Lecture Notes in Electrical Engineering 702

G. T. Chandra Sekhar · H. S. Behera · Janmenjoy Nayak · Bighnaraj Naik · Danilo Pelusi *Editors*

Intelligent Computing in Control and Communication

Proceeding of the First International Conference on Intelligent Computing in Control and Communication (ICCC 2020)

Springer

Lecture Notes in Electrical Engineering

Volume 702

The book series *Lecture Notes in Electrical Engineering* (LNEE) publishes the latest developments in Electrical Engineering - quickly, informally and in high quality. While original research reported in proceedings and monographs has traditionally formed the core of LNEE, we also encourage authors to submit books devoted to supporting student education and professional training in the various fields and applications areas of electrical engineering. The series cover classical and emerging topics concerning:

- Communication Engineering, Information Theory and Networks
- Electronics Engineering and Microelectronics
- Signal, Image and Speech Processing
- Wireless and Mobile Communication
- Circuits and Systems
- Energy Systems, Power Electronics and Electrical Machines
- Electro-optical Engineering
- Instrumentation Engineering
- Avionics Engineering
- Control Systems
- Internet-of-Things and Cybersecurity
- Biomedical Devices, MEMS and NEMS

For general information about this book series, comments or suggestions, please contact leontina.dicecco@springer.com.

To submit a proposal or request further information, please contact the Publishing Editor in your country:

China

Jasmine Dou, Associate Editor (jasmine.dou@springer.com)

India, Japan, Rest of Asia

Swati Meherishi, Executive Editor (Swati.Meherishi@springer.com)

Southeast Asia, Australia, New Zealand

Ramesh Nath Premnath, Editor (ramesh.premnath@springernature.com)

USA, Canada:

Michael Luby, Senior Editor (michael.luby@springer.com)

All other Countries:

Leontina Di Cecco, Senior Editor (leontina.dicecco@springer.com)

**** Indexing: Indexed by Scopus. ****

More information about this series at http://www.springer.com/series/7818

G. T. Chandra Sekhar · H. S. Behera ·
Janmenjoy Nayak · Bighnaraj Naik ·
Danilo Pelusi
Editors

Intelligent Computing in Control and Communication

Proceeding of the First International Conference on Intelligent Computing in Control and Communication (ICCC 2020)

Springer

Editors
G. T. Chandra Sekhar
Department of Electrical and Electronics Engineering
Sri Sivani College of Engineering (SSCE)
Srikakulam, Andhra Pradesh, India

Janmenjoy Nayak
Department of Computer Science and Engineering
Aditya Institute of Technology and Management (AITAM)
Srikakulam, Andhra Pradesh, India

Danilo Pelusi
Faculty of Communication Sciences
University of Teramo, Coste Sant'agostino Campus
Teramo, Italy

H. S. Behera
Department of Information Technology
Veer Surendra Sai University of Technology
Burla, Odisha, India

Bighnaraj Naik
Department of Computer Application
Veer Surendra Sai University of Technology
Burla, Odisha, India

ISSN 1876-1100 ISSN 1876-1119 (electronic)
Lecture Notes in Electrical Engineering
ISBN 978-981-15-8438-1 ISBN 978-981-15-8439-8 (eBook)
https://doi.org/10.1007/978-981-15-8439-8

ICCC-2020 Committees

Chief Patron

Dr. K. Someswara Rao, Chairman, Aditya Institute of Technology and Management (AITAM), Tekkali, Srikakulam, A.P., India

Patrons

Sri L. L. Naidu, Secretary-AITAM, Tekkali, A.P., India
Sri T. Naga Raju, Treasurer-AITAM, Tekkali, A.P., India
Prof. V. V. Nageswara Rao, Director-AITAM, Tekkali, A.P., India
Mrs. V. Sudha Priya, Vice Chairman-AITAM, Tekkali, A.P., India
Dr. K. Ravi Kumar, Joint Secretary-AITAM, Tekkali, A.P., India
Sri K. Madhu Kumar, Director-AITAM, Tekkali, A.P., India
Sri T. Naga Seshu, Director-AITAM, Tekkali, A.P., India
Sri V. Naga Sanketh, Director-AITAM, Tekkali, A.P., India
Dr. K. B. Madhu Sahu, Director-R&D-AITAM, Tekkali, A.P., India
Dr. A. S. Srinivasa Rao, Principal, AITAM, Tekkali, A.P., India

Honorary General Chairs

Prof. V. E. Balas, IEEE Senior Member, Aurel Vlaicu University of Arad, Arad, Romania
Prof. Ahmad Taher Azar, IEEE Senior Member, RIOTU, Prince Sultan University, Saudi Arabia

General Chairs

Dr. Ajith Abraham, MIR LAB, USA
Dr. B. K. Panigrahi, IIT, New Delhi
Dr. H. S. Behera, VSSUT, Burla

Program Chairs

Dr. Asit Kumar Das, IIEST, Shibpur, India
Dr. S. Panda, VSSUT, Burla, Odisha, India
Dr. R. K. Sahu, VSSUT, Burla, Odisha, India
Dr. Bighnaraj Naik, VSSUT, Burla, Odisha, India
Dr. Janmenjoy Nayak, AITAM, Tekkali, A.P., India
Dr. G. T. Chandra Sekhar, SSCE, Srikakulam, A.P., India

Organizing Chairs

Dr. Janmenjoy Nayak, AITAM, Tekkali, A.P., India
Mr. B. Manmadha Kumar, AITAM, Tekkali, A.P., India

Local Organizing Committee

Dr. D. Vishnumurthy, Dean A&P, AITAM, A.P., India
Dr. CH. Ramesh, Associate Dean IQAC, AITAM, A.P., India
Dr. M. Jayamanmadharao, Associate Dean IQAC, AITAM, A.P., India
Dr. C. J. Rao, HOD-Mech., AITAM, A.P., India
Dr. G. S. N. Murty, HOD-CSE, AITAM, A.P., India
Dr. D. Yugandhar, HOD-ECE, AITAM, A.P., India
Dr. B. V. Ramana, HOD-IT, AITAM, A.P., India
Dr. V. Chitti Babu, Incharge HOD-Civil, AITAM, A.P., India
Dr. G. Vasanthi, HOD-BS&H, AITAM, A.P., India
Dr. K. Venugopal, HOD-MBA, AITAM, A.P., India

Conveners

Dr. D. Vijaya Kumar, HOD-EEE, AITAM, A.P., India
Dr. B. Rama Rao, Professor, ECE, AITAM, A.P., India

Co-conveners

Dr. K. Kiran Kumar, Professor, EEE, AITAM, A.P., India
Mr. M. Bala Krishna, Assistant Professor, ECE, AITAM, A.P., India

Website Chair

Student Activity Centre (SAC), AITAM, A.P., India

Publication Chair

Mr. B. Manmadha Kumar, EEE, AITAM, A.P., India

International Advisory Committee

Prof. A. Abraham, Machine Intelligence Research Labs, USA
Prof. Michael Pecht, Chair Professor and Director, University of Maryland, College Park, USA
Prof. Lakhmi C. Jain, University of Technology Sydney, Australia
Prof. Danilo Pelusi, University of Teramo, Coste Sant'agostino Campus, Teramo, Italy
Prof. B. D. Majhi, IIIT, Kanchipuram
Prof. Weiping Ding, Nantong University, China
Prof. Asit Kumar Das, Indian Institute of Engineering Science and Technology, Shibpur, WB
Prof. Margarita N. Favorskaya, Reshetnev Siberian State University of Science and Technology, Russia
Prof. D. P. Mohapatra, NIT, Rourkela, Odisha, India
Prof. Sheng-Lung Peng, National Dong Hwa University, Hualian, Taiwan
Prof. Luca Tallini, University of Teramo, Italy
Prof. Arnab Bhattacharya, Indian Institute of Technology, Kanpur

Prof. Chi-Chang Chang, Chung-Shan Medical University, Taiwan
Prof. Joy I.-Z. Che, Dayeh University, Taiwan
Prof. S. K. Panda, National University of Singapore, Singapore
Prof. Raouf Boutaba, University of Waterloo, Canada
Prof. Asish Ghosh, ISI, Kolkata
Prof. Douligeris Christos, University of Piraeus, Greece
Prof. B. K. Panigrahi, Indian Institute of Technology, Delhi, India
Prof. Hisao Ishibuchi, SUSTech, China
Prof. Santi Prasad Maity, IIEST Shibpur, W.B., India
Prof. Raffaele Mascella, University of Teramo, Italy
Prof. Mohammad S. Khan, East Tennessee State University, USA
Prof. Chin-Teng Lin, University of Technology Sydney, Australia
Prof. Mita Nasipuri, Jadavpur University, West Bengal
Prof. G. Sahoo, Birla Institute of Technology, Meshra
Prof. Ruben G Crespo, University International de La Rioja, Spain
Prof. M. Ramalingaraju, JNTUK, Kakinada
Prof. P. Mallikarjuna Rao, Andhra University, Visakhapatnam
Prof. N. Preamakumar, Andhra University, Visakhapatnam
Prof. G. SasibushanaRao, Andhra University, Visakhapatnam
Prof. N. V. S. N. Sarma, Indian Institute of Information Technology, Tiruchi

International Technical Committee

Prof. Yong Deng, Institute of Fundamental and Frontier Science Chengdu, China
Prof. Subramaniam Ganesan, Oakland University, USA
Dr. Satchidananda Dehuri, Fakir Mohan University, Balasore, Odisha, India
Dr. Santanu Phadikar, Maulana Abul Kalam Azad University of Technology, West Bengal
Dr. Sidhartha Panda, VSSUT, Burla
Dr. Rabindra Kumar Sahu, VSSUT, Burla
Dr. N. P. Patidar, MANIT, Bhopal
Dr. B. Nagaraj, Karpagam College of Engineering, India
Dr. B. Acharya, NIT, Raipur, India
Dr. A. R. Routray, Fakir Mohan University, Balasore, Odisha, India
Dr. J. C. Bansal, South Asian University, New Delhi, India
Dr. Imon Mukherjee, Indian Institute of Information Technology, Kalyani, West Bengal
Dr. B. Murali Krishna, SITAM, Visakhapatnam
Dr. Bighnaraj Naik, VSSUT, Burla
Dr. Sarat Ch. Nayak, CMRCET, Hyderabad, India
Dr. R. Obulakonda Reddy, IARE, Hyderabad, India
Dr. Santosh Ku. Sahoo, CVR College of Engineering, Hyderabad, India
Dr. Sunanda Das, SVCET, Chittoor, A.P., India

Dr. S. K. Hafizul Islam, IIIT, Kalyani
Dr. B. B. Chaudhury, Indira Gandhi Institute for Technology, Dhenkanal, Odisha
Dr. B. Ravikumar, IIT-Hyderabad
Dr. D. M. Vinod kumar, NIT-Warangal
Dr. K. Nagasujatha, JNTU-Hyderabad
Dr. Bidyadhar Subudhi, NIT Rourkela
Dr. R. SrinivasaRao, JNTUK, Kakinada
Prof. D. V. Ramakoti Reddy, Andhra University, Visakhapatnam
Prof. P. Rajesh kumar, Andhra University, Visakhapatnam
Dr. Pilla Ramana, GMR Institute of Technology, Rajam
Prof. L. V. Suresh Kumar, GMR Institute of Technology, Rajam
Dr. P. Devendra, Gayatri Vidya Parishad College of Engineering for Women, Visakhapatnam
Prof. P. V. Sridevi, Andhra University, Visakhapatnam
Prof. B. T. Krishna, JNTUK, Kakinada
Prof. M. Balaji, JNTUK, Kakinada

Publicity Chairs

Mr. G. Ashok, EEE, AITAM, A.P.
Mr. M. Chaitanyakumar, ECE, AITAM, A.P.

Registration Chairs

Mrs. A. Jayalakshmi, ECE, AITAM, A.P.
Mrs. N. Sowjanya, EEE, AITAM, A.P.

Finance Chairs

Mr. N. A. N. Raju, CAO, AITAM, A.P.
Mr. V. Lokesh Raju, ECE, AITAM, A.P.
Mr. K. Kanakaraju, EEE, AITAM, A.P.

Preface

Recent days of computing world have witnessed a colossal amount of intelligent computing and control-based technologies with the escalating computational and control power of computers. These help to extend the focus of researchers and academic experts on providing extraordinary research in intelligent computing and control systems. The major innovations in three important branches of engineering such as electrical, communication and computer always have a direct impact in current and future growth of our society. The 1st International Conference on Intelligent Computing in Control and Communication (ICCC-2020) is organized by Department of Electrical Electronics Engineering and Electronics and Communication Engineering, Aditya Institute of Technology and Management (AITAM), K. Kotturu, Tekkali, Srikakulam District, A.P., India. The conference ICCC-2020 is a collaborative event for the discussion and dissemination of different applications of control engineering, communication and computing technology on the current developing scenario. The conference aims at bringing together the researchers, scientists, engineers, industrial professionals and students in their domain of interest. Also, it concentrates on both theory and practices from around the world in all the areas of related disciplines of intelligent computing for the mentioned areas.

A massive number of control algorithms and intelligent computational with the rising control and computational power of computers have notably extended the concentration of scientists and researchers on presenting exceptional improvements in control as well as intelligent computing systems. This book covers the latest methodologies such as robust fuzzy logic controller, dynamic programming and genetic algorithm advances, hybrid nature-inspired optimizations, artificial intelligence-based control methods, block chain technology, advances designs for wearable applications and advance machine learning approaches as a solution to various research domains of allied engineering domains. The proposed solutions covered in this book are applicable in various cross-disciplinary domains such as IoT sensor-based anomaly detection, photovoltaic fed brushless DC motor system, liver disease prediction, solar cell application, smart grid, solar photovoltaic power system, thermal barrier coatings, hydro-thermal system, smart energy management system, global solar radiation estimation, diabetic retinopathy detection, renewable

energy, induction motor, alcohol classification, wearable applications, wireless mobile cellular networks, wind turbine energy system and so on. More than 170 numbers of articles have been received in different thematic areas of the conference, and with the help of reviewers committee, the editors have selected only 53 high-quality articles thorough rigorous peer-review process. In the peer-review process, several highly knowledgeable researchers/professors with expertise in single/multi-domain have assisted the editors in unbiased decision making of the acceptance of the selected articles. Moreover, valuable timely suggestions of the advisory, program and technical committee members helped the editors for smoothing the peer-review process and choosing the best outcomes.

The proceeding of ICCC-2020 has attracted the researchers and academicians working in the discipline of electrical, electronics and computer science along with other allied engineering disciplines. The accepted manuscripts (original research and survey articles) are the collections of bunch of state-of-the-art technologies applied in the abovementioned engineering domains. As the current world is witnessing the use of various intelligent techniques for their independent problem solving, this book may have a wide importance for all range of researchers and scholars. We are grateful for the authors' contribution and value the choice that is "ICCC-2020" for disseminating the output of their research findings. We are also grateful to each individual reviewer, technical and the program committee members for their continuous support and cooperation.

Srikakulam, India — G. T. Chandra Sekhar
Burla, India — H. S. Behera
Srikakulam, India — Janmenjoy Nayak
Burla, India — Bighnaraj Naik
Teramo, Italy — Danilo Pelusi

Acknowledgements

The editors are opportune to put forward key proposal and significance of ICCC conference. This conference has attracted more than 200 academicians, professionals and researchers all over the globe. The conference showed the gamut of original research findings. We could able to have communes in diversified fields of electrical, electronics and computer engineering.

We would like to thank all the authors for their contributions. We sincerely show our gratitude to the authors who contributed their time and expertise to this conference. We would like to convey our heartfelt thanks to national and international advisory committee to be supportive and guiding us throughout the pre- and post-conference. We have been opportune to have strong eminent reviewers team who holistically did the reviewing process and suggested the critical and strong remarks on the manuscripts.

We profusely thank the organizing committee who has shown the level of eagerness by well organizing and managing all the events throughout the conference.

We are highly thankful to the Management of Aditya Institute of Technology and Management (**AITAM**)—Tekkali, Srikakulam, A.P., India, especially Prof. V. V. Nageswar Rao (Director), Principal, Director, R&D and Head of the Departments for their constant support and motivation for making the conference successful. The editors would also like to thank Springer Editorial Members for their constant support for publishing the proceedings in *Lecture Notes in Electrical Engineering* series. The ICCC conference and proceedings ensured the acknowledgments to a huge congregation of people.

About the Conference

The beginning of ever-augmenting and omnipresent computational and control resources are responsible for the enhancement of the opportunities to develop different intelligent computing and control-based techniques for resolving certain real-time issues like complex problems, uncertainty-based solutions, elusiveness and imprecision techniques. The conference "International Conference on Intelligent Computing in Control and Communication (ICCC 2020)" is an international forum for the discussion on advanced computing methodologies and state-of-the-art tools to solve the present and upcoming complex problems. ICCC is a cross-platform opportunity to share and disseminate the ideas, solutions, theory and methods for different range of problems by the various backgrounds of researchers. The conference provided an opportunity for collaborating their thoughts/ideas in the direction of development of intelligent solutions on a global basis. ICCC is intended in the direction of the knowledge and construction of optimistic research in various applications of electrical engineering, communication and computing technology for leading and governing the technological domain. The proceedings of ICCC aim the academicians, postgraduate students and researchers working in the discipline of electrical, electronics and communication and computer science/information technology. This book addresses the exploitation of budding intelligent computing approaches, optimizing solutions in different disciplines of control and communication.

Contents

About the Editors

Dr. G. T. Chandra Sekhar is working as an Associate Professor in the Department of Electrical & Electronics Engineering, Sri Sivani College of Engineering, Chilakapalem, Srikakulam, Andhra Pradesh. He received Ph.D. degree in Electrical Engineering from Veer Surendra Sai University of Technology, Burla, Odisha, India. He has published more than 40 research papers in various international journals and international/national conferences. He is acting as a member of the editorial/reviewer board of various international journals/ conferences. He is the recipient of Best Young Researcher (Male) Electrical Engineering by ITSR Foundation Award-2017 and Young Leader in Engineering during the Higher Education Leadership Meet (HELM 2018) organized by Venus International Foundation. His research interests include soft computing applications in power system engineering. He has been serving as an active member of reviewer committee of various reputed peer-reviewed journals such as IET Journals (GTD), Springer, International Journal of Computational System Engineering, International Journal of Swarm Intelligence, Elsevier, etc. His area of interest includes intelligent computing, control system and power stability. His research interests include soft computing application in power system engineering. Dr. Chandra Sekhar is a life member of ISTE and AMIE (India), IAENG(Hongkong) and ISAET and associate member of IRED.

Dr. H. S. Behera is working as an Associate Professor in the Department of Information Technology, Veer Surendra Sai University of Technology (VSSUT) (A Unitary Technical University, Established by Government of Odisha), Burla, Odisha. He has received M.Tech. in Computer Science & Engineering from NIT, Rourkela (formerly REC, Rourkela), and Doctor of Philosophy in Engineering (Ph.D.) from Biju Pattnaik University of Technology (BPUT), Rourkela, Government of Odisha, respectively. He has published more than 90 research papers in various international journals and conferences, edited 11 books and is acting as a member of the editorial/reviewer board of various international journals. He is proficient in the field of computer science engineering, served the capacity of program chair and tutorial chair and acts as advisory member of committees of

many national and international conferences. His research interest includes data mining and intelligent computing. He is associated with various educational and research societies like OITS, ISTE, IE, ISTD, CSI, OMS, AIAER, SMIAENG and SMCSTA. He is currently guiding seven Ph.D. scholars, and five scholars have been awarded under his guidance.

Dr. Janmenjoy Nayak is working as an Associate Professor, Department of Computer Science and Engineering, Aditya Institute of Technology and Management (AITAM) (An Autonomous Institution declared by UGC), Tekkali, Andhra Pradesh, India. He has published more than 110 research papers in various reputed peer-reviewed refereed journals, international conferences and book chapters. He is the recipient of best researcher award from Jawaharlal Nehru University of Technology, Kakinada, Andhra Pradesh, for the AY: 2018–2019, Gold Medalist in Computer Science (two times) and many other awards of national repute. Moreover, he is the recipient of Outstanding Reviewer for the Journal "Engineering Applications of Artificial Intelligence" for 2017, by Elsevier Publications. His area of interest includes data mining, nature-inspired algorithms and soft computing. He is the regular member of IEEE and life member of some of the reputed societies like CSI India. He has edited 10 books from various publishers such as Elsevier, Springer and IGI Global. He has been serving as Guest Editor of various journal special issues from Elsevier, Springer and Inderscience. He is the author of one textbook and has served as Volume Editor of the Springer proceedings of six international conferences of various themes of soft computing, intelligent computing, etc.

Dr. Bighnaraj Naik is an Assistant Professor in the Department of Computer Application, Veer Surendra Sai University of Technology (Formerly UCE Burla), Odisha, India. He received his Ph.D. in Computer Science and Engineering, M.Tech. in Computer Science and Engineering and B.E. in Information Technology in 2016, 2009 and 2006, respectively. He has published more than 70 research papers in various reputed peer-reviewed international journals, conferences and book chapters. He has edited four books from various publishers such as Elsevier, Springer and IGI Global. At present, he has more than ten years of teaching experience in the field of computer science and IT. He is a member of IEEE. His area of interest includes data mining, computational intelligence, soft computing and its applications. He has been serving as Guest Editor of various journal special issues from Elsevier, Springer and Inderscience. He has served as Convener & Volume Editor of the International Conference on Computational Intelligence in Data Mining (ICCIDM-2017, ICCIDM-2018) and International Conference on Computational Intelligence in Pattern Recognition – 2019, IIEST, Shibpur, West Bengal.

Dr. Danilo Pelusi has received the Ph.D. degree in Computational Astrophysics from the University of Teramo, Italy. Presently, he is holding the position of Associate Professor at the Faculty of Communication Sciences, University of

Teramo. Associate Editor of IEEE Transactions on Emerging Topics in Computational Intelligence, IEEE Access, International Journal of Machine Learning and Cybernetics (Springer) and Array (Elsevier), he served as Guest Editor for Elsevier, Springer and Inderscience journals, as program member of many conferences and as editorial board member of many journals. Reviewer of reputed journals such as IEEE Transactions on Fuzzy Systems and IEEE Transactions on Neural Networks and Machine Learning, his research interests include intelligent computing, communication system, fuzzy logic, neural networks, information theory and evolutionary algorithms.

A Fuzzy-Based STATCOM Controller for Grid Interconnection of Fuel System to Improve Power Quality

B. Srinivasa Rao and G. Sreenivasan

Abstract The main theme of this paper is to design a concept regarding the grid interconnected system with fuel energy system. A proton exchange membrane-based fuel cell system is considered in this paper as a distribution source. A DC–DC boost converter is proposed with suitable controller to improve the reliability and efficiency of fuel cell system. A STATCOM converter is proposed in this paper to improve the power quality and to mitigate the current harmonics generated by the nonlinear load. The reference signal required for STATCOM controller is generated with the help of power quality-theory concept. In this paper, the proposed system is tested under two different controllers, namely conventional PI and fuzzy logic vontrollers. This system is tested in MATLAB and compared the results.

Keywords Fuel cell · Grid interfaced · STATCOM · Fuzzy logic and THD

1 Introduction

Since last decade, the utilization of renewable systems increases rapidly due to environmental conditions or pollution caused by fossil fuel generating stations. The commonly available renewable systems are solar, wind, fuel and hydrosystems. This paper mainly concentrates on fuel energy-based renewable system. In this, the fuel energy is converted to electrical energy by electrolyte process [1]. The proton exchange membrane-type fuel system is considered in this paper. In this case, the hydrogen fuel is reacted with oxidant to generate electrons.

B. Srinivasa Rao (✉)
Department of EEE, Aditya Institute of Technology and Management, Tekkali, Andhra Pradesh 532201, India
e-mail: bsreee2013@gmail.com

G. Sreenivasan
Department of EEE, Srinivasa Ramanujan Institute of Technology, Ananthapur, Andhra Pradesh 515001, India

G. T. C. Sekhar et al. (eds.), *Intelligent Computing in Control and Communication*, Lecture Notes in Electrical Engineering 702,
https://doi.org/10.1007/978-981-15-8439-8_1

The output of fuel cell is applied to a conventional DC–DC converter to improve the voltage levels to meet the requirements. The DC output from converter is converted to AC by using a PWM-based three-phase inverter. In the second stage of this paper, the proposed fuel cell system is interconnected with grid systems to operate the load applications. The synchronization between these two converters achieved with three-phase inverter.

Figure 1 shows the block diagram for grid interconnected fuel cell system. In this, the fuel cell is applied to battery for backup energy purpose and a DC–DC converter to control the voltage levels. A PWM-based three-phase converter is used to meet the synchronization between these two systems [2]. The control circuit for inverter is

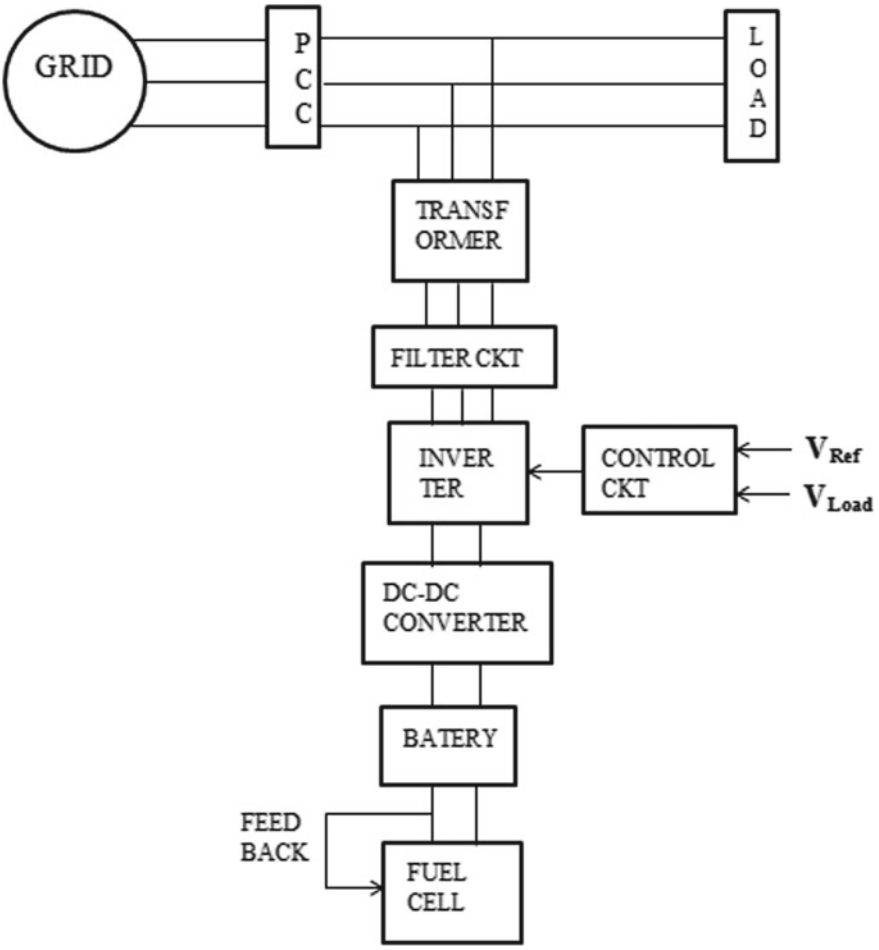

Fig. 1 Block diagram of microgrid

designed with the reference signals from system voltage and load voltage parameters. This hybrid system is tested under different load conditions.

Compensating devices used in this paper to compensate the power quality problems caused by the different load variations. Generally, these problems are voltage unbalances, harmonics in currents, sag/swell conditions, etc. [3]. The main causes for these problems are load changes, system behavior or external fault conditions. In this paper, to mitigate the harmonics caused by the nonlinear loads, a STATCOM controller is proposed. STATCOM is one of the shunt active converters in FACTS family. The required control technique for STATCOM is designed with instantaneous active and reactive power technique.

This paper also focuses on application of fuzzy logic controller for static compensator to get better control action. Fast and reliable operation of system is the main advantage of fuzzy controller over conventional PI controller.

The proposed grid interconnected system with fuel energy is tested under different load conditions with fuzzy and PI-based STATCOM controller to improve power quality in MATLAB environment.

2 Structure and Design of Fuel Cell

The electrical energy from fuel cell is obtained by fuel source with the process of chemical process. In this, fuel energy is converted into electric current by chemical reaction between fuel chemical and oxidant. This chemical reaction is also called as electrolyte. In fuel cells, the electrochemical reaction is done at anode side. In this case, H_2 molecule is considered at anode side and it separates H^- ions through anode side as shown in Eq. 1 [4].

The fuel cell reaction in oxidant is expressed in Eq. 2.

$$\begin{aligned} &\mathrm{H_2} \rightarrow \mathrm{H_2O} + 2e^- (\text{Anode}) \\ &\frac{1}{2}\mathrm{O_2} + 2\mathrm{H^+} + 2e^- \rightarrow \mathrm{H_2O}(\text{Cathode}) \end{aligned} \tag{1}$$

$$\Delta g_g = \Delta g_f^o - \mathrm{RT}_{fc}[\ln(\mathrm{PH_2}) + 0.5\ln(\mathrm{PO_2})] \tag{2}$$

In this chemical reaction, by the activation loss of anode and cathode, the bond between electron–proton chemicals will break at zero current.

The activation voltage of fuel cell system is expressed as

$$V_{\text{act}} = V_0 + V_a(1 - \mathrm{e}^{-C_1 i}) \tag{3}$$

In the above expression (3), V_0 is expressed as voltage at zero current density due to cathode pressure. Here, the terminal voltage of fuel cell system is expressed in the function of fuel temperature, pressure.

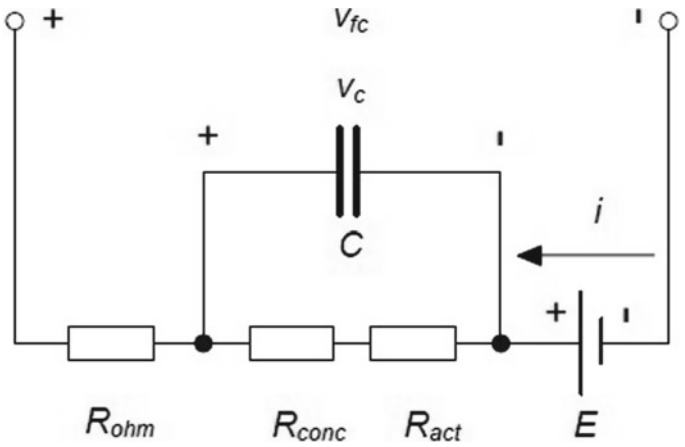

Fig. 2 Fuel cell equivalent system

1. **Fuel cell circuit**

Figure 2 shows the equivalent electrical circuit of fuel cell system. In this, the terminal voltage is obtained with cell temperature, and series and ohmic resistant of system [4].

$$V_{fc} = -(V_e + i R_{\text{ohm}}) + E$$
$$i = \frac{V_C}{R_{\text{act}} + R_{\text{conc}}} + C\frac{\mathrm{d}V_C}{\mathrm{d}t} \tag{4}$$

$$V_{fc} = -i\left(\frac{R_{\text{con}} + R_{\text{act}}}{(sc(1 + R_{\text{con}} + R_{\text{act}}))} + R_{\text{ohm}}\right) + e \tag{5}$$

The expressions for electrical voltage from the system are shown in Eqs. (4) and (5). In order to maintain the fuel cell voltage to suitable level, a DC–DC converter is proposed.

3 Dynamic Modeling of Boost Coverter

In this case, a DC–DC boost converter is proposed to improve the output voltage from the fuel cell system. The purpose of boost converter is to maintain the fuel cell voltage to meet the required level. An MPPT-based DC–DC controller is proposed in this paper to control the IGBT switch. Equations (6)–(8) show expression for output voltage from the boost converter with variable duty cycle is expressed below. Figure 3 shows the structure of DC–DC converter [5].

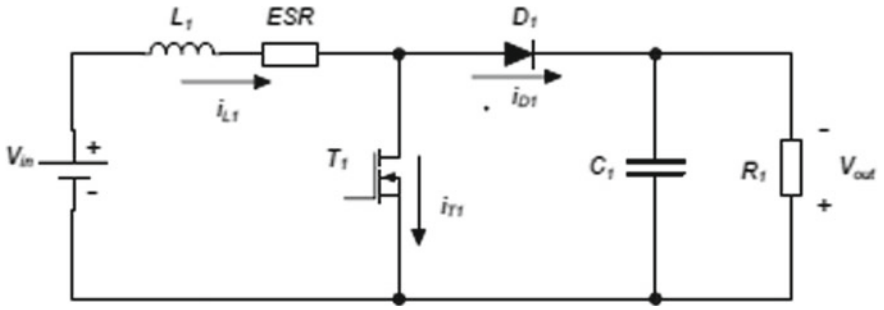

Fig. 3 DC–DC boost chopper circuit

$$V_{\text{in}} - L\frac{\mathrm{d}i_1}{\mathrm{d}t-}(1-D)V_C - \text{ESR}i_1 = 0 \tag{6}$$

$$i_{D1} = i_{C1} + i_{L1} \tag{7}$$

$$\begin{bmatrix} \dot{i}_{L_1} \\ \dot{v}_{C_1} \end{bmatrix} = \begin{bmatrix} \frac{-\text{ESR}}{L_1} & \frac{-(1-D)}{L_1} \\ \frac{1-D}{C_1} & \frac{-1}{R_1 C_1} \end{bmatrix} \begin{bmatrix} i_{L_1} \\ v_{C_1} \end{bmatrix} + \begin{bmatrix} \frac{1}{L_1} \\ 0 \end{bmatrix} [V_{\text{in}}]$$

$$[V_{\text{Out}}] = \begin{bmatrix} 0 & 1 \end{bmatrix} \begin{bmatrix} i_{L_1} \\ v_{C_1} \end{bmatrix} + [0][V_{\text{in}}] \tag{8}$$

The control diagram for DC–DC converter is shown in Fig. 4. The control strategy for four-phase interleaved bidirectional converter is shown in figure. In this controller, the super capacitor DC current and converter currents are compared with conventional reference currents [6] and applied to PI controller and then to PWM controller to generate gate signals required for boost converter.

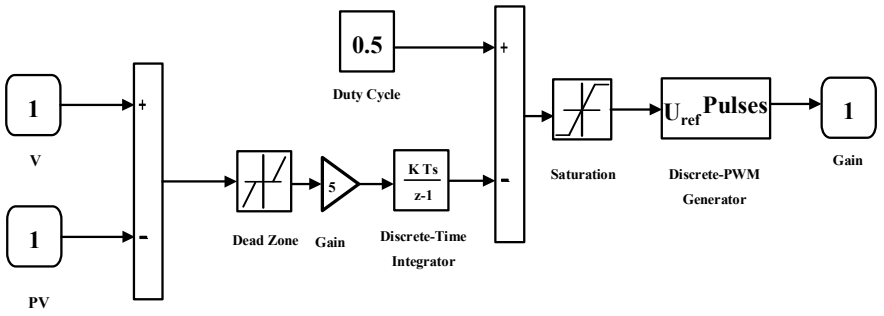

Fig. 4 Boost converter control diagram

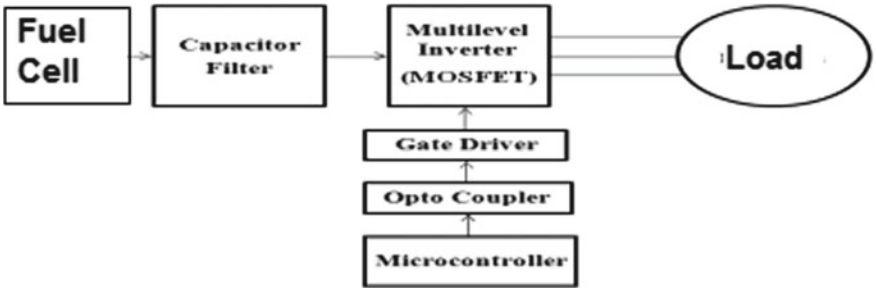

Fig. 5 Control diagram for three-phase inverter

3.1 3-ø Inverter

The output of the FP-IBC bidirectional DC/DC converter is given to a conventional three-phase inverter. The purpose of this inverter is used to regulate the operation of induction motor. Generally, the better harmonic reduction is obtained with multilevel inverter concept; this paper proposes a concept of five-level inverter. The unique nature of multilevel inverter is to generate high voltage levels [7]. Figure 5 shows the closed-loop control structure and diagram for induction motor. This diagram consists of gate driver, IGBT-based 6 pulse three-phase converter.

Figure 5 shows the basic block diagram for inverter circuit. The main blocks in the system are (a) control circuit and (b) power converter. Here, the power converter consists of IGBT switches in three levels, filter capacitor which helps to minimize the harmonic content. And the control circuit is used to generate gate signal pattern, i.e., the switching signals required for IGBT switches in power converter. In this paper, the control circuit for three-phase converter is based on SVM technique.

3.2 SVM Technique

Generally, there are different modulation techniques available in literature to generate pulse required for inverter such as:

1. PWM technique
2. Hysteresis technique.

But this paper proposes a modulation technique based on vector combination of reference signals. This method is called as space vector modulation.

In this SVM concept, the reference signals are transformed in to vectors. This vector consists of magnitude with diameter co-ordinates and angles. The space vector modulation for proposed system is shown in figure. In this vector diagram, the reference signals are spitted into six vectors combinations (i.e., s_0, s_2, … s_6). Here, switching pattern s_0 and s_6 acts positive (or) negative vectors, respectively [8].

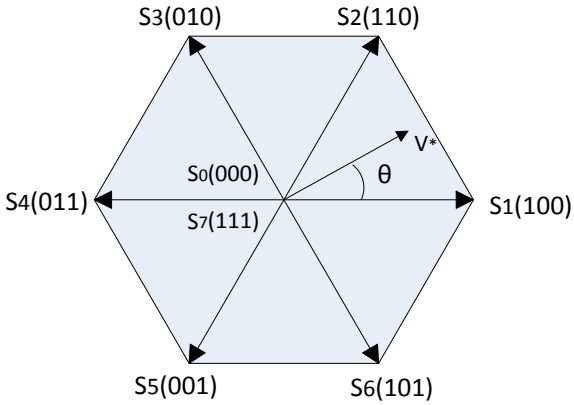

Fig. 6 SVM technique

The gate pulses pattern for three-phase inverter is choose with respect to position of reference voltage (v*).

Consider a cycle, i.e., reference voltage (V^*) between the positions S_1 and S_2, in this period, phase-a is positive and phase-c is negative as shown in Fig. 6, so the output voltage from inverter is Vac. Likewise, the pattern is repeated for next cycle. With the use of SVM technique, the harmonics in voltage and current are reduced.

The implementation of SVM technique is explained in the following two steps:

Identification of reference voltage and its vector by converting three-phase to two-phase transformation.

Identification of switching times T_1, T_2 and T_0.

From the above notations, the expression for reference voltage (V*) in terms of switching times is expressed in (9),

$$V * T_z = S_1 * T_1 + S_2 * T_2 + S_0 * (T_0/2) + S_7 * (T_0/2) \tag{9}$$

4 p-q Theory Power Components

In this three-phase inverter, the reference current signal required for inverter is generated with the help of instantaneous active and reactive powers called as "PQ-Theory" model. In this, two-phase PQ are obtained from the system active and reactive powers of three phases [9]. In order to obtain two quadrant powers, an clark's transformation is used. The α-β-0 coordinates of voltages and currents are calculated by using Eqs. (10–11):

$$\begin{bmatrix} v_0 \\ v_\alpha \\ v_\beta \end{bmatrix} = T \begin{bmatrix} v_a \\ v_b \\ v_c \end{bmatrix}, \begin{bmatrix} i_a \\ i_b \\ i_c \end{bmatrix} = T \begin{bmatrix} i_a \\ i_b \\ i_c \end{bmatrix} \tag{10}$$

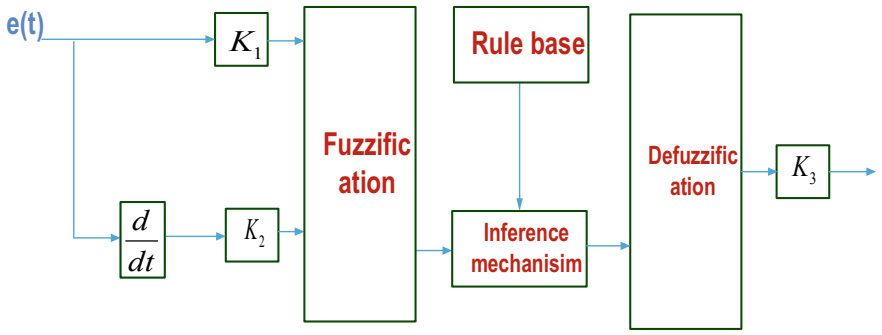

Fig. 7 Structure of fuzzy controller

$$T = \begin{bmatrix} 1/\sqrt{2} & 1/\sqrt{2} & 1/\sqrt{2} \\ 1 & -1/2 & -1/2 \\ 0 & \sqrt{3}/2 & -\sqrt{3}/2 \end{bmatrix} \tag{11}$$

$$p_0 = \bar{p_{01}} + \tilde{p}_{02} \tag{12}$$

Generally, the zero-sequence power for a three-phase system is calculated in neutral wire. The expression for power P_o is expressed in (12).

5 Fuzzy Controller

Excessive mathematical analysis, inaccurate response and time taken analysis are the major concerns in conventional controllers. To overcome this situation, this paper proposes a concept of soft computing controllers called as AI techniques. This paper considered fuzzy logic controller. The operation of fuzzy logic system can be in four stages, i.e., (a) fuzzification, (b) membership function, (c) rule-based formation and (d) defuzzification [10]. The inputs for fuzzy logic controller are chosen as error and change in error as shown in Fig. 7. In this, the number of members chosen for these inputs is {MN, SN, Z, SP, MP). And the number of rules formation for this system is 25 rules.

6 Simulation Diagram and Results

The simulation diagram for proposed fuel cell-based grid interconnected system with STATCOM controller to improve the PQ improvement is implemented based on Fig. 8. In this case, the proposed system is tested under controllers, namely (a) conventional PI controller and (b) fuzzy logic controller.

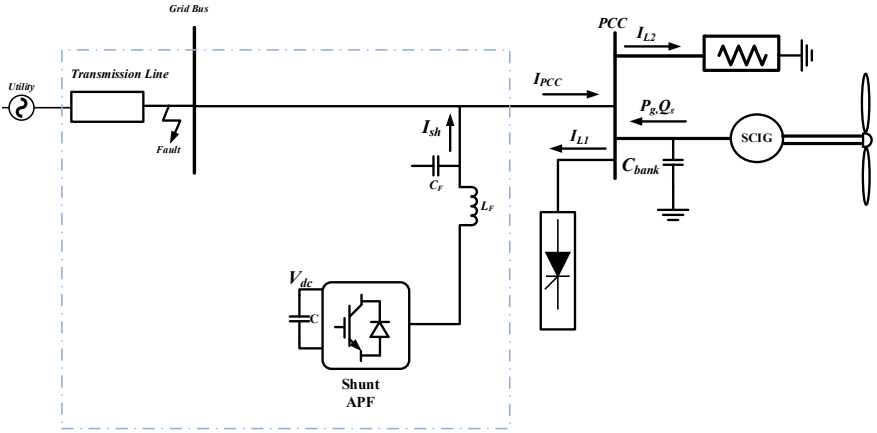

Fig. 8 Structure of proposed system

Output voltage from the fuel cell is shown in Fig. 9. Here, the input oxidation for fuel cell system is taken at 200 ms. and the output voltage from the system is approximately 400v.

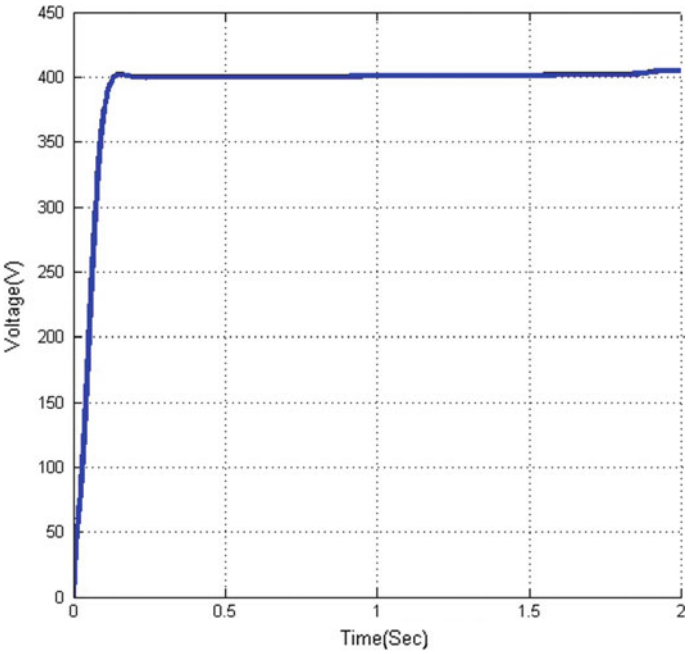

Fig. 9 Output voltage of the DG system

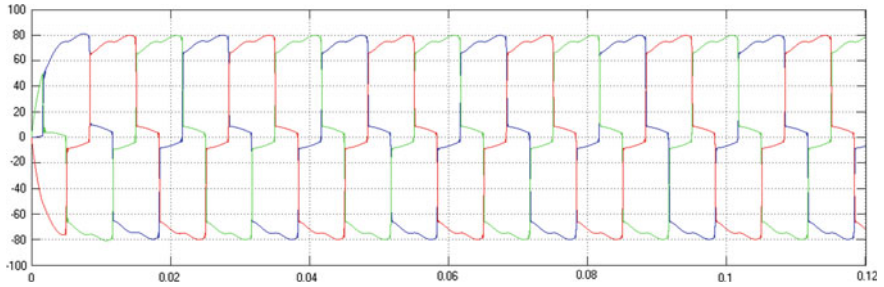

Fig. 10 Three-phase output currents at load

This proposed system is implemented and applied to three-phase nonlinear load. The harmonics caused by the nonlinear loads are shown in Fig. 10. To mitigate this harmonic currents, an STATCOM controller is proposed in this paper. The injected current from the STATCOM controller is shown in Fig. 11.

Figure 12 shows the simulation result for compensated current from shunt controller at grid side. The harmonic distortions in source current are shown in Figs. 13 and 14 with conventional PI and Fuzzy controllers, respectively. Figure 15 shows the simulation result for grid current and voltage to show the in-phase compensation (power factor).

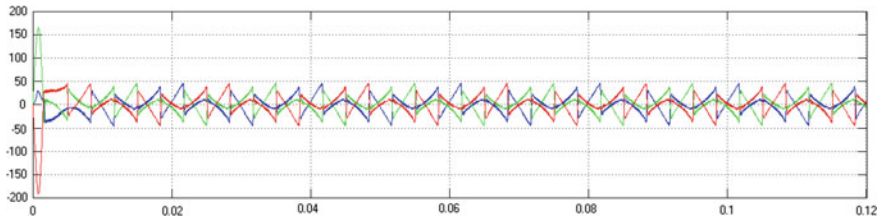

Fig. 11 STATCOM injected current

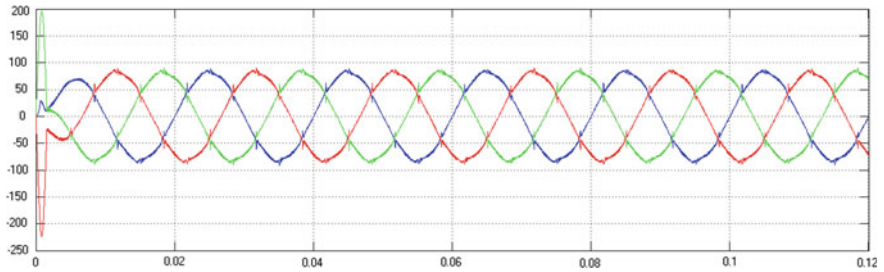

Fig. 12 Grid current after compensation

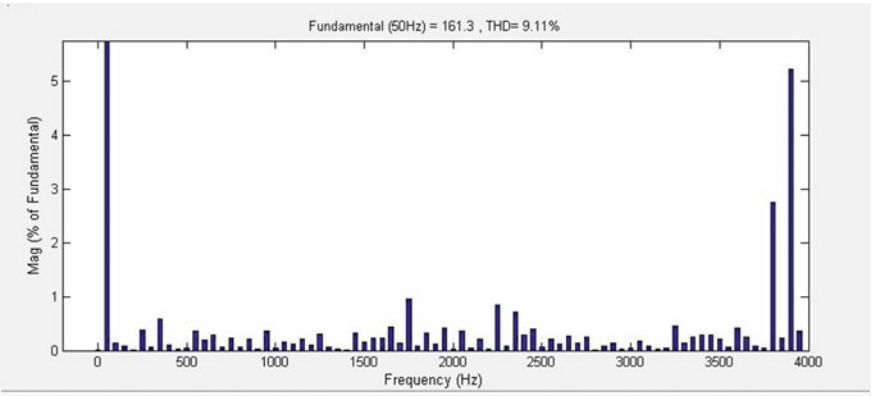

Fig. 13 Current harmonic distortion using PI

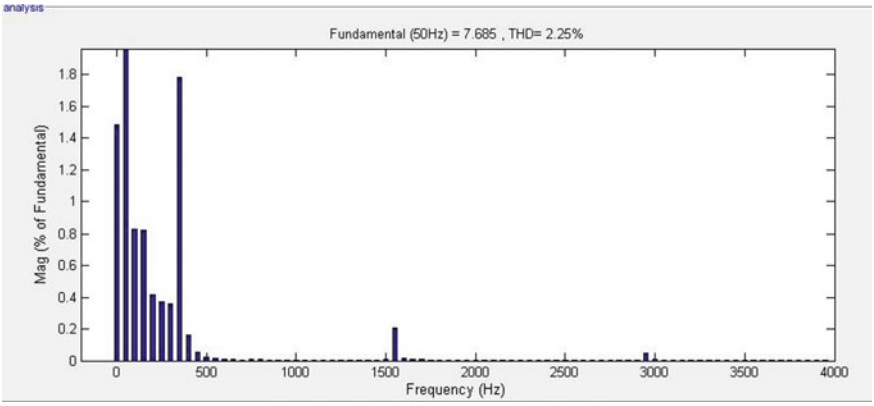

Fig. 14 Current harmonic distortion using fuzzy

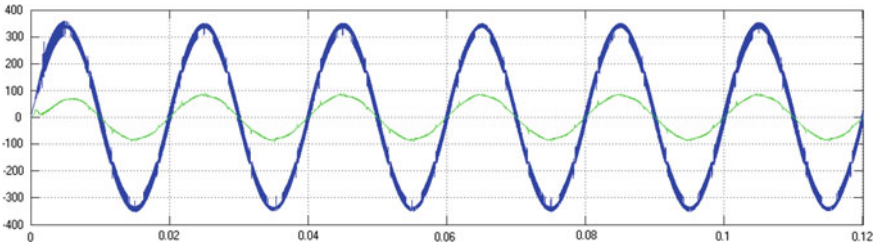

Fig. 15 In-phase representation for voltage and current

7 Conclusion

In this paper, the power quality improvement is achieved for given hybrid system with STATCOM controller using PI and fuzzy Logic controllers. The fuel cell system is designed under proton exchange membrane fuel cell and also a DC–DC converter is used to improve the fuel cell voltage. The control diagram for shunt active filter is designed with instantaneous active and reactive power controller. The proposed system is tested and verified using MATLAB environment. With these results, the fuzzy-based STATCOM controller for proposed gives better result as compared with conventional controller, i.e., the THD under nonlinear load with PI controller is 9.11% while the THD for the same with fuzzy controller is 2.25%.

References

1. Sanjeevi kumar P, Neeraj P, Mahajan Sagar B (2019) A hybrid PV-FC for grid integration with jaya-based MPPT: experimental performance evaluation. IEEE Access vol 7
2. Sun L, Wu G, Xue Y, Shen J, Li D, Lee K (2018) Control strategies for FC power plant in a microgrid. IEEE Trans Energy Convers 33(1)
3. Mojallal A, Lotfifard S (2018) Improving during and post fault response of FC in symmetrical and asymmetrical grid fault cases. IEEE Trans Sustain Energy 9(3)
4. Florian G, Jens S, Arno L, Marc FM (2019) Robust primary protection device for weight-optimized PEMFC systems in HVDC power systems of aircraft. Indus Electron IEEE Trans 66(7)
5. Amit R, Prasenjit B, Gyan RB (2019) Low voltage ride through capability enhancement in a grid-connected wind/fuel cell hybrid system via combined FF and FLC. IET Gener T & D 13(13)
6. Wang Y, Xu J, Feng L, Wang C (2018) A novel hybrid modular 3-level shunt filter. Power Electron IEEE 33(9)
7. Hao Z, Fang Z, Zhu C (2020) An optimal compensation method of shunt filters for system-wide voltage quality improvement. Indus Electron IEEE Trans 67(2)
8. Liu Y, Hong H, Huang AQ (2009) Real-time calculation of switching angles minimizing THD for multilevel inverters with step modulation. IEEE Trans Indus Electron 56(2):285–293
9. Yacine T, Muhammad UM, Mojtaba M, Abderezak L (2019) Adaptive CDSC-based open-loop synchronization technique for dynamic response enhancement of APF. IEEE 7
10. Prakash KR, Soumya RD, Asit M (2019) FLC-designed-PV-based UPQC for PQ enhancement. IEEE Energy Convers 34(1)

Comparison of Uplink Spectral Efficiency in Massive MIMO Systems

B. Ch. Kiran Patrudu and P. V. Sridevi

Abstract The exponential development of wireless communication networks leads to deficient in the capacity of wireless networks. Spectral efficiency can be enhanced by using one of the favorable techniques in 5G wireless communication, i.e., Massive MIMO which configures a huge no. of antennas at the Base Station (BS).This paper figures out the performance comparison of Uplink SE in a single-cell M-MIMO system for MRC, ZF, MMSE receivers at the base station in Rayleigh channel models. For distinct large-scale fading parameters, the SE of all the users on an average is also investigated in detail.

Keywords Massive MIMO (m-MIMO) · Spectral efficiency (SE) · Large scale fading

1 Introduction

MIMO technology has been an interesting subject for many years because of its enormous advantages in spectral and energy efficiency [1]. To fulfill the ever-increasing demand of wireless data services, M-MIMO is one of the advancements in 5G that enhances SE by configuring a huge no. of antennas at the BS [2]. M-MIMO can accomplish remarkable gains and can be able to reduce intra-cell interference extensively with lucid signal processing [3]. The channels of the users become orthogonal as M increases because of channel hardening so that M-MIMO can be able to completely suppress multi-user interference [4]. In M-MIMO, the transmitted power can be decreased proportionally to antennas at the BS, both in uplink and downlink [5]. The system considered is single-cell with N antennas at the BS and one antenna

B. Ch. Kiran Patrudu (✉) · P. V. Sridevi
Department of ECE, Andhra University College of Engineering (A), Visakhapatnam, Andhra Pradesh 530003, India
e-mail: kiranec121@gmail.com

P. V. Sridevi
e-mail: pvs6_5@yahoo.co.in

G. T. C. Sekhar et al. (eds.), *Intelligent Computing in Control and Communication*, Lecture Notes in Electrical Engineering 702,
https://doi.org/10.1007/978-981-15-8439-8_2

for each K user equipment. Using power scaling, the power of each user can be made proportional to $1/N$ for perfect CSI and $1/\sqrt{N}$ for imperfect CSI without any change in SINR, even 'N' tends to infinity [5]. The closed-form expressions of lower bounds on the uplink achievable rates are derived for finite but large N for both perfect and imperfect CSI [4]. The impact of shadow fading on SE with MRT precoding is analyzed for the downlink case [3]. The impact of large-scale fading over a generalized-k fading channel is analyzed in uplink very large MIMO systems [6].The performance of various linear receivers in the uplink is compared in this paper and also analyzed the impact of various path loss exponent values in the spectral efficiency analogous to cell radius.

2 System Model

Considering the Uplink of a Single Cell framework with one BS provided with N antenna array and K mobile users with one antenna operating in TDD mode. The received uplink vector 'y' at the BS is given by Eq. (1)

$$y = \sqrt{P_u} G \mathrm{x} + w \tag{1}$$

where P_u = each user power
$x = K$ by 1 transmitted signal vector of all users.
$w = N \times 1$ AWGN vector with $\mu = 0, \sigma^2 = 1$.
The Uplink channel matrix with channel coefficients is given by

$$G = \begin{bmatrix} g_{11} & g_{12} & \cdots & g_{1K} \\ g_{21} & g_{22} & \cdots & g_{2K} \\ \vdots & \vdots & \ddots & \vdots \\ g_{N1} & g_{N2} & \cdots & g_{NK} \end{bmatrix}$$

Each element of G, i.e., g_{nk} denotes the channel between the user of 'k' and antenna 'n' of the BS. Each coefficient g_{nk} is mentioned in Eq. (2) as

$$g_{nk} = h_{nk}\sqrt{\beta_k}, \quad n = 1, 2 \ldots N, \tag{2}$$

where h_{nk} = the fast fading coefficient between the user of 'k' and nth antenna.
$\sqrt{\beta_k}$ = shadow fading coefficients that are independent of 'n'.
The channel matrix G dimensioned $N \times K$ is defined in Eq. (3)

$$G = H D^{1/2} \tag{3}$$

where $H = N \times K$ small scale fading matrix
$D^{1/2} = K \times K$ diagonal matrix.

3 Spectral Efficiency

Spectral Efficiency is the amount of information that can be transferred per second over one Hz of bandwidth. To make the data rate as large as possible, SE should be maximized. Since Time Division Duplex (TDD) Protocol is considered, the channel response is same for uplink and downlink. The channel response during uplink is calculated from the pilot signals transmitted by each user [7]. Uplink SE is considered in this paper and downlink is for further work.

3.1 Perfect Channel State Information

Perfect CSI implies the channel information is known by the BS. Let the detector matrix whose characteristics depend on G be assumed as A of dimension $N \times K$. The job of the BS is to perform multiplication between the signal received and conjugate-transpose of the estimated channel matrix A. The effective signal vector at the BS is given by Eq. (4)

$$r = A^H y = \left(A^H \sqrt{P_u} G x + A^H w\right) \tag{4}$$

The row corresponding to the user 'k' in the $K \times 1$ vector r is mentioned in Eq. (5) as

$$r_k = \sqrt{P_u} \hat{a}_k^H g_k x_k + \sqrt{P_u} \sum_{i=1, i \neq k}^{K} \hat{a}_k^H g_i x_i + \hat{a}_k^H w \tag{5}$$

where g_k = column 'k' of the matrix G
x_k = input signal of user k
a_k = column 'k' of matrix A
The desired kth user SINR is represented in Eq. (6)

$$\text{SINR} = \frac{P_u \left| \widehat{a_k}^H g_k \right|^2}{P_u \sum_{i=1, i \neq k}^{K} \left| \widehat{a_k}^H g_i \right|^2 + \widehat{a_k}^2} \tag{6}$$

Maximum Ratio Combining

The channel estimate for MRC or the detector matrix A for MRC is the same as that of channel G. so, $a_k = g_k$. SINR for the kth user is given in Eq. (7)

$$\text{SINR} = \frac{P_u g_k^4}{P_u \sum_{i=1, i \neq k}^{K} \left| g_k^H g_i \right|^2 + g_k^2} \tag{7}$$

If power scaling is used from [8] by replacing $P_u = E_u/N$ for Perfect CSI and N tends to infinity, then SINR is represented in Eq. (8)

$$\text{SINR} = E_u \beta_k \quad \text{as} \quad N \to \infty \tag{8}$$

Zero-Forcing Receiver

The channel estimate of the ZF receiver is given by Eq. (9) as [9]

$$A = G\left(G^H G\right)^{-1} \tag{9}$$

then the SINR for the desired user 'k' can be calculated by substituting Eq. (9) in Eq. (6) and is shown in Eq. (10) as

$$\text{SINR} = \frac{P_u}{\left[\left(G^H G\right)^{-1}\right]_{kk}} \tag{10}$$

If we substitute $P_u = E_u/N$ and N grows large then SINR becomes as shown in Eq. (11)

$$\text{SINR} = E_u \beta_k \quad \text{as} \quad N \to \infty \tag{11}$$

MMSE Receiver

The channel estimate of the MMSE receiver is given by Eq. (12)

$$A = G\left(G^H G + \frac{1}{P_u} I_k\right)^{-1} = \left(GG^H + \frac{1}{P_u} I_k\right)^{-1} G \tag{12}$$

So, the conjugate transpose of A is given by Eq. (13)

$$A^H = \left(GG^H + \frac{1}{P_u} I_k\right)^{-1} G^H \tag{13}$$

Considering the kth column of A^H [4]

$$\hat{a}_k^H = \frac{v_k^{-1} g_k}{g_k^H v_k^{-1} g_k + 1} \quad \text{where } v_k \triangleq \sum_{i=1, i \neq k}^{K} g_i g_i^H + \frac{1}{P_u} I_N \tag{14}$$

and Substituting Eq. (14) in Eq. (6), then the SINR is given by Eq. (15)

$$\text{SINR} = g_k^H v_k^{-1} g_k. \tag{15}$$

3.2 Imperfect Channel State Information

In this, the BS does not have information about the channel. The BS will estimate the channel by using pilot symbols sent from the users which are orthogonal. These pilot symbols are transmitted during the first part of each coherence interval under the assumption that channel is constant. In the second part, every user has to send their data to the BS [10]. The pilot matrix is defined by a $\tau \times K$ matrix $\sqrt{P_P}\phi(\tau \geq K)$ where $P_p = \tau P_u$. The pilot matrix received at the BS is mentioned in Eq. (16) as

$$Y_P = \sqrt{P_P} G \phi^T + W \tag{16}$$

where W is an AWGN matrix of dimension $N \times \tau$ with $\mu = 0$ and variance σ^2. The estimate of G using MMSE is given by Eq. (17)

$$\hat{G} = \frac{1}{\sqrt{P_P}} Y_P \phi^H \tilde{D} = \left(G + \frac{1}{\sqrt{P_P}} W \phi \right) \tilde{D} \text{ where } \tilde{D} = \left(\frac{\sigma^2}{P_P} D^{-1} + I_K \right)^{-1} \tag{17}$$

Because of the presence of an error in the estimation, the estimated channel is denoted as $\hat{G} = G + E$ where E is the error in estimating the channel. Each ith element of E is Gaussian RV with a $\mu = 0$ and $\sigma^2 = \frac{\beta_i}{P_P \beta_i + 1}$. After substituting $\hat{G}$ in (16) and considering the vector received at the BS as Eq. (18)

$$\hat{r} = \hat{A}^H \left(\sqrt{P_u} \hat{G} x - \sqrt{P_u} E x + w \right) \tag{18}$$

the signal received from user 'k' is shown in Eq. (19)

$$\widehat{r_k} = \sqrt{P_u} \widehat{a_k}^H \widehat{g_k} x_k + \sqrt{P_u} \sum_{i \neq k}^{K} \widehat{a_k}^H \widehat{g_i} x_i - \sqrt{P_u} \sum_{i=1}^{K} \widehat{a_k}^H \varepsilon_i x_i + \widehat{a_k}^H w \tag{19}$$

in which the ith columns of $\widehat{G}$ and E is represented by $\widehat{g_i}$ and ε_i.In Eq. (19),the signal of the desired user is given by the first term and the remaining three terms are considered as undesired user interference. Then the SINR for user 'k' is represented in Eq. (20) as

$$\text{SINR} = \frac{P_u \left| \widehat{a_k}^H \widehat{g_k} \right|^2}{P_u \sum_{i=1, i \neq k}^{K} \left| \widehat{a_k}^H \widehat{g_i} \right|^2 + P_u \widehat{a_k}^2 \sum_{i=1}^{K} \frac{\beta_i}{\tau p_u \beta_i + 1} + \widehat{a_k}^2} \tag{20}$$

Maximum Ratio Combining

By replacing $\widehat{a_k} = \widehat{g_k}$ for MRC in the Eq. (20) then SINR can be obtained as

$$\text{SINR} = \frac{P_u \widehat{g_k}^4}{P_u \sum_{i=1, i\neq k}^{K} \left|\widehat{g_k}^H \widehat{g_i}\right|^2 + P_u \widehat{g_k}^2 \sum_{i=1}^{K} \frac{\beta_i}{\tau p_u \beta_i + 1} + \widehat{g_k}^2} \tag{21}$$

Using Power Scaling for Imperfect CSI from [2], i.e., Substituting $P_u = E_u/\sqrt{N}$ in Eq. (21) and N tends to infinity, SINR is obtained as $\tau \beta_k^2 E_u^2$.

ZF Receiver

Zero-forcing receiver forces the interference to zero by using $\widehat{a_k}^H \widehat{g_i} = \delta_{ki}$. Substituting this in Eq. (16) we can find the SINR as shown in Eq. (22)

$$\text{SINR} = \frac{P_u}{\sum_{i=1}^{K} \frac{P_u \beta_i}{\tau p_u \beta_i + 1} \left[\left(\hat{G}^H \hat{G}\right)^{-1}\right]_{kk}} \tag{22}$$

By processing with ZF receiver and using imperfect CSI for $N \geq K + 1$, the rate of user 'k' in uplink [5] is bounded as Eq. (23)

$$\frac{\tau P_u^2 (M - K) \beta_k^2}{(\tau P_u \beta_k + 1) \sum_{i=1}^{K} \frac{P_u \beta_i}{\tau p_u \beta_i + 1} + \tau P_u \beta_k + 1} \tag{23}$$

Similarly, with $P_u = E_u/\sqrt{N}$, when $N \to \infty$, the rate of user 'k' in uplink using ZF is same as MRC i.e., $\tau \beta_k^2 E_u^2$.

MMSE Receiver

The vector received at the BS using imperfect CSI can be written as Eq. (24)

$$y = \sqrt{P_u} \hat{G} x - \sqrt{P_u} E x + w \tag{24}$$

the kth column of the estimated channel $\widehat{A}$ using the MMSE receiver is given by [4]

$$\widehat{a_k} = \frac{\hat{V}_k^{-1} \hat{g}_k}{\hat{g}_k^H \hat{V}_k^{-1} \hat{g}_k + 1} \tag{25}$$

where $\hat{v}_k = \sum_{i=1, i\neq k}^{K} \hat{g}_i \hat{g}_i^H + \left(\sum_{i=1}^{K} \frac{\beta_i}{\tau p_u \beta_i + 1} + \frac{1}{P_u}\right) I_N$

Substituting Eq. (25) in Eq. (19) the kth user achievable rate in the uplink for any receiver is given by Eqs. (26) and (27)

$$R = \left\{\log_2(1 + \text{SINR})\right\} \tag{26}$$

$$R_{\mathrm{MMSE}} = E\left\{\log_2\left(\left[\left(I_K + \left(\sum_{i=1}^{K}\frac{\beta_i}{\tau p_u \beta_i + 1} + \frac{1}{P_u}\right)^{-1}\hat{G}^H\hat{G}\right)^{-1}\right]_{kk}\right)\right\} \quad (27)$$

n

The Spectral Efficiency can be calculated as $\mathrm{SE} = \sum_{k=1}^{K} R$ where R is the kth user achievable for any receiver.

4 Simulation and Analysis

An Annular region around the base station with minimum distance r_h of 100 m and the maximum distance of 1000 m for any user is considered [11]. The no. of users in each cell are assumed as $K = 15$. The large-scale fading is expressed as $\beta_k = \frac{z_k}{(r_k/r_h)^v}$ where z_k follows a log-normal shadowing with a standard deviation of 8 dB and path loss exponent $v = 3.8$ and the gap between user 'k' and BS is r_k. The plots are averaged over 1000 Monte-Carlo simulations. Figure 1 gives the theoretical and numerical values of SE of MRC receiver versus N with Perfect and Imperfect CSI for different values of $K = 10, 15, 25$ users. The theoretical bounds are nearer to the numerical values for various configurations of BS antennas. Figure 1 also gives SE,

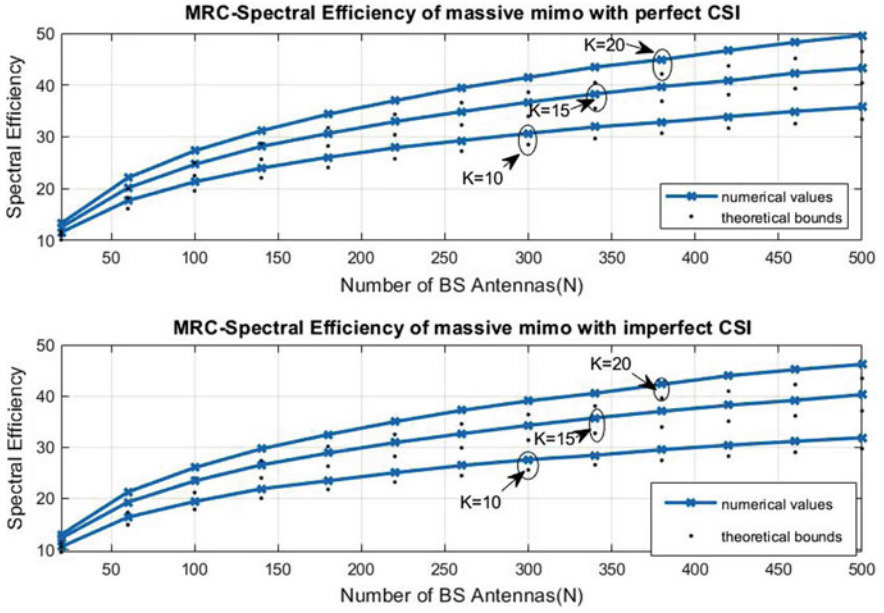

Fig. 1 Spectral efficiency versus No. of antennas at the base station N for different No. of users $K = 10, 15, 20$ at SNR = 20 dB

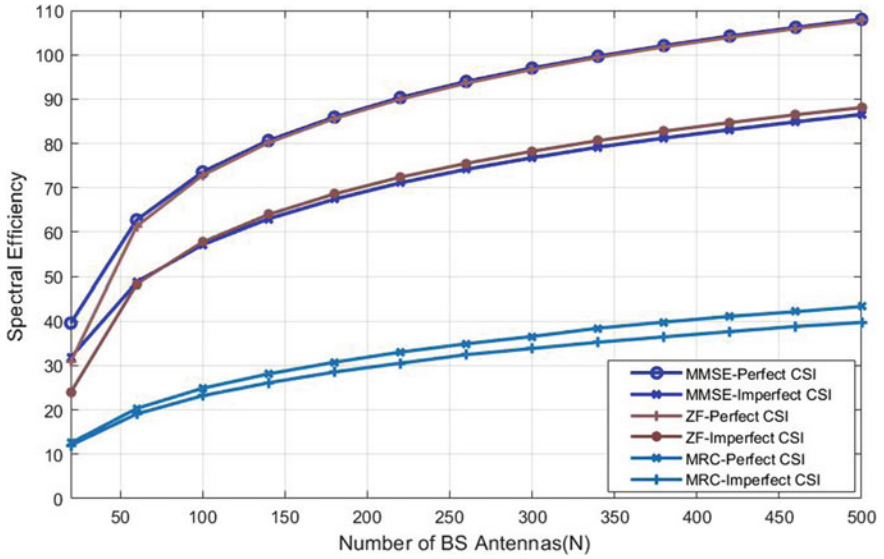

Fig. 2 Spectral efficiency versus No. of antennas at BS for MRC, ZF, MMSE receivers with perfect CSI and imperfect CSI for $K = 15$ SNR $= 20$ dB

which can be enhanced by using a greater no. of antennas at the BS. Figure 2 shows the improvement in spectral efficiency due to increment of antennas at BS for MRC, ZF and MMSE receivers in perfect and imperfect CSI case. It shows that MMSE outperforms than MRC and ZF receiver.

In Fig. 3, incrementing the antennas at the transmitter enhance the SE but observed the reduction in deviation made by Imperfect CSI in SE. However, as the number of users is increased, not only the SE is improved but also SE of imperfect CSI gets nearer to SE of perfect CSI because channel estimation becomes reliable as K increases. The impact of large-scale fading parameter, i.e., for various values of path loss exponent (PLE) on SE is presented in Fig. 4. The values of PLE is 2 for free space, 2.7–3.5 for urban cell radio, 3–5 for shadowed urban cell radio, 4–6 for obstructed in building [2, 12]. The SE is maximum when the radius of the cell is 100 m irrespective of the path loss exponent since the users are very nearer to the base station. The SE is reduced as the radius of the cell is increased but the loss in SE is increased as the path loss exponent is increased. It is observed that the curves of SE are coincident at lower values of radius for perfect and Imperfect CSI but as the radius is increased, SE of imperfect CSI is lower than SE of perfect CSI due to error in the channel estimation and the impact of path loss exponent increases.

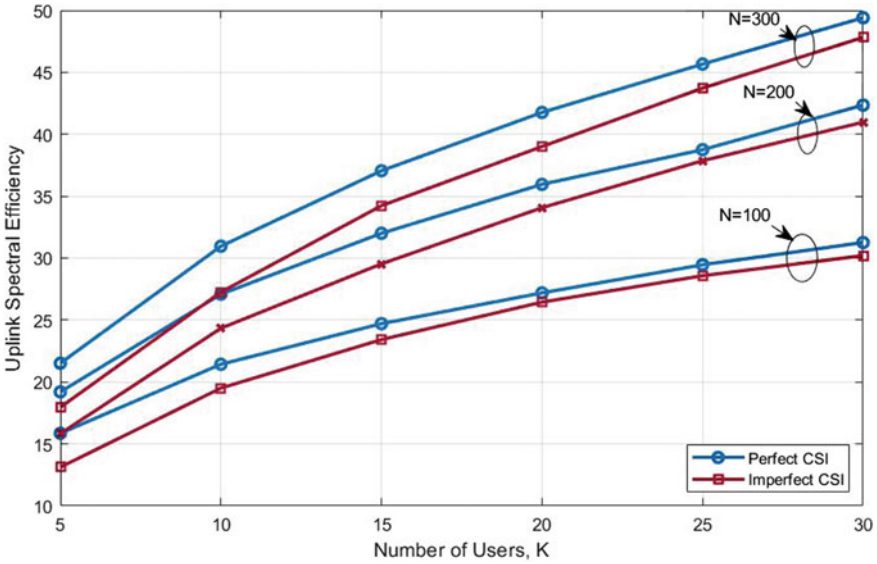

Fig. 3 Spectral efficiency versus No. of users K for different No. of BS antennas for perfect CSI and imperfect CSI at SNR = 20 dB

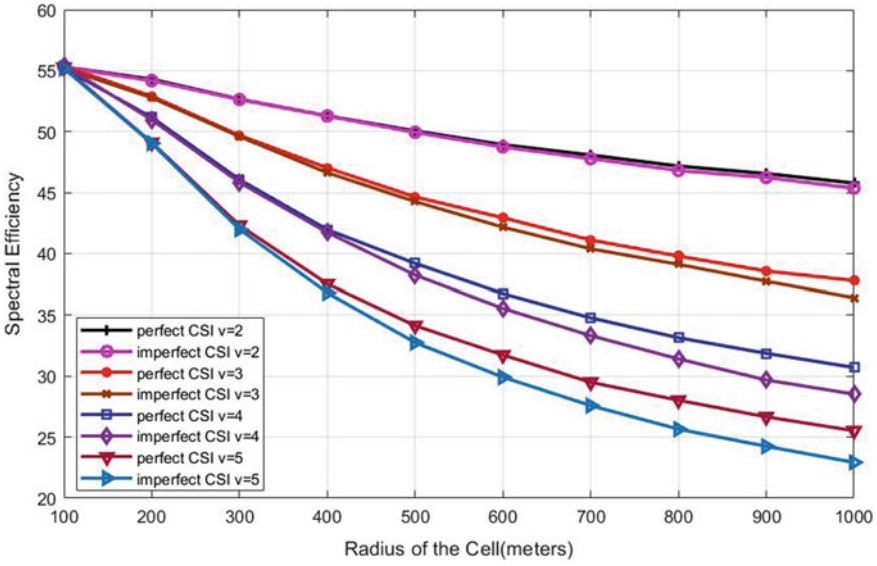

Fig. 4 Spectral efficiency versus radius of the cell with perfect CSI and imperfect CSI for various values of path loss exponent for $N = 200$, $K = 15$, SNR = 20 dB

5 Conclusion

This paper examined the Uplink Performance of Massive MIMO for various receivers, in particular, MRC, ZF and MMSE for perfect CSI and imperfect CSI over Rayleigh Fading Channel. The outcomes show that MMSE outperforms than MRC and ZF receivers. The SE of these receivers increments as the number of BS antennas N increments. This paper also evaluates the performance of MRC receiver over a large-scale fading channel which gives a conclusion that the large-scale fading parameters have considerable effects on the SE for both perfect and imperfect CSI but have limited impact on the decrement in SE arise due to imperfect CSI.

Acknowledgements The authors wish to acknowledge Andhra University College of Engineering (A), Visakhapatnam for providing the resources. Also, acknowledge the University Grants Commission of India for providing the JRF fellowship for doing research.

References

1. Zhao L, Zhao H, Massive MIMO in 5G networks : selected applications
2. Larsson EG, Edfors O, Tufvesson F, Marzetta TL (2014) Massive MIMO for next-generation wireless systems. IEEE Commun Mag 52(2):186–195
3. Lin Y, Li X, Fu W, Hei Y (2015) Spectral efficiency analysis for downlink massive MIMO systems with MRT precoding. China Commun 12(1):67–73
4. Ngo HQ, Larsson EG, Marzetta TL (2013) Energy and spectral efficiency of very large multiuser MIMO systems. IEEE Trans Commun 61(4):1436–1449
5. Ngo HQ, Suraweera HA, Matthaiou M, Larsson EG (2014) Uplink power efficiency of multiuser MIMO with very large antenna arrays uplink power efficiency of multiuser MIMO with very large antenna arrays. IEEE J Sel Areas Commun 32(9):1721–1737
6. Yang A, He Z, Xing C, Fei Z, Kuang J (2016) The role of large-scale fading in uplink massive MIMO systems. IEEE Trans Veh Technol 65(1):477–483
7. Björnson E, Hoydis J, Sanguinetti L (2017) Massive MIMO Networks. IEEE Commun Mag 1(1):4
8. Rusek F et al (2013) Scaling up MIMO: opportunities and challenges with very large arrays. IEEE Sig Process Mag 30(1):40–60
9. Yang A, Xing C, Fei Z, Kuang J (2016) Performance analysis for uplink massive MIMO systems with a large and random number of UEs. Sci China Inf Sci 59(2):1–9
10. Al-Rawi M, Al-Rawi M (2017) Performance of massive MIMO uplink system over Nakagami-m fading channel. Radioelectron Commun Syst 60(1):13–17
11. Chawla A, Jagannatham AK (2019) Spectral efficiency of very large multiuser MIMO systems for time-selective fading. In: IEEE vehicular technology conference, vol 2019, pp 1–5
12. Munoz D, Bouchereau F, Vargas C, Enriquez R (2009) Signal parameter estimation for the localization problem. Position Location Technical Application, pp 23–65

Design and Analysis of Redox Flow Battery for Load Frequency Control of Power System

Thamminaina Uma and Ramana Pilla

Abstract The ability of a redox flow battery (RFB) is analyzed in the present paper to minimize the tie-line power and frequency of the two-area power system. Initially, a power system with two-areas is designed in MATLAB/Simulink environment. For the proposed system, different secondary controllers such as integral (I), proportional integral (PI), proportional integral derivative (PID), and proportional derivative-proportional integral derivative (PD-PID) controllers are evaluated. Results of simulation show that the better transient response is given by PD-PID controller. After that, the redox flow battery (RFB) is installed in area-1 for dynamic response enhancement. Lastly, system robustness under variance of system parameters is tested.

Keywords Dynamic response · PID controller · PD-PID controller · Redox flow battery (RFB) · Robustness · Transient response

1 Introduction

The integrated power system with nominal frequency and terminal voltage aims at producing, transporting and transmitting electric energy. The need for an integrated power system has been increasing due to volatility in demand for electrical energy and the gap between generation and demand due to system blackouts. The total power produced should be equal to the total load plus system losses for better operation of the interconnected power system [1]. If the amount of power produced is less than the demand, the generator unit begins to decrease in speed and frequency, and vice versa. With the deviation of results in scheduled power interchange and nominal system frequency between different areas, undesirable effects may occur, even for a small

T. Uma · R. Pilla (✉)
Department of Electrical and Electronics Engineering, GMR Institute of Technology, Rajam, Andhra Pradesh 532127, India
e-mail: ramana.pilla@gmrit.edu.in; pramana.gmrit@gmail.com

T. Uma
e-mail: umathamminaina@gmail.com

G. T. C. Sekhar et al. (eds.), *Intelligent Computing in Control and Communication*, Lecture Notes in Electrical Engineering 702,
https://doi.org/10.1007/978-981-15-8439-8_3

change in demand. For efficient, economical, and reliable operation, the frequency and tie-line power of the interconnected power system must be kept fixed to their nominal values [2, 3]. This can be done by Automatic Generation Control (AGC).

Different classical controllers responses are analyzed, and it is found that the IDD controller performs better than others [4, 5]. To attain an optimal working point [6], the genetic algorithm (GA) is used to compute the control parameters. For AGC, a two-area 4-unit thermal system with PID along with filter (PIDF) is proposed. Using DE algorithm with ITAE criterion, PIDF controller gains are optimized. This shows DE's optimized PIDF superiority over Fuzzy Logic Controller (FLC) [7]. Different optimization techniques have been suggested, such as GA, DE algorithm, firefly algorithm (FA), artificial bee colony (ABC) algorithm and bacterial foraging optimization algorithm (BFOA) for the LFC problem [2, 8–12]. Having above literature kept in mind, in the present manuscript a cascaded PD-PID controller is proposed with search group algorithm (SGA).

2 Investigated Model

Control area has variety of generating sources such as gas, hydro, nuclear, wind, thermal, solar etc. In the present study, a diverse power system with two-area six unit is designed as shown in Fig. 1 using SIMULINK environment. It consists of gas, hydro and thermal units in both the areas and participated in load frequency control (LFC) with participation factors.

With the power system units, RFB is also included in the power system for better transient response. It becomes very popular due to its quick response, flexible layout, long life cycle, low maintenance, easy state of charge determination and therefore delay in response does not occur [13]. In order to reduce large fluctuations in customer demand, the battery is used for secondary control in power system [14]. To get the better response of the system for small load disturbances in LFC scheme, RFBs have been integrated [15].

For the purpose of LFC, a secondary controller called cascaded PD-PID controller has been implemented. Due to its inherent simplicity PID controller is the finest choice, but to enhance the control action of the system and for LFC in multi-area power system a PD controller is connected in cascade with the PID controller giving rise to PD-PID cascaded controller [16–18]. The optimal values of PD-PID controller employed ITAE objective function are obtained with search group algorithm (SGA). SGA was able to upgrade data from the algorithm's independent runs and provide the latest structures. It is a metaheuristic optimization technique for multimodal, non-smooth, nonconvex, nonlinear, bounded optimization problem. The process of obtaining controller parameters with SGA technique is clearly explained in [19, 20].

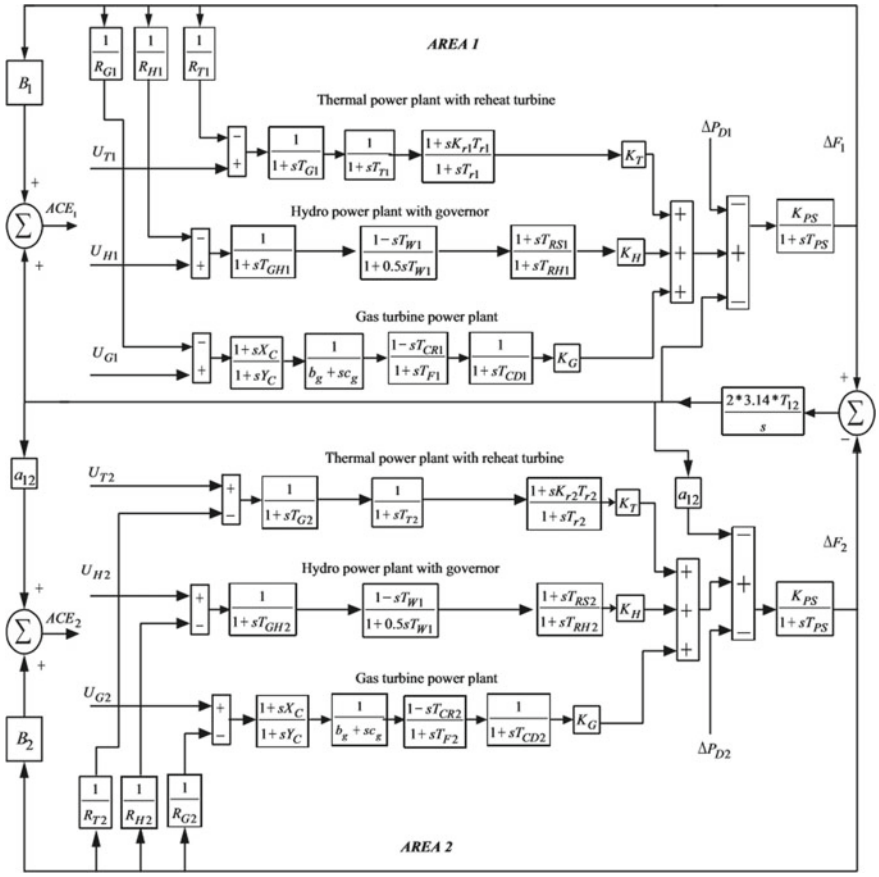

Fig. 1 Simulink diagram of the proposed power system

3 PD-PID Controller

For the purpose of LFC, a secondary controller called cascaded PD-PID controller has been implemented. Due to its inherent simplicity the best choice is PID controller, but to progress the control action of the system and for LFC, a PD controller is connected in cascade with the PID controller giving rise to PD-PID cascaded controller [9]. The cascade control is primarily used to achieve fast rejection in the disturbance. The PD-PID controller comprising of an inner control loop (referred to as a secondary loop or slave loop) and an outer control loop (referred to as the main loop or master loop) as shown in Fig. 2. The inner controller corrects the disturbances that occur in the inner loop before affecting the outer loop controller variable. In the outside loop, the PD controller is implemented while the PID controller is implemented in the inside loop. The t.f. of the proposed PD-PID controller can be given as shown in Eq. (1).

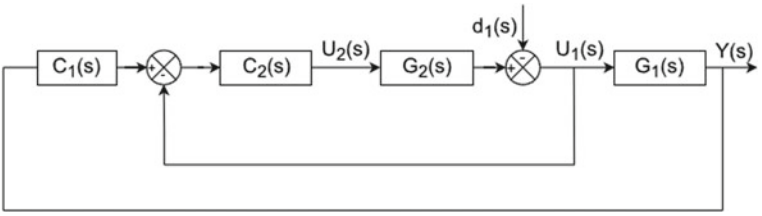

Fig. 2 Proposed PD-PID cascaded controller

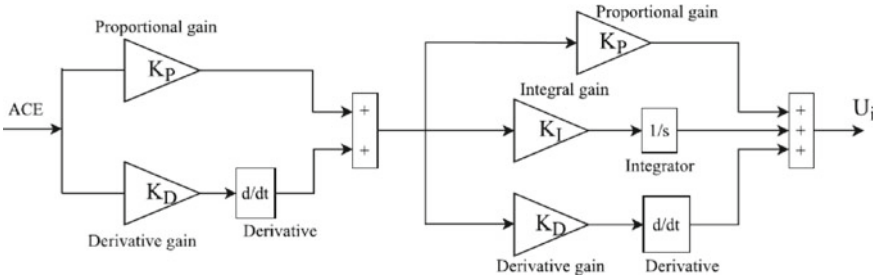

Fig. 3 Simulink diagram of PD-PID controller

$$Y(s) = \left[\frac{G_1(s)G_2(s)C_1(s)C_2(s)}{1 + G_2(s)C_2(s) + G_1(s)G_2(s)C_1(s)C_2(s)}\right]R(s) + \left[\frac{G_1(s)}{1 + G_2(s)C_2(s) + G_1(s)G_2(s)C_1(s)C_2(s)}\right]d_1(s) \quad (1)$$

The SIMULINK implementation diagram of PD-PID controller is as depicted in Fig. 3.

Where $U_1(s)$ is input for outer process, $U_2(s)$ is the input for inner process, $Y_1(s)$ is output for inner process, $Y(s)$ is output for outer process, and $d_1(s)$ is the load disturbance.

4 Objective Function

The objective function is first specified during design of a controller, based on the required needs and constraints. For AGC the suitable criterion for performance is ITAE and hence the ITAE is used as objective function and is given by the Eq. (2)

$$\text{ITAE} = \int_0^t (|\Delta F_1| + |\Delta F_2| + |\Delta P_{\text{tie}}|) \times t\,dt \quad (2)$$

where the frequency variations in area 1 is equal to ΔF_1 and in area 2 is equal to ΔF_2, the variation of the tie-line power between area 1 and 2 is equal to ΔP_{tie} and t is the time. The settling time and peak overshoot can be reduced by ITAE criterion which cannot be achieved by using ISE or IAE. Therefore, the better objective function for load frequency control (LFC) is ITAE.

5 Results Analysis

The machine model under analysis as shown in Fig. 1 is built in the environment of SIMULINK and the software of SGA is written in .m file. Integral controllers are initially considered for each device. The model built is implemented in a distinct program (using .m file) taking into account a disturbance of 1% step load in area-1. Other conventional controllers namely PI and PID controllers are then selected as secondary controllers to improve system performance. Cascade PD-PID controller is checked in the next phase, and then RFB is put in area-1 for better transient response. The min. and max. values of K_P, K_I for PI controller are -2 and 2, and for remaining controllers K_P, K_I, and K_D are preferred in the present work as 0 and 2 respectively. The best end results obtained in the 100 runs and objective function ITAE are:

For I controller:

$K_{\text{I1}} = 0.1523$; $K_{\text{I2}} = 0.0503$; $K_{\text{I3}} = 0.2673$; ITAE = 2.7933

For PI controller:

$K_{P1} = 1.6534$; $K_{P2} = -1.6251$; $K_{P3} = -0.8121$; $K_{\text{I1}} = 1.0805$; $K_{\text{I2}} = 0.0759$; $K_{\text{I3}} = 0.4684$; ITAE = 0.5281;

For PID controller:

$K_{P1} = 1.6805$; $K_{P2} = 1.7642$; $K_{P3} = 1.8534$; $K_{I1} = 1.9066$; $K_{I2} = 0.1250$; $K_{I3} = 1.8156$; $K_{D1} = 1.7371$; $K_{D2} = 0.0221$; $K_{D3} = 0.4819$; ITAE = 0.1860

For PD-PID controller:

$K_{P1} = 1.3491$; $K_{P2} = 0.0363$; $K_{P3} = 1.4796$; $K_{I1} = 1.4432$; $K_{I2} = 0.4941$; $K_{I3} = 1.8937$; $K_{D1} = 0.2323$; $K_{D2} = 0.2693$; $K_{D3} = 0.2996$; $K\_1 = 1.8664$; $K\_2 = 0.3166$; $K\_3 = 0.2359$; $K\_4 = 0.7308$; $K\_5 = 1.6638$; $K\_6 = 1.9104$; ITAE = 0.1115;

For PD-PID controller with RFB:

$K_{P1} = 1.9594$; $K_{P2} = 0.7710$; $K_{P3} = 1.4658$; $K_{I1} = 1.7638$; $K_{\text{I2}} = 0.0270$; $K_{I3} = 1.4557$; $K_{D1} = 1.3690$; $K_{D2} = 1.1289$; $K_{D3} = 1.2345$; $K\_1 = 1.7643$; $K\_2 = 1.5856$; $K\_3 = 1.5055$; $K\_4 = 0.1157$; $K\_5 = 1.9907$; $K\_6 = 0.4291$; ITAE = 0.1311;

For area-1 at $t = 0$ s a 1% step load is applied and the values of performance index are shown in Table 1. From Table 1 it is clear that, the PD-PID controller performance with RFB is better compared to other techniques. From these figures it is perceived that the PD-PID controller with RFB provides excellent transient response specifications for area-1 frequency change, area-2 frequency change and tie-line power change.

In addition, the PD-PID controller's ability is evaluated by varying device parameters ranging from −25 to +25% of nominal values. In the present study, T_{G} and T_{T} are varied. The dynamic responses are plotted under varied conditions without

Table 1 Values of performance index

Controller	Settling time			Peak overshoot ($\times 10^{-3}$)			Undershoot ($\times 10^{-3}$)		
	ΔF_1	ΔF_2	ΔP_{Tie}	ΔF_1	ΔF_2	ΔP_{Tie}	ΔF_1	ΔF_2	ΔP_{Tie}
I	41.5	45.5	45	7.85	7.4	0.48	−38.36	−42.65	−7.7
PI	15.5	19	18.2	11.8	7.2	0.58	−28.86	−25.2	−5.36
PID	10.9	13.4	11.3	3.28	3.145	0.231	−18.0	−12.0	−3.035
PD-PID	10.3	11.5	0	1.025	0.452	0.144	−9.865	−5.94	−1.734
PD-PID with RFB	14.0	14.8	0	0.33	0.23	0.112	−2.7	−1.96	−0.665

returned the controller parameters. The Figs. from 4a–c, 5a–c and 6a–c shows the corresponding responses. This robustness was analyzed for RFB incorporated power system, as it is the best system.

6 Conclusion

An attempt was made to design a PD-PID controller in multi-area power system employed with SGA technique for LFC. It demonstrates the performance of proposed PD-PID controller by comparing with classical controllers. A suitable model of RFB is developed for LFC applications and kept in area-1. From the results of simulation, it reveals that with the incorporation of RFB in area-1 the improvement in the transient response has been obtained. Further, the analysis of robustness was carried out for testing the ability of proposed technique with variation of system parameters. Simulation results show that there is no need of retuning controller parameters for variation of system parameters.

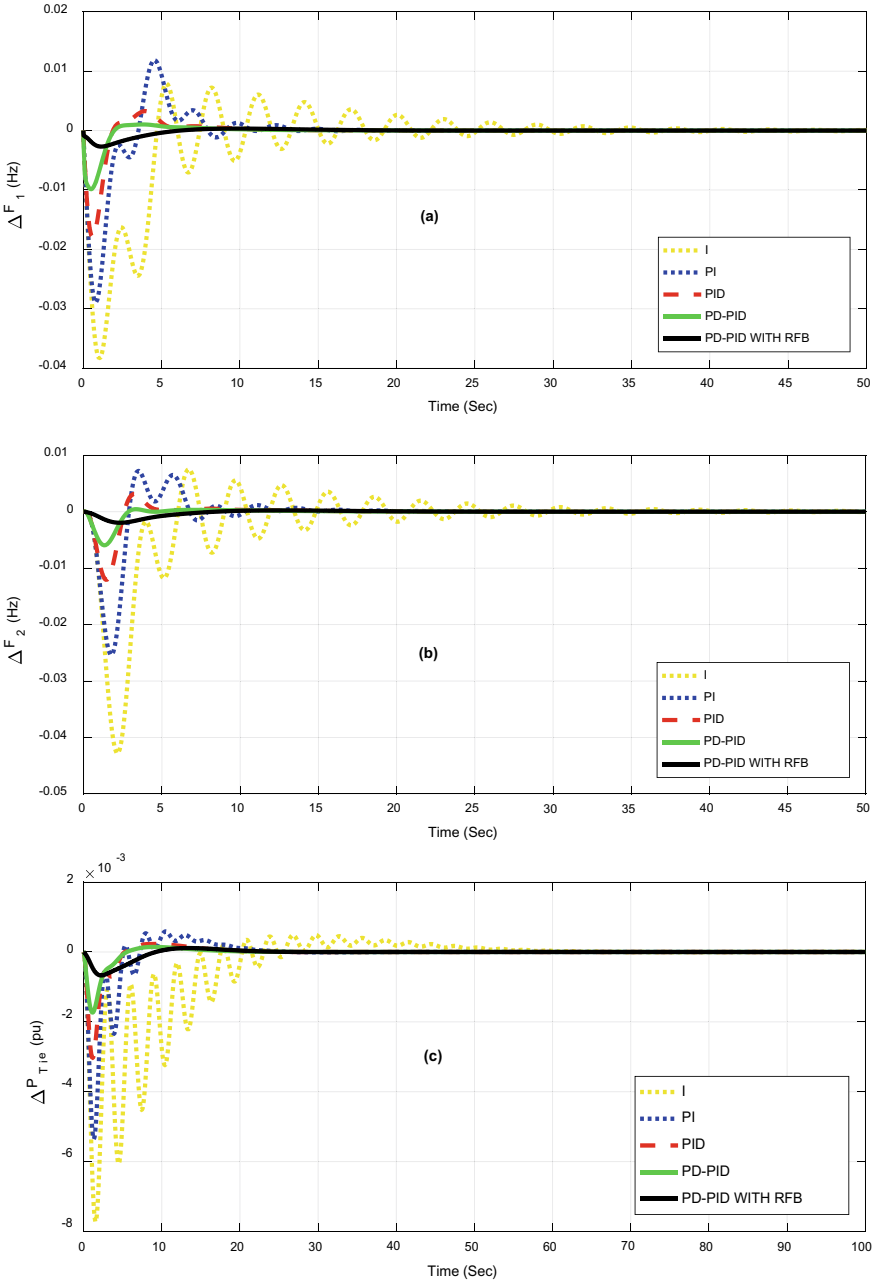

Fig. 4 **a–c** Responses for 1% SLP in area-1

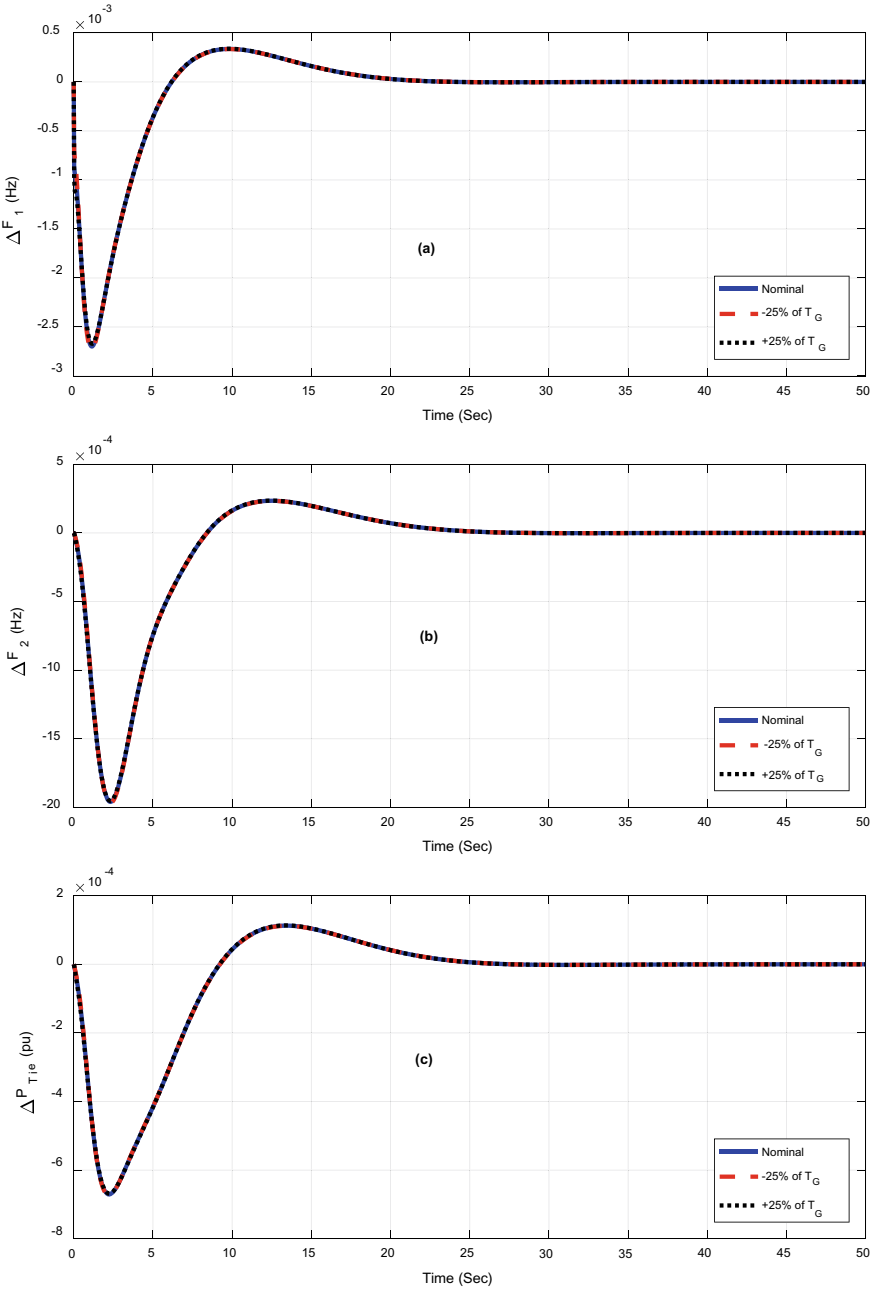

Fig. 5 **a–c** Responses for variation of T_G

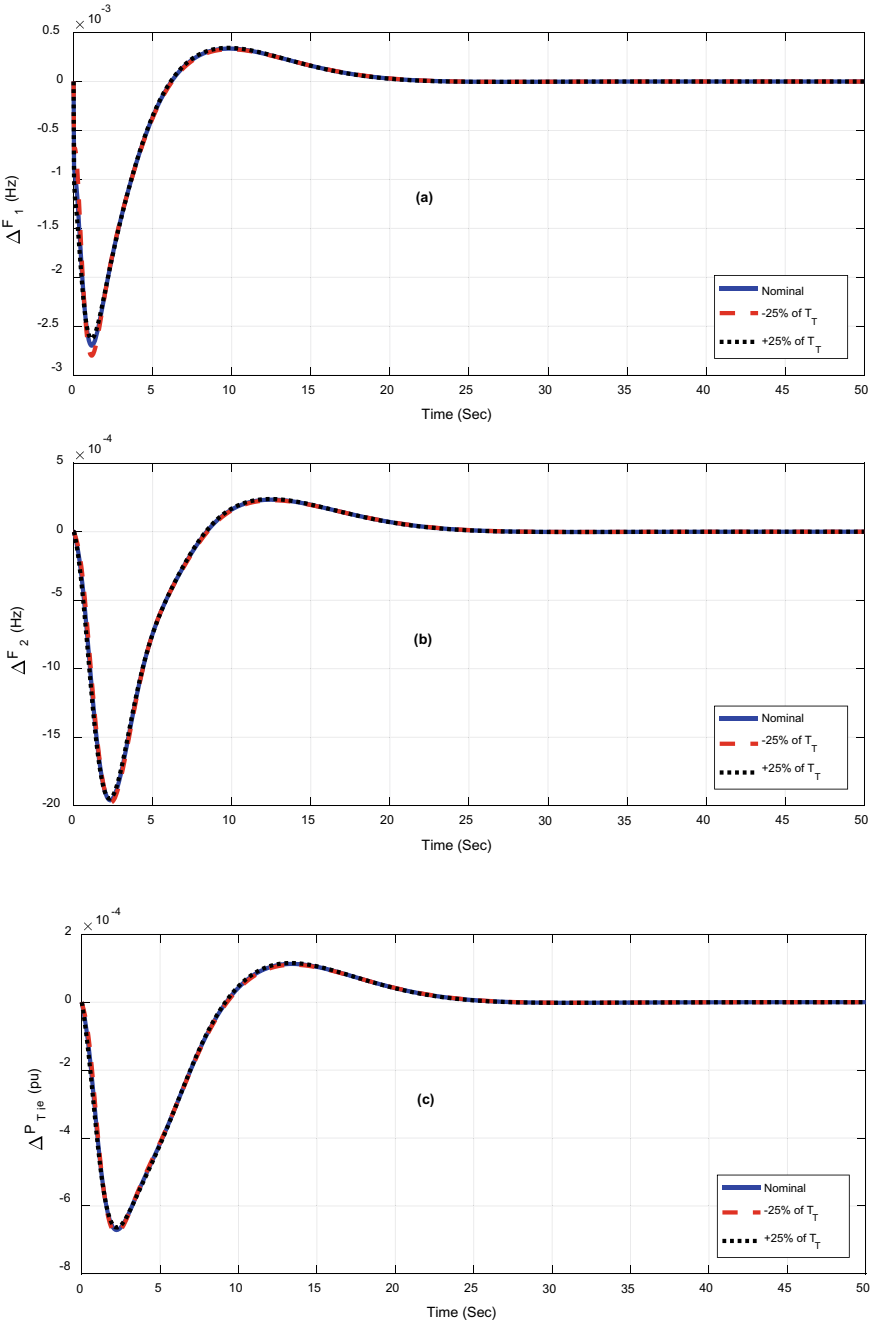

Fig. 6 **a–c** Responses for variation of T_T

Appendix

$B_1 = B_2 = 0.4312$ P.U. MW/Hz, $R_{G1} = R_{H1} = R_{T1} = R_{G2} = R_{H2} = R_{T2} = 2.4$ Hz/p.U., $T_{G1} = T_{G2} = 0.08$ s, $K_{r1} = K_{r2} = 0.3$, $T_{r1} = T_{r2} = 10$ s, $T_{t1} = T_{t2} = 0.3$ s, $T_{GH1} = T_{GH2} = 0.2$ s, $T_{RS1} = T_{RS2} = 5$ s, $T_{RH1} = T_{RH2} = 28.75$ s, $T_{w1} = T_{w2} = 1.0$ s, $T_{CR1} = T_{CR2} = 0.01$ s, $T_{F1} = T_{F2} = 0.23$ s, $T_{CD1} = T_{CD2} = 0.2$ s, $X_c = 0.6$ s, $Y_c = 1$ s, $c_g = 1$ s, $b_g = 0.05$ s, $K_T = 0.543478$, $K_H = 0.326084$, $K_G = 0.130438$, $T_{12} = 0.0433$ s, $T_{p1} = T_{p2} = 1.49$ s, $a_{12} = -1$, $K_{p1} = K_{p2} = 68.9566$ Hz/p.U. MW, $K_{RFB} = 1.67$, $T_{RFB} = 0$

References

1. Pilla R, Azar AT, Gorripotu TS (2019) Impact of flexible AC transmission system devices on automatic generation control with a metaheuristic based Fuzzy PID controller. Energies 12(21):4193
2. Dash P, Chandra Saikia L, Sinha N (2014) Comparison of performances of several Cuckoo search algorithm based 2DOF controllers in AGC of multi-area thermal system. Electr Power Energy Syst 55:429–436
3. Pilla R, Botcha N, Gorripotu TS, Azar AT (2019) Fuzzy PID controller for automatic generation control of interconnected power system tuned by glow-worm swarm optimization. In: Nayak J, Balas V, Favorskaya M, Choudhury B, Rao S, Naik B (eds) Applications of robotics in industry using advanced mechanisms. ARIAM 2019. Learning and analytics in intelligent systems, vol 5. Springer, Cham
4. Saikia LC, Sahu SK (2013) Automatic generation control of a combined cycle gas turbine plant with classical controllers using firefly algorithm. Electr Power Energy Syst 53:27–33
5. Saikia LC, Nanda J, Mishra S (2011) Performance comparison of several classical controllers in AGC for multi-area interconnected thermal system. Electr Power Energy Syst 33:394–401
6. Golpîraa H, Bevrania H, Golpîrab H (2011) Application of GA optimization for automatic generation control design in an interconnected power system. Energy Convers Manage 52:2247–2255
7. Gorripotu TCS, Sahu RK, Panda S (2015) AGC of a multi-area power system under deregulated environment using redox flow batteries and interline power flow controller. Eng Sci Technol Int J, 1–24
8. Gozde H, Taplamacioglu M, Kocaarslan I (2012) Comparative performance analysis of artificial bee colony algorithm in automatic generation control for interconnected reheat thermal power system. Electr Power Energy Syst 42:167–178
9. Panda S, Yegireddy NK (2013) Automatic generation control of multi-area power system using multi-objective non-dominated sorting genetic algorithm-II. Electr Power Energy Syst 53:54–63
10. Dey R, Ghosh S, Ray G, Rakshit A (2012) H1 load frequency control of interconnected power systems with communication delays. Electr Power Energy Syst 42:672–684
11. Bhatt P, Roy R, Ghoshal SP (2010) Optimized multi area AGC simulation in restructured power systems. Electr Power Energy Syst 32:311–322
12. Chandra Sekhar GT, Vijay Kumar D, Manmad Kumar B, Ramana P (2018) Design and analysis of BFOA optimized PID controller with derivative filter for frequency regulation in distributed generation system. Int J Autom Control 12(2): 291–323

13. Singh Parmar KP (2014) Load frequency control of multi-source power system with redox flow batteries: an analysis. Int J Comput Appl 88
14. Chen R, Kim S, Chang Z (2017) Redox flow batteries: fundamentals and applications. INTECH, pp 103–118
15. Arenas LF, Ponce de León C, Walsh FC (2017) Engineering aspects of the design, construction and performance of modular redox flow batteries for energy storage. J Energy Stor 11:119–153
16. Zeynelgil HL, Demiroren A, Sengor NS (2002) The application of ANN technique to automatic generation control for multi-area power system. Electr Power Energy Syst 24:345–354
17. Chandrasekhar GT, Pilla R (2019) Black hole optimized cascade proportional derivative-proportional integral derivative controller for frequency regulation in hybrid distributed power system. Int J Swarm Intell 4:155–174
18. Debnath MK, Jena T, Mallick RK (2016) Novel PD-PID cascaded controller for automatic generation control of a multi-area interconnected power system optimized by Grey Wolf optimization (GWO). In: 1st IEEE international conference on power electronics, intelligent control and energy systems (ICPEICES-2016), pp 1–6
19. Khamari D, Sahu RK, Panda S (2019) Application of search group algorithm for automatic generation control of multi-area multi-source power systems. In: E3S web of conferences, 87
20. Panigrahi BK, Ravikumar Pandi V, Sharma R, Das S, Das S (2011) Multiobjective bacteria foeaging algorithm for electrical load dispatch problem. Energy Convers Manag 52:1334–1342

DE-Assisted LFC of Three-Area Six-Source Interconnected Power System with Wind Model and Fuel Cell Under Restructured Environment

G. Pavan Kumar and R. Srinu Naik

Abstract The area frequency control named as load frequency control (LFC) of three-area six-machine power system with asynchronous power transfer links in the presence of the combination of wind generating system and fuel cell is studied in this paper. Instead of concentrated conventional environment, deregulated environment with different scenarios is presented in this work. The test system influences the frequency in the presence of the combination of wind and fuel cell under constant load conditions leads the frequency oscillations. The overall system performance is improved in the presence of asynchronous tie-lines along with sudden load disturbances with proportional–integral–derivative controller as secondary controller. The secondary controller parameters are optimized using differential evaluation technique. The observations from results show that the powerful differential evaluation technique validates with renewable energy sources under open market system. The peak values and settling time are reduced with the insertion of both AC and DC links. The simulations are done in MATLAB/Simulink environment.

Keywords Load frequency control · Open market system · Secondary controller · Wind system · Fuel cell · Differential evaluation technique

1 Introduction

The input power change effects the system frequency along with load perturbations [1]. This change is maximum particularly in the presence of renewable energy sources like photovoltaic, wind, and solar system since the input of these systems varies random in nature. The basic models of interconnected power system under

G. Pavan Kumar (✉) · R. Srinu Naik
Department of EE, AU College of Engineering (A), Visakhapatnam, Andhra Pradesh 530003, India
e-mail: gpavan16@gmail.com

R. Srinu Naik
e-mail: naiknaiknaik@gmail.com

G. T. C. Sekhar et al. (eds.), *Intelligent Computing in Control and Communication*, Lecture Notes in Electrical Engineering 702,
https://doi.org/10.1007/978-981-15-8439-8_4

open market system are discussed in [2, 3]. The effect of asynchronous tie-line under deregulated environment is presented in [4–6]. Two degrees of freedom PID controller tuned by differential evaluation technique under restructured system are provided in [7, 8]. Load frequency control of multi-area multi-machine power system is presented in [9–11]. In [12–15], the influence of renewable energy sources like wind turbines in open market system is discussed in literature survey.

From the above discussions, most of the articles deal with power system models with EHVAC links. Therefore, authors made an attempt by considering asynchronous tie-line with combination of wind and fuel system and PID as secondary controller in this work. The utilization of HVDC link in parallel with EHVAC results improvement of dynamic response and stability margin. The performance measure integral square error is used under restructured system. The contract relations among DISCO and GENCOs for different scenarios are presented [2, 3].

2 System Investigated

The investigated system consists of two generation companies named reheat thermal units in area 1, and area 2 consists of two generation companies of the same units as in area 1 and two more generation companies named hydro units in area 3. The system under investigation is incorporated with DC links acting as asynchronous tie-line in all the areas under the combination of wind and fuel cell. The complete transfer model of investigated three-area interconnected power system with wind–fuel cell under deregulated domain is shown in Fig. 1.

In restructured domain, distribution companies have a chance to choose any number of generation companies for contract between them. The relation of contracts between DISCO and GENCOs are represented in matrix form named as distribution participation matrix (DPM) which is discussed in results section.

2.1 DFIG System

The impact of DFIG model under restructured system in the presence of asynchronous tie-lines is an important aspect. The operating conditions of wind generating system model influence the system frequency in large manner. Differential evaluation algorithm is used for tuning and controlling pitch control parameters. In this work, the DFIG model [12, 13] is considered in all the three areas.

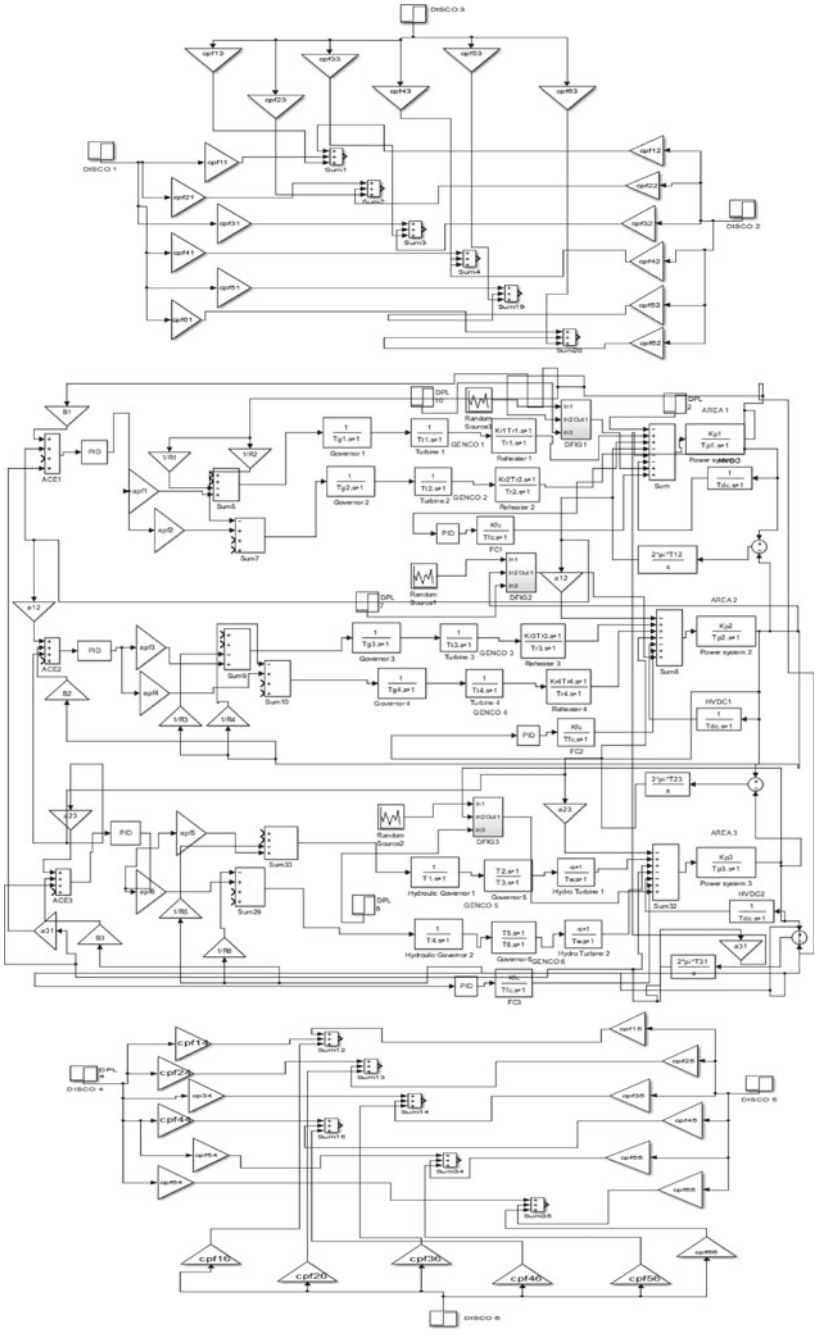

Fig. 1 Complete modeling of investigated system under deregulated domain

2.2 *Fuel Cell*

The complexity of the investigated system is increased by adding another renewable energy source named fuel cell where the power is generated through the electrochemical reaction between hydrogen and oxygen. Fuel cell is an alternative to conventional system which is having an advantage of producing power without noise [14, 15]. Fuel cell generator transfer function is approximated as first-order model and is given in Eq. (1).

$$G_{\mathrm{FC}}(S) = \frac{K_{\mathrm{FC}}}{T_{\mathrm{FC}} + 1} \tag{1}$$

Wind and fuel cell systems are participated to have a short-term active power support in open market domain which significantly improves the dynamic response of the system in case 1 and case 2. The present work is concentrated on the impact of DFIG for the optimization purpose. The detailed description of the participation given in reference [13].

3 Control Strategy

The conventional proportional–integral–derivative controller is used in this work as secondary controller since most of the literature survey suggests PID controller is acceptable for open system market. There are different optimization methods that are available in which the differential evolution (DE) technique is opted in this work which is developed by Stron and Price in 1995 for optimization problems [16, 17]. Differential evolution algorithm is a simple, efficient and mainly depends on randomly sampled pair of solutions. For setting optimum values of PID controller, the performance measure considered in this paper is integral square error (ISE) given in Eq. (2).

$$J = \mathrm{ISE} = \int_0^t \sum_{\substack{i=1 \\ j=1 \\ i \neq j}}^{n} [(\Delta f_i)^2 + \left(\Delta P_{tieij}\right)^2 \mathrm{d}t \tag{2}$$

The optimized control parameters are obtained using differential evaluation technique for investigated system without HVDC link and with asynchronous tie-line. The change in frequency and tie-line powers in all the three areas is shown in results section for unilateral and bilateral transaction scenarios.

4 Results and Discussions

The investigated system model is developed in MATLAB/Simulink environment with 10% load demand on each DISCO. The analysis and results of dynamic response plots under unilateral and bilateral scenarios are mentioned below:

Case 1, poolco-based transaction:

The disco participation matrix for poolco-based transaction is given in Eq. (3).

$$\text{DPM} = \begin{bmatrix} 0.5 & 0.5 & 0 & 0 & 0 & 0 \\ 0.5 & 0.5 & 0 & 0 & 0 & 0 \\ 0 & 0 & 0 & 0 & 0 & 0 \\ 0 & 0 & 0 & 0 & 0 & 0 \\ 0 & 0 & 0 & 0 & 0 & 0 \\ 0 & 0 & 0 & 0 & 0 & 0 \end{bmatrix} \tag{3}$$

The area participation factor for the investigated system is taken as apf1 = apf2 = apf3 = apf4 = apf5 = apf6 = 0.5. The values of PID controller parameters in all three areas for the case 1 are optimized using proposed algorithm without and with renewable energy sources and obtained as −5.85, −4.291, −4.8329, −4.1652, −12.0528, −4.2855, −0.1, −0.0989, −20.8637 and −5.7803, −4.1, −4.6618, −4.4, −12.9, −3.6, −0.2, −0.0935, −20.56, respectively. The peak values and settling time (t_s) for all control strategies are given in Table 1. The best objective values obtained from the minimization of objective function with asynchronous tie-line and along with renewable sources are 0.0056 and 0.0042, respectively.

Table 1 Dynamic response specifications

Control strategy ⇒	Without HVDC	With HVDC (QOHS-SFL)	With HVDC (DE)	With HVDC-WIND + FC (DE)
Δf_1(peak)	−0.162	−0.133	−0.1126	−0.0749
Δf_2(peak)	−0.05	−0.024	−0.0187	−0.0066
Δf_3(peak)	−0.0937	−0.02	−0.014	−0.0084
ΔP_{12}(peak)	−0.0205	−0.0146	−0.0105	−0.0082
ΔP_{23}(peak)	0.0163	−0.001	−0.0008	−0.0017
ΔP_{31}(peak)	0.021	0.0184	0.011	0.009
$\Delta f_1(t_s)$	22	15	13	11
$\Delta f_2(t_s)$	25	23	21	20
$\Delta f_3(t_s)$	23	21	20	19
$\Delta P_{12}(t_s)$	27	26	25	23
$\Delta P_{23}(t_s)$	26	25	22	20
$\Delta P_{31}(t_s)$	25	26	25	24

The responses of system investigated with wind and fuel cell for poolco-based transaction are shown in Fig. 2. The change in frequency in area 1 is settled at 13 s in asynchronous tie-line and 11 s with renewable sources compared to 22 s in AC tie-line only. Similarly, change in frequency in area 2 is settled at 21 seconds in asynchronous tie-line and 20 s with renewable sources compared to 25 s in AC tie-line only. The change in frequency in area 3 is settled at 20 s in asynchronous tie-line, 19 s with renewable sources compared to 23 s in AC tie-line only. Though there is not much difference in the settling time values after including the renewable sources, the peak values are drastically reduced results, a low frequency oscillation damping, which produces new results in open market system using powerful DE technique under asynchronous tie-line.

From the waveforms, it is clearly showing that the proposed differential evaluation algorithm produces new results where a drastically reduction in the peak values even after incorporating wind and fuel cell with asynchronous tie-line under open market domain.

Case-2, Bilateral transaction:

In this case, distribution companies have freedom to contract with any generation companies under control of independent system operator in area 1 or area 2 or area 3. The contracts relation for case 2 is represented in Eq. (4).

$$\mathrm{DPM} = \begin{bmatrix} 0.3 & 0.25 & 0 & 0.4 & 0.1 & 0.6 \\ 0.2 & 0.15 & 0 & 0.2 & 0.1 & 0 \\ 0 & 0.15 & 0 & 0.2 & 0.2 & 0 \\ 0.2 & 0.15 & 1 & 0 & 0.2 & 0.4 \\ 0.2 & 0.15 & 0 & 0.2 & 0.2 & 0 \\ 0.1 & 0.15 & 0 & 0 & 0.2 & 0 \end{bmatrix} \tag{4}$$

The values of PID controller parameters in all three areas for the case 2 are optimized using proposed algorithm without and with renewable energy sources and obtained as −5.1448, −2.925, −3.4004, −3.1331, −11.664, −3.3957, −0.1047, −0.1339, −20.972 and −4.9036, −3.2066, −3.5027, −3.6957, −11.2, −3.8221, -0.15, −0.104, −20.6642, respectively. The peak values and settling time (t_s) for all control strategies are given in Table 2. The best objective values obtained from the minimization of objective function with asynchronous tie-line and along with renewable sources are 0.7385 and 0.6527, respectively.

The responses of system investigated with DFIG model and fuel cell for bilateral transaction are shown in Fig. 3. The frequency change in area 1 is settled at 12 s in asynchronous tie-line and 11 s with renewable sources compared to 18 s in AC tie-line only. Similarly, change in frequency in area 2 is settled at 16 seconds in asynchronous tie-line and 15 s with renewable sources compared to 18 s in AC tie-line only. The frequency change in area 3 is settled at 14 seconds in asynchronous tie-line and 13 s with renewable sources compared to 18 s in AC tie-line only. Also,

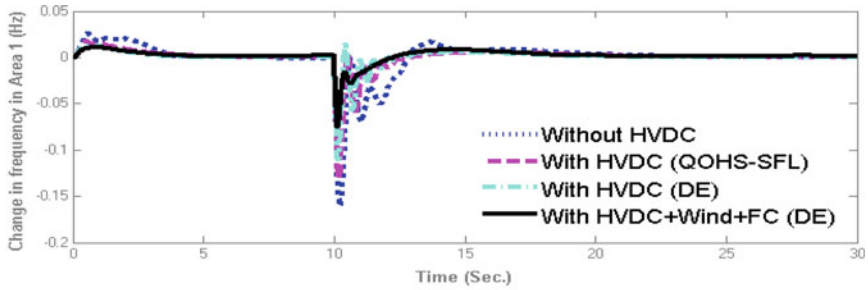

(a) Δf_1

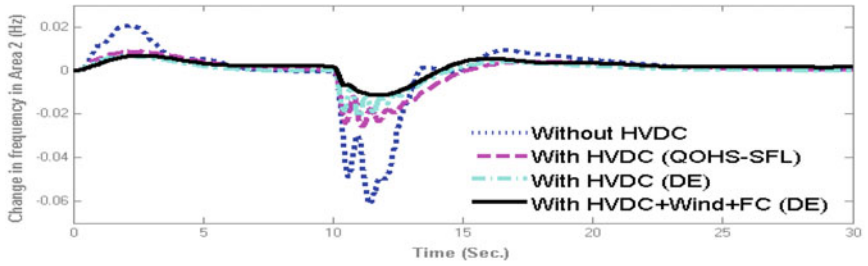

(b) Δf_2

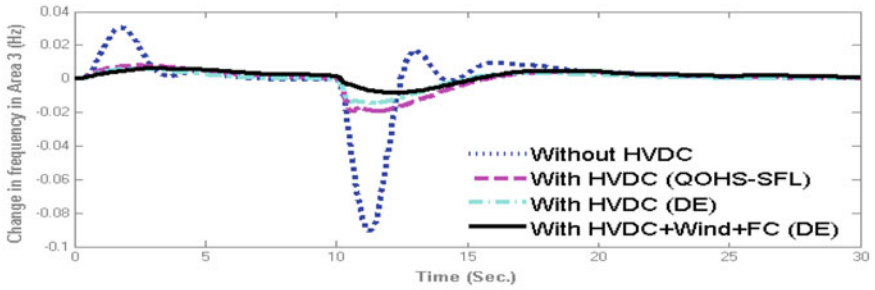

(c) Δf_3

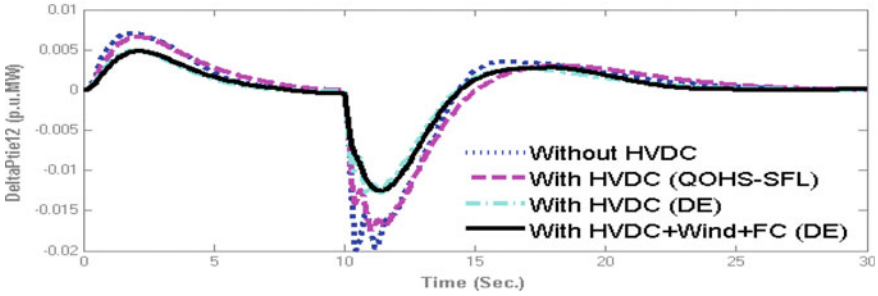

(d) $\Delta Ptie_{12}$

Fig. 2 Response plot of frequency and tie-line power

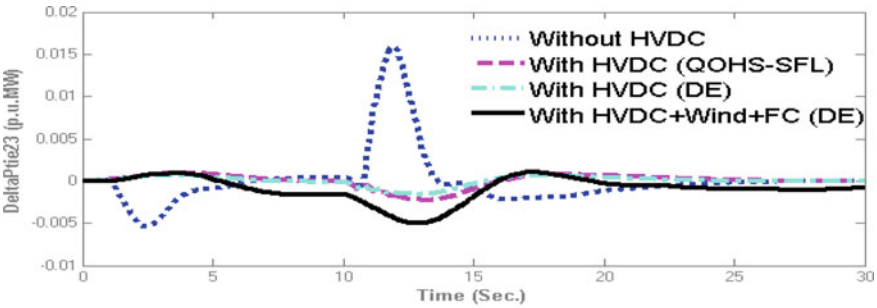

(e) $\Delta Ptie_{23}$

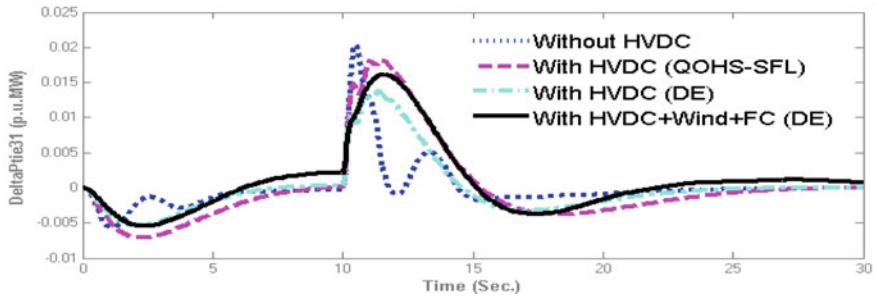

(f) $\Delta Ptie_{31}$

Fig. 2 (continued)

Table 2 Dynamic response specifications

Control strategy ⇒	Without HVDC	With HVDC (QOHS-SFL)	With HVDC (DE)	With HVDC-WIND + FC (DE)
Δf_1(peak)	−0.265	−0.0673	−0.06	−0.018
Δf_2(peak)	−0.23	−0.0675	−0.055	−0.019
Δf_3(peak)	−0.58	−0.1876	−0.1865	−0.0575
ΔP_{12}(peak)	−0.038	−0.0245	−0.0225	−0.02
ΔP_{23}(peak)	0.184	0.075	0.075	0.0495
ΔP_{31}(peak)	−0.157	−0.06	−0.058	−0.034
$\Delta f_1(t_s)$	18	12	12	11
$\Delta f_2(t_s)$	18	17	16	15
$\Delta f_3(t_s)$	18	15	14	13
$\Delta P_{12}(t_s)$	28	26	25	22
$\Delta P_{23}(t_s)$	20	19	18	15
$\Delta P_{31}(t_s)$	27	25	24	22

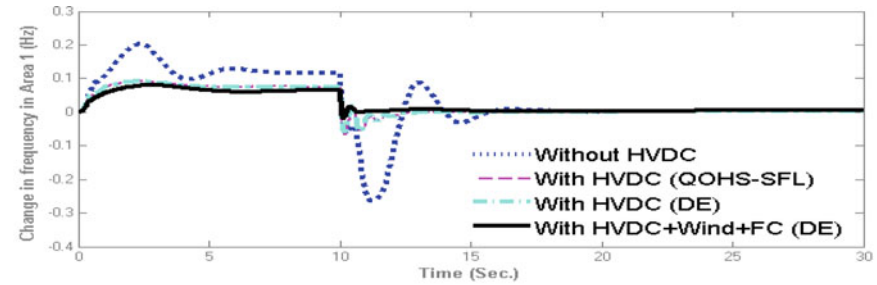

(a) Δf_1

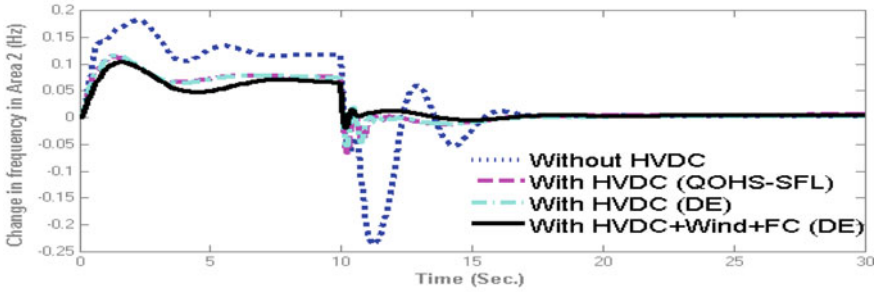

(b) Δf_2

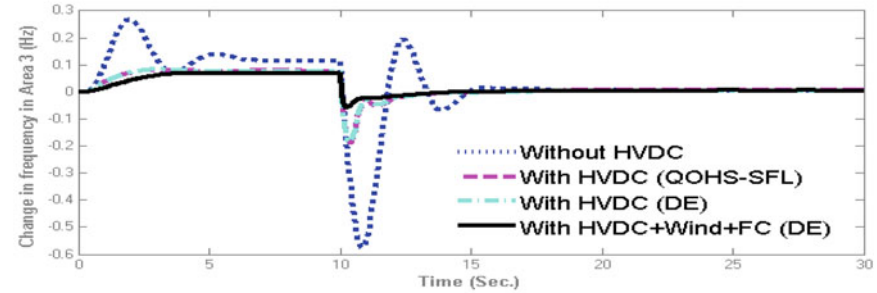

(c) Δf_3

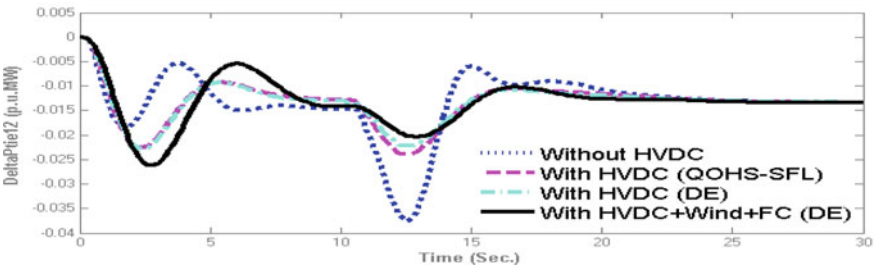

(d) $\Delta Ptie_{12}$

Fig. 3 Response plot of frequency and tie-line power

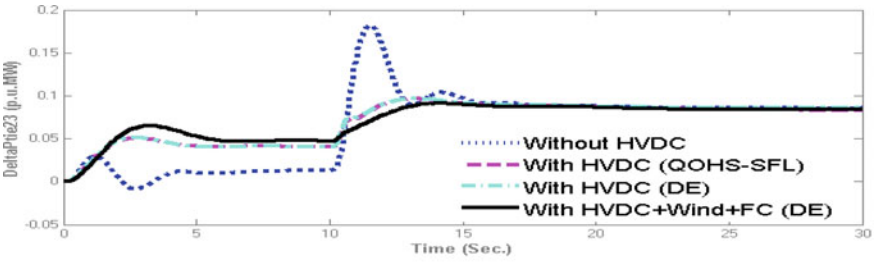

(e) $\Delta Ptie_{23}$

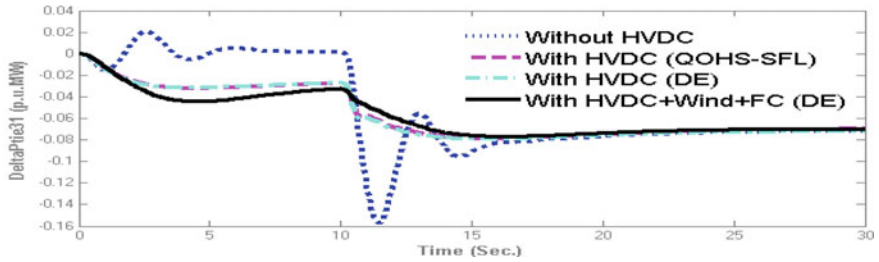

(f) $\Delta Ptie_{31}$

Fig. 3 (continued)

the peak values are reduced even after including the renewable energy sources using powerful DE technique under asynchronous tie-line.

5 Conclusion

This work discusses the contribution of the combination of wind system and fuel cell in area frequency control of three-area six-source interconnected power system with asynchronous tie-line under open market scenario. Differential evaluation algorithm is used for optimizing the controller parameters. The observations from the results show that the powerful differential evaluation algorithm improves the dynamic response leads to reduction in the peak values and settling time after inserting renewable energy sources with combination of DFIG model and fuel cell.

References

1. Saadat H (2002) Power system analysis. Tata McGraw- Hill Edition
2. Chandra Sekhar GT, Sahu RK, Baliarsingh AK, Panda S (2016) Load frequency control of power system under deregulated environment using optimal firefly algorithm. Int J Electr Power Energy Syst Sci Direct 74:195–211

3. Shiva CV, Mukherjee V (2016) A novel quasi-oppostional harmony search algorithm for AGC optimization of three- area multi- unit power system after deregulation. Eng Sci Technol Int J 19:395–420
4. Srinivasa Rao C, Naghizadeh Z, Mahdavi S (2008) Improvement of dynamic performance of hydrothermal system under open market scenario using asynchronous tie-lines. World J Modell Simul 4(2): 153–160. ISSN 1 746-7233
5. Arya Y, Kumar N (2016) AGC of a multi-area multi- source hydrothermal power system interconnected via AC/DC parallel links under deregulated environment. Electr Power Energy Syst 75:127–138
6. Prakash A, Murali S, Shankar R, Bhushan R (2019) HVDC tie-link model ing for restructured AGC using a novel fractional order cascade controller. Electr Power Syst Res Sci Direct 170:244–258
7. Bengiamin N, Wang L, Salehfar H (2000) Assessment of automatic generation control in deregulated environment. IEEE Power Eng Soc Winter Mtg 2:1331–1336
8. Sahu RK, Panda S, Rout UK (2013) DE optimized parallel 2-DOF PID controller for load frequency control of power system with governor dead-band nonlinearity. Int J Electr Power Energy Syst 49(1):19–33
9. Parmar KPS, Majhi S, Kothari DP (2014) LFC of an interconnected power system with multi-source power generation in deregulated power. Environ. Int J Electr Power Energy Syst 57:277–286
10. Kumar J, Ng K-H, Sheble G (1997) AGC simulator for price- based operation: Part- II. IEEE Trans Power Syst 12(2):533–538
11. Tyagi B, Srivastava SC (2006) A decentralized automatic generation control scheme for competitive electricity markets. IEEE Trans Power Syst 21:312–319
12. Supriyadi C, Nandar A (2013) Robust PI control of smart controllable load for frequency stabilization of microgrid power system. Renew Energy 56:16–23
13. Bhatt P (2014) Short term active power support from DFIG with coordinated control of SSSC and SMES in restructured power system. 978-1-4799-7537-2/14/$31.00 ©2014 IEEE.
14. Amin H, Golkar Masoud A (2010) Control of hybrid fuel cell/energy storage distributed generation system against voltage sag. Int J Electr Power Energy Syst 32(5):488–497
15. Wang C, Nehrir MH (2008) Power management of stand-alone wind/photovoltaic/fuel cell energy system. IEEE Trans Energy Conver 23(3):957–967
16. Price K, Storn R (1996) Minimizing the real functions of the ICEC'96 contest by differential evolution. In: IEEE international conference on evolutionary computation (ICEC'96), May 1996, pp 842–844
17. Mahanthi B, Panda S, Hota PK (2014) Controller parameters tuning of differ ential evealution algorithm and its application to load frequency control of multi-source power system. Int J Electr Power Energy Syst Sci Direct 54(9): 77–85

Performance Analysis of PID Controller and Sliding Mode Control for Electric Vehicle Applications in Interleaved Double Boost Converter

J. S. V. Siva Kumar and P. Mallikarjuna Rao

Abstract The impacts of a global temperature rise are becoming extreme with increased carbon emanations in weather. For this reason, people in the automotive industry are paying more attention to green technology—hybrid electric vehicles. Among the green technology available, the fuel cell has a higher energy density but it is costly. In view among this, it is important to infer a valid scheme to use energy efficiently to make electric vehicles rational. Because of the fuel cell's low voltage output, boost converters are used to meet the load demands. Interleaved double boost (IDDB) converters are recommended to improve converter efficiency and, in turn, to minimize vehicle overall weight. In this paper, the control technique for both PID and sliding mode is implemented to improve the transient response of the IDDB converter operated by the fuel cell for different load conditions. In addition, they compare the performance of both controllers. In the simulated environment, IDDB converter output voltages, output currents, and input currents with sliding mode and PID controller are obtained and tested using MATLAB/Simulink.

Keywords Hybrid electric vehicles · Fuel cell · IDDB converter · High voltage gain · PID and sliding mode controller

1 Introduction

One of the key reasons for introducing electric vehicles on the market is the concern about greenhouse gas emissions and their contribution to global warming. In any event, the use of petroleum derivatives and carbon-based mixtures, in vehicles, results

J. S. V. S. Kumar (✉)
Department of EEE, GMR Institute of Technology , Rajam, Andhra Pradesh 532127, India
e-mail: jsvsivakumar99@gmail.com; electricalprofessor@gmail.com

J. S. V. S. Kumar · P. Mallikarjuna Rao
Department of Electrical Engineering, Andhra University, Visakhapatnam, Andhra Pradesh 530003, India

G. T. C. Sekhar et al. (eds.), *Intelligent Computing in Control and Communication*,
Lecture Notes in Electrical Engineering 702,
https://doi.org/10.1007/978-981-15-8439-8_5

in enormous ozone-depleting substances. A significant portion of the thickly populated urban areas are faced with poor air quality, as demonstrated by a few examinations. Interestingly, electric cars use electrical energy to operate in an environmentally friendly way [1]. Electrical vehicles use battery, fuel cell (FC), and ultra-capacitor, as energy source for the propulsion system. Of these, fuel cell was shown to be a superior decision as an integral source of energy in EV, due to the high power density and renewable source of electrical energy. Due to FC's slower response, however, they cannot respond faster to unexpected load changes, and therefore an ultra-capacitor is suggested for propulsion during dynamic condition. Ultra-capacitors have high energy density but low power densities, allowing them to charge and discharge at a quicker rate. This design allows the ultra-capacitor to supply energy during transients [1].

Usually, FC voltage level is extremely low, but high voltage is required to run the vehicle. Therefore, to boost the FC voltage level, a step-up chopper is required. Maintaining high performance at such voltage gain criteria is quite a challenging task [2, 3]. Low-input voltage results in high input current for a given power [2–6]. This high current enforces the boost converter to work on a short duty cycle that affects inductor size and capacitor performance, resulting in increased losses and reduced capacity. Therefore, for high-power applications, such as EV, a high-power converter is required to improve the FC voltage level, which can handle high-power and high-voltage input and output without affecting efficiency, respectively. The most successful way to solve this issue is by making multiple traditional boost converters interleave.

This paper verifies the feasibility of the proposed interleaved double boost with the goal of achieving higher voltage gain compared with the classic boost converter, [7–9]. Among other things, this topology has been selected with high gaining properties due to the possibility of phase interleaving enabling the flexible characteristics of the converter for high-power applications.

An appropriate controller is required to regulate the nominal value of the output voltage even under load disturbances usually occurring in electric vehicles[10–13]. In this paper, sliding mode and PID-based controller are tested for IDDB converter and the output voltages, currents, and input currents are tested and compared using MATLAB/Simulink in simulation environment.

2 N-Phase IDDB Converter Modeling

The two-phase IDDB is described in Fig. 1, where "R_O" stands for load. There is an inductor in traditional boost module and its corresponding switch pair in each step of the converter. "Module-1" is Phase 1 and capacitor C_1 whereas "module-2" is Phase 2 and capacitor C_2 and both the modules are assumed to be symmetric.

This topology, as pointed out, promotes modular structure allowing for more than two phases. An even several phases are favored for achieving symmetry. This section is intended to generalize the modeling of converters to topology in N-phase.

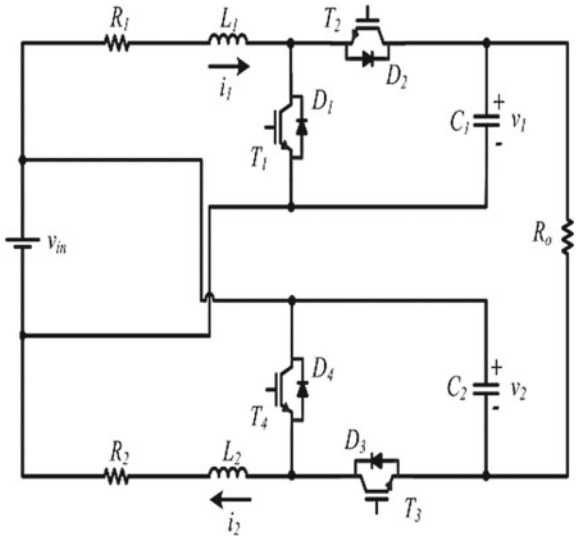

Fig. 1 Two-phase IDDB

For module-2, the combination of the stages attached to the C_1 capacitor and the C_2 capacitor itself forms module-1 and vice versa. The six-phase converter is indicated in Fig. 2, as a demonstration to represent multiple stages. The source current is given by Eq. (1):

$$i_{\text{in}} = i_1 + i_2 + i_3 + \cdots + i_N - i_0 \tag{1}$$

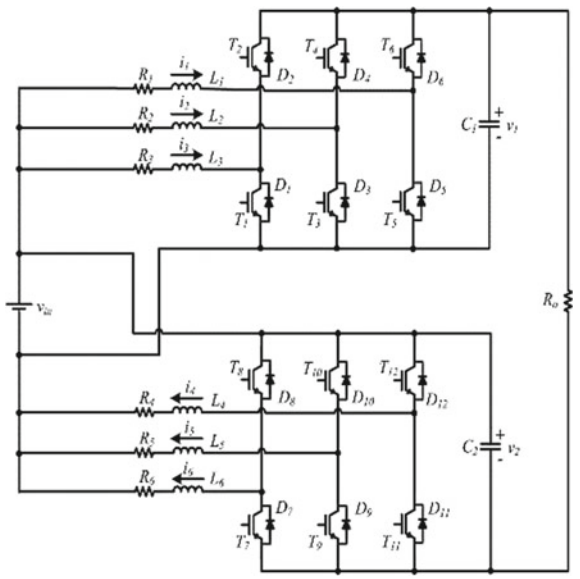

Fig. 2 Six-phase IDDB converter

The IDDB N-phase has state variables of $N + 2$, here the inductor currents representing "N" and two capacitor voltages are chosen.

The current differential equation in each of the module-1$N/2$ inductors is given by

$$\frac{\mathrm{d}}{\mathrm{d}t} I_k = \frac{1}{L_k}\left(-R_k I_k - V_1 \bar{\delta}_k + V_{\text{in}}\right) \tag{2}$$

for $k = 1, 2, 3 \ldots, N/2$. Correspondingly for $k = (N/2) + 1$ to N.

V_1 gives the differential equation for the voltage at C_1

$$\frac{\mathrm{d}}{\mathrm{d}t} V_1 = \frac{1}{C_1}\left[\left(\sum_{k=1}^{\frac{N}{2}} I_k \bar{\delta}\right) + \frac{-V_1 - V_2 + V_{\text{in}}}{R_0}\right] \tag{3}$$

Similar expression will be obtained for the voltage across C_2 by using Eqs. (2) and (3).

Exploring the symmetry of the above-described system (Fig. 1), it can be generalized for N-phase system, then $I_1 = I_2 = \ldots = I_N = I$ and $\delta_1 = \delta_2 = \ldots = \delta_N = \delta$

$$\frac{\mathrm{d}}{\mathrm{d}t} I = \frac{1}{L}\left(-RI - V\bar{\delta} + V_{\text{in}}\right) \tag{4}$$

$$\frac{\mathrm{d}}{\mathrm{d}t} V = \frac{1}{C}\left[\frac{\left(N\bar{\delta} I\right)}{2} + \frac{-2V + V_{\text{in}}}{R_0}\right] \tag{5}$$

The state vector in the state-space form is

$$X = \begin{bmatrix} I & V \end{bmatrix}^I \tag{6}$$

By using Equations from (1) to (6), the input and function matrices can be written as

$$A = \begin{bmatrix} -\frac{R}{L} & -\frac{\bar{\delta}}{L} \\ \frac{N\bar{\delta}}{2C} & \frac{-2}{R_o C} \end{bmatrix} \quad B = \begin{bmatrix} \frac{1}{L} \\ \frac{1}{R_o C} \end{bmatrix} \tag{7}$$

The set of achievable equilibrium points for the converter is provided by

$$X_{\text{eq}} = -A^{-1} B U \tag{8}$$

where $U = [v_{\text{in}}]$ and from above, Eqs. (7) and (8) the set of points of equilibrium can be as

$$X_{\text{eq}} = \begin{bmatrix} I_{\text{eq}} \\ V_{\text{eq}} \end{bmatrix} = \begin{bmatrix} \frac{2+2\delta}{4R+NR_0(1-\delta)^2} \\ \frac{2R+NR_0(1-\delta)}{4R+NR_0(1-\delta)^2} \end{bmatrix} \tag{9}$$

The equivalent linear system near the equilibrium point is given by using the state-space averaging method, and assuming the small-signal approximation

$$\dot{\tilde{x}} = A\tilde{x} + [(A_1 - A_2)X + (B_1 - B_2)U]\tilde{\delta} \tag{10}$$

In Eq. (10), A_1 is the matrix when δ value for 1 and A_2 is the matrix when δ value for 0, respectively, and $B_1 = B_2$, X is equilibrium point and the above values can be used to simplify the equation.

$$\dot{\tilde{x}} = A\tilde{x} + [(A_1 - A_2)X]\tilde{\delta} \tag{11}$$

Finally, after substituting of all the above values in Eqs. (9) and (11), the expression becomes as shown in Eq. (12)

$$\dot{\tilde{x}} = \begin{bmatrix} \dot{\tilde{i}} \\ \dot{\tilde{v}} \end{bmatrix} = \begin{bmatrix} \frac{-R}{L}\tilde{i} - \frac{\bar{\delta}}{L}\tilde{v} + \frac{V_{\text{in}}}{L}\left\{\frac{2R+NR_0(1-\delta)}{4R+NR_0(1-\delta)^2}\right\}\tilde{\delta} \\ \frac{N\bar{\delta}}{2C}\tilde{i} - \frac{2}{R_0C}\tilde{v} - \frac{NV_{\text{in}}}{2C}\left\{\frac{(2+2\delta)}{4R+NR_0(1-\delta)^2}\right\}\tilde{\delta} \end{bmatrix} \tag{12}$$

The linearized system transfer functions around the point of operation are given by

$$H(s) = (sI - A)^{-1}(A_1 - A_2)X_{\text{eq}} \tag{13}$$

Expression (13) can turn into

$$\begin{bmatrix} G_{id}(s) \\ G_{vd}(s) \end{bmatrix} = \begin{bmatrix} \frac{(2R_0CV_{\text{eq}})s+\left[4V_{\text{eq}}+NR_0(1-\delta)I_{\text{eq}}\right]}{2R_0LCs^2+(2RR_0C+4L)s+4R+NR_0(1-\delta)^2} \\ \frac{-NR_0LI_{\text{eq}}s-NI_{\text{eq}}RR_0+NR_0(1-\delta)V_{\text{eq}}}{2R_0LCs^2+(2RR_0C+4L)s+4R+NR_0(1-\delta)^2} \end{bmatrix} \tag{14}$$

where $G_{id}(s) = I(s)/\Delta(s)$ and $G_{vd}(s) = V(s)/\Delta(s)$ from Eq. (14), the transfer function $G_{vi}(s) = V(s)/I(s)$ can be applied in relation to current, voltage as

$$G_{vi}(s) = \frac{V(s)}{I(s)} = \begin{bmatrix} \frac{-NR_0LI_{\text{eq}}s - NI_{\text{eq}}RR_0 + NR_0(1-\delta)V_{\text{eq}}}{(2R_0CV_{\text{eq}})s + \left[4V_{\text{eq}} + NR_0(1-\delta)I_{\text{eq}}\right]} \end{bmatrix} \tag{15}$$

3 Controller Design

In addition, due to high current and low performance, high duty cycle values were unacceptable, and thus the duty cycle was reduced to 0.85. A nominal equilibrium point, which belongs to the set defined by Eq. (9), is selected for calculating the small-signal model of the converter.

Using the current mode control [8], the control loops can be built using the transfer function of the current to the duty cycle as shown in Eq. (14) and the voltage to current provided in Eq. (15).

The current controller (inside loop) determines the duration of the duty cycle. The voltage controller produces the average reference current. Figure 3 shows the voltage control diagram displayed in one module, and the current in one stage.

The current duty cycle transfer function of (14) is evaluated using the parameters given below, resulting in the transfer function described in Eq. (16).

$$G_{id}(s) = \frac{I(s)}{\Delta(s)} = \frac{407 \times 10^3 (s + 134.3)}{s^2 + 352.5s + 8.9 \times 10^5} \tag{16}$$

The voltage controller and the current controller are preferred as an PI controller along with a low-pass filter. The transfer function of the controller is given by the

$$G_{pi}(s) = \left(k_p + \frac{k_i}{s}\right)\left(\frac{\omega_p}{s + \omega_p}\right) = \frac{k_i}{s}\left(\frac{s + \omega_z}{\omega_z}\right)\left(\frac{\omega_p}{s + \omega_p}\right) \tag{17}$$

Everywhere the proportional gain is k_p, the integral gain is k_i, the pole angular frequency is ω_p, and the zero angular frequency is $\omega_z = k_i/k_p$.

The closed-loop cutoff frequency $f_{ci} = 1$ kHz and the phase margin $PM_i = 80°$ are selected. The resulting parameters are $k_{ic} = 1002$ rad/s, $\omega_{zc} = 6637$ rad/s, $\omega_{pc} = 59{,}479$ rad/s are determined by using K-factor method. From this, the transfer function of voltage to current is determined and utilized in the design of voltage controller Eq. (17).

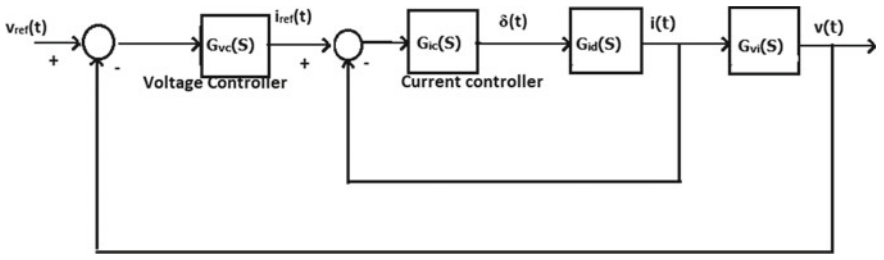

Fig. 3 Control loop of each module

$$G_{vi}(s) = \frac{V(s)}{I(s)} = \frac{-0.123\left(s - 1.37 \times 10^4\right)}{s + 134.3} \tag{18}$$

Cutoff frequency $f_{cv} = 100$ Hz and the phase margin $PM_v = 80°$ of the closed loop are chosen. The resulting parameters are $k_{iv} = 40.9$ rad/s, $\omega_{zv} = 107.7$ rad/s, $\omega_{pv} = 3667$ rad/s are determined by using K-factor method in Eq. (18).

4 Sliding Mode Controller Methodology

The inductors reference currents are obtained by applying limited analysis of the signal. The feedback controller is designed to provide good response. A sliding mode controller is designed because of the converter's fast and robustness requirement, which is a large signal model, resulting in global stability. A sliding surface is described by

From this $S = \tilde{v} + k\tilde{i}$ then $\dot{S} = \dot{\tilde{v}} + k\dot{\tilde{i}}$

$$\begin{aligned}\dot{S} = {} & \frac{N\bar{\delta}}{2C}\tilde{i} - \frac{2}{R_0 C}\tilde{v} - \frac{NV_{in}}{2C}\left\{\frac{(2+2\delta)}{4R + NR_0(1-\delta)^2}\right\}\tilde{\delta} \\ & + k\left[\frac{-R}{L}\tilde{i} - \frac{\bar{\delta}}{L}\tilde{v} + \frac{V_{in}}{L}\left\{\frac{2R + NR_0(1-\delta)}{4R + NR_0(1-\delta)^2}\right\}\right]\tilde{\delta}\end{aligned} \tag{19}$$

From Eq. (19)$\tilde{v}$, $\tilde{i}$ and $\tilde{\delta}$ terms are separated, then

$$\begin{aligned}\dot{S} = {} & \frac{N\bar{\delta}}{2C}\tilde{i} - \frac{2}{R_0 C}\tilde{v} - k\frac{R}{L}\tilde{i} - k\frac{\bar{\delta}}{L}\tilde{v} \\ & + \left[k\frac{V_{in}}{L}\left\{\frac{2R + NR_0(1-\delta)}{4R + NR_0(1-\delta)^2}\right\} - \frac{NV_{in}}{2C}\left\{\frac{(2+2\delta)}{4R + NR_0(1-\delta)^2}\right\}\right]\tilde{\delta}\end{aligned} \tag{20}$$

Can reflect the above equation as $\dot{S} = f(x) + u$ when $\dot{S} = 0$ then the sliding mode is existing generally representation of control structure with $u = -f(x) - k_1 \text{sign}(S)$ controlling signal $\tilde{\delta}$ is obtained by using Eq. (20) and above

$$\tilde{\delta} = \frac{\left[\left\{-\frac{N\bar{\delta}}{2C}\tilde{i} + \frac{2}{R_0 C}\tilde{v} + k\frac{R}{L}\tilde{i} + k\frac{\bar{\delta}}{L}\tilde{v}\right\} - k_1 \text{sign}(s)\right]}{\left[k\frac{V_{in}}{L}\left\{\frac{2R+NR_0(1-\delta)}{4R+NR_0(1-\delta)^2}\right\} - \frac{NV_{in}}{2C}\left\{\frac{(2+2\delta)}{4R+NR_0(1-\delta)^2}\right\}\right]} \tag{21}$$

The implemented controller Eq. (21) function diagram is shown in Fig. 4. Where V_1 and V_2 are the capacitor voltages of module-1 and module-2, respectively. The i_1, i_2, i_3, i_4, i_5 and i_6 are phase currents, respectively. V_1 is the input of the DC connection voltage to the module-1 SM controller, while V_2 is for the module-2. Similarly, i_1, i_2 and i_3 are the inputs to module-1 and i_4, i_5 and i_6 are the inputs to

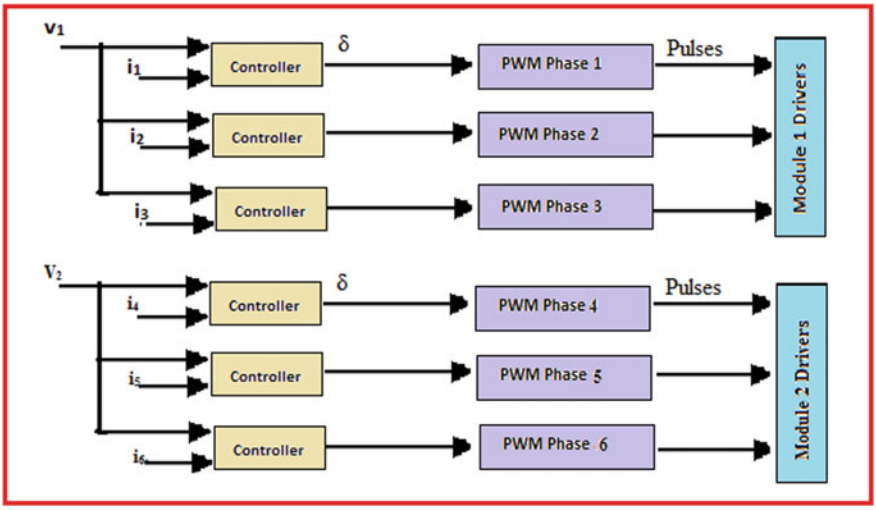

Fig. 4 SM control diagram for the modules

module-2 SM controllers. SMC output is duty cycle and is used for the generation of PWM pulses to operate the switches in the converter.

5 Results and Conversation

The IDDB converter is modeled, and its device output is tested on MATLAB/Simulink by using sliding mode and PID controllers. Below are the effects of the entire system parameters. Simulation results are described in these two phases and six-step IDDB converters with Sliding mode and PID-based controllers. The nominal parameters are $V_{\text{in}} = 60$ V, $R = 0.15\ \Omega$, $L = 535\ \mu$H, $C = 470\ \mu$F, $R_{\text{o}} = 59\ \Omega$, $f_{\text{sw}} = 10$ kHz $\delta = 0.73$, $V_{\text{eq}} = 217.9$ V, and $I_{\text{eq}} = 7.86$ A are considered for simulation [8].

The inductor current of the two phases of sliding mode and PID controllers are presented in Figs. 5 and 6. Clearly, it is observed that the current ripples in each inductor of 7A in SM and 9 A in PID-based controller of IDDB.

The output current flowing through the load of the sliding mode and PID-based controllers-based two-phase IDDB are presented in Figs. 7 and 8. It is clearly identified that in the SM control, the output current is nearly 7A whereas 6A in PID-based controller IDDB. From this, for the same input voltage, sliding mode controller is giving more output current as compared to PID-based control of IDDB converter.

The output voltage across the load of the sliding mode and PID-based controllers-based two-phase IDDB is presented in Figs. 9 and 10. It is clearly observed that the output voltage across load in SM is nearly 450 V whereas 380 V in PID-based

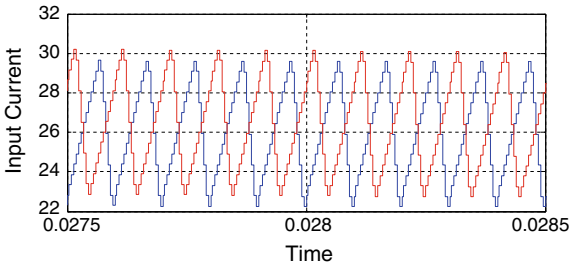

Fig. 5 Two-phase IDDB Input current with SM

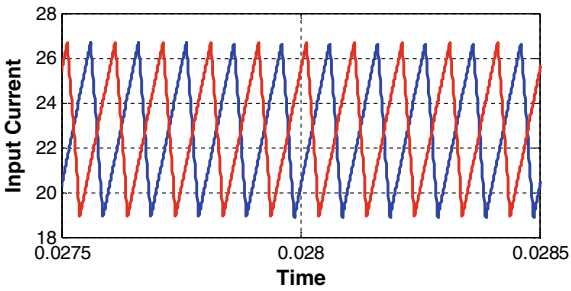

Fig. 6 Two-phase IDDB Input current with PID

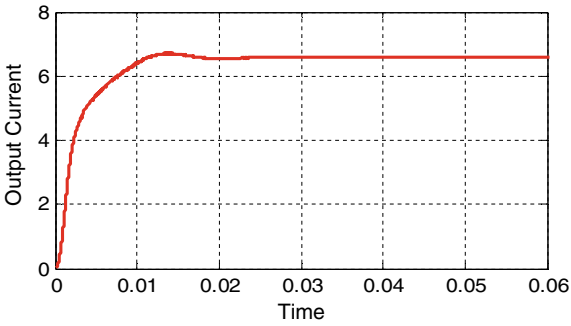

Fig. 7 Output current to two-phase IDDB with SM IDDB

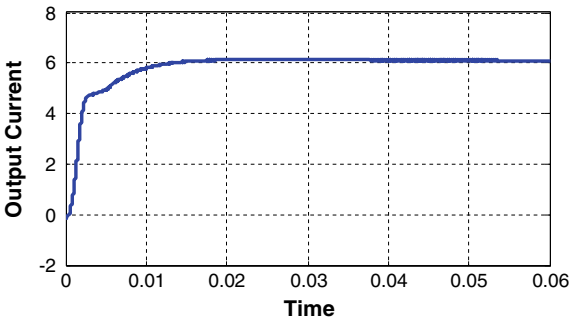

Fig. 8 Output current to two-phase With PID

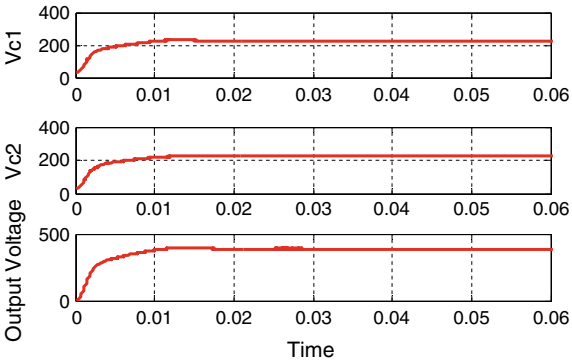

Fig. 9 Output voltage of two-phase IDDB with SM

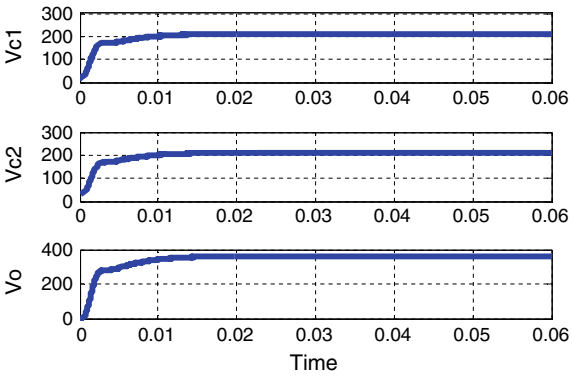

Fig. 10 IDDB output voltage of with PID

controller IDDB. From this, for the same input voltage, sliding mode controller is giving more output Voltage as compared to PID-based control of IDDB converter.

The inductor current of the six phases of sliding mode and PID-based controllers are presented in Figs. 11 and 12. It is clearly observed that the current in each inductor has a current ripple of 7 A in SM and 9 A in PID-based controller IDDB. But the magnitude of the input current through the inductor decreases with the increasing

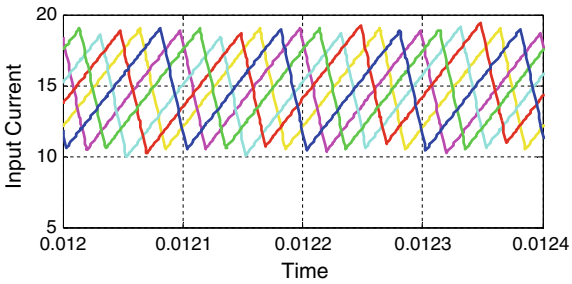

Fig. 11 Six-phase IDDB input current with SM

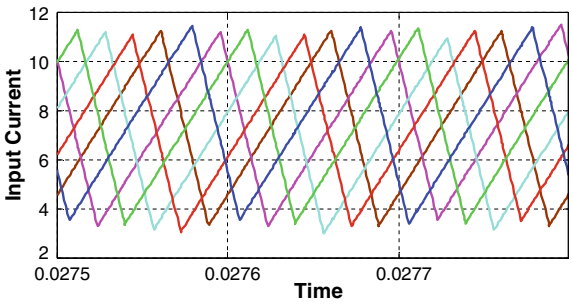

Fig. 12 Six-phase IDDB input current with PID

number of phases. In two-phase, its value is nearly 30 A whereas in six-phase the value is 18A only.

The output current through the load of the sliding mode and PID-based controllers-based six-phase IDDB are presented in Figs. 13 and 14. It is observed that the output current in load in SM is nearly 9 A whereas 6 A in PID-based controller IDDB. From this, for same input voltage, sliding mode controller is giving more output current as compared to PID-based control of IDDB. In addition, these values are more as compared to two-phase IDDB.

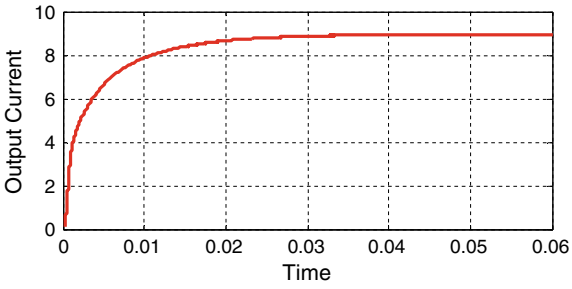

Fig. 13 Six-phase IDDB output current with SM

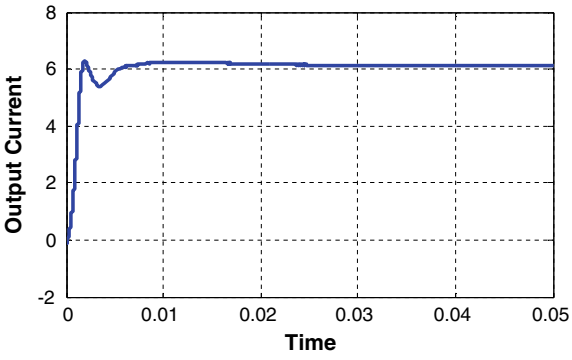

Fig. 14 Six-phase IDDB output current with PID

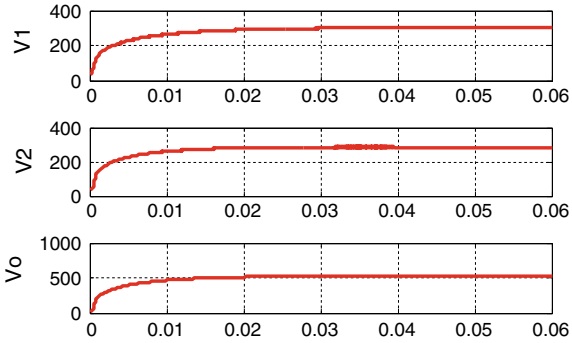

Fig. 15 Six-phase IDDB output voltage with SM

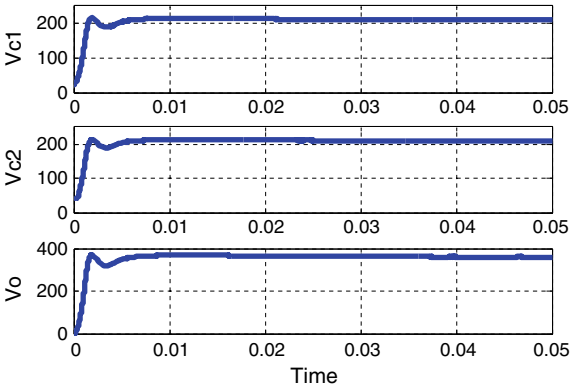

Fig. 16 Six-phase IDDB output voltage with PID

The output voltage across the load of the sliding mode and PID-based controllers-based six-phase IDDB are presented in Figs. 15 and 16. It is clearly observed that the output voltage across load in SM is nearly 500 V whereas 400 V in PID-based controller IDDB. From this, for same input voltage, sliding mode controller giving more output voltage as compared to PID-based control of IDDB. In addition, these values are more as compared to two-phase IDDB.

6 Conclusions

This paper briefed the general IDDB converter with *N*-phase small-signal analysis and simulation. Sliding mode and PID-based control mechanism for this converter are demonstrated both for two and six phases. From the tests, it is apparent that the power handling capacity of the converter is found to increase as the number of phases increases. Therefore, the converter can be upgraded according to the load requirements, with more phases. The converter symmetry and control behavior are used to reduce the model's complexity. In comparison, sliding mode controller compared

to PID-based controller is robust in design. In support of the theoretical research, simulation results were given in MATLAB/Simulink. In future, this DC output will be connected to the inverter to test electric vehicle performance.

References

1. El Fadil H, Giri F, Ieee SM, Guerrero JM, Member S (2014) Modeling and nonlinear control of FC/super capacitor hybrid energy storage system for electric vehicles. IEEE Trans Veh Technol 63(7):3011– 3018
2. Shahin A, Hinaje M, Martin J-P, Pierfederici S, Rael S, Davat B (2010) High voltage ratio dc–dc converter for fuel-cell applications. IEEE Trans Ind Electron 57(12):3944–3955
3. Yang LS, Liang TJ, Lee HC, Chen JF (2011) Novel high step-up dc–dc converter with coupled-inductor and voltage-doubler circuits. IEEE Trans Ind Electron 58(9):4196–4206
4. Kumar, Siva JSV, Mallikarjuna Rao P (2017) Design and simulation of front end converter for fuel cell based electric vehicle applications. In: 2017 IEEE international conference on power, control, signals and instrumentation engineering (ICPCSI). IEEE
5. Kumar, JSV Siva, Mallikarjunarao P (2019) Design and simulation of a DC–DC converter for fuel cell-based electric vehicles with closed-loop operation. Soft computing in data analytics. Springer, Singapore, pp 387–396
6. Siva Kumar JSV, Venkata Sateesh P (2017) Design and simulation of a current fed full bridge voltage doubler converter with high voltage gain for fuel cell based electric vehicle. J Adv Res Dyn Control Syst 9(16):110–121
7. Thounthong P, Sethakul P, Davat B (2009) Modified 4-phase interleaved fuel cell converter for high-power high-voltage applications. In: Proceedings of IEEE international conference on industrial technology, pp 1–6
8. Garcia FS, Pomilio JA, Spiazzi G (2010) Modeling and control design of the six-phase interleaved double dual boost converter. In: Proceedings of 9th IEEE/IAS international conference industrial applications, pp 1–6
9. Choi S, Agelidis VG, Yang J, Coutellier D, Marabeas P (2011) Analysis, design and experimental results of a floating- output interleaved-input boost-derived dc–dc high-gain transformer-less converter. IET Power Electron 4(1):168–180
10. Yang J, Li S, Yu X (2013) Sliding-mode control for systems with mismatched uncertainties via a disturbance observer. IEEE Trans Indus Electron 60(1): 160–164
11. Adirak K, Ekkachai M (2019) An improved back stepping sliding mode control for power systems with superconducting magnetic energy storage system. Int J Innov Comput Inf Control 15(3):891–904
12. Bouziane HA, Bouiadjra RB, Debbat MB (2015) Design of robust LQR control for DC-DC multilevel boost converter. In: The 2015 4th international conference on electrical engineering (ICEE), 13–15 Dec 2015
13. Kanchanaharuthai A, Mujjalinvimut E (2019) An improved backstepping sliding mode control for power systems with superconducting magnetic energy storage system. Int J Innov Comput Inf Control 15(3):891–904

A Comparative Study of Unit Commitment Problem by Dynamic Programming and Genetic Algorithm

R. Krishna Mohan, M. Gopichand Naik, and S. Rajendra Prasad

Abstract Unit commitment (UC) is a famous problem in electrical power systems which desire the minimization of total power generation cost at a specific period by determining acceptable scheduling of the generation units. Several methodologies and algorithms have been proposed to solve the UC problem. This research provides a blend of unit commitment problem implemented with genetic algorithm and the dynamic programming and also describes the best technique in solving the same. This problem involves an optimization task that involves schedule ON/OFF of generating units that satisfy various constraints for minimum cost generation of load demand at an hour. This problem improves network reliability and yields a technique to decrease the generation cost. The short-term unit commitment approach requires a quick technique to reduce system changes and scheduled errors. The definite solution for this problem can be achieved by the entire combination of all appropriate generating different combinations focusing on cost optimization. Genetic algorithms are stochastic search algorithms; they will maintain the population solutions to a problem in an encoded form so that the information will evolve in time. The optimal outcomes from the unit commitment problem for this technique are compared with the standard IEEE 10-unit system data.

Keywords Optimization · Economic dispatch · Dynamic programming · Unit commitment · Genetic algorithm

R. Krishna Mohan (✉) · M. Gopichand Naik · S. Rajendra Prasad
Department of Electrical Engineering, Andhra University, Visakhapatnam, Andhra Pradesh 530003, India
e-mail: rkrishnamohan1@gmail.com

M. Gopichand Naik
e-mail: professor.gopichand@gmail.com

S. Rajendra Prasad
e-mail: rajendra29.eee@gmail.com

G. T. C. Sekhar et al. (eds.), *Intelligent Computing in Control and Communication*, Lecture Notes in Electrical Engineering 702,
https://doi.org/10.1007/978-981-15-8439-8_6

Abbreviations

TPC	Total production cost
P_{mq}	The generation yield of mth unit at qth hour
$\mathrm{FC}_m(P_{mq})$	Fuel price of mth unit with generation yield P_{mq} at qth hour
ST_m	Start-up expense of mth unit
SD_m	Shutdown expense of mth unit
G	Number of generation units available
T	Number of hours
U_{mq}	ON/OFF situation of mth unit at qth hour that is $U_{mq} = 0$ When OFF &$U_{mq} = 1$ when ON
a_m, b_m, c_m	Cost coefficients of mth unit
HSC_m	Hot start cost of mth unit
CSH_m	Cold start hours of mth unit
CSC_m	Cold start cost of mth unit
up_m	Minimum uptime of mth unit
down_m	Minimum downtime of mth unit
$P_{m(\max)}$	Max generation range of mth unit
$P_{m(\min)}$	Min generation range of mth unit
P_{Dq}	Load demand at qth hour
P_{Lq}	System losses at qth hour
R_q	Spinning reserve at qth hour

1 Unit Commitment Problem (UCP)

Unit commitment problem (UCP) involves the most critical tasks which implement various power engineers in day-to-day operation of power systems domain. This load demand differs throughout, as the demand reaches the peak value daily and hence the generated power cannot be kept constant [1]. This is a big challenge today and an urgent task that is needed to be resolved in systems operation. This will facilitate UCP with generation cost reduction, fuel cost reduction, shutdown and start-up costs over a scheduling time of 24-h or 168-h with 1-h time interval subject to unit constraints and several systems [2].

Generally, there are three categories of generation units in electrical power systems: Thermal, hydro, and renewable energy sources (RES). In UCP, the total production cost (TPC) is to be minimized, and this depends on several constraints which are related to system power equilibrium and operation of generating units [3].

The UCP optimization is in the form, TPC = Fuel cost + Start-up cost + Shutdown cost + Maintenance cost.

This UCP is a complex reduction issue with a combination of continuous and integer variables. The precise answer for a unit dedication hassle may be done by the entire enumeration of all appropriate producing unit combos, which are a huge variety, while the financial dispatch hassle is resolved for every viable aggregate and it cannot be implemented to realistic energy systems due to huge computational time necessities [4]. The unit commitment can be viewed as a mixed-integer nonlinear programming (MINLP) problem where finding an optimal solution in finite time is quite challenging. Various traditional algorithms and many techniques have been adopted for this purpose.

1.1 Optimization Techniques for Solving UCP

Several optimization strategies have been recommended in the past to solve UCP and are classified into three groups; they are [5]:

1. Classical or mathematical techniques
2. Stochastic or heuristic techniques
3. Hybrid techniques.

1. **Classical techniques** produce accurate and optimal solutions, but it requires large computational time even for a medium-sized unit commitment problem (UCP). Mathematical programming techniques are alternatives to heuristic approaches. Mostly used mathematical techniques are

a. Priority list (PL) method
b. Lagrangian relaxation (LR) method
c. Mixed-integer linear programming (MILP) method
d. Branch-and-bound (BAB) method
e. Dynamic programming (DP) method
f. Interior point semi-definite programming (IPSDP) method
g. Mixed-integer nonlinear programming (MINLP) method

Among the above-mentioned methods, the priority list (PL) method is rapid but offers a sub-optimal solution. Dynamic programming (DP) method faces dimensionally problem as the problem size increases, and it is easy to add constraints for an operating hour. The main motive for selecting MILP method is its availability of high-performance optimization solution [6].

2. **Stochastic techniques** are parameter-sensitive and they are highly heuristic thus they require proper tuning to attain the global optimal solution for minimum execution time. Improper tuning of these parameters results in slow or premature convergence which may lead to a local optimum solution. The stochastic UCP manages the scheduling of generating units under ambiguity [7]. Mostly used stochastic techniques are

a. Genetic algorithm (GA) method
b. Harmony search algorithm (HAS) method
c. Evolutionary programming (EP) method
d. Imperialistic competition algorithm (ICA) method
e. Memetic algorithm (MA) method
f. Differential evolution (DE) method
g. Simulated annealing (SA) method
h. Particle swarm optimization (PSO) method
i. Tabu search (TS) method

3. **Hybrid techniques** are proposed to overcome the drawbacks of one method to another. The hybridization of massive-scale unit commitment problem (UCP) reduces the execution time and thereby, search space reduces. Frequently used hybrid techniques are [8]:

a. Tabu search (TS) and genetic algorithm (GA) methods
b. Combination of genetic algorithm (GA) and Lagrangian relaxation (LR) methods
c. Artificial neural network (ANN) combined with dynamic programming (DP) methods
d. Lagrangian relaxation (LR) and memetic algorithm (MA) methods
e. Particle swarm optimization (PSO) and Lagrangian relaxation (LR) methods
f. Simulated annealing (SA) and genetic algorithm (GA) methods.

1.2 Constraints of UCP

There are some constraints for solving this unit problem; they are [9]:

1. The total power produced should touch the system loss and its load demand.
2. There needs to be sufficient spinning reverse.
3. Constraints related to energy factor have to be reached.
4. The flexible power output range of each generation unit ranges from minimum to maximum.
5. The min up and downtime constraints of every generating unit are taken into consideration.
6. The thermal generating units must not violate the ramp rate limits.
7. The storage reservoirs must meet level constraints.

1.3 Problem Formulation (UCP)

The main objective of UCP is to reduce the total system cost which satisfies the load demand, spinning reverse, and other constraints and which overcomes the scheduled time interval is shown in Eq. (1) below

$$\text{MinTPC} = \sum_{m=1}^{G} \sum_{q=1}^{T} \left[\text{FC}_m\left(P_{mq}\right) + \text{ST}_m\left(1 - U_{m(q-1)}\right)\right] U_{mq} \tag{1}$$

The operation cost of individual systems is accumulated with the scheduled time horizon which contains various cost utilization factors like start-up expense and shutdown cost for all committed units. Equation (1) represents the fuel cost of the individual unit which is characterized as the quadratic polynomial form shown below Eq. (2)

$$\text{FC}_m\left(P_{mq}\right) = \sum_{m=1}^{G} a_m\left(P_{mq}\right)^2 + b_m\left(P_{mq}\right) + c_m \tag{2}$$

The second and third terms of the first equation shown above can be described as the start-up and shutdown expenses of each unit generated, respectively. In general, shutdown cost is consistent for every unit and the beginning up cost depends on the boiler temperature of a thermal unit that can be shown in below Eqs. (3) and (4)

$$\text{ST}_m = \begin{cases} \text{HSC}_m, \text{ if} \ldots \text{down}_m \leq \text{CSH}_m \\ \text{CSC}_m, \text{ otherwise} \end{cases} \tag{3}$$

$$\text{SD}_m = 0 \quad \text{for all units} \tag{4}$$

The minimization of the objective function will be based on practical inequality and equality constraints which affect the optimization problem process due to the operational requirements.

The implementation of the above UCP model must satisfy several constraints which are formulated as follows [10]:

1.3.1 Power Balance (PB) Constraints

Power accumulation of each generated unit should match the load demand with an appropriate interval of time, and the equation is stated as shown in Eq. (5) as shown below

$$\sum_{m=1}^{G} P_{mq} U_{mq} = P_{Dq} + P_{Lq} \tag{5}$$

1.3.2 Spinning Reserve Constraints

The greatest yield power from generating units ought to be capable to feed the load demand for an hour. The adequate spinning reserve should obtain a stable and reliable operational process. The spinning reserves constraints stated as shown in Eq. (6) are as follows

$$\sum_{m=1}^{G} U_{mq} P_{m(\max)} \geq P_{Dq} + R_q \tag{6}$$

1.3.3 Generation Limit Constraints

For the safe operation and system stability of every generating unit, the generated power must be within the specified upper and lower limits as shown in Eq. (7)

$$P_{m(\min)} \leq P_{mq} \leq P_{m(\max)} \tag{7}$$

1.3.4 Minimum up and Downtime Constraints

In thermal power plants, each generating unit depends on the temperature and pressure of the steam and has to stay in ON and OFF state for a specific time period before the actual change. This online unit is adequate to minimize its minimal uptime unit factor. Similarly, a downtime or offline unit factor is capable to turn ON; it should pass the minimal downtime hours as in Eqs. (8) and (9).

1. *Uptime constraints*:

$$U_{mq} = 1 \quad \text{for} \sum_{t=q-up_q}^{q-1} U_{mt} < \text{up}_m \tag{8}$$

2. *Downtime constrains*:

$$U_{mq} = 0 \quad \text{for} \sum_{t=q-\text{down}_m}^{q-1} (1 - U_{mt}) < \text{down}_m \tag{9}$$

2 Dynamic Programming (DP)

The dynamic programming is one of the best techniques to determine the unit commitment problem. This algorithm evaluates several possible decisions by reducing the overall cost of a system in a multistate scheduling problem [11]. It takes a long time to process due to enumeration so that the length of the problem increases exponentially and arrives at a level that it is unable to compute. So that in practical cases, various heuristic strategies are incorporated to decrease the dynamic search of large systems. Also, the priority list search method is incorporated to decrease computation time.

Practically, a precise unit commitment approach requires a quick technique to diminish the system changes and scheduled errors [12]. In general, the dynamic programming technique can efficaciously compute small-to-medium-sized troubles. However, it is a continuous programming technique it requires a large quantity of calculations results in an increase in size.

The primary objective of this dynamic programming approach is to minimize overall expenses which consist of fuel expense, start-up price, shutdown price, and operation and maintenance costs. Fuel costs are determined by fuel price, heat rate, and efficiency. Start-up prices are estimated as the quantity of hours the unit is shut down. Maintenance and operation costs are calculated in $/MBtu and $/h. The constraints which satisfy the optimal cost solution search with different parameters like system load with high and lower limits, max and minimum unit limits, and many more [13].

Different unit commitment methods are used and in that the complete priority order method comes first [14]. It is based completely on the prioritization list where the generated units are shortlisted according to low operation cost. This list facilitates load demand using an ON state where the optimal solution can be accessed quite fast. The main disadvantage of this priority list method is high operating costs for generation scheduling and they are highly heuristic.

However, if a strict priority order is introduced, there will be only four combinations exists; they are [15]:

Priority unit 1
Priority unit 1 + Priority unit 2
Priority unit 1 + Priority unit 2 + Priority unit 3
Priority unit 1 + Priority unit 2 + Priority unit 3 + Priority unit 4.

The main advantage of this dynamic programming technique is minimum quantity of loading k units which are simple and easy to decide on $(K + 1)$ units.

The cost function $F_X(n)$ is determined as follows:

$F_X(n) =$ The minimum cost price for generating n MW by X units is $/h.
$F_X(m) =$ The generation cost of m MW by Xth unit.

$F_{X-1}(n-m)$ = The minimum generation cost of $(n-m)$ MW by the remaining $(X-1)$ units.

Thus, the application of this dynamic programming technique results in the successive recursive relation as shown in Eq. (10) [16]

$$F_X(n) = \min_m \{F_X(m) + F_{X-1}(n-m)\} \tag{10}$$

The above recursive equation shows that it is easy to define the sequence of units, results in the least operating prices for loads ranging inconvenient steps from the least acceptable load to the sum of the available units. In this process, the loads contributed by every unit and the total minimum operating cost of least combinations are defined for a single load level individually (see Fig. 1).

A dynamic programming algorithm will execute to the final stage starting from the initial level using forward and reverse approaches. The forward DP technique has many advantages in determining a unit commitment problem. The recursive dynamic programming approach will execute at least cost hour T with R combinations is shown in Eq. (11) [15]:

$$F_{\cos t}(T, R) = \min_{\{P\}} \{P_{\cos t}(T, R) + S_{\cos t}(T-1, P:T, R) + F_{\cos t}(T-1, P)\} \tag{11}$$

where $F_{\cos t}(T, R)$ = Minimum cost price at state (T, R)
$P_{\cos t}(T, R)$ = The Production cost price at state (T, R)

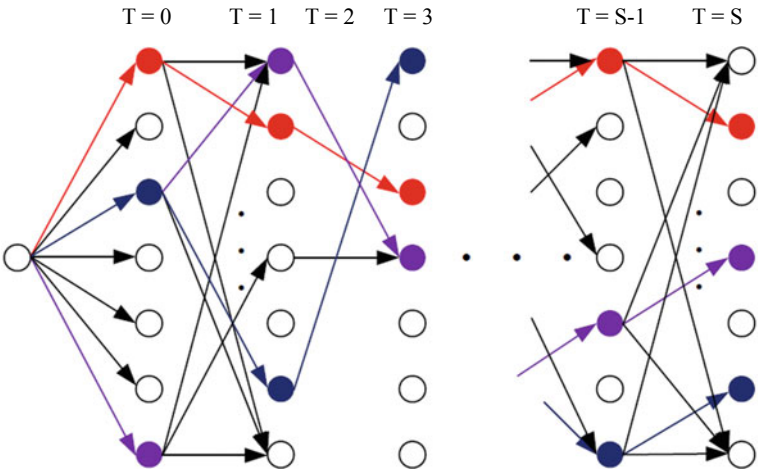

Fig. 1 DP method for a unit commitment problem [17]

$S_{\cos t}(T-1, P:T, R)$ = The transition cost price from the state $(T-1, P)$ to (T, R)

The flowchart of the above dynamic programming problem is shown in Fig. 2.

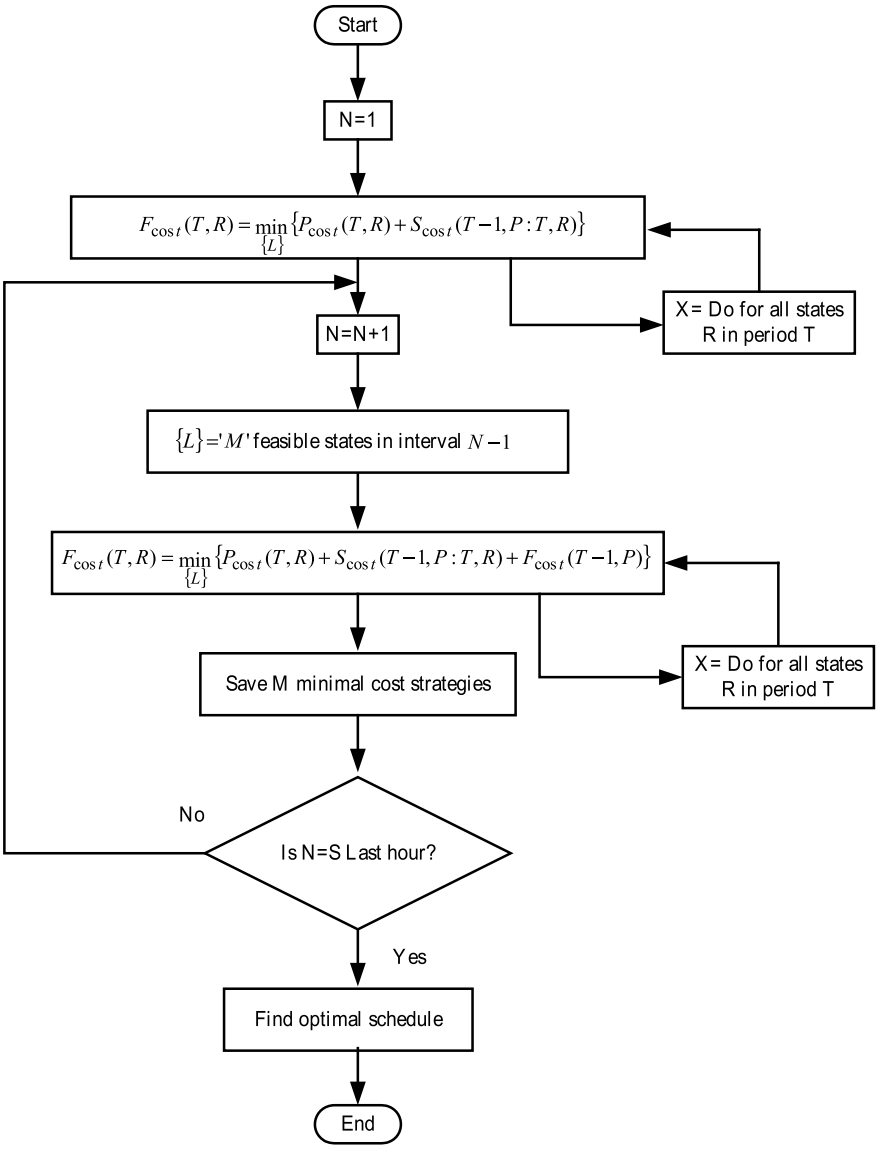

Fig. 2 Flowchart of unit commitment through dynamic programming [13]

3 Genetic Algorithm

These algorithms come under stochastic search algorithms which are based on the biological evaluation. The necessary principle of this genetic algorithm technique is that it maintains the population solutions to a problem in an encoded form so that the information will evolve in time. It also depends on the principles inspired by evaluation mechanisms and genetic principles. This evaluation is based on combining different genetic knowledge data depending on natural selection criteria with the overall population count.

After completion of the evaluation, the individual chromosomes from the overall population are divided into pairs which replicate with different offspring. The selection of individual chromosomes is implemented probabilistically, and probability selection is directly proportional to its stimulus of a chromosome. Thus, large-quality solutions are chosen at a different point in time to develop various solutions.

3.1 Genetic Operators

Genetic operators are stochastic transition steps of the genetic algorithms. These are applied to each string to achieve a new population which is an improved one compared to the old one. The population could have a gene and a gene is a key to the trouble. Every gene is calculated with a suitable positive fitness rate depending on its probability and optimality factors. An individual is determined by its fitness rate and gene. Based on fitness rate, some proportion of the population is selected and deleted, now the remaining individuals in the population are selected and mutated. After evaluation of the population, the process of selection starts again and it continues [2].

The major operators used in the genetic algorithm are selection, reproduction, crossover, and mutation [5].

1. **Selection** of the whole population comprises of its parent and child chromosomes which are ordered in a decreasing manner. These parent chromosomes are chosen according to the fitness values using the Roulette wheel selection mechanism. The best solutions are marked along with the element chromosomes to obtain the next generation.
2. **Reproduction** lies on a principle in which each string is replaced with their objective function values. This operator indicates the genetic algorithm which is fit for survival. The population of individual strings is selected according to its fitness values where its algorithm efficiency is affected by the population size.
3. **Crossover** simply combines two genotype strings to generate new genotype with the different chromosome that incorporates the solution-driven characteristics. There commended offspring genotypes are in corporated in the next-generation population (See Fig. 3).

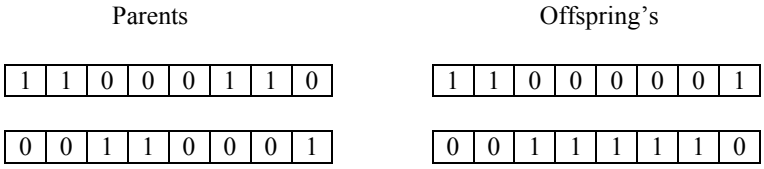

Fig. 3 Binary genetic algorithm crossover [18]

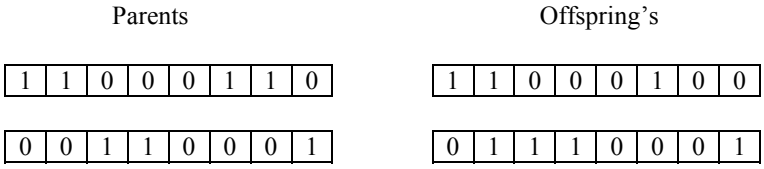

Fig. 4 Binary genetic algorithm mutation [19]

4. **Mutation** introduces a new genotype information gene at a low rate. The injection of a gene is done randomly by alerting symbols of the new chromosome. A user-defined factor regulates the probability of mutation occurrence. During the evaluation process, different solution strings are indicated in new generation and they are replaced by the parent chromosomes. The probability of the randomly chosen bits of different offspring can vary from 0 to 1 and vice versa (See Fig. 4).

3.2 Steps for the Genetic Algorithm

The genetic algorithm follows the major steps [20]:

1. The problem domain of a chromosome is fixed. The quantity of the chromosome as M, the crossover probability as Q_c, and the mutation probability as Q_m will be selected.
2. Describe the fitness function to regulate individual chromosome fitness. The fitness function chooses chromosomes that will mate during reproduction.
3. Randomly develop the chromosomes of the initial population having size M:

$$a_1, a_2, \ldots a_M$$

4. Individual fitness function values of chromosomes are calculated as:

$$f(a_1), f(a_2), \ldots f(a_M)$$

5. Choose a pair of chromosomes that are mated with the current population. Related to fitness function, the probabilities of parent chromosomes are selected.

6. Generate a pair of offspring individuals by incorporating the genetic operators such as the mutation and crossover.
7. Replace the generated offspring individual chromosomes with a new population.
8. Step 5 will be repeated until the size of the initial population M is equal to the size of the new chromosome population.
9. Restore the individual parent chromosomes with the new offspring chromosome population.
10. Step 4 will be repeated until the process terminates.

The genetic algorithm is the iterative procedure; every iteration is related to its generation. The integrated arrangement of each generation is known as the run. For easy genetic algorithm technique, the total number of generations is in limit ranging from 50 to 500. We will discover one or more extremely fit chromosomes at the end of a run. The flowchart for the above-discussed genetic algorithm is shown in below Fig. 5.

4 Simulation Results

Table 1 shows the data of standard IEEE 10-unit System [21].

Table 2 shows the data load demand for 24 h [21].

Table 3 shows the generated ON/OFF states of 10-unit load demand for each hour in a day.

Table 4 shows the comparison of the operation cost and start-up cost for dynamic programming and the genetic algorithm.

Table 5 shows the output results for the genetic algorithm and dynamic programming and it also shows the genetic algorithm is best in both of them.

5 Conclusion

A unit commitment problem is considered. Flowchart of unit commitment through dynamic programming and genetic algorithm is developed. Genetic algorithm technique is implemented through the major operators such as selection, reproduction, crossover, and mutation. Using a multistate scheduling technique of dynamic programming, the overall cost of the system is minimized. ON/OFF state of generating units for an hour demand is computed. The operation costs for 24 h are measured. A comparison of genetic algorithm with dynamic programming is made. It is observed that the genetic algorithm will converge in less time and the operating cost is also low, under the IEEE standard.

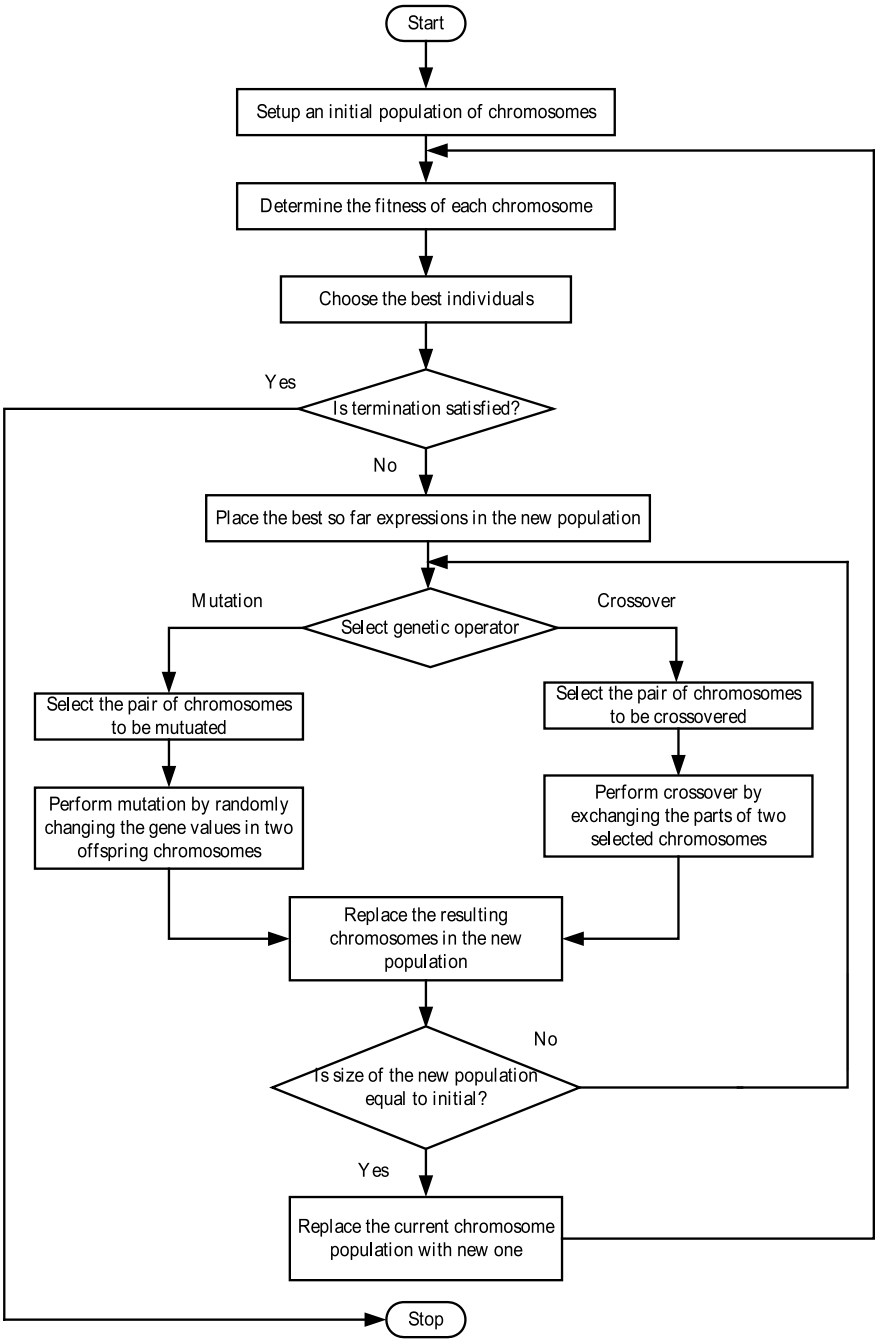

Fig. 5 Flowchart of genetic algorithm [20]

Table 1 Data for standard IEEE 10-unit system

	Unit 1	Unit 2	Unit 3	Unit 4	Unit 5	Unit 6	Unit 7	Unit 8	Unit 9	Unit 10
P_{max}(MW)	455	455	130	130	162	80	85	55	55	55
P_{min}(MW)	150	150	20	20	25	20	25	10	10	10
a ($/h)	1000	970	700	680	450	370	480	660	665	670
b ($/MWh)	16.19	17.26	16.60	16.50	19.70	22.26	27.24	25.92	27.27	27.79
c ($/MW^2 h)	0.00048	0.00031	0.002	0.00211	0.00398	0.00712	0.00079	0.00413	0.00222	0.00173
Min up (h)	8	8	5	5	6	3	3	1	1	1
Min down (h)	8	8	5	5	6	3	3	1	1	1
Hot start cost ($)	4500	5000	550	560	900	170	260	30	30	30
Cold start cost ($)	9000	10,000	1100	1120	1800	340	520	60	60	60
Cold start hrs. (h)	5	5	4	4	4	2	2	0	0	0
Initial status (h)	8	8	−5	−5	−6	−3	−3	−1	−1	−1

Table 2 Load demand for 24 h

Hour	**1**	**2**	**3**	**4**	**5**	**6**	**7**	**8**	**9**	**10**	**11**	**12**
Demand (MW)	700	750	850	950	1000	1100	1150	1200	1300	1400	1450	1500
Hour	**13**	**14**	**15**	**16**	**17**	**18**	**19**	**20**	**21**	**22**	**23**	**24**
Demand (MW)	1400	1300	1200	1050	1000	1100	1200	1400	1300	1100	900	800

Table 3 ON/OFF state of generating units for hour demand

Units	Hrs																							
	1	2	3	4	5	6	7	8	9	10	11	12	13	14	15	16	17	18	19	20	21	22	23	24
Unit 1	1	1	1	1	1	1	1	1	1	1	1	1	1	1	1	1	1	1	1	1	1	1	1	1
Unit 2	1	1	1	1	1	1	1	1	1	1	1	1	1	1	1	1	1	1	1	1	1	1	1	1
Unit 3	0	0	0	0	0	1	1	1	1	1	1	1	1	1	1	1	1	1	1	1	1	0	0	0
Unit 4	0	0	0	1	1	1	1	1	1	1	1	1	1	1	1	1	1	1	1	1	1	0	0	0
Unit 5	0	0	0	1	1	1	1	1	1	1	1	1	1	1	1	1	1	1	1	1	1	1	1	0
Unit 6	0	0	0	0	0	0	0	0	0	1	1	1	1	1	1	0	0	0	0	0	1	1	1	1
Unit 7	0	0	0	0	0	0	0	0	0	1	1	1	1	1	1	0	0	0	0	0	0	0	0	0
Unit 8	0	0	0	0	0	0	0	0	0	0	1	1	1	1	0	0	0	0	0	0	0	0	0	0
Unit 9	0	0	0	0	0	0	0	0	0	0	0	1	1	0	0	0	0	0	0	0	0	0	0	0
Unit 10	0	0	0	0	0	0	0	0	0	0	0	0	1	0	0	0	0	0	0	0	0	0	0	0

Table 4 Calculation of the costs for 24-h

Hour (h)	Dynamic programming		Genetic algorithm	
	Operation cost ($)	Start-up cost ($)	Operation cost ($)	Start-up cost ($)
1	13,683	0	13,683	0
2	14,554	0	14,555	0
3	16,809	900	16,809	900
4	19,146	560	18,598	0
5	20,020	0	20,020	560
6	22,387	1100	22,387	1100
7	23,262	0	23,261	0
8	24,150	0	24,150	0
9	27,251	860	27,251	860
10	30,058	60	30,057	60
11	31,916	60	31,916	60
12	33,890	60	33,890	60
13	30,058	0	30,057	0
14	27,251	0	27,251	0
15	24,150	0	24,150	0
16	21,514	0	21,513	0
17	20,642	0	20,641	0
18	22,387	0	22,387	0
19	24,150	0	24,150	0
20	30,058	920	30,058	490
21	27,251	0	27,251	0
22	22,736	0	22,735	0
23	17,645	0	17,645	0
24	15,427	0	15,427	0
Total	**560,395**	**4520**	**559,842**	**4090**

Table 5 Comparison of genetic algorithm with dynamic programming

Method	Operational cost ($)	Start-up cost ($)	Average time (s)	No. of units
Genetic algorithm	559,842	4090	221	10
Dynamic programming	560,395	4520	471.11	10

References

1. Franz A, Rieck J, Zimmermann J (2020) A long-term unit commitment problem with hydrothermal coordination for economic and emission control in large-scale electricity systems, vol 42. Springer, pp 235–259. https://doi.org/10.1007/s00291-020-00576-y
2. Kazarlis SA, Bakirtzis AG, Petridis V (1996) A genetic algorithm solution to the unit commitment problem. IEEE Trans Power Syst 11(1):83–92
3. Abdou I, Tkiouat M (2018) Unit commitment problem in electrical power system: a literature review. Int J Electr Comput Eng (IJECE) 8(3):1357–1372
4. Mantawy AH, Abdel-Magid YL, Selim SZ (1997) A new genetic algorithm approach for unit commitment. In: IEEE, second international conference on genetic algorithms in engineering systems: innovations and applications. IEEE, Glasgow, pp 215–220. https://doi.org/10.1049/cp:19971183, ISBN: 0-85296-693-8
5. Singhal PK, Naresh R, Sharma V, Goutham Kumar N (2014) Solution of unit commitment problem using enhanced genetic algorithm. In: IEEE, 18th national power systems conference (NPSC) 2014. IEEE, Guwahati, India. https://doi.org/10.1109/NPSC.2014.7103861, ISBN: 978-14799-5141-3
6. Brito BH, Finardi EC, Takigawa FYK (2020) Mixed-integer nonseparable piecewise linear models for the hydropower production function in the unit commitment problem. Electr Power Syst Res 182 (106234)
7. Haberg M (2019) Fundamentals and recent developments in stochastic unit commitment. Electr Power Energy Syst 109:38–48
8. Deka D, Datta D (2019) Optimization of unit commitment problem with ramp-rate constraint and wrap-around scheduling. Electr Power Syst Res 177 (105948)
9. Rudolf A, Bayrleithner R (1999) A genetic algorithm for solving the unit commitment problem of a hydro-thermal power system. IEEE Trans Power Syst 14(4):1460–1468
10. Senthil Kumar V, Mohan MR (2010) Solution to security constrained unit commitment problem using genetic algorithm. Int J Electr Power Energy Syst 32(2):117–125
11. Ouyang Z, Shahidehpour SM (1991) An intelligent dynamic programming for the unit commitment application. IEEE Trans Power Syst 6(3):1203–1209
12. Ouyang Z, Shahidehpour SM (1992) A hybrid artificial neural network-dynamic programming approach to unit commitment. IEEE Trans Power Syst 7(1):236–242
13. Hobbs WJ, Hermon G, Warner S, Sheble GB (1988) Enhanced dynamic programming approach for unit commitment. IEEE Trans Power Syst 3(3):1201–1205
14. Pang CK, Sheble GB, Albuyeh F (1981) Evaluation of dynamic programming based methods and multiple area representation of thermal unit commitments. IEEE Trans Power Syst PAS-100(3):1212–1218
15. Wood AJ, Wollenberg BF (1984) Power generation operation and control, 2nd edn. Wiley, New York
16. Kothari DP, Nagarth IJ (2003) Modern power system analysis, 3rd edn. Tata McGraw-Hill, New Delhi
17. Park J-H, Kim S-K, Park G-P, Yoon Y-T, Lee S-S (2010) Modified dynamic programming based unit commitment technique. In: IEEE, power & energy society general meeting. IEEE, Providence, RI. https://doi.org/10.1109/PES.2010.5588184, ISBN 978-1-4244-6551-4
18. Pavez-Lazo B, Soto-Cartes J (2011) A deterministic annular crossover genetic algorithm optimisation for the unit commitment problem. Expert Syst Appl 38(6):6523–6529
19. Saber NA, Salimi M, Mirabbasi D (2016) A priority list based approach for solving thermal unit commitment problem with novel hybrid genetic-imperialist competitive algorithm. Energy 117(1):272–280

20. Negnevitsky M (2005) Artificial intelligence: a guide to intelligent systems, 2nd edn. Addison Wesley, England
21. Singhal PK, Naresh Sharma R (2011) Dynamic programming approach for solving power generating unit commitment problem. In: IEEE, 2nd international conference on computer and communication technology (ICCCT - 2011) 2011. IEEE, pp. 298–303. IEEE, Allahabad. https://doi.org/10.1109/ICCCT.2011.6075161, ISBN: 978-1-4577-1386-6 (2011)

Robust Fuzzy Logic Controller for DC Motor Stability Enhancement Under Load Disturbances

Venu Yarlagadda, G. Sasi kumar, G. Radhika, Ramavath Gnanendar, and K. Rajesh

Abstract The fuzzy logic control draws the attention of researchers to improve the system robustness under disturbed conditions, especially when system is non-deterministic and involves ambiguity. The article is focussed to test the DC machine to obtain its transfer function model. It deals with the design of PID controller for improving machine stability by using Ziegler–Nichols tuning method. The performance and stability of the machine requires further enhancement which can be implemented using fuzzy logic controller (FLC), for all load scenarios. The output of the fuzzy controller is fed to the root locus-based designed PID controller to enhance its effectiveness. The machine is tested for all load disturbances from 0 to 10% variation, and case study has been performed with simulation results. Comparative analysis of ZN-tuned PID controller with fuzzy controller has been performed when the machine is subjected to the disturbances. The performance of the machine with fuzzy logic controller is robust and much superior to other method for all load disturbances.

Keywords ZN-tuned PID controller · Ziegler–Nichols tuning · Fuzzy logic controller · Dynamic performance of DC motor · Root locus-based design · FLC controlled DC motor

V. Yarlagadda · G. Sasi kumar · G. Radhika · R. Gnanendar (✉) · K. Rajesh
Department of EEE, VNR Vignana Jyothi Institute of Engineering and Technology, Hyderabad, Telangana 500090, India
e-mail: r.gnanender@gmail.com

V. Yarlagadda
e-mail: venu_y@vnrvjiet.in

G. Sasi kumar
e-mail: sasikumar_g@vnrvjiet.in

G. Radhika
e-mail: radhika_g@vnrvjiet.in

K. Rajesh
e-mail: kasalarajesh566@gmail.com

G. T. C. Sekhar et al. (eds.), *Intelligent Computing in Control and Communication*, Lecture Notes in Electrical Engineering 702,
https://doi.org/10.1007/978-981-15-8439-8_7

1 Introduction

DC shunt motors are widely used, due to the advantages they offer like adjustable speed characteristics with good speed regulation and frequent starting, reversing, and braking operations. There are many methods available in literature to control the speed and position of the DC shunt motor. The PID controller has been widely used in the process industries. The output of a PID controller relies on the error between desired value and actual value. The tuning of PI and PID controllers can be obtained using Ziegler–Nichols tuning method [1–7].

The performance and stability of the machine that require further enhancement which can be implemented based on PID/FOPID controller is explained and recently, the inspiration is taken from nature to develop a host of nature-inspired algorithms namely genetic algorithms from evolution artificial neural networks, fuzzy logic control, ant colony optimization, artificial bee colony optimization, and particle swarm optimization. Out of these techniques, stochastic search, fuzzy logic control, particle swarm optimization, and ant bee colony optimization techniques are widely used for optimal tuning of the parameters [8–12].

In this work, the stability of a DC motor is attained for all load disturbances using fuzzy logic controller. The paper is organized and explained as follows. Section 2 presents mathematical modeling of DC motor, Sect. 3 deals with obtaining the TF model parameters from the laboratory-based testing, and Sect. 4 explains the design of PID controller using Ziegler–Nichols (ZN) tuning method. Section 5 deals with design of fuzzy logic controller, along with the root locus-based designed PI controller, and Sect. 6 analyzes the simulation results of all load disturbances; the machine is tested with ZN-tuned PID controller and fuzzy controller. The testing of machine with all load scenarios has been performed and highlighted the robustness and influence of fuzzy controller on enhancement of dynamic stability of machine. The comparisons have been made for ZN-tuned PID controller with fuzzy controller [2, 4, 8, 13–15].

2 Mathematical Modeling of DC Motor

The basic block diagram of armature controlled DC shunt motor model with field circuit operation of separately excited machine as illustrated in Fig. 1 [1].

Case (i): When $V_a = 0$ and load disturbance alone is considered then the transfer function is given by Eq. (1)

$$\frac{\varpi_1(s)}{T_L(s)} = \frac{-(L_a s + R_a)}{L_a J s^2 + (R_a J_m + L_a B_m)s + (R_a B_m + K_b K_t)} \tag{1}$$

Case (ii): When $T_L = 0$ and armature voltage alone is considered then the transfer function is given by Eq. (2)

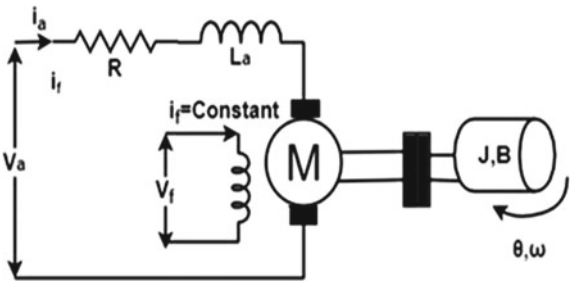

Fig. 1 Armature controlled DC motor

$$\frac{\varpi_2(s)}{V_a(s)} = \frac{K_t}{L_a J s^2 + (R_a J_m + L_a B_m)s + (R_a B_m + K_b K_t)} \tag{2}$$

Case (iii): when both V_a and T_L are present in the circuit, i.e., speed control with load disturbances.

When $V_a = 1$ and $T_L = 0.01$, 0.05, and 0.1 of three load disturbances from 1 to 10% load variations, then the overall transfer function is given by Eq. (3)

$$G(s) = \frac{\varpi_1(s)}{T_L(s)} + \frac{\varpi_2(s)}{V_a(s)} \tag{3}$$

3 Experimental Determination of Dynamical Model

The testing is performed on the DC shunt motor of ratings as 220 V, 5HP, 1500 rpm DC shunt motor with 19 A armature current and 0.8 A field current ratings. The retardation test circuit is shown in Fig. 2, and it is performed on the machine to obtain moment of inertia and friction of machine rotor. The armature resistance and impedance tests have been performed to compute armature resistance and inductance

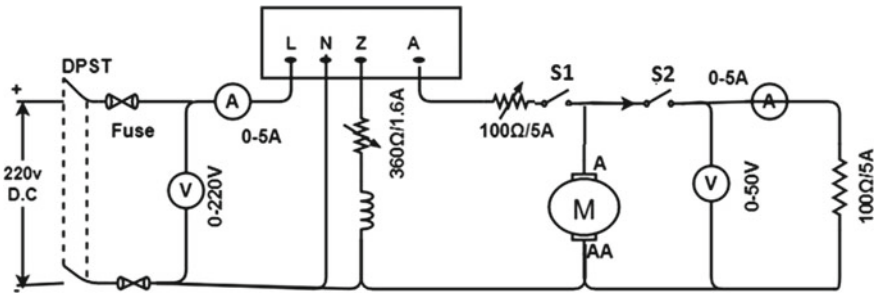

Fig. 2 Retardation test for finding J and B values

Fig. 3 Experimental setup of retardation test with field excited separately

respectively. The transfer function model of armature controlled DC shunt motor has been obtained from these test results [1].

Figure 3 shows the experimental setup of retardation test and its computation results of moment of inertia: J and friction: B values, E_b (voltmeter reading) = 206 V, I_a(ammeter reading) = 0.75 A, $t_1 = 51.3$ s and $t_2 = 23$ s, from Eqs. (4) and (5) we can compute the J and B values as follows:

$$P = \omega\left(\frac{J\mathrm{d}\omega}{\mathrm{d}t_1} + B\omega\right) \tag{4}$$

$$P - W_1 = \omega\left(\frac{J\mathrm{d}\omega}{\mathrm{d}t2} + B\omega\right) \tag{5}$$

By substituting the values, the computed rotor parameters are as $J = 0.002366$ and $B = 0.017$ and from the armature resistance and impedance test as in Fig. 4, the computed values of armature resistance as 2 ohms and armature inductance of 0.0256 H. The transfer function model of DC motor [6], determined by the laboratory-based testing.

$$GH(s) = \frac{0.124}{0.00512s^2 + 0.0547525s + 0.051076} \tag{6}$$

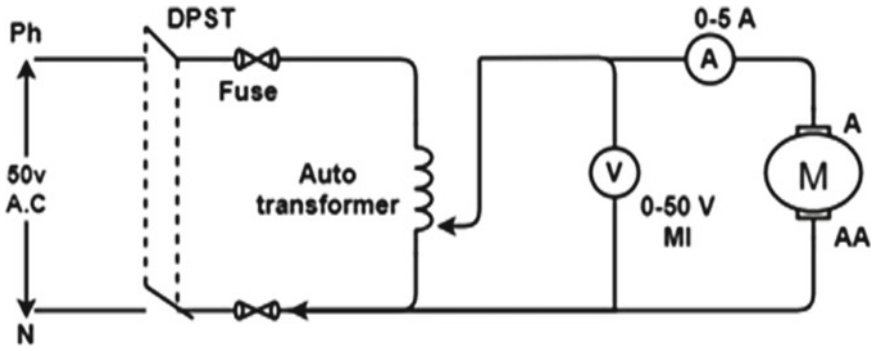

Fig. 4 Experimental setup of impedance test

4 Ziegler–Nichols Tuning of PID Controllers

Equation (6) represents open-loop transfer function which is specified by $GH(s)$, the characteristic equation of the system which is given by Eqs. (7) and (8), to find critical gain K_c and critical time period T_c corresponding to critical gain at imaginary axis of s-plane [2].

$$1 + K_c GH(s) = 0 \tag{7}$$

The characteristic equation of the system

$$0.00512s^2 + 0.0547525s + 0.051 + 0.124K_c = 0 \tag{8}$$

The critical gain K_c of the system computed using Ziegler–Nichols tuning is 0.41129, and the critical time constant or ultimate time constant corresponding to critical gain is 1.39 s corresponding frequency is 4.518 rad/s. The proportional, derivative, and integral controller parameters are computed as $K_p = 0.246774$, $K_i = 0.355$ and $K_d = 0.042877$. Here, limits of PID parameters are decided based on root locus.

5 Fuzzy Logic Control

Figures 5 and 6 show that the input membership functions are taken as triangular type, which is varying from minimum value to a maximum value and mean is at its peak of the triangle, and five input functions have been taken from −2.5 to +2.5 range as input 1 similarly input 2 and output variables are illustrated in Figs. 5, 6 and 7 including fuzzy rule surface followed by rules shown in Table 1. Here, the fuzzy rules and membership functions are decided based on error and derivative of error

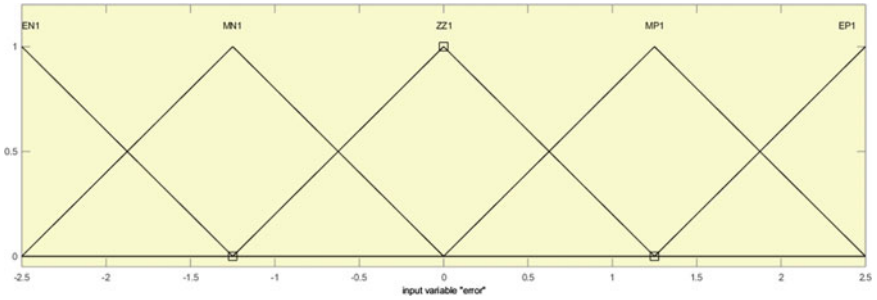

Fig. 5 Fuzzy input 1 triangular membership functions varying from −2.5 to +2.5 for error

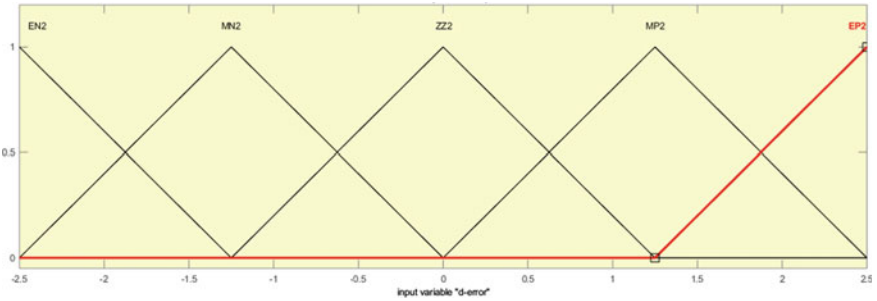

Fig. 6 Fuzzy input 2 triangular membership functions varying from −2.5 to +2.5 for derivative error

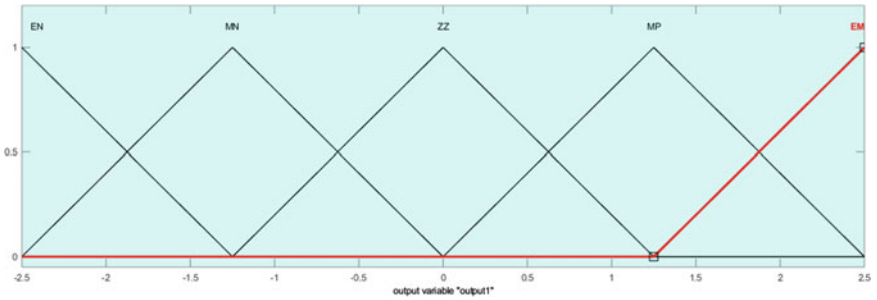

Fig. 7 Fuzzy output triangular membership functions varying from −2.5 to +2.5 for error

variations and fuzzy parameters have been selected to fit for any kind of disturbances. Initially, we have plotted dynamic response with various disturbances and M_p, t_s and error values. Disturbances have been increased to 10%. Based on disturbances and responses error, we have designed fuzzy parameters to get robustness [4, 8, 14].

Table 1 Membership function inputs and output relationship

e	d*e*/d*t*				
	EN2	MN2	Z2	MP2	EP2
EN1	EN	EN	MN	Z	Z
MN1	EN	MN	MN	Z	MP
Z1	MN	Z	Z	MP	MP
MP1	Z	Z	EP	EP	EP
EP1	Z	MP	MP	EP	EP

6 Case Study and Results

The case study and result analysis have been presented in two major cases which consist of four subcases. The comparative analysis among without any controller, with ZN-tuned PID controller and fuzzy logic controllers with all four subcases are mentioned below.

Case I: Without any load disturbance
Case II: With load disturbance of one percent
Case III: With load disturbance of five percent
Case IV: With load disturbance of ten percent.

Figure 8 shows the Simulink diagram without any controller, Fig. 9 shows the Simulink diagram with ZN-tuned PID controller and Fig. 10 shows the Simulink diagram of fuzzy logic controller.

Figure 11 shows the dynamic responses for without controller, with ZN-tuned PID and fuzzy logic controllers without any load disturbance, Fig. 12 shows the dynamic responses for all three cases without controller, with ZN-tuned PID and fuzzy logic controllers with 1% load disturbance, and Figs. 13 and 14 show the dynamic responses for all three cases without controller, with ZN-tuned PID and

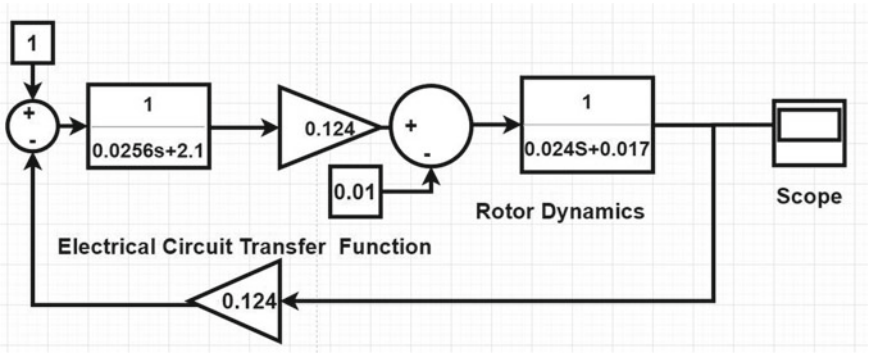

Fig. 8 Simulink model without any controller

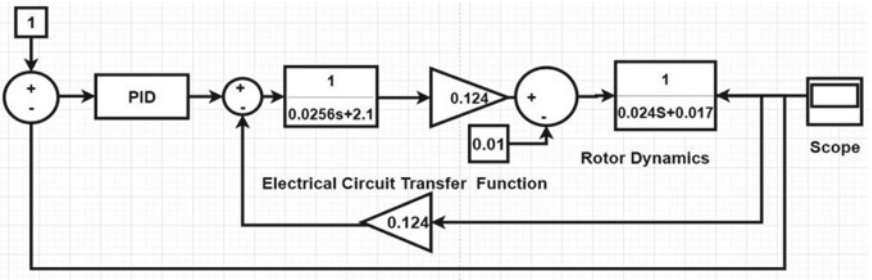

Fig. 9 Simulink model with ZN-tuned PID controller

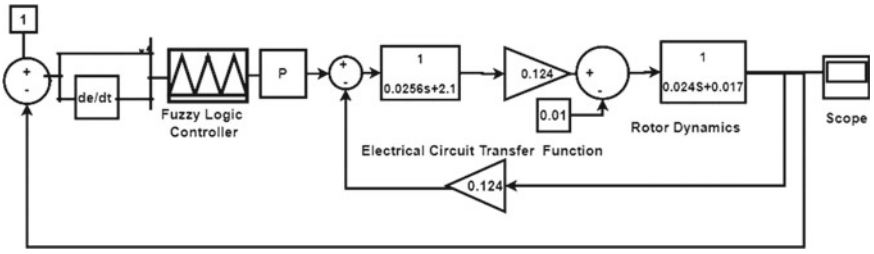

Fig. 10 Simulink model with fuzzy logic controller

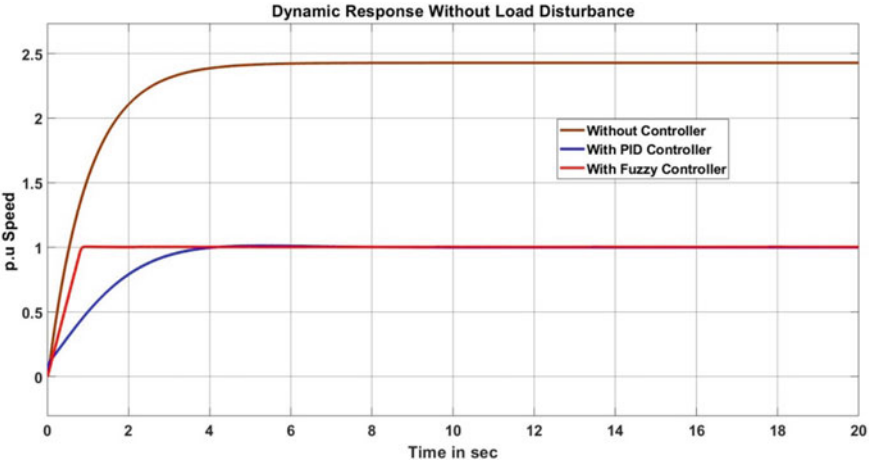

Fig. 11 Dynamic responses for all three cases without controller, with ZN-tuned PID and fuzzy logic controllers without any load disturbance

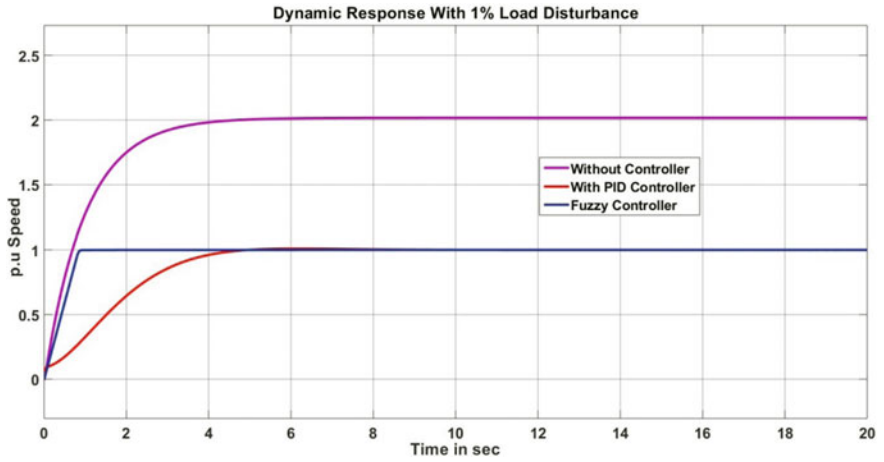

Fig. 12 Dynamic responses for all three cases without controller, with ZN-tuned PID and fuzzy logic controllers with 1% load disturbance

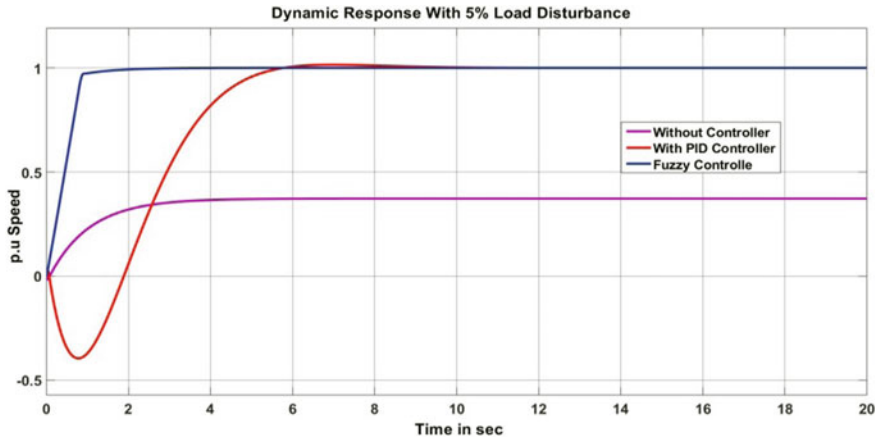

Fig. 13 Dynamic responses for all three cases without controller, with ZN-tuned PID and fuzzy logic controllers with 5% load disturbance

fuzzy logic controllers with 5 and 10% load disturbance, respectively, [2, 3, 7, 8, 13, 15].

Comparative analysis without any controller, with ZN-tuned PID controller and fuzzy logic controllers

Case I. Without Any Load Disturbance

Simulation results without any load disturbance shows that the simulation results of uncontrolled machine is completely unstable with the steady-state error of −142%. The simulation results of ZN-tuned PID controller is also stable with settling time

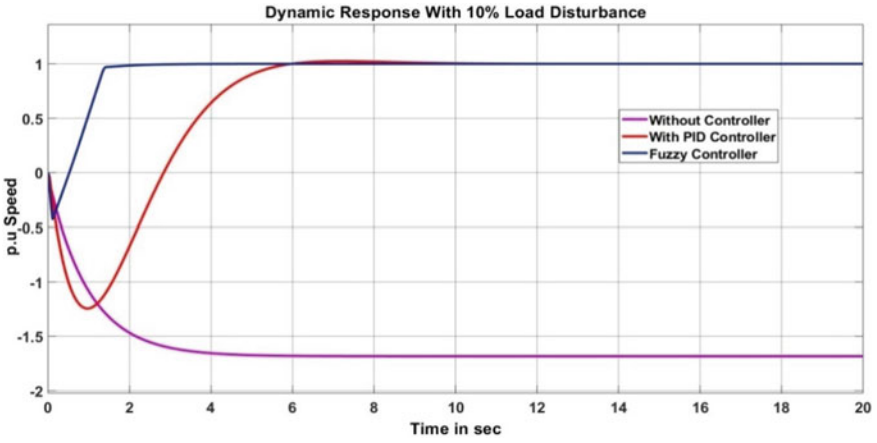

Fig. 14 Dynamic responses for all three cases without controller, with ZN-tuned PID and fuzzy logic controllers with 10% load disturbance

of 7 s with zero steady-state error, and that of the fuzzy logic controller result shows that the controller is more robust and adaptive with a very fast settling time of 0.91 s with zero error.

Case II: With Load Disturbance of One Percent
Simulation results with one percent load disturbance shows that the uncontrolled machine is completely unstable with the steady-state error is of −100%. The simulation results of ZN-tuned PID controller are also stable with settling time of 8 s with zero steady state error, and that of the fuzzy logic controller result shows that the controller is more robust and adaptive with a very fast settling time of 0.91 s with zero error.

Case III: With Load Disturbance of Five Percent
Simulation results with five percent load disturbance shows that the uncontrolled machine is completely unstable with the steady-state error is of −43%. The simulation results of ZN-tuned PID controller is stable with a settling time of 10 s and zero error, and that of the fuzzy logic controller result shows that the machine is stable with a very fast settling time of 1.5 s with zero error.

Case IV: With Load Disturbance of Ten Percent
Simulation results with ten percent load disturbance show that the uncontrolled machine is completely unstable. The simulation results of ZN-tuned PID controller is more prone to instability with an undershoot of −125% with a settling time of 6 s, and that of the fuzzy logic controller result shows that the machine is stable with a settling time of 2.5 s with zero error as shown in Figs. 11, 12, 13 and 14 respectively.

7 Conclusion

The simulation results reveal that the performance of fuzzy logic controller is adaptive and robust controller for load disturbances from 0 to 10% variations. For all load scenarios, fuzzy logic controller fed machine is completely stable with very fast settling time and zero steady-state error compared to Ziegler–Nichols-tuned PID controller, which is more prone to instability under disturbed conditions with quite high steady-state error. It is analyzed from the simulation results with 5% load disturbance that ZN-tuned PI controller is more prone to instability with an under shoot of −78% with a settling time of 15 s. With ten percent load disturbance, the ZN-tuned PI controller is more prone to instability with an undershoot of −143% with a settling time of 15 s, and for ten percent disturbance, the ZN-tuned PID controller is more prone to instability with an undershoot of −125% with a settling time of 6 s. The fuzzy controller is robust and machine is completely stable with a very fast settling time of 0.9 s with zero steady state error for both 5 and 10% load disturbances.

References

1. Elsrogy WM, Fkirin MA, Moustafa Hassa MA (2013) Speed control of DC motor using PID controller techniques based on artificial intelligence. In: International conference on control, decision and information technologies, CoDIT
2. Kushwah M, Patra A (2014) Pid controller tuning using Ziegler-Nichols method for speed control of Dc motor. Int J Sci Eng Technol Res 03(13)
3. Rajasekhar A, Abraham A (2011) Fractional order speed control of DC motor using levy mutated artificial bee colony algorithm. World Congress on Information and communication Technologies, IEEE, pp 7–13
4. Sharma K, Palwalia DK (2017) A modified PID control with adaptive fuzzy controller applied to DC motor Instrumentation and control ICICIC. In: IEEE international conference on information, communication
5. Astrom K, Hagglund T (1995) PID controllers: theory, design, and tuning, 2nd edn. Instrument Society of America
6. Nagrath IJ, Gopal M (2017) Control systems engineering. New Age International Publishers
7. Bhimbra PS (1973) Electrical machinery. Khanna Publications
8. Adepoju GA, Adeyemi IA (2014) Application of fuzzy logic to the speed control of DC motor. Int J Eng Trends Technol (IJETT) 15
9. Karaboga D, Basturk B (2007) Artificial bee colony (ABC) optimization algorithm for solving constrained optimization problems IFSA 2007. LNAI 4529:789–798
10. Int J Comput Appl 77(15):0975–8887 (2013)
11. Int J Digit Appl Contemp Res 2(3) 2013
12. Sundareswaran K (2008) D.C. motor speed controller design through a colony of honey bees. TENCON (IEEE region) conference, pp 1–6
13. Ercin O, Coban R (2011) Comparison of the artificial bee colony and the bees algorithm for PID controller tuning. In: Innovations in intelligent systems and applications (INISTA) IEEE conference, pp 595–598

14. Tohamy IA, Ahmed A, El Koshairy D (2019) Enhancement of the dynamic performance of a Dc motor using fuzzy logic algorithm. Int J Eng Res Technol (Ijert) 8(10):2278–0181 Ijertv8is100117 Published by Www.Ijert.Org
15. Kushwah M, Patra A (2014) Tuning PID controller for speed control of dc motor using soft computing techniques-a review. Adv Electron Electr Eng 4:141–148

Optimal Scheduling for Delay Management in Railway Network Using Hybrid Bat Algorithm

Poulami Dalapati and Kaushik Paul

Abstract This paper aims to solve the timetable rescheduling problem of a railway network to minimize the total delay in journey time of trains under any disastrous situation. Here, multiple tracks and platforms are taken into account to dynamically update the timetable. A Bat Algorithm (BA) based meta-heuristic approach is proposed to solve it. The results obtained from the proposed approach depicts that it can readily solve such problems in an efficient and optimized way. Moreover, the comparative study shows that this approach outperforms the existing method in this domain.

Keywords Railway · Optimization · Railway network · Intelligent system · Bat algorithm · Heuristic method

1 Introduction

The increasing demand of railway transportation in recent days throws a challenge to the system authority as the Railway Scheduling Problem (RSP) involves huge number of constraints to be handled. Moreover, disaster occurred in such large, complex, distributed network make pre-defined schedule less effective in terms of delay minimization of trains. As extension of stations (number of platforms and tracks) are not possible in long term or immediately, RSP becomes vulnerable time to time. The best solution to RSP in this research work hence aims to determine

Supported by BIT Sindri.

P. Dalapati (✉)
Department of CSE, BIT Sindri, Dhanbad, India
e-mail: dalapati89@gmail.com

K. Paul
Department of EE, BIT Sindri, Dhanbad, India
e-mail: kaushiksunnypaul@gmail.com

G. T. C. Sekhar et al. (eds.), *Intelligent Computing in Control and Communication*, Lecture Notes in Electrical Engineering 702,
https://doi.org/10.1007/978-981-15-8439-8_8

an optimized schedule for trains while minimizing total journey time delay of it maintaining the system safety.

Among various state-of-the-art methods, FCFS [11] serves as the most common approach to solve RSP, mainly where there is only one track between two stations. Various other methods to solve this include dynamic programming [6], heuristic methods [7, 8], branch and bound [4]. Researchers in recent times brought various natural phenomenon under microscopic lens, based on heuristic or meta-heuristic which can solve real world problems like transportation scheduling [1–3, 12, 16]. Some of them include Ant Colony Optimization (ACO) [9, 10], chicken swarm optimization [17], bionomic algorithm [5],Particle Swarm Optimization (PSO) [22, 26], hybrid meta-heuristics [15, 20].

In [19] a new TBR method is discussed , minimizing negative effect in rescheduling after disaster. But here only line-topology ia addressed from the same. An MILP based rescheduling model, taking the threshold delay, is highlighted in [18]. Though this works well for small network, it shows the loop-hole for large network in real world. Some other related work for RSP are discussed in [12, 14, 16]. Yang proposed a meta-heuristic method named Bat Algorithm (BA) [27], which inspired from the echolocation behavior of micro bats. BA gained popularity in solving numerous optimization problems, which can be found in details in [21, 22, 25]. In [13, 28] Gandomi and his team solves many engineering problems which include constrained optimization tasks. A differential operator and the DLBA based bat algorithm is proposed by Xie et al. in [24]. A new bat algorithm based path planning problem is described in [23] to solve uninhabited combat air vehicle (UCAV).

With the notion of the above-discussed literature, the main *contribution* of the paper is, it considers multiple platform and track based railway network to solve RSP with the aim to minimize the journey time delay of all the trains and a hybrid bat algorithm (HBA) is developed to accomplish the proposed approach. The efficiency and diversified application areas make BA a very popular one in the area of optimization for complex, dynamic systems. This is our main motivation to incorporate the notion of BA in solving RSP. Moreover, BA shows faster convergence in the aforementioned domain, which promises better results in a time-critical system.

The rest of the paper is organized as follows: Sect. 2 models RSP into a mathematical model and the basics of BA is also discussed here. A hybrid algorithm with the notion of BA is proposed in Sect. 3. Experimental results and comparative analysis have been discussed in Sect. 4. Finally Sect. 5 concludes the proposed work.

2 Problem Description

This section describes the inline framework of a distributed railway system followed by the basics of Bat Algorithm, which is later used to achieve the optimized results.

2.1 Railway Architecture

Being a geographically distributed network, consisting of multiple number of tracks, stations, platforms railway system is a very large complex architecture (see Fig. 1). Multiple trains are in circulation in this network at any time instant. These trains are at stations (on a platform) or on track connecting two stations. When disaster happens, rescheduling of the existing timetable is executed in such a pattern that consider the rescheduling of the premium trains (marked as top most priority) are performed in first place. These priorities change dynamically to reduce total journey time delay of trains depending on the current scenario.

The objective of railway scheduling problem (RSP) is to find the optimized solution for arrival time (AT), departure time (DT), platform (P), and tracks (L) for running trains so that the delay is minimized ensuring the headway distance between any pair of trains. For mathematical formulation of RSP, we define some indices, parameters, and decision variables in Table 1.

The objective function for this is formulated as follows:

$$\min\ \Delta = \min \sum_{j} \delta_j = \min \sum_{\mathrm{Rou}(T_j)} (\delta_{ji}^{\min} + \delta_{jl}^{\min}) = \min \sum_{P_{jik}} \delta_{ji} + \min \sum_{L_{jil}} \delta_{jl} \quad (1)$$

Subject to constrains:

$$x_{ji}^{AT} \geq x_{ji'}^{DT} + x_{jl}^{J} \quad (2)$$

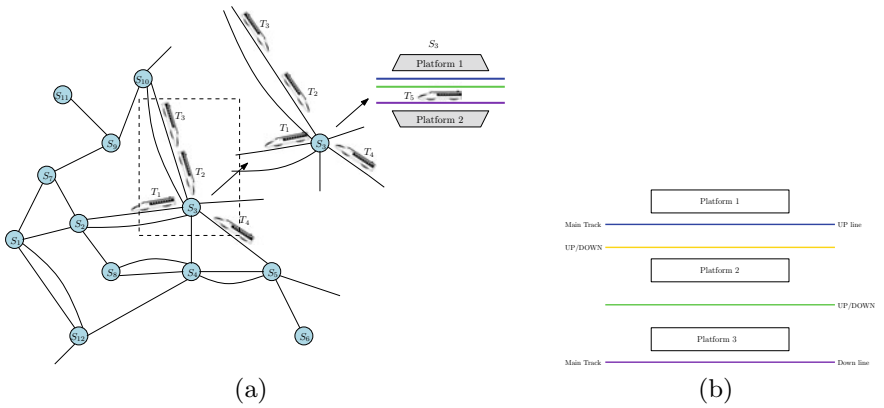

Fig. 1 Railway system framework. **a** Railway architecture represented as a graph. **b** Broad representation of a station

Table 1 Notation

Indices and Parameters	
S Station	o_{ji}^{J} Train j's original journey time
T Trains	o_{ji}^{d} Train j's original dwell time at S_i station
i Index of a station	x_{jl}^{J} Train j's journey time on l^{th} track
j Index of a train	a Index of an agent
l Index of a track	q Total agents, here $q = m + n$
k Index of a platform	t Time instant
n Total count of stations	t_D Time of disaster
m Total count of trains	t_R Time of recovery
p Maximum number of platforms at each station	t_{Busy} Busy Time of day
o_{ji}^{AT} Train j's original time of arrival at i^{th} station	$i' \in [1, n]$ i Station index except i^{th} station.
o_{ji}^{DT} Train j's original time of departure from i^{th} station	$j' \in [1, m]$ j Train index except j^{th} train.
δ_{ji} Train j's delay at i^{th} station	$i'' \in [1, n]$ i, i' Station index except i^{th} and i'^{th} station.
δ_{jl} Train j's delay on track l	$j'' \in [1, m]$ j, j' Train index except train j and j'.
δ_{Th} Threshold delay	Δ Total delay
Decision Variables	
x_{ji}^{AT} Train j's original time of arrival at i^{th} station after disaster	x_{ji}^{DT} Train j's original time of departure at i^{th} station after disaster
P_{jik} Platform indicator, $P_{jik} = 1$ when T_j occupies k^{th} platform of S_i, otherwise 0	L_{jil} Track indicator, $L_{jil} = 1$ if T_j occupies l^{th} track connecting to S_i, otherwise 0 and when $L_{jil} = 1$, $L_{j'il} = 0$
$Prio(T_j)$ T_j's priority	x_{ji}^{d} Actual operation time of T_j at S_i

$$\left.\begin{array}{l} x_{ji}^{AT} \geq o_{ji}^{AT} \\ x_{ji}^{AT} - o_{ji}^{AT} = \delta_j \\ x_{ji}^{DT} \geq o_{ji}^{DT} \\ x_{ji}^{DT} - o_{ji}^{DT} = \delta_j \end{array}\right\} \tag{3}$$

$$\forall j \in [1, m] \; \exists \; P_{jik} \in [0, 1], \text{ where } 1 \leq k \leq p, \; \forall \; S_i \tag{4}$$

$$\sum_{k} P_{jik} \leq p, \text{ where } 1 \leq k \leq p \tag{5}$$

$$\text{if } L_{jil} = 1, \text{ then } L_{j'il} = 0 \tag{6}$$

$$\left.\begin{array}{l} Re(T_j)|^t = L_{jil} \; or \; Re(T_j)|^t = P_{jik} \\ L_{jil} \cap P_{jik} = \Phi \end{array}\right\} \tag{7}$$

$$\text{Rou}(T_j) = (\bigwedge_{i=1}^{n-1} P_{jik} L_{jil}) \cup P_{jnk}, \text{ where } j \in [1, \; m] \tag{8}$$

Equation (1), as formulated in objective function, minimizes total delay of journey time of trains in the railway system. Equation (2) conveys the train's time of arrival depends on the time of departure from its earlier station and journey time to reach the current station.

Equation (3) represents the time delay, which is calculated from the differences between actual and original time of arrival and/or departure of trains. It is also noted that a train faces delay iff actual arrival and/or departure time is greater than the original one. Equations (4) and (5) ensures that the platform index of a station of occupying train cannot be greater than the maximum number of platforms of that particular station. Equation (6) restricts train $T_{j'}$ to occupy the same track as T_j at the same time. Equation (7) signifies that the resource requirements of a train T_j at time t is any one of the tracks or platforms. Route of train T_j is introduced by Eq. (8) as a series connection of platforms (P) and track (L).

2.2 Bat Algorithm

Inspired from the preying strategy of bats, the Bat Algorithm (BA) is initially proposed in 2010 by Yang [27]. This algorithm adopts echolocation strategy of bats. The meta heuristic follows several ideal rules and the algorithmic steps for BA can be described as follows:

- Echolocation characteristics is used by each bat to differentiate between a barrier and a prey.
- Every bat flies randomly at a position with a particular frequency. The velocity, position, and frequency is denoted by v_i, x_i, and $f_{\min}$ respectively for each bat i. The wavelength and loudness to look for prey is denoted by λ and $\mathcal{L}_o$ where λ is varying parameter ranges 2–14 mm, when frequency varies from 25 to 150 kHz. Each bat can control automatically the frequency of pulse released and modulate pulse emission rate $\mathcal{R}$, where $\mathcal{R} \in [0, 1]$, depending upon the distance from its aim. Similarly, values of the component x_i and v_i are updated during each iteration process for each bats. v_i, x_i, and $f_{\min}$ can be updated using Eqs. (9), (10), (11).

$$f_i = f_{\min} + (f_{\max} - f_{\min})\alpha \tag{9}$$

$$v_i^{t+1} = v_i^t + (x_i^t - x_*) f_i \tag{10}$$

$$x_i^{t+1} = x_i^t + v_i^t \tag{11}$$

Here $\alpha \in [0, 1]$ is a random vector which follows uniform distribution. The recent global best solution for location is denoted by x_*. The global solution is fetched based on the comparative analysis of the location corresponding to each bats. The frequency of each bat varies from $[f_{\min}, f_{\max}]$ and is assigned randomly during implementation. The generation of the new solution is achieved locally based on random walk. The new solution is represented in Eq. (12).

$$x_{\text{new}} = x_{\text{old}} + \varepsilon \mathcal{L}^t \tag{12}$$

Here $\varepsilon \in [-1, 1]$ and the mean loudness is represented as $\mathcal{L}^t$ at a time instant for all bats.

- For each bat, the parameters like pulse emission rate and loudness varies. The idea behind these variations is for exploring and exploiting the mechanism.
- Loudness varies from $\mathcal{L}_o$ (larger value) to $\mathcal{L}_{\min}$ (minimum value) when bat gets its prey. Here $\mathcal{L}_{\min}$ is assumed to be zero.
- At this time bat stops radiating any sound.Thus,

$$\left.\begin{aligned} \mathcal{L}_i^{t+1} &= \beta \mathcal{L}_i^t \\ \mathcal{R}_i^{t+1} &= \mathcal{R}_i^0 [1 - \exp(-\gamma t)] \end{aligned}\right\} \tag{13}$$

Here, $\beta \in [0, 1]$ and $\gamma > 0$. When $t \to \infty$, $\mathcal{L}_i \to 0$ and $\gamma_i^t = \gamma_i^0$. Loudness $\mathcal{L}$ decreases with the increase of pulse emission rate $\mathcal{R}$.

3 Solution Based on BA for Railway Rescheduling Problem

Being a continuous optimization, the basic BA can not be always applicable to solve real-world distributed optimization problem like RSP. Therefore, to solve such problem, a hybrid BA (HBA) is proposed in this paper. The initial candidate solution is taken as a sequence $\mathcal{S} = (s_1, \ldots, s_n)$ with $s_i \in \{1, \ldots, p\} \vee \{1, \ldots, l\}$. Here, s_i denotes either a station or a track and $|\mathcal{S}|$ denotes number of trains in circulation, where $|\mathcal{S}|$ can be m at max. In this paper, l is taken as 3, p is taken as 4, and m is taken as 10 as shown in Fig. 2.

From Fig. 2 it is understood that train 3, 5, 9 take track 1, train 4, 6, 7, 10 take track 2, and train 1, 2, 8 take track 3 to reach to the next station. Whereas, after reaching the station train 1, 2, 7 are allocated platform 1, train 3, 6 are allocated platform 2, train 5, 10 are allocated platform 3, and train 4, 8, 9 are at platform 4.

To minimize the delay of trains, the arrival as well as departure time of trains are very crucial. The new rescheduled arrival time (x_{ji}^{AT}) and departure time (x_{ji}^{DT}) are determined depending upon the original arrival time (o_{ji}^{AT}), original departure time

Train	1	2	3	4	5	6	7	8	9	10
Track	3	3	1	2	1	2	2	3	1	2
Platform	1	1	2	4	3	2	1	4	4	3

Fig. 2 Candidate solution for RSP

(o_{ji}^{DT}), journey time taken on track L and dwell time at platform P. For this, priority of trains are taken into account so that the high priority trains can be rescheduled earlier to minimize the delay. If $T_{j'}$ is having higher priority than T_j, then $x_{j'i}^{AT} < x_{ji}^{AT}$ if both T_j and $T_{j'}$ are requesting for same platform and $x_{j'i}^{AT} = x_{ji}^{AT}$ if they request for different platforms. Similarly, $x_{j'i}^{DT} < x_{ji}^{DT}$ if both trains request for same track and $x_{j'i}^{DT} = x_{ji}^{DT}$ if they request for two different tracks. These conditions hold for any number of trains in the sequence $\mathcal{S}$. The rescheduled timetable becomes effective iff all the constrains from Eqs. (2) to (8) are satisfied. Initially, when all the platforms and tracks are unoccupied, a random selection is made as a solution for each train. It is observed from the experiments, that such initialization results into good initial timetable schedule for railway network. But for further improvement towards achieving an optimized schedule, a bat algorithm is proposed for RSP.

With the notion of position updation in BA, we prepare the updation in following way:

1. Choose any platform (as frequency f) or track (as frequency f') randomly.
2. Choose any train related to that platform or track and allocate the alternative resource to it.

In this paper we assume frequency $f = 3$, means platform 3 is selected randomly. There are two trains which are approaching to stop at platform 3, T_5 and T_{10}. Suppose, the first one i.e., T_5 is selected and platform 2 is assigned to it. Similarly, if we assume $f' = 1$, i.e. track no. 1 is selected, then we select T_5 among T_3, T_5, T_9 to be assigned of track 3 (*see* Fig. 3).

	Train	1	2	3	4	5	6	7	8	9	10
Track	*before*	3	3	1	2	1	2	2	3	1	2
	after	3	3	1	2	3	2	2	3	1	2
Platform	*before*	1	1	2	4	3	2	1	4	4	3
	after	1	1	2	4	2	2	1	4	4	3

Fig. 3 Track and platform updation of train for RSP

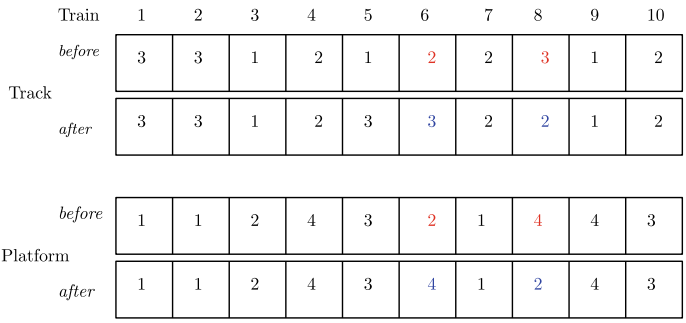

Fig. 4 Swapping of track and platform of trains after local search for RSP

Local search swapping is done by swapping the resources of randomly chosen trains. The idea behind this swap is based on mutation of recent global best solution to get the improved solution around optimal solution. Figure 4 illustrates this, where two trains T_6 and T_8 having different resource requirements are chosen randomly. So, the platform as well as track assignment are just swapped between them. This local search is done depending upon $\mathcal{R}$ as updated in Eq. (13), the pulse emission rate. If $\mathcal{R}$ is less than a random number, swapping is done. This is to find out different structures in neighborhood.

Parameter $\mathcal{L}$ (loudness) is used for the acceptance of solution found by the local search. In this paper $\mathcal{L}$ is used to manage congestion on tracks and at platforms. Initially number of trains are counted which want to access same platform or track at the same time and also total number of trains (max and min) competing for a resource (either platform or track). If max and min value are same, then resources are selected randomly. The iteration terminates when the difference is greater than or equal to 1. $\mathcal{L}$ is updated using Eq. (13).

3.1 Computational Complexity of Proposed RSP

In this section, we discuss the computational complexity for RSP in brief. The proposed RSP solution includes initialization of parameters of HBA for candidate solution followed by updation of the same until the termination condition meet. The worst case complexity of the solution is estimated as follows:

- In initialization stage, RSP initializes all BA parameters: v_i in D-dimension, x_i, and $f, \mathcal{R}, \mathcal{L}, \alpha$. For population size $\mathcal{P}_{size}$ the computational complexity of initialization phase found out to be $O(\mathcal{P}_{size} D + 5\mathcal{P}_{\text{size}}) = O(\mathcal{P}_{size} D)$.
- In next phase f is determined as well as each bat, which takes $O(\mathcal{P}_{\text{size}} D)$ computations for $t = 1$. So, total complexity after maximum generation is $O((\mathcal{P}_{\text{size}} D) t_{\max})$.
- The local search swapping and congestion management can be computed within $O(t_{\max})$ computations.

- Lastly, the final solution can be found in constant time.

Taking all these into thoughtful consideration and assuming $D << t_{\max}$, the overall computational complexity of proposed RSP comes out to be $O(\mathcal{P}_{\text{size}} t_{\max})$.

4 Results and Discussion

All experiments in this research work are done in MATLAB 2016b in Windows 10 platform 3.6 GHz processor and 32 GB memory. The experiments end when either the optimal solution is met or the number of iteration to the maximum generation ($t_{\max} = 500$).

Table 2 Comparison of total delay Δ and computation time $\mathcal{T}_e$ for the instances

				HBA [proposed]		PACO [9]		FCFS [11]		PSO [26]	
$\mathcal{I}$	m	p	l	Δ	$\mathcal{T}_e$	Δ	$\mathcal{T}_e$	Δ	$\mathcal{T}_e$	Δ	$\mathcal{T}_e$
RSP1	10	2	1	59	0.09	141	1.43	57	0.08	132	1.41
		3		47	0.08	147	1.49	52	0.07	128	1.29
RSP2	15	2	1	79	0.11	139	1.47	69	0.91	24	0.03
		3		75	0.10	152	1.66	61	0.91	17	0.02
RSP3	20	2	2	57	0.09	189	1.84	520	3.41	129	1.45
		3		62	0.10	224	2.08	489	3.32	121	1.42
RSP4	25	2	2	83	0.65	231	2.10	214	2.18	244	2.41
		3		72	0.60	249	2.52	214	2.17	218	2.39
RSP5	30	2	3	67	0.43	201	1.97	193	2.05	115	1.26
		3		93	1.01	215	2.02	210	2.11	118	1.26
		4		59	0.58	195	1.93	203	2.10	129	1.29
RSP6	40	2	3	118	1.20	272	2.89	216	2.50	156	1.60
		3		105	1.11	259	2.77	211	2.31	171	1.63
		4		111	1.13	451	3.03	211	2.31	158	1.62
RSP7	50	2	2	187	1.22	588	3.96	220	3.10	248	2.51
		3		162	1.15	756	3.77	232	3.09	247	2.50
		4		98	1.09	889	4.25	217	3.01	239	2.47
RSP8	60	2	2	49	0.08	876	4.81	289	4.01	112	1.19
		3		47	0.08	893	5.07	276	3.89	102	1.09
		4		121	1.11	902	5.47	272	3.82	123	1.20
RSP9	80	2	2	201	2.01	856	5.47	316	4.15	253	2.53
		3		215	203	1011	6.95	311	4.15	271	2.57
		4		197	198	1121	8.25	303	3.98	279	2.55
RSP10	100	2	3	158	1.77	3215	18.87	448	4.88	149	1.49
		3		213	1.92	3116	17.16	516	4.93	138	1.42
		3		118	2.45	3341	34.82	414	3.89	153	1.51

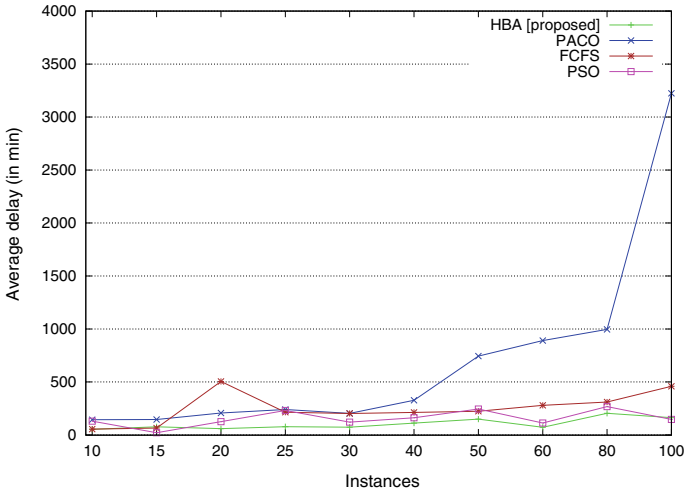

Fig. 5 Comparison of average delay faced by trains of each instance

Sensitivity analysis is made to evaluate the effectiveness of the parameter values chosen for the experiments. It is observed from the rigorous experiments of sensitivity analysis, population size $\mathcal{P}_{size}$ and parameter α can be set to 15 and 0.9 respectively for the proposed algorithm.

Table 2 shows the comparative analysis among HBA (proposed), PACO [9], FCFS [11], PSO [26], where for each instance $\mathcal{I}$, m number of trains, p number of platforms, l number of tracks. The instances involve 10 to 100 trains, maximum 4 platforms, and 3 tracks. Each instance is ran 20 times. The system taken for the experiments follows network topology, where network elements like stations (nodes), tracks (links) are arranged as depicted in Fig. 1 and communication between them is done based on the protocol. It is observed from Table 2 that delay (Δ) faced by the trains in RSP and the computation time ($\mathcal{T}_e$) both are far less in proposed algorithm than the other methods taken from literature survey.

Figures 5 and 6 depicts comparison of average delay and average execution time of aforementioned algorithms under the same experimental conditions. Figure 7 shows the convergence characteristics of proposed algorithm. Taking one of terminating conditions as $t_{\max} = 500$, it is observed that for the proposed HBA for railway scheduling problem delay of trains gets minimized while number of iteration increases.

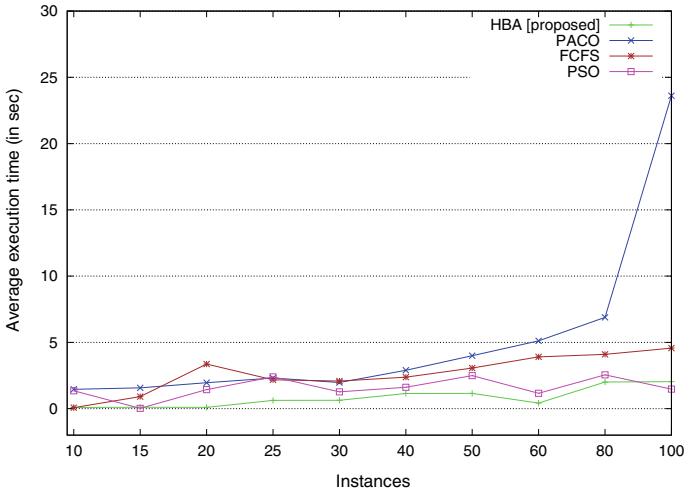

Fig. 6 Comparison of average execution time of each instance

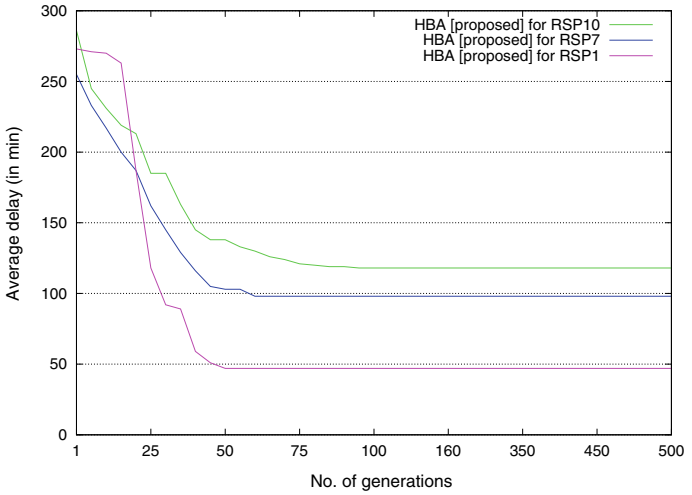

Fig. 7 Convergence graph for proposed HBA

5 Conclusion

This paper addresses railway scheduling problem (RSP) with multiple tracks and platforms. The main goal of this is to minimize the total journey time delay of the trains. To solve this, the notion of hybrid bat algorithm (HBA) is incorporated in this research work, where candidate solution is taken depending upon the problem and number of local searches are made in the BA framework. The results obtained

from the proposed approach shows that this algorithm can efficiently handle RSP and gives high quality solutions for such large complex network. The comparative analysis also shows this proposed method outperforms the other existing methods in this domain.

Acknowledgements This research work is a part of the project [Project Id No.: 1-5728195821] named "Multi-Agent Based Modelling for Collision Handling and Delay Optimization in Indian Railway System" and funded by MHRD and World-bank under TEQIP Collaborative Research Scheme, Govt. of India.

References

1. Abid MM, Khan MB (2015) Sensitivity analysis of train schedule of a railway track network using an optimization modeling technique. Eur Transp Res Rev 7:2–7
2. Acuna-Agost R, Michelon PcDF, Gueye S (2011) Sapi: statistical analysis of propagation of incidents. a new approach for rescheduling trains after disruptions. Eur J Oper Res 215:227–243
3. Alwadood Z, Shuib A, Hamid NA (2012) A review on quantitative models in railway rescheduling. Int J Sci Eng Res 3:1–7
4. Beasley JE, Krishnamoorthy M, Sharaiha YM, Abramson D (2000) Scheduling aircraft landings-the static case. Transp Sci 34(2):180–197
5. Beg S, Khan A, Nauman U, Mohsin S (2011) Performance evaluation of bionomic algorithm (ba) in comparison with genetic algorithm (ga) for shortest path finding problem. Int J Comput Sci Issues (IJCSI) 8(6):238
6. Brentnall AR, Cheng RC (2009) Some effects of aircraft arrival sequence algorithms. J Oper Res Soc 60(7):962–972
7. Corman F, D'Ariano A, Marra AD, Pacciarelli D, Samà M (2017) Integrating train scheduling and delay management in real-time railway traffic control. Transp Res Part E Logist Transp Rev 105:213–239
8. D'Ariano A, Pacciarelli D, Sama M, Corman F (2017) Microscopic delay management: minimizing train delays and passenger travel times during real-time railway traffic control. In: 2017 5th IEEE international conference on models and technologies for intelligent transportation systems (MT-ITS). IEEE, pp 309–314
9. Eaton J, Yang S, Gongora M (2017) Ant colony optimization for simulated dynamic multi-objective railway junction rescheduling. IEEE Trans Intell Transp Syst 18(11):2980–2992
10. Eaton J, Yang S, Mavrovouniotis M (2016) Ant colony optimization with immigrants schemes for the dynamic railway junction rescheduling problem with multiple delays. Soft Comput 20(8):2951–2966
11. Gafarov ER, Dolgui A, Lazarev AA (2015) Two-station single-track railway scheduling problem with trains of equal speed. Comput Indus Eng 85:260–267
12. Gaied M, Lefebvre D, M'halla A, Othmen KB (2018) Modelling and performance evaluation of railway transport systems using p-timed petri nets. In: 2018 5th international conference on control, decision and information technologies (CoDIT). IEEE, pp 841–846
13. Gandomi AH, Yang XS, Alavi AH, Talatahari S (2013) Bat algorithm for constrained optimization tasks. Neural Comput Appl 22(6):1239–1255
14. Giglio D, Sacco N (2016) A petri net model for analysis, optimisation, and control of railway networks and train schedules. In: 2016 IEEE 19th international conference on intelligent transportation systems (ITSC). IEEE, pp 2442–2449
15. Hancerliogullari G, Rabadi G, Al-Salem AH, Kharbeche M (2013) Greedy algorithms and metaheuristics for a multiple runway combined arrival-departure aircraft sequencing problem. J Air Transp Manage 32:39–48

16. Hassan GM, Reynolds M (2018) Genetic algorithms for scheduling and optimization of ore train networks. In: GCAI, pp 81–92
17. He D, Lu G, Yang Y (2019) Research on optimization of train energy-saving based on improved chicken swarm optimization. IEEE Access 7:121675–121684
18. Kersbergen B, van den Boom T, Schutter BD (2013) Reducing the time needed to solve the global rescheduling problem for railway networks. In: Proceedings of the 16th international IEEE annual conference on intelligent transportation systems (ITSC 2013), pp 791–796
19. Li X, Shou B, Ralescu D (2014) Train rescheduling with stochastic recovery time: a new track-backup approach. IEEE Trans Syst Man Cybern Syst 44(9):1216–1233
20. Salehipour A, Modarres M, Naeni LM (2013) An efficient hybrid meta-heuristic for aircraft landing problem. Comput Operat Res 40(1):207–213
21. Taha A, Hachimi M, Moudden A (2017) A discrete bat algorithm for the vehicle routing problem with time windows. In: 2017 international colloquium on logistics and supply chain management (LOGISTIQUA). IEEE, pp 65–70
22. Talal R (2014) Comparative study between the (ba) algorithm and (pso) algorithm to train (rbf) network at data classification. Int J Comput Appl 92(5):16–22
23. Wang G, Guo L, Duan H, Liu L, Wang H (2012) A bat algorithm with mutation for UCAV path planning. Sci World J
24. Xie J, Zhou Y, Chen H (2013) A novel bat algorithm based on differential operator and lévy flights trajectory. Comput Intell Neurosci
25. Xie J, Zhou Y, Zheng H (2013) A hybrid metaheuristic for multiple runways aircraft landing problem based on bat algorithm. J Appl Math
26. Yaman O, Karakose E, Karakose M (2018) PSO based traffic optimization approach for railway networks. In: 2018 international conference on artificial intelligence and data processing (IDAP). IEEE, pp 1–4
27. Yang XS (2010) A new metaheuristic bat-inspired algorithm. In: Nature inspired cooperative strategies for optimization (NICSO 2010). Springer, pp 65–74
28. Yang XS, Gandomi AH (2012) Bat algorithm: a novel approach for global engineering optimization. Eng Comput

Optimal Rescheduling of Real Power to Mitigate Congestion Using Elephant Herd Optimization

Kaushik Paul and Poulami Dalapati

Abstract Transmission line congestion has evolved as one of the vital issues in the deregulated power system framework. This paper proposes an efficient congestion management strategy based on the rescheduling of the generators. The Generator Sensitivity Factor has been incorporated to select the most efficient generator to reschedule their power output. Elephant Herd Optimization has been used to optimally reschedule the real power delivery of the generators to minimize the congestion cost. 39-bus New England Test framework is considered to analyse the performance of the proposed approach. The proposed approach has been compared with other algorithms and it is observed that the proposed strategy efficiently minimizes the congestion cost when compared to other optimization approaches. The adopted approach also enhances the voltage limits and reduces the real power losses providing a better system stability.

Keywords Congestion management · Generator rescheduling · Generator sensitivity factor · Elephant Herd optimization

1 Introduction

The deregulated framework of the power system has intensified the competition among the market players [19]. This scenario has resulted into extensive transaction of power from generation source to consumer end causing the transmission channel to be overloaded. The transmission line is identified as congested when the transfer limits are violated [14]. The Independent System Operator (ISO) initiates necessary

K. Paul (✉)
Department of Electrical Engineering, BIT Sindri, Dhanbad, India
e-mail: kaushiksunnypaul@gmail.com

P. Dalapati
Department of Computer Science and Engineering, BIT Sindri, Dhanbad, India
e-mail: dalapati89@gmail.com

G. T. C. Sekhar et al. (eds.), *Intelligent Computing in Control and Communication*, Lecture Notes in Electrical Engineering 702,
https://doi.org/10.1007/978-981-15-8439-8_9

actions to relive the congested status of the transmission lines to maintain the security and reliability of the power system [11, 13].

There has been ample of techniques adopted to manage congestion in the power system network. A brief discussion of several Congestion Management (CM) approaches, implemented in the electricity market, can be found in [8, 15]. In [1] Conejo et al. controlled the transmission congestion monitoring the voltage stability. Sang et al. utilized the FACTS devices to relive congestion [17]. In [6] a penalty emission cost was considered with the the optimal positioning of the thyristor controlled series capacitors to control congestion. In [9] the locational marginal pricing has been computed considering the bilateral transaction to alleviate the congestion. Rajamanickam et al. have focused their research to regulate congestion using distribution generation. The distribution generations were located optimally to at the best possible sites to control the excessive power flow [18]. A stochastic CM model was formulated by Hojjat et al. using constrained programming approach to reduce congestion in the transmission channels [5].

The increment in the load demand is satisfied with the optimal balance in the power generation [12]. The generator rescheduling has been proved competent to diminish congestion in transmission lines [14]. In [21] the authors adopted generator rescheduling to lessen the effect of congestion based on the Relative Electrical Distance (RED) methodology. The CM problem also considered the better voltage stability with reduction in transmission losses. In [3], the Generator Sensitivity Factor (GSF) and Particle Swarm Optimization (PSO) was implemented to curtail the congestion by modulating the generator power output. The GSF has been used for the identification of most prominent generators for rescheduling. Artificial Bee Colony (ABC) algorithm has been utilized by Deb et al. to reduce congestion cost occurred due to generator rescheduling phenomenon. In this work, the GSF approach has been implemented to select most influential generators for power management. [2]. A CM approach considering the load shedding and generator rescheduling has been implemented by Reddy [16]. The CM was formulated as a multi-objective problem to control congestion cost with social-welfare maximization.

In this research work, the generator rescheduling technique for the real power is taken into account to manage congestion. The generators are engaged in the power rescheduling process according to their GSFs. The integral contribution of this work is the implementation of Elephant Herd Optimization (EHO) to optimally reschedule the real power output of the generators and minimize the rescheduling cost.

2 Problem Formulation

The definition of GSF can be stated as power variation in the congested line for a minor variation in the power generation. The GSF is represented in Eq. (1) as:

$$\mathrm{GSF}_{\mathrm{g}} = \frac{\Delta P_{\mathrm{lm}}}{\Delta P_{\mathrm{g}}} \tag{1}$$

Here, ΔP_{lm} and ΔP_{g} states the deviation in flow of power in the over loaded line and change in the generated power respectively. Equation (2) represents the active power flow in the transmission channel:

$$P_{\mathrm{lm}} = -V_{\mathrm{l}}^2 G_{\mathrm{lm}} + V_{\mathrm{l}} V_{\mathrm{m}} G_{\mathrm{lm}} \cos(\theta_{\mathrm{l}} - \theta_{\mathrm{m}}) + V_{\mathrm{l}} V_{\mathrm{m}} B_{\mathrm{lm}} \sin(\theta_{\mathrm{l}} - \theta_{\mathrm{m}}) \tag{2}$$

Here V_{l} and V_{m} corresponds to the bus voltages at the lth and mth buses respectively. G_{lm} and B_{lm} are the conductance and susceptance of line connecting the buses $'l'$ and $'m'$. θ_{l} and θ_{m} are the magnitudes of the phase angles corresponding to $'l'$ and $'m'$ buses respectively. The Eq. (1) can be represented as:

$$\mathrm{GSF}_{\mathrm{g}} = \frac{\delta P_{\mathrm{lm}}}{\delta \theta_{\mathrm{l}}} . \frac{\delta \theta_{\mathrm{l}}}{\delta P_{\mathrm{g}}} + \frac{\delta P_{\mathrm{lm}}}{\delta \theta_{\mathrm{m}}} . \frac{\delta \theta_{\mathrm{m}}}{\delta P_{\mathrm{g}}} \tag{3}$$

The detail derivation of the $\mathrm{GSF}_{\mathrm{g}}$ in Eq. (3) has been illustrated in [3].

The congestion cost based on real power rescheduling for the CM approach can be represented as:

$$\min\ \mathcal{C} = \min \sum_{\mathrm{g}=1}^{N_{\mathrm{g}}} C_{\mathrm{g}}(\Delta P_{\mathrm{g}}) \Delta P_{\mathrm{g}} \tag{4}$$

Here, in Eq. (4), ΔP_{g} = amount of active power rescheduled by the generator $'g'$ in MW. C_{g}= generators price bids submitted for CM (\$/MWh). The constraints considered for the optimization problem are as follows:

$$\sum_{\mathrm{g}=1}^{N_{\mathrm{g}}} ((\mathrm{GSF}_{\mathrm{g}}) * \Delta P_{\mathrm{g}}) + PF_k^0 \leq PF_k^{\max} \tag{5}$$

$$\Delta P_{\mathrm{g}}^{\min} \leq \Delta P_{\mathrm{g}} \leq \Delta P_{\mathrm{g}}^{\max} \tag{6}$$

$$\Delta P_{\mathrm{g}}^{\min} = P_{\mathrm{g}} - P_{\mathrm{g}}^{\min} \tag{7}$$

$$\Delta P_{\mathrm{g}}^{\max} = P_{\mathrm{g}}^{\max} - P_{\mathrm{g}} \tag{8}$$

$$\sum_{\mathrm{g}=1}^{N_{\mathrm{g}}} \Delta P_{\mathrm{g}} = 0 \tag{9}$$

$P_{\mathrm{g}}^{\max}$= maximum real power output limit of generator.
$P_{\mathrm{g}}^{\min}$= minimum real power output limit of generator.
PF_k^0= power flow in kth line considering all the contracts.
$PF_k^{\max}$= maximum limit of power flow for kth line (line limit).
N_{g}= number of generators taking part in CM.

Equations (5) and (6) show the in-equality constraints governing the maximum limit for the power flow in the transmission lines and the generation limits respectively. Equations (7) and (8) represents the computation of upper and lower generation limits for the generators. The equality constraints for the power generation is represented in Eq. (9).

The fitness function for CM with EHO is represented in Eq. (10) as:

$$\sum_{g=1}^{N_g} C_g(\Delta P_g)\Delta P_g + \mathcal{P}_{\mathbf{M}} * [(\sum_{g=1}^{N_g}((\mathrm{GSF}_g) * \Delta P_g) + PF_k^0 \leq PF_k^{\max}) + P_g - P_g^{\min} + \sum_{g=1}^{N_g} \Delta P_g = 0)] \tag{10}$$

where $\mathcal{P}_{\mathbf{M}}$ is the penalty multiplier.

3 Elephant Herd Optimization

The Elephant Herd Optimization (EHO) has been implemented in several engineering sectors with appreciable results [4, 7, 10] which was first developed in 2016 by Wang et al. [20]. EHO has certain advantages like it is easy to implement, better convergence rate and does not fall into local optima. The primary framework of the EHO has been developed based on the following rules:

- The elephant population corresponding to various clans stays together and is regulated by a matriarch. The count of elephants in each clan is same and is kept constant.
- The position updating of the elephants in the clans is performed depending on its relation with matriarch. An updating operator is used to perform this ask.
- A certain number of male elephants gets separated from their clans during each generation to live alone. This process is performed based on the separating operator.
- The matriarch is considered as the most eldest and fittest entity in the group.

3.1 Clan Updating Operator

The updating procedure for EHO [20] has been illustrated in Eq. (11) and is represented as:

$$x_{n,ci,j} = x_{ci,j} + \alpha \times (x_{b,ci} - x_{ci,j}) \times r \tag{11}$$

Here, $x_{n,ci,j}$, $x_{ci,j}$ represent updated position and previous position of elephant j of clan ci respectively. In addition to this, the matriarch of ci is denoted as $x_{b,ci}$. The range of scale factor α is taken as $\alpha \in [0, 1]$. This helps in determining the effect of matriarch on $x_{ci,j}$. A stochastic distribution $r \in [0, 1]$ is taken to provide a substantial amount of improvement in the population diversity during the later duration of the search phase. The proposed work considers an uniform distribution.

It is observed that the position update cannot be performed when $x_{ci,j} = x_{n,ci,j}$. In order to circumvent this situation, the position update of the matriarch can be done considering the Eq. (12):

$$x_{n,ci,j} = \beta \times x_{c,ci} \tag{12}$$

Here $\beta \in [0, 1]$ and modulates the effect of $x_{c,ci}$ on $x_{n,ci,j}$. $x_{c,ci}$ is the center of c_i for the d^{th} dimension is represented in Eq. (13):

$$x_{c,ci,d} = \frac{1}{n_{ci}} \times \sum_{j=1}^{n_{ci}} x_{ci,j,d} \tag{13}$$

where $1 \leq d \leq D$ and D is as the total dimension. n_{ci} is taken as the number of elephants present in ci. $x_{ci,j,d}$ is represented as the individual of $x_{ci,j}$ at dth dimension.

3.2 Separating Operator

The male elephants at the time of their puberty leave the elephant group and start to leave alone. This phenomenon has been modeled as a separating operator in the EHO optimization strategy. The search ability of EHO can enhanced based on the following equation:

$$x_{w,ci} = x_{\min} + (x_{\max} - x_{\min} + 1) \times r_{\text{num}} \tag{14}$$

In Eq. (14) the highest and lowest limit for the elephant positions are denoted as $x_{\max}$ and $x_{\min}$ respectively. $x_{w,ci}$ signifies the worst elephant in herd. In the optimization problem, $r_{\text{num}} \in [0, 1]$ denotes the uniform distribution. The EHO flowchart for CM is shown in Fig. 1

The EHO adopts the strategy to protect the best elephant from group of elephants in the clan. In this optimization approach the best elephant individual is secured and this replaces the worst elephant. This strategy is maintained at the end of each search procedure. The CM problem analysed with EHO in this paper, the EHO parameters selected are as follows: number of kept elephants = 2, number of clan $nClan$ = 5, $\alpha = 0.5$, $\beta = 0.1$. The work in this article consider that all the clan has the same number of elephant $n_{ci} = 20$.

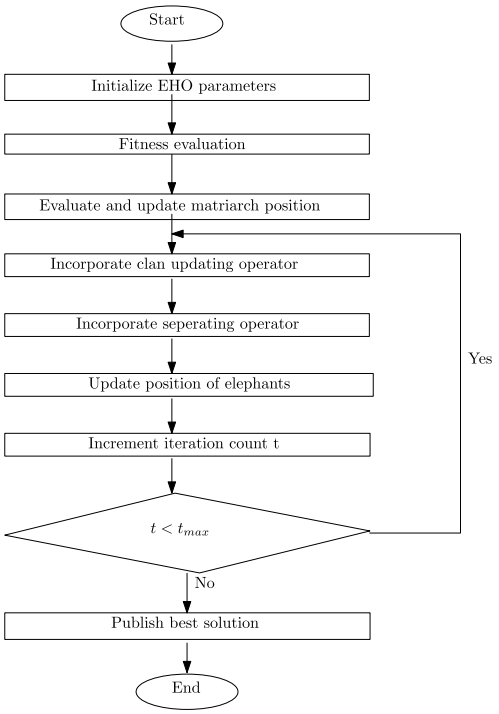

Fig. 1 Flowchart of Elephant Herd optimization

4 Results and Discussions

The work presented in this manuscript utilizes EHO to mitigate the over burden of the lines while minimizing the congestion cost. The proposed approach has been implemented on 39-bus New England to analyse its effectiveness [3]. The representation of 39-bus New England system is shown in Fig. 2. The results obtained with EHO has been compared with RED [21], PSO [3] and ABC [2].

The adopted test case system portrays that, the transmission path (L14-L34) existing between buses 14 and 34 has a flow limit of 600 MVA, which is loaded to 262 MVA. In the proposed work, line outage is done for the line L_{14-34}, which leads to the over loading of the line L_{15-16}. The power flow in the line L_{15-16} has been increased to 628.4 MVA (Line limit 500 MVA). The line outage can be carried out based on any other line to analyse the proposed work, but line L_{14-34} has been subjected to outage performed to establish a comparative analysis with RED [21], PSO [3], and ABC [2].

The GSF values are represented in Table 1. The generators numbers 4,5,6,7 have uniform GSF values and does not provide significant contribution in power flow reduction for the designated congested line. Generators 2, 3, 8, 9, 10 have the most deviated GSF values which influence maximum power flow modulation in congested

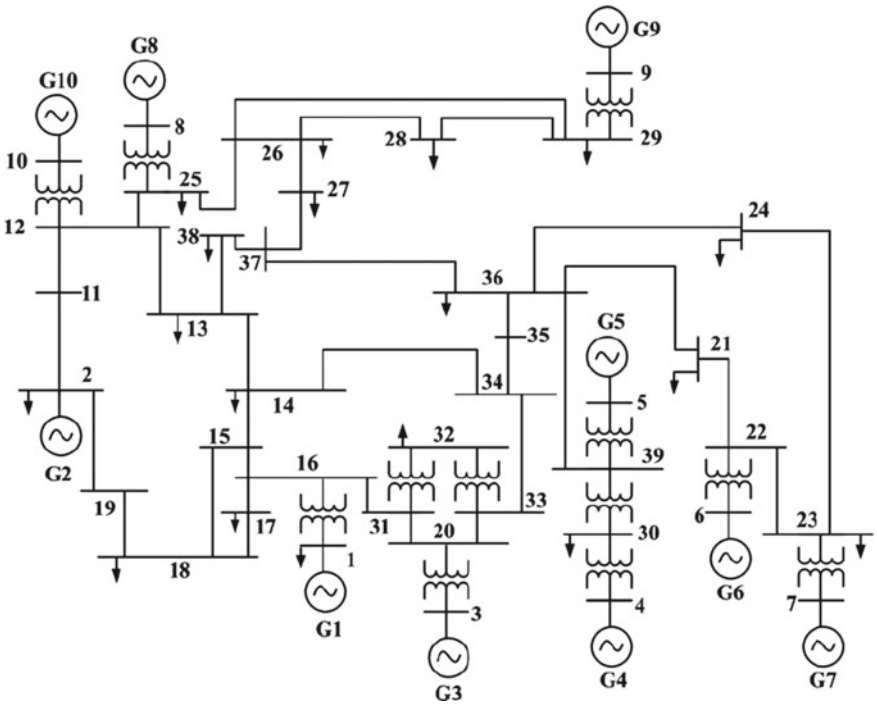

Fig. 2 39-bus New England framework

Table 1 Generator sensitivity factor for 39 bus

Gn. No.	1	2	3	4	5	6	7	8	9	10
GSF	0.00	−0.49	−0.12	−0.35	−0.35	−0.35	−0.35	−0.53	−0.46	−0.58

Table 2 Generator price bids for 39 bus

Gn. No.	1	2	3	4	5	6	7	8	9	10
Bids($/MWh)	15	20	17	16	12	17	13	11	14	19

line. The system losses are met by rescheduling generator no. 1, which is the slack bus generator. The generator price bids are represented in Table 2.

The comparison between EHO and other algorithms [2, 3, 21] are shown in Table 3. It is observed that the GSF analysis have led to the reduction in count of generators from ten to six. Thus leading to the minimum number of generators to participate in the rescheduling process to manage the congestion. In order to establish a comparative analysis, the results obtained with other algorithms [2, 3, 21] are also represented in Table 3 along with EHO. It is observed that the rescheduled cost obtained with EHO

Table 3 Comparative analysis of results with EHO for 39 bus

	RED [21]	PSO [3]	ABC [2]	EHO [proposed]
Rescheduling cost ($/h)	8640.2	8873.1	8451.8	8107.78
Power flow of L_{15-16} (MW) after CM	510	490	499.50	496.90
ΔP_1 (MW)	−99.59	−149.1	−131.0	−132.63
ΔP_2 (MW)	98.75	65.6	63.2	43.12
ΔP_3 (MW)	−159.64	−129	−132.0	−125.32
ΔP_4 (MW)	12.34	Not involve	Not involve	Not involve
ΔP_5 (MW)	24.69	Not involve	Not involve	Not involve
ΔP_6 (MW)	24.69	Not involve	Not involve	Not involve
ΔP_7 (MW)	12.34	Not involve	Not involve	Not involve
ΔP_8 (MW)	24.69	75.4	72.2	92.78
ΔP_9 (MW)	12.34	52.1	49.1	46.95
ΔP_{10} (MW)	49.38	83.0	78.8	76.19
Total amount (MW)	518.45	554.2	526.3	516.99

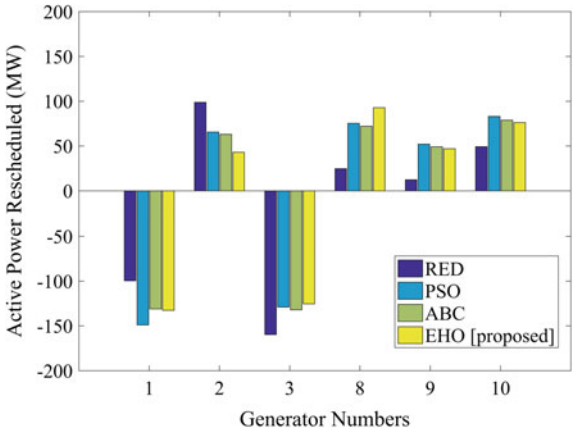

Fig. 3 Active power rescheduled with RED [21],PSO [3], ABC [2] and EHO [proposed]

is 8107.78 $\$/h$ which is minimum among all the other optimization approaches [2, 3, 21]. The power flow in the congested line has been reduced to 496.90 MW and signifies that EHO has successfully relieved the state of congestion in the transmission network.

The total rescheduled amount of real power achieved with EHO is also minimum among the other opted algorithms in the referred literature. The pictorial representation of the amount of real power adjusted by the generators are represented in Fig. 3.

Table 4 Comparative analysis of system parameters

System parameters	Before rescheduling	RED [21]	PSO [3]	ABC [2]	EHO [proposed]
P_{loss}(MW)	59.64	57.31	58.00	59.36	57.09
V_{min}(p.u)	0.941	0.945	0.932	0.940	0.956

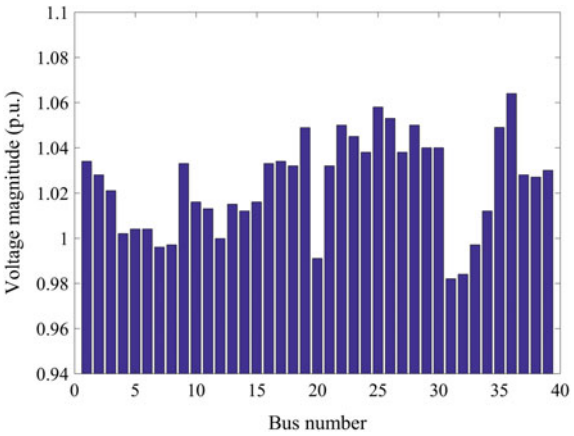

Fig. 4 Voltage levels at each buses after CM

Table 5 Analysis of Line overload factor

Line number	Before rescheduling	RED [21]	PSO [3]	ABC [2]	EHO [proposed]
L_{15-16}	1.25	1.02	0.98	0.99	0.97

Table 4 shows that the implementation of EHO has led to the reduction in the system losses to 57.09 MW and has also led to the enhancement in voltage levels to 0.956 p.u. It is observed that the system losses and the improvement in the voltage levels are better than the other reported results in Table 4. The voltages at each buses post CM are represented in Fig. 4. The line overload factors are indicated in Table 5. It is observed that with EHO the line overload factor for the congested line is 0.97 and better than the overload factor achieved with other optimization approaches.

The EHO has resulted in the successful elimination of the overburdening of transmission channel. The convergence characteristic portrays that with the increase in the iteration the congestion cost reaches its minimum with EHO. The convergence profile is shown in Fig. 5.

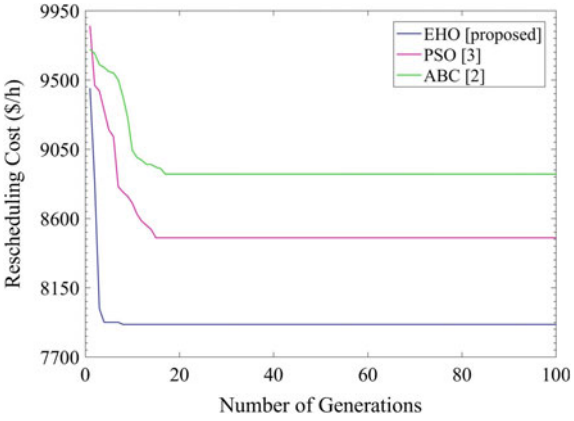

Fig. 5 Convergence profile with EHO for optimal congestion cost

5 Conclusion

This paper introduces generator rescheduling strategy for congestion control in power system framework. The sensitivity approach based on the GSF has led to selection of the most prominent generators that could participate in the rescheduling process. The nature inspired EHO technique has been successfully implemented to minimize the congestion cost with the elimination of congestion in the transmission lines.The rescheduling cost achieved with EHO is minimum among the cost achieved with other referred algorithms. The adopted approach also leads to the reduction in the system losses and enhancement in the system voltage, thus ensuring a reliable and stable power system network.

References

1. Conejo AJ, Milano F, García-Bertrand R (2006) Congestion management ensuring voltage stability. IEEE Trans Power Syst 21(1):357–364
2. Deb S, Gope S, Goswami AK (2013) Generator rescheduling for congestion management with incorporation of wind farm using artificial bee colony algorithm. In: 2013 Annual IEEE India conference (INDICON). IEEE, pp 1–6
3. Dutta S, Singh S (2008) Optimal rescheduling of generators for congestion management based on particle swarm optimization. IEEE Trans Power Syst 23(4):1560–1569
4. Elhosseini MA, El Sehiemy RA, Rashwan YI, Gao X (2019) On the performance improvement of elephant herding optimization algorithm. Knowl-Based Syst 166:58–70
5. Hojjat M, Javidi DB MH (2013) Probabilistic congestion management considering power system uncertainties using chance-constrained programming. Electric Power Compon Syst 41(10): 972–989
6. Hooshmand RA, Morshed MJ, Parastegari M (2015) Congestion management by determining optimal location of series facts devices using hybrid bacterial foraging and Nelder-Mead algorithm. Appl Soft Comput 28:57–68

7. Jayanth J, Shalini V, Kumar TA, Koliwad S (2019) Land-use/land-cover classification using elephant herding algorithm. J Indian Soc Remote Sens 47(2):223–232
8. Kumar A, Srivastava S, Singh S (2005) Congestion management in competitive power market: a bibliographical survey. Electr Power Syst Res 76(1–3):153–164
9. Liu M, Gross G (2008) Congestion rents and FTR evaluations in mixed-pool-bilateral systems. Int J Electr Power Energy Syst 30(8):447–454
10. Meena NK, Parashar S, Swarnkar A, Gupta N, Niazi KR (2017) Improved elephant herding optimization for multiobjective der accommodation in distribution systems. IEEE Trans Indust Inf 14(3):1029–1039
11. Pal Verma Y, Sharma AK (2015) Congestion management solution under secure bilateral transactions in hybrid electricity market for hydro-thermal combination. Int J Electr Power Energy Syst 64:398–407
12. Paul K, Kumar N (2018) Cuckoo search algorithm for congestion alleviation with incorporation of wind farm. Int J Electr Comput Eng 8:2088–8708
13. Paul K, Kumar N, Agrawal S (2017) Optimal rescheduling of real power to mitigate congestion with incorporation of wind farm using gravitational search algorithm in deregulated environment. Int J Renew Energy Research (IJRER) 7(4):1731–1740
14. Paul K, Kumar N, Agrawal S, Paul K (2019) Optimal rescheduling of real power to mitigate congestion using gravitational search algorithm. Turk J Electr Eng Comput Sci 27(3):2213–2225
15. Pillay A, Karthikeyan SP, Kothari D (2015) Congestion management in power systems-a review. Int J Electr Power Energy Syst 70:83–90
16. Reddy SS (2016) Multi-objective based congestion management using generation rescheduling and load shedding. IEEE Trans Power Syst 32(2):852–863
17. Sang Y, Sahraei-Ardakani M (2017) The interdependence between transmission switching and variable-impedance series facts devices. IEEE Trans Power Syst 33(3):2792–2803
18. Sasiraja RM, Kumar VS, Ponmani S (2015) An elegant emergence of optimal siting and sizing of multiple distributed generators used for transmission congestion relief. Turk J Electr Eng Comput Sci 23(6):1882–1895
19. Shahidehpour M, Yamin H, Li Z (2003) Market operations in electric power systems: forecasting, scheduling, and risk management. Wiley, New York
20. Wang GG, Deb S, Gao XZ, Coelho LDS (2016) A new metaheuristic optimisation algorithm motivated by elephant herding behaviour. Int J Bio-Inspired Comput 8(6):394–409
21. Yesuratnam G, Thukaram D (2007) Congestion management in open access based on relative electrical distances using voltage stability criteria. Electr Power Syst Res 77(12):1608–1618

Adiabatic Logic-Based Area- and Energy-Efficient Full Adder Design

Krishna Saladi and B. Leela Kumari

Abstract Low energy- and area-efficient digital circuit design is unique among the significant navigational challenges of digital VLSI design suitable for real-time applications. Full adders are essential functional elements in complex arithmetic circuits; a 1-bit adder is developed by using adiabatic logic in this operation to get low power consumption. The intended 1-bit adder cell with adiabatic logic results in very less heat dissipation with its surrounding circuit atmosphere. As a result, this logic has minimal energy loss due to overheating dissipation. The proposed adiabatic logic circuit is compared with CMOS and pass transistor logic (PTL) with TG 1-bit adder topologies. The results show that there are significant advantages in power saving compared to CMOS and pass transistor cells. The proposed adiabatic logic full adder requires 18 transistors to design. The proposed adiabatic logic 1-bit adder, designed with three inputs, produces the output response as true and complementary outputs in a single architecture. All full adder cells were designed with 65 nm technology and compared area and power consumption.

Keywords Full adder cell · Adiabatic logic · PTL logic

1 Introduction

In VLSI technology, engineers can easily implant more than a million gates into a single IC. In handhelds and convenient electronic devices, the power saving of a full adder circuit is essential [1]. Most of these circuit blocks are slots in processor-based blocks, requiring a variety of arithmetic blocks. For example, this arithmetic block is part of a microprocessor, digital signal, and digital image processor, encryption

K. Saladi (✉)
Department of ECE, Aditya Engineering College, Surampalem, Andhra Pradesh 533437, India
e-mail: krishna.s@aec.edu.in

K. Saladi · B. Leela Kumari
Department of ECE, JNTU kakinada, Kakinada, Andhra Pradesh 533003, India
e-mail: leela8821@yahoo.com

G. T. C. Sekhar et al. (eds.), *Intelligent Computing in Control and Communication*, Lecture Notes in Electrical Engineering 702,
https://doi.org/10.1007/978-981-15-8439-8_10

processor [2, 3]. In each of the above processor's arithmetic and logical units, adders, multipliers, and dividers remain essential components. Various design styles have been implemented to reduce power consumption. This proposed adiabatic logic is a widely studied technique for low-power VLSI design due to its energy recycling operation. Recently, different adiabatic logic or energy recovery logic circuits have been proposed [4]. Adiabatic circuits have achieved better energy and area savings compared to conventional CMOS circuit designs. The level restore transfer event in conventional CMOS is a VDD to GND productivity voltage swing that produces energy transfer between the VDD to the output node or output node to GND.

Introducing adiabatic logic in the circuit reduces energy dissipation during switching events from power supply toward output, otherwise output to ground. It offers the prospect of reprocessing or reusing, approximate energy drained from the power supply. As the silicon area decreases during the manufacturing process, power consumption is reduced by selecting a low-power design style during the logic design phase. Due to this constraint, the design of a low-power 1-bit adder cells are achieved by choosing a low-power design style such as conventional 28-transistor cell [5], 16-transistor PTL with TG logic adder cell, 14-T PTL with TG adder cell and proposed low-power adiabatic logic full adder cell [6].

In VLSI circuit design, there is always an optimization between area, power, and delay. Adopting adiabatic logic overcomes the challenges of standard technologies such as CMOS and adder cells before PTL topologies. This paper is organized as follows: (i) various adder topologies, (ii) proposed adiabatic adder, and (iii) comparison of static CMOS and adiabatic switching activity. The performance of all designed full adder topologies is analyzed along with their area and power intake results.

2 Design of Various Full Adder Topologies

The following 1-bit adder topologies are discussed to compare with proposed adiabatic adder topology.

- Conventional 28-Transistor 1-bit adder cells.
- TG with PTL-based 1-bit adder topologies.

2.1 Conventional 28-Transistor 1-bit Adder Cells

The conventional 28-transistor full adder logic cell is shown in Fig. 1. To get the sum and carry outputs of this topology, the designed dimensions for PMOS pull-up network and NMOS pull-down network are [7] 0.5u/0.07u and 0.3u/. 07u, respectively.

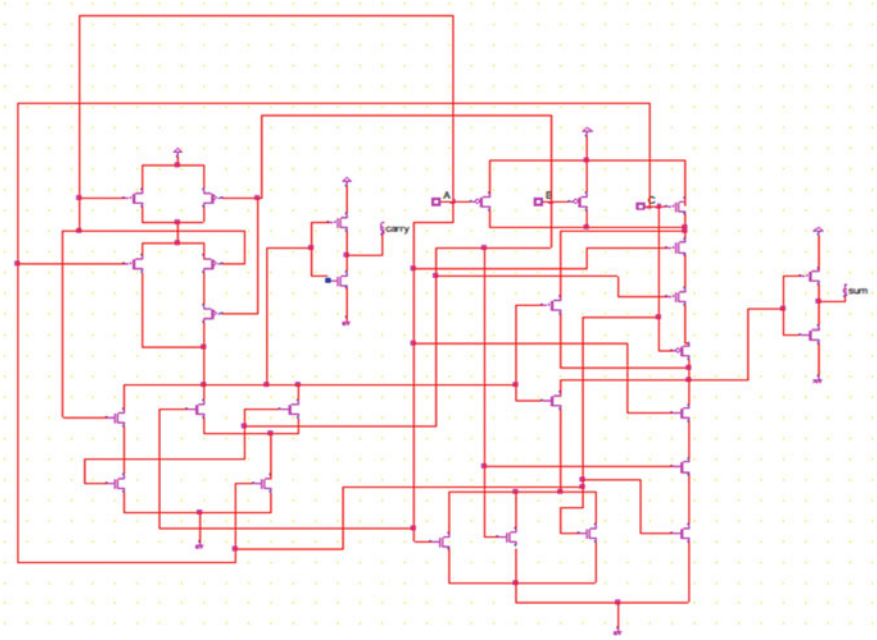

Fig. 1 28-T CMOS 1-bit adder topology

2.2 TG with PTL-Based 1-Bit Adder Topologies

The advantage of using PTL over static CMOS is that the less transistor count achieves desired logic levels. The bottleneck of this PTL logic is that the degradation of logic levels when inputs are passed through them. By inserting TG in this topology, the logic levels can be restored without degradation.

2.2.1 16-Transistor TG with PTL 1-bit Adder Cell

16-T PTL using TG constructed 1-bit adder cell is presented in Fig. 2. The simulation model result shows that this logic has a smaller amount of power dissipation than the 28-T CMOS full adder logic cell.

2.2.2 14-Transistor TG with PTL 1-Bit Adder Cell

The PTL with 14-T 1-bit adder is presented in Fig. 3. Simulation output shows that it has a lesser power intake than CMOS dynamic power consumption.

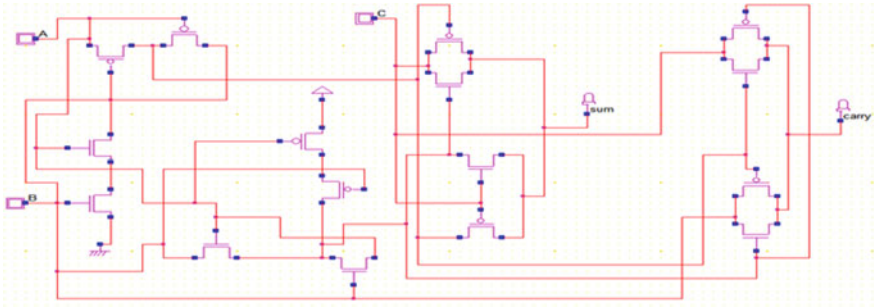

Fig. 2 PTL with TG-based 16-T 1-bit adder

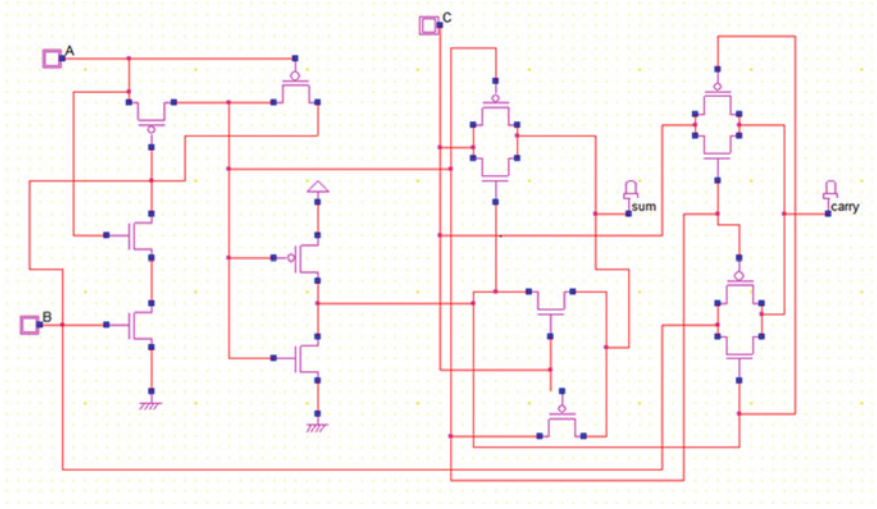

Fig. 3 PTL with TG-based 14-T 1-bit adder

3 Proposed Adiabatic 1-bit Adder Cell

Adiabatic logic reduces power consumption compared to CMOS and other logic families. This type of logic circuit model is a low-power circuit using charge recovery logic to conserve energy [8]. In this logic, the energy stored in the capacitor is recycled back to the power supply during the discharge period, in this way, there is less energy loss in this circuit topology.

3.1 Comparison of CMOS and Adiabatic Logic Switching Activity

Static CMOS switching activity and adiabatic switching activity is compared and advantages of adiabatic switching activity are discussed.

3.1.1 Conventional CMOS Logic Switching

In CMOS logic, a static voltage source VDD is used for its switching operation. In this, the switching event of the circuit causes the energy transfer between VDD to output or output to the ground, as presented in Fig. 4. During 0 to VDD transitions of output, the total output charge is given by Eq. (1).

$$Q = C_L V_{DD} \tag{1}$$

Thus, the energy per transition is given by

$$E = \frac{1}{2} C_L V_{DD}^2 \tag{2}$$

In Eq. (2), it is evident that only part of the energy drawn from the VDD is presented across the output node; the remaining power is dissipated across the PMOS pull-up network. In the next VDD to ground transition, the stored energy is discharged to ground through the NMOS pull-down network. To optimize power consumption, circuit designers can adopt dimensions scaling of devices, reducing the output node capacitance, voltage scaling, or use a combination of these methods.

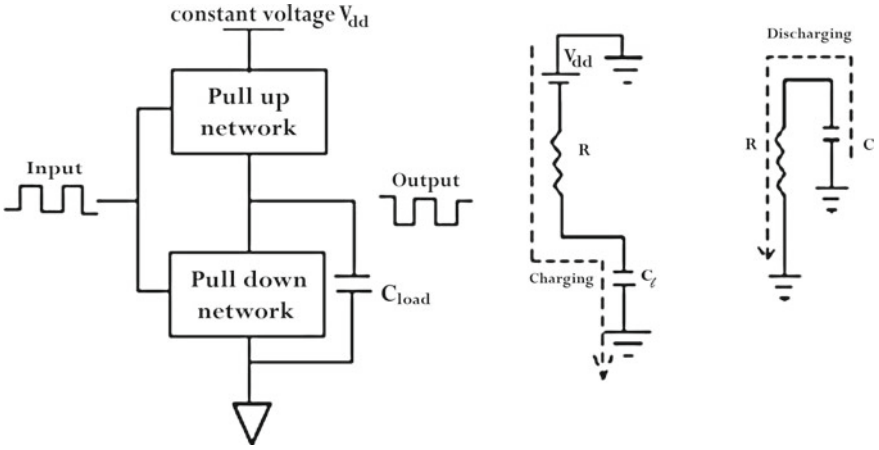

Fig. 4 Conventional CMOS charging and discharging

3.1.2 Adiabatic Switching

To increase the energy efficiency of the circuit, the circuit topology needs to be improved as required. In this, the energy stored in the charging phase is restored in the discharging phase; in other words, there is no energy loss like in CMOS logic.

Figure 5 shows a model for adiabatic-based circuits topology, and it consists of complimentary clock power sources, a resistor, and a switch. The constant current source has been used rather than a constant voltage source. The following equation describes the transition behavior in the adiabatic process.

Current across the capacitor can be written as shown in Eq. (3)

$$I(t) = C\_L \mathrm{d}V/\mathrm{d}T \tag{3}$$

Equation (4) describes the energy across the capacitor during charging.

$$E = I^2 * R * T \tag{4}$$

The voltage across the switch $= I * R$

$$Q = C\_L * V\_DD$$

$$I = C\_L * V\_DD/T$$

Therefore

$$E\_\text{Adiabatic} = I^2 * R * T \tag{5}$$

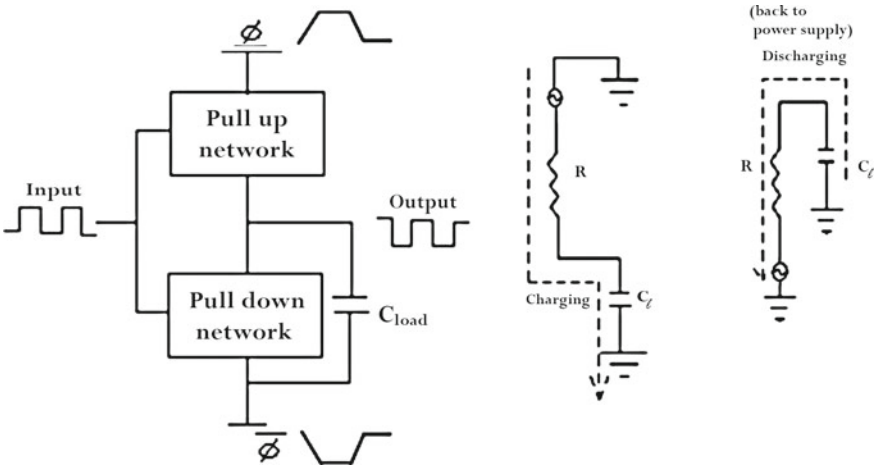

Fig. 5 Adiabatic charging and discharging [9]

$$E\_\text{Adiabatic} = R * C * V\_DD^2/T. \tag{6}$$

From the above expressions (5) and (6), it is evident that the total switching power is inversely proportional to the capacitor charging time. Hence, this logic can achieve very low energy loss by slowing down the operation speed and the AC power supply is used to recycle the energy stored in the capacitor rather than DC supply.

3.2 *Adiabatic Full Adder*

The proposed 18 transistors adiabatic full adder cell as shown in Fig. 6 not merely provide the sum and C_{out}, it also delivers a compliment of actual outputs. The property of energy recycling or restoring leads to energy and area-efficient design compared to other logic designs. The following Eq. (7)–(10) represents the adiabatic logic output expressions

$$\text{Sum} = (BC_{\text{in}} + B(C_{\text{in}}))A + \left(BC_{\text{in}} + \bar{B}\overline{C_{\text{in}}}\right)A \tag{7}$$

$$\text{SumBar} = \left(\bar{B}C_{\text{in}} + B\overline{C_{\text{in}}}\right)A + \left(BC_{\text{in}} + \bar{B}\overline{C_{\text{in}}}\right)\bar{A} \tag{8}$$

$$C_{\text{out}} = (A\overline{B}C_{\text{in}} + AB\overline{C_{\text{in}}} + BC_{\text{in}}) \tag{9}$$

$$\text{Cout Bar} = (\overline{A\overline{B}C_{in}} + \overline{A}B\overline{C_{\text{in}}} + \overline{BC_{\text{in}}} \tag{10}$$

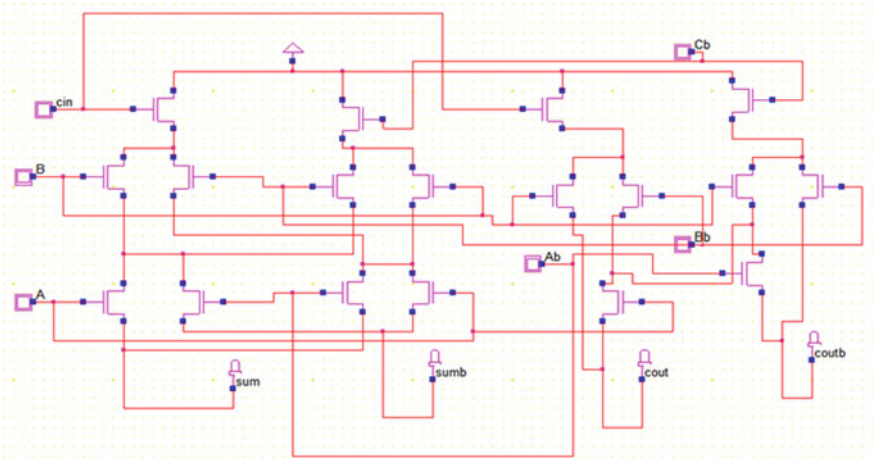

Fig. 6 Adiabatic logic 1-bit adder cell

Table 1 Adiabatic full adder truth table

A	b	c_{in}	S	SBar	Co	Co bar
0	0	0	0	1	0	1
0	0	1	1	0	0	1
0	1	0	1	0	0	1
0	1	1	0	1	1	0
1	0	0	1	0	0	1
1	0	1	0	1	1	0
1	1	0	0	1	1	0
1	1	1	1	0	1	0

Table 1 shows the Truth table of the adiabatic full adder cell.

4 Results and Discussion

Associated with CMOS conventional full adder, pass transistor logic (PTL) has achieved better area optimization and less area power consumption with the degraded logic levels. Using adiabatic logic to design full adder gives the lesser amount of power consumption and area-efficient compared toward conventional CMOS and pass transistor logic full adders. The simulation model results and the layout of the proposed adiabatic cell are presented in Figs. 7 and 8.

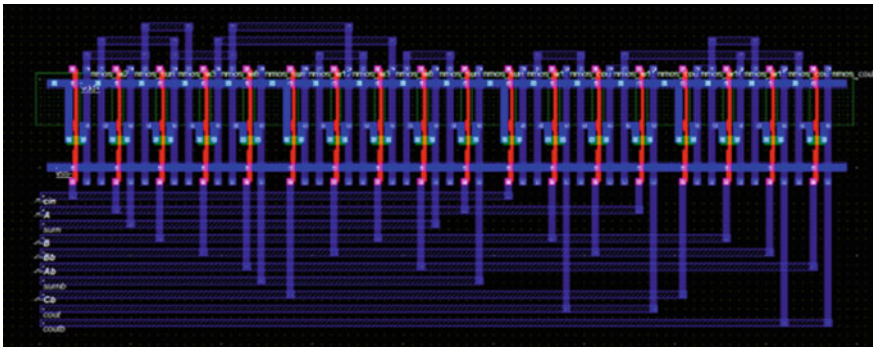

Fig. 7 Layout of proposed adiabatic full adder

Fig. 8 Simulation results

Table 2 Power consumption of adiabatic full adder in different technologies

Technologies (nm)	Power (μw)
90	1.429
65	0.290
45	0.061
32	0.037

Table 3 Power consumption for four sets of dynamic input combinations

Proposed ALFA	Input set 1 $A = 0, B = 0, C = 0$	Input set 2 $A = 0, B = 1, C = 0$	Input set 3 $A = 1, B = 0, C = 0$	Input set 4 $A = 1, B = 1, C = 1$	Average
Power (μw)	0.203	0.186	0.160	0.187	0.184

4.1 Power Consumption of Proposed Adiabatic Full Adder

Tables 2 and 3 illustrate the power consumption at different technologies and for different input combinations.

4.2 Power and Area Comparison with Other Adder Technologies

Table 4 illustrates the performance of proposed 1-bit adder with other technologies

Table 4 Area and power comparison

Full adder design topology	Power (μw)	Area $(\mu m)^2$
Conventional 28-transistor logic	19.600	145.48
16-T PTL and TG	2.937	65.00
14-T PTL and TG	4.095	57.2
18-T adiabatic full adder logic	0.290	94.878

5 Conclusion

From the above results, the proposed adiabatic 1-bit adder minimizes the power consumption by energy recycling. The proposed adiabatic cells individually reduce power consumption through 98.53,88 and 93.5 compared to conventional CMOS full adders, 16-T PTL and TG, and 14-T PTL logic full adders. Also, it occupies less area than 28T CMOS full adder. As a result, for example, the proposed 1-bit adder cell based on adiabatic logic provides better power consumption, which can be adequately integrated into the logic circuit inside the VLSI chip and utilized for small and handheld applications.

References

1. Goel S, Kumar A, Bayoumi MA (2006) Design of robust, energy-efficient full adders for deep-sub micrometer design using hybrid-CMOS logic style. IEEE Trans Very Large-Scale Integr (VLSI) Syst 14(12):1309–1321
2. Tajasob S, Rezaalipour M, Dehyadegari M (2019) Designing energy-efficient imprecise adders with multi-bit approximation. Microelectron J 89:41–55
3. Rakesh S, Vijula Grace KS (2019) A comprehensive review on the VLSI design performance of different parallel prefix adders. Mater Today Proc
4. Sunil Gavaskar Reddy Y, Rajendra Prasad VVGS (2011) Power comparison of CMOS and adiabatic full adder circuits. Int J VLSI Des Commun Syst (VLSICS) 2(3)
5. Wei Y, Shen J-Z (2011) Design of a novel low power 8-transistor 1-bit full adder cell. J Zhejiang Univ Sci C 12(7):604–607
6. Goel S, Kumar A, Bayoumi MA (2006) Design of robust, energy-efficient full adders for deep-sub micrometer design using hybrid-CMOS logic style. IEEE Trans Very Large Scale Integr (VLSI) Syst 14(12):1309–1321
7. Shams AM, Bayoumi MA (2000) A novel high-performance CMOS 1-bit full-adder cell. IEEE Trans Circ Syst II Anal Dig Sig Process 47(5):478–481
8. Murugan K, Baulkani S (2019) VLSI implementation of ultra power optimized adiabatic logic-based full adder cell. Microprocess Microsyst 70:15–20
9. Sanadhya M, Vinoth Kumar M (2015) Recent development in efficient adiabatic logic circuits and power analysis with CMOS logic. Procedia Comput Sci 57:1299–1307

Comparative Analysis of Rapid Single Flux Quantum (RSFQ) Circuit Technique Multipliers

Yamini Devi Ykuntam and Katta Pavani

Abstract The primary operation of any processor is to perform basic arithmetic operations. In all basic arithmetic operations, multiplication consumes more time to be performed. Multiplier is the component which performs the multiplication operation. Its performance speed is going to affect the speed of the entire processing unit. The major operation of multiplier is to generate final product from partial products. To perform this major operation, the required architecture may require more area which intends to increase in latency in operation**.** In order to improve the performance of processor with minimum area, fast multiplier must be employed to perform multiplication operation. With high speed, the multiplier should occupy less area and consume low power. In the design of multipliers, a new technology called superconductor RSFQ logic is extensively used in order to achieve a multiplier design with less area and minimum latency in operation. From the time of introduction of this technology, different types of RSFQ multipliers are proposed. This paper gives an comparative analysis of rapid single flux quantum(RSFQ) technology multipliers like integer multiplier, matrix multiplier, parallel carry-save pipelined multiplier, floating-point multiplier in terms of area (number of Josephson junctions) and latency.

Keywords Rapid single flux quantum (RSFQ) · Josephson junctions (JJs) · Integer multiplier · Matrix multiplier · Parallel carry-save pipelined multiplier · Floating-point multiplier

Y. D. Ykuntam (✉) · K. Pavani
Department of Electronics and Communication Engineering, Aditya Engineering College, Surampalem, Andhra Pradesh 533437, India
e-mail: yaminieie@gmail.com

K. Pavani
e-mail: k.pavani.k@gmail.com

G. T. C. Sekhar et al. (eds.), *Intelligent Computing in Control and Communication*, Lecture Notes in Electrical Engineering 702,
https://doi.org/10.1007/978-981-15-8439-8_11

1 Introduction

In most of digital signal processing applications and data paths, a multiplier plays major role in terms of performance which is going to affect the execution time of the complete system. A fast speed multiplier is required in order to enhance the DSP system performance. At the same time, the multiplier design should consume low power as most of the electronic gadgets are portable. Therefore, the multiplier employed in any DSP processors, data paths and VLSI architectures should be designed with low power consumption and high speed execution characteristics.

There are three stages in multiplier to obtain the final product. The performance of these three stages should be enhanced to get a multiplier with low power and high speed features. By employing traditional multiplication algorithms for designing, a multiplier does not achieve the required features of low power and high speed. In order to achieve the desired characteristics for a multiplier design, new ways in technology should be used. RSFQ [1] circuits are a technology having superconducting elements like Josephson junctions, to process digital signals with high speed and low power consumption [2]. So RSFQ circuits can be used in designing a multiplier. Also the multiplier should be designed for parallel or pipelined processing techniques rather than a serial processing to achieve high speed operation. But parallel processing hardware occupies more area which leads to increase in cost of the design. Figure 1 shows physical principle, symbol and junction model of a Josephson junction.

In this paper, different multiplier design techniques based on RSFQ circuits are studied and compared with each other. A 32-bit floating-point multiplier is designed with IEEE-745 notation [3]. A 32-bit bit-slice integer multiplier [4, 5] and 8-bit parallel carry-save pipelined RSFQ multiplier are designed to operate with gigahertz frequencies [6]. A 32-bit bit-slice matrix multiplier is designed to achieve low latency [7].

The subsequent sections of the papers explain about literature survey on various RSFQ multipliers, operation of different RSFQ multipliers, analysis of multipliers which is depicted in result analysis part and application of RSFQ multiplier which is given. Finally, the paper ends with conclusion.

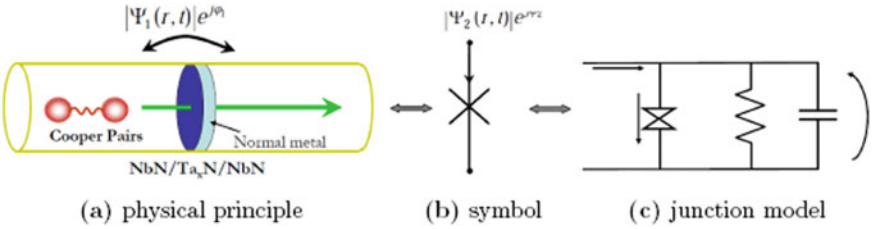

Fig. 1 Josephson junction [3]

2 Literature Survey on RSFQ Multipliers

In CMOS circuits as the threshold voltage is scaled down, leakage power is increasing in circuit. Also, temperature shows major impact on leakage power consumption. The leakage power consumption is increasing exponentially with the scaling feature [8]. Moreover, by scaling a MOS transistor power consumption of particular logic function decreases in which scaled MOS transistor is employed. But as the numbers of transistors on chip are increasing, the overall power consumption of the chip increases.

An alternative technology for CMOS is required in order to overcome the drawbacks of it. Superconductor is the most advanced technology which offers high speed with low power consumption, i.e., the circuit developed using superconductor technology consumes 1/10th of the power consumed by CMOS circuits[9,10]. The basic building block of today's superconductor circuit is Josephson junction which is built using two superconducting metals (usually niobium) separated by a very thin insulating layer [11].

An innovative step forward in superconductor computing was marked by the discovery of rapid single flux quantum (RSFQ) in 1991 [12] which is not only fast but also dissipates less amount of power. In superconductor computing, RSFQ logic became a standard and is used widely today. Multiple Josephson junctions, inductors and bias resistors are combined to build RSFQ gates. With the evolution of superconducting RSFQ technology, various types of multipliers are designed. The first RSFQ multiplier is a bit-serial design using carry-save path in 1989 which can be expanded into parallel design [13].

In 2001, Wallace tree-based 32-bit multiplier with carry look-ahead adder is proposed [14]. In simulation results, it is showed that Wallace-based RSFQ multiplier maximum speed limit is 10-GHz. An AND gate array-based serial-parallel multiplier is designed which has maximum speed of 14 GHz [15].

Later, RSFQ parallel multiplier–accumulator with a carry-save array type compressor of maximum speed limit 24-GHz was proposed [16]. A 32-bit floating-point RSFQ multiplier with IEEE-745 standard with a processing speed of 11 GHz is proposed in[3] with a overall latency of 1.772 ns.

A 32-bit bit-slice integer RSFQ multiplier which can perform both signed and unsigned multiplication with operating speed of 50 GHz is proposed [4]. A 8 X 8-bit parallel carry-save pipelined RSFQ multiplier with processing speed of 20 GHz is proposed in [6]. The latest RSFQ multiplier based on bit-slice matrix multiplication process which achieves latency in terms of picoseconds is proposed in [7].

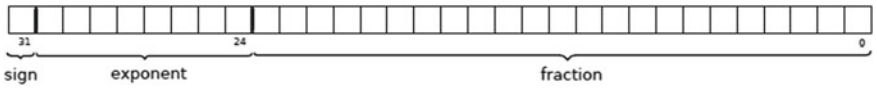

Fig. 2 Representation of IEEE-745 single-precision floating-point number format [3]

3 Operation of Different RSFQ Multipliers

Different types of RSFQ multipliers are proposed since the evolution of superconducting RSFQ technology. In this section, mainly operation of latest three multipliers is explained.

3.1 Precision Floating-Point RSFQ Multiplier

Using single-precision IEEE-745 floating-point arithmetic standard, a 32-bit precision floating-point multiplier is designed. The IEEE-745 standard supports rounding process and excluding denormalized numbers. The floating-point numbers in IEEE-745 notation are represented using a sign bit, an 8-bit wide exponent and a 23-bit wide fraction as shown in Fig. 2.

The multiplier is composed of three major blocks—sign bit calculation, exponent calculation unit and mantissa calculation unit. A binary floating-point number, say x, is represented as a significant s and exponent e as in $x = s$ *2^e the formula.

$$\left(s1 * 2^{e1}\right) \cdot \left(s2 * 2^{e2}\right) = (s1 \cdot s2) * 2^{e1+e2} \tag{1}$$

Expression (1) shows that the floating-point multiplication process has numerous parts. A normal multiplier is used to multiply significant in first part. The rounding process is done in second part, whereas new exponent value is computed in third part.

3.2 Bit-Slice Integer RSFQ Multiplier

In this multiplier, multiplicands are divided into bit slices. The bit slices are multiplied by using integer multiplier. The structure of multiplier is based on systolic-like multiplication algorithm proposed in [5]. A 32-bit multiplicand can be divided into eight slices of 4 bits each.

The main structure of multiplier consists of a partial product generator, accumulator, registers and D flip-flops. To process slices of bits, pipelining technique is used. The pipelining technique used is fully pipelined synchronous RSFQ logic design. Every pipeline stage consists of a row of RSFQ logic gates composed of AND, XOR,

NOT, DFF and NDRO (non-destructive read-out) and wiring elements: Josephson transmission line (JTL), splitter (SPL) and confluence buffer (CB) in the cell library [17] for the AIST ADP2 are used.

3.3 Bit-Slice RSFQ Matrix Multiplier

In this multiplier also, input multiplicands are divided as bit slices and output the result in the form of matrix. The multiplication process performed is unsigned integer matrix multiplication. An 8-bit bit-slice 4 × 4 matrix multiplication is carried out through 131 steps. Matrix multiplication algorithm is used to carry out multiplication process in this multiplier [7]. A 32-bit multiplier consists of four 8-bit bit-slice multipliers and three 8-bit bit-slice adders. The proposed matrix multiplier uses concurrent flow clocking to design fully pipelined synchronous RSFQ logic circuits. D flip-flops are used to form register structures. The bit-slice adders used are parallel prefix adder called Sklansky adder with six pipeline stages. The carry signal delay in feedback loop to the next slice is minimized by method proposed in [18].

4 Result Analysis

To analyze the current design trends of RSFQ multipliers, recent three designs are studied which are 32-bit precision floating-point RSFQ multiplier proposed by Kasperek [3], 32-bit bit-slice integer RSFQ multiplier by Tang et al. in 2017 [4] and 32-bit bit-slice RSFQ matrix multiplier by Tang et al. in 2018 [7]. All the three multipliers are of 32-bit size which is analyzed in terms of number of Josephson junctions in design and latency which is shown in Table 1.

As shown in Table 1, precision floating-point RSFQ multiplier has latency of 1.772 ns with 89,000 Josephson junctions, whereas bit-slice RSFQ matrix multiplier has least latency of 13,344.1 ps but more number of Josephson junctions, i.e., 342,238. But bit-slice integer RSFQ multiplier has least number of Josephson junctions, i.e., 56,885 with a moderate latency of 3.125 ns.

From the comparison table, it is clear that bit-slice integer RSFQ multiplier is better in terms of number of Josephson junctions and latency.

Table 1 Different RSFQ multiplier's comparison in terms of no. of Josephson junctions and latency [3, 4, 7]

RSFQ multiplier	No. of Josephson junctions	latency
32-bit precision floating-point RSFQ multiplier	89,000	1.772 ns
32-bit bit-slice integer RSFQ multiplier	56,885	3.125 ns
32-bit bit-slice RSFQ matrix multiplier	3,42, 238	13,344.1 ps

5 Applications

In many processor designs, signal and video processing units multiplier design plays a vital role. Multiply and accumulate unit is major component for any signal and video processing units. By using RSFQ technology, a parallel multiply-accumulate unit is developed in [16]. A 32 × 32-bit 4-bit bit-slice integer multiplier for RSFQ microprocessors has been proposed in [4]. A 4-bit bit-slice arithmetic logic unit is designed for 32-bit RSFQ microprocessors [18]. These types of multipliers have a wide area of application which motivates the researchers to work foremost on these multiplier designs.

6 Conclusion

In this paper, majorly three different types of multiplier designs of 32-bit size are analyzed, namely precision floating-point RSFQ multiplier, bit-slice integer RSFQ multiplier and bit-slice RSFQ matrix multiplier which are designed using RSFQ technology. From the result analysis section, it is clear that precision floating-point RSFQ multiplier latency and number of Josephson junctions are moderate, whereas bit-slice RSFQ multiplier has least latency but more number of Josephson junctions. For bit-slice integer RSFQ multiplier, the latency is little bit high but has the least number of Josephson junctions when compared with the two other RSFQ multipliers in this paper. Finally, it can be concluded that if least latency is required without bothering about area, then bit-slice matrix RSFQ multiplier can be used, whereas if least area is required with latency as not a major constraint, then bit-slice integer RSFQ multiplier can be employed.

Reference

1. Likharev KK, Semenov VK (1991) RSFQ logic/memory family: a new Josephson-junction technology for sub-terahertz-clock-frequency digital systems. IEEE Trans Appl Supercond 1(1):3–28
2. Takagi N, Tanaka M (April, 2010) Comparisons of synchronous-clocking SFQ adders. IEICE Trans Electron E93-C(4):429–434
3. Kasperek AK (2012) 32-bit superconductor integer and floating-point multiplier, Ph.D. dissertation. Dept Comput Eng Stony Brook Univ (Stony Brook, NY, USA)
4. Tang G, Takagi K, Takagi N (April, 2017) 32 × 32-bit 4-bit bit-slice integer multiplier for RSFQ microprocessors. IEEE Trans Appl Supercond 27(3):Art. no. 1301005
5. Tang G, Takagi K, Takagi N (June, 2016) RSFQ 4-bit bit-slice integer multiplier. IEICE Trans Electron E99-C(6):697–702
6. Dorojevets M, Kasperek AK, Yoshikawa N, Fujimaki A (June, 2013) 20-GHz 8 × 8-bit parallel carry-save pipelined RSFQ multiplier. IEEE Trans Appl Supercond 23(3): Art. no. 1300104
7. Tang GM, Qu PY, Ye XC, Fan DR, Sun NH (October, 2018) A 32-Bit 4 × 4 bit-slice RSFQ matrix multiplier. IEEE Trans Appl Supercond 28(7)

8. White M, Chen Y (November, 2010) Scaled CMOS technology reliability users guide. NASA, Tech Rep WBS: 939904.01.11.10 (Cited on page 2)
9. Superconducting Technology Assessment (STA) (August, 2005) National Security Agency—Office of Corporate Assessments. Available: https://www.nitrd.gov/pubs/nsa/sta.pdf (Cited on pages 2, 3, 5, 6 and 9)
10. Mukhanov OA (2011) Energy-efficient single flux quantum technology. IEEE Trans Appl Supercond PP(99):1 (Cited on pages 2, 6 and 7)
11. Josephson B Possible new effects in superconductor tunneling.Phys Lett 251 {253, 1962} (Cited on page 3)
12. Likharev K, Semenov V (March, 1991) RSFQ logic/memory family: a new Josephson-junction technology for sub-terahertz-clock-frequency digital systems. IEEE Trans Appl Supercondu 1(1):3 {28} (Cited on pages 3, 5, 6 and 34)
13. Mukhanov OA, Rylov SV, Semonov VK, Vyshenskii SV (1989) RSFQ logic arithmetic. IEEE Trans Magn 25(2):857 {860} (Cited on page 25)
14. Onomi T, Yanagisawa K, Seki M, Nakajima K (2001) Phase-mode pipelined parallel multiplier. IEEE Trans Appl Supercond 11(1):541–544 (Cited on page 25)
15. Akahori A, Tanaka M, Sekiya A, Fujimaki A, Hayakawa H (2003) Design and demonstration of SFQ pipelined multiplier. IEEE Trans Appl Supercond 13(2):559–562 (Cited on pages 25 and 26)
16. Kataeva I, Engseth H, Kidiyarova-Shevchenko A (May, 2006) New design of an RSFQ parallel multiply accumulate unit. Supercond Sci Technol 19:381+ (Cited on pages 26 and 27)
17. Yamanashi Y, et al (April, 2010) 100 GHz demonstrations based on the single-flux quantum cell library for the 10 kA/cm2 Nb multi-layer process. IEICE Trans Electron E93-C(4):440–444
18. Tang G, Takata K, Tanaka M, Fujimaki A, Takagi K, Takagi N (January, 2016) 4-bit bit-slice arithmetic logic unit for 32-bit RSFQ microprocessors. IEEE Trans Appl Supercond 26(1):Art. no. 1300106

Techno-Economic Material Demand-Based Model in Plastic Waste Management Using Metaheuristic Algorithms

Gopalamma S. L. K. Aravelli and R. Srinu Naik

Abstract In the world, the waste volume increases day by day in modern communities. It ensures the level of requirement of waste management policies to reduce the effect of dumping waste and toward incineration. In this paper, we proposed a balanced material demand-based plastic waste management optimization model, and the following model results in the economic parameters on different stages of recycling. The model primarily depends on the demand of by-products of each step and the rate of recycling and dumping. Cuckoo search algorithm and vibration particle optimization algorithm used to evaluate the dependency of economic parameter values and the effective minimal cost of each stage in waste management. Comparative analysis between the metaheuristic techniques and respective results and discussions is shown.

Keywords Waste management · Material demand-based model · Cuckoo search algorithm · Vibration particles algorithm · Environment economics

1 Introduction

The increasing waste volume results in severe health issues and environmental impacts. Industries and individuals must follow the right way of separating solid and liquid waste coming from both the residential and industrial sectors. According to the waste management policies available now, less than 50% recycled today in all industries. As some initiatives like swatch Bharat, the level little bit improved.[1–3] The barriers of this sector involve the cost for each stage, and some returns invested are low. The limited size of the market, particularly in materials like plastic, is limited

G. S. L. K. Aravelli (✉) · R. S. Naik
Andhra University College of Engineering (A), Visakhapatnam, Andhra Pradesh 530003, India
e-mail: gopika.aravelli@gmail.com

R. S. Naik
e-mail: naiknaiknaik@gmail.com

G. T. C. Sekhar et al. (eds.), *Intelligent Computing in Control and Communication*, Lecture Notes in Electrical Engineering 702,
https://doi.org/10.1007/978-981-15-8439-8_12

to 10% of the annual volume of waste. There are two significant roadblocks for recycling plastic materials because of the limited market and low profitability. With proper policies, one should overcome these problems.[1].

Waste management plays a vital role in reducing the volume of waste generated and minimizes carbon emissions.

1.1 Technical Aspects

Waste handling units were facing so many challenges technically and economically. Some technical aspects discussed as follows.

1. *Prevention of waste*: This parameter can affect the economic parameters in both the production and consumption sides. Reducing throw away type plastic materials and using eco-friendly materials can reduce waste volume.
2. *Recycling Products*: Recycling products become ease with proper communication between manufacturing units, and also, it makes the possibility of reusing the same material with minimal modifications
3. *Recycling Materials*: The residual materials from the products have two types of applications, such as high-quality and low-quality products, but the major disadvantage behind this is it is not possible to use for the same product manufacturing. Several materials combined with each other and pollute the quality of the materials, and the separation costs also increased. The quality of materials is even less than their original materials. Another way of recycling products in efficient manner possible with proper maintenance and garbage collection system from household units to Industrial units. Cost-effective techniques involve a financial burden. Depending on the process, they classified as a fully automatic and semi-automatic process of waste handling.
4. *Thermal Conversion*: Thermal conversion involves different stages, such as hydrolysis, pyrolysis, and gasification. In the case of plastics recycling, the final stage is thermal recycling, and the residues coming from these stages used as secondary by-products in other new fabrication products.

1.2 Economical Parameters

An important aspect of recycling materials is about economic feasibility. The recycling industry should focus on the financial parameters and opportunities in cost–benefit analysis [2, 4]. Different costs involved commonly in waste management are

- Recuperation costs which include transport costs, storage costs, primary treatment costs, etc.
- Garbage collection cost

- Residual treatment costs
- Dumping costs
- Revenue from recycled secondary materials.

2 Material-Based Optimization Model

The optimization model derived on the basis of the demand for the materials(by-products) and the number of stages involved, procedures, and analysis as per the cost and quality of the products.

2.1 Cost–Benefit Analysis

According to VNCI,1989, there are three stages for recycling any product. Variables such as quality of material, rate of change in the quality of the material, and pollution levels in content play a vital role in the design. In this study, we considered the plastic waste management [4].

1. *Original material Applications*: The quality of materials used for this application is high, and the materials not yet used in other applications. For Example, the packing of materials in food and drinks involves more quality than the cost involved.
2. *Second-level high standard applications*: In these applications, the primary product granulates required. These are substitutes for the origin materials.
3. *Third-level low standard applications*: In this type of low standard applications, the low-quality residues are more than sufficient. Small defects and pollution of materials are acceptable here.

Value-added = (revenues from secondary materials) + (Costs for dumping waste − garbage collection cost) − (cost of recuperation − residual treatments).

The value-added depends on the type of waste, and the analysis of potential value-added depends on three categories of waste.

1. Waste produced by manufacturing primary product
2. Waste generated by manufacturers of secondary product
3. Waste produced at the consumer level of products.

The third category involves high separation costs because of more involved locations for large/small quantities. The value added is negative.

2.2 Modeling Waste Management Structure

In this section, the model of waste management structure studied as per the quality of material obtained from each stage. The process involved in each stage involves in–out cost flow as per the type of material used and its cost—similarly, the cost analysis of the by-products, which as used as raw material for another production.

2.2.1 Plastic Recycling Structure Model

High-quality applications need high-quality recycled products. At the manufacturing level of plastics, using crude oil and origin materials, plastic material manufactured and the recycled residues collected at the industry level used for product recycling in second-level high-grade applications. The high-quality by-products obtained from the residues of the primary manufacturing level used for secondary products. After usage, the products could be recycled. Recuperation units clean the waste material coming from stage 1, which contains useful materials with some unwanted materials. Thus, in the recuperation unit, the residues washed and sent to the re-granulated section. Low-level material production Unit 3 in Fig. 1 contains the materials mixed with polluted waste material, which would be used for low-grade applications.

An alternate and final path of processing waste material having low quality is the thermal process, which is complicated and costly. But the obtained raw material can again be reused in other manufacturing units and product fabrication units. The final model gives a direct way to recycle products of plastic.

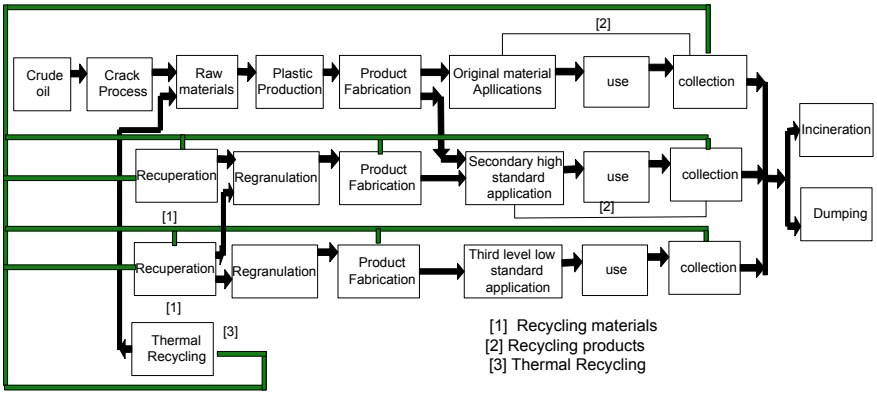

Fig. 1 Plastic waste handling design model

2.2.2 Optimization of the Model

The proposed model is a linear and static optimization model, and the design variables are the number of products at each level. And the cost–benefit analysis is categorized as 1. Original products application 2. High-grade quality application 3. Low-quality grade application. The demands of the following products are D_1, D_2, respectively.

The objective function with Design Variables is as follows: $((P_{oil} * X_{oil}) + (C_{CRA} * X_{CRA}) + (C_{PRO} * X_{PRO}) + (C_{FAB1} * X_{FAB1}) + (C_{FAB2} * X_{FAB2}) + (C_{FAB3} * X_{FAB3}) + (C_{COL} * X_{COL}) + (C_{PROR} * X_{PROR}) + (C_{REC} * X_{REC}) + (C_{THER} * X_{THER}) + (C_{INC} * X_{INC}) + (C_{DUM} * X_{DUM}))$

$$X_{\text{oil}}, X_{\text{CRA}}, X_{\text{PRO}}, X_{\text{FAB1}}, X_{\text{FAB2}}, X_{\text{FAB3}}, X_{\text{COL}},$$
$$X_{\text{PROR1}}, X_{\text{PROR2}}, X_{\text{PROR3}}, X_{\text{REC}}, X_{\text{THER}}, X_{\text{INC}}, X_{\text{DUM}}$$

The most important constraints are

$$X_{\text{FAB1}} + X_{\text{PROR1}} > D_1 \tag{1}$$

$$X_{\text{FAB1}} + X_{\text{FAB2}} - X_{\text{PROR2}} > D_2 \tag{2}$$

$$X_{\text{FAB1}} + X_{\text{FAB2}} + X_{\text{FAB3}} - X_{\text{PROR3}} > D_3 \tag{3}$$

$$X_{\text{COL}} = X_{\text{DUM}} + X_{\text{INC}} + (1/r * X_{\text{THER}}) + (1/s * X_{\text{REC}}) + (1/t * X_{\text{PROR}}) \tag{4}$$

$$X_{\text{FAB1}} + X_{\text{FAB2}} + X_{\text{FAB3}} = (u * X_{\text{REC}}) \tag{5}$$

where

P_{OIL}	Price of crude oil.
D_1	Demand of products for original application.
D_2	Demand of products for high-grade application.
D_3	Demand of products for the low-grade application.
C_{CRA}	Cost of cracking process.
C_{PRO}	Cost of production.
C_{Fab1}, C_{Fab2}, C_{Fab3}	Cost of fabrication in three stages, respectively.
C_{COL}	Cost of collection of materials.
C_{PROR}	Cost of product recycling.
C_{REC}	Cost of recuperation.
C_{THER}	Cost of thermal process.
C_{INC}	Cost of incineration process.
C_{DUM}	Cost of dumping process.

r, s, t, u	Conversion parameters for recuperation, thermal, product recycling, fabrication.
X_{oil}	Quantity of oil (in barrels).
X_{CRA}	Quantity in cracking process (in barrels).
X_{PRO}	Quantity in production.
X_{FAB1}	Quantity in fabrication of original product.
X_{FAB2}	Quantity in fabrication of high-grade application product.
X_{FAB3}	Quantity in fabrication of low-grade application product.
X_{COL}	Quantity in the collection of recycled materials.
X_{PROR1}, X_{PROR2}, X_{PROR3}	Quantity of recycled products in three stages, respectively.
X_{REC}	Quantity of recuperation products (in kgs).
X_{THER}	Quantity of material in thermal process(in kgs).
X_{INC}	Quantity of material in incineration process (in kgs).
X_{DUM}	Quantity of material in dumping process (in kgs).
X_I	Quantity of material in Incineration Process (in kgs).
X_D	Quantity of material in Dumping Process (in kgs).

3 Metaheuristic Optimization Models

The design model optimized using metaheuristic techniques such as vibration particle search algorithm and cuckoo search algorithm. The methodology and principle of both algorithms discussed in this section and the corresponding flow charts incorporated in Fig. 1.

3.1 Vibration Particles Algorithm

Vibration particles (VP) algorithm is a budding metaheuristic optimization technique developed by IlchiGhazaan and kaveh [2]. This algorithm developed by the motivation of free vibration of systems(single degree freedom) with viscous damping. By considering each vibrating system with under-damped conditions, it will experience oscillations and comes to their respective equilibrium positions, and those parameters verified by the differential equations. Every particle that attains the equilibrium position consists of three parts, good particle, the best position in the entire population, and bad particle. The basic essence of the theory stands on concepts like self-adaption and the cooperation between the good particle, bad particle, and competition among the particles. The essence of the main algorithm and methodology has shown in Fig. 2a.

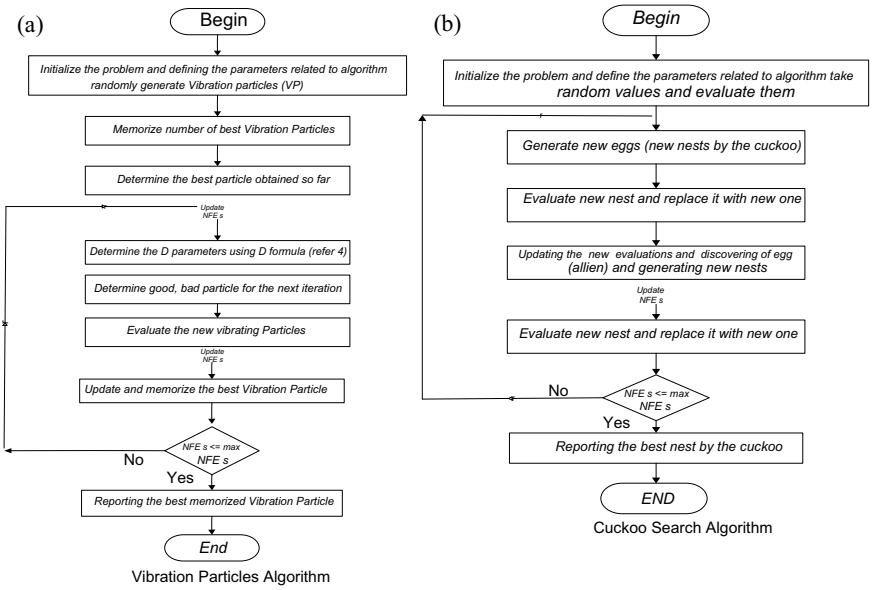

Fig. 2 **a** Vibration particle algorithm flowchart [1]. **b** Cuckoo search algorithm flowchart [5]

3.2 Cuckoo Search Algorithm

The cuckoo search algorithm was one of the most famous metaheuristic techniques based on the behavior of cuckoo species with the levy flight. The principal methodology of this technique is analogous to the nature of cuckoo breeding with levy flight behavior. Each excellent solution should be considered as nest and cuckoo improves the quality of solution candidate by changing step size until they attain the quality comparison with levy flight [5]. The essence of the main algorithm and methodology has shown in Fig. 2b.

4 Results and Discussions

The material demand-based model cost–benefit analysis has done with the help of some metaheuristic techniques under some assumptions—the comparison between the two algorithms concerning the population size and iterations, the findings incorporated in Table 1. The decision variables values are taken from ref [4], as shown in Table 2.

Table 1 Cost–benefit analysis (cost in $ and taken as nominal)

Population size	Min cost function (for n iterations using cuckoo search algorithm)			Min cost function (for n iterations using vibration particles algorithm)		
	200	500	1000	200	500	1000
30	25,995	17,007	13,524	35,988	24,680	20,464
40	32,791	17,705	13,754	28,458	29,133	25,305
50	31,772	14,504	14,504	31,607	36,870	36,870

Table 2 Cost coefficient values taken for study [4]

Cost coefficient	Cost coefficient expression	Cost (in $)
Cracking process cost coefficient	C_cra	100
Price of oil (in $/ Barrel)	P_oil	200
Product cost coefficient	C_pro	100
First stage fabrication cost coefficient	C_fab1	150
Second stage fabrication cost coefficient	C_fab2	100
Third stage fabrication cost coefficient	C_fab3	100
Cost coefficient for collection of materials	C_col	50
Cost coefficient for recycling of product 1	C_pror1	100
Cost coefficient for recycling of product 2	C_pror2	50
Cost coefficient for recycling of product 3	C_pror3	75
Cost coefficient of recuperation	C_rec	175
Cost coefficient for thermal process	C_ther	200
Cost coefficient for inceranation process	C_inc	100
Cost coefficient for dumping	C_dum	75
The demand for product A	D_a	80 (%)
The demand for product B	D_b	60 (%)
The demand for product C	D_c	50 (%)

4.1 Assumptions and References

The cost–benefit analysis performed under some assumptions such as 80% output available for level 1 fabrication 70% for the fabrication of materials under high, 60% for low-level material applications. We assumed only 60% from the collection site, and recycling rates for three-level products below 30%. We are taken the values as a reference and applied metaheuristic techniques such as cuckoo search algorithm and vibration particles algorithm.

4.2 Test Results and Findings

We performed the execution of the proposed material demand optimization model to the optimization technique and comparative analysis done under the same search space. The results carried out with 30, 40, 50 populations and 200, 500, 1000 maximum iterations. The results are shown in Table 1. The costs involved in the process are taken as low values such that the cost-effective solution is also deficient with practical.

The variation of cost with max iterations shown in Fig. 3; the variation of cost vs.the number of populations represented in Figs. 4 and 5, respectively.

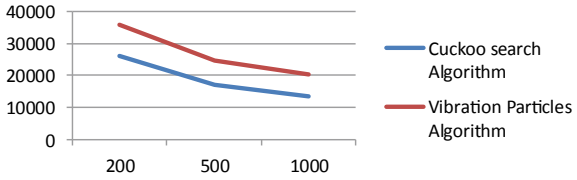

Fig. 3 Cost evaluation under dynamic iterations

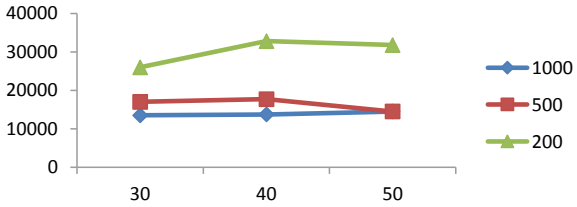

Fig. 4 Cost evaluation between the number of populations and number of iterations (cuckoo search algorithm)

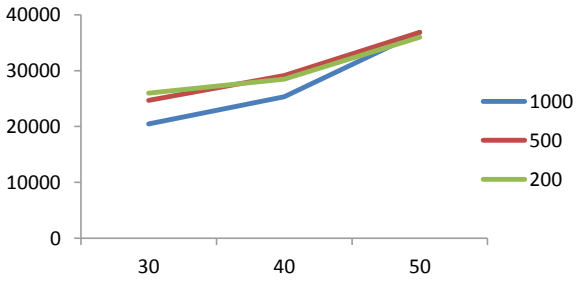

Fig. 5 Cost evaluation between the number of populations and number of iterations (vibration particles algorithm)

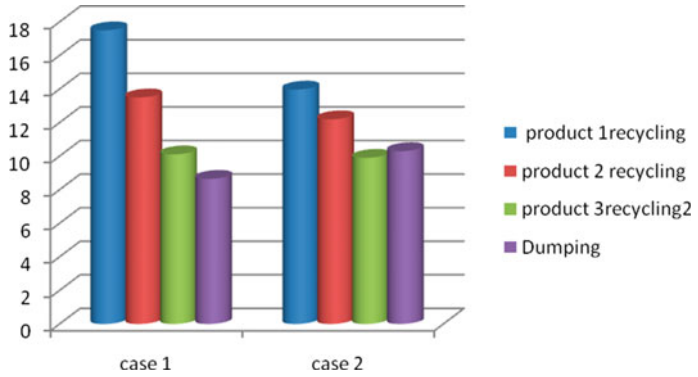

Fig. 6 Recycling and dumping percentage using vibration particle and cuckoo search algorithm, respectively

In Fig. 6, the optimum values of product recycling rates and dumping rate for two cases are shown. The cost evaluations are based on the vibration particle optimization model as case 1 and cuckoo search optimization model as case 2.

5 Conclusions

This paper aims to study the techno-economic impacts and solutions. with the Motivation, this study proposed a optimisation model based on the demands of By–products obtained from three stages mentioned such as fabrication level, reuse, and recycling levels to establish the practical, efficient analysis by calculating the impact of cost in every stage in recycling to dumping. Based on the demand, we designed a model to get the optimum values of design variables to get minimum cost using metaheuristic techniques 1. cuckoo search algorithm 2. vibration particle algorithm. The respective changes based on the population size and number of iterations shown in graphical representation and the cost values are nearly equal. But, the cuckoo search algorithm gives minimized outputs compared with the vibration particle system.

In this analysis, the dynamic nature of the demand of by-products and the rate of recycling and dumping carried out and the results itself shown that the values obtained reveal the comparative analysis between two techniques. The product recycling rate and dumping rate are high in the VPS technique, but the minimum cost has received in the cuckoo search technique under the same search space.

References

1. Kaveh A, IlchiGhazaan M (2017) A new meta-heuristic algorithm: vibrating particle system. Sci Iran Trans a CivEng 24(2):551–566
2. Yang XS, Deb S (2010) Engineering optimization by cuckoo search. Int J Math Model Numer Optim 1:330–343
3. Baumol W, Oates W (1998) The theory of environmental policy. Cambridge
4. Folkert Starreveld P, Van Ierland EC (1994) Recycling Plastics: A materials balance OptimisationModel. Environ Resource Econ 4(251–264):1994
5. Kaveh A, Bakhshpoori T, Afshari E (2011) An optimization-based comparative study of double-layer grids with two different configurations using a cuckoo search algorithm. Int J OptimCivEng 1:507–520

Breaking Down and Reduplication of Information in Cloud for Best Overall Performance and Protection

G. NageswaraRao, B. Venkateswarlu, and G. JagadeeswaraRao

Abstract As an increase in the usage of the database, the data security and storage of data become a very big issue. To overcome this, cloud computing comes first. All the data will be stored in a third-party location and retrieve whenever the user wants to access it. In order to achieve this, we came up with "Disintegration and reduplication of data in cloud for safety and security." In this methodology, when the user sends the file on the cloud server it gets fragmented. Fragmentation is a process of dividing the file into some fragments in a way that it is impossible to attack the total file at a time. Each node stores a single fragment of a particular file. The main aim of this work is to give security, protection, and performance against all types of attacks.

Keywords Fragmentation · Reduplication · Cloud security · Encryption · Decryption · Performance

1 Introduction

Traditional business applications are expensive and complicated. The amount of hardware and software required to run them are difficult. With cloud computing, you can eliminate the problems that come with storing of data because you are not managing hardware and software that becomes the responsibility of the software vendor. Cloud computing is a platform that is configuring, manipulating, and accessing the hardware

G. NageswaraRao (✉) · G. JagadeeswaraRao
Department of Information Technology, Aditya Institute of Technology and Management, Tekkali, Andhra Pradesh 532001, India
e-mail: gnraoaitam@gmail.com

G. JagadeeswaraRao
e-mail: jagadish4u.g@gmail.com

B. Venkateswarlu
Department of Computer Engineering, Dayananda Sagar University, Bengaluru 560078, India
e-mail: iambondu@yahoo.com

G. T. C. Sekhar et al. (eds.), *Intelligent Computing in Control and Communication*, Lecture Notes in Electrical Engineering 702,
https://doi.org/10.1007/978-981-15-8439-8_13

and software resources remotely. It offers online infrastructure, data storage, and software applications. In cloud computing, the software is not going to be installed locally on the private computer, i.e., it is platform-independent. Cloud can have four sorts of access: public, private, hybrid, and community. Public cloud is that in which entire infrastructure is found on the premises of a cloud computing company that gives the cloud surface. Due to this, the safety level is low. In a private cloud, all the computing infrastructure is with yourself and not shared. Due to this, the safety and control level is high. In a hybrid cloud, it comprises both public and personal cloud, user can use depending upon their purpose. In a community cloud, the cloud is shared between an organization that matches into a selected community like geographic community, professional community, etc. The cloud services were categorized into majorly three types: IaaS, PaaS, and SaaS.

The IT infrastructure usage and maintenance are completely changed after development of these cloud services. Cloud computing had become a popular computing model, which provides on-demand dynamic service by facilitating virtual hardware and software resources [1]. The data that was stored in cloud severs must be secured and allow for modification based on the user authentication. The cloud was built upon basic cryptographic technique, which will encrypt any data files coming into the cloud to guarantee their privacy and security [2]. Cloud computing provides a large amount of storage for different clients. The main advantages are: users can access, manipulate, and configure the applications as utilities over the Internet at any time. It is more reliable as it offers a load balance. Cloud provides low cost and good reliability [3, 4].

To develop effective and efficient end solutions, first we need to understand the security and privacy risks in the cloud. All though cloud allows its users to avoid initial costs, less operating costs, and increase their activity by immediately acquiring infrastructural resources, services when needed, their unique architectural features raise many security and privacy concerns [5]. Whether it is a public, private, or hybrid cloud, cloud security is the protection of data involved in cloud computing. The security measures protect customers' privacy as well as framing authentication rules for individual users and other devices.

Cryptography is often mentioned because of the practice of the study of hiding and securing the data. Cryptography is the science of keeping data secret and safe. There has always been an urge among humans to stay sensitive data safe and secure in order that it might not cause unwanted intrusion into sensitive information which could lead to severe problems. Thus, cryptography has been practiced by humans from olden times to keep their data secure [6].

The cloud computing paradigm allows accessing the services and data from remote data centers. Nowadays, companies are moving data to the cloud, and they are trying to protect their data against threats.

The major security goals are confidentiality, integrity, and availability. Cryptography is a mixture of three kinds of algorithms: (1) symmetric, (2) asymmetric, and (3) hashing. Cryptography is nothing but encoding the information like text and media from understandable to meaningless, and make it not visible during the data transfer and storage, this conversion of information from understandable to not

understandable format is referred to as encryption. Decipherment is the process of getting the initial information from encrypted information. To encipher information in cloud each symmetric or asymmetric key are often used, but for the large-sized databases and the data which is stored on the cloud, the symmetric key algorithms are meaningfully good [7].

The information in the cloud will be partitioned for security, those partitions are commonly called fragments, and these fragments will be allocated at some locations among the cloud data servers. The file fragmentation will be done in a way that, no individual fragments may not contain any meaningful data, and this will be performed based upon the user criteria. A cloud node may be anything which can be a computing VM, storage VM. These nodes contain a definite fragment to extend the information security. We have to keep our file fragments at different locations and unaware from an attacker. The selection of the cloud nodes are also important in this context, they are not neighbors, and they are at a meaningful distance from each other [8].

The community should take predefined measures to ensure security. A displacement of the file information exists to adopt global standards (e.g., open source) to make sure interoperability among service providers [9].

Storing data in an exceedingly public cloud could be one more security issue in cloud computing. Normally, clouds will be implemented at centralized storage facilities like data centers, which may be a selective target for hackers. Public clouds are more vulnerable for the attacks. Maintaining a personal cloud if possible for very sensitive data is recommended to avoid these security issues [10].

Privacy and security are the main concerns in the usage of the cloud for data. Features of knowledge like privacy, integrity, and protection must be upheld. Different mechanisms and policies are employed by different service providers counting on the sort of knowledge, size of knowledge, and nature of knowledge. In cloud computing, the most advantage is that various organizations can share the info. But, the advantage causes data to be in danger. Therefore, the risk to the info must be overcome, and thus, data protection is extremely much required [11].

First the file is going to be fragmented, and these file fragments will be distributed over the different cloud nodes. To ensure the security of the file, each cloud node stores singly one fragment of a specific record, this makes no data has been revealed to the attacker.

1.1 Objective of the Paper

The objective of the paper is as follows.

- To achieve optimal performance and security by division and replication of data in the cloud.
- We break the file into several fragments and distribute by replicating the fragments on the cloud nodes.

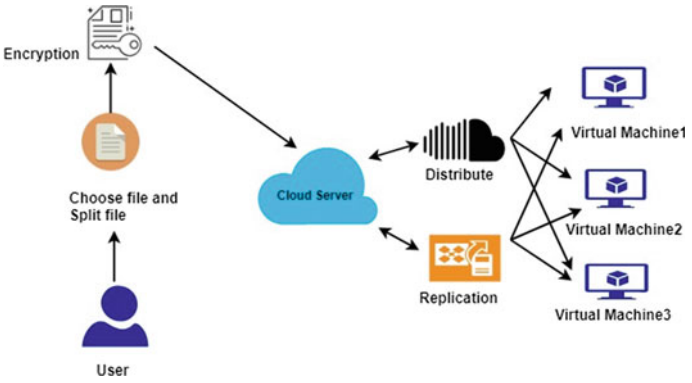

Fig. 1 Methodology

The methodology of this work is shown in Fig. 1. The sections in this paper are organized as follows. In Sect. 2, we gave an overview of the related work. In Sect. 3, we discussed the preliminary concepts of the work. Section 4 discusses the system model and methodology. Section 5 gives the experimental setup and results, and Sect. 6 is concluding the paper.

2 Related Work

M. Ali et al. [12] proposed a division and replication of data for optimal performance and security (DROPS) to answer the performance and security issues in the cloud. Juels et al. [13] introduced an approach of Iris document framework for the information movement to the cloud. The proposed procedure in [13] vigorously relies upon the user's utilized to plan for information secrecy. Additionally, the likely measure of misfortune just if there should arise an occurrence of information hardening because of interruption or access by different VMs can't be diminished. Our proposed methodology doesn't rely on ordinary cryptographic systems for information security. In addition, the proposed approach doesn't store the whole record on one hub to stay away from the bargain of the entirety of the data just in the event of a fruitful assault on the hub. The creators in [14] drew nearer the multi-tenure kind of issues in the distributed storage by using the combined stockpiling and local access control. The Dike approval configuration is arranged that blends the local access to the executives and subsequently the inhabitant name house separation. The proposed technique handles the spillage of basic data by dividing documents and utilizing different hubs to store one record.

Jansen [15] proposed the method where the issues of the cloud are sorted out into a few general classes: trust, engineering, personality board, software disengagement, information insurance, and accessibility. Episodes may include different sorts of extortion, the harm of information assets, and robbery of information by present

or previous representatives, temporary workers, and different gatherings that have obtained access to other private information. Both the customer- and server-side security is unavoidable in distributed storage.

Information segregation and information area are significant inside the information security part inside the cloud. The data put away on the cloud hubs ought to be accessible for approved clients at any expense whenever. Tang et al. [16] depict redistributing information reinforcements off-site to outsider distributed storage administrations. Blur is to accomplish fine-grained, strategy-based access control, and document-guaranteed erasure.

3 Preliminary Concepts

Before we dive into the proposed methodology, let's look at the related concepts in the following.

3.1 Data Encryption and Decryption

Encryption is the process of converting plain text information into a not understandable format meaningless data called ciphertext. Decryption is the procedure of converting ciphertext again to plaintext. To encrypt more than a small number of facts, symmetric encryption is used. The symmetric key is used at some stage in each of the encryption and decryption processes. The intention of each encryption is to make it as difficult as feasible to decrypt the generated ciphertext. The longer the key, the harder it is to decrypt a piece of ciphertext.

3.2 Elliptic Curve Cryptography (ECC)

One of the approaches to public key cryptography is elliptic curve cryptography.

3.2.1 Basic Algorithm

Alice, Bob agree with a non-secret fixed curve point F on the elliptic curve. Alice chooses a random integer A_k, which is her secret key. Now Alice computes curve point $A_P = A_k F$ and publishes it as her public key. Bob will do the same, let $B_p = B_k F$. Consider a scenario, Alice needs to communicate with Bob. One way is, Alice has to simply compute, $R_k = A_k B_p$. The result R_k will be used as the secret key for a conventional symmetric block cipher (say DES). Bob can compute the same number by calculating $B_k A_p$ [17],

$$\text{Since } B_k A_P = B_k \cdot (A_k F) = A_k \cdot (B_k F) = A_k B_P.$$

The security lies in this algorithm is that it is difficult to compute k for a given F and kF.

3.2.2 RSA vs ECC

Menezes and Jurisic [18] mentioned following observations by which we can assess the working of RSA and ECC. To get a considerable amount of security, 160-bit modulus should be sufficient for ECC, whereas RSA system takes 1024-bit modulus. The strength comparison of RSA and ECC is given in Table 1.

4 System Model

The system model contains the system architecture, which is a two-tier client–server architecture and also discussed the algorithms for encryption and decryption.

4.1 System Architecture

System architecture mainly consists of the user, cloud server, and server machines.

4.2 User

1. User makes registration by providing their details.
2. Users will log in by using a username and password.
3. After login, they choose the file and split that file into the number of fragments.
4. After splitting the files into fragments, they can view the fragments and details of the fragments.

Table 1 RSA versus ECC strength comparison

Time to break (in MIPS–years)	RSA key-size (in bits)	ECC key-size (in bits)
10^4	512	106
10^8	768	132
10^{11}	1024	160
10^{20}	2048	210
10^{78}	21000	600

5. Next, distribute the fragments by selecting distribute operation to the server machines.

4.3 Server

1. Receive the fragments from the user which is converted into the encrypted format and store the fragments. The server receives the request details from the user and gives a response for the particular request what the user has requested.
2. Disintegration and reduplication of data in the cloud can be done by the servers.

The algorithm 1 is for data encryption of the given file which takes a random number and multiplies it with a prime number which will be stored in a big integer format. Here we are using the ECC algorithm for encryption. Algorithm 2 decrypts the encrypted messages where the cipher text is converted into a string.

4.4 Algorithm 1: Algorithm for Data Encryption

The algorithm for the data encryption is given below.

```
Random r1 = new Random();
BigInteger I = BigInteger.probablePrime(3, r1);
BigInteger J = BigInteger.probablePrime(3, r1);
BigInteger K = I.multiply(J);
Random rand = new Random();
int kval = K.intValue();
int kres = rand.nextInt(kval-1);
BigInteger p = BigInteger.valueOf(kres);
BigInteger i1 = k.multiply(I);
BigInteger N = new BigInteger(msg.getBytes());
BigInteger i2 = N.add(i1);
encmsg = i1 + "," + i2;
```

Table 2 File content size versus no. of fragments

File content size	No. of fragments
275	1
854	1
5482	6
7543	8
11,642	12

4.5 Algorithm 2: Algorithm for Data Decryption

The algorithm for the data decryption is given below.

String spt[] = cipher.split(",");

BigInteger i1 = new BigInteger(spt[0]);

BigInteger i2 = new BigInteger(spt[1]);

BigInteger n = i2.subtract (i1);

String filedata = new String (n.toByteArray());

return filedata;

5 Result Analysis

Here, we are showing the results, comparison between file content size, and number of fragments. Also shown the performance of our method when compared to DROPS method [12].

5.1 File Content Size v/s number of Fragments

The following Table 2 shows the number fragments with respect to the size of the file and graph. Figure 2 shows the relation between size of the file and number of fragments in our methodology.

5.2 For Performance

Here, we are showing the performance results of our method when compared to DROPS method.

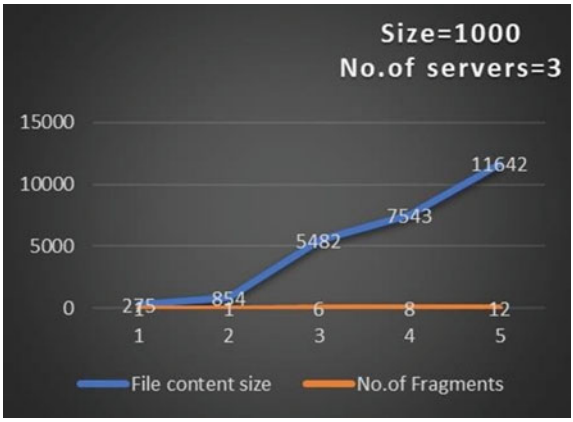

Fig. 2 File content size versus no. of fragments

5.2.1 Read, Replicate, and Retrieval Time Comparison

The read and replicate time comparison between our methodology and DROPS methodology for different fragment size were shown in Table 3. The retrieval time comparison between our methodology and DROPS methodology for different fragment size was shown in Table 4. Here in graph Fig. 3, we see the read and replicate time for our methodology and DROPS methodology, and we see the read and replicate time is optimal when the fragments are between 6 and 8 and therefore gives better performance than DROPS for those numbers of fragments.

Table 3 Read and replicate time comparison

No. of fragments	Read and replicate time for our methodology (ms)	Read and replicate time for DROPS methodology (ms)
1	83	80
6	63	76
8	69	78
12	78	83

Table 4 Retrieval time comparison

No. of fragments	Retrieval time for our methodology (ms)	Retrieval time for DROPS
1	46	32
6	16	27
8	24	30
12	47	31

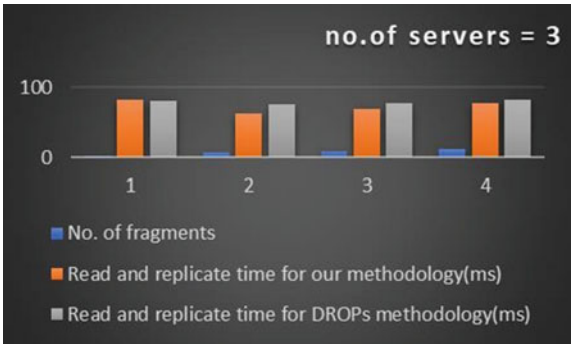

Fig. 3 File content size versus no. of fragments

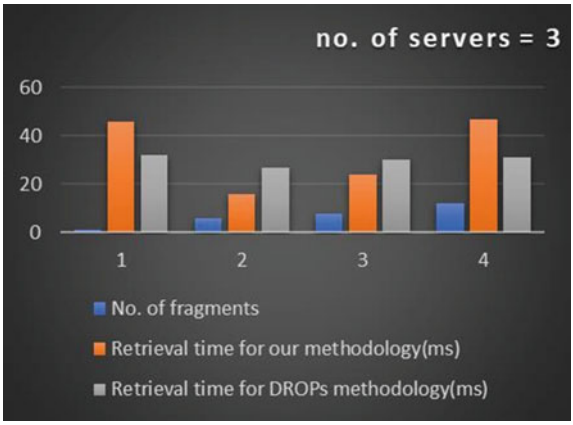

Fig. 4 Comparison with DROPS

5.2.2 Retrieval Time Comparison

Here in graph Fig. 4 we see the retrieval time for our methodology and DROPS methodology, and we see that the retrieval time is optimal when the fragments are between 6 and 8, and therefore, gives better performance than DROPS for those number of fragments. But there is a slight drop in the overall performance.

6 Conclusion

In this paper, we proposed a model for high security through file disintegration, encryption, and performance by retrieval time. This is achieved by dividing the file into small chunks and distributing it in different nodes of the cloud. The data

inside the fragments will be converted into an encrypted format for better security and also contains one replication of that data, so that if there is any sort of attack no meaningful information is revealed, only corrupted information is gained. As shown in the result, the comparison between our model and DROPS technology gives detailed information about performance through minimizing retrieval time for some range of fragments. Therefore, the obtained results increase the security of the user files and avoids the success of unauthorized party attacks of accessing the data, also in better optimizing the performance. User can download their file successfully in the original format after decrypting the data inside the file.

References

1. Zissis D, Lekkas D (2012) Addressing cloud computing security issues. Future Generat Comput Syst 28(3):583–592
2. Tang Y, Lee PP, Lui JCS, Perlman R (November, 2012) Secure overlay cloud storage with access control and assured deletion. IEEE Trans Dependable Secure Comput 9(6):903–916
3. Khan AN, Kiah MLM, Khan SU, Madani SA (2013) Towards secure mobile cloud computing: a survey. Future Generat Comput Syst 29(5):1278–1299
4. Rao GJ, Babu GS (2017) Energy analysis of task scheduling algorithms in green cloud. In: 2017 international conference on innovative mechanisms for industry applications (ICIMIA), Bangalore, pp 302–305
5. Takabi H,James B, Joshi D (January, 2011) Security and privacy challenges in cloud computing environments. Article IEEE Secur Privacy Mag
6. Agarwal P (May–June, 2017) Cryptography Based Security for Cloud Computing System. Int J Adv Res Comput Sci Res Paper 8(5). Available Online at www.ijarcs.info © 2015–19. IJARCS All Rights Reserved 2193 ISSN No. 0976–5697
7. Ramadan HH, Djamilou MA Using cryptography algorithms to secure cloud computing data and services engineering. Am J Eng Res AJER 6(10):334–337, e-ISSN: 2320–0847, p-ISSN: 2320–0936
8. Khan AN, Kiah MLM, Madani SA, Ali M (2013) Enhanced dynamic credential generation scheme for protection of user identity in mobile-cloud computing. J Supercomput 66(3):1687–1706
9. Kaufman LM (2009) Data security in the world of cloud computing. IEEE Secur Priv 7(4):61–64
10. Ahmed A, et al (2016) Data security in cloud computing. In: 2016 Fifth international conference on future generation communication technologies (FGCT), pp 55–59
11. Poonguzhali E, Suhas Rao MV (2017) Protection and security of data in cloud computing. Int J Eng Res Technol (IJERT) ISSN: 2278–0181. Published by, www.ijert.org ICPCN - 2017 Conference Proceedings
12. Ali M, Bilal K, Khan SU, Veeravalli B, Li K, Zomaya AY (2015) DROPS: division and replication of data in cloud for optimal performance and security. IEEE Trans Cloud Comput 6(2):303–315
13. Juels A, Opera A (2013) New approaches to security and availability for cloud data. Commun ACM 56(2):64–73
14. Kappes G, Hatzieleftheriou A, Anastasiadis SV (2013) Dike: virtualization-aware access control for multitenant file systems. University of Ioannina, Greece, Technical Report No. DCS2013–1
15. Jansen WA (2011) Cloud hooks: security and privacy issues in cloud computing. In: Proceedings of the 44th Hawaii international conference on system sciences

16. Tang Y, Lee PPC, Lui JSC, Perlman R (Nov/Dec, 2012) Secure overlay cloud storage with access control and assured deletion. IEEE Trans Depend Secure Comput 9(6)
17. Kapoor V, Abraham VS, Singh R (May, 2008) Elliptic curve cryptography. ACM Ubiquity 9(20), 20–26
18. Jurisic A, Menezes AJ (1997) Elliptic curves and cryptography. Dr. Dobb's J

A Novel Modulating PID Controller for a Speed Control of BLDC Motor Adopting Flower Pollination Algorithm

Yamima Nuthalapati and R. S. R. Krishnam Naidu

Abstract Brushless DC (BLDC) motor is recognized for its more capability and amp; less maintenance. To advance the speed control of the BLDC motor, modulation of proportional plus integral plus derivative (PID) controller uses Flower Pollination Algorithm (FPA) as an optimization technique. It progresses the transient response of the motor by comparing the terms of rise time (t_r), peak overshoot ($\%M_p$), and settling time (t_s). The three gains (proportional (K_p), integral (K_I), and derivative (K_D) of the PID controller have been optimized by the FPA technique to control the speed of the BLDC motor. By estimating the other existing approaches for the same investigated BLDC motor, the simulation numerical results exhibit that the adopted FPA modulated PID controller has greater control performances. The core of the presented study points out that the proposed approach may successfully be claimed for the BLDC motor.

Keywords BLDC motor · PID controller · Flower pollination algorithm (FPA)

1 Introduction

To the full extent of operating conditions, PID controllers are established in a broad range of utilization for industrial operation management because of its simple structure and vigorous conduct [1]. The PID controller advances the nature of transient response along with compressing the steady-state error. So, it has been absolutely tiring to modulate K_P, K_I, and K_D of PID controllers. Each mode in a PID controller has to be modulated, which results in the modulating process [2]. For the speed control of BLDC motor, there is no exact technique for the modulation of PID controller.

Y. Nuthalapati · R. S. R. K. Naidu (✉)
Department of Electronics and Electrical Engineering, Nadimpalli Satyanarayana Raju Institute of Technology, Sontyam, Visakhapatnam, Andhra Pradesh 531173, India
e-mail: naidueee06@gmail.com

Y. Nuthalapati
e-mail: yamiesther1318@gmail.com

G. T. C. Sekhar et al. (eds.), *Intelligent Computing in Control and Communication*, Lecture Notes in Electrical Engineering 702,
https://doi.org/10.1007/978-981-15-8439-8_14

So, the various optimization techniques have been implemented for the gains of PID controllers to converge the best values required to improve the performance [3]. In this paper, flower pollination algorithm is implemented to the parameters of the PID controller. Based on the nature inspired and biological system of flower pollination, Yang proposed a FPA algorithm which is applied for multi objective optimizations. The improved optimization is obtained by this algorithm. With a suggested switch probability, the FPA can discipline the balance of exploration and exploitation properties [4].

2 Research Background

Brushless DC (BLDC) motors are universally habituated in industries for ages ago considering its lower maintenance, simple structure, high efficiency, and high starting torque including dropping speed characteristics and help to avert abrupt load increment [5]. These motors are driven by DC voltages. While managing the speed with better efficiency; it is viable to setup four-quadrant operations from the motor variations using modern drives. Quasi-rectangular current waveforms and trapezoidal back EMF are produced by this motor [6].

A simple BLDC motor simulink model is shown in Fig. 1. For position and speed control, hall-effect sensors are used by varying flux/pole, armature resistance, and applied voltage [7]. Based on the requirement of the switching for a rated speed of the motor, the electronic circuitry arrangement adjusts the speed of the motor and turns ON the transistor to energize the motor winding. Generally, these speed control

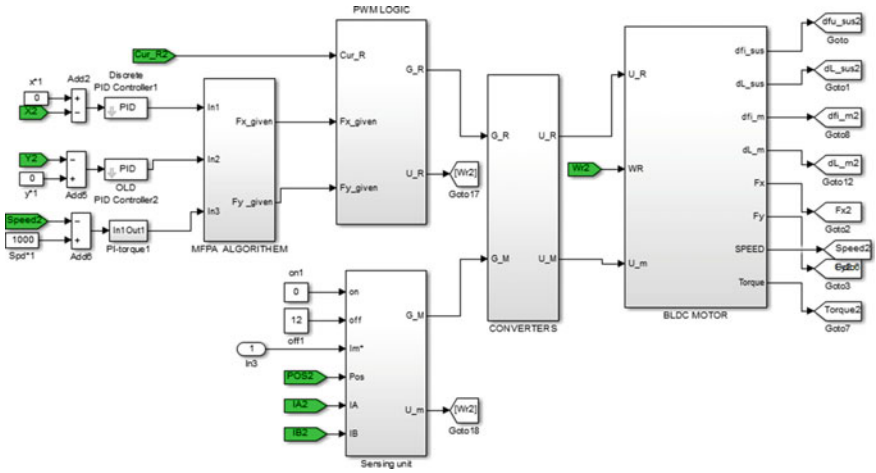

Fig. 1 Simulink model of brushless DC motor

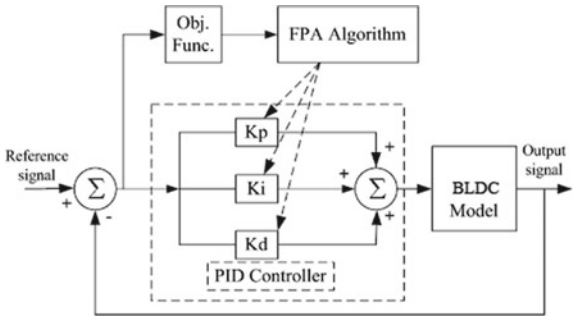

Fig. 2 Block diagram of PID controller

units are carried out with PID controller to have proper control. In both single phase and three phases, BLDC motors can operate.

BLDC motor is a durable magnet which produces required air gap flux. The BLDC motors are electronically commutated thus no need of any brushes for commutation. It has the advantage of no mechanical commutator [8, 9]. Modeling, simulation, tuning of parameters, and control scheme selection are involved in the design of BLDC drive.

3 PID Controller

The proportional plus integral plus derivative controller used to improve the response quality [10]. The block diagram of PID controller is shown in Fig. 2.

If there is an increase in the value of K_P (proportional gain), then the t_r and $\%M$ are shortened. The system will become unstable when K_P increases to a certain limit which produces overshoot [11, 12]. Similarly, the rise time decreases by increasing the value of K_I (integral gain), with eliminating steady-state error. After increasing K_I to a specific limit, worse transient response is produced with overshoot. With improved optimization, when K_D increases then the value of settling time and overshoot decreases [13, 14].

4 Flower Pollination Algorithm

Pollination is a phenomenon where the pollen grains of one plant which are present on the anthers and are transferred to the stigma of other plant or flower of the same species either by biotic (animals, birds), or abiotic (wind, water) factors. This leads to reproduction of a plant. Both the biotic and abiotic factors which help in carrying the pollen grains are called pollinators and play a role in transferring the pollen grains of a flower over wide range. There are two modes of pollination in FPA viz global and local.

Local pollination is a type of pollination where the pollination and fertilization occur within the plant. Global pollination is a type of pollination where the pollination and fertilization occur with the plant which is far away from each other. Global pollination gives the best result than the local pollination [15].

1. Global pollination mode categories into biotic and cross-pollination.
2. Local pollination mode categories into abiotic and self-pollination.
3. The process of pollination is administered by switch possibility, $\rho \in [0, 1]$.

5 Mathematical Modeling

Mathematical modeling gives the insight on overall plant model by considering the higher-order transfer function $G(s)$ and reduced order transfer function $R(s)$ as shown in Eqs. (1) and (2).

Consider a high-order transfer function,

$$G(s) = \frac{N_r(s)}{D_r(s)} = \frac{c_1 + c_2 s + c_3 s^2 + \ldots + c_n s^{n-1}}{d_1 + d_2 s + d_3 s^2 + \ldots + d_n s^{n-1}} \tag{1}$$

Here, $G(s) =$ high-order transfer function.

$$R(s) = \frac{n_r(s)}{d_r(s)} = \frac{c_1^{/} + c_2^{/} s + c_3^{/} s^2 + \ldots + c_k^{/} s^{k-1}}{d_1^{/} + d_2^{/} s + d_3^{/} s^2 + \ldots + d_k^{/} s^{k-1}} \tag{2}$$

Here, $R(s)$ is low-order transfer function. c_1, $c_1^{/}$ are the scalar coefficients of numerator and denominator of $G(s)$ and $R(s)$, respectively.

5.1 Modeling of FPA

Modeling of FPA is carried out in following two sections. In Sect. 5.1.1, it is discussed about global pollination development; in this probability of reproduction is defined step size which is determined. In Sect. 5.1.2, local pollination process is explained, which increases the probability of reproduction within the plant.

5.1.1 Global Pollination Development

Pollen grains increases the probability of reproduction and is defined as shown in Eq. (3).

$$y_i^{t+1} = y_i^t + L\left(y_i^t h^*\right) \tag{3}$$

Here, y = Solution; h^* = best current solution.

To determine the step size valid for $s > 0$, Levy flight distribution [13] is used, shown in Eq. (4)

$$L \approx \frac{\lambda\Gamma(\lambda)\sin(\pi\lambda/2)}{\pi} \cdot \frac{1}{s}, \quad (s >> s_0 >> 0) \tag{4}$$

Here, L = step size of pollination strength; $\Gamma(\lambda)\Gamma(\lambda)$ = basic gamma function, $\lambda = 0.5$.

5.1.2 Local Pollination Process

Pollinators carry the pollen grains within the narrow range, which increases the probability of reproduction within the plant, represented in Eq. (5)

$$y_i^{t+1} = y_i^t + \in (y_j^t - y_k^t) \tag{5}$$

Here, y_j^t and y_k^t = pollens different flowers of same population; $\in$ = uniform distribution, range [0, 1].

y_j^t and y_k^t are the neighboring flower pollens. Neighborhood constancy is considered in this distribution.

FPA is carried out in both global and local pollination. The local pollination occurs within the flower whereas the global pollination occurs among faraway flowers. This condition is controlled by switch probability. Flowchart for FPA is shown in Fig. 3.

6 Methodology

In this section, step-wise procedure is carried out for coefficients of numerator, reduced SISO systems, coefficients of the ROM, transfer function for second-order system as follows in steps.

Step 1: Using FPA, evaluate the coefficients of numerator and denominator of the reduced high-order transfer function.

Step 2: To reduce the SISO system design an objective function which is shown in Eq. (6) and fitness of the above-mentioned function in Eq. (7).

$$\text{ISE} = \int_0^\infty |h(t) - r(t)|^2 \mathrm{d}t \tag{6}$$

$$\text{fitness} - \min(\text{ISE}) \tag{7}$$

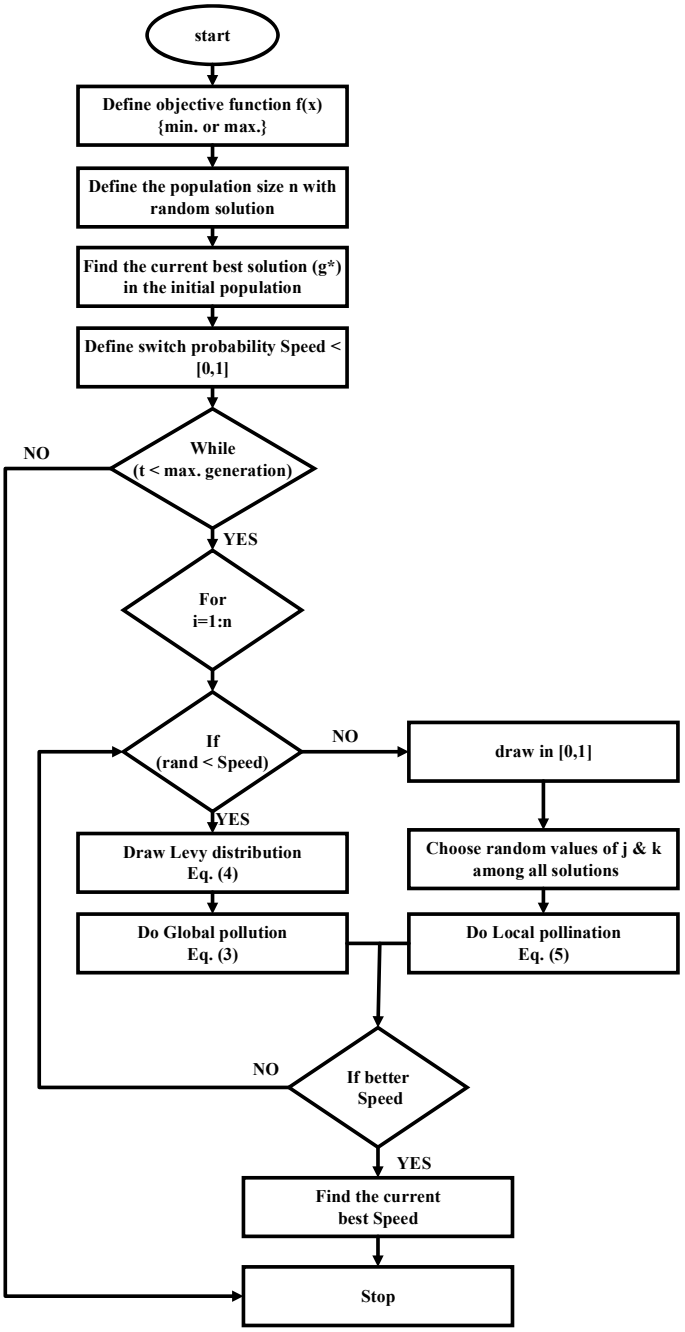

Fig. 3 Flowchart for FPA

Step 3: The numerator (Nr) and denominator (Nd) coefficients of the ROM are given when the fitness function is reduced. Else repeat form Step 1.
Step 4: The ROM transfer function for second order is shown in Eq. (8).

$$R(s) = \frac{c_2 s + c_1}{s^2 + d_2 s + d_1} \tag{8}$$

Here, c_1, c_2 and d_1, d_2 are the numerators and denominators of an unknown coefficients of the reduced high-order transfer function, respectively. IAE and ITAE are shown below in Eqs. (9) and (10).

$$\text{IAE} = \int_0^\infty |h(t) - r(t)| \, \mathrm{d}t \tag{9}$$

$$\text{ITAE} = \int_0^\infty t|h(t) - r(t)| \, \mathrm{d}t \tag{10}$$

The pseudocode of the algorithm is as follows:

1. Initialize the objective function f(X) for minimum or maximum, X = (x_1, x_2, x_3,…, x_n).
2. Insert the population size n for flower/pollens with random solution.
3. Identify the best solution (h*) from initialize population.
4. Insert the switch probability ρ ϵ [0, 1]
5. while (t < Maximum Generation)
6. for i = 1:n
7. if rand < p
8. Calculate a step size or Levy distribution (L)
9. Calculate global pollination using $y_i^{t+1} = y_i^t + L(y_i^t - h^*)$
   else
10. Draw ρ ∈ from a uniform distribution in [0, 1].
11. Select different j and k from all the solutions.
12. Calculate local pollination using $y_i^{t+1} = y_i^t + \in (y_j^t - y_k^t)$
    end if
13. Find new values
14. If new values are better, substitute and store in place of new population
    end for
15. Find for new best solution h*
    end while

Table 1 Controller parameters

Controller type	Controller parameters		
	K_P	K_I	K_D
PID	1.4671	0.3261	0.0371
FPI	1.5204	0.1687	0.1284
FPID	5.7874	0.4515	0.8182
GPID	11.8316	1.1612	1.3247
FPA	12.110	2.1901	1.1010

Table 2 Transient response parameters

Controller type	(t_r) (sec)	$(\%M_p)$	(t_s) (sec)
PID	0.07	7.0	0.4
FPI	0.05	4.0	0.36
FPID	0.06	2.5	0.31
GPID	0.05	0	0.63
FPA	0.01	0	0.024

7 Results and Discussion

In this work, proposed FPA is utilized for the enhancement of the PID controller for the speed control of BLDC Motor. The simulation is carried out in MATLAB/Simulink. This speed response of the PID controller of the BLDC motor adopted FPA is compared with the other existing approaches such as FPI, FPID, and GPID for the same investigated BLDC motor.

Table 1 shows the controller parameters of the different approaches utilized for the BLDC speed control.

Table 2shows the speed response profiles based on the values of parameters of the controller. Speeds comparison of BLDCM using different algorithms with step is shown in Fig. 4.

The adopted FPA algorithm is showing the improved results during rise time (t_r), peak overshoot $(\%M_p)$, and settling time (t_s). It also gave a smooth operating performance when compared with the other controllers. Thus, the proposed FPA algorithm is easy to implement for controlling the speed in various electric motors.

8 Conclusion

Here, the transient response of BLDCM motor is advanced by modulating the PID controller using FPA. By estimating the other existing approaches, numerical simulation results show that the proposed FPA modulated PID controller gives smooth

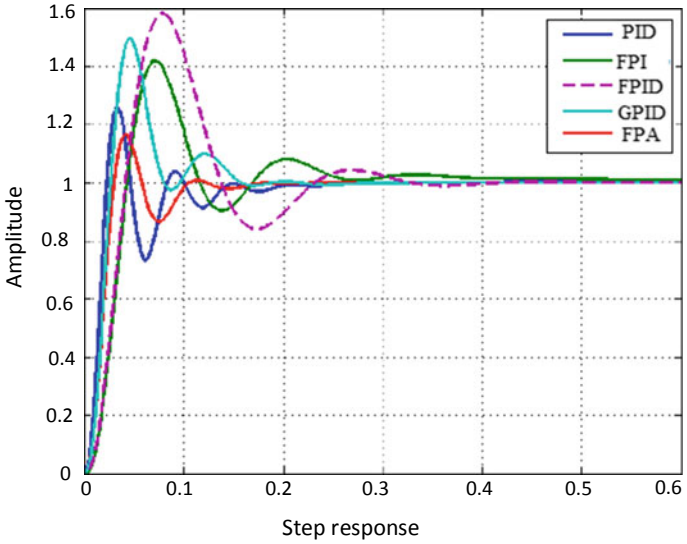

Fig. 4 Speeds comparison of BLDCM using different algorithms with step i/p

and greater control performances and have an advanced capability to explore the optimal solution when comparing the rise time (t_r), peak overshoot ($\%M_p$), and settling time (t_s). Hence, the presented study points out that the proposed approach may successfully be claimed for the BLDC motors.

References

1. Gaing ZL (June, 2004) Member, IEEE, A particle swarm optimization approach for optimum design of PID controller in AVR system. IEEE Trans Energy Conver 19(2)
2. Sharma P, Gupta R (2014) Tuning of PID controller for a linear BLDC motor using TLBO technique. In: Sixth international conference on computational intelligence and communication networks
3. Chatterjee S, Dalel MA, Palavalasa M (August, 2019) Speed control of DC motor using whale optimization algorithm based PID controller. Think India J 22(16), ISSN: 0971–1260
4. Sambariya DK, Gupta T (2018) An application of flower pollination algorithm in model order reduction of LTI systems. Am J Electr Electron Eng 6(3):77–84
5. Abedini S, Zarabadipour H (2011) Tuning of an optimal PID controller with iterative feedback tuning method for DC motor. In: 2nd international conference on control, instrumentation and automation (ICCIA)
6. Suganthi P, Nagapavithra S, Umamaheswari S (2017) Modeling and simulation of closed loop speed control for BLDC motor IEEE
7. Setiyono WB, Surnardi MR (2018) Design of self-tuning regulator for brushless dc motor speed control. ICSGTEIS
8. Pelczewski PM, Kunz UH (October, 1990) The optimal control of a constrained drive system with brushless dc motor. IEEE Trans Ind Electron 37:342–348

9. Lin FJ, Shyu KK, Lin YS (March, 1999) Variable structure adaptive control for PM synchronous servo motor drives. IEE Proc IEE B Elect Power Appl 146:173–185
10. Sambariya DK, Paliwal D (2016) Optimal design of PIDA controller using firefly algorithm for AVR power system. In: International conference on computing, communication and automation (ICCCA), pp 987–992
11. Panda S, Sahu BK, Mohanty PK (2012) Design and performance analysis of PID controller for an automatic voltage regulator system using simplified particle swarm optimization. J Franklin Inst 349(8):2609–2625
12. Sambariya DK, Gupta T (2017) Optimal design of PID controller for an AVR system using monarch butterfly optimization. In: 2017 international conference on information, communication, instrumentation and control (ICICIC), pp 1–6
13. dos Santos Coelho L (2009) Tuning of PID controller for an automatic regulator voltage system using chaotic optimization approach. Chaos, Solitons Fractals 39(4):1504–1514
14. Sambariya DK, Gupta T (2018) Optimal design of PID controller for an AVR system using flower pollination algorithm. J Auto Control 6
15. Wang Z, Xie H, He D (2019) Member, IEEE, Sammy Chan, Member IEEE, Wireless sensor network deployment optimization based on two flower pollination algorithms in IEEE (2019)

Shaped Beams from Circular Aperture Antennas

J. Babu, B. Ramesh Reddy, J. Doondi Kumar, N. Siva Govind, and Baji Babu Mutte

Abstract The design of circular apertures for generating radiation pattern with controlled side lobe levels is attractive in communication and radar applications. The aperture distribution would cause the innermost side lobes to have individually specified heights. The research on circular aperture distribution to produce sum patterns with controlled side lobe levels is limited in the open literature. Hence, an attempt is made to obtain the shaped beams with controlled side lobe levels from circular aperture antennas. This is possible with a proper set of root positions. These root positions will yield the proper shaped beams from circular apertures. Different shaped beams are generated with new root positions. These shaped beams will have specified and controlled side lobe level.

J. Babu (✉)
Department of Electronics and Communication Engineering, Dadi Institute of Engineering and Technology, Anakapalle, Visakhapatnam, Andhra Pradesh 531002, India
e-mail: jettisanjay@gmail.com

B. R. Reddy
Department of Electronics and Communication Engineering, Lakireddy Bali Reddy College of Engineering, Mylavaram, Krishna, Andhra Pradesh 521230, India
e-mail: brrece73@gmail.com

J. D. Kumar
Department of Electronics and Communication Engineering, Karunya Institute of Technology and Sciences, Coimbatore, Tamil Nadu 641114, India
e-mail: jdoondikumarece@gmail.com

N. S. Govind
Department of Electronics and Communication Engineering, MVR College of Engineering and Technology, Paritala, Krishna 521180, Andhra Pradesh, India
e-mail: nandamuri429@gmail.com

B. B. Mutte
Department of Electronics and Communication Engineering, Godavari Institute of Engineering and Technology, Rajahmundry, Andhra Pradesh 533296, India
e-mail: bajibabumutte@gmail.com

G. T. C. Sekhar et al. (eds.), *Intelligent Computing in Control and Communication*, Lecture Notes in Electrical Engineering 702,
https://doi.org/10.1007/978-981-15-8439-8_15

Keywords Aperture distribution · Radiation pattern · Circular aperture antenna · Side lobes

1 Introduction

The most commonly used beam shapes in communication and radar applications are fan beam and pencil beam. The beam width of pencil beam will be narrow, whereas the beam width of fan beam is wide. The fan beams are used to simultaneously cover some degrees of azimuth and elevation.

Antenna aperture [1] is a measure of how effective an antenna is at receiving the power of radio waves. The antenna apertures which are mainly in use are circular aperture, rectangular aperture, and square aperture. The circular apertures are widely used when compared to other apertures, as they do not have any discontinuities while radiating. Usually the parabolic dish antenna and horn antenna will have circular apertures.

The circular aperture antennas [2] which produces the shaped beams are used in space communication. The shaped beams are produced by well-designed aperture distributions. The present work is centered on circular apertures. Taylor [3] has reported a method for design of circular apertures for generating radiation pattern with narrow beam width and low side lobe levels. The aperture distribution was further elaborated by Hansen [4].

Graham et al. [5] also presented a method for design of circular apertures for producing sum patterns with ring side lobes of arbitrary heights. A perturbation procedure has been devised that will determine the proper set of root positions once the height of each side lobe has been specified. The resultant patterns are called modified Taylor patterns.

Orchard et al. [6] presented a method aimed to produce a shaped pattern with controlled ripple and controlled side lobe levels from linear arrays with equal spacing. A pattern synthesis procedure was developed by Elliott and Stern [7, 8] using aperture antenna with a circular boundary.

The aperture distribution plays important role in producing shaped beams. It would cause the innermost side lobes (of a pattern) to have individually specified heights. This is possible with set of root positions. These root positions can also be modified with different methods, which will yield the proper shaped patterns from circular apertures. Hence, a method has been implemented that will determine the proper set of root positions with the specified side lobe level. In the present work, Elliott and Stern method has been extended to obtain the shaped patterns.

2 Shaped Patterns from Circular Aperture Antennas

The shaped beams can be generated from properly designed circular apertures [3]. The circular aperture with a radius R is shown in Fig. 1.

Here, θ is observation angle.

Φ is azimuthal angle measured from x-axis. It is assumed to be zero.

r is the distance from center of aperture to the point of observation.

The radiation pattern of circular aperture with radius R is given n Eq. 1

$$E(u) = \int_0^{\pi} pg(p)J_0(pu)\,\mathrm{d}p \tag{1}$$

where $g(p)$ is the aperture distribution function.

Here, $u = \frac{2R}{\lambda}\sin\theta$

The normalized radius is $p = \frac{\pi}{R}\rho$

Let $\overline{n}$ is a number controlling the degree of uniformity of the side lobes.

It assumes a finite positive integer more than 1.

If the circular aperture is uniformly excited, then $g(p) = 1$.

This will produce a sum pattern in the form as Eq. 2

$$E(u) = \frac{J_1(\pi u)}{\pi u} \tag{2}$$

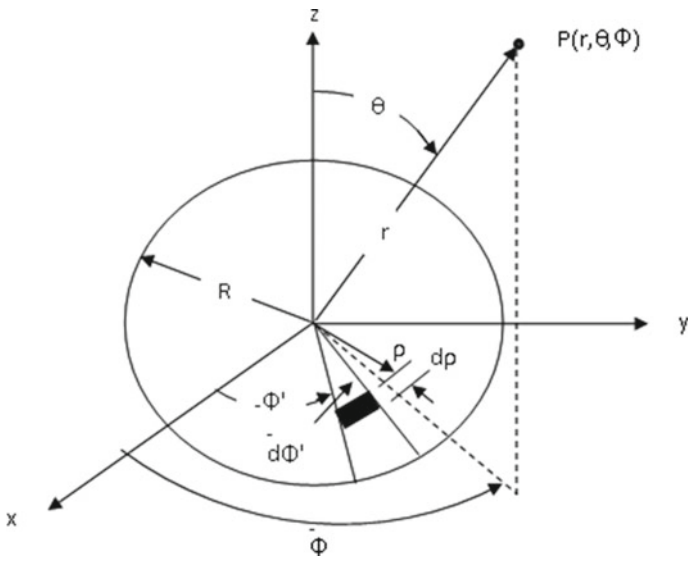

Fig. 1 Circular aperture

Here, $J_1(\pi u)$ is the Bessel function of first kind and first order.

The pattern shown in Fig. 2 has a main lobe and a family of side lobes that decay in height as the side lobe position becomes more remote from the main beam. Since this pattern is rotationally symmetric, the main lobe is observed to be pencil beam, surrounded by ring side lobes. How many of these side lobes are in visible space that depends on the aperture size. Since $u = 2a\sin\theta/\lambda$, the range of u corresponding to visible space is $0 < u < 2a/\lambda$.

The nulls of this pattern are given by Eq. 3

$$J_1(\pi \Upsilon_{1n}) = 0, \quad n = 0, 1, 2, 3, \ldots \tag{3}$$

The nth roots "Υ_{1n}" are called as Bessel function zeros.

In order to have the near-in side lobes at a quasi-constant controlled height, the aperture distribution function $g(p)$ should be expressed in a suitable form. Then, the pattern given by Eq. 2 is modified.

Taylor [3] has reported the solution to this problem. He has presented a method of circular aperture design to produce the radiation patterns with specific beam width and side lobe level. This analysis consists of moving the innermost $\overline{n} - 1$ nulls of Fig. 2 to achieve the desired level for the intervening side lobes. The pattern of circular aperture [3] is represented by Eq. 4

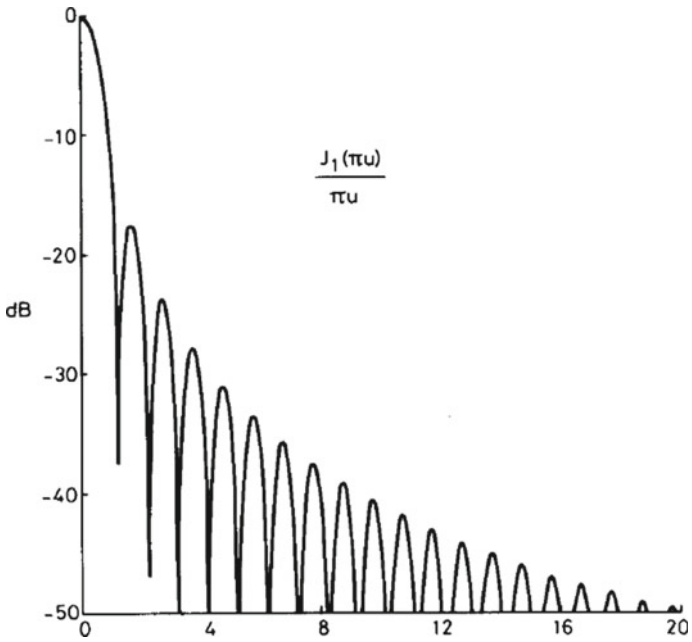

Fig. 2 Radiation pattern for circular aperture with uniform excitation.

$$E(u) = \frac{J_1(\pi u)}{\pi u} \prod_{n=1}^{\bar{n}-1} \left\{ \frac{1 - \frac{u^2}{\sigma^2[A^2+(n-0.5)^2]}}{1 - \frac{u^2}{\Upsilon_{1n}^2}} \right\} \tag{4}$$

Here, "A" is a parameter that describes the desired side lobe level. It is given by

$$A = \frac{1}{\pi} \cosh^{-1}(10^{\frac{-\text{SLL}}{20}})$$

The beam broadening factor σ is given by $\sigma = \frac{u_{\bar{n}}}{\sqrt{A^2+(\bar{n}-0.5)^2}}$

By letting $u_{\bar{n}} = \sigma\left[A^2 + (\bar{n} - 0.5)^2\right]$, Eq. (4) can be expressed as

$$E(u) = \frac{J_1(\pi u)}{\pi u} \frac{\prod_{n=1}^{\bar{n}-1}\left[1 - \frac{u^2}{u_n^2}\right]}{\prod_{n=1}^{\bar{n}-1}\left[1 - \frac{u^2}{\Upsilon_{1n}^2}\right]} \tag{5}$$

The relation between desired side lobe level (SLL) and side lobe ratio η is given by SLL (in decibels) $= -20\log_{10}(\eta)$ dB.

The designed aperture distribution function [3], which produces the radiation pattern of Eq. (5), is given by

$$g(p) = \frac{2}{\pi^2} \sum_{m=0}^{\bar{n}-1} \frac{E(\Upsilon_{1m})}{J_0^2(\Upsilon_{1m}\pi)} J_0(\Upsilon_{1m} p) \tag{6}$$

Here, $J_0(\pi u)$ is Bessel function of first kind and zero order.

It is observed that Eq. (5) removes the first $\overline{n} - 1$ root pairs of Eq. (2) and replaces them with $\overline{n} - 1$ root pairs at the new positions $\pm u_n$.

If there are $\overline{n} - 1$ side lobes, then the analysis is to move the innermost $\overline{n} - 1$ nulls of starting pattern to new positions.

The new positions of the selected inner most side lobes are given by Eq. (7)

$$u_n^2 = \Upsilon_{1n}^2 \frac{A^2 + \left(n - \frac{1}{2}\right)^2}{A^2 + \left(\bar{n} - \frac{1}{2}\right)^2} \tag{7}$$

These new root positions are substituted in Eq. (5) to obtain desired pattern.

3 Null Filling and Optimization of Desired Shaped Patterns from Circular Apertures

Graham et al. [5] presented a method for design of circular apertures for producing sum patterns with side lobes of different heights. The resultant patterns are called

modified Taylor patterns. The aperture distributions for these modified Taylor patterns can be determined from Eq. (6). Orchard et al. [6] presented a pattern synthesis method to produce patterns from equi-spaced linear arrays. The array excitations are varied. Elliott et al. [7] presented a new method for shaped beam synthesis from equispaced arrays. Elliott et al. [8] reported a pattern synthesis procedure for circular apertures.

Usually, a sum pattern consists of a main lobe with adjacent side lobes. The height of each side lobe can be individually controlled. Such patterns find applications in radar and space communications.

Further flat-topped beams can also be obtained. In the present work, Elliott and Stern method has been extended to obtain the shaped patterns with controlled side lobes.

In order to obtain desired shaped patterns, the starting pattern will be taken as base to find out the starting root positions u and null locations γ. We can use Fig. 2 as the starting pattern. There is no null filling in this particular case. The root positions for this pattern is [1.21972.23313.23834.2411 5.2427]. For this, $u_n = \Upsilon_{1n}$ and $v_n = 0$.

If we anchor all the roots (of Taylor pattern) $u_n = \Upsilon_{1n}$ for $n > \bar{n}$, and move the inner roots for $n = 1, 2, \ldots, \bar{n} - 1$ to the new positions $u_n + jv_n \neq \Upsilon_{1n}$, the pattern takes the form of [8–10].

$$E(u) = f(u) \prod_{n=1}^{\bar{n}-1} \left[1 - \frac{u^2}{(u_n + j v_n)^2} \right] \tag{8}$$

where $f(u)$ is given as Eq. (9)

$$f(u) = 2 \frac{J_1(\pi u)}{\pi u} \frac{1}{\prod_{n=1}^{\bar{n}-1} \left[1 - \frac{u^2}{\Upsilon_{1n}^2} \right]} \tag{9}$$

It is possible to find complex root positions $u_n + jv_n$ that will yield a pattern with properly filled nulls in the shaped region while maintaining controlled side lobe levels in the unshaped region [8]. A flat-topped beam with specified ripple level and specified side lobe level can also be obtained.

Usually, 2^M different continuous aperture distributions corresponding to the same shaped beams are obtained if there are M complex roots. These aperture distributions are all complex.

The u_n and v_n values can be placed in Eq. (8) to obtain the field pattern. This field pattern can be used in Eq. (6) to find the aperture distribution function.

4 Results

The Taylor radiation pattern of circular aperture with $\bar{n} = 4$, SLL $= -30$ dB is generated from Eq. (5). It is shown in Fig. 3. The respective aperture distribution is generated from Eq. (6). It is shown in Fig. 4.

For the case of inner most ring side lobe at -35 dB, and next adjacent four side lobes at -25 dB, the new root positions u_n are calculated with the help of Eq. (6). The u_n values are found to be [1.4839 1.8933 2.9268 3.9622 5.0416]. There is no null filling in this case. So, the v_n values are zeros.

By substituting these values in Eq. (8), the radiation pattern can be obtained. It is shown in Fig. 5. In this case, the five inner most side lobes are moved to [-35 -25 -25 -25 -25] (in dB).

For the case of side lobe levels at [00 -25 -25 -25] (in dB), the new root positions u_n are found to be at [0.6322 1.9308 3.7674 4.3929 5.2633]. The generated pattern is shown in Fig. 6.

For the above pattern, the first two nulls can be filled. So the values for v_1 and v_2 are taken as 0.1 instead of zero as was the value for earlier case. Using these values, the pattern is obtained and is shown in Fig. 7. For this case, the inner most side lobes are at [00 -25 -25 -25] and null filling $v_1 = v_2 = 0.1$.

The pattern of Fig. 7 can be converted to the flat-topped beam with a ripple of ± 0.5 dB. For this case, the new root positions and the null-filling values are given

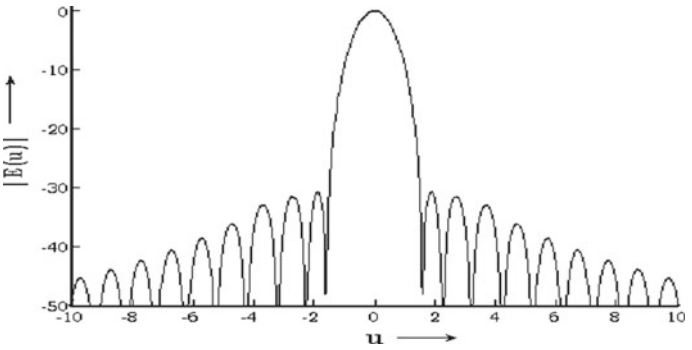

Fig. 3 Radiation pattern of circular aperture with $\bar{n} = 4$, SLL $= -30$ dB

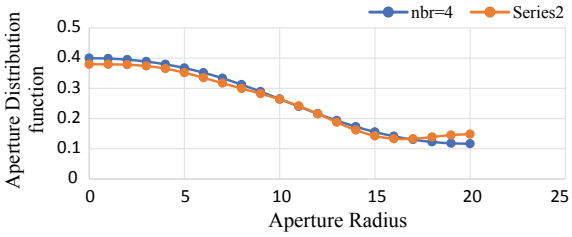

Fig. 4 Taylor circular aperture distribution for SLL $= -30$ dB

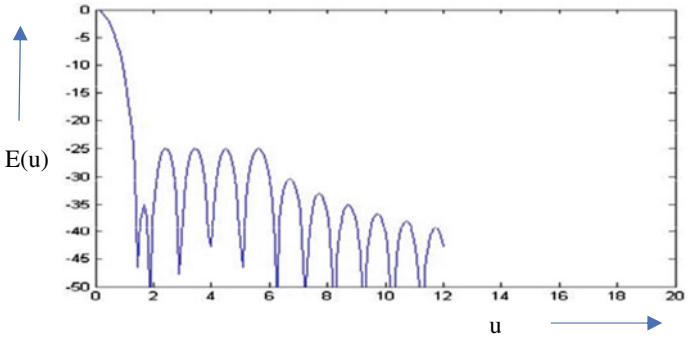

Fig. 5 Shaped pattern with inner side lobe at −35 dB, four side lobes at −25 dB

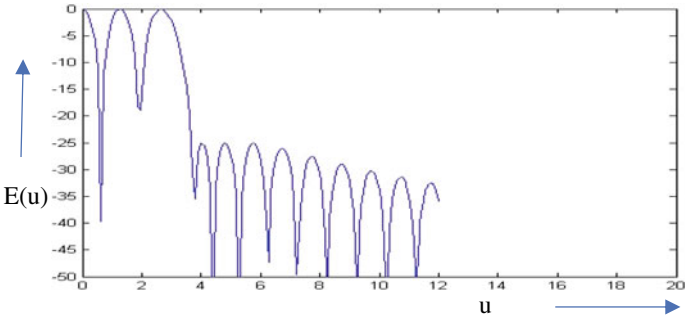

Fig. 6 Shaped pattern with two inner side lobes raised to zero dB

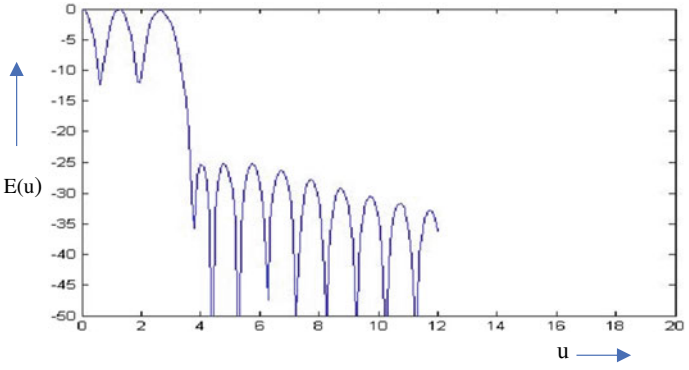

Fig. 7 Starting radiation pattern for a flat-topped beam with SLL = −25 dB

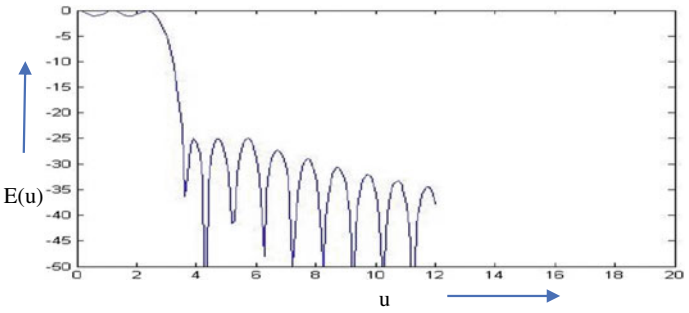

Fig. 8 Flat-topped radiation pattern with a ripple ±0.5 dB and SLL = −25 dB

as $u_n = [0.5967\ 1.7837\ 3.6420\ 4.3039\ 5.2119]$ and $v_n = [0.5225\ 0.5268\ 0\ 0\ 0]$.By substituting these values, the flat-topped radiation pattern can be obtained. It is shown in Fig. 8.

5 Conclusion

The Taylor patterns from circular aperture have been generated. These patterns are having narrow beam width and low side lobe levels. The aperture distribution reported by Taylor has been modified. The new aperture distribution which causes the innermost side lobes to have individually specified heights is considered. This is possible with set of new root positions. The patterns are generated with the modified roots. These new root positions are useful in obtaining the patterns with a specified and controlled side lobe level. This method can also be applied to many modern antenna design applications which are aimed to produce the shaped beams with low and controlled side lobe level.

References

1. Raju GSN (2006) Antennas and wave propagation. Pearson Education India
2. Elliot RS (2006) Antenna theory and design. Wiley
3. Taylor TT (January, 1960) Design of circular apertures for narrow beam width and low sidelobes. IRE Trans Antennas Propagat AP-8:17–22
4. Hansen RC (1960) Tables of taylor distributions for circular aperture antennas. IRE Trans Antenna Propagat
5. Graham O, Johnson RM, Elliott RS (1978) Design of circular apertures for sum patterns with ring side lobes of individually arbitrary heights. Alta Frequenza J 47:21–25
6. Orchard HJ, Elliott RS, Stern GJ (February, 1985) Optimizing the synthesis of shaped beam antenna patterns. IEE Proc Microw Antennas Propagat Part H, 132(1):63–69
7. Elliott RS, Stern GJ (Octo) A new technique for shaped beam synthesis of equispaced arrays. IEEE Trans Antennas Propag 32(10):1129–1133

8. Elliott RS, Stern GJ (December, 1988) Shaped patterns from a continuous planar aperture distribution. IEE Proc Pt H. 135(6):366–370
9. Kim YU, Elliott RS (November, 1988) Shaped-pattern synthesis using pure real distributions. IEEE Trans Antennas Propagat 36(11):1645–1649
10. Elliott RS, Stern GJ (April, 1990) Footprint patterns obtained by planar arrays. IEE Proc Pt. H, 137(2)

A Simple and Low-Cost HIL Solution for Control of Power Electronic Converters

Pydimarri Manoj Kumar and Y. V. Pavan Kumar

Abstract Power electronic converters play a crucial role in converting the available voltage to the required voltage ratings in both AC and DC. Generation of pulse width modulation (PWM) signals plays a crucial part in the overall working of a power electronic converter. The controlled PWM signals can effectively regulate the converter output according to the user requirement. So, supplying these PWM signals is the prime focus in the entire converter design. These PWM signals can be generated through hardware controller boards such as FPGA and microcontroller, or through software and hardware co-simulation platforms such as hardware in the loop (HIL) environment. However, direct hardware controller-based PWM generation needs thorough expertise on relevant programming languages. So, HIL solutions are normally preferred over this. There are many HIL simulators available such as Typhoon-HIL, RTDS, eMEGAsim, dSPACE, HRTSim, and RT-Lab, which serves the purpose. However, the cost of these simulators and the design complexity may limit their usage for research works conducted in academic institutions. With this intent, this paper suggests a low-cost HIL setup which requires data acquisition (DAQ) board and MATLAB/Simulink software to develop. The usefulness of the proposed HIL setup is validated by comparing with the actual results produced by the simulation environment and found it as satisfactory.

Keywords Hardware in the loop (HIL) setup · Power electronics' control · Step-down converter · Pulse width modulation

This work was supported by Project Grant No: SRG/2019/000648, sponsored by Start-up Research Grant (SRG) scheme of Science and Engineering Research Board (SERB), a statutory body under the Department of Science and Technology (DST), Government of India.

P. M. Kumar · Y. V. P. Kumar (✉)
School of Electronics Engineering, Vellore Institute of Technology-Andhra Pradesh (VIT-AP) University, Amaravati 522237, India
e-mail: pavankumar.yv@vitap.ac.in

P. M. Kumar
e-mail: manojkumar.pydi@vitap.ac.in

G. T. C. Sekhar et al. (eds.), *Intelligent Computing in Control and Communication*, Lecture Notes in Electrical Engineering 702,
https://doi.org/10.1007/978-981-15-8439-8_16

1 Introduction

Development of a direct product in real-time environment always may lead to several problems such as the malfunctioning due to ineffective design, wastage of material due to damages, injuries to the engineers in some cases, investment loss, and time wastage. If it is in the case of large-scale industries or systems, it may lead to the damage in a greater extent such as overall plant shutdown. Hence, the prototyping plays a major role in the product development lifecycle to ensure the correctness of a given design. However, before going for the prototype development, an effective product development cycle suggests simulation and hardware-software co-simulation. Hence, a simulator is required, which can emulate the real-time environment and testing scenarios to match its characteristics with the actual product [1]. This can be achieved by using a microcontroller or FPGA but there are some disadvantages such as these devices has lower efficiency, high complexity in coding when realizing in large scale, and lesser processing capabilities.

So, there is a need to develop a software–hardware co-simulation setup which reduces the disadvantages mentioned above. Hence, with this motive, hardware In the loop (HIL) solutions came into existence to fill this gap. HIL setup provides easier implementation and helps to analyze the design issues without much damage to the system [2, 3]. There are some HIL setups available in the market such as Typhoon-HIL, RTDS, eMEGAsim, dSPACE, HRTSim, and RT-Lab. These solutions are widely used in various research studies as mentioned in the following literature.

Power system and virtual synchronous generator interactions are tested using RTDS simulation in [4]. Power drives simulation using RT-Lab HIL setup was discussed in [5]. Similarly, implementation of desired control and testing techniques for AC and DC electrical drives was done using RT-Lab setup [6]. eMEGAsim real-time simulator-based simulations were successfully executed for phasor measurement units in [7]. For managing the grid transmission, a static convertible transmission controller was discussed using HIL based simulation in [8]. Automotive applications are also being tested using dSPACE HIL simulator which makes the testing process easier and convenient [9]. Simulation of a distribution system with high percentage of photovoltaic energy which is difficult task was made possible by using a RTDS and dSPACE simulator, which allows to change the testing environment various times to test the system subjected to dynamic operating conditions [10]. But all these above-mentioned HIL setups are very much expensive which may not be suitable for research works carried in low and medium range academic institutions or industries. This motivates to the idea of developing a low-cost HIL setup that helps the academic research.

Besides, as the world is progressing toward renewable energy usage, there are a lot of issues in terms of efficiency, power conversion, impedance mismatching, etc., have to be addressed to get maximum benefits out of these green energy systems. The voltage at the generation usually available is higher or lower than the need according to various applications or loads such as battery charging, mobile charging, switch mode power supplies, and uninterrupted power supplies. Similarly, other applications

need power conversion from DC to AC or vice versa. All these applications use power electronic converter as a major device to perform the required conversions such as AC-to-DC, DC-to-AC, and voltage step-up or step-down.

So, in this paper, a step-down converter is considered as a test case, for which the required control signals (PWM signals) are generated through the proposed HIL setup. The behavior of the converter is studied with different duty-cycled pulses given to its switching device. To validate the effectiveness, the proposed HIL based hardware results and the direct software results are compared as discussed in the results section.

2 Description of the Proposed HIL Setup

The proposed HIL setup can be briefly segregated into three parts, namely software environment, hardware under test, and software–hardware interfacing medium as shown in Fig. 1. Here, the data acquisition (DAQ) hardware is considered as the required interfacing medium to develop communication between software and hardware environments [11]. The hardware system is the step-down converter hardware, which consists of the components such as resistor, capacitor, inductor, diode, and switch (MOSFET). The software environment consists of the PWM signal generator, which is developed using MATLAB/Simulink software. Hence, the hardware and the software environments are connected in a closed loop via the DAQ interfacing hardware. Thus, the generated control pulses (PWM signal) in software are supplied to the MOSFET hardware continuously. Further, these PWM signals are regulated according to the converter output requirements.

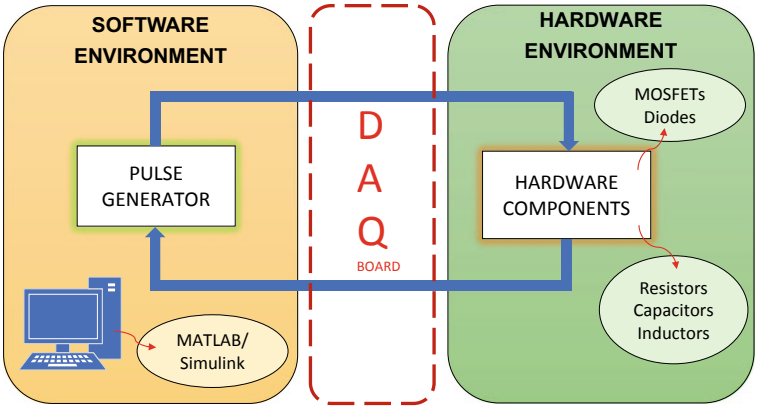

Fig. 1 Depiction of proposed HIL setup and its constituents

2.1 Detailed Design

The setup of the proposed HIL configuration is shown in Fig. 2. It consists of the host setup that provides the simulation environment, the target setup that provides real-time environment with DAQ facility, the actual hardware (power electronic converter), etc. Further, the input and output monitor provides the observation of the output and input signals. A PC with MATLAB/Simulink software acts as the host PC in which the controller model is developed. This model is converted to real-time executable file using a target PC, which facilitates for data acquisition to or from peripheral equipment. The connection between host PC and target PC is established via RS-232 cable or Ethernet. Any DAQ, for example, this work uses NI-PCI 6229 based DAQ board whose specifications are given in Table 1 which can be used for the input and output communication with peripherals [12].

Here, in the case of power electronic converter control, PWM signals are continuously generated from the software control model and sent out for the control of the switching device. Similarly, the output of the converter is fed back to the model via voltage/current sensors as shown in Fig. 2; thus, it forms a closed loop between the real hardware and the software control logic [13]. Hence, this way, various control

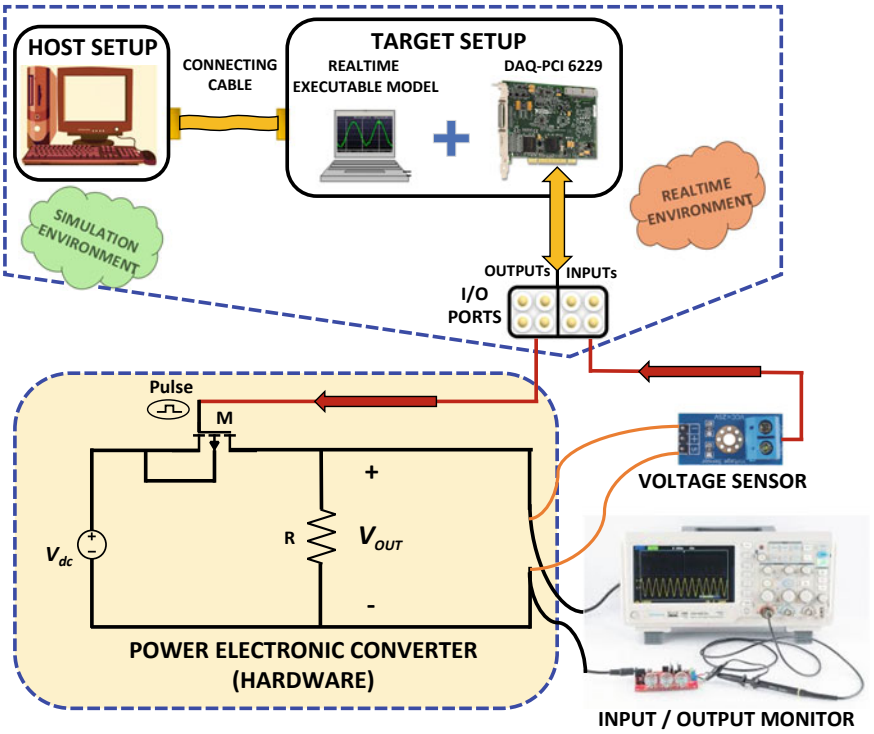

Fig. 2 Schematic of the proposed HIL setup

Table 1 Specifications of data acquisition board used for HIL setup

S. No.	Parameter	Type	Number of pins
1.	Input port	Analog	16
		Digital	32
2.	Output port	Analog	16
		Digital	4

logics can be implemented simply in the software environment and used for the hardware converter, and hence, more accurate validation can be realized.

2.2 Test Case Description

In order to understand the usefulness of the proposed HIL setup, a power electronic step-down converter shown in Fig. 3, which reduces the input voltage based on the given duty ratio of the PWM signal is considered [14]. The component specifications used in the hardware design are given in Table 2.

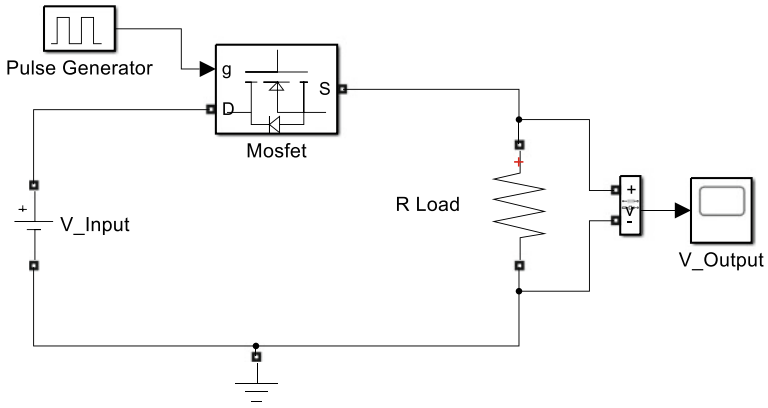

Fig. 3 Circuit diagram of the step-down converter for validating the proposed HIL setup

Table 2 Circuit parameters of step-down converter

S. No.	Parameter	Values
1.	Resistor	100Ω
2.	MOSFET	Enhancement mode NMOS (IRF 740-A)
3.	Input voltage	15 V
4.	Control pulse (pulse generator)	Switching frequency: 25 kHz
		Duty ratio: (0–100)%

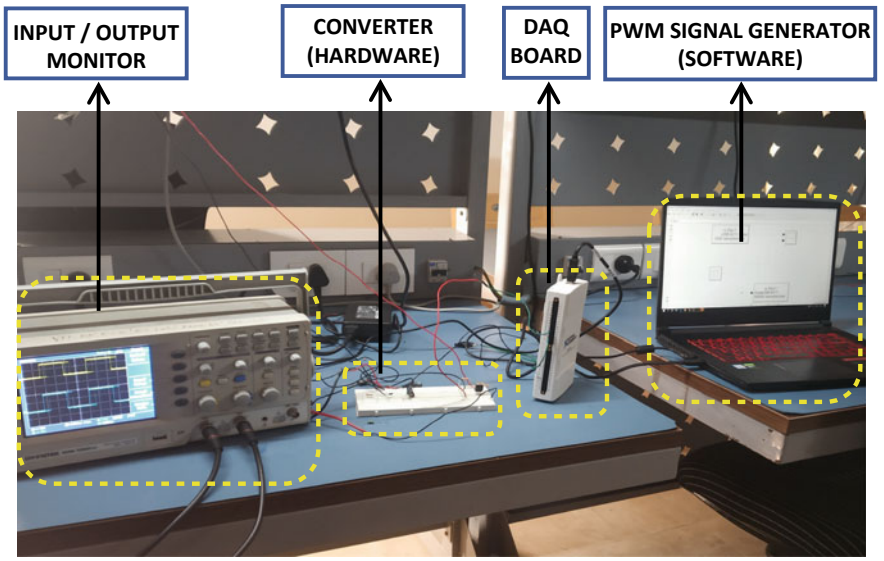

Fig. 4 Hardware prototype of the proposed HIL setup

A MOSFET is used as switch which is driven by the controlled PWM signal that is generated in the software [15, 16]. Based on this signal, step-down converter operates in two modes. The output voltage is the average of these two modes [17, 18]. The real-time prototype of the proposed HIL setup is given in Fig. 4. Further, by changing the pulse width, the average output voltage will be changed as given in Eq. (1).

- *Mode-1*: MOSFET—ON (HIGH pulse) state—The output voltage will be equal to the input voltage
- *Mode-2*: MOSFET—OFF (LOW pulse) state—The output voltage will be zero as the circuit opens near MOSFET

$$v_{\text{out}} = v_{\text{in}}\left[\frac{T_{\text{ON}}}{T_{\text{ON}} + T_{\text{OFF}}}\right] = v_{\text{in}} \times k \tag{1}$$

where 'k' denotes the duty ratio, T_{ON} is ON time, and T_{OFF} is OFF time of the pulse. V_{in} is the input and V_{out} is the output voltages, respectively.

3 Results and Analysis

The effectiveness of the proposed method is verified by conducting simulation studies as well as studies on experimental prototype as mentioned follows.

3.1 Analysis Through Simulation Results

To test the developed model, it is simulated in MATLAB/Simulink, and the corresponding outputs are given below. The simulation result for the duty ratio of 50%, 25%, and 75% are shown by Figs. 5, 6, and 7, respectively. The cumulative quantitative results for various duty ratios are mentioned in Table 3.

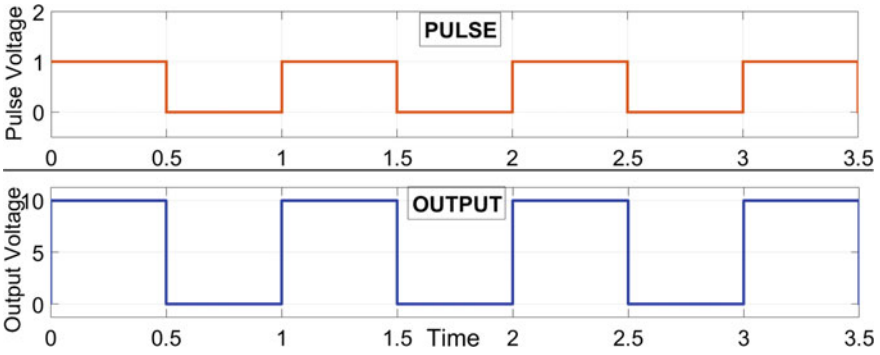

Fig. 5 Software simulation result for the input pulse of duty ratio 50%

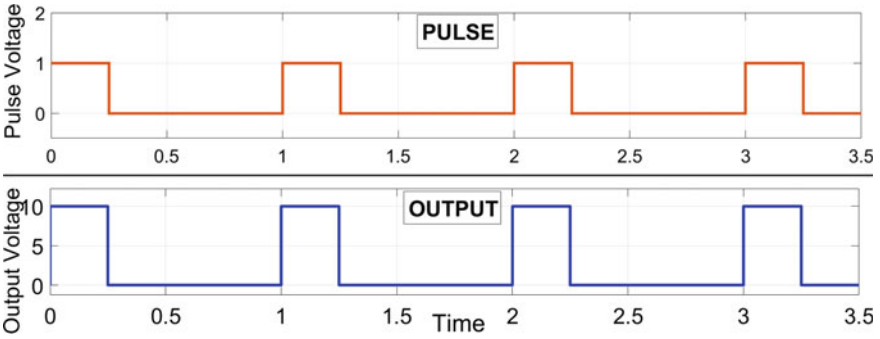

Fig. 6 Software simulation result for the input pulse of duty ratio 25%

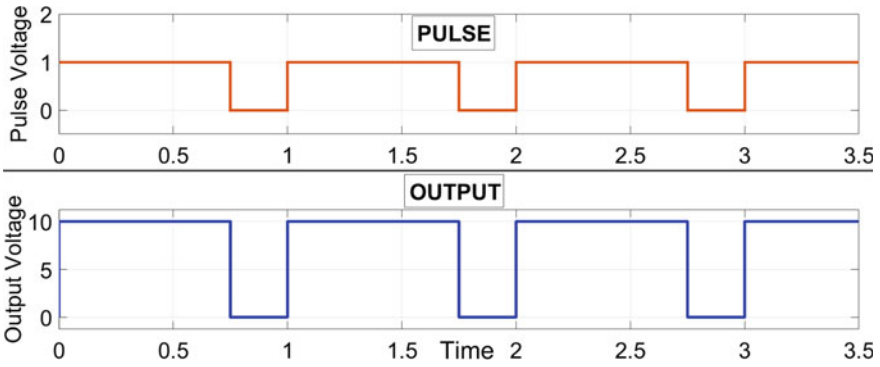

Fig. 7 Software simulation result for the input pulse of duty ratio 75%

Table 3 Software simulation quantitative results

S. No.	Input voltage (V)	Duty cycle of gate pulse (%)	Average output voltage (V)
1.	15	50	7.50 (0.50 × 15)
2.		25	3.75 (0.25 × 15)
3.		75	11.25 (0.75 × 15)

3.2 Analysis Through Hardware Results

The results are taken through the proposed HIL hardware setup. The control pulses generated in the software are given to the hardware step-down converter through the DAQ. When the pulse of 50, 75, 25% of duty cycles are sent to the hardware, the output waveforms are obtained as shown in Fig. 8, where the upper trend represents the output and the lower trend represents the gate pulse signal in each sub-figure. The cumulative gains computed are given in Table 4. The simulation and HIL results are compared in Table 5, from which, it is seen that both these are almost equal.

4 Conclusions

To reduce the cost of real-time testing of the proposed hardware equipment such as power electronic converters, this paper proposes a simple and low-cost HIL setup. The salient features of this proposed HIL setup are given as follows.

- The cost of this proposed HIL setup is low as compared to the solutions available in the current market.
- This is simple and can be easily implemented, so very helpful for academic research.

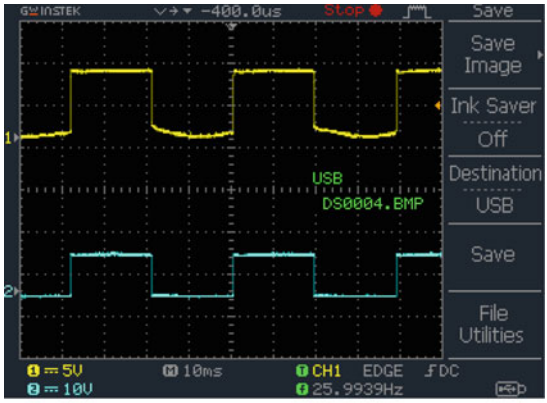

(a) For the duty ratio of 50%

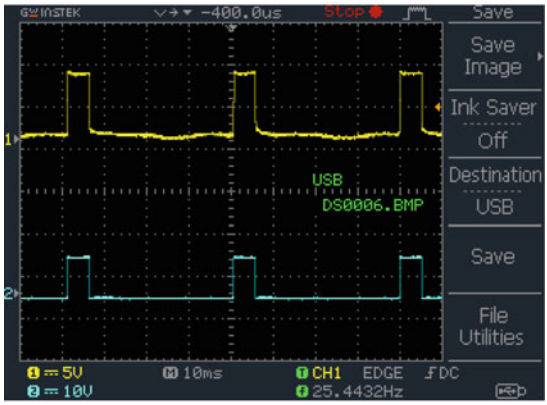

(b) For the duty ratio of 25%

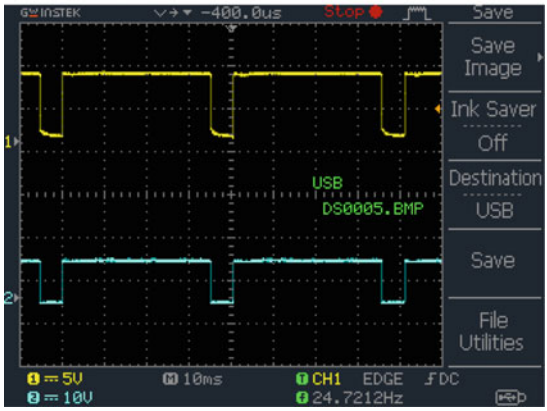

(c) For the duty ratio of 75%

Fig. 8 Proposed HIL setup results for various duty cycles of the input pulses

Table 4 HIL simulation quantitative results

S. No.	Input voltage (V)	Applied duty ratio (%)	Average output voltage (V)
1.	15	50	7.43
2.		25	3.71
3.		75	11.18

Table 5 Proposed HIL and conventional software results comparision

S. No.	Input voltage (V)	PWM duty ratio generated in software (%)	Average output voltage obtained in simulation (V)	Average output voltage obtained in hardware HIL (V)
1.	15	50	7.50	7.43
2.		25	3.75	3.71
3.		75	11.25	11.18

- No need of having thorough knowledge on programming software. It is enough to have the knowledge on basic modeling tool, such as MATLAB/Simulink.
- It supports extensive libraries to work with. So, wide variety of control logics can be implemented and tested for their effectiveness.

A simple step-down converter is tested using this proposed setup, and the results are validated with the help of results obtained in simulation. From this comparison given in Table 5, it is found that both the results (i.e., the results obtained through simulation and results obtained through proposed hardware HIL) are reasonably similar, which is desirable. So, finally, it is concluded that this proposed HIL can be used for the analysis of any similar circuits, especially helps for the implementation of control logics for power electronic converters.

References

1. Yujia H, Gruosso G, Luigi P (2017) Power hardware in the loop simulator of photovoltaic plant for smart grid interation analysis. In: 2017 IEEE International Conference on Environment and Electrical Engineering and 2017 IEEE Industrial and Commercial Power Systems Europe (EEEIC/I&CPS). Milan, Italy
2. Yangkai L, Shi X, Chao F, Meng J (2014) Hardware in-the-loop simulation system based on NI-PXI for operation and control of microgrid. In: 2014 9th IEEE Conference on Industrial Electronics and Applications. Hangzhou, China
3. Bacic M (2005) On hardware-in-the-loop simulation. In: Proceedings of the 44th IEEE Conference on Decision and Control. Seville, Spain
4. Mahdi D, Arindam G, Gerard L, Firuz Z (2012) Studies in power hardware in the loop (PHIL) simulation using real-time digital simulator (RTDS). In: 2012 IEEE International Conference on Power Electronics, Drives and Energy Systems (PEDES). Bengaluru, India

5. Dufour C, Simon A, Belanger J (2005) Hardware-in-the-loop simulation of power drives with RT-LAB. In: 2005 International Conference on Power Electronics and Drives Systems. Kuala Lumpur, Malaysia
6. Aghalmolki HG, Miao Z (2017) Real-time digital simulator enabled hardware-in-the-loop electric machine drive lab. In: 2017 Australasian Universities Power Engineering Conference (AUPEC). Melbourne, Australia
7. Paolo R, Pignati M, Mario P (2015) Integration of an IEEE Std. C37.118 compliant PMU into a real-time simulator. In: 2015 IEEE Eindhoven PowerTech Eindhoven Netherlands
8. Nima Y, Ali A, Bhattacharya S, Babak P, Ivan C, Adrien G (2013) Real-time hardware-in-the-loop simulation of convertible static transmission controller for transmission grid management. In: 2013 IEEE 14th Workshop on Control and Modeling for Power Electronics. COMPEL). Salt Lake City, UT, USA
9. Taksale A, Vishwas V, Shahane P, Goutham D, Deulkar V (2015) Low cost hardware-in-loop for automotive application. In: 2015 International Conference on Industrial Instrumentation and Control (ICIC). Pune, India
10. Musse BF, Silva NL, Dalmo SC, de Oliveira LW, de Oliveira JG (2017) Controller-hardware-in-the-loop simulation of a distribution system with PV penetration using RTDS and dSPACE. In: 2017 Brazilian Power Electronics Conference (COBEP). Juiz de Fora, Brazil
11. Haifeng D, Wei X, Zechang S, Wang J (2012) A hardware-in-the-loop system for development of automotive battery management system. Lecture Notes Electr Eng 135:27–36
12. Getting started with Simulink real-time (2020). https://in.mathworks.com/help/xpc/getting-started-with-xpc-target-1.html?s_tid=CRUX_lftnav. Accessed on 23rd March, 2020
13. Kumar YVP, Bhimasingu R (2016) Alternative hardware-in-the-loop (HIL) setups for real-time simulation and testing of microgrids. In: 2016 IEEE 1st International Conference on Power Electronics, Intelligent Control and Energy Systems (ICPEICES). Delhi, India
14. Miguez MR, Arnaud A, Alejandro RO, Pedro J (2016) Step down DC/DC converter for micro-power medical applications. Analog Integr Circuits Signal Process Springer Int J 89(3):531–539
15. An J, Shengdong H (2019) SiC trench MOSFET with heterojunction diode for low switching loss and high short-circuit capability. IET Power Electron 12(8):1981–1985
16. Cristina AA, Zhu D (2020) Exploitation of MOSFET-based AC switches in capacitive impedance matching networks in inductive wireless power transfer systems. IET Power Electron 13(4):713–719
17. Zishun P, Wang J, Zeng L, Dai Y, Zeng G, John ZS (2020) Fault-tolerant inverter operation based on si/sic hybrid switches. IEEE J Emerg Sel Topics Power Electron 8(1):545–556
18. Yifei Z, Smedley KM (2020) Analysis and design of a single-switch high step-up coupled-inductor boost converter. IEEE Trans Power Electron 35(1):535–545

Improved Harmonic Profile of Multilevel Inverter Topology with Shifted Carrier Modulation Technique

G. Vivek and Y. V. Pavan Kumar

Abstract With the surge in the technological development and advancements in modern machinery, a better-quality voltage waveform with reduced harmonics is much desired for an application. It is also desired to avoid various other issues including voltage stress on individual power switches, complexity of the inverter design, voltage balancing at the capacitors, etc. This has been a constant goal for various power electronic research works and numerous topologies have been presented in the literature to compensate several such issues. Along with the general existing modulation schemes, a number of newer modulation schemes have also been presented till date, with each scheme having its own limitation from one perspective or the other. All these topologies focusing on reducing harmonics or producing a better-quality waveform at the output comparatively require a greater number of components. But the increase in the components of the inverter topology leads to an increased number of harmonics at output and the increase in the requirement of the gate driving circuits. Focusing on various such issues, a modified inverter topology has been identified from the literature with a reduced number of components but the harmonic content at the output is observed to be exceedingly high. So, to this inverter, it is proposed to use phase-shifted pulse width modulation to operate the switches. From results, it is observed that this proposed combination reduces harmonics of the voltage output. This overall inverter module is simulated in Simulink®.

Keywords Shifted carrier pulse width modulation · Multilevel inverter · Total harmonic distortion (THD) · Voltage swell · Voltage sag

This work was supported by Project Grant No: SRG/2019/000648, sponsored by Start-up Research Grant (SRG) scheme of Science and Engineering Research Board (SERB), a statutory body under the Department of Science and Technology (DST), Government of India.

G. Vivek · Y. V. P. Kumar (✉)
School of Electronics Engineering, Vellore Institute of Technology-Andhra Pradesh (VIT-AP) University, Amaravati 522237, India
e-mail: pavankumar.yv@vitap.ac.in

G. Vivek
e-mail: g.vivek@vitap.ac.in

G. T. C. Sekhar et al. (eds.), *Intelligent Computing in Control and Communication*, Lecture Notes in Electrical Engineering 702,
https://doi.org/10.1007/978-981-15-8439-8_17

1 Introduction

With the increase in the drastic use of multilevel inverters by various classes of consumers, the problems faced by the inverter modules including the individual voltage stress on the inverter switches, harmonic content in the output waveform, overall cost of the system, voltage balancing at the capacitor, etc., also started to be increasingly noticed. To overcome many such issues various topologies have been presented in the recent literature, that either includes the existing general topologies namely Flying Capacitor Multilevel Inverter (FCMI), Cascaded H-Bridge Multilevel Inverter (CHBMI), and Diode Clamped Multilevel Inverter (DCMI) [1], the modified topologies of the general ones [2, 3] or the modified hybrid topologies, each serving its own purpose and design, targeting issues mentioned previously [4, 5]. Also, various modulation schemes have been presented to optimize the output of the inverter by suitable control of the switches that include either the general existing modulation schemes like unipolar pulse width modulation (PWM), bipolar PWM, In-Phase Disposition PWM (IPD PWM), space vector modulation, Phase Opposition Disposition PWM (POD PWM), Alternative Opposition Disposition PWM (AOD PWM), etc., or modified versions of the existing modulation schemes. Through various such inverter topologies and control schemes have been presented till date, each topology or switching scheme comes with its own drawback, providing an unsatisfactory result at the output. Also, the quality of the voltage output produced, if improper would lead to various concerns including damage of device connected at the output, increase in the current drawn, increased switching losses or damage of individual inverter components. Focusing on various such concerns, this paper is aimed at identifying and analyzing a multilevel inverter topology from the literature as mentioned follows, along with the identification of the best suitable modulation scheme to improve the output quality when compared to the output of the original inverter module.

1.1 Analysis of State-of-the-Art Multilevel Inverter Topologies

The output of any considered suitable inverter is generally preferred to have less total harmonic distortion (THD) value and according to IEEE 519 guideline, it should be less than or equal to 8% [6]. Many of the inverter topologies presented till date violate this rule, which reduces the quality of the output waveform. Analysis presented in [7] provides a general comparison on the harmonic distortion values of three typical inverter topologies and it has been clearly presented to have values that show a great deviation from the preferred total harmonic distortion value (17.10%, 17.24% and 17.34%, respectively, for CHBMI, DCMI and FCMI topologies). Similar harmonic study performed on the same three general inverter topologies focused especially for photoelectric application has presented high THD values of 32.04,

32.47 and 36 respectively for CHBMI, DCMI and FCMI topologies [8]. Apart from the general topologies, modified topologies do exhibit greater THD values. The modified CHMI in [9] presents a THD value of 26.97% compared to the THD value of the general CHBI topology which has been presented to show distortion values of 29.07%, 29.84% and 29.63%, respectively, for IPD, POD, APOD control schemes, thus showing THD being a control scheme dependent attribute.

One another major issue is the increased device count of the modified or presented topologies compared to the general ones which have been designed focusing on reducing harmonics at the output or various other issues, thus increasing the total cost of the system. THD% of a topology given in [10] presents a reduced value of 11.91% with a drawback of increased components. Other issue to be focused during inverter design is fault tolerance. Topologies designed focusing on such issues usually come with an additional fault tolerance module, increasing the overall component requirement, thereby increasing the overall module cost [11]. Topologies with reduced device count pose another problem, the voltage stress on the remaining switches increases, leading to the increase in the requirement of switches with high voltage standing capability, which further increases the system cost [12, 13]. Requirement of different DC voltage sources is another major issue in these topologies. Considering the wide range of issues explained, and various topologies presented in the literature, the topology presented in [14] has been observed to require a comparatively lower number of components and presenting a fault-tolerant circuit, but the harmonic content at the output is observed to be reasonably high. Hence, as discussed above, there were various multilevel inverter topologies explained in the literature that have been evolved to continuously enrich the harmonic distortion level of the output. However, along with the topological advancements, design of suitable modulation technique plays a crucial role to further enhance the fruitfulness of the inverter. A suitable switching method can further lessen the harmonic content in the output voltage profile of the inverter [15, 16]. From the analysis presented in [17–19], it is observed that the shifted carrier modulation technique helps to diminish the harmonic distortion in the voltage profile.

With the above-mentioned analysis on various topologies and modulation schemes, this paper is intended to propose an improved inverter module which is obtained by the combination of above-mentioned best inverter topology and modulation technique.

2 Description of the Proposed Concept to Improve Harmonic Profile of the Inverter

In this paper, Shifted Carrier PWM is suggested to improve the harmonic profile. In order to implement the proposed modulation technique, latest better multilevel inverter topology mentioned in [14] is considered. This multilevel inverter topology possesses least number of components namely lower number of switches, and no

capacitors or inductors, thus reducing the cost drastically when compared to similar topologies generating equal number of levels in the output. However, the harmonic profile of this inverter topology can be further improved as observed from [19]. So, to further reduce the harmonic content shown by this topology, shifted carrier PWM is used to drive the switches as shown in Fig. 1. The output of the improved module is expected to produce an enhanced-quality waveform, with least possible harmonic distortion. Since the required number of gate-driving signals are six (three-pairs), three carrier signals with a phase shift angle of 120° have been used with the sinusoidal signal as per Eq. (1) as the reference, which is given in Fig. 2.

$$\text{Phase Shift Angle (in Degrees)} = \frac{360^\circ}{N} \tag{1}$$

where, N is number of pairs of gate-driving signals required.

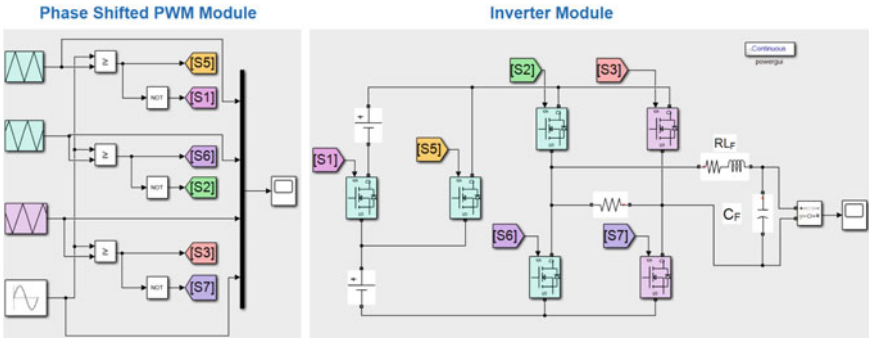

Fig. 1 Implemented inverter topology with the proposed phase-shifted modulation

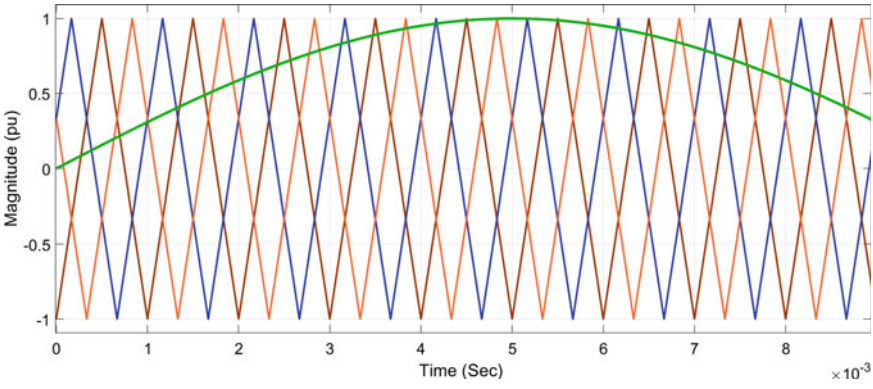

Fig. 2 Reference and carrier waveforms of the phase-shifted PWM

For the simulated inverter module, three triangular waveforms have been used as carriers with a phase shift of 120° and a sinusoidal waveform has been used as the reference. The pulse generated on comparing each triangular wave and the sinusoidal wave produces two complementary pulse signals, which are in turn used to control each respective pair of switches of the inverter. This continuous operation produces an improved stepped waveform at the inverter output, that is further filtered to produce a approximated sinusoidal waveform.

3 Results and Analysis

To check the fruitfulness of the implemented inverter module, and enhancement in the quality of the output with the improved inverter module, the harmonic analysis has been performed under various conditions including harmonic analysis at steady-state, transient state, when subject to dominant inductive and capacitive loads. The obtained values with the proposed inverter module have been compared with the conventional inverter module. From results, the following observations could be made.

- *Harmonic analysis during the steady-state of the output waveform*: The FFT analysis of the multilevel inverter topology with conventional PWM and proposed PWM during steady-state operation has been referred in Figs. 3 and 4 respectively. The specifications include: Start time 1 s and cycles considered 10, projecting a THD of 6.68% and 6.37% respectively.
- *Harmonic analysis of the output waveform when subjected to dominant capacitive load*: The FFT analysis of the multilevel inverter topology with conventional PWM and proposed PWM when driving dominant capacitive load has been presented in Figs. 5 and 6, respectively. Dominant capacitive load has been connected for the time duration of 1–1.03 s with a fundamental frequency of 50 Hz. The FFT

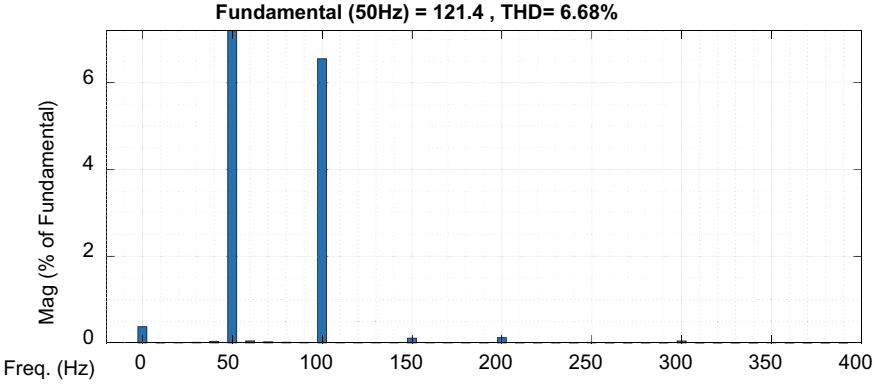

Fig. 3 FFT plot of multilevel inverter with conventional PWM during steady-state operation

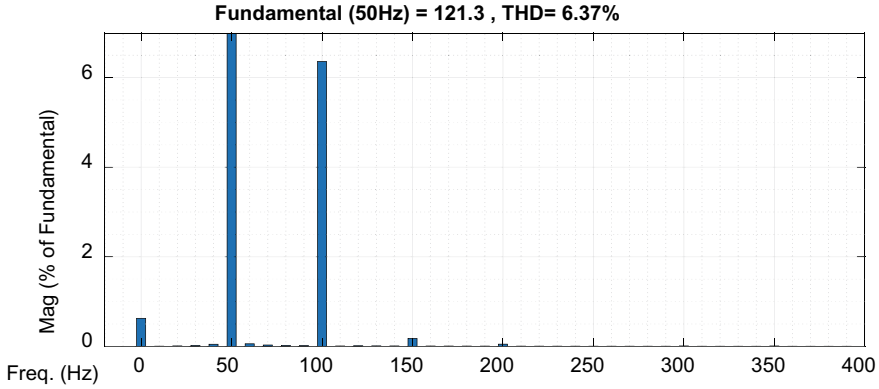

Fig. 4 FFT plot of multilevel inverter with proposed PWM during steady-state operation

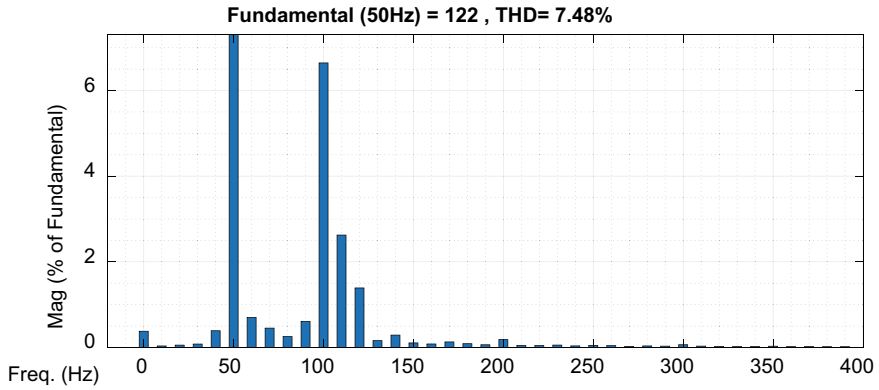

Fig. 5 FFT plot of inverter with conventional PWM when driving dominant capacitive load

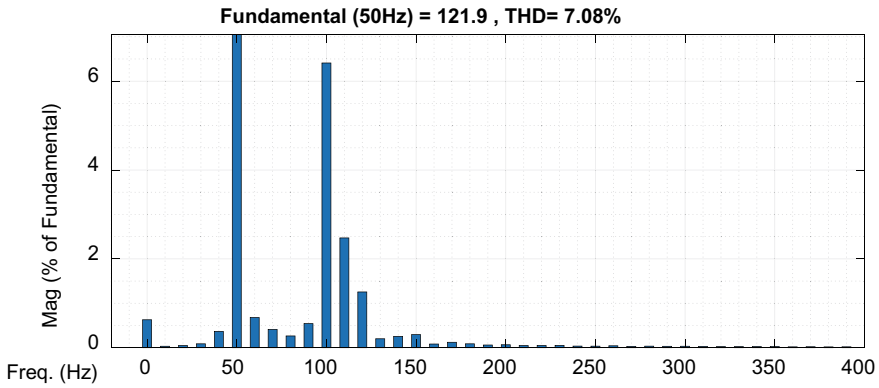

Fig. 6 FFT plot of inverter with proposed PWM when driving dominant capacitive load

analysis has been performed from 1 s for three cycles with a capacitive reactive power of 200kVAR, projecting a THD of 7.48% and 7.08%, respectively.

- *Harmonic analysis of the output waveform when subjected to dominant inductive load*: The FFT analysis of the multilevel inverter topology with conventional PWM and proposed PWM when driving dominant inductive load has been presented in Fig. 7 and 8 respectively. Dominant inductive load has been connected for the time duration of 1 to 1.03 seconds with a fundamental frequency of 50 Hz. The FFT analysis has been performed from 1 second for three cycles with an inductive reactive power of 200kVAR, projecting a THD of 6.89% and 6.61% respectively.

From this abovementioned harmonic analysis, it is clearly seen that the harmonic profile has been improved from conventional to proposed combination of inverter topology and modulation. Further, voltage quality in terms of sag and swell

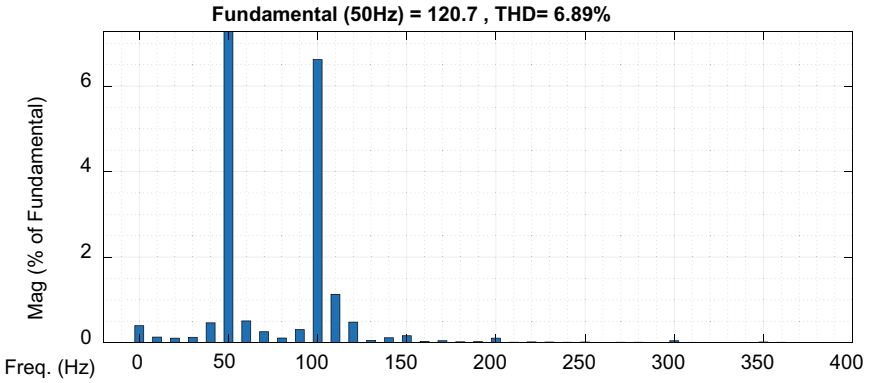

Fig. 7 FFT plot of inverter with conventional PWM when driving dominant inductive load

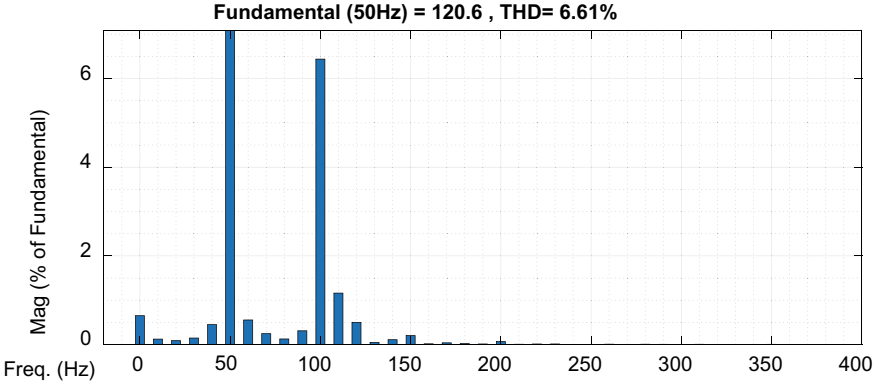

Fig. 8 FFT plot of inverter with proposed PWM when driving dominant inductive load

is observed as mentioned follows to persuade the fruitfulness of the proposed combination of the inverter topology and modulation.

- *Voltage analysis of the output waveform when subjected to dominant inductive load and dominant capacitive load*: The key reason for sag and swell is an abrupt change in the current drawn through the source impedance. Voltage sag at the output waveform is caused because of a sudden huge rise in the source current requirement that would demand development of a larger voltage across the source impedance causing a reduction in the voltage at the load. In the same way, an abrupt fall in current flow in the event of surges would result in the rise of load voltage. This change of flow of current at the source is usually caused by various factors and the action of high nonlinearities is one such factor. In the simulated inverter, when the inverter output is subjected to a dominant inductive load or a dominant capacitive load of 2000 kVAR, it undergoes a voltage sag and voltage swell respectively, which can be observed in Figs. 9 and 10 respectively. The respective values of voltage swell (%) and voltage sag (%) have been calculated

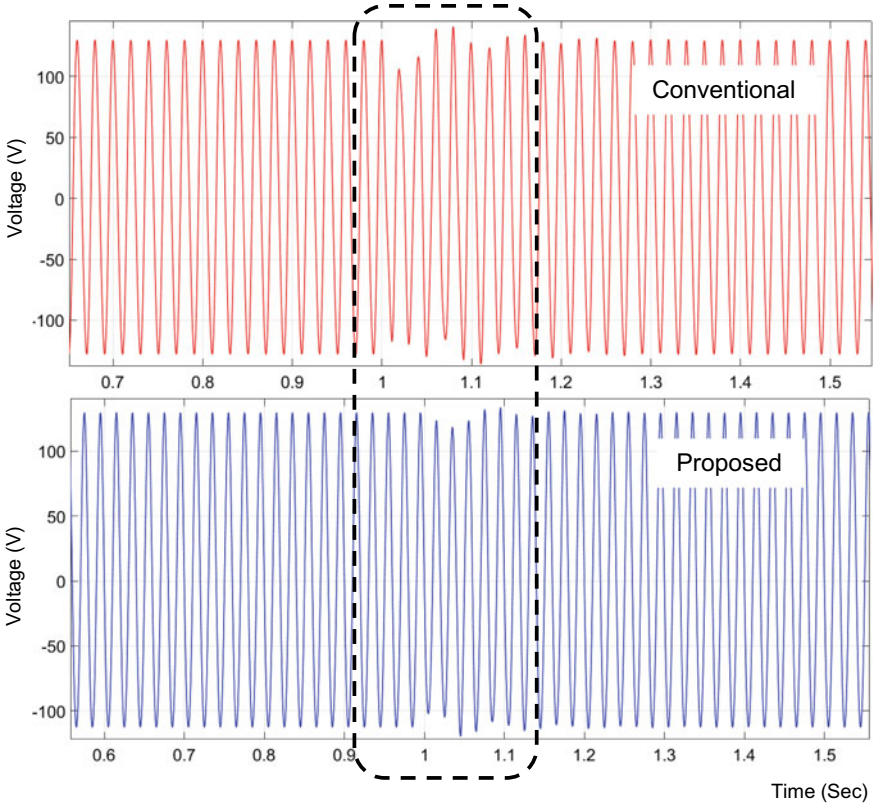

Fig. 9 Voltage sag in conventional and proposed units when driving dominant inductive load

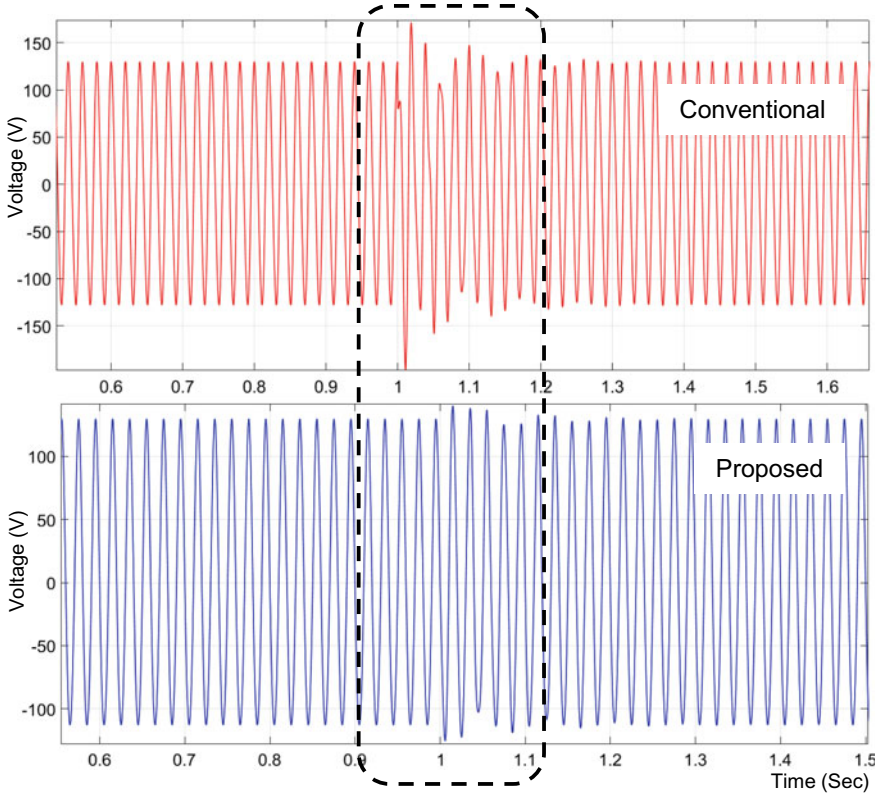

Fig. 10 Voltage swell in conventional, proposed units when driving dominant capacitive load

for the multilevel inverter topology with conventional PWM and proposed PWM and presented in Table 1.

4 Conclusion

This paper proposes a shifted carrier PWM technique for one of the latest and best modular multilevel inverter topology to further improve its harmonic profile. From the simulation results and values consolidated in Table 1, the following improvements are to be noted:

- THD% at the steady-state showed an improvement from 6.68 to 6.37%
- THD% of the output when connected dominant inductive load has improved from 6.89 to 6.61%.
- THD% of the output when connected dominant capacitive load has improved from 7.48 to 7.08%.

Table 1 Comparison of effective power quality performance parameters obtained with conventional and proposed inverters

S. No.	Parameter observed	Conventional inverter module	Proposed inverter module	Benchmark regulation
1.	THD % at steady-state with no disturbance	6.68	6.37	8% (IEEE 519 [20])
2.	THD % at steady-state with dominant capacitive load	7.48	7.08	
3.	THD % at steady-state with dominant inductive load	6.89	6.61	
4.	Voltage sag (%)	16.66	14.54	
5.	Voltage swell (%)	52.17 (violation)	26.9	40% (IEC 61,000-4-34 [21])

- Voltage swell (%) at the output showed an improvement from 52.17 to 26.9%.
- Voltage sag (%) at the output showed an improvement from 16.66 to 14.54%.

Hence, by observing the above improvements, it can be concluded that the proposed phase-shifted carrier PWM modulation approach can enhance the effectiveness of the modular multilevel inverter topology.

References

1. Fri A, El RB, El GA (2013) A comparative study of three topologies of three-phase (5L) inverter for a PV system. Energy Procedia 42:436–445
2. Ali MH, Sarbanzadeh M, Sarebanzadeh E, Rivera M, Munoz J (2018) Reduced modified T-type topology for cascaded multilevel inverters. In: IEEE International conference on automation/XXIII congress of the Chilean association of automatic control, concepcion. Chile
3. Kannan R, Rathinam A, Baharudi ZBH, Karthikeyan T (2016) Modified APO PWM based multilevel inverter topology for solar power conversion system. In: 4th IET clean energy and technology conference. Kuala Lumpur, Malaysia
4. Farsadi M, Kalashani MB (2015) A new hybrid topology for multilevel inverter for power quality improvement. In: IEEE power, communication and information technology conference. Bhubaneshwar, India
5. Alian C, Xiangning H (2006) Research on hybrid-clamped multilevel-inverter topologies. IEEE Trans Ind Electron 53(6):1898–1907
6. 519-2014—IEEE recommended practice and requirements for harmonic control in electric power systems (2014)
7. Aparna P, Sanjay B (2016) A comparative analysis of classical three phase multilevel (five level) inverter topologies. In: 1st IEEE international conference on power electronics. Intelligent control and energy systems. Delhi, India

8. Batool BA, Aliya, Noor M, Athar SO (2018) A study of asymmetrical multilevel inverter topologies with less number of devices and low THD: a review. In: 4th International conference on power generation systems and renewable energy technologies. Islamabad, Pakistan
9. Kumawat RK, Dheeraj KP (2016) A novel PWM control for asymmetric multilevel inverter based on half bridge module. In: IEEE 7th power India international conference. Bikaner, India
10. Farsadi M, Kalashani MB (2017) A novel hybrid multiphase multilevel inverter topology. In: 10th international conference on electrical and electronics engineering. Bursa, Turkey
11. Salimian H, Houssein I (2017) Fault-tolerant operation of three-phase cascaded h-bridge converters using an auxiliary module. IEEE Trans Ind Electron 64(2):1018–1027
12. Javad E, Ebrahim B, Goverg GB (2011) A new topology of cascaded multilevel converters with reduced number of components for high-voltage applications. IEEE Trans Power Electron 26(11):3109–3118
13. Ahmad M, Mehmood MU, Nawaz H, Umair M, Hussian Q, Raza MA (2018) A multilevel inverter topology with reduced switches. In: IEEE 21st multitopic conference. Karachi, Pakistan
14. Javad E, Ebrahimi B, Gevorg GB (2012) A new multilevel converter topology with reduced number of power electronic components. IEEE Trans Ind Electron 59(2):655–667
15. Athanasios M, Dimitrios P, Charis D (2011) A new modulation technique for reduced harmonic distortion of current in PV inverters. In: 2011 IEEE EUROCON−international conference on computer as a tool. Lisbon, Portugal
16. Concettina B, Maria CG, Carlo C, Babaei E (2016) Comparison between harmonic reduction procedures for 5-level inverters. In: 2017 AEIT International Conference. Cagliari, Italy
17. Kumar YV P, Bhimasingu R (2016) A simple modular multilevel inverter topology for power quality improvement in renewable energy based green building microgrids. Electric Power Syst Res 140:147–161
18. Narendra KG, Srinivas S (2016) Carrier phase shifted SPWM for CMV reduction in a three-level inverter using open-end winding induction motor drive. In: IEEE Region 10 Conference. Singapore
19. Agarwal S, Rahul SK (2018) Carrier phase shift modulation for reducing the common mode voltage in a two-level three-phase inverter. In: 44th annual conference on IEEE industrial electronics society. Washington, DC, USA
20. IEEE Standard 519: IEEE recommended practice and requirements for harmonic control in electrical power system, pp 1–29 (2014)
21. IEC Standard 61000–4–34:2005: Electromagnetic Compatibility (Part 4-34)—Testing and measurement techniques-voltage dips, short interruptions and voltage variations immunity tests for equipment with input current more than 16A Per Phase (2005)

Artificial Intelligence Based Control Methods for Speed Control of Wind Turbine Energy System

Karthik Ramireddy, A. Sri Hari, and Y. V. Pavan Kumar

Abstract Many of the practical control systems utilize PID based control logic for their functionality. So, the fruitfulness of product making or the economics of an industry depends on how well these controllers are performing. The conventional way of PID tuning basically follows offline procedures, where the controller parameters are designed offline and substituted into the controller for its real-time operation. Due to this offline mechanism, the controller may not work well when they face online/real-time disturbances. This is the typical issue with the traditional offline PID tuning methods. So, the tuning procedure has to be changed to online, so that the controller gain parameters will be updated continuously with respect to the system disturbance rather than having fixed values in offline methods. By motivating from this idea, this paper proposes the use of artificial intelligence techniques, viz., fuzzy logic and neural networks for tuning the PID gain parameters. The effectiveness of these proposed online tuning methods over traditional offline tuning methods is validated by injecting various real-time disturbances into the system. The overall system simulation is done using MATLAB/Simulink tool. From the results, it is observed that the proposed methods provide better system response over the conventional methods.

Keywords Wind power · Renewable energy · PID controller design · Fuzzy logic controller · Artificial neural network controller

K. Ramireddy · A. S. Hari · Y. V. P. Kumar (✉)
School of Electronics Engineering, Vellore Institute of Technology-Andhra Pradesh (VIT-AP) University, Amaravati 522237, India
e-mail: pavankumar.yv@vitap.ac.in

K. Ramireddy
e-mail: karthik.18bev7028@vitap.ac.in

A. S. Hari
e-mail: sarihariharn.18bec7103@vitap.ac.in

G. T. C. Sekhar et al. (eds.), *Intelligent Computing in Control and Communication*, Lecture Notes in Electrical Engineering 702,
https://doi.org/10.1007/978-981-15-8439-8_18

1 Introduction

Normally, we use fossil fuels for the generation of electrical energy, but in recent years, there is a vast demand for the utilization of renewable energy. Burning of fossil fuels is one of the main reasons for the global warming and in turn leads to the depletion of the ozone layer, which has become a major threat to the earth these days. To control this global warming and to match the electricity needs of the increasing population, many researches are going on to produce electricity from natural resources like air, sun light, water and from other gases. This type of utilization of renewable energy resources results in less use of fossil fuels and reduces the emission levels of greenhouse gases like carbon dioxide drastically. There are different forms of renewable energy sources like solar energy, wave energy, hydropower energy, wind energy, etc. Among all these sources, wind energy production is the fastest growing technology because of its low-cost electricity production, and it is the cleanest and more effective source of energy among all the remaining energy resources. Wind turbine is used to generate the electricity from wind energy, generally, permanent magnet synchronous generator (PMSG) is widely used because of its rigorous construction. The speed of the wind is unpredictable and there will be many variances in the speed of wind, which in turn produces the variable voltage which may affect the connected load. So, one of the major challenges in the wind power system is the design of the control system to control the output speeds of the turbine against all kinds of uncertain wind velocities to operate the generator faithfully.

Usually, the wind turbine works in two different modes, one is regulated speed mode and the other is fixed speed mode. For variable speed wind turbine systems, variable voltages are produced, this may damage the load. This shall be solved by modelling the variable speed wind turbine system with suitable PID controller and then interfacing it with artificial intelligence like fuzzy logic or artificial neural networks. When the wind turbine system is interfaced with artificial intelligence, it can adjust the controller values according to the varying wind speeds so that the load will remain safe and also produces the maximum output from the generator. Hence, there will be no concern about whether the wind speed is low or high the wind turbine system produces the maximum electricity. In recent years, researches have started working on interfacing the artificial intelligence with the wind turbine energy system for control operations. There were some state-of-the works carried such as modelling of various constituents as well as overall wind energy system as presented in [1–3], neural networks based control philosophies [4], fuzzy logic based control philosophies [5–10], neuro-fuzzy based control logics [11, 12], etc. Besides, artificial intelligence techniques play a crucial role in estimating or forecasting wind availability, thereby predicting the capacity of the wind turbine energy system for a given time [13–16]. Some other research works focused on speed control through MPPT control and pitch angle control using classical PID and fuzzy logic PID [17–19].

As the classical PID tuning method is an offline tuning method, where the parameters cannot be adjusted as per the real-time disturbance of varying wind speed, and based on the motivation from literature works to use artificial intelligence in

wind power, this paper proposes the online tuning methods established on fuzzy logic and neural networks. In these proposed online tuning methods, the controller gain parameters are adjusted as per the disturbance occurred in real-time, thereby, effective control is possible in any conditions.

2 Modelling of Wind Turbine Energy System

The basic block diagram representation of wind turbine energy system is given in Fig. 1. Basically, it is a combination of three subdivisions such as mechanical model, PMSG model, and DC-DC boost converter model with a step-up transformer connected to the grid. Here, when the fans of the wind turbine rotate the gear box increases the revolution speed of the shaft thereby the power is generated at the PMSG. This is passed through the DC-DC converter and then supplied to the grid. The modelling of all these elements and thereby, the overall system model is given as follows. The classical offline PID controller possesses fixed gain parameters. Whereas, in the proposed artificial intelligence methods (fuzzy logic/neural networks) based control, PID gains are trained in such a way that they can autotune their values as per the change occurred in the real-time applications. The block diagram model of the system with PID/fuzzy/ANN based controller is represented in Fig. 2.

$$P = 0.5 \times \pi \times \rho \times R^2 \times (C_P(\lambda, \beta)) \times v_w^3 \tag{1}$$

$$\lambda = \frac{\omega \times r}{v} \tag{2}$$

$$C_p(\lambda) = 0.44\left(\frac{125}{\lambda_i} - 6.94\right)e^{\left(\frac{-16.5}{\lambda_i}\right)} \tag{3}$$

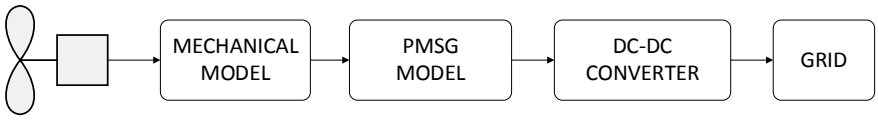

Fig. 1 Schematic diagram of wind turbine energy system without controller

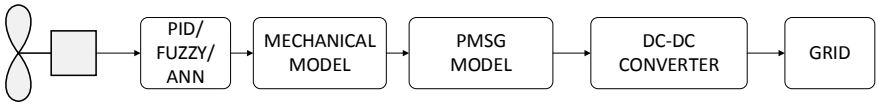

Fig. 2 Schematic diagram of wind turbine energy system with PID/fuzzy/ANN controller

$$\text{where,} \quad \frac{1}{\lambda_i} = \frac{1}{\lambda} + 0.002 \tag{4}$$

$$T_M = \frac{1}{Js + F} \tag{5}$$

$$T_p = \frac{\phi p}{Z + R + Ls} \tag{6}$$

$$T_B = \frac{(1 - D)V_{\text{op}} - LI_{\text{ip}}}{V_{\text{op}}Cs + 2(1 - D)I_{\text{ip}}} \tag{7}$$

$$\left| \begin{array}{l} T_T = (T_M) \times (T_P) \times (T_B) \\ T_T = \left(\frac{1}{Js + F}\right)\left(\frac{\phi p}{z + R + Ls}\right)\left(\frac{(1 - D)V_{\text{op}} - LI_{\text{ip}}}{V_{\text{op}}Cs + 2(1 - D)I_{\text{ip}}}\right) \end{array} \right. \tag{8}$$

$$T_T = \frac{1693.32}{0.000631s^3 + 4.499s^2 + 254.465s + 1.5573} \tag{9}$$

In these relations, the power generated through the turbine is denoted by Eq. (1). Tip speed ratio (λ) is given as the ratio of blade tip speed to the wind speed as given in Eq. (2). The wind turbine generator's power coefficient is given by Eq. (3) and Eq. (4). The transfer functions for the mechanical model of wind turbine (T_M) and PMSG are given in Eqs. (5) and (6) respectively that are derived based on [2]. The transfer function for the dc-dc boost converter is given by Eq. (7). Finally, the whole wind turbine energy system's transfer function shown in Eq. (8) is achieved by multiplying all the sub transfer functions given by Eqs. (5), (6), and (7). The same with parameter substitution is given by Eq. (9). The parameters that are used are taken from [1] and are given as follows.

Here, ρ is density of the air, λ (=0.07) is tip-speed ratio, v_w is the wind speed, β is pitch angle, ω is the angular velocity of the wind turbine, C_P is the efficiency of overall system, J (=0.11 kgm^2) is the equivalent inertia of the overall system, F (=0.05 N) is total friction that includes coulomb friction, static friction, viscous friction, ϕ is the flux linkage of the rotor, p (=8) is the number of poles of PMSG, Rs (=0.3 Ω) is the resistance of the stator winding, Ls (=0.174 mH) is the inductance of the stator winding, Z is the load impedance of the PMSG, D (=0.8) is the duty cycle, V_{op} is the steady-state peak output voltage, L (=4 mH) is the inductance of boost converter, I_{ip} is the input current, C is the capacitance of the boost converter.

3 Implementation of the Proposed AI-Based Control Logics

This paper implements two verities of AI controllers, one is based on the fuzzy logic concept and the second is based on the artificial neural networks. These two methods are explained as follows.

3.1 Fuzzy Logic Based Controller Design

The fuzzy logic controller (FLC) is trained in such a way that it can give the better outputs even when the disturbance varies from −20 to 20%, i.e. it can autotune the parameters over that disturbance range. To train the FLC, different disturbances are injected into the system operation and calculated the corresponding gain parameters to nullify the deviations. The data sheet representing the disturbance and the corresponding gain parameter values are displayed in Table 1. The trained FLC is given in Fig. 3. In this, Mamdani interfaced fuzzy system is considered for the controller design. FLC is trained with values in the form of ranges and it uses fuzzifier to convert them into fuzzy values and defuzzifier to convert the fuzzy values into crisp values and feeds to the system. The input membership functions for FLC are divided into four quarters as shown follows with respect to the deviation as represented in Fig. 4. Similarly, the output membership functions for FLC gives the K_d value which is also divided into four quarters as shown in Fig. 5. Based on this, the relation between the input values and the output values are derived and matched as given in Table 1.

- Input membership function1 (mf1) = −20 to −10%
- Input membership function2 (mf2) = −10 to 0%
- Input membership function3 (mf3) = 0 to 10%
- Input membership function4 (mf4) = 10 to 20%

The rule viewer for the membership functions in which the output (K_d) value changes with the input (deviation) are given in Fig. 6. The overall system modelled

Table 1 Datasheet that is used to train the fuzzy logic controller

S. No	Input (deviation) (%)	Output (K_d)
1.	−20 to −15	0.09–0.1021
2.	−15 to −10	0.1021–0.1061
3.	−10 to −5	0.1061–0.1086
4.	−5 to 0	0.1086–0.112
5.	0 to 5	0.112–0.121
6.	5 to 10	0.121–0.127
7.	10 to 15	0.127–0.134
8.	15 to 20	0.134–0.15

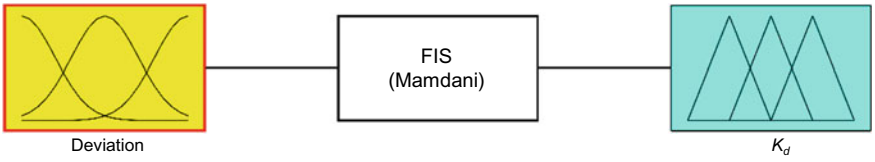

Fig. 3 Block diagram of FLC designed to control the system

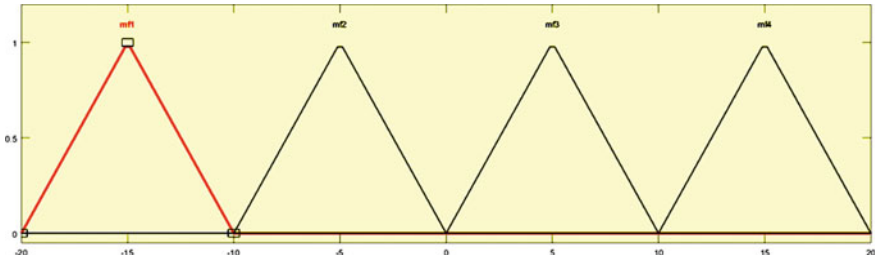

Fig. 4 Input membership function (deviation) designed for FLC

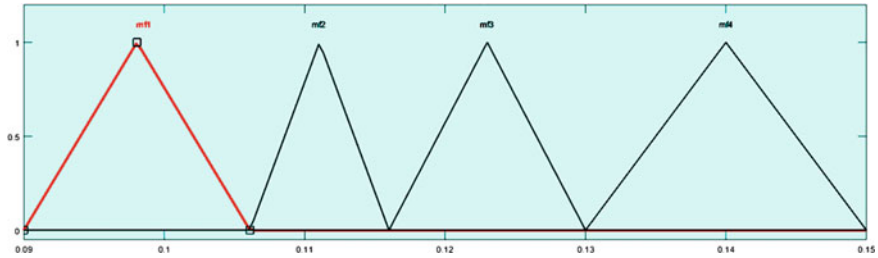

Fig. 5 Output membership function (K_d) designed for FLC

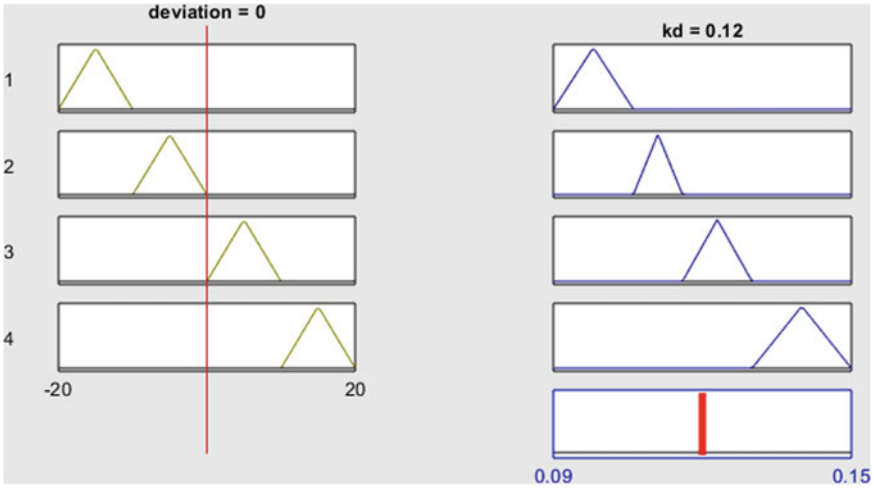

Fig. 6 Input versus output relation for FLC design

in Simulink is shown in Fig. 7. The extended subsystem of the trained FLC is shown in Fig. 8.

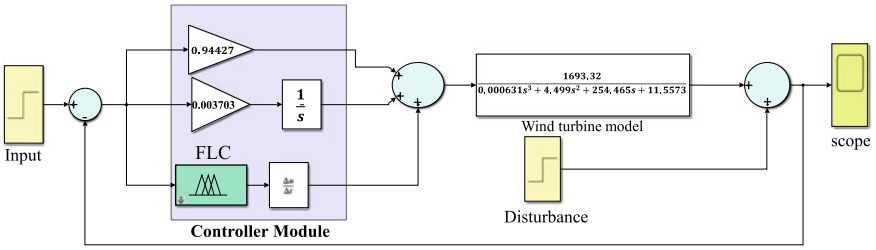

Fig. 7 Simulink model for the FLC based wind turbine energy system

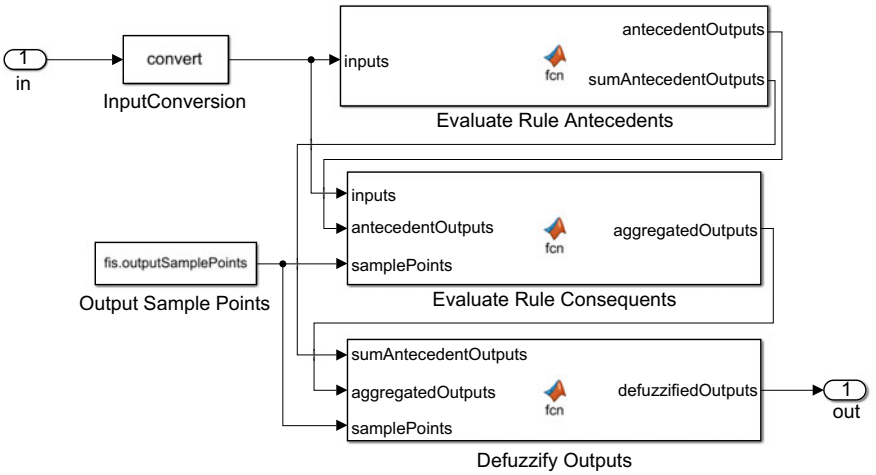

Fig. 8 FLC implementation—fuzzification and defuzzification process

3.2 Neural Network Based Controller Design

Artificial neural network (ANN) working process is similar to the function of the biological characters of how neurons work, which consists of many layers. In this paper, the ANN is trained for disturbance over a range of −20 to 20% which gives a better output. The working process of ANN is shown as simple diagram with two hidden layers in Fig. 9. Here, the information is transferred from the inputs and collected at the outputs, through the hidden layers, where the information is processed and generate the outcomes. In Fig. 9, two hidden layers are taken into consideration for the implementation of the proposed ANN. Basically, there are three different types of training algorithms used to train the ANN, namely, "Levenberg–Marquardt method, Bayesian Regularization method, and Scaled Conjugate Gradient method". This paper uses Levenberg–Marquardt method to train the ANN. The function for the output and the target is shown in Fig. 10. The datasheet that is used to train the neural networks system is given in Table 2, where, 42 samples are taken to train the

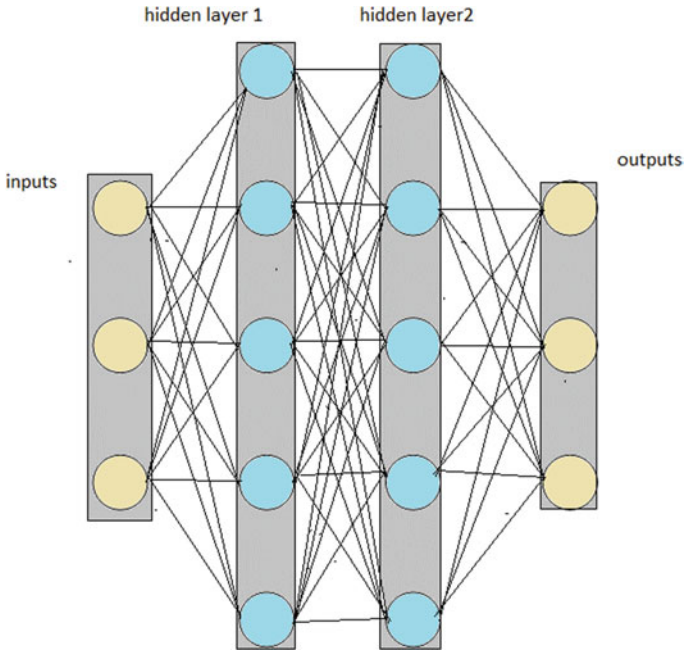

Fig. 9 ANN internal structure with two hidden neurons

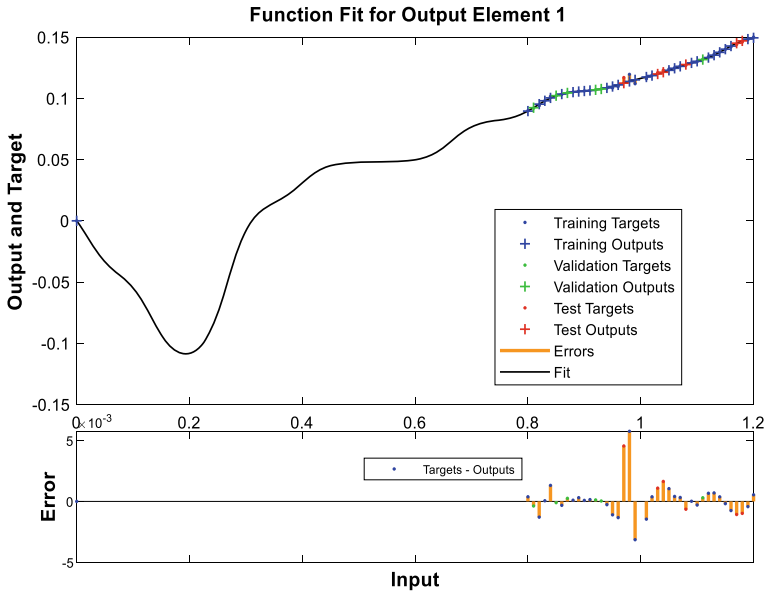

Fig. 10 Function fit plot for the output element of ANN

Table 2 Datasheet that is used to train the neural network controller

% of deviation	Actual deviation	Computed K_d	% of deviation	Actual deviation	Computed K_d
0	0	0	0	0	0
−1	0.99	0.112	1	1.01	0.116
−2	0.98	0.1196	2	1.02	0.119
−3	0.97	0.117	3	1.03	0.121
−4	0.96	0.1097	4	1.04	0.123
−5	0.95	0.1086	5	1.05	0.124
−6	0.94	0.1083	6	1.06	0.125
−7	0.93	0.1077	7	1.07	0.1265
−8	0.92	0.1071	8	1.08	0.127
−9	0.91	0.1066	9	1.09	0.129
−10	0.9	0.1061	10	1.1	0.13
−11	0.89	0.1059	11	1.11	0.132
−12	0.88	0.1052	12	1.12	0.134
−13	0.87	0.1047	13	1.13	0.136
−14	0.86	0.1032	14	1.14	0.138
−15	0.85	0.1021	15	1.15	0.14
−16	0.84	0.1017	16	1.16	0.142
−17	0.83	0.0981	17	1.17	0.144
−18	0.82	0.094	18	1.18	0.146
−19	0.81	0.092	19	1.19	0.148
−20	0.8	0.09	20	1.2	0.15

ANN efficiently with a disturbance ranging from −20 to +20%. Further, 10 hidden neurons are used for the 2 hidden layers.

The training is verified by using the error histogram shown in Fig. 11, which compares the input values and output values. The efficiency of the trained ANN is verified using Regression curve shown in Fig. 12. Based on it, if the majority of the sample points taken lie on the regression line, then the system is said to be trained efficiently and if the sample points do not lie on the regression line, then system is worst trained. The Simulink diagram developed for the simulation of the wind turbine with ANN controller is shown in Fig. 13. The function fitting neural network design of ANN with two layers is shown in Fig. 14. The elaborated structures of layer 1, layer 2 the LW (2, 1) used to design the proposed ANN are shown in Fig. 15.

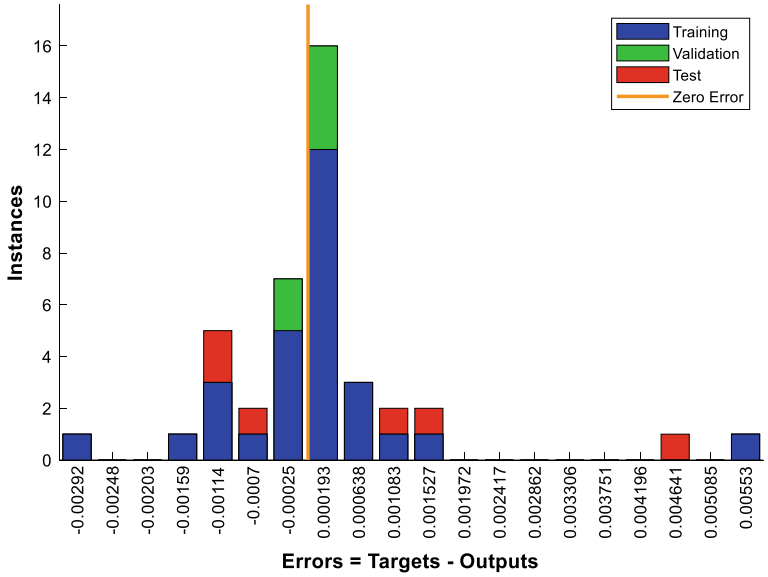

Fig. 11 Error histogram to test the training process of ANN

4 Simulation Results and Analysis

In order to validate the efficacy of the artificial intelligence based control logic, various wide raged disturbances are injected into the system and their respective impact on the system characteristics is observed. The corresponding simulation results obtained with the proposed FLC and ANN controllers along with their comparison with classical PID controller are displayed in Figs. 16, 17 and 18 respectively. The cumulative time domain response performance index is shown in Table 3, which depicts the parameters such as, delay time, rise time, peak overshoot, settling time, and peak time. From these plots and the cumulative index, it is witnessed that the proposed Fuzzy controller and ANN controller based system exhibits better responses when compared to the response produced by the conventional PID controller based system. Further, out of the two proposed artificial intelligence techniques, the fuzzy logic controller based system produces better responses under steady-state as well as all in the duration of application of various disturbances to the system for testing purpose.

5 Conclusion

This paper emphasizes the importance of artificial intelligence for the design of control logics for wind turbine energy system applications. From the simulation

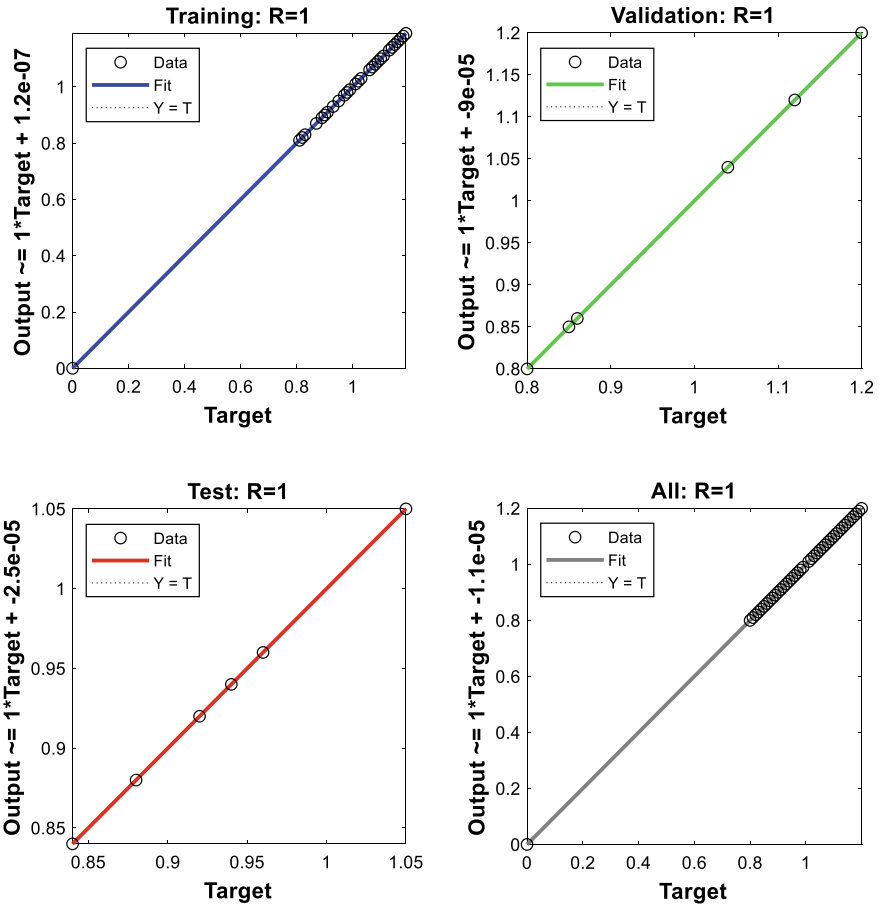

Fig. 12 Regression plot to test the training process of ANN

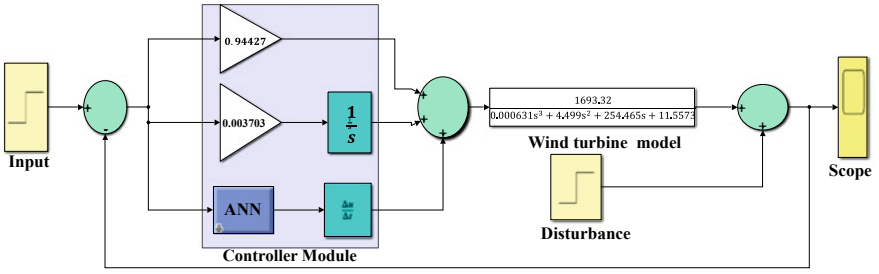

Fig. 13 Simulink model of the ANN controller based wind turbine energy system

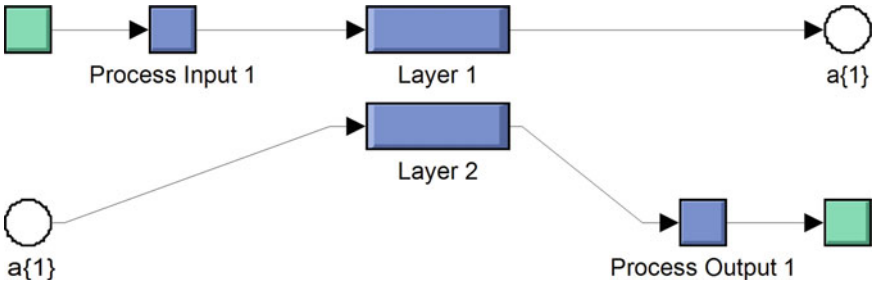

Fig. 14 The function fitting network design of ANN with two layers

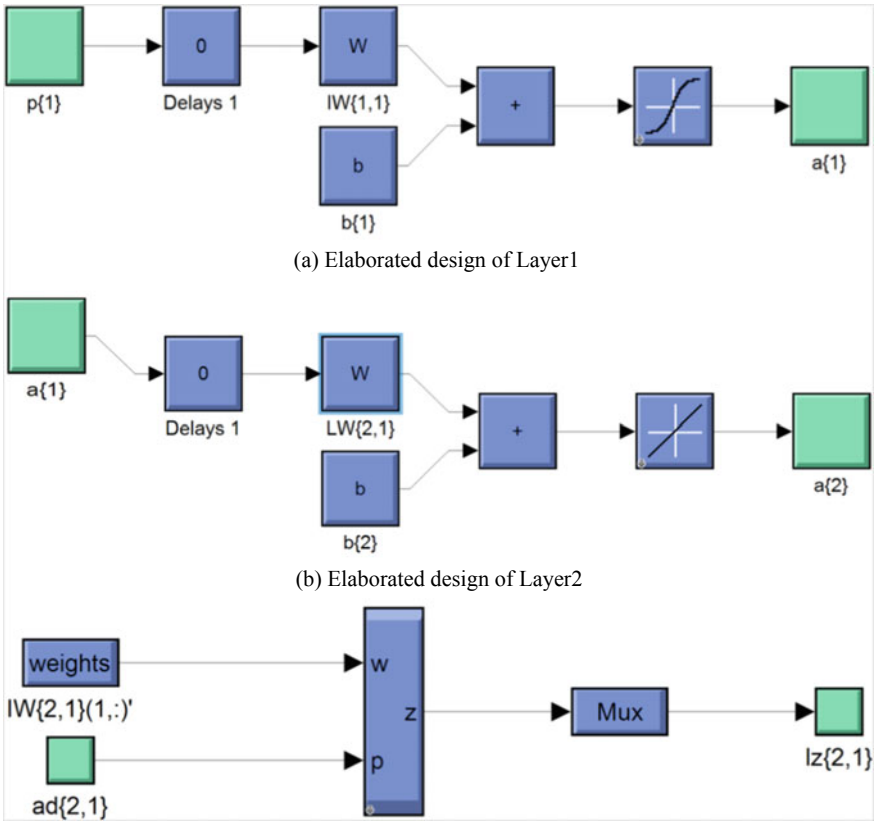

Fig. 15 Elaborated designs of different layers of ANN

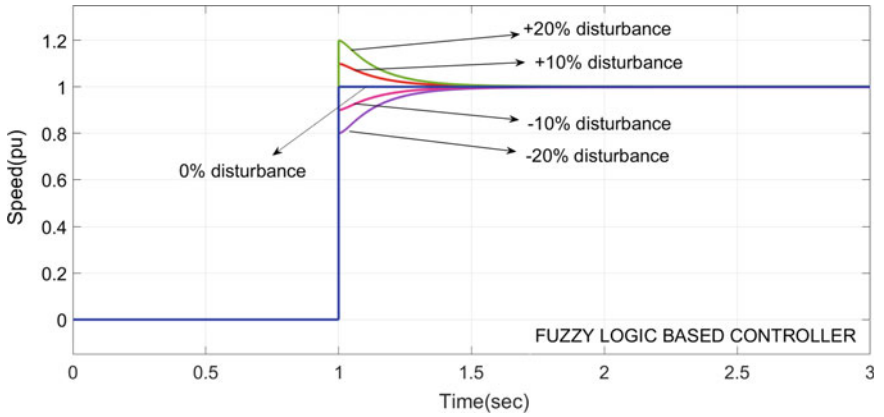

Fig. 16 Response of FLC based wind turbine system

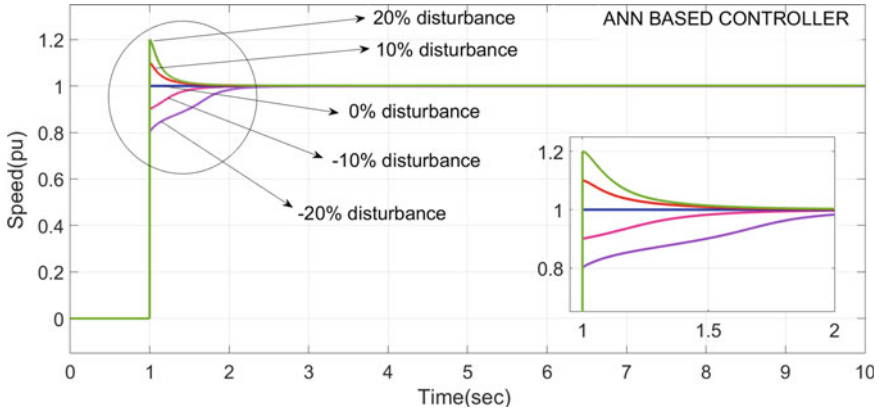

Fig. 17 Response of ANN-based wind turbine system

results and the summary projected in Table 3, the following observations could be made.

- The system response during all the practical disturbance conditions has been improved with the artificial intelligence based controllers when compared to the response produced by classical PID controller.
- Further, fuzzy logic based control design shows superior behaviour when compared to ANN based control design. This improves the fruitfulness of the wind turbine energy system deployments by effectively regulating its speed during the uncertain wind velocities.

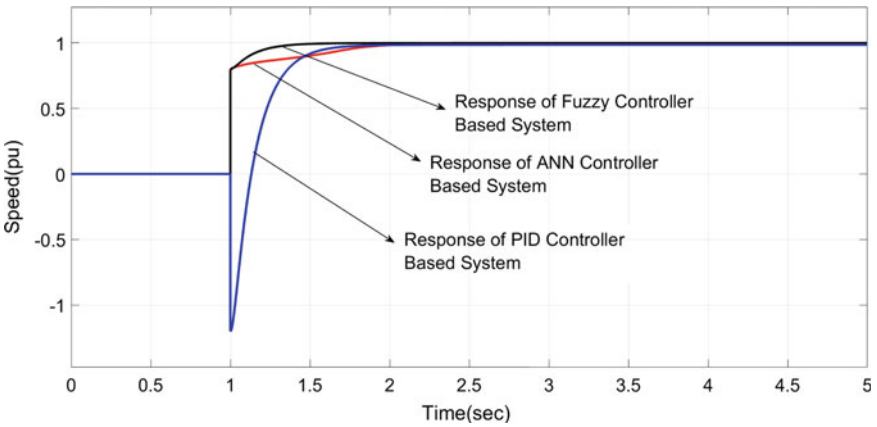

Fig. 18 Response with PID, FUZZY and ANN for a random disturbance of −20%

Table 3 Performance index computed for PID, FUZZY and ANN for various disturbances

Method	Deviation (%)	Rise time	Delay time	Peak time	Peak overshoot (%)	Settling time
ANN-based control method	−20	2.11	1	2.1	0	3.1
	−10	2.03	1	2.2	0	2.4
	0	1	1	1	0	1
	+10	1.7	1	1	0.7	2.1
	+20	1.8	1	1	0.8	1.91
Fuzzy logic based control method	−20	1.7	1	1.75	0	1.81
	−10	1.5	1	1.6	0	1.75
	0	1	1	1	0	1
	+10	1.5	1	1	0.4	1.49
	+20	1.53	1	1	0.58	1.61
Classical PID based control method	−20	2.1	1.2	2.2	0	2.15
	−10	2.2	1.21	2.2	0	2.26
	0	1.51	1.265	1.80	0	2.1
	+10	2.1	1.13	1.9	0	2.3
	+20	2.3	1.38	2.5	0	2.54

References

1. Karthik R, Hari AS, Kumar YVP, Pradeep DJ (2020) Modelling and control design for variable speed wind turbine energy system. In: International conference on artificial intelligence and signal processing (AISP), pp 1–6, Amaravati, India

2. Mahdi AJ, Tang WH, Wu QH (2011) Derivation of a complete transfer function for a wind turbine generator system by experiments. In: 2011 IEEE power engineering and automation conference, vol 1, pp 35–38
3. Hand MM (1999) Variable-speed wind turbine controller systematic design methodology: a comparison of non-linear and linear model based designs. National Renew Energy Lab
4. Liu Z, Gao W (2012) Wind power plant prediction by using neural networks. In: IEEE energy conversion conference and exposition raleigh, pp 15–20. North Carolina
5. Simoes MG, Bimal BK, Spiegel RJ (1997) Design and performance evaluation of a fuzzy logic-based variable speed wind generation system. IEEE Trans Ind Appl 33:956–965
6. Badrana O, Abdulhadib E, El-Tousc Y (2011) Fuzzy logic controller for predicting wind turbine power generation. Int J Mech Mater Eng (IJMME) 6(1):51–66
7. Aissaoui AG, Tahour A, Abid M, Essounbouli N, Nollet F (2013) Power control of wind turbine based on fuzzy controllers. The Mediterranean Green Energy Forum 2013 (MGEF-13). Energy Procedia 42:163–172
8. Simani S, Alvisi S, Venturini M (2019) Fuzzy control techniques applied to wind turbine systems and hydroelectric plants. In: 2019 IEEE international conference on fuzzy systems (FUZZ-IEEE), pp 1–6. New Orleans, LA, USA
9. Zubova NV, Achitaev AA (2018) Application of neuro-fuzzy control systems for increasing the energy efficiency of wind turbines. In: 2018 XIV international scientific-technical conference on actual problems of electronics instrument engineering (APEIE), pp 518–521. Novosibirsk
10. Cheikh R, Hocine B, Drid S, Arezki M, Tiar M (2013) Fuzzy logic control algorithm of grid connected doubly fed induction generator driven by vertical axis wind turbine in variable speed. In: 3rd international conference on systems and control, pp 439–444
11. Aarthi Sindu P, Anbarasu P (2014) Comparison of pi, fuzzy logic and neural networks based control of doubly fed induction generator in wind energy generation. Int J Innov Sci Eng Technol (IJISET) 6(4):499–508
12. Anjaneyulu Babu U, Satish T, Kumar NY (2019) Comparative analysis of fuzzy/ann techniques for compensation of unbalanced voltages in grid connected pmsg based wind turbine. Int J Res Advent Technol 7:285–289
13. Singh S, Bhatti TS, Kothari DP (2007) Wind power estimation using artificial neural network. J Energy Eng 133(1)
14. Marugan AP, Arquez FPG, Perez JMP, Ruiz HD (2018) A survey of artificial neural network in wind energy systems. Appl Energy 228:1822–1836
15. Fazelpour F, Tarashkar N, Rosen MA (2016) Short-term wind speed forecasting using artificial neural networks for Tehran, Iran. Int J Energy Environ Eng 7:377–390
16. Mishra A, Ramesh L (2009) Application of neural networks in wind power (generation) prediction. In: International conference on sustainable power generation and supply
17. Andrea T, Christian C (2011) Speed control for medium power wind turbines: an integrated approach oriented to mppt. IFAC Proc Vol 44(1):544–550
18. Yishuang Q, Qingjin M (2012) The application of fuzzy pid control in pitch wind turbine. Energy Procedia 16:1635–1641
19. Silpa B, Abdulla I (2017) Design and control of the pitch of wind turbine through pid. Int Res J Eng Technol (IRJET) 4(9)

Recent Trends and Challenges in Blockchain Technology

J. S. Shyam Mohan, Nagendra Panini Challa, V. V. Kalyan Chakravarthy, G. P. Siva Kumar, R. Subba Rao, and P. Venkata Rama Raju

Abstract With the increasing utilization of Internet in majority areas such as banking and social security, which produces an enormous amount of data, the data integrity of the customers has turned to be a major challenge for the organizations which are dependent on third-party software organizations. This challenge led to evolve the expert's interest in Blockchain technology which focuses on transaction decentralization with effective data management. Hence, this paper tries to concentrate on facilitating with an effective study of various works related to Blockchain technology. This technology acts as a backbone of the crypto-currency system. The main objective of this review is to provide a complete overview of the current research,

J. S. Shyam Mohan (✉)
Department of Computer Science and Engineering, Sri Chandrasekharendra Saraswathi Viswa Mahavidyalaya University (SCSVMV), Kanchipuram, Tamil Nadu 631561, India
e-mail: jsshyammohan@kanchiuniv.ac.in

N. P. Challa
Department of Information Technology, Sri Vishnu Engineering College for Women, Bhimavaram, Andhra Pradesh 534202, India
e-mail: cnpanini@svecw.edu.in

V. V. K. Chakravarthy
Department of Mechanical Engineering, Sri Chandrasekharendra Saraswathi Viswa Mahavidyalaya University (SCSVMV), Kanchipuram, Tamil Nadu 631561, India
e-mail: kalyanchakravarthy@kanchiuniv.ac.in

G. P. S. Kumar
Department of Instrumentation Engineering, Sri Chandrasekharendra Saraswathi Viswa Mahavidyalaya University (SCSVMV), Kanchipuram, Tamil Nadu 631561, India
e-mail: sivakumar43@gmail.com

R. S. Rao
Department of Maths, SRKR Engineering College, Bhimavaram, Andhra Pradesh 534204, India
e-mail: rsubbarao9@gmail.com

P. V. R. Raju
Department of Information Technology, Sri Vishnu Engineering College for Women, Bhimavaram, Andhra Pradesh 534202, India
e-mail: vpenmetsa@yahoo.com

G. T. C. Sekhar et al. (eds.), *Intelligent Computing in Control and Communication*, Lecture Notes in Electrical Engineering 702,
https://doi.org/10.1007/978-981-15-8439-8_19

challenges and their solutions related to Blockchain technology that mainly focuses on wide range of applications. This review helps the researchers to understand the technology and its advancements in the Blockchain mechanism.

Keywords Blockchain · Data management · Crypto-currency system · Security · Cryptography · Telecommunication

1 Introduction

Blockchain is basically an increasing list or sequence or chain of public records [1]. This technology is known for its public data management system which maintains the data integrity without disturbing the sequence of transactions. This technology is mainly used for the generation of crypto-currency, but it can also be used in many other fields like telecommunication and banking [2]. This feature is mainly implemented as the value of the currency is maintained without any involvement of organization or government. These transactions encounter constant increase within that Bitcoin network which has gained the attention of various communities and main application for Blockchain technology. This technology uses a Public Key Infrastructure (PKI) mechanism [3] where the client consists of a private and public key. The former is used to authenticate the Bitcoin wallet, and the later is used for user authentication.

All the transactions are aligned in a continuous chain mode called nodes as shown in Fig. 1 which are stored in the user's disk. Once the transaction has been approved by all the nodes [4] in the Blockchain network, it is not possible to delete or modify the transaction, which is the main advantage of this technology. Blockchain technique can be used to improvise and maximize the profit [5] of the telecommunication industry and its related sectors using their three main properties of Blockchain technology which are as follows: decentralization, transparency, and immutability. Decentralized systems [6] allow each entity of the network to have its own information rather than storing it in single entity as depicted in Fig. 2. Interactions are done directly without third-party intervention.

Transparency ensures that all the personal identities are hidden using complex crypto-graphic mechanisms, and only public addresses are used for transactions. The data packets which are not tampered due to any external agent called as immutability. There are many challenges and limitations which are identified using Blockchain technology like throughput [7], latency, security, scalability, and many more. There are three different types of Blockchain technologies as given in Table 1:

1. Public
2. Federated
3. Public

The innovative use of Blockchain mechanism [8] can do a pretty much change to every possible industry. Blockchain involves simple records which are duplicated in crosswise manner over different partners in the system. The system will maintain

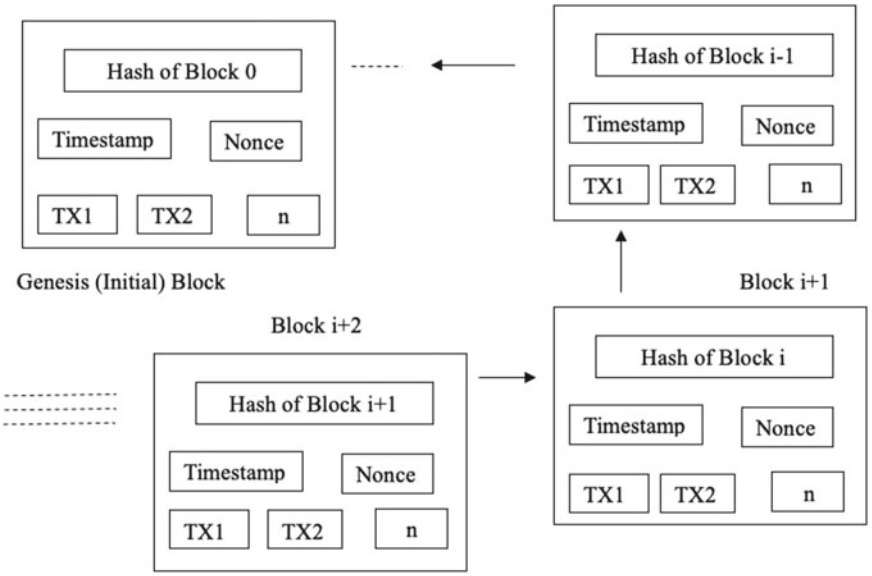

Fig. 1 Blockchain architecture [1]

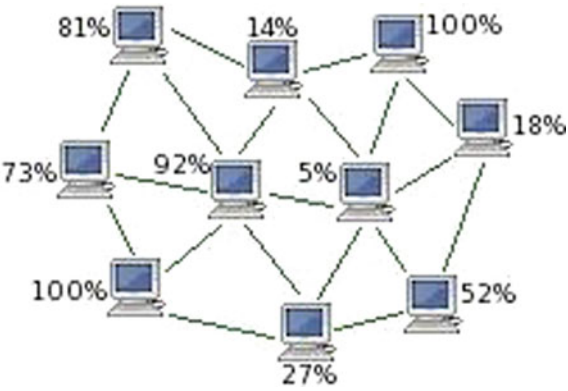

Fig. 2 Decentralized systems [2]

Table 1 Types of blockchains [3].

Transaction	Public	Federated		Private
Send	Anyone	Limited		Centralized
Approve	Anyone	Few members		Centralized
Read	Anyone	Limited		Limited

total history of all the exchanges made. Different parties [9] will give confirmation on history, so that it cannot be messed up with the others. However, the exchanges are often limited to certain extent. This restriction ensures security, straight forwardness and reduces the involvement of middle people.

The procedure of transaction in Blockchain technology has following steps [10].

1. A system containing excavators will check against each other in order to provide the right approval.
2. Once approval has been given, then they will be included to the consecutive chain of exchanges.

2 Literature Survey

For the past few years, because of increased commoditization and administrative difficulties [11], media transmission business is facing some confronting difficulties resulting in low income and productivity rates. So, we are obviously in the need for unquestionable changes and redesigns in the system. As stated, to survive in the new era of virtualization and digitization [12], selecting Blockchain technique is the far better option. The reason is that it will possibly lead to many future advancements and enhancements in all possible channels. There are many key characteristics for Blockchain technology which define different aspects like [13]:

1. Decentralization: All the transactions in the Blockchain network are monitored and validated by the central server which results in efficient cost and performance management between any two peers.
2. Persistency: The transactions are generally disturbed or manipulated in a network due to different reasons. To minimize this problem Blockchain technology facilitates with verification and validation at every node of Blockchain network which reduces the error easily.
3. Anonymity: As node-to-node (P2P) monitoring and validation of data being transmitted [14], it is enabled in Blockchain network privacy, and other security is preserved according to the transactions.
4. Auditability: Transparency of the data stored in Blockchain network is improved by verifying all the transactions at every peer node that facilitates tracing back the transactions.

The Blockchain network is divided into different strategies as in Table2 based on various properties given below [15].

There are different benefits of Blockchain technology.

Nonpartisan and transparent: Blockchain framework [16] is completely open and transparent in full scale, so there is no place for counterfeit or fraud. The record that holds data of each and every client is completely visible to every other client. Also, every hub on the system has a duplication of each record. This method offers us a complete decentralized approach.

Table 2 Comparison between public, consortium, and private blockchain

	Consensus determination	Read permission	Immutability	Efficiency	Centralized	Consensus process
Public	All mining algorithms	Public	Not possible to tamper	Low	No	Permission-less
Consortium	Selected number of nodes	Restricted	Tampering possibility	High	Partial	Permissioned
Private	One central hub	Public or restricted	Tampering possible	High	Yes	Permissioned

Increased speed [17]: In many applications, superior speed check became an important factor in case of shared exchanges or transactions. Bitcoin arrangements do not show much focus on such factor. But our Blockchain arrangements have many up to date techniques to settle down this issue.

Security: The use of decentralized approach [18] guarantees much security. Apart from this two-level security, keys and various encryption techniques are used which further more increases the level of security. Thus, the possibility of any malicious impact is altogether effectively handled by the Blockchain mechanism.

Blockchain technology is facing much new advancement day by day. Each advancement has its own appropriate value which effectively manages the distributed information in a decentralized system. We can consider bitcoin as such an example. It started as a basic cryptographic form of money, and now, it is extended to various dimensions such as banking, medicinal services, media transmission, production, and protection.

3 Algorithmic Survey

Blockchain-based algorithms provide an idea about the communication and verification between all the nodes in the Blockchain network [19]. Some of the algorithm comparisons are mentioned below in Table 2. The value chain of telecommunication sector [19] involves a major system framework for voice, information, media, and other related entities. The information trade or exchange between the systems will call for security, trustworthiness, examination, and possible counteractive actions for the information involved. Recently, new infra-sharing models are coming up to add new flavors to the existing techniques (Tables 3 and 4).

Additionally, new plans of action and advanced eco-frameworks [20] play an integral part in telecom value support. Blockchain technique helps us to detangle this complex procedure. It also makes them secure, straightforward, and effective thereby leading to new income streams.

1. Finance
2. IoT

Table 3 Comparison of different blockchain algorithms [8]

	Node identity management	Energy saving	Tolerated power of adversary	Example
PoW	Open	No	<25% computing power	Bitcoin
PoS	Open	Partial	<51% stake	Peer coin
PBFT	Permissioned	Yes	<33.33% fault replicas	Hyper ledger fabric
DPOS	Open	Partial	<51% validators	Bit shares
Ripple	Open	Yes	<20%	Ripple
Tendermint	Permissioned	Yes	<33.33%	Tendermint

Table 4 Blockchain applications [9]

	Domain	Applications
Blockchain	Finance	Financial services, enterprise transmission, P2P financial marketing, risk management, and many more
	IoT	E-business, security, and privacy
	Public and social service	Land registration, energy saving, and education
	Reputation system	Academics and Web community

3. Public and social services
4. Reputation system
5. Security and privacy.

Recent advancements of digital transformation include virtualization, artificial intelligence, robotic process automation, etc., so including Blockchain techniques in the above-mentioned areas will lead to further more advancements, thereby maximizing the profit. Some of them are mentioned below.

3.1 Fraud Prevention

The critical on-going consideration of many companies across the world is the fraud detection. We are in the need of perfect and secured accounting information system in order to reduce or even prevent the fraud risks [19]. The system which handles tampering from both inside and outside parties is required. Blockchain mechanism as a public decentralized system does the above-mentioned work effectively. The computer jointly supervises the overall system operations and prevents the information from being tampered. So, the companies may incorporate Blockchain into their information systems to maintain a much clean and secure database.

3.2 Identity Management

A Telco is most commonly used to search for a forward concentrated identity management. But for a crosswise connection over various gadgets and applications, we can use Blockchain mechanism. It effectively supports by recognizing numerous crosswise connections over various stages. Decentralized Blockchain rule with personality confirmation is employed to achieve this effective crosswise connection.

3.3 Internal Process Support

By making more advancements and procedure improvement, Blockchain mechanism can support a number of BSS/OSS procedures [20]. Some of the examples include billing SIM provisioning, number versatility, and activation of mobile services onto a network. Utilizing the advancements of Blockchain can easily stir down the time consumption by robotizing many of the procedures.

3.4 Readiness for 5G

Blockchain mechanism helps the administrators to easily overcome with the complex procedures required for executing 5G systems. It usually defeats the boundaries around system provisioning. By utilizing smart contracts and with the help of constant supply of system assets, Blockchain innovation will surely accelerate the overall administration process, thereby gaining a good esteem from outside clients.

4 Future Work

Blockchain technology has no ending for its advancements and enhancements. The research work can be extended in other domains by taking Blockchain technique as base because it always ensures an innovative end. An end always leads to a fresh start, and so the development process will continue to progress. There are certain zones in media transmission that needs to be concentrated much. Many organizations are facing considerable amount of loss because of fake plans. To cope with this, the organizations can utilize the security feature of Blockchain technology. Overseeing a personality allows us to deal with client's Id, applications, gadgets, and organizations with just a single secret key. On the other hand, the client will have an ace key and with the help of that he/she can check their character in any digital platform. We can consider certain domains like IOT, AI, etc., to pursue the research work

in combination with Blockchain mechanism. Such combined work with the above-mentioned domains will surely result in an unpredictable growth and advancements.

5 Conclusions

1. From the extensive survey of various published research, many experts have seen the possibilities through which the Blockchain technology can lead us to move toward development and advancement in the field of data management.
2. Every technology has its own problems, and Blockchain is no different from others in this context, but the most promising feature of Blockchain technology can be understood from the theories that this technology can never be compromised in terms of security issues related to client or user (evidences or proofs needed).
3. Many experts and researchers also concluded that many features mentioned in this paper are required in telecommunication industry as it relies more on its client's safety and continue to work with it only if they are ensured that they are safe and secure. If we are able to work on other domains as well, then it leads to a glorious development in that field.

References

1. Bentov I, Lee C, Mizrahi A, Rosenfeld M (2014) Proof of activity: extending Bitcoin's proof of work. ACM SIGMETRICS Perform Evaluati Rev 42(3):34–37
2. Axon L (2015) Privacy-awareness in blockchain-based PKI. CDT Technical Paper Series
3. Zyskind G, Nathan O et al (2015) Decentralizing privacy: using blockchain to protect personal data. Security and Privacy Workshops (SPW), 2015 IEEE, pp180–184
4. Azure (2016) Microsoft azure: blockchain as a service. https://azure.microsoft.com/en-us/solutions/blockchain/
5. Buterin V (2015) On public and private blockchains. https://blog.ethereum.org/2015/08/07/on-public-and-private-blockchains/
6. Carboni D (2015) Feedback based reputation on top of the bitcoin blockchain. arXiv preprint arXiv:1502.0150
7. Habib K, Torjusen A, Leister W (2015) Security analysis of a patient monitoring system for the internet of things in eHealth. In: The seventh international conference on eHealth, telemedcine, and social medicine (eTELEMED)
8. IBM (2016) IBM blockchain. https://www.ibm.com/blockchain/ISO
9. Kraft D (2016) Difficulty control for blockchain-based consensus systems. Peer-To-Peer Netw Appl 9(2):397–413
10. Mazieres D (2015) The stellar consensus protocol: a federated model for internet-level consensus. Stellar Development Foundation
11. Zhang Y, Wen J (2015) An IoT electric business model based on the protocol of bitcoin. In: Proceedings of 18th international conference on intelligence in next generation networks(ICIN), pp 184–191. Paris, France
12. Devine P (2015) Blockchain learning: can crypto-currency methods be appropriated to enhance online learning?. ALT Online Winter Conference

13. Micheler E, vonder Heyde L (2016) Holding, clearing and settling securities through Blockchain technology creating an efficient system by empowering asset owners. Soc Sci Res Net
14. Morini M (2016) From blockchain hype to a real business case for financial markets. Soc Sci Res Netw
15. Noyes C (2016) Bitav: fast anti-Malware by distributed blockchain consensus and feed forward scanning. arXiv preprint arXiv:1601.01405.
16. Pilkington M (2016) Does the fintech industry need a new risk management philosophy? A blockchain typology for digital currencies and e-money services in Luxem- bourg. Soc Sci Res Netw
17. Olat S, Potop-Butucaru M (2016) Zero block: timestamp-free prevention of block-withholding attack in bitcoin. Technical Report, Sorbonne Universities, UPMC University of Paris
18. Eyal I, Gencer AE, Sirer EG, Van Renesse R (2016) Bitcoinng: a scalable Blockchain protocol. In: Proceedings of 13th USENIX symposium on networked systems design and implementation (NSDI 16), pp 45–59. Santa Clara, CA, USA
19. Tschorsch F, Scheuermann B (2016) Bitcoin and beyond: a technical survey on de-centralized digital currencies. IEEE Commun Surveys Tutorials 18(3):2084–2123
20. Zheng Z, Xie S, Dai H, Chen X, Wang H (2017) An overview of blockchain technology: architecture, consensus, and future trends. In: Proceedings of the 2017 IEEE bigdata congress, pp 557–564. Honolulu, Hawaii, USA

A Study on Static Call Admission Control Policies for Wireless Mobile Cellular Networks

Promod Kumar Sahu, Hemanta Kumar Pati, and Sateesh Kumar Pradhan

Abstract In wireless mobile cellular networks call admission control (CAC) plays an important role in Quality of Service (Qos) provisioning. During last three decades it has been acquiring enormous interest due to the growing demand of wireless communication. In wireless systems for first and second generations CAC schemes were designed considering a single class of service i.e. voice. However, third generation (3G) and further wireless systems providing multimedia services such as voice, video and data are extended with different QoS forms under homogeneous and heterogeneous networks. Accordingly, more refined CAC methods are developed to confront with the above-mentioned changes. In this paper, we provide an overall study on the static CAC schemes used in wireless mobile cellular networks.

Keywords Call admission control · Quality of service · Bandwidth reservation · Guard channel · Mobile networks

1 Introduction

The demand of wireless network is increasing in the recent years because of the rapid advancement in wireless technology and development of more efficient handheld wireless terminals [1–5]. Since mid-1980 cellular mobile communication has been experiencing incredible growth and the number of wireless network subscribers has risen above 700 million at the end of 2000. It is normal that the number will exceed 50 billion by 2020 [6]. The wireless networks should handle as many mobile users

P. K. Sahu (✉) · S. K. Pradhan
Department of CSA, Utkal University , Bhubaneswar, Odisha 751004, India
e-mail: promod_sahu@yahoo.com

S. K. Pradhan
e-mail: sateesh.cs@utkaluniversity.ac.in

H. K. Pati
Department of CSE, IIIT Bhubaneswar, Odisha 751003, India
e-mail: hemanta@iiit-bh.ac.in

G. T. C. Sekhar et al. (eds.), *Intelligent Computing in Control and Communication*, Lecture Notes in Electrical Engineering 702,
https://doi.org/10.1007/978-981-15-8439-8_20

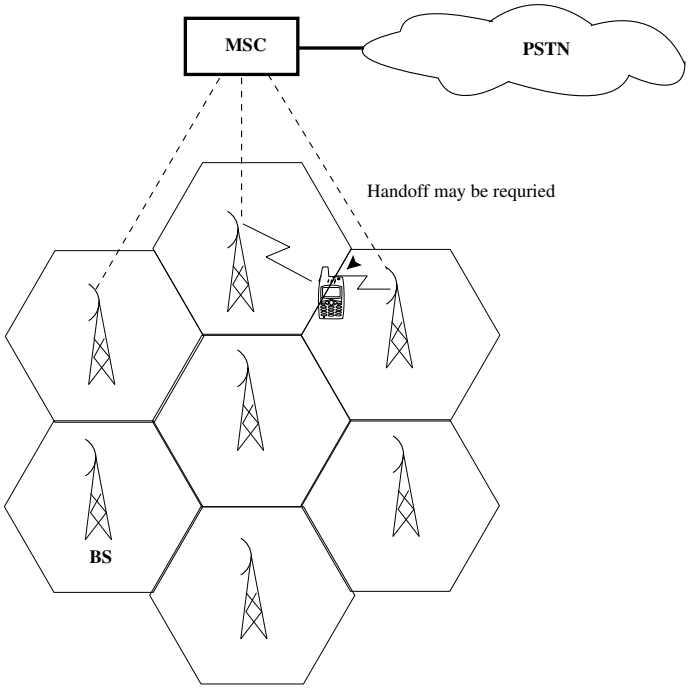

Fig. 1 Architecture of the wireless cellular network

as possible with limited wireless resources (e.g. bandwidth) as the number of mobile subscribers is progressively growing. Also, QoS provisioning is highly expected because the network provides various types of services such as voice, video and data. These two fulfillments are challenging against each other. To have a good balance between system user capacity and providing QoS to various types of services, radio resource allocation plays a key role. For effective usage of network radio resources and for providing QoS guarantee to different applications resource allocation is responsible. The difficulties present in any wireless mobile cellular network such as limited bandwidth, user mobility and error prone wireless channel make it difficult to carry out.

Commonly as shown in Fig. 1 the wireless cellular network is formed by deploying base station (BS)s to cover the geographical region under consideration for providing the service. Here the geographical area under a single BS is called a cell. The same radio channels or frequencies may repeat some distance away in other cells [7]. In the cell a BS handles its mobile users. To communicate with other mobile users, a new connection request must be issued by a mobile user to the BS, in which a set of QoS specifications as required by the application are implicitly or explicitly described. The BS after receiving the connection request will initiate the call admission procedure to decide whether to accept the request or not. The admission control unit in the BS

while taking the decision has to ensure QoS of the existing connections and also QoS of the newly arrived call in its service period. So, to satisfy QoS requirement for each of the connected service and to maximize network utilization, the BS allocates resources established through connection admission scenario.

Certain issues should be considered while designing CAC scheme. First, the handoff connect request is an ongoing call in the process of moving from one cell to one of its neighbor cell and so it has higher priority than newly originated call requests. Second, the network provides different types of services with varying traffic characteristics. Their QoS demand may vary in provisions of delay, connection dropping probabilities and bandwidth. So, it is the duty of the network to specify distinctive priorities to the above-mentioned services based on individual traffic characteristics and QoS demand. Lastly, it is important for the network to maintain fairness among the services at the same time satisfying their particular QoS demand specifically when the different types of services coincide in the network. The network requirement is to properly assign resources through various users such that individualized Quality of Service demands for individual type of service can be satisfied independent of others. In this paper we focus some handoff prioritization CAC schemes to address this matter. Call admission can take place based on the type of traffic used in the system, the type of information used in the admission control, the number of cells in which call admission is performed and the way handoff requests are handled. All these schemes are divided into two main classes i.e. static CAC schemes and dynamic CAC schemes. In this paper we present static CAC schemes . So in this regard in Sect. 2 we discuss some major challenges in providing user services over wireless networks. In Sect. 3 we present static CAC schemes. Finally, in Sect. 4 we conclude this paper.

2 Some Major Challenges

The wireless network has emerged from second generation (2G) Frequency Division Multiple Access (FDMA) / Time Division Multiple Access (TDMA) to third generation (3G) Code Division Multiple Access (CDMA) technology [8], and carried traffic from voice service to multimedia service such as voice, video and data, and further in case of fourth generation (4G) wireless systems supportive to multimedia applications with divergent QoS requirements in the presence of varying wireless access technologies [9–13]. This introduces new challenges for making optimal resource allocation while designing appropriate CAC scheme. We identify some challenges in the following.

2.1 Increased Handoff Frequency

With rapidly growing wireless network subscribers the bandwidth attach into a cell becomes inadequate and the total capacity of the system has to be raised. Suppose the systems frequency spectrum remain fully stable. Then to enhance the network capacity the size of the cell has to be reduced achieving frequency reuse. This results in the development of micro-cell or pico-cells from a macro-cell. By reducing cell size the system capacity can be enhanced but this also increases handoff frequency as users steady in a call are more anticipated to cross over the cell edge during lifetime of the calls. The handoff call is an ongoing call, so its dropping is more unacceptable than blocking of new call request. So, it is more demanding for the network to guarantee a acceptable handoff call dropping probability in the influence of added on handoff frequency. So it is usefulness for observing the hard handoff in FDMA/TDMA cellular networks where a mobile end user disconnects its connection from the present BS prior to establishing a new connection to the new BS. In CDMA network the soft handoff gives seamless connectivity to a mobile end user. It does not disconnect the connection when the mobile end user moves from its current cell to an immediate neighbor cell. Later establishing a new connection from the new BS, the connection to the old BS is dropped.

2.2 Multiple Service Types

The next generation wireless cellular network is awaited to meet a broad chain of applications with divergent media types that may constitute voice, video and data. They need different Quality of Service requirements in provisions of bit error rate, delay jitter and delay due to their divergent traffic characteristics. In Universal Mobile Telecommunications Service (UMTS) [14], the four different traffic classes supported are Conversational, Streaming, Interactive and Background. The *Conversational* class has stiff demands on delay jitter and delay , and are not very easily affected to bit error rate. Examples of applications belong to this traffic class include video telephony and voice. The *Streaming* class is normally less flexible to delay jitter or delay than the conversational class. Real-time streaming video is an example of this application class. The *Interactive* class requires the response time to be inside certain range and the bit error rate to be really low so that the payload contented can be preserved. Examples of this class of application include database retrieval and web browsing. The *Background* class includes applications like data services using file transfer or email. In these class of traffic the target can accept delays differing from seconds to minutes but the data transferred has to remain received error free.

2.3 Traffic Asymmetry

The traffic asymmetry between uplink and downlink turn into a remarkable attribute in the next generation wireless network because the traffic expands from voice-centric to multimedia [15–17]. In the classes of traffic mentioned above, the conversational traffic is approximately symmetric or symmetric, the web browsing or streaming video are actually asymmetric and generally require large bandwidth for downlink than for uplink. The traffic asymmetry handling depends not only on the asymmetric allocation of bandwidth in a system but also the CAC scheme should take this into account explicitly.

2.4 Heterogeneous Networking

In 4G system a call in one specific network essentially be allowed to roam and hand over to another network clearly due to global mobility requirement and smooth connection. This is named as vertical handoff, and various relevant points need to be addressed. The handoff initiation based on signal strength cannot be enough, and at the network congestion level system parameter must be considered. For that, in order to alleviate congestion in a cellular network the mobile end users with non-real time application can be hand over to Wireless Local Area Network (WLAN). All these elements will impact on the distribution call holding time in all network. The vertical handoff determination is a new sub type of handoff call from the call admission control point of view. A CAC algorithm should specify the priority of vertical handoff call around the new calls. A new performance metric that is vertical handoff call dropping probability shall be resolved and must be conserve below the admissible threshold. Again issue connected to call queuing and/or dropping essential to be addressed because if a wireless cellular network cannot acquire a vertically handover call from a WLAN, the call stay linked with the WLAN or may be dropped and wait till the wireless cellular network is able to hold the call.

2.5 Adaptive Bandwidth Allocation and Cross Layer Design

With multimedia applications, system usage and Quality of Service achievement can be enhanced by arranging the bandwidth distribution, build upon the users Quality of Service requirement and the network state [18]. To design CAC algorithm both QoS of call and packet level demand to be studied, such that not alone the call blocking probability and call dropping probability but again packet dropping probabilities and packet delay can be keep up at the target [19].

3 Static CAC Approaches

In a cellular network commonly some amount of resource such as wireless channels or bandwidth is assigned to each cell. This channel assignment to the cell in a network can be either fixed or dynamic. The number of wireless channels or bandwidth allot to any cell is fixed in fixed channel allocation. A new or handoff call initiated in any cell will be blocked when there is no unreserved channel usable [20]. In case of dynamic channel allocation, the number of wireless channels or bandwidth allotted to any cell is not rigid and changing according to co-channel interference restriction. More information on the allocation of fixed channel and the allocation of dynamic channel can be found from [21]. In the following we present fixed channel allocation schemes.

3.1 Guard Channel Based CAC Approaches

A set or group of channels called GC are reserved for the use of handoff calls in GC concept. The flowchart for GC concept is shown in Fig. 2. Based on guard channel concept four different schemes are presented in the following.

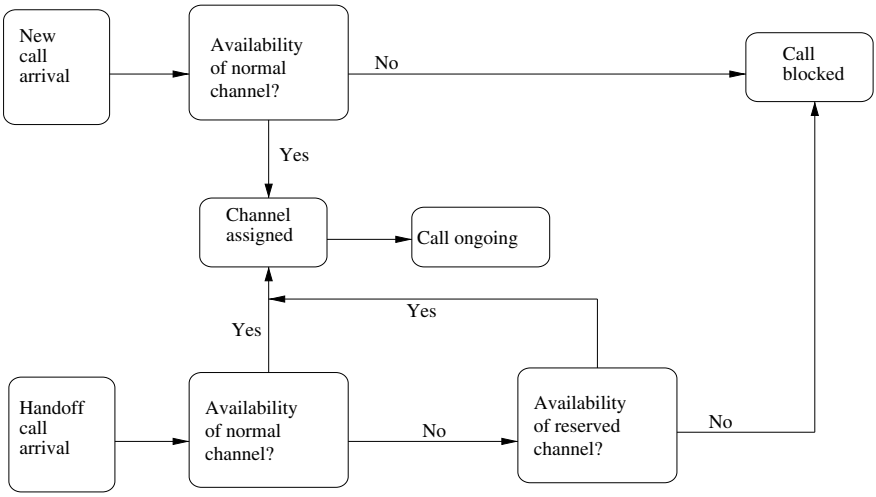

Fig. 2 Flowchart for the guard channel (GC) concept

3.1.1 The Cutoff Priority Scheme

In this scheme, a new call will be blocked when the number of free channels or bandwidths available in a cell is either less than or equal to the number of GC reserved for handoff calls [22–27]. In [22], for handoff calls some channels are reserved i.e. called guard channels. In a cell let C_t be the total number of radio channels and C_T is a threshold. In this guard channel scheme up to use of $C_T - 1$ channels both new and handoff calls are allowed and after that up to C_t only handoff calls are allowed. Here the number of GC (i.e. $C_t - C_T + 1$) is reserved for handoff calls. The state transition diagram is shown in Fig. 3.

3.1.2 The Fractional Guard Channel Based Scheme

In this scheme, a new call is allowed based on some certain probability that depend on the active or occupied number of bandwidths or channels present at that moment in the cell. In [28], a Fractional Guard Channel (FGC) scheme is proposed using the guard channel concept. This scheme, for handoff calls reserves a non-integral number of GC and accepts the new call with some certain probability that is established on present network situation such as channel occupancy at that moment. The state transition diagram obtained for FGC scheme based on guard channel assumptions is shown in Fig. 4. Here the new call acceptance probability is β_i, $1 \leq i \leq C_t$ whereas in the cell there are $i - 1$ active radio channels. Let $\alpha = \frac{\lambda_h}{\lambda_n + \lambda_h}$ and $\rho = \frac{\lambda_n + \lambda_h}{\mu}$. Further let $\gamma_i = \alpha + (1 - \alpha)\beta_i$ and $1 \leq i \leq C_t$. The fractional guard channel policies are conventional CAC policies, here the new call will be accepted based on probability β_i while the number of engaged or busy channels in the cell is $i\,(i = 0 \ldots C_t - 1)$. If no channel is available the handoff call will be rejected otherwise always the handoff call will be admitted. Fractional guard channel method use a vector B=[$\beta_0, \ldots, \beta_{C_t-1}$] for deciding whether new call can be accepted and elements of the same vector define the scheme. When $\beta_0 = \cdots = \beta_{C_t-1} = 1$, the fractional guard channel scheme becomes the non prioritization method and when $\beta_0 = \cdots = \beta_{C_t-g-1} = 1$ and $\beta_{C_t-g} = \cdots = \beta_{C_t-1} = 0$ the FGC method becomes the GC method with reserved channels of an

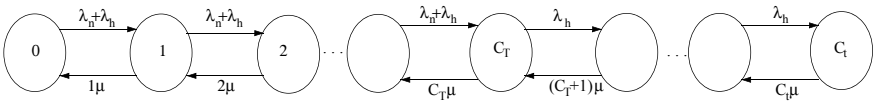

Fig. 3 State transition diagram for GC scheme [22]

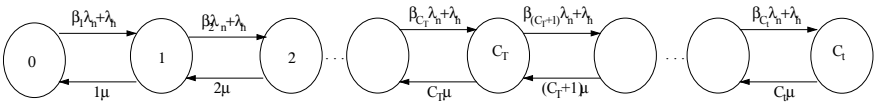

Fig. 4 State transition diagram for fractional guard channel (FGC) scheme [28]

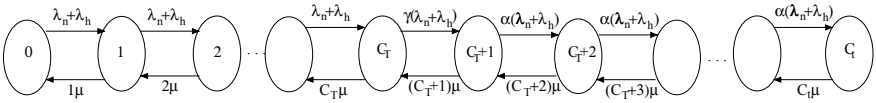

Fig. 5 State transition diagram for LFGC [28]

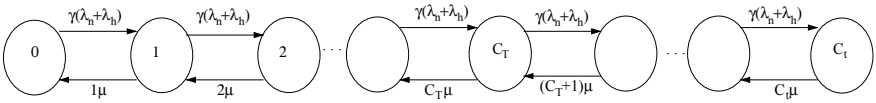

Fig. 6 State transition diagram for UFGC [31]

integer number g. On the other side while $\beta_0 = \cdots = \beta_{C_t-\lfloor g \rfloor-2} = 1$, $\beta_{C_t-\lfloor g \rfloor-1} = 1-(g-\lfloor g \rfloor)$ and $\beta_{C_t-\lfloor g \rfloor} = \cdots = \beta_{C_t-1} = 0$ the fractional guard channel method became limited fractional guard channel method with reserved channels of a real number g [29]. When $\beta_0 = \cdots = \beta_{C_t-1} = \beta$, the FGC method becomes uniform fractional guard channel (UFGC) method with admission probability β [30, 31]. The state transition diagrams for limited fractional guard channel (LFGC) and UFGC methods are shown in Figs. 5 and 6 respectively. Performance analysis for different guard channel methods can be found from [32].

In [33], a two level FGC method is outlined based on priority given to handoff calls. It controls switching between levels based on a dropped call. Smaller number of GC are used in the first level like as fixed guard channel scheme and large number of GC and smaller number of FGC used in the second level. Under light load this method is almost same as fixed GC method. The advantage of this scheme is that the handoff call dropping probability is better as compared to fixed GC method under heavy load. In [34], a new uniform fractional band (UFB) scheme is proposed by combining non-priority scheme, uniform fractional guard channel scheme and priority scheme. As reported in [34], this UFB scheme shows better overall connection block probability compared to other fractional channel schemes. In [35], performance analysis for different fractional guard channel policies are specified. It concluded that, LFGC concept performs better than GC and UFGC schemes under all mobility conditions.

3.1.3 The New Call Bounding Scheme

New call bounding scheme is discussed in [36, 37]. This scheme applies some restriction to admit new calls into the wireless network. It work out as follows. Here the request of a new call will be blocked in the cell when the number of new calls (i.e. calls originated in the same cell, accepted by the network and neither handoffed nor completed) exceed a threshold, otherwise the new call will be accepted. Here handoff call will be blocked if all channels in the cell are in use. The concept behind for this method is to relatively accept a small number of customers than dropping the ongoing calls in the future as a result of, customers are easily hurt to dropping of call

than to blocking of call [36, 37]. This new call bounding scheme may be applied to situations where the call arrivals are bursty.

3.1.4 The Rigid Division Based Scheme

In [38], the rigid division based GC method is presented. In this method all available channels in a cell is split into two groups i.e. common channel group (CCG) and guard channel group (GCG). Channels in the CCG can be used by both handoff and new calls and channels in the GCG can be used by only handoff calls. In the traditional guard channel scheme this rigid division is not present. Based on how the handoff calls bring about the use of these two channel groups different channel share schemes named as methods 1–3 are proposed. In *Method 1*: the mobile switching center (MSC), first checks for a free channel in the GCG to allot it to the handoff call if it is available. In the absence of a free channel in that group it looks at the CCG to allot a free channel to the handoff call if it is available. If the free channel is also not available in the CCG the handoff call terminates. In *Method 2*: the MSC first looks for a free channel in the CCG to allot it to the handoff call if it is available. In the absence of a free channel in that group it looks at the GCG to allot a free channel to the handoff call if it is available. If the free channel is also not available in the GCG, the handoff call terminates. In *Method 3*: The MSC generates an arbitrary value within the range 0 and 1. If that random value lies between 0.0 and 0.5 then channel allocation Method 1 is applied for the handoff call. Otherwise, Method 2 of channel allocation is applied. The detail of these schemes can be found from [38]. This rigid division-based handover priority method improves performance for the system. It outperforms the traditional guard channel scheme. We summarize above schemes in Table 1.

3.2 Queueing Schemes

The blocking probability of handoff call is enhanced in the original guard channel method. However, this improvement in handoff call blocking is achieved by increasing the blocking probability of new call. So, the entire network total carried traffic is decreased. The carried traffic is to be improved if blocked new calls would be queued. Further to improve the carried traffic, the handoff calls or both the handoff calls and new calls also be queued. Some such queuing schemes are studied in [22, 39–44].

3.2.1 The Guard Channel Scheme with Handoff Calls Queueing

The scheme presented in [22] is working similar to the original guard channel scheme except if there is no idle channel available the handoff call will be queued. In the

Table 1 Classification of Static CAC schemes based on guard channel

Name	Comments	References
Cutoff priority scheme	It allows some integer number of channels only to handoff calls based on threshold applied. The probability of new call blocking is more and dropping probability of handoff call is less as compared to fixed channel allocation scheme	[22–27]
Fractional guard channel scheme	This model for handoff calls reserve some non-integer number of channels. Here new call blocking probability is improved compared to cutoff priority scheme	[28]
Limited fractional guard channel scheme	It allows non-integer number of channels only for handoff calls by using an additional parameter for accepting new calls when the number of busy channels is equal to the threshold. It further improves new call blocking probability improved compared to cutoff priority scheme	[29]
Uniform fractional guard channel scheme	Independent of channel occupancy, allows new calls with some probability. This method is better than cutoff priority method under low handoff traffic condition	[30, 31]
Two level fractional guard channel scheme	It reserves channels for handoff calls in two levels. It improves handoff blocking probability compared to fractional guard channel schemes under heavy load and it performs same as to fractional guard channel schemes in light load	[33]
New call bounding scheme	It restrict the new call for entering into the wireless network based on some threshold used for new call. This scheme may be preferred to handle bursty traffic	[36, 37]
Rigid division based scheme	Total available channels in a cell is divided into two groups. One group is used by both types of calls and the other group is used by only handoff calls. Here handoff blocking probability is less as compared to cutoff priority scheme and it is ideal for micro-cellular personal communication networks	[38]

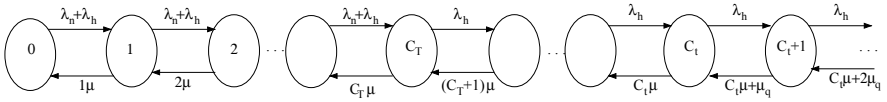

Fig. 7 State transition diagram for GC with queueing [22]

queue the calls will be served on the basis of first-come-first-served (FCFS). Time for handoff calls stay in the queue is equal to the time for handoff calls in handoff area. If the common signal power lined up from a BS drops down the handoff threshold, still it is quite more than the minimum receiver threshold that area is called the handoff area. Based on size of the cell, travelling speed of the mobile user, direction and based on the nature of landscape it varies. The state transition diagram of GC method with handoff call queueing is shown in Fig. 7. In [43], a measurement based prioritization scheme (MBPS) is proposed. For the queued handoff calls it uses non-preemptive dynamic priority based on first-come-first-served (FCFS) queueing discipline. In this scheme, the current handoff request is put at the end of the queue if no unoccupied channel is usable. The power level is measured regularly for all the handoff calls in the queue to update their priority dynamically. If the measured power level of a queued handoff call is decreased to the minimum receiver threshold from the handoffed threshold it will be attached with a high priority. A handoff call assigned with the maximal or highest priority, gets served whenever there is a free channel. As a consequence, this MBPS method can farther lower the handoff call drop probability. In terms of QoS and spectrum efficiency compared to FIFO method this MBPS method offers better performance. In [45], a signal prediction priority queueing method is proposed to improve the measurement based prioritization method by using both received signal strength and change in received signal strength to determine the priority ordering in the handoff queue. Under non-ideal condition they show that signal prediction priority queueing scheme (SPPQ) performs better than first in first out (FIFO) and measurement based prioritization method (MBPS). Signal prediction priority queueing (SPPQ) scheme discussed above is extended in [46] for handling the multimedia traffic. This extended scheme is called as Signal Strength of Multimedia Communication (SSMC) scheme. In this scheme, when all channels of the BS are busy then the handoff requests are queued for that cell and request for the new call are simply blocked within the cell. The queued handoff requests are ordered according to a priority value which is based on received signal strength, change in received signal strength and traffic type. In [47] by queueing handoff calls a mobility aware CAC algorithm is proposed for mobile hotspots. This algorithm introduces two phases i.e stop and moving. In stop phase guard channels are assigned to prioritize handoff calls and in the moving phase no guard channels are used to maximally utilize the wireless local area network capacity.

3.2.2 The Guard Channel Scheme with New Calls Queueing

In [39], a scheme is proposed by considering new call and handoff call as the two different kinds of incoming traffic. The concept which is used in guard channel, the same concept is used in this method except if a new call is arrived and no channel is available then the new call will be queued. In this method with no restriction all free channels the handoff calls can access. It is found that by queueing new calls the dropping probability of handoff calls is slightly increased as compared to guard channel but there is a considerable increase in the total carried traffic.

3.2.3 The Guard Channel Scheme with Queueing Both New and Handoff Calls

In [40], performance of a system is examined by using GC method and by allowing both handoff and new calls are to be queued with bounded buffer size. Again, due to caller impatience the queued new call, may leave the system and before successful completion whenever the user moves out of the handoff area the handoff call may be dropped. It was concluded that we can find appropriate queue size for both new and handoff calls. In such a system for minimizing the overall blocking probability there exist an optimal guard channel threshold. In [44], performance of guard channel schemes are compared by applying new and handoff call queueing strategies. We summarize queueing schemes in Table 2.

3.3 The Guard Channel Scheme for Multiple Traffic Classes

In this sub section we describe some CAC policies that are used for multiple traffic classes for example voice and data. Here we divide it into two categories i.e. single threshold GC policy for multiple traffic classes and multi-threshold GC policy for multiple traffic classes.

3.3.1 Single Threshold Guard Channel Scheme for Multiple Traffic Classes

In single threshold scheme there is no priority to voice calls over data calls. In this subsection we describe some single threshold CAC schemes for multiple traffic classes. In [48], for multimedia traffic CAC of wireless networks is studied by using fixed channel allocation. In this work, narrowband voice calls and wideband images, these two kinds of traffic are studied. Three different admission control policies are evaluated namely complete partitioning (CP), complete sharing (CS), and hybrid policies in provisions of dropping probability of handoff call and blocking probability of new call and the QoS requirement is guarantee. The study revealed several

Table 2 Static CAC schemes based on queueing

Name	Comments	References
Queueing handoff call scheme	Reduce handoff call dropping probability compared to GC method and increases blocking probability of new call	[22]
Queueing new call scheme	Reduce blocking probability of the new call and dropping probability of the handoff call slightly increases	[39]
Queueing new call and handoff call scheme	Based on appropriate queue size it minimizes both blocking probability of new call and dropping probability of handoff call	[40]

conclusions. First, CS favors narrowband users and for handoff traffic it does not provide high priority. It favors narrowband users over wideband users accordingly more bandwidth is required to admit wideband traffic. It can achieve higher channel utilization in heavy load compared to other two schemes. Second, in CP the total bandwidth in a cell is divided into subgroups, so that the QoS requirements of different traffic classes accept with different priority levels can be satisfied. However, in the process of achieving this it may further reduce channel utilization. Third, the hybrid policy using the appropriate reservation algorithms adapts the desired QoS to obtain the minimized cost function that is measured based on the call dropping or blocking probabilities and can be examined as the total performance. In [49], a CAC scheme for multiple-class calls with user mobility is described. For the deravitation of connection level QoS numerical method is used and verifiable with computer simulation final result. The result shows that user mobility can have a greater impact on the connection level Quality of Service in addition to offered load. In [50], CAC policy for a wireless system supporting both available-rate data calls and constant-rate voice calls is presented. The objective of this scheme is, for mobile users Quality of Service is guaranteed and efficiency for utlization of resource is high. The parameters of this proposed policy are determined by using optimization approach. In [51], a new adaptive bandwidth allocation method known as the measurement-based preassignment (MPr) technique is presented to avoid handoff failure in cellular wireless networks. It also discussed how this MPr algorithm can be used both in multi-service with complete partitioning and resource sharing environments.

3.3.2 Multi Threshold Guard Channel Scheme for Multiple Traffic Classes

In multi threshold method priority is given to real time calls (such as voice) over non-real time calls (such as data). A dual threshold reservation scheme (DTR) is proposed in [52] which is a general extension of guard channel scheme that supports voice traffic in cellular network. The idea behind this scheme is that here two thresholds are used. One threshold is used to reserve channel for voice handoff and another threshold is used to block data traffic to the network. Here in terms of call blocking and handoff dropping probability it safe the performance of the voice. Based on complete sharing approach a dual threshold bandwidth reservation policy is outlined in [53]. In this policy, to meet the specific QoS requirement multiple thresholds are used and channels are shared among different traffic types in each cell. By extending limited fractional guard channel a dual threshold CAC policy is proposed in [54]. This scheme minimizes the new call blocking probability for both voice and data traffic while satisfying the hard constraints on handoff call dropping probabilities. In [55], a CAC scheme is proposed for integrated voice/data traffic. For maintaining the corresponding service quality for data and voice traffic and for voice calls the target handoff dropping probability is guaranteed this uses two acceptance ratio. One acceptance ratio is for voice call and other acceptance ratio for data. Here two variations of extended fractional guard channel scheme are proposed. One is EFGC-REST which is a conservative approach, this preserves the corresponding service quality by sacrifice the bandwidth utilization and second is EFGC-UTIL which is a greedy approximation, for voice calls at the expense of increased handoff failure probability it achieves higher bandwidth utilization.

For two classes of voice users a two threshold GC method for cellular wireless network is proposed in [56]. This method used three type oftraffic classes i.e. new calls, handoff voice calls of class 1 and class 2. For different classes to provide the level of Quality of Services two threshold are used. Based on the dropping probabilities for two classes of calls this scheme minimizes the new call blocking probability. In [57], the idea given in [56] is generalized for multi-classes. The performance analysis of call admission control for multiple traffic class is given in [58–60]. The performance is analyzed in terms of data loss probability, voice call blocking probability and mean data delay in each cell. When the number of channel assigned to voice call increases the voice call blocking probability decreases and when the number of channels assigned to data traffic increases the voice call dropping probability increases. When the number of channels assigned to data traffic increases the mean data delay and data loss probability decrease. The data loss probability and mean data delay increase when the number of channels assigned to voice call increases. We summarize the multiple traffic schemes in Table 3.

Table 3 Static CAC schemes based on multiple traffic classes

Name	Comments	References
Single threshold scheme	There is no priority to real time call over non-real time call	[48, 51]
Multi threshold scheme	There is priority to real time call over non-real time call	[52–57]

4 Conclusion

In this paper we studied some of the important static CAC schemes. It is found that these schemes determine the admission control specification such as bandwidth or the reserved channel size, and length of the queue corresponding to a prior knowledge of the traffic pattern. These cannot be modified during course of system activity once determined because these methods are static in nature. These schemes have merits and demerits as stated in the following. *Merits*:1. They are simple and can be mathematically modelled to derive the important performance metrics like the handoff call dropping and new call blocking probabilities. 2. For further improvement they provide benchmark for us. 3. These schemes are effective whereas control specification set properly to carry out QoS requirements. *Demerits*:1. Due to static character they are incapable to compete with dynamically varying network environment where users exhibit high mobility and traffic pattern changes unexpectedly. 2. Static schemes cannot provide QoS guarantee and inefficient in system utilization.

References

1. Rappaport TS, Annamalai A, Buehrer RM, Tranter WH (2002) Wireless communications: past events and a future perspective. IEEE Commun. Mag. 40:148–161
2. Brockwell PJ, Davis RA (1991) Time series: theory and methods, 2nd edn. Springer Verlag, New York
3. Zhang T, Berg E, Chennikara J, Agrawal P, Chen JC, Kodama T (2001) Local predictive resource reservation for handoff in multimedia wireless IP networks. IEEE JSAC 19:1931–1941
4. Li VOK, Qiu X (1995) Personal communication systems (PCS). Proc IEEE 83:1210–1243
5. Cox DC (1995) Wireless personal communications: what is it? IEEE Pers Commun 2:20–35
6. Gupta A, Jha RK (2015) A survey of 5G network: architecture and emerging technologies? IEEE Access 3:1206–1232
7. Rappaport TS (2002) Wireless communications: principles and practice, 2nd edn. Prentice-Hall Inc, New York
8. Holma H, Toskala A (2002) WCDMA for UMTS: radio access for third generation mobile communications, 2nd edn. Wiley, New York
9. Niyata D, Hossian E (2005) Call admission control for QoS provisioning in 4G wireless networks ossues and approachs. IEEE Netw 19:5–11
10. Sun J-Z, Sauvola J, Howie D (2001) Features in future: 4G visions from a technical perspective. In: IEEE GLOBECOM, vol. 6, pp 3533–3537
11. Varshney U, Jain R (2001) Issues in emerging 4G wirless networks. IEEE Comput 34:94–96

12. Hui SY, Yeung KH (2003) Challenges in the migration to 4G mobile systems. IEEE Commun Mag 41:54–59
13. Zahariadis T, Kazakos D (2003) (R)Evolution toward 4G mobile communication systems. IEEE Wirel Commun 10:6–7
14. 3GPP. Universal mobile telecommunications system (UMTS); QoS concept and architecture. TS 23.107 version 4.1.0 release 4
15. Jeong DG, Jeon WS (1999) CDMA/TDD system for wireless multimedia services with traffic unbalance between uplink and downlink. IEEE JSAC 17:939–946
16. Jeon WS, Jeong DG (2001) Call admission control for mobile multimedia communications with traffic asymmetry between uplink and downlink. IEEE Trans Veh Technol 50:59–66
17. Kim D, Jeong DG (2000) Capacity unbalance between uplink and downlink in spectrally overlaid narrow-band and wide-band CDMA mobile systems. IEEE Trans Veh Technol 49:1086–1093
18. Chau CT, Shin KG (2004) Analysis of adaptive bandwidth allocation in wireless networks with multilevel degradable quality of service. IEEE Trans Mobile Comput 3:5–17
19. Carneiro G, Ruela J, Ricardo M (2004) Cross layer design in 4G wireless terminals. IEEE Wirel Commun 11:7–13
20. Sgora A, Vergados DD (2009) Handoff prioritization and decision schemes in wireless cellular networks: a survey. IEEE Commun Surv Tutor 11:57–77
21. Katzela I, Naghshineh M (1996) Channel assignment schemes for cellular mobile telecommunication systems: a comprehensive survey. IEEE Pers Commun 3:10–31
22. Hong D, Rappaport SS (1986) Traffic model and performance analysis for cellular mobile radio telephone systems with prioritized and nonprioritized handoff procedures. IEEE Trans Veh Technol VT-35:77–92
23. Li B, Lin C, Chanson ST (1998) Analysis of a hybrid cutoff priority scheme for multiple classes of traffic in a multimedia wireless network. Wirel Netw 4:279–290
24. Lin YB, Mohan S, Noerpel A (1994) Queueing priority channel assignment strategies for PCS hand-off and initial access. IEEE Trans Veh Technol 43:704–712
25. Oh S-H, Dong-wan T (1992) Prioritized channel assignment in a cellular radio network. IEEE Trans Commun 40:1259–1269
26. Purzynski C, Rappaport SS (1993) Traffic performance analysis for cellular communication system with mixed platform types and queued handoffs. In: IEEE 43rd vehicular technology conference, pp 172–175
27. Hai X, Simon K (1994) Priority handoff analysis. Int J Wirel Inf Netw 1(2):141–148
28. Ramjee R, Towsley D, Nagarajan R (1997) On optimal call admission control in cellular networks. ACM Wirel Netw 3:29–41
29. Cruz-pérez FA, Lara-Rodríguez D, Lara M (1999) Fractional channel reservation in mobile communication system. IEE Electron Lett 35:2000–2002
30. Beigy H, Meybodi MR (2002) Uniform fractional guard channel policy. In: Proceding Sixth SCI, Orlando FL, vol 15
31. Beigy H, Meybodi MR (2004) A new fractional channel policy. J Speed Netw 13(1):25–36
32. Cruz-Pérez FA, Toledo-Marín R, Hernańdez-Valdez GH (2011) Approximated mathematical analysis methods of gurad-channel-based call admission control in cellular networks. Cellular networks-positioning. Perform Anal Reliab 151–168
33. Wong DTC, Mark JW, Chua KC (2006) Two-level fractional channels for priority access in cellular systems. In: IEEE vehicular technology conference, vol 1, pp 383–387
34. Asadur M, Chowdhury MZ, Jang YM (2015) Uniform fractional band CAC for QoS provisioning in wireless networks. J Inf Process Syst 11:583–600
35. Avila JLV, Cruz-Perez FA, Oritigoza-Guerrero L (2006) Performance analysis of fractional guard channel policies in mobile cellular networks. IEEE Trans Wirel Commun 5:301–305
36. Fang Y, Zhang Y (2002) Call admission control schemes and performance analysis in wireless mobile networks. IEEE Trans Veh Technol 51:371–382
37. Rahman MA, Hossain MA, Ahmed S, Chowdhury MZ (2014) A new guard-band call admission control policy based on acceptance factor for wireless cellular networks. In: ICIEV, pp 1–5

38. Kulavaratharasah MD, Aghvami AH (1999) Teletraffic performance evaluation of microcell personal communication networks (PCN) with prioritized handoff procedures. IEEE Trans Commun 36:137–152
39. Guérin R (1988) Queueing-blocking system with two arrival streams and guard channels. IEEE Trans Commun 36:153–163
40. Chung-Ju C, Su T-T, Yueh-Yiing C (1994) Analysis of a cutoff priority cellular radio system with finite queueing and reneging/dropping. IEEE/ACM Trans Netw 2:166–175
41. Chung-Ju C, Po-Chiun H, Su T-T (1996) A Channel borrowing scheme in a cellular radio system with guard channels and finite queues. IEEE ICC 2:1168–1172
42. Samanta RK, Bhattacharjee P, Sanyal G (2009) Performance analysis of cellular wireless network by queuing priority handoff calls. Int J Electr Electron Eng 3(8):472–477
43. Tekinay S, Jabbari B (1992) A measurement-based prioritization scheme for handovers in cellular and microcellular networks. IEEE JSAC 10:1343–1350
44. Abdulova V, Aybay I (2014) Performance evaluation of non-prioritized and prioritized call admission control schemes in wireless cellular networks. Wirel Person Commun 78:69–84
45. Ebersman HG, Tonguz OK (1999) Handoff ordering using signal prediction priority queuing in personal communication system. IEEE Trans Veh Technol 48:20–35
46. Chang RS, Leu SJ (2004) Handoff ordering using signal strength for multimedia communication in wireless network. IEEE Trans Wirel Commun 3:1526–1532
47. Younghyun K, Haneul K, Sangheon P, Wonjun L, Xuemin S (2013) Mobility-aware call admission control algorithm with handoff queue in mobile hotspots. IEEE Trans Veh Technol 2:3903-3912
48. Epstein B, Schwartz M (1995) Reservation strategies for multi-media traffic in a wireless environment. IEEE VTC 1:165–169
49. Chao C-C, Chen W (1997) Connection admission control for mobile multiple-class personal communications networks. IEEE JSAC 15:1618–1626
50. Leong CW, Zhuang W (2002) Call admission control for voice and data traffic in wireless communication. Comput Commun 25:972–979
51. Luo X, Li B, Thng I, Lin YB, Chlamtac I (2002) A measurement-based pre-assigment scheme with connection-level QoS support for multi-service mobile network. IEEE Trans Wirel Commun 1:521–530
52. Yin L, Li B, Zhang Z, Lin Y-B (2000) Performance analysis of a dual-threshold reservation (DTR) scheme for voice/data integrated mobile wireless networks. In: IEEE WCNC, vol 1, pp 258–262
53. Li B, Li LZ, Li B, Sivalingam K, Cao XR (2004) Call admission control for voice/data integrated cellular networks: performance analysis and comparative study. IEEE JSAC 22:706–718
54. Chau TC, Wong KYM, Li B (2006) Optimal call admission control with QoS guarantee in a voice/data integrated cellular network. IEEE Trans Wirel Commun 5:1133–1141
55. Ghaderi M, Bouta R (2006) Call admission control for voice/data integration in broadband wireless networks. IEEE Trans Wirel Commun 5:193–207
56. Beigy H, Meybodi MR (2004) A two threshold guard channel scheme for minimizing blocking probability in communication networks. IJE Trans B: Appl 17:247–264
57. Beigy H, Meybodi MR (2005) A general call admission policy for next generation wireless networks. Comput Commun 28:1798–1813
58. Haung YR, Lin YB, Ho JM (2000) Performance analysis for voice/data integration on a finite-buffer mobile system. IEEE Trans Vehi Technol 49:367–378
59. Li B, Li L, Li B, Cao X (2003) On handoff performance for an integrated voice/data cellular system. ACM Wirel Netw 9:393–402
60. Wang J, Zeng QA, Agrawal DP (2003) Performance analysis of a preemptive and priority reservation handoff scheme for integrated service-based wireless mobile networks. IEEE Trans Mobile Comput 2:65–75

Design of Low PDP Ternary Circuits Utilizing Carbon Nanotube Field-Effect Transistors

Nancharaiah Vejendla, Priyanka Jamanchipalli, Sreevidhya Bontha, Jahnavi Dendeti, Bhavana Bolloju, and Kishan Kumar Kuppili

Abstract The future of the electronic industry is the nanotechnology which witnessed a tremendous change in the world of electronics. To increase the performance of the silicon-based industry, there are promising alternatives which shown a greater superiority like carbon nanotube field-effect transistors (CNTFET). Multi-valued circuits (MVL) act as novel gadgets for optimizing the power. When the Ternary circuits are built with CNTFET's, we can achieve the advantages of reduction in power dissipation and increase in the speed. This paper talks much about the implementation of various logic gates, combinational circuits and sequential circuits using CNTFETs and multi-valued circuits. The proposed designs aim at decreasing the power delay product (PDP). The intended designs include ternary inverter, ternary NAND, ternary decoder, ternary half adder, ternary multiplier, ternary multiplexer and ternary full adder. We optimize the power at the basic gate level which would in turn help to reduce the power at any complex circuit we use.

Keywords Nanotechnology · CNTFET · Ternary circuits · Decoder · Multiplier · Multiplexer · Half adder · Full adder

N. Vejendla · P. Jamanchipalli · S. Bontha (✉) · J. Dendeti · B. Bolloju · K. K. Kuppili
Department of ECE, Lendi Institute of Engineering and Technology, Jonnada, Viziangaram, Andhra Pradesh 535005, India
e-mail: sreevidhyab.1999@gmail.com

N. Vejendla
e-mail: nanch84@gmail.com

P. Jamanchipalli
e-mail: jpriyanka102@gmail.com

J. Dendeti
e-mail: dendetijahnavi@gmail.com

B. Bolloju
e-mail: bhavanabolloju@gmail.com

K. K. Kuppili
e-mail: rohit.kishan487@gmail.com

G. T. C. Sekhar et al. (eds.), *Intelligent Computing in Control and Communication*, Lecture Notes in Electrical Engineering 702,
https://doi.org/10.1007/978-981-15-8439-8_21

1 Introduction

The digital technology of today's era goes round about the binary logic since the day Shannon expressed the behavior of the electrical switches. But to the researchers all around, the globe multi-valued logic (MVL) has been an inspiration. The three-valued logic popularly known as ternary logic has brought about an evolution in optimizing the power and thereby improving the efficiency of the circuits. The MVL operates in two important operating modes: voltage mode and current mode. The voltage modes are of two types: balanced mode (−Vdd, 0, Vdd); unbalanced mode (0, Vdd/2, Vdd). MVL has a wide range of applications and can be used in designing of the circuits of transistors, logic gates, memory circuits like SRAM, logic arrays (PLAs), quantum logic and wireless sensor networks (WSN).

To provide better trade-off and optimize the power, various transistor logics have been evolved. Starting the journey of transistors from BJT progressed to the world of silicon field-effect transistor (FET) like metal oxide semiconductor field-effect transistor (MOSFET), metal semiconductor field-effect transistor (MESFET) and FINFET and now diversified to CNTFET. The former paper makes use of both the CNTFET technology and ternary logic system to reduce the power delay product (PDP).

This paper uses the Hewlett Simulation Program with Integrated Circuit Emphasis (HSPICE), a modern tool for simulation. The project emphasizes the development of various logic gates like standard ternary inverter (STI), ternary NAND (TNAND), ternary decoder (TDECODER), ternary multiplier (TMUL), ternary half adder (THA), ternary full adder (TFA) and ternary multiplexer (TMUX). The designs give us optimized results as we are reducing the transistor count by using the CNTFETs and also supplying the dual power supplies, i.e., Vdd (0.9) and Vdd/2 (0.45). The proposed design helps to save the battery power as well as helps to improve the battery life. The paper is organized into the following sections: CNTFET preliminary which provides the basics of carbon nanotube field-effect transistors, while the next section deals with the existing methodologies of logic gates and various combinational circuits. Furthermore, the next section deals with the comparison and simulation results of various circuits.

2 Literature Review

The researchers Oseily and Haidar work on the multi-input floating gates using CMOS technology. They have used quaternary digital system. Their work mainly focuses on converting the hexadecimal and octal values into binary system. The major application of the paper reflects in the use of neural systems [1].

The researchers aim at developing parallel full adder. The parallel full adder was constructed using encoders and decoders. The paper focuses on optimizing the power

using a proposed technique. A 4-bit full adder was developed decreasing the power consumption and delay [2].

The development of the D latch by CNTFET transistors was proposed by two Indian researchers. The D latch was developed using inverters, NAND, NOR gates which were built using the CNTFET transistors. The authors believe that carbon nanotube is a promising alternative for the silicon transistors and reduces the delay as well [3].

The crew of researchers published a paper on the development of quaternary full adder cells using CNTFETs. There are two proposed circuits in the paper. One is developed using multiplexers which brings the results as the other circuits. The other proposed circuit is a novel circuit which brings utmost optimization which is built using the binary to quaternary and quaternary to binary converters [4].

The young researchers of India proposed two new designs of building a half adder circuit. Their aim is to build circuits with the ternary logic as it reduces the number of interconnections and reduces the chip overhead as well as chip area. The results depict that there is a decrease of about 40% in the delay and 39% in the power consumption. The designs reflect NAND_NOR implementation and transistor level implementation of three AND & one OR circuits which show impact on the efficiency [5].

The research enthusiasts made use of FINFETs to provide better energy optimization. The basic gates like the standard ternary inverter, NAND, decoder and half adder were developed using the FINs [6].

This paper underlines the development of quaternary adders and a variety of applications. The applications developed as a part of the project are the quaternary to binary and binary to quaternary converters and the development of Mod-4 adder circuits. The paper emphasizes the usage of max-min voltage logic instead of the current mode which reduces the power consumption [7].

The researchers develop novel circuits of the multiplexer and half adder and analyze the results with a resistive load. The proposed designs were made up of the ternary decoder and binary AND & OR gate and transmission gates [8].

The article underlines the use of quaternary logic system and the use of CNTFETs for building circuits. The paper states that the threshold voltage can be determined by changing the diameter of the carbon nanotube which works as an advantage. The max and min circuits were built using quaternary multiplexers and specific ternary buffers. The results speak that they have 51 and 63% reduced power delay product for Qmax and Qmin circuits [9].

The paper underlines the development of a novel architecture for ternary content addressable memory using the gate-based area efficient ternary content addressable memory cells. The proposed design has no restrictions on the size and there is also no need for the pre-processing. The proposed design utilized unique matrix combinations [10].

The authors discuss a new algorithm which was developed to translate a ternary function into equivalent classes. For a two-variable function, there are 11 equivalent classes. They found that the utility is much more for the radix—2 classes than any other. The classification of the ternary function into spectral translation equivalent

classes is prototype software. The application of the work targets at checking if two functions fall in the same equivalence class and gives a chance to interchange if needed [11].

The paper underlines the development of energy-efficient circuits for wireless sensor applications in healthcare applications. The paper depicts two new models. The first model is to develop quaternary transceiver instead of a binary one wherein it uses quaternary to binary modulator and binary to quaternary demodulator. The other model developed is the NN-SRAM, i.e., neural network SRAM. The target runs after developing of low cost storage which is well equipped by the neural networks [12].

The paper completely discusses about the benefits and energy efficiency of the CNTFET. The authors analyze many important factors like clock frequencies, metal contact resistance for various FETs like FINFET, Si/Ge nanowire FET and CNTFET. The results show that CNTFET has nine times more EDP than the others, also the resistance is better even in deeply scaled sub-nodes at 10 nm technology [13].

The authors of the paper perform a complete analysis of the simultaneous switching noise effects in multi-walled carbon nanotube bundle and Cu power interconnects in CNTFET-based ternary digital logic circuits. Using the HSPICE simulation tool, the analysis has been done for both 14 and 7 nm technologies. The results show that the CNTFET interconnects consume nearly 50% power less than the usual copper connected wires. Also, the results depict that the delay is 80% reduced with the CNTFET interconnect with respect to the copper interconnects [14].

3 CNTFET Preliminary

A promising alternative to MOSFET which is made up of silicon is the CNTFET which is made up of carbon. Need for CNTFET has come up with the drawbacks of MOSFETs like short channel consequences, huge leakage current and reliability issues which are the drawbacks of scaling of devices. CNTFET provides a high performance channel material and also the mobility characteristics are enhanced. CNTFET has the capability to drive high current. The above reasons make CNTFET the most opted solution in this nanoelectronic world.

Graphene, an allotrope of carbon, is rolled up into sheets to form carbon nanotubes. The carbon atoms are well arranged in honeycomb structure. Figure 1 depicts the two types of carbon nanotube (CNT). They are single-walled carbon nanotube and multi-walled carbon nanotube. Figure 1 depicts the different types of carbon nanotubes.

The CNT can act as a semiconductor or as a conductor. The channel of a FET is a semiconductor. To make the CNT work as channel of a field-effect transistor, CNT must act as a semiconductor. There are several factors that influence the working of the CNTFET like the chirality, threshold voltage, diameter of the carbon nanotube and the number of the tubes used. The abovementioned factors enable it to work like a CNTFET. Chirality gives the orientation of the atoms in the carbon nanotube. All the other parameters such as diameter and the limit voltage which is the treshold of

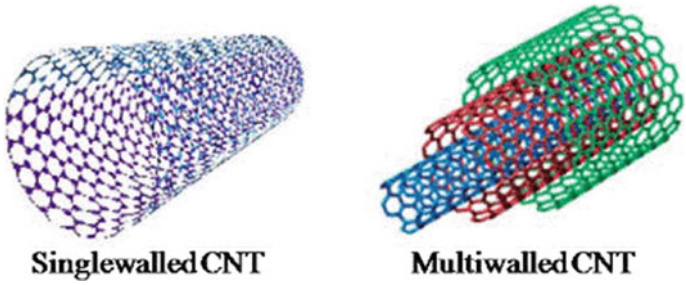

Fig. 1 Types of carbon nanotube

the CNTFET depend on the mathematical calculations of few parameters of CNT. The chiral vector is represented by Eq. 1.

$$Cj = na1 + ma2 \tag{1}$$

where Cj is the chiral vector.

$a1$, $a2$ are the vectors of the cells of CNT.

(m, n) is the integer pair.

The Eq. 1 decides whether the carbon nanotube acts as a semiconductor or a conductor. If $n = m$ (or) $n - m = 3j$, then the CNT acts as a metal, and in all the other cases, it works as a semiconductor.

The diameter (D) of the carbon nanotube FET depends on the chiral vector and is given by Eq. 2.

$$D_{\text{CNT}} = \frac{\sqrt{3} \cdot a0}{\pi} * \sqrt{n^2 + m^2 + nm} \tag{2}$$

where $a0$ is the inter-atomic distance and is usually 0.142 nm.

The threshold voltage varies with respect to the chiral vector and differs from the threshold of the MOS.

The peak voltage or the threshold of a CNTFET is represented with the Eq. 3.

$$V_{\text{TH}} = \frac{\sqrt{3}}{3} * \frac{a}{e} * \frac{V_\pi}{D_{\text{CNT}}} \tag{3}$$

where 'e' is the charge of electron,

$V\pi = 3$ eV,

'a' is the atom to atom distance and a = 2.49 Å.

CNT works as semiconductor only for a certain chiral vector pairs. The (m, n) integer pair of the three chiral vectors are: (19, 0), (13, 0), (10, 0).

4 Proposed Ternary Methodologies

In this section, we will discuss about the proposed designs of various logic gates and combinational circuits.

4.1 Ternary Logic Gates

The constituent element of any digital system is the logic gate. The logic gates can be made up of CNTFET and use ternary digital system to optimize the PDP and make an efficient building block.

4.1.1 Standard Ternary Inverter

Based on the diameter of the carbon nanotube, the inverters are classified into three types:

1. Negative ternary inverter (NTI) is a low-skew ternary inverter.
2. Positive ternary inverter (PTI) is a high-skew ternary inverter.
3, Standard ternary inverter.

Both NTI and PTI have a high speed than the STI. STI is capable of producing the intermediate level. So, STI is generally used as a basic block for all the ternary circuits. The truth index of the ternary inverter is shown in Table 1.

The chirality of the different transistors in the above circuit is: $T1$ has (19, 0); $T2$, $T4$ and $T5$ has (10, 0) and $T3$ has (13, 0) chiral integer pairs. Figure 2 depicts

Table 1 Truth index of inverters

Ternary input	NTI	PTI	STI
Logic 0	2	2	2
Logic 1	1	0	2
Logic 2	0	0	0

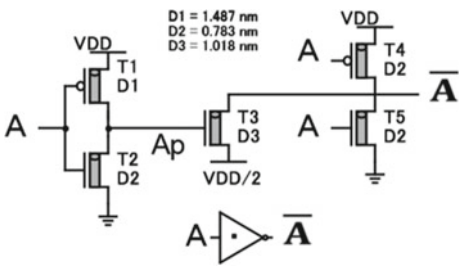

Fig. 2 Circuit diagram of ternary inverter

Table 2 Condition of various transistors

Transistor	Logic low	Logic intermediate	Logic high
$T1$	On	On	Off
$T2$	Off	Off	On
$T3$	On	On	Off
$T4$	On	Off	Off
$T5$	Off	Off	On
Output	High	Intermediate	Low

the circuit diagram of the standard ternary inverter. Table 2 depicts the condition of various transistors when given various inputs:

4.1.2 Standard Ternary Nand

NAND is a universal gate which reflects the inverted output of the AND gate. The circuit diagram of a ternary NAND is given in Fig. 3. The transistors $T1$, $T3$, $T7$, $T8$, $T9$, $T10$ use the integral pair (10,0), transistors $T5$ and $T6$ use the integral pair (13, 0) and the transistors $T2$ and $T4$ use the integral pair (19, 0) to obtain the chirality which reflects CNT to be a semiconductor. Figure 3 depicts the circuit diagram and Table 3 depicts truth table of a ternary NAND gate. Table 4 depicts the condition of various transistors at various inputs and the final input at certain inputs.

4.2 Combinational Ternary Circuits

The proposed combinational circuits in the paper include TDECODER, ternary half adder, ternary multiplier, ternary multiplexer and ternary full adder.

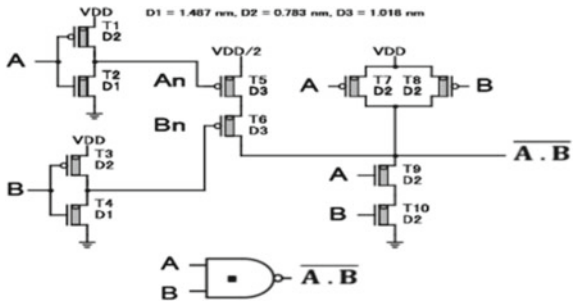

Fig. 3 Circuit diagram of ternary NAND

Table 3 Truth index of NAND

Input		Output
INPUT_1	INPUT_2	Out
L	L	H
L	I	H
L	H	H
I	L	H
I	I	I
I	H	I
H	L	H
H	I	I
H	H	L

L low, *I* intermediate, *H* high

Table 4 Condition of various transistors

Transistor	Logic low	Logic intermediate	Logic high
*T*1	On	Off	Off
*T*2	Off	On	On
*T*3	On	Off	Off
*T*4	Off	On	On
*T*5	Off	On	On
*T*6	Off	On	On
*T*7	On	Off	Off
*T*8	On	Off	Off
*T*9	Off	Off	Off
*T*10	Off	Off	On
Output	High	Intermediate	Intermediate

4.2.1 Ternary Decoder

The ternary decoder enacts a combinational circuit which is capable of producing unique outputs which when provided with n bits of information. The circuit description of the ternary decoder is shown in Fig. 4.

The truth table of a ternary decoder is depicted in Table 5 and the condition of various transistors is depicted in Table 6. Decoders are vitally used in A/D and D/A converters and in binary to decimal conversions and serve a variety of applications.

Fig. 4 Ternary decoder

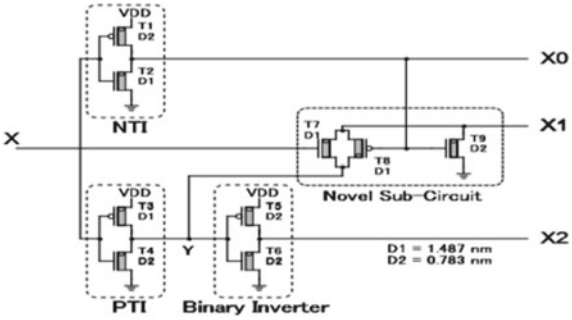

Table 5 Truth table of TDECODER

Input	Outputs		
X	*X*0	*X*1	*X*2
0	2	0	0
1	0	2	0
2	0	0	2

Table 6 Condition of various transistors

Input	Logic 0	Logic 1	Logic 2
*T*_1	On	Off	Off
*T*_2	Off	On	On
*T*_3	On	On	Off
*T*_4	Off	Off	On
*T*_5	On	Off	On
*T*_6	On	On	Off
*T*_7	Off	On	On
*T*_8	Off	On	On
*T*_9	On	Off	Off
*X*0	High	Low	Low
*X*1	Low	High	Low
*X*2	Low	Low	High

4.2.2 Ternary Half Adder

The ternary **half adder** is a digital circuit which is responsible to add two binary bits called as augend and addend and produce two outputs respectively as the sum and the carry. The half adder has been constructed using a TDECODER and a TNAND circuit and a few binary inverters and ternary inverters. The proposed system is efficient to be built just with 85 transistors which makes the model versatile to be used for the portable electronics of today's world.

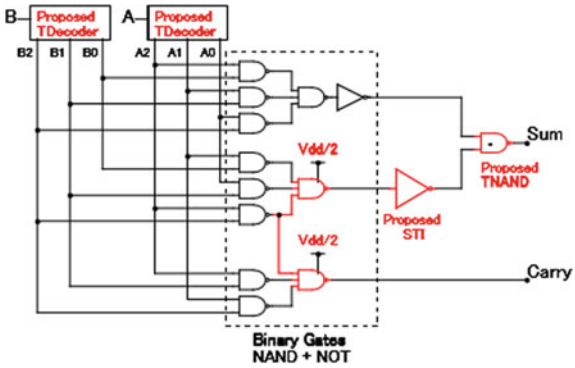

Fig. 5 Ternary half adder

Table 9 depicts the truth table of a ternary half adder. Figure 5 depicts the circuit diagram of a half adder. The carry becomes high when any of the input is at logic 1 and other at logic 2 or both the inputs are at logic 2. The sum becomes high when any one of the inputs is at logic 2 or both the inputs are at logic 1 or both the inputs are at logic 1. The sum attains logic 1 when only one of the inputs is at logic 1 or both the inputs are at logic 2.

4.2.3 Ternary Multipler

A ternary multiplier is a digital circuit which emphasizes multiplication of two bits which results in product and a carry. The multiplier serves its application in arithmetic and logical units and also in various logical circuits as a basic block.

The ternary multiplier is made of a ternary decoder, binary inverters, binary NAND gates, ternary inverter (STI) and a ternary NAND gate.

The ternary multiplier contains product and carry as the end results. The product of the multiplier is at logic high when either of the input is at logic high and the other is at logic intermediate. The product is at logic intermediate when both the inputs are at logic intermediate or at logic high. At all the rest of cases, the product is at logic Low.

The carry of the multiplier is at logic high when both the inputs are at high level, else they are at low level. Table 7 depicts the truth index of the ternary multiplier. Figure 6 depicts the circuit diagram of a half adder.

4.2.4 Ternary Full Adder

Ternary full adder is a digital circuit which sums up three input bits which emphasize the sum and carry as outputs. The three inputs comprise of the three ternary inputs which includes carry in as one of the inputs. The ternary full adder is built of two half adders and two binary NAND gates and one ternary NAND gate. The first half adder

Table 7 Truth index of ternary multiplier

Inputs		Outputs	
Input_1	Input_2	Product	Carry
L	L	L	L
L	I	L	L
L	H	L	L
I	L	L	L
I	I	I	L
I	H	H	L
H	L	L	L
H	I	H	L
H	H	I	H

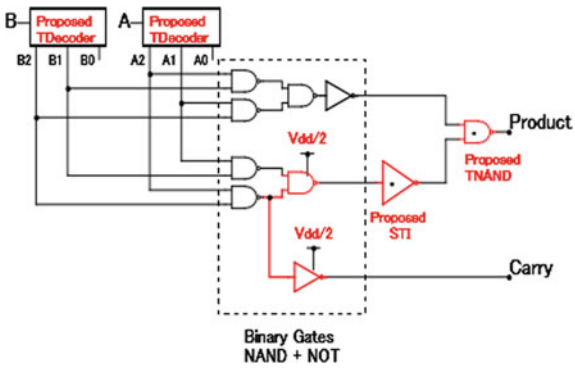

Fig. 6 Ternary multiplier

outputs are provided to the second half adder to produce the outputs. The ternary full adder truth table is depicted in Table 8. Figure 7 depicts the circuit diagram of a ternary full adder.

4.2.5 Ternary Multiplexer

Multiplexer enacts as a combinational circuit which is a data selector, i.e., it serves any one of the inputs at the output based on the selection line. Multiplexer finds its application mainly in the communication devices and in telephone networks. In the case of a ternary system (3ˆn), inputs are fed as input with n selection lines to obtain t one output.

The multiplexer is designed using a ternary decoder and a few inverters. Figure 8 depicts the circuit diagram of a ternary multiplexer. The truth table of a multiplexer is depicted in Table 10. When the selection line is at low level, then the output reflects the first input, i.e., A. When the selection line is at intermediate level, then the output

Table 8 Truth index of ternary full adder

Input			Output	
Input_1	Input_2	Input_3	sum	carry
L	L	L	L	L
L	L	I	I	L
L	L	H	H	L
L	I	L	I	L
L	I	I	H	L
L	I	H	L	I
L	H	L	H	L
L	H	I	L	I
L	H	H	I	I
I	L	L	I	L
I	L	I	H	L
I	L	H	L	I
I	I	L	H	L
I	I	I	L	I
I	I	H	I	I
I	H	L	L	I
I	H	I	I	I
I	H	H	H	I
H	L	L	H	L
H	L	I	L	I
H	L	H	I	I
H	I	L	L	I
H	I	I	I	I
H	I	H	H	I
H	H	L	L	I
H	H	I	H	I
H	H	H	H	H

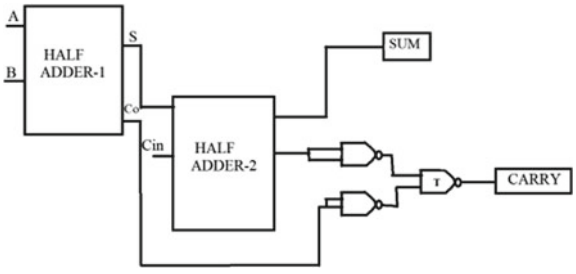

Fig. 7 Ternary full adder

Table 9 Truth index of ternary half adder

Inputs		Outputs	
Input_1	Input_2	Sum	Carry
L	L	L	L
L	I	I	L
L	H	H	L
I	L	I	L
I	I	H	L
I	H	L	H
H	L	H	L
H	I	L	H
H	H	I	H

Fig. 8 Ternary multiplexer

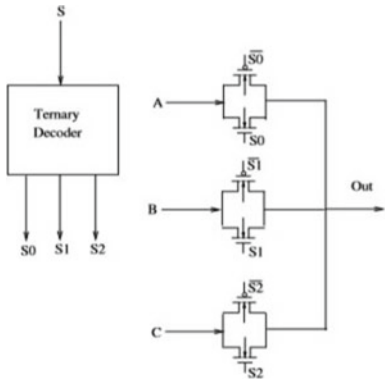

Table 10 Truth index of ternary multiplexer

Selection input	Output (out)
0	A
1	B
2	C

reflects the second input, i.e., B. When the selection line input is high, then the output reflects the third input, i.e., C.

5 Transient Response Results

The preferred circuits are extensively simulated in HSPICE software tool and transient response of the circuits is observed.

Fig. 9 Transient response of STI

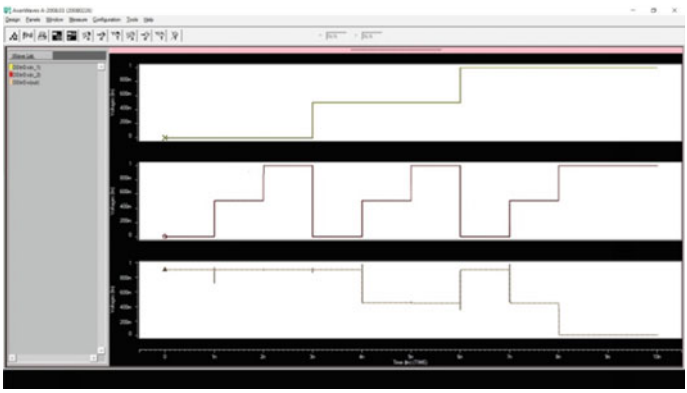

Fig. 10 Transient response of TNAND

The above pictures depict the transient response of various combinational circuits. Figure 9 depicts the transient response of ternary inverter. Figures 10 and 11 depict the transient response of ternary NAND and ternary decoder circuits, respectively. Figures 12 and 13 depict the transient response of ternary half adder and multiplier, respectively. Figures 14 and 15 depict the transient response of the ternary multiplexer and ternary full adder, respectively.

6 Extensive Simulation Reports

All the proposed circuits have been extensively simulated to analyze the ternary circuit's efficiency. The ternary circuits have undergone three types of analysis. They

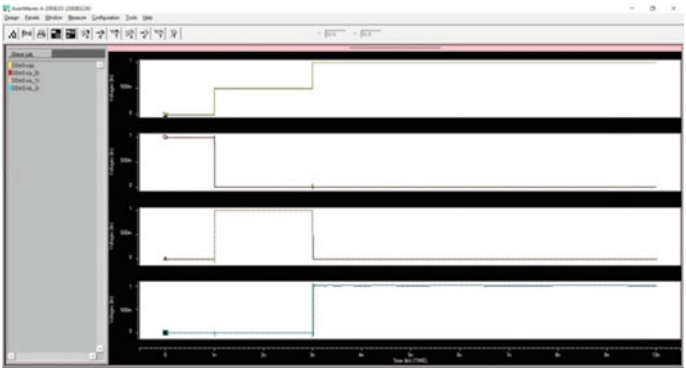

Fig. 11 Transient response of TDECODER

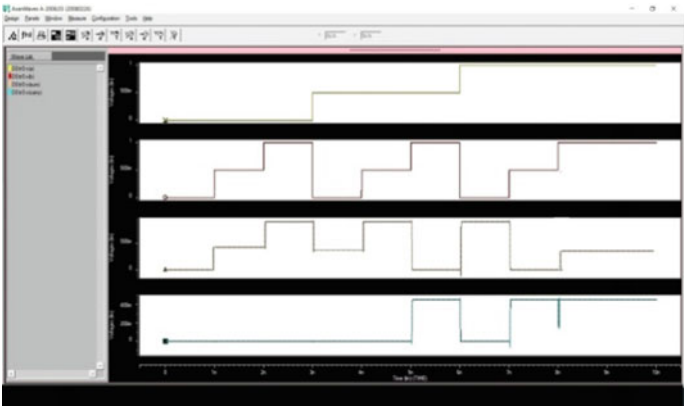

Fig. 12 Transient response of half adder

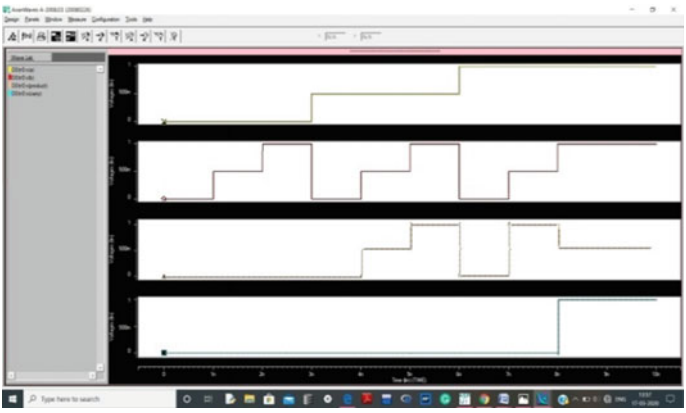

Fig. 13 Transient response of multiplier

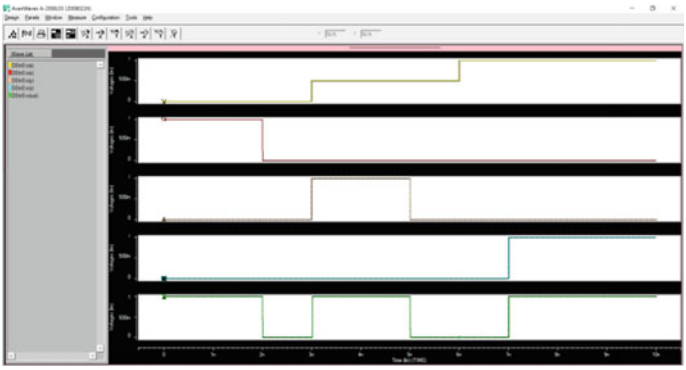

Fig. 14 Transient response of multiplexer

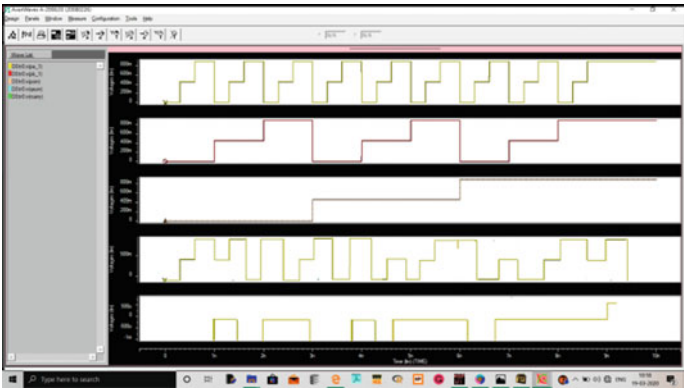

Fig. 15 Transient response of a ternary full adder

are voltage analysis, temperature analysis and frequency analysis. In voltage analysis, the circuits have been tested at various voltages like 0.8, 0.9 and 1.0 V maintaining a constant temperature at 27 °C and 1 GHz frequency. The graphs are plotted to compare the performance metrics with the power delay product (PDP). In temperature analysis, the circuits have been tested at various temperatures like 10, 27 and 70 °C maintaining a constant voltage at 0.9 V and 1 GHz frequency. The graphs are plotted to compare the performance metrics with the power delay product (PDP). In frequency analysis, the circuits have been tested at various frequencies like 0.5, 1, 2 GHz maintaining a constant voltage at 0.9 V and 27 °C temperature.

Figures, i.e., from Figs. 16, 17, 18, 19, 20, 21 and 22 depict the various simulations analysis of basic logic gates as well as combinational circuits. There are three graphs in each figure which depict three kinds of analysis starting with the voltage analysis succeeded by the temperature analysis and concluded with the frequency analysis. The reports depict the variation in the range of the power delay product.

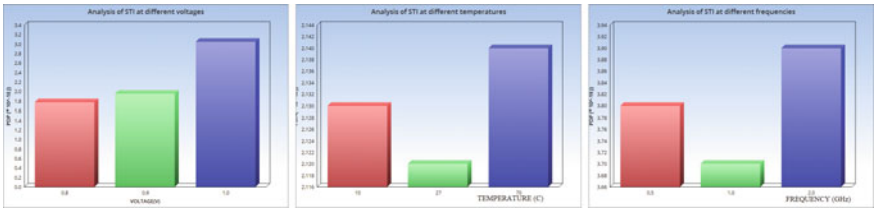

Fig. 16 Analysis of standard ternary inverter

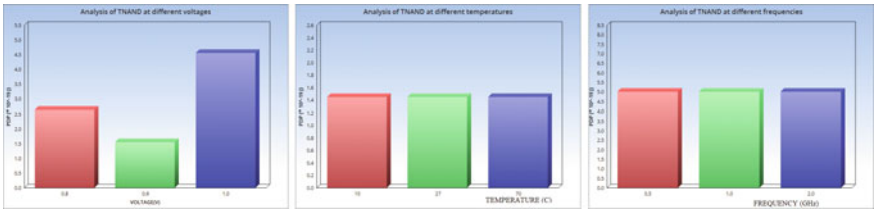

Fig. 17 Analysis of ternary NAND

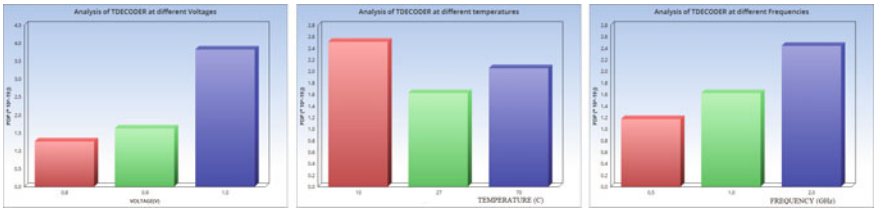

Fig. 18 Analysis of ternary decoder

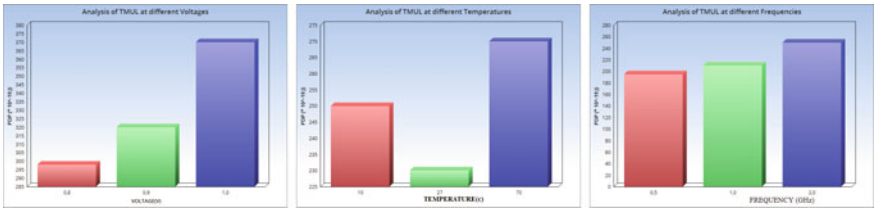

Fig. 19 Analysis of ternary multiplier

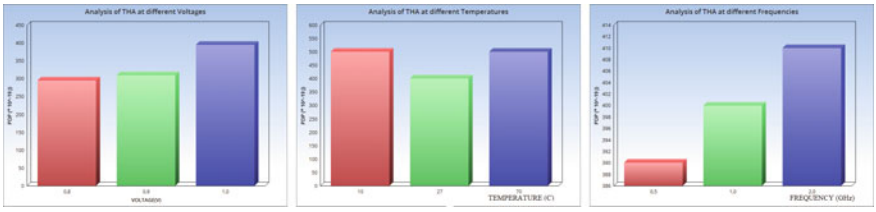

Fig. 20 Analysis of ternary half adder

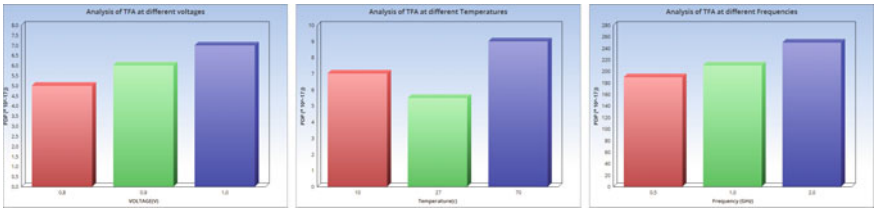

Fig. 21 Analysis of ternary full adder

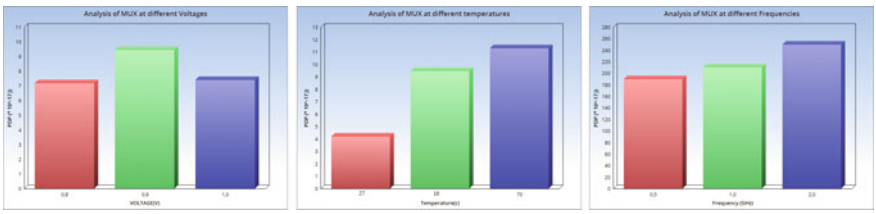

Fig. 22 Analysis of ternary multiplexer

7 Conclusion

The paper discusses about various ternary circuits which act as a basic building blocks for many applications in today's portable electronics. They not only optimize the power delay product but also reduce the area compared to that of the silicon chips. The dual power supplies, i.e., Vdd and Vdd/2, act as an added advantage to optimize the use of resources. In the world that runs with portable electronics, energy efficiency is highly needed. When we start the journey of increasing the efficiency at gate level, it increases the efficiency at the combinational circuit level, thereby improving the capability at the sequential circuits which reflects impact at the application level. The extensive simulations at various voltages, power supplies and frequencies give a scope for understanding the behavior of the circuit at various levels. Thus, the proposed circuits of this paper pave a path to create circuits with less power delay product and give a lot of future scope.

References

1. Oseily H, Haidar AM (2015) Hexadecimal to binary conversion using multi-input floating gate complementary metal oxide semiconductors. In: International conference on applied research in computer science and engineering (ICAR), Beirut, Lebanon, pp 1–6 (2015)
2. Patil M, Mahesh RK (2015) Power efficient parallel adder design using CNTFET. Int J Ethics Eng Manag Educ (IJEEE) 2(4)
3. Supriya SJ, Narkhede S (2015) Design of ternary D latch using carbon nanotube field effect transistors. In: Proceedings of 2nd international conference on electronics and communication

systems (ICECS), pp 1–9, June 2015
4. Sharifi F, Moaiyeri MH, Navi K, Bagherzadeh N (2015) Quaternary full adder cells based on carbon nanotube FETs. J Comput Electron 14(3), 762–772
5. Muglikar M, Sahoo R, Sahoo SK (2016) High performance ternary adder using CNTFET. In: 3rd international conference on devices, circuits and systems (ICDCS), Coimbatore, India
6. Jyoti K, Narkhede S (2016) An approach to ternary logic gates using FinFET. In: Proceedings of the international conference on advances in information communication technology & computing (AICTC 2016), Bikaner, India
7. Jane V, Tembhurne S (2016) Design Low Power Quaternary Adder Using Multi-Value Logic. Int J Adv Eng Technol Manag Appl Sci (IJAETMAS) 03(07):181–187
8. Samadi H, Shahhoseini A, Aghaei-liavali F (2017) A new method on designing and simulating CNTFET-based ternary gates and arithmetic circuits. Microelectron J 63:41–48. https://doi.org/10.1016/j.mejo.2017.02.018
9. Moaiyeri MH, Rahi A, Sharifi F, Navi K (2017) Design and evaluation of energy-efficient carbon nanotube FET based quaternary minimum and maximum circuits. J Appl Res Technol 15(3):233–241
10. Irfan M, Ullah Z (2017) G-AETCAM: gate-based area-efficient ternary content-addressable memory on FPGA. IEEE Access 5:20785–20790. https://doi.org/10.1109/ACCESS.2017.2756702
11. Miller D, Soeken M (2018) A spectral algorithm for ternary function classification. In: IEEE 48th international symposium on multiple-valued logic (ISMVL), Linz, Austria
12. Saleh N, Kassem A, Haidar AM (2018) Energy-efficient architecture for wireless sensor networks in healthcare applications. IEEE Access 6:6478–6486. https://doi.org/10.1109/ACCESS.2018.2789918
13. Hills G, Bardon MG, Doornbos G, Yakimets D, Schuddinck P, Baert R, Jang D, Mattii L, Sherazi SY, Rodopoulos D, Ritzenthaler R, Lee C-S, Thean A, Radu I, Spessot A, Debacker P, Catthoor F, Raghavan P, Shulaker M, Philip Wong H-S, Mitra S (2018) Understanding energy efficiency benefits of carbon nanotube field-effect transistors for digital VLSI. IEEE Trans Nanotechnol 17(6):1259–1269. https://doi.org/10.1109/TNANO.2018.2871841.
14. Khezeli MR, Moaiyeri MH, Jalali A (2019) Comparative analysis of simultaneous switching noise effects in MWCNT bundle and Cu power interconnects in CNTFET-based ternary circuits. IEEE Transact Very Large Scale Integr (VLSI) Syst 27(1):37–46. https://doi.org/10.1109/TVLSI.2018.286976.

Detection and Estimation of Multiple Point Targets for LFM Echo Using Compressed Sensing

Sudha Hanumanthu and P. Rajesh Kumar

Abstract Detection of high bandwidth linear frequency modulated (LFM) echo signal at Nyquist rate with traditional Matched Filter (MF) requires very high sampling rate that necessitates a high rate ADC which is expensive. With large amount of sampled data, storage capacity and power consumption increase. Also low resolution and range sidelobes of MF cause false alarms and masking of weak targets. Compressed Sensing (CS) enables the reconstruction of a sparse signal from a small set of measurements. In this paper, target ranges are estimated directly from compressed measurements without echo reconstruction. Receiver operating characteristic (ROC) curves for probability of detection were plotted. A comparative study is made for CS with MF in noise-free and noisy conditions. Target detection and estimation is done with just 8% of original echo samples in noise-free case and with 20% samples in noisy case of SNR = 20 dB. Also closely spaced targets could be detected with high resolution than MF. No Side lobes appear with CS and hence no false alarms can occur.

Keywords Compressed sensing · Sparsity · Matched filter

1 Introduction

In classical radar system target detection with high resolution requires transmission of a shorter pulse (reducing the average transmitted power) or wider bandwidth. Wide bandwidth requires high sampling rate which necessitates fast ADC's and also large amount of sampled data requires vast memory capacity [1]. Processing of such data results in high power consumption that drives up the cost of a system.

S. Hanumanthu (✉) · P. Rajesh Kumar
ECE Department, Andhra University College of Engineering, Visakhapatnam 530003, India
e-mail: sudha.klce@gmail.com

P. Rajesh Kumar
e-mail: rajeshauce@gmail.com

G. T. C. Sekhar et al. (eds.), *Intelligent Computing in Control and Communication*, Lecture Notes in Electrical Engineering 702,
https://doi.org/10.1007/978-981-15-8439-8_22

CS technique reduces the sampling rate much lower than Nyquist rate and compresses the signal as it is measured [2], i.e. acquisition of samples from echo and compression takes place simultaneously (unites sampling and compression) as opposed to traditional pulse compression technique that involves a MF which has limitation due to time–frequency uncertainties [3]. CS avoids the use of a MF [4]. UWB signal detection at a low sampling rate is possible with CS if the signal has sparse representation in certain space. To sparsely represent the echo signal, waveform-matched dictionary according to the prior knowledge of the transmitted signal is used [5]. In this paper point targets are detected and their ranges from transmitter are found with far fewer samples measured from received echo by exploiting target sparsity nature. Detection probability of point targets is measured and plotted by ROC curves [6]. MF and CS are compared and also the effectiveness of CS in presence of noise-free and noisy conditions is realized.

2 Theory of CS Framework

CS is the technique in which sparsity of a signal can be exploited to recover it from far fewer samples than required by Nyquist sampling theorem. CS allows sub-Nyquist sampling of sparse signals. Promise of CS is to transmit or store signals using fewer bits [7]. Sparse signal is the one with only a few non-zero values. Some signals are inherently sparse, such as images that only have a few non-zero pixel values. However CS has a wide range of applications because many signals can be made sparse through particular transform; for example, the Fourier transform of a sine wave is very sparse because the wave contains only one frequency. The two conditions under which recovery is possible are as follows [8]:

1. Sparsity, which requires the signal to be sparse in some domain.
2. Incoherence, which is applied through the isometric property and is sufficient for sparse signals. We must use a special kind of measurement matrix that satisfies restricted isometric property (RIP).

If we sample the signal y, using a matrix A, we get the smaller vector z such that $Ay = z$, z must be smaller than y, otherwise no compression of the signal has occurred. This means that the matrix A must have fewer rows (m) than columns (n) and the system is "underdetermined", having more unknowns than equations. A is $m \times n$ matrix and $m \ll n$. Reconstruction is summarized as seeking a solution to under-determined linear equation $Ay = z$, y is the sparsity coordinates and z is the compressed coordinates. The equation has infinitely many solutions, but only the one with correct sparsity, computationally though; we seek the y with the least l1-norm. The sparse representation of signal y can be reconstructed by solving the minimization problem in Eq. (1), known as Basis Pursuit (BP) [9]:

$$\min_{y} \|y\|_1 \quad \text{subject to} \quad z = Ay \tag{1}$$

2.1 Linear Frequency Modulated Signal

LFM signal is commonly used to achieve wider bandwidth since a long pulse can have same bandwidth as a short pulse if modulated in frequency or phase. A typical LFM waveform can be expressed by Eq. (2)

$$r(t) = \text{Rect}\left(\frac{t}{\tau_0}\right) e^{j(2\Pi f_0 t + C\Pi t^2)} \tag{2}$$

where the pulse width is τ_0, $C = B/\tau_0$, B is the bandwidth, f_0 is the radar center frequency, $\text{Rect}\left(\frac{t}{\tau_0}\right)$ is rectangular pulse of width τ_0.

2.2 Waveform-Matched Dictionary

In the design of waveform-matched dictionary, the prior knowledge of transmitted signal and the model of echo should be taken into consideration. An echo signal can simply be modeled as sum of scaled and shifted versions of transmitted signal, without taking into effect, the interferences like noise or Doppler shift. Let T_s be the sampling interval of echo signal. All the time shifted versions of $r(t)$ at integral multiples of T_s forms the redundant dictionary represented by $A2$ (of order $n1 \times n$) in Eq. (3)

$$A2 = r(t + j * T_s), \quad j = 1, 2, \ldots n_1 \tag{3}$$

where $n1 = n - \text{N}$, n is number of samples of composite received echo signal and N is number of samples of transmitted signal. All the individual components in $A2$ have exactly same waveform as the transmitted waveform, hence the name waveform-matched dictionary. The received echo signal of order $n \times 1$ can be described in Eq. (4)

$$H = \sum_{j=1}^{\text{nscat}} \text{rcs}_j * r\left(t + \left(\frac{2 * \text{range}_j}{c}\right)\right) \tag{4}$$

where rcs represents the receiver cross section area of target, nscat is the total number of targets and range is the location of target from transmitter. If we multiply $A2$ with received echo signal H we get a sparse signal y given by Eq. (5)

$$y = A2 * H \tag{5}$$

Now to apply CS technique, multiply received echo signal H by a sensing matrix $A1$ (of order $m \times n$), which in my case is a random Gaussian matrix (as it satisfies

RIP), given by Eq. (6).

$$z = A1 * H \tag{6}$$

Now if we replace H by $A2' * y$, we get $z = A1 * A2' * y = A * y$.

where $A = A1 * A2'$. By multiplying the sparse signal y with A makes the signal compressible, therefore z is the compressed signal with only m measurements (as we know $m \ll n$). We can now store or transmit the compressed signal with just few bits, m, which are far lesser than n bits of original echo signal.

2.3 Sparse Signal Recovery

To estimate the target information we can reconstruct the sparse signal y that contains target locations with one of the several optimization algorithms [10]. Matrix A and z values are fed to optimization algorithm. In this paper Basis Pursuit De-Noising (BPDN) algorithm which solves Eq. (7) is used as it provides better optimization with high under sampling when compared to other algorithms.

$$\min_{y} ||y||_1 \quad \text{subject to} \quad ||Ay - z||_2 \leq \varepsilon \tag{7}$$

where, ε is threshold proportional to noise variance (σ^2) given by Eq. (8).

$$\varepsilon = m * \sigma^2 \tag{8}$$

3 Probability of Detection

Signal processing system has two tasks: 1st task is to detect the presence of signal in noise. 2nd task is information extraction. Detection theory provides the foundation for 1st task i.e. it says whether target (targets in multiple target scenario) is present or only noise is present in the received signal. Estimation theory deals with 2nd task i.e. it gives information about location (range) of targets, Doppler shift etc. One cannot move to 2nd task unless 1st task is fulfilled i.e. without targets present no meaning in estimation of targets.

Detection theory implements hypothesis testing.

H0: Received signal = Noise alone

H1: Received signal = Target + Noise

Detection after MF/CS is based on whether the power or magnitude of MF/CS output is greater or lesser than threshold v_{th}, given by Eq. (9)

$$v_{\text{th}} = \sqrt{-2\sigma^2 \ln \text{pfa}} \tag{9}$$

where σ^2 is the variance of noise and pfa is the probability of false alarm which represents probability that received signal exceeds the threshold under hypothesis $H0$. Probability of detection (Pd) is the probability that received signal exceeds the threshold under hypothesis $H1$. Probability of Detection of targets is calculated and plotted by employing Marcum function, given by Eq. (10)

$$\begin{aligned} \text{Pd}_{\text{CS}} &= \text{marcum}(a_{\text{CS}}, b) \\ \text{Pd}_{\text{MF}} &= \text{marcum}(a_{\text{MF}}, b) \end{aligned} \tag{10}$$

where Pd_{CS} is the probability of detection of CS and Pd_{MF} is the probability of detection of MF, where a_{CS}, a_{MF} and b are given by Eq. (11)

$$\begin{aligned} b &= \sqrt{-2 \ln \text{pfa}} \\ a_{\text{CS}} &= \sqrt{2\text{SNR}_{\text{CS}}} \\ a_{\text{MF}} &= \sqrt{2\text{SNR}_{\text{MF}}} \end{aligned} \tag{11}$$

where output SNR of CS/MF outputs can be measured by Eq. (12), given below

$$\text{SNR} = \frac{||x||_2^2}{||x_n - x||_2^2} \tag{12}$$

where x is recovered/true signal (i.e. MF/CS output) when noise-free with exact amplitudes (rcs values) and x_n is recovered signal in presence of noise.

4 Simulation Results

The transmitted signal used is an LFM waveform with center frequency f_0 set to zero, pulse width tau of 1 μs and a bandwidth, b of 30 MHz is shown in Fig. 1.

Sampling frequency of transmitted signal Fs = 5*b gives number of samples of transmitted signal N = tau * Fs = 150. Simulations are carried out for 4 target positions set at 100 m, 103 m, 380 m and 620 m with amplitudes 1, 0.7, 0.2 and 0.8 respectively. Individuals echo signals from 4 targets is shown in Fig. 2.

Composite received echo signal with all the 4 targets when noise-free and noisy with SNR = 0 dB is shown in Fig. 3, that results into number of samples $n = 848$.

Sample ratio SR = normal sampling rate/CS sampling rate, that leads to SR = n/m, where n is number of samples of received echo and m is under sampling number of CS. Therefore new sampling rate using CS = normal sampling rate/SR.

Radar echo after sparse decomposition using BPDN algorithm for $m = 65$ (i.e. SR = 13) using CS compared to MF is shown in Fig. 4.

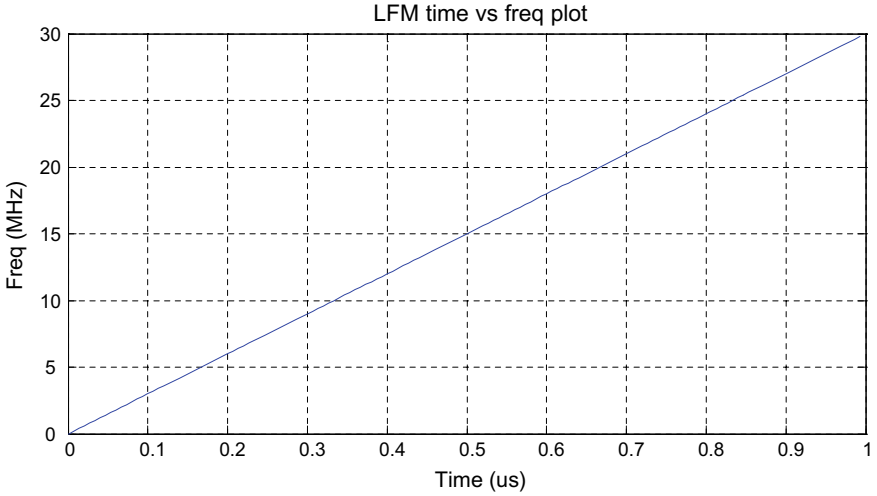

Fig. 1 LFM

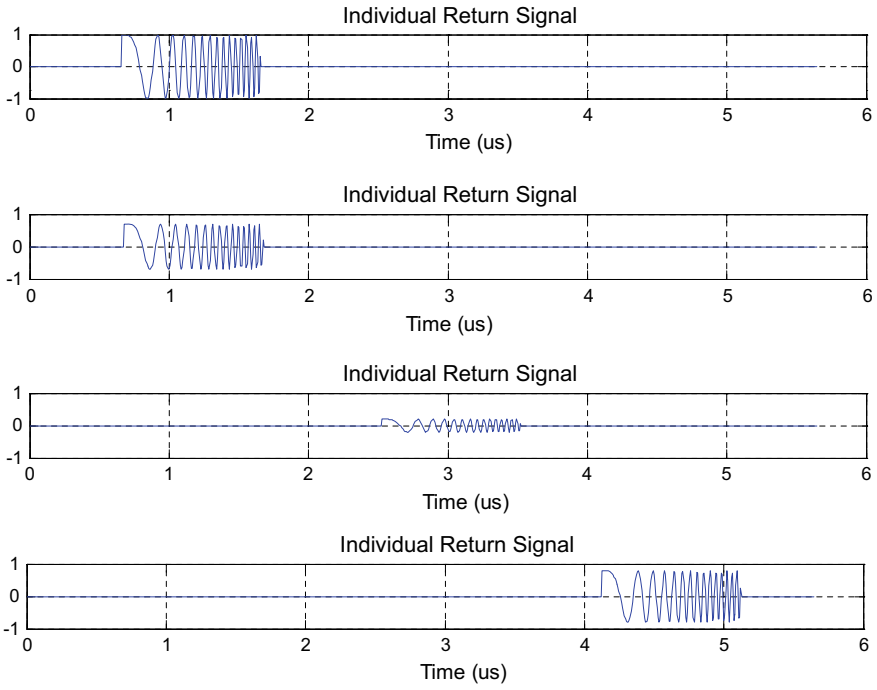

Fig. 2 Individual echo signals

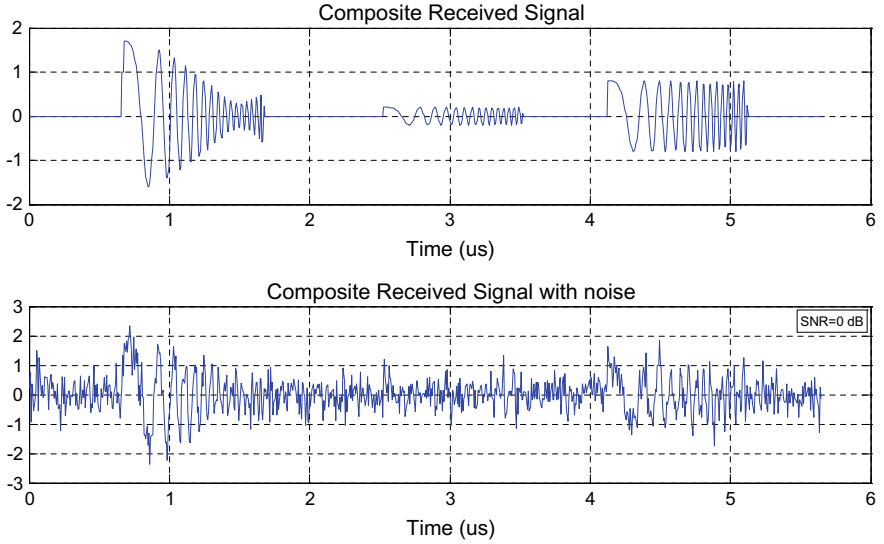

Fig. 3 Composite received echo signal

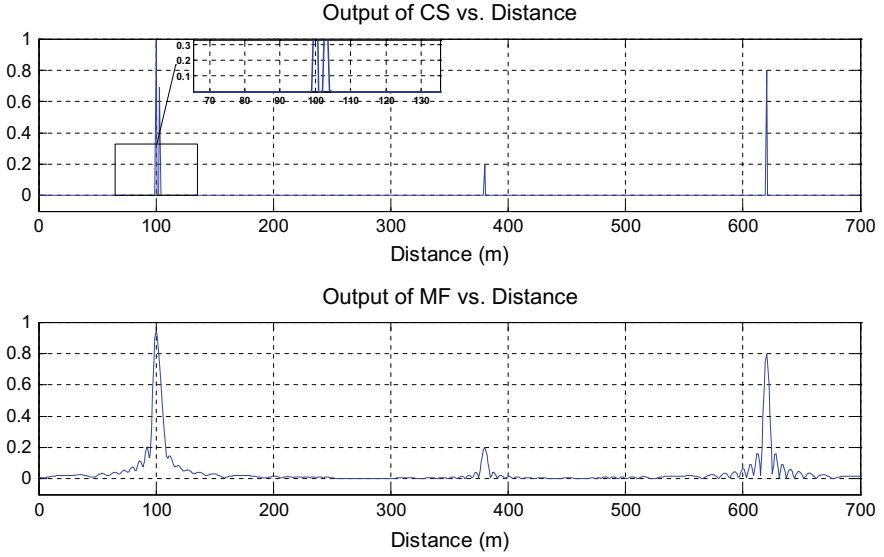

Fig. 4 Detection of targets using CS and MF

The result above shows how CS outperforms traditional MF. The observations that can be made are:

1. No Sidelobes using CS.
2. Resolution of CS is very much improved than MF i.e. main lobe width is narrower than that of MF.
3. The 2 closely spaced targets located at 100 m and 103 m are not distinguished by MF where as CS could distinguish them. Resolution $\Delta R = c/2b = 5m$. MF cannot detect targets below $\Delta R = 5m$, whereas CS could detect targets up to $3m$ i.e. below ΔR.
4. Weak target of 0.2 amplitude located at $380m$ could be detected by both CS and MF.
5. Rather than full Nyquist samples of $n = 848$ using MF, CS could estimate the targets with exact locations and amplitudes using just $m = 65$ samples (SR = 13) i.e. with an under sampling of <8% (for noise-free case).
6. New sampling rate = Fs/SR = 5*b/SR = 150 MHz/13 = 11 MHz. Therefore with CS, ADC requirement would be reduced from sampling frequency of 150 MHz to just 11 MHz.

A comparative study is made for noise-free and noisy conditions (with SNR = 20 dB) and ROC is plotted between probability of detection (Pd) versus sample ratio (SR) by performing Montecarlo simulations as shown in Fig. 5 and tabulated in Table 1. Here Gaussian noise is assumed to have added to Received echo signal and probability of false alarm taken is Pfa = 10^{-3}.

As can be observed from the above result that an under sampling of greater than 8% of samples (i.e. SR $\leq$ 13) is acceptable for 100% detection of targets for noise-free case and an under sampling of greater than 20% of samples (i.e. SR $\leq$ 5) is

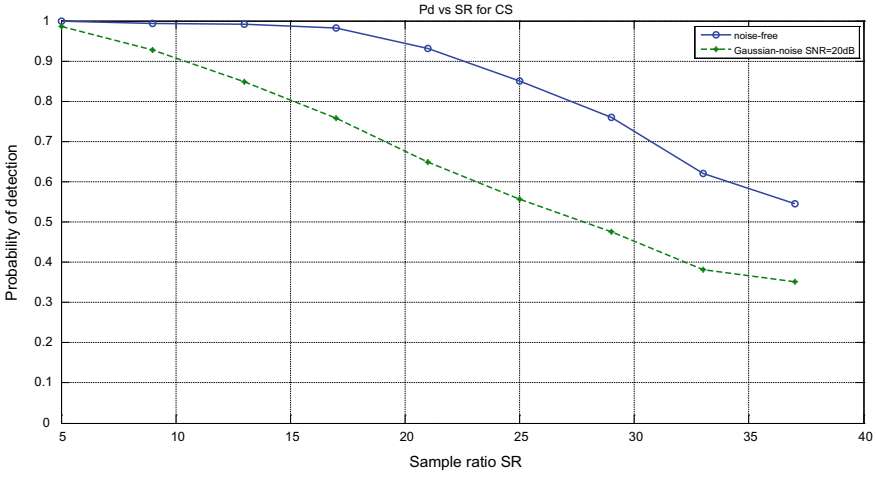

Fig. 5 Probability of detection Pd versus sample ratio SR

Table 1 Probability of detection versus sample ratio SR

SR	m	Probability of detection ($n = 848$)	
		Noise-free	Noisy (20 dB)
5	169.60	1	0.9855
9	94.22	0.9928	0.9281
13	65.23	0.9906	0.8491
17	49.88	0.9822	0.7576
21	40.38	0.9305	0.6485
25	33.92	0.8504	0.5566
29	29.24	0.7593	0.4752
33	25.69	0.6213	0.3815
37	22.91	0.5445	0.3504

acceptable for 100% detection of targets for noisy case of SNR = 20 dB. The curve also indicates that detection probabilities are higher for noise-free case.

In order to study the performance of CS and MF under high noisy condition for different cases of input SNR values output of CS and MF is observed and detection probabilities are computed which can be viewed in Table 2.

At SNR = 0 dB, MF is better compared to CS as it could better optimize noise which can be seen from Fig. 6.

The detection performance is also analyzed for CS and traditional MF and plot of Pd versus SNR is shown in Fig. 7.

Simulation results indicate that for noisy case MF could better optimize noise than CS. Therefore detection probability for MF is good compared to CS. However for SNR $\geq$ 20 dB detection probability of CS is 100% with just 8% of samples rather than full Nyquist samples of MF.

ROC of Pd versus Pfa plot is shown in Fig. 8 and values are noted in Table 3.

The above plot indicates that when SNR = 0 dB for different values of Pfa, MF has better detection compared to CS as MF could better optimize noise than CS.

Figure 9 and Table 4 give the change of number of false alarms with SNR.

Table 2 Probability of detection versus SNR

SNR	Probability of detection ($n = 848$)	
	MF	CS ($m = 65$, SR = 13)
−5	0.0880	0.0059
0	0.5829	0.0302
5	0.7497	0.1837
10	0.9321	0.3553
15	1	0.5498
20	1	0.8137
25	1	0.9893

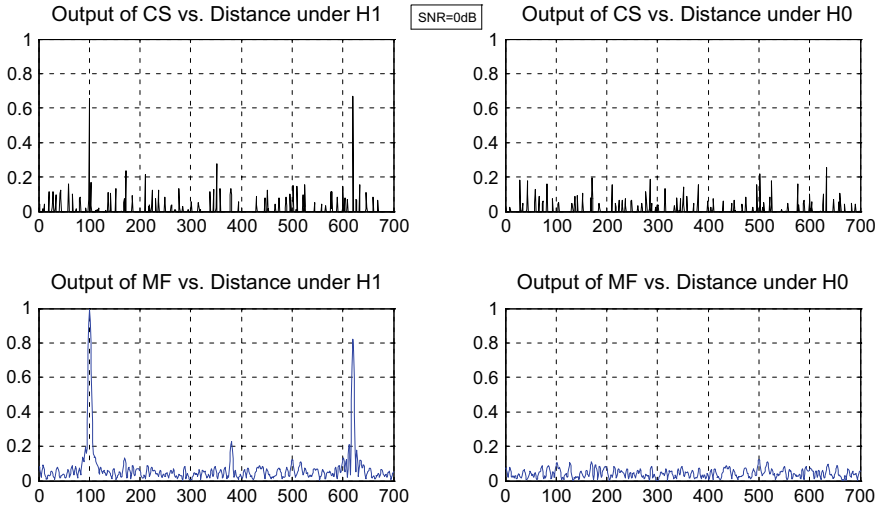

Fig. 6 Comparison of CS and MF output for SNR = 0 dB under hypothesis $H1$ and $H0$ conditions

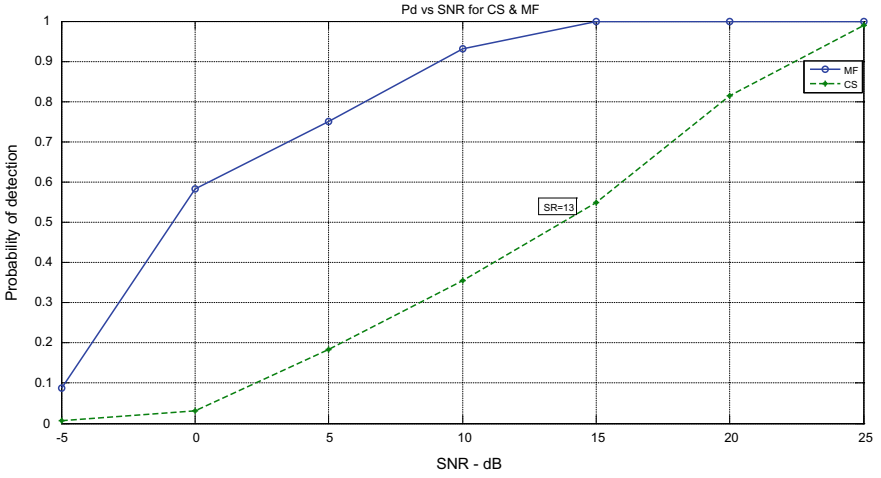

Fig. 7 Probability of detection versus SNR

For SNR = 25 dB, range estimates is computed by finding the number of peaks that exceed the threshold of 0.15 (which is slightly lesser than the weak target amplitude of 0.2 at 380 m). This resulted in: Range estimates for CS = [100 103 380 620] m and Range estimates for MF = [92 100 112 380 613 620 628] m.

This implies that all the 4 targets are correctly estimated by CS without any false alarms, whereas the closely spaced target 103 m is not estimated by MF and also 4

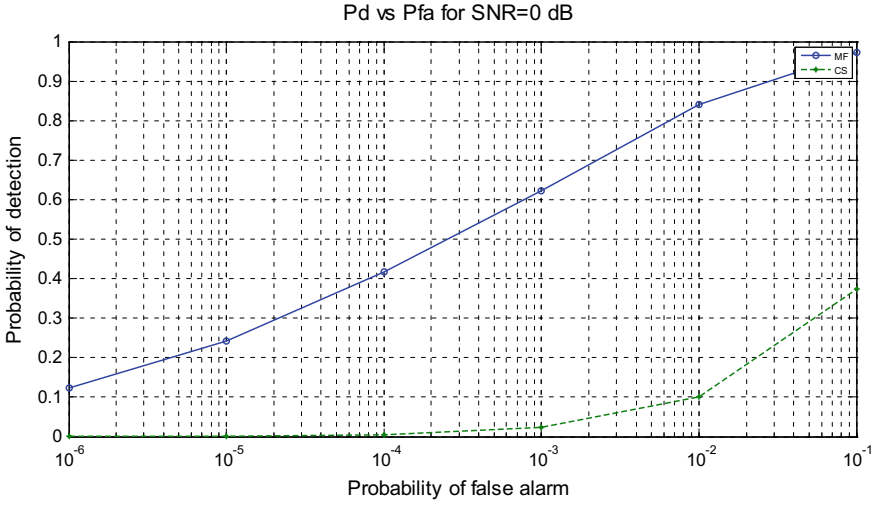

Fig. 8 Probability of detection versus probability of false alarm for CS and MF

Table 3 Probability of detection versus Pfa

Pfa	Probability of detection $n = 848$, SNR $= 0$ dB	
	MF	CS ($m = 65$, SR $= 13$)
10^{-6}	0.1225	0.0002
10^{-5}	0.2419	0.0009
10^{-4}	0.4174	0.0048
10^{-3}	0.6216	0.0229
10^{-2}	0.8405	0.1002
10^{-1}	0.9735	0.3731

false targets are identified at locations 92 m, 112 m, 613 m and 628 m. Therefore disadvantage with MF is there is a missed target along with 4 false alarms.

The above result indicates that because of the presence of sidelobes even at high SNR there are few false alarms for MF and zero false alarms for CS since no sidelobes appear for CS output.

5 Conclusion

In this paper, target ranges are estimated using compressed sensing and their probability of detection curves are plotted. A comparative study is made for noise-free and noisy conditions of both CS and MF. Results indicate that CS outperforms traditional MF approach in many ways. Using CS no sidelobes appear and hence no false

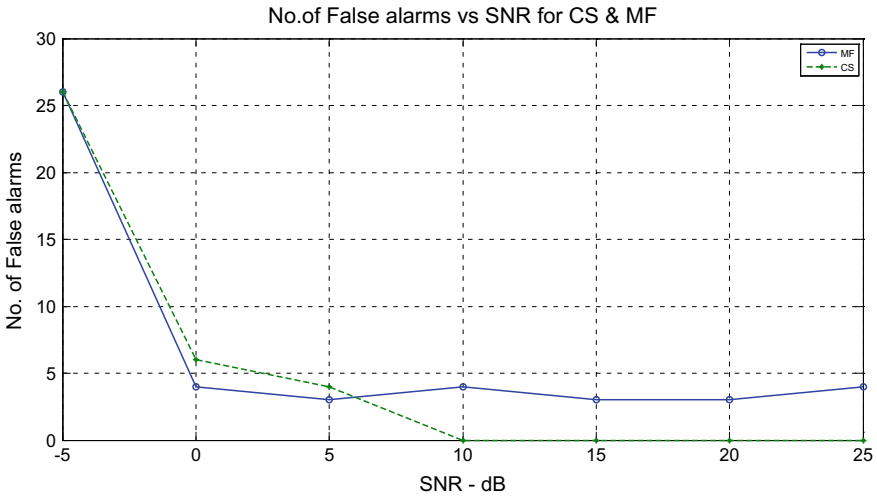

Fig. 9 No. of false alarms versus SNR for CS and MF

Table 4 No. of false alarms versus SNR

SNR	No. of false alarms	
	MF	CS ($m = 65$, SR $= 13$)
-5	26	26
0	4	6
5	3	4
10	4	0
15	3	0
20	3	0
25	4	0

alarms. Weak targets as well as close targets can be accurately estimated as resolution is improved very much. Above all CS could estimate the targets with exact locations and amplitudes using 8% of samples (SR $= 13$) for noise-free case and using 20% of samples (SR $= 5$) for noisy (SNR $= 20$ dB) case which greatly reduces the storage space and high rate ADC requirement from 150 to 11 MHz for noise-free case and to 30 MHz for noisy case.

References

1. Shen F, Zhao G, Shi G, Jin D (2011) Compressed sensing based ultra-wideband radar system. In: IEEE CIE international conference on radar, vol 2, pp 1850–1853
2. Donoho D (2006) Compressed sensing. IEEE Trans Inf Theory 52(4):1289–1306

3. Varshney LR, Thomas D (2003) Sidelobe reduction for matched filter range processing. In: Proceedings of IEEE radar conference
4. Abdul Hadi M, Alshebeili S, Jamil K, Abd El-Samie FE (2015) Compressive sensing applied to radar systems: an overview. Signal, image and video processing, vol 9, pp 25–39. Springer, Berlin
5. Shi G, Lin J, Chen X, Qi F, Liu D, Zhang L (2008) UWB echo signal detection with ultra-low rate sampling based on compressed sensing. IEEE Trans Circuits Syst II Exp Briefs 55(4):379–383
6. Anitori L, Otten M, Hoogebroom P (2011) Detection performance of compressive sensing applied to Radar. In: IEEE radar conference
7. Majumdar A (2018) Compressed sensing for engineers. CRC Press, Taylor & Francis Group. ISBN-13: 978-0-8153-6556-3.
8. Candes E, Romberg J (2007) Sparsity and incoherence in compressive sampling. Inverse Probl. 23:969
9. Candes E, Romberg J, Tao T (2006) Robust uncertainty principles: exact signal reconstruction from highly incomplete frequency information. IEEE Transact Inf Theory 52(2):489–509
10. Pope G (2009) Compressive sensing: a summary of reconstruction algorithm. Master's thesis, ETH, Swiss Federal Institute of Technology Zurich, Department of Computer Science

A Comparative Analysis of Fractional Filter PID Controller for Integrating Processes with Time Delay

R. Ranganayakulu and G. Uday Bhaskar Babu

Abstract This article deals with the performance and fragility analysis of fractional filter PID controller designed for several integrating time-delay processes. The controller performance is assessed with the variation of fractional IMC filter time constant as it greatly affects the closed-loop performance. This is achieved with the help of different performance measures. Further, the fragility analysis is accomplished for variation in the controller parameters to assess the robustness and performance of the controller. This is executed for variation in individual controller parameters. Later, the controller parameter which is affecting the robustness and performance of the controller is presented. Three examples representing three different integrating processes are considered for illustrating the performance and fragility analysis of the controller.

Keywords Performance · Robustness · Fragility

1 Introduction

Control of integrating processes is difficult as they show unbounded behavior in their output for changes in the input [1]. Extensive efforts are required for proper designing and tuning of the controller for such processes. There were several works on this topic in the literature and majority of the researchers designed integer order PID controller and its alternate forms for integrating processes [2–4]. The design of fractional controller for integrating processes has been in focus in the last decade

R. Ranganayakulu
Department of ECE, Vignan's Foundation for Science, Technology & Research (Deemed To Be University), Vadlamudi, Andhra Pradesh 522213, India
e-mail: drr_ece@vignan.ac.in

G. Uday Bhaskar Babu (✉)
Department of Chemical Engineering, National Institute of Technology, Warangal, Telangana 506004, India
e-mail: udaybhaskar@nitw.ac.in

G. T. C. Sekhar et al. (eds.), *Intelligent Computing in Control and Communication*, Lecture Notes in Electrical Engineering 702,
https://doi.org/10.1007/978-981-15-8439-8_23

[5]. However, there is little effort on the fractional controller design applying widely accepted internal model control (IMC) scheme using fractional IMC filter based on maximum sensitivity (M_s) [6, 7]. The current work concentrates on the investigation of performance [8] and fragility analysis [9] of the novel fractional filter PID (FFPID) controller created for various types of integrating systems employing higher order fractional IMC filter structures and time-delay approximation utilizing higher order Pade's procedure [10].

In this work, the system performance is analyzed for variation in the tuning parameter of the controller, i.e., fractional IMC filter time constant for identification of optimum FFPID controller. Further, the fragility analysis is done to know which controller parameter is affecting the system performance and robustness.

This article is presented as follows: Sect. 2 describes the different integrating processes and proposed controller expressions used for analysis. The performance and fragility analysis with measures used in this work are briefly presented in Sect. 3. The discussion regarding results with illustrations is in Sect. 4, and Sect. 5 concludes the article.

2 Background

The closed-loop system diagram is shown in Fig. 1. The expressions for FFPID controllers for the three integrating processes are listed in Table 1 [10].

The methods Proposed 1 to Proposed 6 are named according to the fractional IMC filter structure plus Pade's procedure for representing e^{-Ls} used in their design [10]. Proposed 1 ($((\beta s + 1/(\gamma s^{\mathrm{p}} + 1)^2) + M)$ and Proposed 2 ($((1/(\gamma s^{\mathrm{p}} + 1) + M)$ methods are the controllers designed for IPTD process; Proposed 3 ($((\beta s + 1/(\gamma s^{\mathrm{p}} + 1)^3) + N)$ and Proposed 4 ($((1/(\gamma s^{\mathrm{p}} + 1) + N)$ methods are the controllers designed for IFPTD process; Proposed 5 ($((\beta s + 1/(\gamma s^{\mathrm{p}} + 1)^3) + M)$ and Proposed 6 ($((1/(\gamma s^{\mathrm{p}} + 1)^3) + M)$ methods are the controllers designed for DIPTD process.

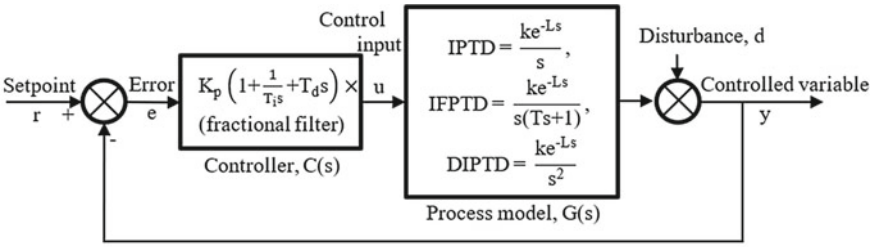

Fig. 1 Block diagram of feedback loop

Table 1 Expressions for proposed FFPID controllers [10]

Method	Controller
Proposed 1	$\left[\frac{\beta s^2+s}{(\gamma^2L^2/12)s^{2p+1}+(\gamma^2L/2)s^{2p}+(\gamma L^2/6)s^{p+1}-(\beta L^2/12)s^2+\gamma^2s^{2p-1}+\gamma Ls^p+(\beta L/2)s+2\gamma s^{p-1}+(L-\beta)}\right]$ $\left(\frac{L}{2K}\right)\left[1+\frac{1}{(L/2)s}+\left(\frac{L}{6}\right)s\right]$
Proposed 2	$\left[\frac{s}{(\gamma L^2/12)s^{p+1}+(\gamma L/2)s^p+\gamma s^{p-1}+L}\right]\left(\frac{L}{2K}\right)\left[1+\frac{1}{(L/2)s}+\left(\frac{L}{6}\right)s\right]$
Proposed 3	$\left[\frac{\beta L^3s^5+(9\beta L^2+L^3)s^4+(36\beta L+9L^2)s^3+(36L+60\beta)s^2+60s}{\gamma^3L^3s^{3p+2}+9\gamma^2L^3s^{3p+1}+3\gamma^2L^3s^{2p+2}+36\gamma^3Ls^{3p}+27\gamma^2L^2s^{2p+1}+3\gamma L^3s^{p+2}+60\gamma^3s^{3p-1}+108\gamma^2Ls^{2p}}\right.$ $\left.+27\gamma L^2s^{p+1}+(L^3-3\beta L^2)s^2+180\gamma^2s^{2p-1}+108\gamma Ls^p+(24\beta L+6L^2)s+180\gamma s^{p-1}+(60L-60\beta)\right]$ $\left(\frac{T}{K}\right)\left[1+\frac{1}{Ts}\right]$
Proposed 4	$\left[\frac{L^3s^3+9L^2s^2+36Ls+60}{\gamma L^3s^{p+2}+9\gamma L^2s^{p+1}+L^3s^2+36\gamma Ls^p+6L^2s+60\gamma s^{p-1}+60L}\right]\left(\frac{1}{K}\right)[1+Ts]$

(continued)

Table 1 (continued)

Method	Controller
Proposed 5	$\left[\frac{\beta s^3 + s^2}{(\gamma^3 L^2/12)s^{3p+1} + (\gamma^3 L/2)s^{3p} + (\gamma^2 L^2/4)s^{2p+1} + \gamma^3 s^{3p-1} + (3\gamma^2 L/2)s^{2p} + (\gamma L^2/4)s^{p+1} - (\beta L^2/12)s^2 + 3\gamma^2 s^{2p-1} + (3\gamma L/2)s^p + (\beta L/2)s + 3\gamma s^{p-1} + (L-\beta)}\right]$ $\left(\frac{L}{2K}\right)\left[1 + \frac{1}{(L/2)s} + \left(\frac{L}{6}\right)s\right]$
Proposed 6	$\left[\frac{s^2}{(\gamma^3 L^2/12)s^{3p+1} + (\gamma^3 L/2)s^{3p} + (\gamma^2 L^2/4)s^{2p+1} + \gamma^3 s^{3p-1} + (3\gamma^2 L/2)s^{2p} + (\gamma L^2/4)s^{p+1} + 3\gamma^2 s^{2p-1} + (3\gamma L/2)s^p + 3\gamma s^{p-1} + L}\right]$ $\left(\frac{L}{2K}\right)\left[1 + \frac{1}{(L/2)s} + \left(\frac{L}{6}\right)s\right]$

Note: M = 2nd Pade approximation of e^{-Ls}: $(0.0833L^2s^2 - 0.5Ls + 1)/(0.0833L^2s^2 + 0.5Ls + 1)$;

N = 2/3rd Pade approximation of e^{-Ls}: $(3L^2s^2 - 24Ls + 60)/(L^3s^3 + 9L^2s^2 + 36Ls + 60)$.

3 Performance and Fragility Analysis

The performance and fragility analysis are briefly described in the following subsections.

3.1 Performance Analysis

The measures for determining the performance and robustness used in this paper are integral absolute error (IAE/J_E); total variation (TV) and M_s (Eqs. 1–3).

$$J_E = \int_0^\infty |e(t)|\mathrm{d}t \tag{1}$$

$$\mathrm{TV} = \sum_{i=0}^{\infty} |u_{i+1} - u_i| \tag{2}$$

$$M_s = \max_{0<\omega<\infty} \left| \frac{1}{1 + C(j\omega)G(j\omega)} \right| \tag{3}$$

The performance analysis is carried out by varying the tuning parameter fractional filter time constant γ. The parameter γ is varied in steps and the measures J_E, TV and M_s are recorded for each variation in γ until the closed-loop response becomes unstable. Then, IAE versus TV and M_s graphs are plotted to identify the optimum proposed method based on trends of the plots.

3.2 Fragility Analysis

This section describes the fragility indices [9] calculated based on individual controller parameter variation based on performance (J_E) and robustness (M_s). These indices are calculated for +20% and −20% variation in each parameter of the controller.

The robustness fragility index (RFI) for controller parameter variation (Eq. 4) is

$$\mathrm{RFI}_{\delta\varepsilon p} = \frac{M_{s\delta\varepsilon p}}{M_\mathrm{s}} - 1 \tag{4}$$

where M_s is the nominal maximum sensitivity and $M_{s\delta\varepsilon p}$ is the M_s for variation in controller parameter.

The robustness fragility of the controller is determined based on the following criteria: robustness fragile if $\mathrm{RFI}_{\Delta 20} > 0.5$; robustness nonfragile if $\mathrm{RFI}_{\Delta 20} \leq 0.5$; and robustness resilient if $\mathrm{RFI}_{\Delta 20} \leq 0.1$. A resilient controller gives robust performance for +20% variation in controller parameter and if the controller is nonfragile, it is possible to derive the robust performance by retuning the controller. But a fragile controller does not allow for retuning and hence robust performance.

The performance fragility index (PFI) for controller parameter variation (Eq. 5) is

$$\mathrm{PFI}_{\delta\varepsilon p} = \frac{J_{E\delta\varepsilon p}}{J_\mathrm{E}} - 1 \tag{5}$$

where J_E is the nominal value of IAE and $J_{\mathrm{E}\delta\varepsilon p}$ is the IAE for variation in controller parameter.

The performance fragility of the controller is determined based on the following criteria: performance fragile if $\mathrm{PFI}_{\Delta 20} > 0.5$; performance nonfragile if $\mathrm{PFI}_{\Delta 20} \leq 0.5$; and performance resilient if $\mathrm{PFI}_{\Delta 20} \leq 0.1$.

4 Results and Discussion

The performance and robustness of the FFPID controller are discussed in this section with three examples representing three different integrating processes.

4.1 Example 1

The IPTD process example [4, 10] is $G(s) = \frac{0.2e^{-7.4s}}{s}$ and Table 2 presents the controller settings, nominal values of IAE, and M_s.

It is evident from Fig. 2 that the change in IAE, TV, and M_s values are small with the Proposed 1 method compared to Proposed 2 method except for one value. Hence, the Proposed 1 method ensures better performance of the closed-loop system followed by Proposed 2 method.

The RFI values and PFI values for 20% variation in each controller parameter of the two proposed methods are displayed in Figs. 3 and 4. It can be observed from Fig. 3 that the Proposed 1 and Proposed 2 controllers are robustness nonfragile for +20% variation in K_p, K_d, β and γ and hence gives robust performance after retuning the controller. The two proposed controllers are robustness resilient for +20% variation

Table 2 Controller settings and nominal performance measures for the three examples [10]

Example	Method	K_P	T_i	T_d	B	γ	p	IAE	M_s
Example 1	Proposed 1	18.5	3.7	1.23	1.1	1.78	1.02	20.86	2
	Proposed 2	18.5	3.7	1.23	–	2.54	1.02	20.82	2
Example 2	Proposed 3	20	4	–	0.2	0.16	1.02	2.78	1.98
	Proposed 4	5	–	4	–	0.25	1.02	2.95	1.98
Example 3	Proposed 5	0.5	0.5	0.17	0.6	0.3	1.02	3.13	2.01
	Proposed 6	0.5	0.5	0.17	–	0.14	1.02	3.22	2.01

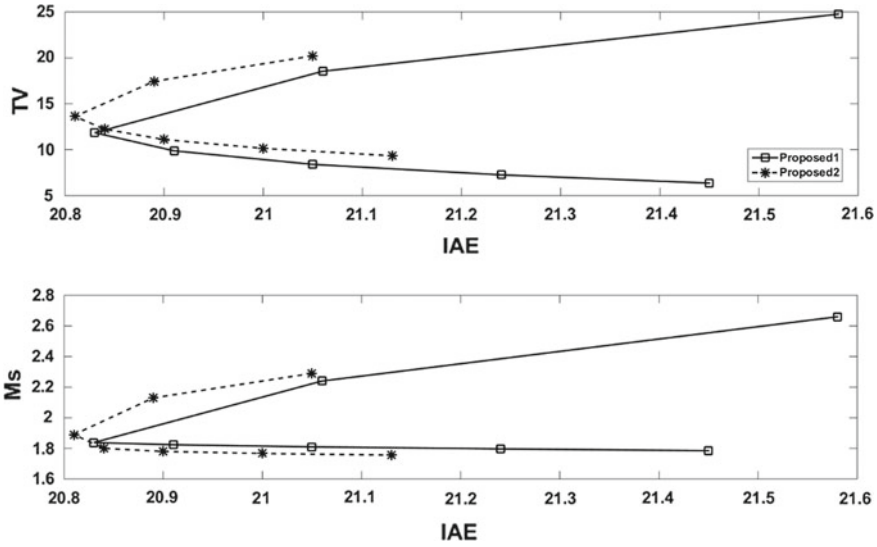

Fig. 2 IAE versus TV and M_s graphs for Example 1

in K_i ensuring robust and stable performance without retuning the controller. The Proposed 1 controller is fragile for +20% variation in p whereas Proposed 2 controller is nonfragile. Similarly, Fig. 3 shows that the proposed controllers are robustness resilient for −20% variation in K_p, K_i, K_d and β. For γ variation, the Proposed 1 controller is fragile and Proposed 2 controller is nonfragile. The two controllers are nonfragile for −20% variation in p.

The PFI values in Fig. 4 shows that the Proposed 1 controller is either performance resilient or nonfragile for +20% variation in K_p, K_i, K_d, β and γ and fragile for variation in p whereas the Proposed 2 controller is either resilient or nonfragile for + 20% change in controller parameters. The two proposed controllers are performance resilient for −20% variation in K_p, K_d, β and nonfragile for −20% variation in K_i, γ and p.

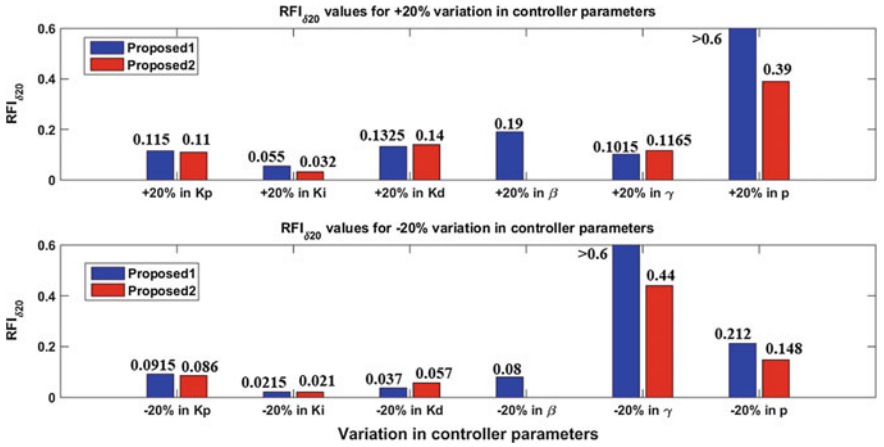

Fig. 3 Comparison of RFI values of Example 1

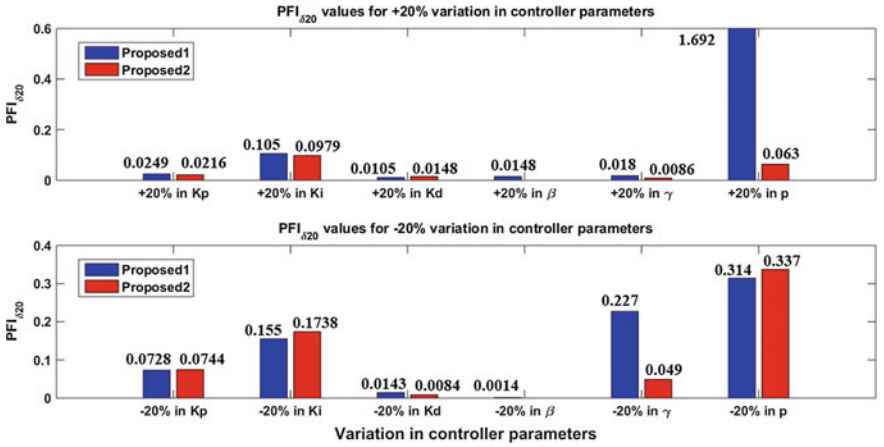

Fig. 4 Comparison of PFI values of Example 1

4.2 Example 2

The IFPTD process model [4, 10] is $G(s) = \frac{0.2e^{-s}}{s(4s+1)}$; the controller settings and the nominal values of IAE and M_s are in Table 2. It is noticed from the trends of IAE versus TV and M_s (Fig. 5) that there is superior performance of Proposed 3 method compared to Proposed 4 method with less change in IAE, TV, and M_s for variation in γ.

The Proposed 3 and Proposed 4 controllers are robustness resilient/nonfragile for +20% variation in controller parameters (Fig. 6). The above statement holds for − 20% variation except the Proposed 3 controller is robustness fragile for variation

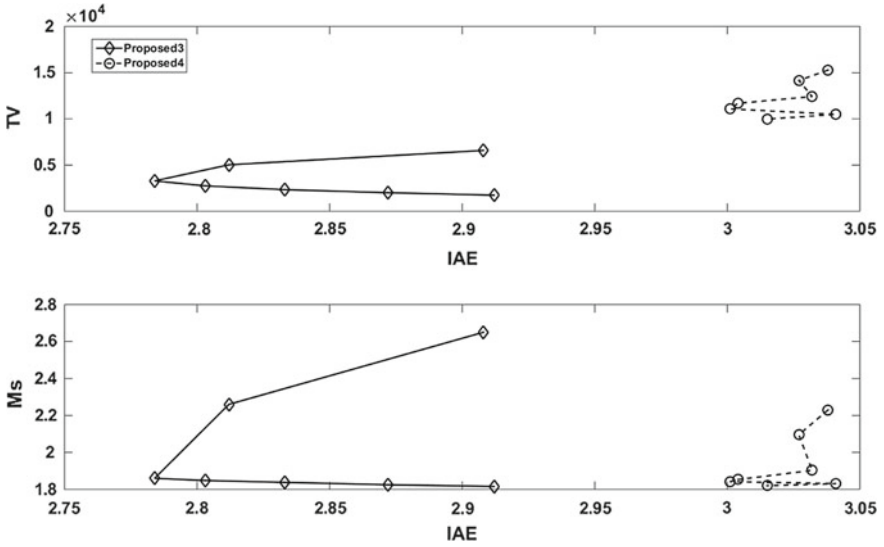

Fig. 5 IAE versus TV and M_s graphs for Example 2

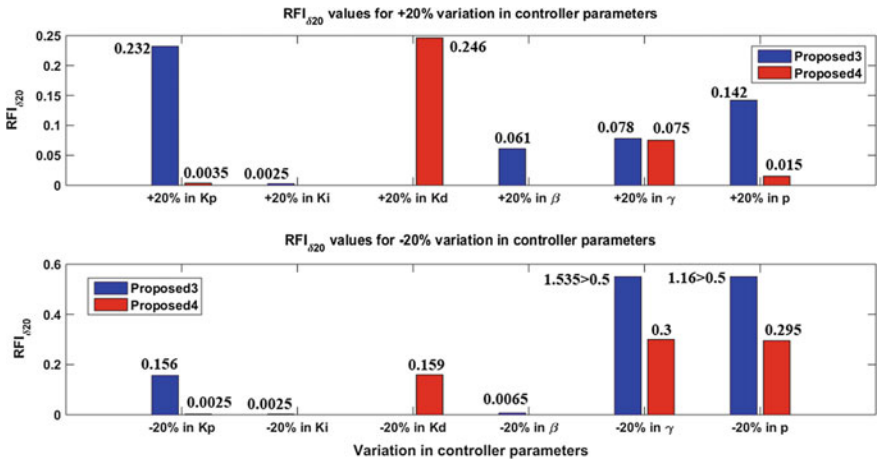

Fig. 6 Comparison of RFI values of Example 2

in γ and p. It is clear from Fig. 7 that the Proposed 3 and Proposed 4 controllers are performance resilient/performance nonfragile for $\pm 20\%$ variation in controller parameters.

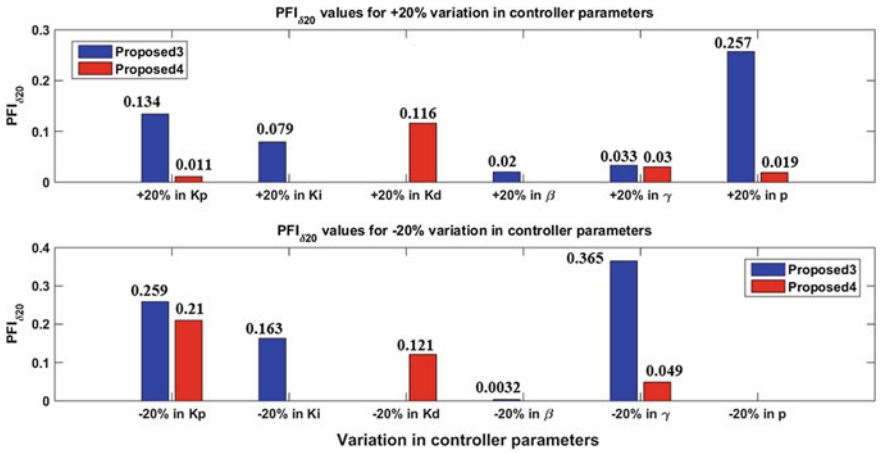

Fig. 7 Comparison of PFI values of Example 2

4.3 Example 3

The DIPTD model is $G(s) = \frac{e^{-s}}{s^2}$ and the controller settings along with nominal values of performance measures are listed in Table 2 [10].

The IAE versus TV and M_s graphs obtained after simulating the system for variation in γ is illustrated in Fig. 8. The Proposed 5 method is preferable with improved performance rather Proposed 6 method which is evident from the Fig. 8. The Proposed

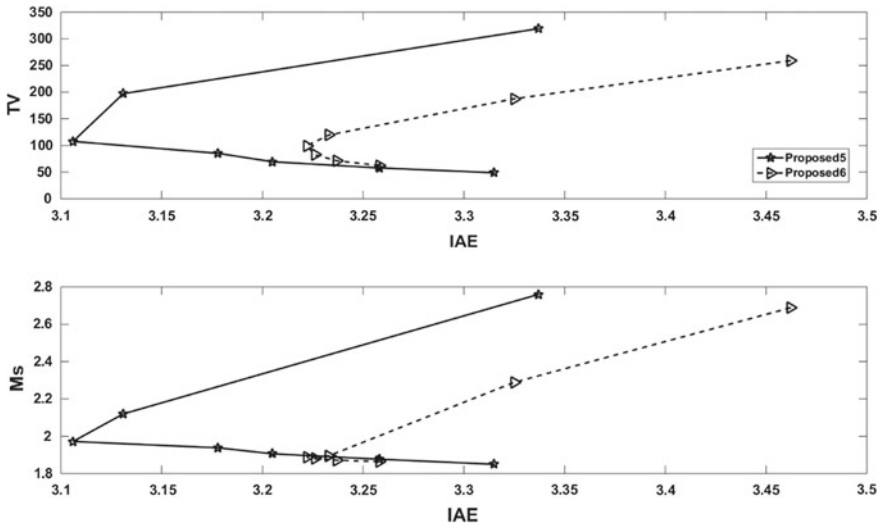

Fig. 8 IAE versus TV and M_s graphs for Example 3

5 and Proposed 6 methods are robustness resilient/robustness nonfragile (Fig. 9) for +20% change in controller settings. They are resilient for −20% variation in K_p, K_i, K_d and β. Both the methods are fragile for −20% variation in γ, whereas Proposed 5 is fragile for 20% change in p and Proposed 6 is resilient (Fig. 9). With respect to PFI values in Fig. 10, the Proposed 5 and Proposed 6 methods are resilient for ±20% variation in K_p, K_i, K_d and β. The proposed methods are resilient for +20% variation in γ and fragile for −20% variation in γ. The Proposed 5 method is fragile for + 20% variation in p and nonfragile for −20% variation and the Proposed 6 method is nonfragile for ±20% variation in p.

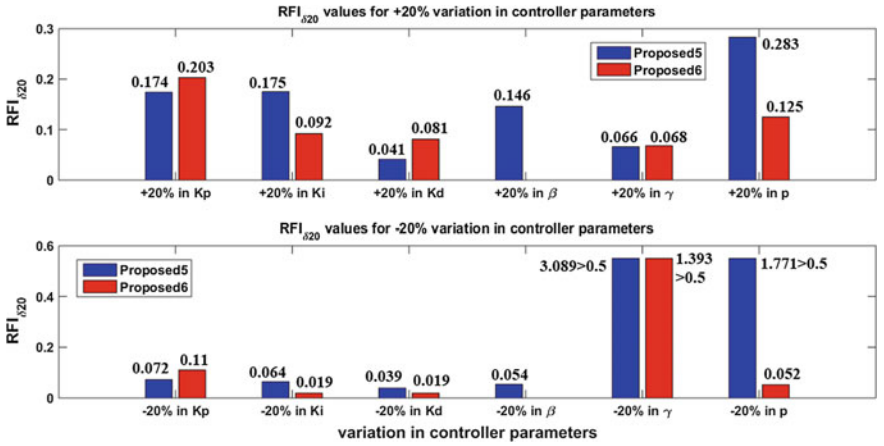

Fig. 9 Comparison of RFI values of Example 3

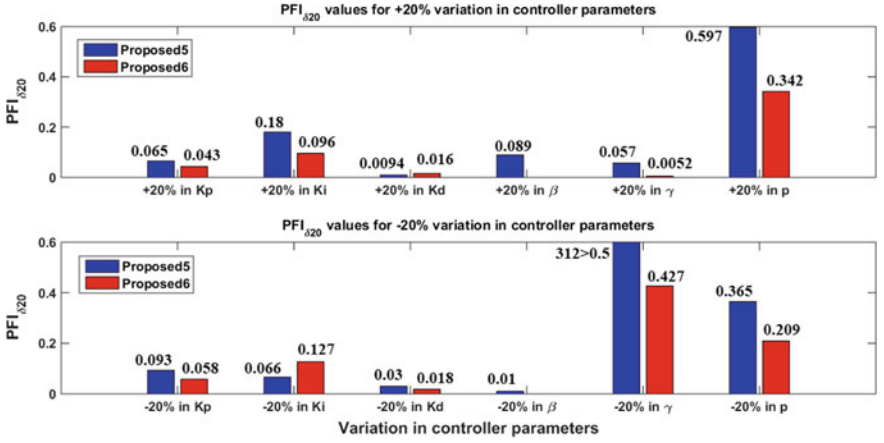

Fig. 10 Comparison of PFI values of Example 3

5 Conclusion

The performance and robustness of FFPID controller designed for different integrating processes are presented through performance and fragility analysis. It is found that the Proposed 1, Proposed 3, and Proposed 5 methods are giving better performance compared to Proposed 2, Proposed 4, and Proposed 6 methods for variation in tuning parameter. The proposed controllers are found to be resilient or nonfragile with respect to robustness and performance for $\pm 20\%$ variation in K_{p}, K_{i}, K_{d} and β. The FFPID controllers produced using higher order fractional IMC filter structures are mostly becoming fragile for -20% variation in γ and p with respect to robustness and rarely with respect to performance. Hence, care should be taken while choosing the parameters γ and p as they affect the robust closed-loop performance.

References

1. Rice B, Cooper D (2002) Design and tuning of PID controllers for integrating (non-self regulating) processes. Techn Pap ISA 422:437–448
2. Vilanova R, Visioli A (2012) PID control in the third millennium. Springer, London
3. Jin QB, Liu Q (2014) Analytical IMC-PID design in terms of performance/robustness tradeoff for integrating processes: from 2-Dof to 1-Dof. J Process Control 24(3):22–32
4. Kumar DS, Sree RP (2016) Tuning of IMC based PID controllers for integrating systems with time delay. ISA Trans 63:242–255
5. Padula F, Visioli A (2015) Advances in robust fractional control. Springer, Chum
6. Maâmar B, Rachid M (2014) IMC-PID-fractional-order-filter controllers design for integer order systems. ISA Trans 53(5):1620–1628
7. Bettayeb M, Mansouri R (2014) Fractional IMC-PID-filter controllers design for non-integer order systems. J Process Control 24(4):261–271
8. Ranganayakulu R, Babu GUB, Rao AS, Patle DS (2016) A comparative study of fractional order PI/PID tuning rules for stable first order plus time delay processes. Resour Efficient Technol 2:S136–S152
9. Alfaro VM (2007) PID controllers' fragility. ISA Trans 46(4):555–559
10. Ranganayakulu R, Rao AS, Babu GUB (2019) Improved fractional filter IMC–PID controller design for enhanced performance of integrating plus time delay processes. Indian Chem Eng 1–18

Design of Dumbbell-Shaped MIMO Antenna for Wearable Applications

B. Ramamohan, S. Usha, P. Ananth, V. Sai Lalitha, and S. Jaswanth

Abstract A wearable textile wideband multi-input and multi-output (MIMO) antenna for wireless communication with low mutual coupling and better isolation is presented in this paper. This design consists of three rectangular copper patches on the front side and dumbbell-shaped stub on the ground which gives high port-to-port isolation and operated in the frequency spectrum from 2 to 8 GHz with a maximum gain of 6.5 dB. The minimum isolation is 38.55 dB at 4.32 GHz and 60.4791 dB is maximum isolation achieved at 4.8 GHz. The envelope correlation coefficient and diversity gain of the MIMO antenna are given by 0.001729 and 10 dB, respectively, which are operated in c-band which is used for many satellite communication transmissions, some Wi-Fi devices as well as surveillance and weather radar systems. This modern epoch demands low power and high data requirements so that designing of a MIMO antenna becomes essential.

Keywords Wearable antenna · Multi-input and multi-output (MIMO) antenna · Textile antenna · Dumbbell-shaped stubs · Mutual coupling · Port-to-port isolation and diversity gain (DG)

B. Ramamohan (✉) · S. Usha · P. Ananth · V. S. Lalitha · S. Jaswanth
Department of ECE, Lendi Institute of Engineering and Technology, Jonnada, Viziangaram 535005, India
e-mail: ramamohanmailid@gmail.com

S. Usha
e-mail: sunkariusha98@gmail.com

P. Ananth
e-mail: ananth.penta@gmail.com

V. S. Lalitha
e-mail: sailalithavadavalli98@gmail.com

S. Jaswanth
e-mail: jaswanths.yadav@gmail.com

G. T. C. Sekhar et al. (eds.), *Intelligent Computing in Control and Communication*, Lecture Notes in Electrical Engineering 702,
https://doi.org/10.1007/978-981-15-8439-8_24

1 Introduction

Wearable antenna has more demand in terms of high performance, simplicity, robustness, and less operating power. It should provide safe power levels to be operated with other interfacing devices. This special purpose antenna configured to interface freely with several sensor elements inside and outside of the body and with these wireless wearable devices we have so many applications in military and health care. The wearable antenna design depends on cloth material, reflection, radiation, efficiency, and also on cloth material which is located on the body. A compact wearable MIMO antenna consists of patches and dumbbell-shaped antenna on the ground plane given the mutual coupling less than 17 dB and reflection coefficient less than 10 dB with operating frequency 2.8–8 GHz [1]. Antenna with a good isolation 30 dB with operating frequency 2.5 GHz can be achieved by designing with electric and magnetic fields [2]. Mutual coupling of an MIMO antenna can be reduced by using different parameters of dumbbell-shaped antenna [3]. To achieve better isolation, novel dumbbell-shaped MIMO antenna array for three inputs for wireless applications is implemented which gives the return loss of 10 dB for 2.45–5.8 GHz and isolation lower than 27 dB at 2.45 GHz and 28 dB at 5.8 GHz [4]. A slotted pattern etched into a single ground plane achieves the isolation more than 20 dB [5]. By introducing a coupling element, we can enhance the coupling factor of a MIMO antenna. For this purpose, a coupling element is placed between antenna elements which results gain more than 30 dB [6]. A canonical two-port MIMO antenna with arbitrary even number of ports has been proposed which is operated in the frequency of 2.6 GHz with a bandwidth of 100 MHz [7]. Three or more than three polarized MIMO antennas can effectively increase the capacity of channel in wireless communication systems which is having operating frequency at 2.4 GHz and achieves isolation less than 17 dB [8]. To diminish the mutual coupling parameter, further a multi-layered structure is designed by placing more substrates integrated cavity slot antenna elements having operating bandwidth 2.396–2.45 GHz [9]. Three ports are placed on a substrate and feeding network, with a required antenna design placed on ground plane results a dumbbell-shaped antenna with operating frequency 3–6 GHz and the three ports are extremely isolated and fine matched [10]. Thus, the designing of wearable wideband MIMO antennas with better gain, better isolation, less mutual coupling, and maximum port-to-port isolation is very important.

2 Antenna Structure and Designing

The objective of this paper is to design a MIMO antenna with less mutual coupling and maximum port-to-port isolation. So, here we are examining three antennas with different structures.

1. Triple patch MIMO antenna without any stub on ground
2. Triple patch MIMO antenna with only one dumbbell-shaped stub on the ground

Fig. 1 Arrangement of MIMO antenna front view

3. Triple patch MIMO wearable antenna with double dumbbell twisted stub on ground

2.1 Designing of Triple Patch MIMO Antenna Without Any Stubs on Ground

The face view of this proposed antenna is shown in Fig. 1. This special structure consists of three rectangular copper patches on the substrate. The back of this antenna is shown in Fig. 1b which consists of ground only. The gain of this antenna is 4.3 dB which is operated in the frequency spectrum from 2 to 8 GHz. The minimum isolation of this antenna is 21.74320 dB at 4.48 GHz and maximum isolation is 26.440 dB at 4.6800 GHz. The Envelope correlation coefficient of this antenna is given by 1 with diversity gain 0 dB.

2.2 Designing of Triple Patch MIMO Antenna with Single Dumbbell-Shaped Stub on Ground

The top view of the MIMO antenna with single dumbbell-shaped stub on the ground is shown in Fig. 2. The back of this antenna is shown in Fig. 2c which consists of ground with single dumbbell-shaped stub with acts as a waveguide. The gain of this antenna is 5.4 dB which is operated in the frequency spectrum from 2 to 8 GHz. The minimum isolation of this antenna is 29.99 dB at 4.149 GHz and maximum isolation is 48.3664 dB at 4.3601 GHz. The envelope correlation coefficient of this antenna is given by 0.03120 with diversity gain of 9.995 dB.

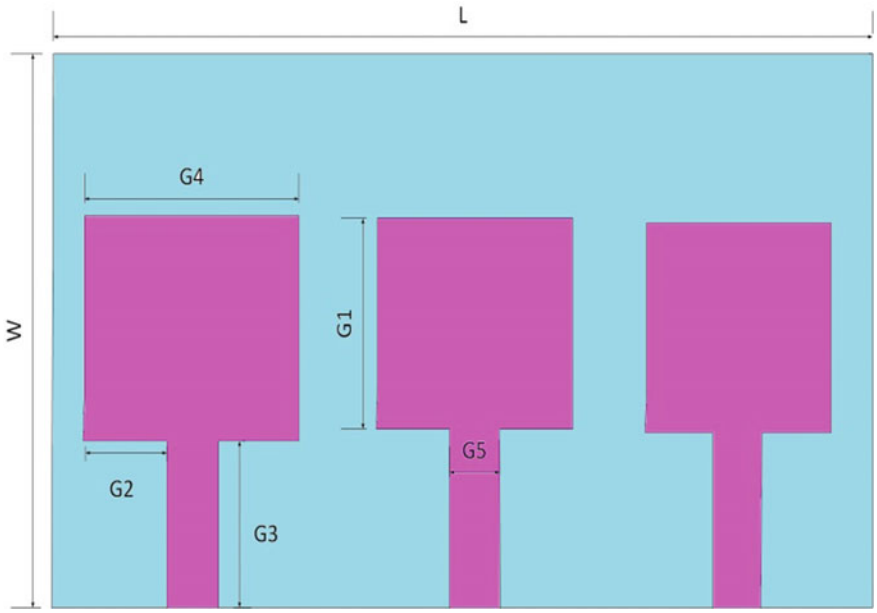

Fig. 2 Back view without any stub on ground

2.3 Designing of Triple Patch MIMO Antenna with Double Dumbbell-Shaped Stub on the Ground

After the simulation of a simple MIMO antenna with single stub on ground, we further implemented it as double stub on ground in order to achieve the better bandwidth requirements. By placing the dumbbell-shaped stub on ground with some gap, we can create an inductive and capacitive environment which results an equivalent stop band filter. This, this dumbbell-shaped stub reduces the current flow from excited port to coupled port on MIMO operated in the frequency spectrum from 2 to 8 GHz. The minimum isolation of this antenna is 38.554 dB at 4.3200 GHz and maximum isolation is 60 dB at 4.800 GHz. The envelope correlation coefficient of this antenna is given by 0.00729 with diversity gain of 10 dB which is shown in Fig. 3. The dimensions for designing above three antennas are shown in Table 1.

3 Simulation

Figure 4 shows the *S* parameters plot of the triple patch antenna without any stub on ground. It consists of *S*11, *S*12, *S*13, *S*21, *S*22, *S*23, *S*31, *S*32, *S*33 parameters. Here, *S*11, *S*22, *S*33 represents reflection coefficient and *S*12, *S*13, *S*23 represents port-to-port isolation of this antenna. The frequency spectrum of this antenna is from

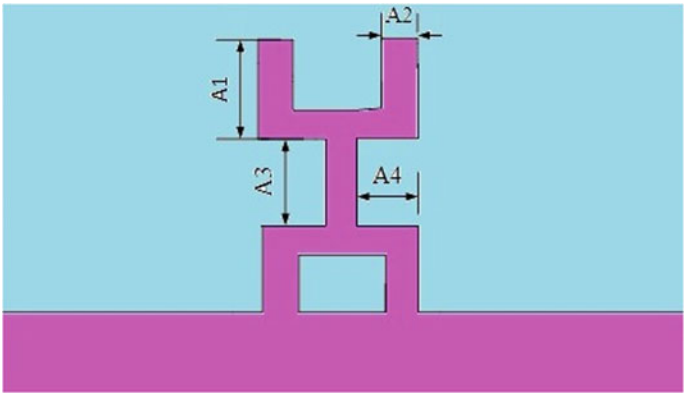

Fig. 3 Back view with single dumbbell stub on ground

Table 1 Dimensions of designed MIMO antenna

Parameters	Dimensions (mm)	Parameters	Dimensions (mm)
L	120	*A*2	4
W	80	*A*4	10
H	10	*U*1	4
d	6	*U*2	10
*G*1	40	*U*3	4
*G*2	15	*U*4	9
*G*3	20	*U*5	14
*G*4	30	*U*6	4
*G*5	10	*U*7	14
*A*1	14		

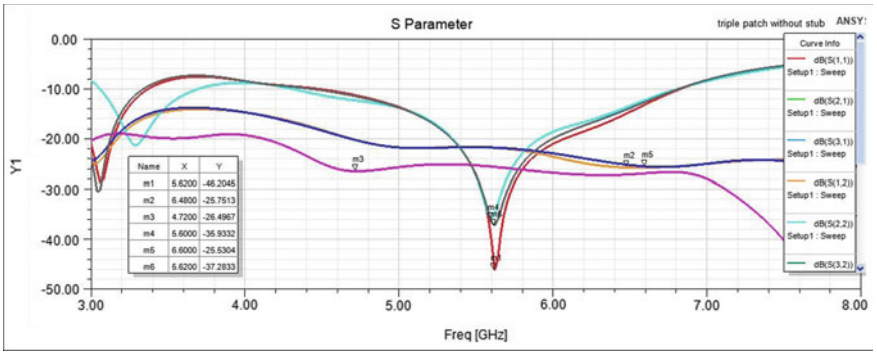

Fig. 4 Scattering parameters of triple patch MIMO antenna without any stub on ground

2 to 8 GHz. The minimum isolation of this antenna is 21.74320 dB at 4.48 GHz and maximum isolation is 26.440 dB at 4.6800 GHz. The envelope correlation coefficient of this antenna is given by 1 with diversity gain 0 dB.

Figure 5 shows the *S* parameters plot of the triple patch MIMO antenna with single dumbbell-shaped stub on ground. The frequency spectrum of this antenna is from 2 to 8 GHz. The minimum isolation of this antenna is 29.99 dB at 4.1449 GHz and maximum isolation is 48.366 dB at 4.3601 GHz. The envelope correlation coefficient of this antenna is given by 0.03120 with diversity gain 9.995 dB.

Figure 6 shows the *S* parameters plot of double dumbbell-shaped stub on ground. The MIMO antenna with double dumbbell-shaped stub on ground gives the gain of 6.5 dB with mutual coupling 0.001729 and minimum isolation 38.55 dB achieved at 4.32 GHz and maximum isolation 60.47 dB at 4.8 GHz with operating frequency 2 to 8 GHz.

3.1 Results with Explanations

Figure 7 shows the 3D polar plot and radiation pattern of triple patch MIMO antenna without any stub on ground and single dumbbell-shaped stub on ground.

The gain of simple antenna is given by 4.3 dB which is shown in Fig. 7. This is implemented by using HFSS software. Calculated gain values at frequency 5 GHz and at different phase values −168°, −170°, −172°, −174°, −178°, −18°, respectively.

Figure 8 shows the 3D polar plot and radiation pattern of triple patch MIMO antenna with single dumbbell-shaped stub on ground. The gain of simple antenna is given by 5.4 dB which is shown in Fig. 8. This is implemented by using HFSS software. Calculated gain values at frequency 5.92 GHz and at different phase values −168°, −170°, −172°, −174°, −178°, −180°, respectively, are shown in different colors in Fig. 6.

Figure 9 shows the 3D polar plot and radiation pattern of triple patch MIMO antenna with double dumbbell-shaped stub on ground. The gain of MIMO antenna with double dumbbell-shaped stub on ground is given by 6.5 dB. This is implemented by using HFSS software. Calculated gain values at frequency 5 GHz and at different phase values −168°, −170°, −172°, −174°, −178°, −180°, respectively, are shown in different colors in Fig. 7.

Table 2 shows the comparison of MIMO antenna without, with single dumbbell, and with double dumbbell antennas on the ground. So, based on that, we can conclude that by placing the stubs on ground we can change the some parameters of the antenna. Based on the shape of the stub, we can improve some important parameters like mutual coupling, isolation, and diversity gain of the MIMO antenna.

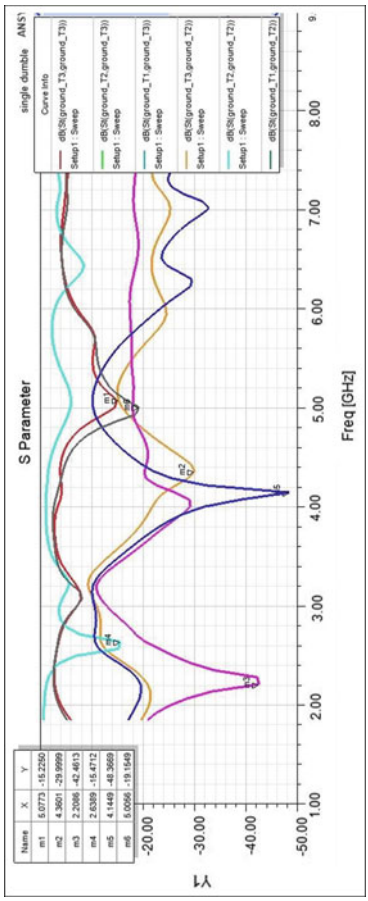

Fig. 5 Scattering parameters of triple patch MIMO antenna with single dumbbell-shaped stub on ground

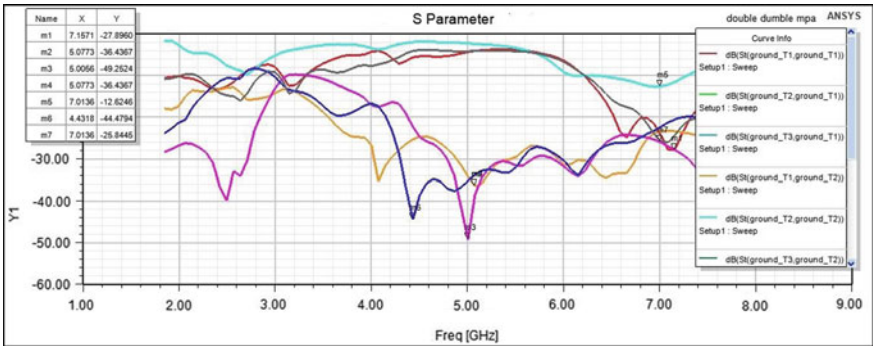

Fig. 6 Scattering parameters of triple patch MIMO antenna with double dumbbell-shaped stub on ground

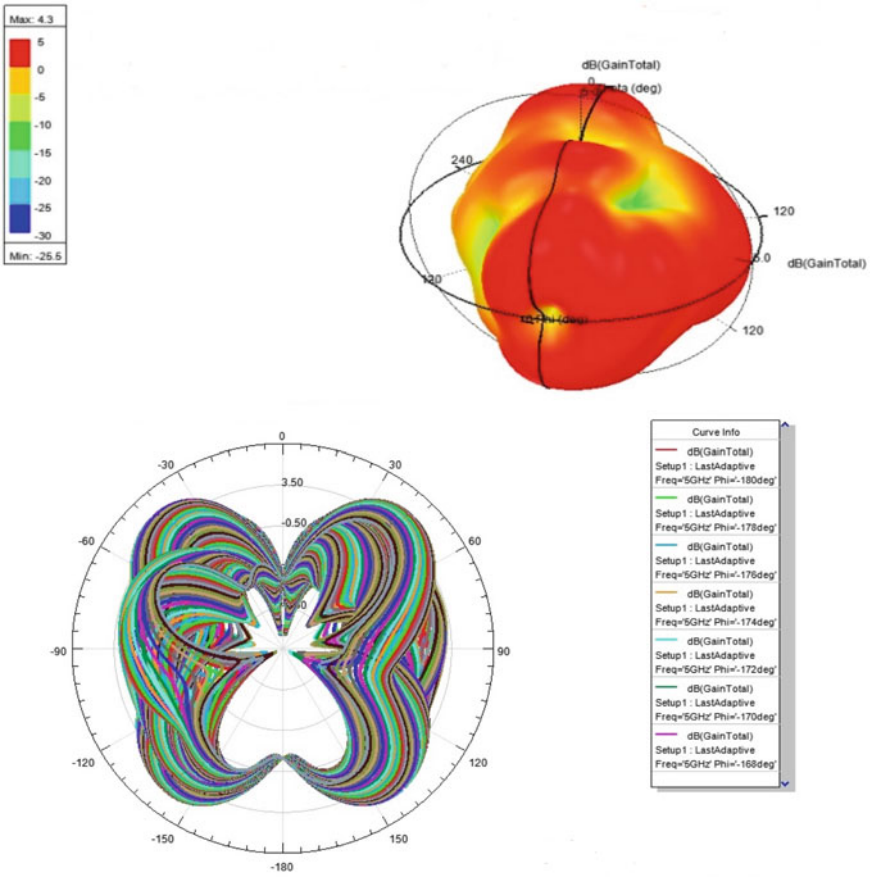

Fig. 7 3D polar plot and radiation pattern of triple patch MIMO antenna without any stub on ground

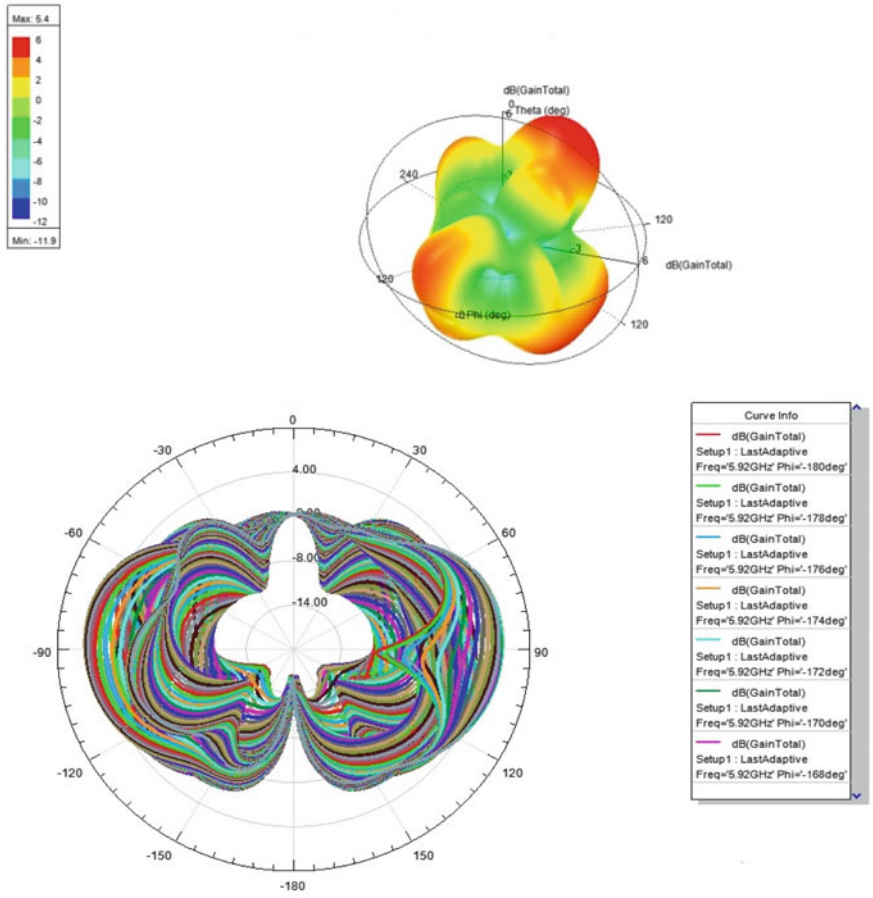

Fig. 8 3D polar plot and radiation pattern of triple patch MIMO antenna with single dumbbell-shaped stub on ground

4 Conclusion

A three-input and three-output wearable wideband textile MIMO antenna for wireless applications is proposed in this paper. This special structure antenna is implemented by placing three rectangular copper patches on the front side and double dumbbell-shaped stub on the ground to achieve better isolation and low mutual coupling. The gain of this antenna is given by 6.5 dB which is operated in the frequency spectrum from 2 to 8 GHz with high isolation of 60 dB which occurred at 4.800 GHz. The envelope correlation coefficient and diversity gain are given by 0.001749 and 10 dB, respectively.

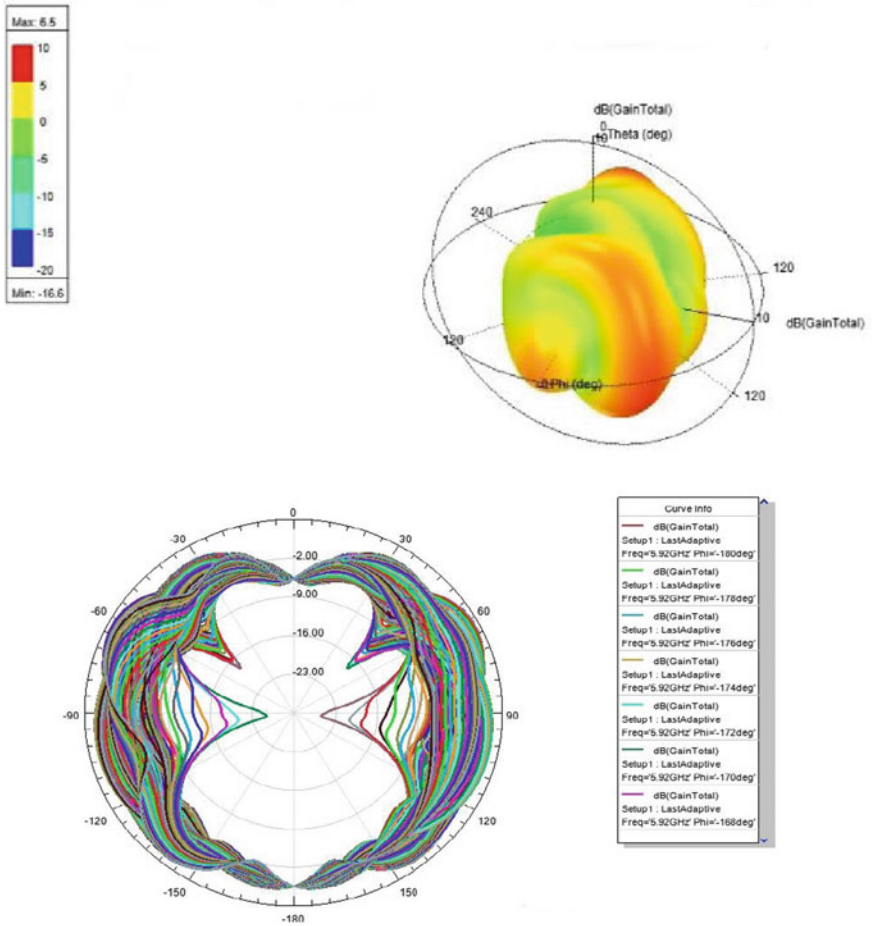

Fig. 9 3D polar plot and radiation pattern of triple patch MIMO antenna with double dumbbell-shaped stub on ground

Table 2 Comparison table of three proposed antennas

Parameter	MIMO antenna without any stub on ground	MIMO antenna with single dumbbell stub on ground	MIMO antenna with double dumbbell stub on ground
Operating frequency	2–8 GHz	2–8 GHz	2–8 GHz
Gain	4.3	5.4	6.5
Minimum isolation	21.743 dB	29.99 dB	38.554 dB
Maximum isolation	26.440 dB	48.3664 dB	60 dB
ECC	1	0.03120	0.001729
DG	0	9.995 dB	10 dB

References

1. Jusoh M, Jamlos MFB, Kamarudin MR, Malek MFBA (2012) A MIMO antenna design challenges for UWB application. Prog Electromag Res B 36:357–371
2. Xue C-D, Zhang XY, Cao YF, Hou Z, Ding CF (2017) MIMO Antenna Using Hybrid Electric and Magnetic Coupling for Isolation Enhancement. IEEE Trans Antennas Propag 65(10):5162–5170
3. Zhao L, Wang Z, Shen X, Li Y (2018) Introduction of the meta-surface antenna array decoupling (MAAD) method for 5G systems. In: 2018 IEEE Asia-Pacific conference on antennas and propagation (APCAP). https://doi.org/10.1109/apcap.2018.8538231
4. Ling X, Li RL (2011) A novel dual-band MIMO antenna array with low mutual coupling for portable wireless devices. IEEE Antennas Wireless Propag Lett 10:1039–1042
5. Chiu C-Y, Cheng C-H, Murch RD, Rowell CR (2007) Reduction of mutual coupling between closely-packed antenna elements. IEEE Trans Antennas Propag 55(6):1732–1738
6. Mak ACK, Rowell CR, Murch RD (2008) Isolation enhancement between two closely packed antennas. IEEE Trans Antennas Propag 56(11):3411–3419
7. Soltani S, Murch RD (2015) A compact planar printed MIMO antenna design. IEEE Trans Antennas Propag 63(3):1140–1149
8. Zhou H, Piao D (2016) Design of a dual-polarized MIMO antenna with high isolation. In: 2016 progress in electromagnetic research symposium (PIERS)
9. Zhai G, Chen ZN, Qing X (2015) Enhanced isolation of a closely spaced four-element MIMO antenna system using metamaterial mushroom. IEEE Trans Antennas Propag 63(8):3362–3370
10. Su W, Zhang Q, Alkaraki S, Zhang Y, Zhang XY, Gao Y (2018) Radiation energy and mutual coupling evaluation for multimode MIMO antenna based on the theory of characteristic mode. IEEE Trans Antennas Propag

QCM Sensor-Based Alcohol Classification by Advance Machine Learning Approach

B. Kameswara Rao, P. Suresh Kumar, Dukka Karun Kumar Reddy, Janmenjoy Nayak, and Bighnaraj Naik

Abstract The consumption of alcohol is a general trend in many persons. But intense drinking will be disruptive and dangerous. The excessive intake of alcohol is allied with a selection of unconstructive consequences that include nonfatal and fatal issues, academic failure, assault, violence and many other consequences that could lead to jeopardizing future prospects. So, the classification prototype approaches with the exploit of sensors for gas detection collectively play an excellent job in the classification and recognition of alcohol chemical compounds and their detrimental effects. Alcohols comprise a vast portion of chemical compounds, as given in "QCM Sensor Dataset" with QCM3, QCM6, QCM7, QCM10, QCM12. The five special types of alcohols: 1-octanol, 1-propanol, 2-butanol, 2-propanol, and 1-isobutanol are classified using quartz crystal microbalance (QCM) sensors with varied structures. The objective of this study is to establish the most affluent classification for the QCM sensor. In this research, Gradient boosting classifier based classification approach is proposed and its performance is compared with other competent methods such as Linear discriminant analysis, Logistic regression, Decision tree. The results are

B. K. Rao · J. Nayak (✉)
Department of Computer Science and Engineering, Aditya Institute of Technology and Management (AITAM), K Kotturu, Tekkali, Andhra Pradesh 532201, India
e-mail: mailforjnayak@gmail.com

B. K. Rao
e-mail: kamesh3410@gmail.com

P. S. Kumar · D. K. K. Reddy
Department of Computer Science and Engineering, Dr. Lankapalli Bullayya College of Engineering, Visakhapatnam, Andhra Pradesh 530013, India
e-mail: reshu.suri@gmail.com

D. K. K. Reddy
e-mail: karun.redy@gmail.com

B. Naik
Department of Computer Application, Veer Surendra Sai University of Technology, Burla, Odisha 768018, India
e-mail: mailtobnaik@gmail.com

G. T. C. Sekhar et al. (eds.), *Intelligent Computing in Control and Communication*, Lecture Notes in Electrical Engineering 702,
https://doi.org/10.1007/978-981-15-8439-8_25

evident that, Gradient boosting is the most successful technique compared to the other classification methods on the all the five sensor data from QCM.

Keywords QCM sensors · Machine learning · Gradient boosting · Ensemble learning

1 Introduction

The quartz crystal microbalance (QCM) is a type of wave sensor that senses the gas, vapor and often used for humidity detection. The QCM contains a thin film of quartz and 2 channels on top of it, and it is an electromechanical oscillator. The oscillation frequency of the quartz crystal is differentiated based on the thickness of the crystal. During operation, the various influencing variables remain constant; in this manner an adjustment in thickness relates directly to an adjustment in the frequency [1]. In a QCM-based estimation framework, the Oscillator circuits are having quartz sensors. The estimation of the quartz reverberation frequency relies upon chemical reference conditions, sensitive layer, and crystal. The crystal's characteristic resonance frequency is in the megahertz range, whereas the film deposition on the substance causes change in the resonance frequency up to a few hundreds of ppm.

The different types of alcohols, perfumes and other ingredients give different smells. So, here the alcohols are classified by their odors by using QCM sensors [2]. QCM sensors function like electrical e-noses that resemble the human nose through the use of sensor array. So, for the alcohol classification QCM sensors were used [3]. QCM sensors are isolated and placed in a thermally stabilized measurement chamber [1]. The gas is passed directly into the sensitive layer surface. At the point when the gas gets into contact with the layer, the molecules are caught up in the sensitive film. This results a mass variety of the sensor and the resonance frequency. It estimates the gas concentration in the preliminary stage that results in frequency shift measure. Different types of alcohol have diverse types of frequencies. Hence the gases can be classified by its frequencies, which are resulted based on QCM layer thickness.

Various machine learning algorithms are used in QCM sensors and among those artificial neural networks provide maximum favored outcomes due to their high learning ability. Moreover, Neural networks with QCM sensor data performed well [4]. ANN is a processing model that can be applied to both hardware and software [5]. The ANN imitate the biological process of the brain. So, the data is trained like how our brain recognizes each object and its characteristics like the smell, color, size, etc. The learning algorithms such as support vector machine, decision trees, random forest, and K-nearest neighbor were best suited for the classification of the alcohols [6]. The machine learning models employ prediction, decision making which is the main operation to differentiate the alcohols and predict its type [6].

There are many applications for the QCM sensors in neurobiology and neurochemistry. The neurobiology applications have been seen in medical industry like Anesthetic dose level detection [7], effective approach for the early detection of

cancer [8], pathophysiology of AUD [9], Machine learning approaches as an supplement to clinical decision making in alcohol dependence treatment [10], detection of drunk drivers by alcohol percent in blood [11], alcohol rehabitation [12]. There are also neurochemical applications like knowing harmful alcohol percentages in hygiene products [4], identification of Chinese Liquor Flavors [3], alcohol content in fruit juices [5], sensing polar and low-polar/nonpolar VOC gases [13], classification of student alcohol consumption [14] etc. It has vivid applications that mainly focus on the medical category for the safety of the people.

Zhu et al. [9] stated further improvement in curative meditation or treatment effectiveness. They focused on information patterns and linked the processing mechanism between the networks. Applying machine learning methods to classify the alcohols have the advantages of comprehending large-scale variations in addiction-related neurobiology. Liu et al. [8] reported the statistical approach in their work and can be used in molecular recognition materials for systematic screening process. The accuracy of alcohol prediction and classification is higher in QCM sensors than other sensors. It also provides high sensitivity and low-cost facility.

Adak et al. [4] developed a model called classification of alcohols acquired by QCM sensors with various characteristics. Where ABC (artificial bee colony) based neural network performed well in contrast to back propagation algorithm for training the neural network. Five different alcohol types are classified by utilizing five QCM sensor structures. After the performance comparison it is evident that, ANN-ABC method performed significantly good over the other methods.

Li et al. [3] improved a model which is an application of alcohol classification by QCM sensors named random forest classifier using a QCM-based e-nose in the identification of Chinese liquor flavors. RF classifier method has been used in the paper to predict the flavors of Chinese liquors. The dataset is divided into the subsets and then by the training process, decision trees are obtained. The proposed method is compared with linear discriminant analysis, ANN optimized with BP algorithm, and support vector machine. From the prediction and computation time, it is concluded that the proposed method performed well.

Katardjiev et al. [6] projected machine learning approaches, such as Support vector machine, Decision trees, Random forest, and k-nearest neighbor algorithm with Uppsala-based company named kontigo care data, where the simulation results favored with respective to random forest method in comparison to RMSE factor.

Saraoğlu and Edin [7] analyzed about the anesthetic dose levels and proposed a multilayer feed-forward neural network structure which is used to establish the relation between anesthetic dose levels and frequency. The MLNN is trained with Levenberg–Marquardt algorithm and the performance is evaluated using MRAE factor. The MLNN shows permissible results compared to ANN based estimation on anesthetic dose level using E-Nose system.

Zhu et al. [9] developed a model that outperforms random forest model and classifies the patients based on alcohol and healthy controls based on resting-state MRI. The dataset is obtained from patients of 1-SE, those withdraw the treatment unit at the national institutes of health clinical research center. From the results they concluded that, executive control network and reward network are very useful in classifying

alcohol use disorder. The authors claim that, machine learning delivers unconventional techniques to determine large-scale networks and to categorize the biomarkers for diagnosis.

In this present research, ensemble learning technique such as Gradient boosting algorithm has been proposed for classification problem. The remaining paper is organized into 5 sections: Sect. 2 explained about the proposed method which consists of the methodology of gradient boosting and its architectural diagram. Section 3 demonstrates experimental setup having an evolutionary measure, and parameter setting of the experimentation. Section 4 represented the results of the experimentation with comparative performance analysis. Lastly Sect. 5 concludes the paper with future scopes.

2 Gradient Boosting Machine (GBC)

In data science, Boosting is one of the most effectively utilized algorithmic calculations. Boosting bestows machine learning models with the capacity to advance their prediction accuracy. The name 'Boosting' alludes to a group of algorithms that develop strong learners from the weak learner (base learner). The transformation into a strong learner from the weak learner is the process of merging the prediction of every individual weak learner through techniques like using an average, weighted average and maximum voting for precise predictions.

The boosting techniques assemble base learners to shape into a strong rule. The weak rule is identified through the base learning algorithms of machine learning with a different distribution. By applying the base learner every time, it produces a new rule of weak prediction. This complete iterative process following numerous iterations integrates all these weak rules in the form of a strong single prediction rule. Selecting the correct distribution for each round is given by the general boosting algorithm.

Boosting Algorithms	
Step 1:	The base learner collects various distributions and allocates them with identical weight to every observation
Step 2:	In case of any error caused by the prediction, through the first base machine learning algorithm, at that point we give higher consideration to the observations that are having prediction error. At that point, the next base machine learning algorithm is applied
Step 3:	Repeat Step 2 until the high accuracy is accomplished using base learning algorithm

Lastly, it integrates the weak learner outputs and produces a strong learner which ultimately enhances the prediction capacity of the model.

In this paper we focused on Gradient Boosting technique, as it trains the model into various sub-models sequentially, where every sub-model progressively minimize the loss function by using gradient descent method [15]. This procedure successively

fits all the sub-models through learning and provides higher accurate estimation for the variables. The GBM integrates all the predictions from various base learners to produce the final output predictions, where decision trees are the base learners in a GBM. In GBM various decision trees confine the nodes of every sub tree that takes various features of subset for choosing the best split. Here every new tree (sub-model) considers the errors made by the previous tree and taking these considerations into account, a consecutive decision trees is built from previous tree errors, by ensemble all the previous predecessors' decision trees model (Fig. 1).

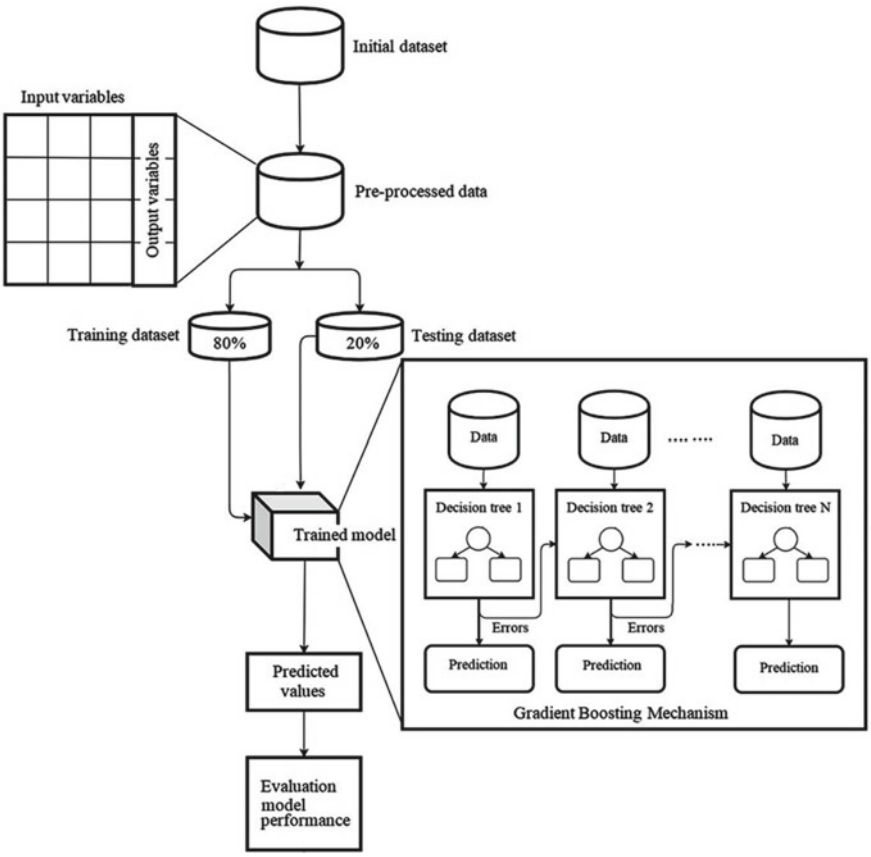

Fig. 1 Proposed method architecture

3 Experimental Setup

In this section, we have discussed various evaluating factors that are considered to confirm the accomplishment of the proposed model with different machine learning methods.

3.1 Evaluation Measures

This section comprises various measurements used to verify the performance of the classification of 5 different types using QCM sensors. Evaluation metrics such as TP, TN, FP, FN, TPR/Recall, FPR, precision, support, and accuracy are taken into major constraints.

True positive (TP): it is the number of predictions where data related to a particular class model *accurately* predicts the *positive* class.

False positive (FP): it is the number of predictions where data related to a particular class model *accurately* predicts the *positive* class in a negative way.

True negative (TN): it is the number of predictions where data related to a particular class model *accurately* predicts the *negative* class.

False negative (FN): it is the number of predictions where data related to a particular class model *incorrectly* predicts the *negative* class.

Accuracy: It is the ratio between the total number of classifications and correct classification. It is conveyed in Eq. 1.

$$\text{Accuracy} = {}^{(\text{TP}+\text{TN})}\!/_{(\text{TP}+\text{TN}+\text{FP}+\text{FN})} \tag{1}$$

Precision: It is a measure to know the accuracy in terms of prediction of a specified class. It is shown in Eq. 2.

$$\text{Precision} = {}^{\text{TP}}\!/_{(\text{TP}+\text{FP})} \tag{2}$$

True positive rate (TPR): It is also called as recall or sensitivity. It is the ratio among true positives of a specified class to the summation of true positives and false negatives. It is expressed in Eq. 3.

$$\text{TPR} = \text{recall} = \text{sensitivity} = {}^{\text{TP}}\!/_{(\text{TP}+\text{FN})} \tag{3}$$

False positive rate (FPR): It is the ratio among false positive of a specified class to the summation of true negative and false positive. It is demonstrated in Eq. 4.

$$\text{FPR} = {}^{\text{FP}}\!/_{(\text{TN}+\text{FP})} \tag{4}$$

True Negative rate: It is also named as specificity. It is the ratio between the summation of true negatives and false positives to the true negatives of that specified class. It is represented in Eq. 5.

$$\text{TNR} = {}^{\text{TN}}/_{(\text{TN} + \text{FP})} \tag{5}$$

***F*-Measure**: It is one of the measurements of test accuracy and it is weighted harmonic average between precision and recall, which is expressed in Eq. 6.

$$F\text{-Measure} = 2 \times \frac{\text{Precision} \times \text{Sensitivity}}{\text{Precision} + \text{Sensitivity}} \tag{6}$$

3.2 Environmental Setup

In this section, we assessed the performance of the alcohol dataset that is obtained by QCM sensor data from the UCI machine learning repository [16]. Experimentation is done by using gradient boosting algorithm and various machine learning models such as logistic regression, decision tree, linear discriminant analysis, and multi-layer perceptron. Parameters considered for experimentation in gradient boosting and machine learning algorithms are shown in Table 1. The performance is evaluated using various metrics such as confusion matrix, TP, TN, FP, FN, TPR/Recall, FPR, precision, support, and accuracy.

Table 1 Parameter setting of the considered methods

Dataset	Technique	Parameter Setting
Alcohol QCM sensor dataset	Gradient boosting	loss: Logistic regression n_estimators: 40 criterion: friedman_mse max_depth: 3
	Decision tree	criterion: gini splitter: best max_depth: none
	Logistic regression	solver: newton-cg random_state: 1 max_iter:100
	Linear discriminant analysis	solver: svd tol: 0.0001
	Multi-layer perceptron	Activation: logistic batch_size: 10 random_state: 2 solver: adam

4 Result Analysis

This section describes the obtained results on alcohol QCM sensor dataset with the proposed gradient boosting algorithm and various machine learning algorithms. The considered dataset contains 125 scenarios from the UCI machine learning repository and it is splitted into 15 cross-folds. To validate the performance of our proposed method with different machine learning methods, we considered the performance measures such as confusion matrix, TP, TN, FP, FN, TPR/Recall, FPR, precision, support, and accuracy (Table 2). The confusion matrix of the gradient boosting classification is shown in Fig. 2. From the confusion matrix it is observed that '2-propanol' scenarios are predicted as '1-propanol', '1-isobutanol' is classified as '1-propanol', '1-propanol' is predicted as '2-butanol', and '1-propanol' is predicted as '2-propanol'. The remaining scenarios are classified correctly. Table 3 shows the results such as TP, TN, FP, FN, TPR, FPR, precision, and f-score using

Table 2 Evaluation factors using gradient boosting

Gradient boosting	1-octanol	1-propanol	2-butanol	2-propanol	1-isobutanol
True positive	19	18	20	18	19
True negative	80	76	78	78	79
False positive	0	3	1	1	0
False negative	0	2	0	2	1
TPR/recall	1.00	0.90	1.00	0.90	0.95
FPR	0.00	0.04	0.01	0.01	0.00
$F1$ score	1.00	0.88	0.98	0.92	0.97
Precision	1.00	0.86	0.95	0.95	1.00
Accuracy	1.00	0.95	0.99	0.97	0.99
Over all accuracy	0.95				

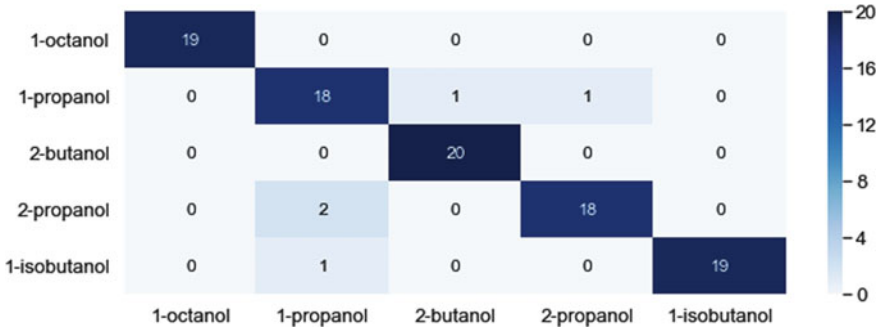

Fig. 2 Confusion matrix of proposed method

Table 3 Performance measure using decision tree

Decision tree	1-octanol	1-propanol	2-butanol	2-propanol	1-isobutanol
True positive	19	17	20	19	18
True negative	80	77	77	77	79
False positive	0	2	2	2	0
False negative	0	3	0	1	2
TPR/recall	1.00	0.85	1.00	0.95	0.90
FPR	0.00	0.03	0.03	0.03	0.00
$F1$ score	1.00	0.87	0.95	0.93	0.95
Precision	1.00	0.89	0.91	0.90	1.00
Accuracy	1.00	0.95	0.96	0.97	0.96
Over all accuracy	0.94				

gradient boosting, where the accuracy is 95 and remaining machine learning algorithms logistic regression, decision tree, Linear discriminant analysis, and multi-layer perceptron are having the accuracy such as 94, 90, 90, and 79 respectively.

The performance of different machine learning algorithms is presented in Tables 3, 4, 5 and 6. In the case of '1-octanol' class, all proposed and machine learning algorithms are performed well in terms of TPR, $f1$-score, precision, and accuracy. In the same way, all values in the false positive rate are zero as the performance in this class is well. Next in the class '1-propanol', the proposed method is performed well with the value 0.90, where machine learning method's performance is less than the proposed method in terms of TPR. Moreover, all the false positives rates are 0 and in comparison with $f1$-score, the performance of ML method is less. In terms of accuracy, gradient boost and decision tree are having same values. Next in case of '2-butanol', the proposed method and decision tree performed well in terms of TPR. However, the FPR value is less in case of the proposed method as compared

Table 4 Performance measure using logistic regression

Logistic regression	1-octanol	1-propanol	2-butanol	2-propanol	1-isobutanol
True positive	19	16	16	18	20
True negative	80	75	75	77	79
False positive	0	4	4	2	0
False negative	0	4	4	2	0
TPR/recall	1.00	0.80	0.80	0.90	1.00
FPR	0.00	0.05	0.05	0.03	0.00
$F1$ score	1.00	0.80	0.80	0.90	1.00
Precision	1.00	0.80	0.80	0.90	1.00
Accuracy	1.00	0.92	0.92	0.96	1.00
Over all accuracy	0.90				

Table 5 Performance measure using linear discriminant analysis

Linear discriminant analysis	1-octanol	1-propanol	2-butanol	2-propanol	1-isobutanol
True positive	19	16	16	18	20
True negative	80	75	75	77	79
False positive	0	4	4	2	0
False negative	0	4	4	2	0
TPR/recall	1.00	0.80	0.80	0.90	1.00
FPR	0.00	0.05	0.05	0.03	0.00
$F1$ score	1.00	0.80	0.80	0.90	1.00
Precision	1.00	0.80	0.80	0.90	1.00
Accuracy	1.00	0.92	0.87	0.87	1.00
Over all accuracy	0.90				

Table 6 Performance measure using Multi-Layer perceptron

Multi-layer perceptron	1-octanol	1-propanol	2-butanol	2-propanol	1-isobutanol
True positive	19	12	10	17	20
True negative	80	72	73	74	76
False positive	0	7	6	5	3
False negative	0	8	10	3	0
TPR/recall	1.00	0.6	0.5	0.85	1.00
FPR	0.00	0.09	0.08	0.06	0.04
$F1$ score	1.00	0.62	0.56	0.81	0.93
Precision	1.00	0.63	0.63	0.77	0.87
Accuracy	1.00	0.85	0.84	0.92	0.97
Over all accuracy	0.79				

to other machine learning algorithms. Similarly $f1$-score, precision, and accuracy values are high in gradient descent algorithm compared to other algorithms. In '2-propanol', performance of gradient boosting, decision tree, and logistic regression is almost equal in terms of accuracy. TPR of decision tree is better as compared to gradient boosting and logistic regression. In the class '1-isobutanol', all the models are having high accuracy, and especially logistic regression, linear discernment analysis and gradient boosting are proved to be efficient classifier. Every model TPR is 1 and in case of precision, all the models performed well except multi-layer perceptron. Graphical representation of all the performance comparison is presented in Figs. 3, 4, 5, 6 and 7.

AUC-ROC curves of the proposed method and various machine learning methods shown in Figs. 8, 9, 10, 11 and 12.

Table 7 presented the comparative analysis in terms of accuracy among the proposed method and other previously developed ML based models. The results

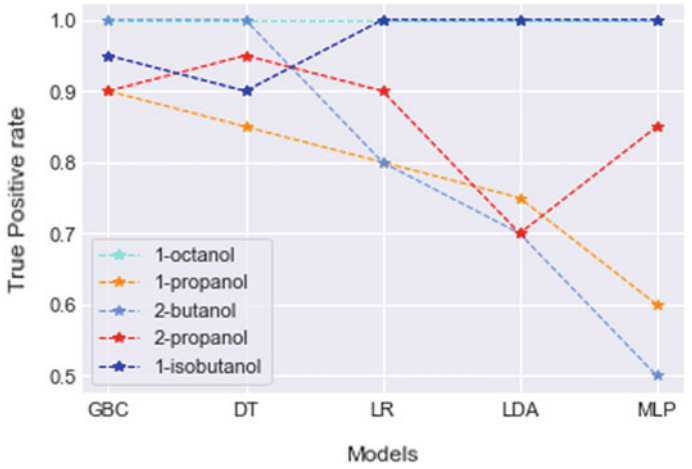

Fig. 3 TPR versus various models

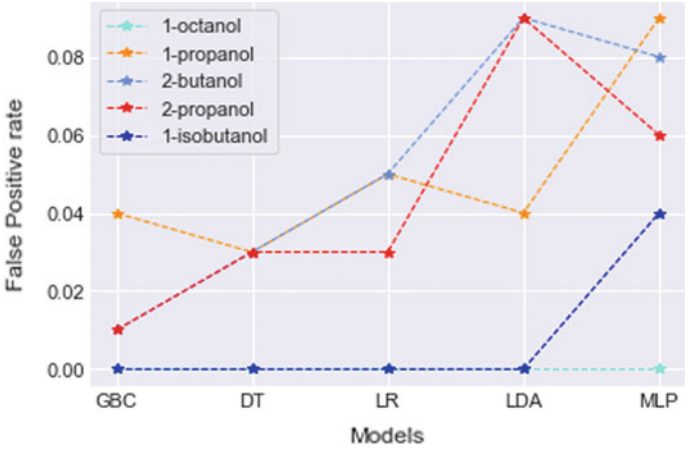

Fig. 4 FPR versus various models

are clearly evident that, the proposed method is a robust classifier and is significant to classify the alcohols.

5 Conclusion

In the examination of 1-octanol, 1-propanol, 2-butanol, 2-propanol, and 1-isobutanol, from the five different alcohols datasets QCM3, QCM6, QCM7, QCM10, QCM12

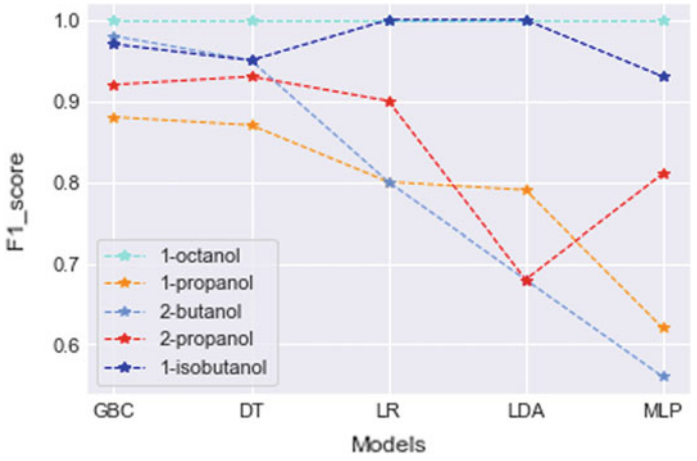

Fig. 5 *F*1_score versus various models

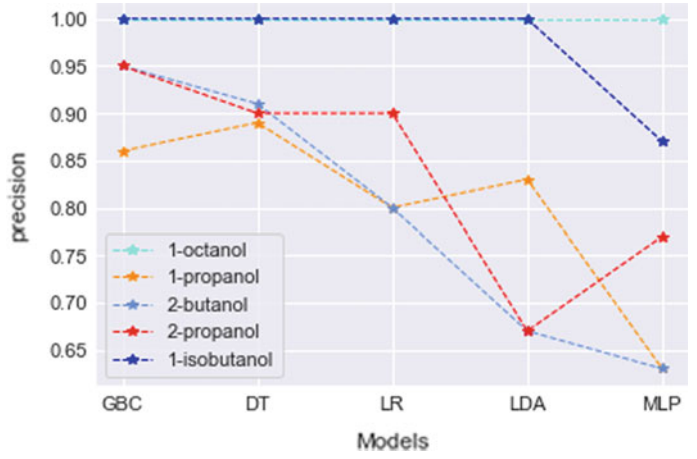

Fig. 6 Precision versus various models

sensors obtained by using QCM sensors are classified by using multi-layer perceptron, linear discriminant analysis, logistic regression, decision tree, and gradient boosting. The gradient boosting is an efficient classifier with an overall accuracy of 95%, when compared to traditional machine learning classifiers. The recall values for 1-octanol, 2-butanol is 100% whereas the class's 1-propanol, 2-propanol gives 90% and 1-isobutanol gives 95%. The F1-score for 1-octanol is 100% and 2-butanol is 98% and the precision values of 1-octanol give 100% and 1-isobutanol gives 100%. The Decision tree classifier gives the second-best results with an overall accuracy of 94%. The recall values for 1-octanol, 2-butanol is 100%. The F1-score for 1-octanol is 100%, 95% for 2-butanol and 1-isobutanol and the precision values of 1-octanol

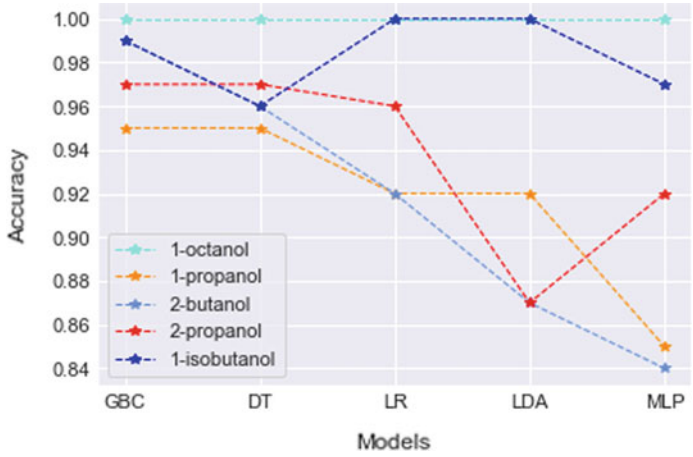

Fig. 7 Accuracy versus various models

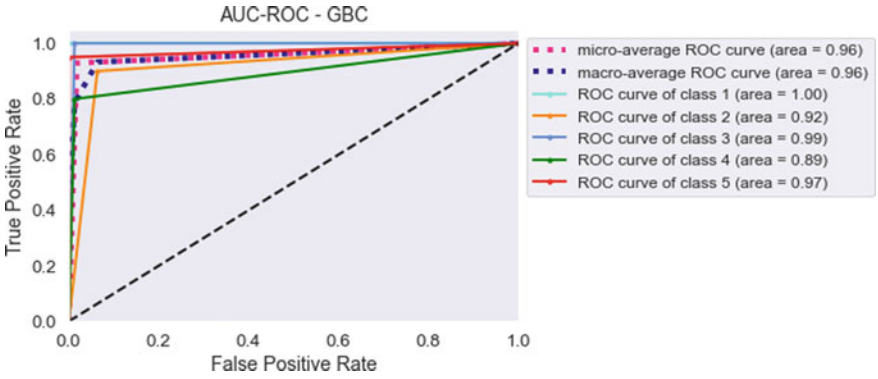

Fig. 8 AUC-ROC curve of gradient boosting

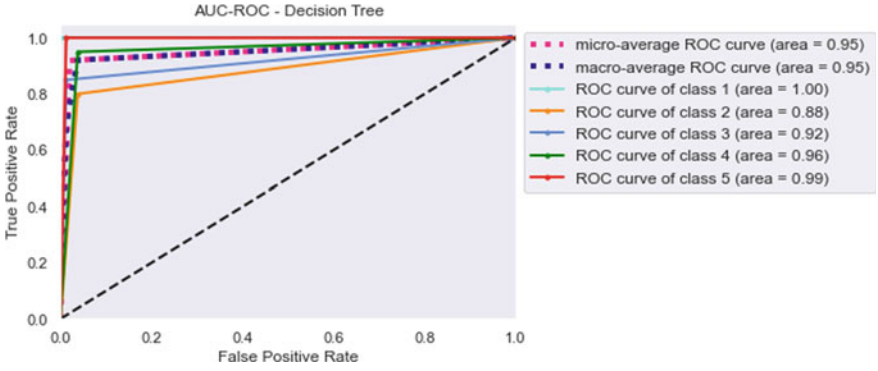

Fig. 9 AUC-ROC curve of decision tree

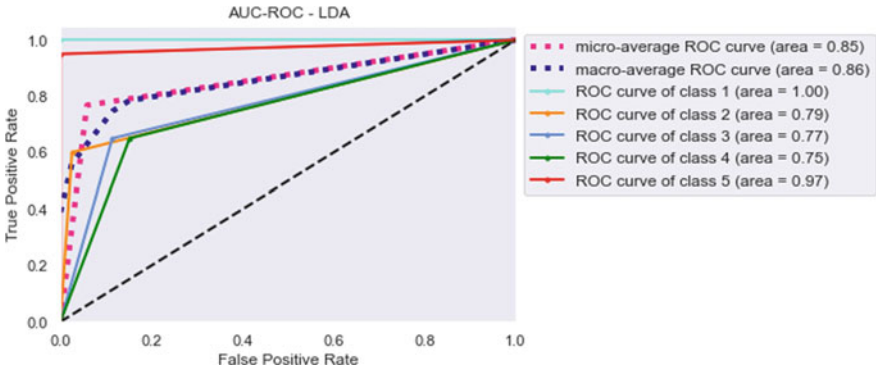

Fig. 10 AUC-ROC curve of linear discriminant analysis

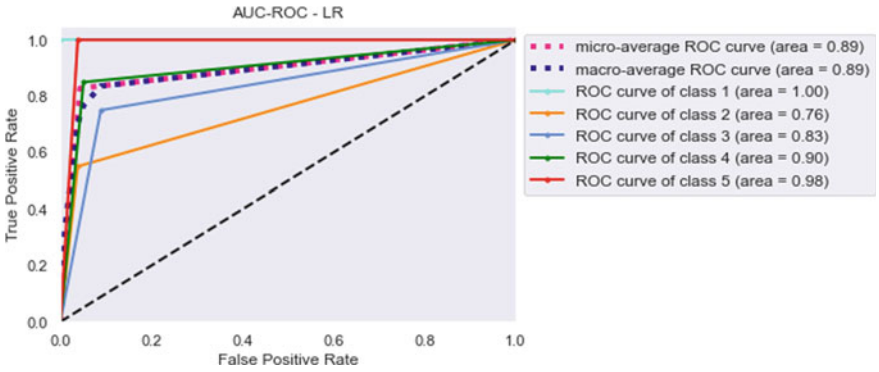

Fig. 11 AUC-ROC curve of Logistic regression

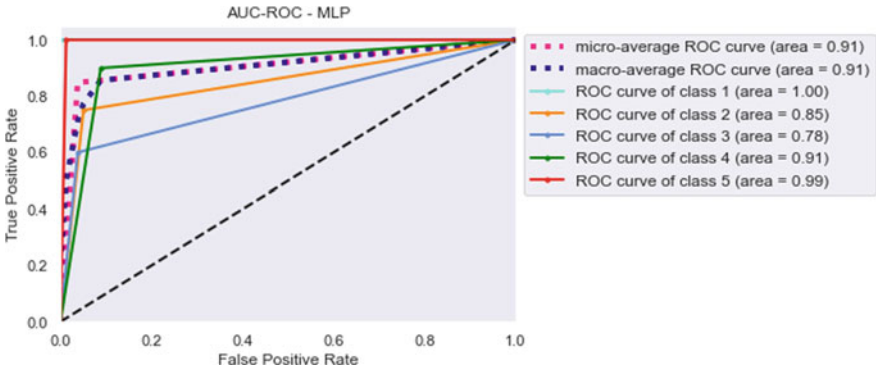

Fig. 12. AUC-ROC curve of multi-layer perceptron

Table 7 Comparison among some other methods in the literature

S. No.	Year	Intelligent method	Accuracy	Reference
1	2019	Decision tree	64.6	[6]
2	2019	Random forest	84.1	[6]
3	2019	*K*-nearest neighbor	78.1	[6]
4	2019	Alternating decision tree	78.0	[17]
5	2019	Random forest	73.3	[17]
6	2019	Random tree	70.0	[17]
7	2019	Logistic model	72.5	[17]
8	2019	Simple logistic model	77.5	[17]
9	2018	Random forest	87	[9]
10	2017	Neural network	61.78	[18]
11	2017	PCA-BPNN	93.3	[3]
12	2017	Support vector machine	90.8	[3]
13	2017	Decision tree	74.3	[19]
14	2014	Linear SVM	91	[20]
15	2014	Bayesian logistic regression	93	[20]
16	2014	Random Forest	94	[20]
17	2010	PCA	90.9	[21]

are 100% (same with 1-isobutanol). The overall accuracy of logistic regression and linear regression is 90% and the multi-layer perceptron is 79%. This study enlightens for the future scope of work such as, QCM sensors alcohol dataset with various structures can be successfully classified by using advance machine learning approaches for precise prediction.

References

1. Di Nucci C et al (2003) A measurement system for odor classification based on the dynamic response of QCM sensors. IEEE Trans Instrum Meas 52(4):1079–1086
2. Leung YC, Yip DHF, Yu WWH (1997) An analogue ANN for classification of alcohol. In: 1997 IEEE international conference on systems, man, and cybernetics. Computational cybernetics and simulation, vol 4, no. 852, pp 4010–4015
3. Li Q, Gu Y, Wang N (2017) Application of random forest classifier by means of a QCM-based E-nose in the identification of Chinese liquor flavors. IEEE Sens J 17(6):1788–1794
4. Adak MF, Lieberzeit P, Jarujamrus P, Yumusak N (2019) Classification of alcohols obtained by QCM sensors with different characteristics using ABC based neural network. Eng Sci Technol Int J. https://doi.org/10.1016/j.jestch.2019.06.011.
5. Ordukaya E, Karlik B (2016) Fruit juice-alcohol mixture analysis using machine learning and electronic nose. IEE J Trans Electr Electron Eng 11(July):S171–S176
6. Katardjiev N, Mckeever S, Hamfelt A (2019) A machine learning-based approach to forecasting alcoholic relapses. In: ITISE 2019 (6th international conference on time series and forecasting).

At: 25th-27th Sept, Granada, Spain, Oct 2019
7. Saraoğlu HM, Edin B (2007) E-nose system for anesthetic dose level detection using artificial neural network. J Med Syst 31(6):475–482
8. Liu C, Wyszynski B, Yatabe R, Hayashi K, Toko K (2017) Molecularly imprinted sol-gel-based QCM sensor arrays for the detection and recognition of volatile aldehydes. Sensors (Switzerland) 17(2):1–15
9. Zhu X, Du X, Kerich M, Lohoff FW, Momenan R (2018) Random forest based classification of alcohol dependence patients and healthy controls using resting state MRI. Neurosci Lett 676:27–33
10. Connor JP, Symons M, Feeney GFX, Young RM, Wiles J (2007) The application of machine learning techniques as an adjunct to clinical decision making in alcohol dependence treatment. Subst Use Misuse 42(14):2193–2206
11. Robinel A, Puzenat D (2013) Multi-user blood alcohol content estimation in a realistic simulator using artificial neural networks and support vector machines. In: ESANN 2013 proceedings, 21st European symposium on artificial neural networks, Computational Intelligence and Machine Learning, April, pp 431–436
12. Kanna PS, Palaniappan R, Ravi KVR (2005) Classification of alcohol abusers: an intelligent approach. In: Third international conference on information technology and applications (ICITA'05), vol 1, pp 470–474
13. Si P, Mortensen J, Komolov A, Denborg J, Møller PJ (2007) Polymer coated quartz crystal microbalance sensors for detection of volatile organic compounds in gas mixtures. Anal Chim Acta 597(2):223–230
14. Pisutaporn A, Chonvirachkul B, Sutivong D (2018) Relevant factors and classification of student alcohol consumption. In: 2018 IEEE international conference on innovative research and development (ICIRD), pp 1–6
15. Friedman JH (2001) Greedy function approximation: a gradient boosting machine'. Ann Stat 29(5):1189–1232
16. Dua D, Graff C (2019) UCI machine learning repository [https://archive.ics.uci.edu/ml]. University of California, School of Information and Computer Science, Irvine, CA
17. Lee MR et al (2019) Using machine learning to classify individuals with alcohol use disorder based on treatment seeking status. EClinicalMedicine 12:70–78
18. Boutamine M, Lezzar OC, Bellel A, Aguir K, Sahli S, Raynaud P (2018) Determination of volatile organic compounds using quartz crystal microbalances coated with hexamethyldisiloxane. Anal Lett 51(3):387–400
19. Perveen S, Shahbaz M, Keshavjee K, Guergachi A (2018) A systematic machine learning based approach for the diagnosis of non-alcoholic fatty liver disease risk and progression. Sci Rep 8(1):2112
20. Aphinyanaphongs Y, Ray B, Statnikov A, Krebs P (2014) Text classification for automatic detection of alcohol use-related tweets: a feasibility study. In: Proceedings of the 2014 IEEE 15th international conference on information reuse and integration (IEEE IRI 2014), pp 93–97
21. Escuderos ME, Sánchez S, Jiménez A (2011) Quartz crystal microbalance (QCM) sensor arrays selection for olive oil sensory evaluation. Food Chem 124(3):857–862

Effect of Different Load Models on Estimation of Maximum Acceptable Load at a Weak Bus Using Line-Based Voltage Stability Indices

Trinadha Burle and V. V. S. Bhaskara Reddy Chintapalli

Abstract This paper is a test case study based paper. In this paper, line indices-based approach is utilized for testing the effect of various load models on estimation of maximum acceptable load at weak bus of a particular power system. It has lot of importance for the voltage stability analysis. Based on result analysis, most preferable load at a bus or substation is also identified. Different exponential-type load models and composite load models are considered in this work. The change of weak bus voltage and maximum load for various load models are analyzed. Each line loss and total loss in the system for different load models are also analyzed. Methodology of this work is implemented on standard IEEE 14 bus test case system. All the simulations of this work are implemented in MATLAB 2019a.

Keywords Line voltage stability index · Load model · Maximum load · Voltage stability

1 Introduction

Due to deregulation initiatives, environmental conditions and high transmission line construction costs, the existing power system network forces to function under strained conditions [1]. Voltage collapse may occur for any minor disruptions under this state. Hence, for a reliable and secure operation of power system, voltage stability analysis is essential [2]. Generally, dynamic or static approaches can be used to analyze the system's voltage stability. More processing time is required for dynamic stability analysis unlike static stability analysis. There are several static techniques

T. Burle (✉) · V. V. S. B. R. Chintapalli
Department of Electrical Engineering, Andhra University College of Engineering (A), Visakhapatnam 530003, India
e-mail: trinadha.burle@gmail.com

V. V. S. B. R. Chintapalli
e-mail: profbhaskara@andhrauniversity.edu.in

G. T. C. Sekhar et al. (eds.), *Intelligent Computing in Control and Communication*, Lecture Notes in Electrical Engineering 702,
https://doi.org/10.1007/978-981-15-8439-8_26

available in the literature to analyze a system's voltage stability [3]. The line-based static techniques are used in this work.

Generally, the active and reactive power load models used in conventional load flow are independent on voltage and frequency variations [4]. The frequency variations in a power system are usually very small, and hence, it can be assumed that constant frequency load model but voltage variations must be considered in load model, otherwise it will give inaccurate results. In recent years, it is clearly understood that load modeling is playing an important role in the estimation of voltage stability [5]. Accurate load modeling poses a big challenge to the power engineers. It is well known that different load models may lead to different conclusions. Constant power load models are independent on bus voltage, whereas constant current and constant impedance load models are dependent on bus voltage. Therefore, as load bus voltage changes, the voltage dependent load also changes its magnitude. It is also important in estimation of power system voltage stability [6].

In this paper, line voltage stability based static approach is used. The estimation of maximum acceptable load of a weak bus for different load models is studied, and corresponding voltage levels are also analyzed. Most preferable load that can be connected to a bus is also identified. The proposed method is implemented on standard IEEE 14 bus power system. Section 2 gives information about different indices used in this work, and Sect. 3 explains various load models considered in this work. Section 4 explains incorporation of various load models into load flow problem, Sect. 5 explains the results and discussions, and finally, Sect. 6 gives the conclusions of this work.

2 Line-Based Voltage Stability Indices

The following line voltage stability indices are used for estimation of maximum load at a weak bus.

2.1 Line-Based Stability Index (L_{mn})

Mahmoud Moghavvemi et al. developed an index L_{mn}, and it is derived from line power flow equation [7].

$$L_{\mathrm{mn}} = (4XQ_r)/(V_s \sin(\theta - \delta))^2 \tag{1}$$

2.2 Fast Voltage Stability Index (FVSI)

Ismail Musirin et al. developed a line-based voltage stability index *FVSI* as given below [8]

$$\mathrm{FVSI} = \left(4Z^2 Q_r\right)/\left(V_s^2 X\right) \tag{2}$$

2.3 Line Voltage Reactive Power Index (VQI_{line})

Althowibi et al. derived an index VQI_{line}, based on the same concept like above two indices, and it is given as [9]

$$\mathrm{VQI_{line}} = (4Q_r)/\left(|B_{sr}|\left|V_s^2\right|\right) \tag{3}$$

2.4 New Voltage Stability Index (NVSI)

This index *NVSI* was developed by Kanimozhi et al. based on single-line power flow concept. Active and reactive power effects both are included in this index. It is expressed as [10]

$$\mathrm{NVSI} = \left(2X\sqrt{\left(P_r^2 + Q_r^2\right)}\right)/\left(2Q_r X - V_s^2\right) \tag{4}$$

2.5 New Line Voltage Stability Index (NLVSI)

The Index *NLVSI* is derived by Burle et al. using the power flow in a line. It is expressed as follows [11]

$$\mathrm{NLVSI} = (4Z|S_r|\cos(\phi_r - \theta))/(V_s \cos\delta)^2 \tag{5}$$

3 Different Load Models in Power System

The following load models are used in this work for testing the effect of load model on estimation of maximum acceptable load at a weak bus.

3.1 Constant Impedance Load Model

It is the load model which depends on bus voltage, and it can mathematically be written as

$$P_Z = P_0\left(\frac{V_i}{V_0}\right)^2 \tag{6}$$

$$Q_Z = Q_0\left(\frac{V_i}{V_0}\right)^2 \tag{7}$$

3.2 Constant Current Load Model

It is also one load model, which depends on bus voltage, and it can be written as

$$P_I = P_0\left(\frac{V_i}{V_0}\right) \tag{8}$$

$$Q_I = Q_0\left(\frac{V_i}{V_0}\right) \tag{9}$$

3.3 Constant Power Load Model

This load model is independent on voltage, and it can be expressed as

$$P_p = P_0 \tag{10}$$

$$Q_p = Q_0 \tag{11}$$

The above three load models can be commonly written as

$$P_{exp} = P_0\left(\frac{V_i}{V_0}\right)^a \tag{12}$$

$$Q_{exp} = Q_0\left(\frac{V_i}{V_0}\right)^b \tag{13}$$

This load model is called as exponential load model.
Where

P_0 Active power demand at rated voltage,
Q_0 Reactive power demand at rated voltage,
V_0 Rated voltage of the system,
V_i Operating voltage of the system,
a, b are the exponential powers for the load model and $a = b = 2$ for constant impedance load model, $a = b = 1$ for constant current load model, $a = b = 0$ for constant power load model [4].

3.4 Composite Load Model or ZIP Load Model

The combination of above three load models can be written as

$$P_{\text{ZIP}} = P_0\left[Z_p\left(\frac{V_i}{V_0}\right)^2 + I_p\left(\frac{V_i}{V_0}\right) + P_p\right] \tag{14}$$

$$Q_{\text{ZIP}} = Q_0\left[Z_q\left(\frac{V_i}{V_0}\right)^2 + I_q\left(\frac{V_i}{V_0}\right) + P_q\right] \tag{15}$$

where

Z_p, I_p, P_p are the active power ZIP coefficients and Z_q, I_q, P_q are the reactive power ZIP coefficients. These values are taken from [11].

4 Incorporation of Load Models into the Load Flow Problem

The basic load flow equations in rectangular coordinates are given below

$$P_p = \sum_{q=1}^{n}\left\{e_p\left(e_q G_{pq} - f_q B_{pq}\right) + f_p\left(f_q G_{pq} + e_q B_{pq}\right)\right\} \tag{16}$$

$$Q_p = \sum_{q=1}^{n} \{ f_p (e_q G_{pq} - f_q B_{pq}) + e_p (f_q G_{pq} + e_q B_{pq}) \} \tag{17}$$

where

e_p, f_p	the real and imaginary components of p^{th} bus voltage,
e_q, f_q	the real and imaginary components of q^{th} bus voltage,
G_{pq}, B_{pq}	the line conductance and susceptance between the p^{th} bus and q^{th} bus.
$P_{sp} = P_g - P_l$	For all buses
$Q_{sp} = Q_g - Q_l$	For all buses

The above two equations for conventional load models

$P_{sp} = P_g - P_{lm}$	For all buses
$Q_{sp} = Q_g - Q_{lm}$	For all buses

Where

P_{lm} and Q_{lm} are the load models active and reactive power demands, respectively [12]. Instead of P_{lm} and Q_{lm} equations from (6) to (15) can be used. Hence, from Eqs. (16) and (17) the power mismatch equations can be written as

$$\Delta P = P_{sp} - \sum_{q=1}^{n} \{ e_p (e_q G_{pq} - f_q B_{pq}) + f_p (f_q G_{pq} + e_q B_{pq}) \}$$

For all buses except slack bus

$$\Delta Q = Q_{sp} - \sum_{q=1}^{n} \{ f_p (e_q G_{pq} - f_q B_{pq}) + e_p (f_q G_{pq} + e_q B_{pq}) \}$$

For all buses except slack bus

These mismatches can be made zero using Jacobian matrix analysis. The following procedure is used in this work:

Step 1: Run the base case load flow using NR method.
Step 2: Incorporate the required load model (from Eqs. (6) to (15)) into the load flow problem.
Step 3: Select the weak bus (from the literature).
Step 4 Increase the reactive load demand at weak bus randomly by keeping generation constant.
Step 5. Calculate the line voltage stability indices using the formulas from Eqs. (1) to (5).
Step 6. If any one of the indices shows unity, stop the process and note down the bus voltages, angles, each line loss, total loss of the system and maximum load at that weak bus. Otherwise go to step 4.
Step 7. Change the load model and repeat the same process from step 3

5 Results and Discussions

The proposed approach is tested on IEEE 14 bus system. It is having 3 generators, two synchronous compensators totally 5 generator buses, 9 load buses and 20 interconnected transmission lines. The bus data and branch data of this system are taken from [13]. The single line diagram of the test case system is shown in Fig. 1. In this system, bus 14 is the weak bus which is selected from [11]. First this system is executed under conventional load case, and next, it is extended to different load models. The simulation results are combined and compared that are given in below figures and tables.

From Fig. 2, it is observed that constant current-type load model offering good voltage profile at all buses compared to remaining load models for large loading at a weak bus. Next constant power-type load models having better voltage profile for the same condition. The bus angle will reduce if the active power loading increases at that bus. From Fig. 3, it is well known that constant power and constant impedance-type load models maintain good angle profile for the maximum load at weak bus.

From Fig. 4, it is understood that the first line having more active power loss compared to other lines. It is acceptable because it is connected slack bus. From lines 2 to 7, it is clear that constant current-type load models give less losses compared to other load models. For the remaining lines, constant power-type load models give less losses.

From Fig. 5 it is clear that for the first ten lines in the maximum cases constant current-type load models having less losses compared to other load models. In the

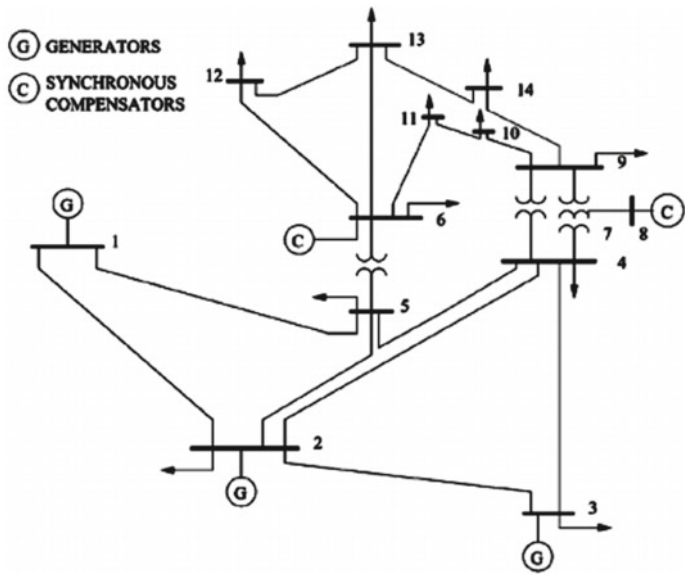

Fig. 1 IEEE standard 14 bus test case system

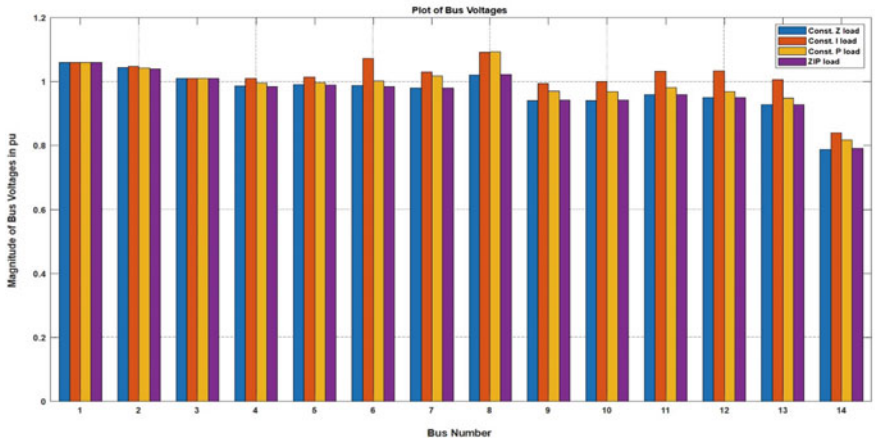

Fig. 2 Bus voltages for various load models at large loading condition of weak bus

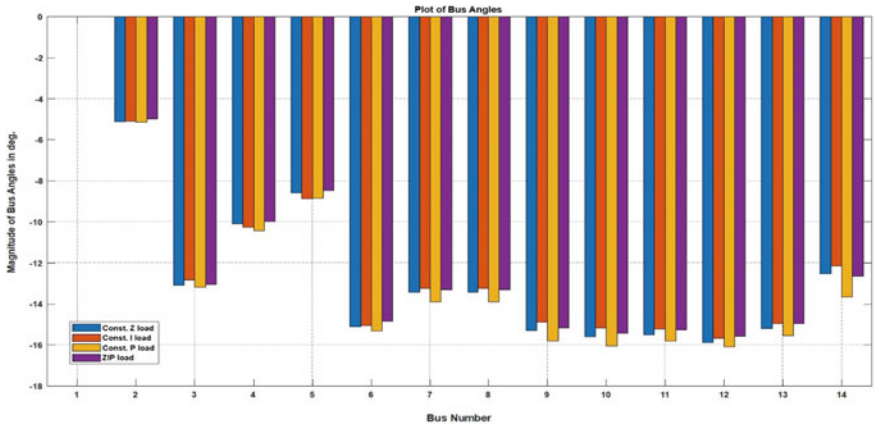

Fig. 3 Bus angles for various load models at large loading condition of weak bus

next ten lines for the maximum cases, constant power-type load models giving less losses.

From Table 1, the maximum acceptable load at a weak bus is less for constant power load model and next low for ZIP load model.

From Table 2, it is observed that total system active power loss is less for constant power load model, but reactive power loss is less with ZIP load model. Both the losses are more for constant current-type load model.

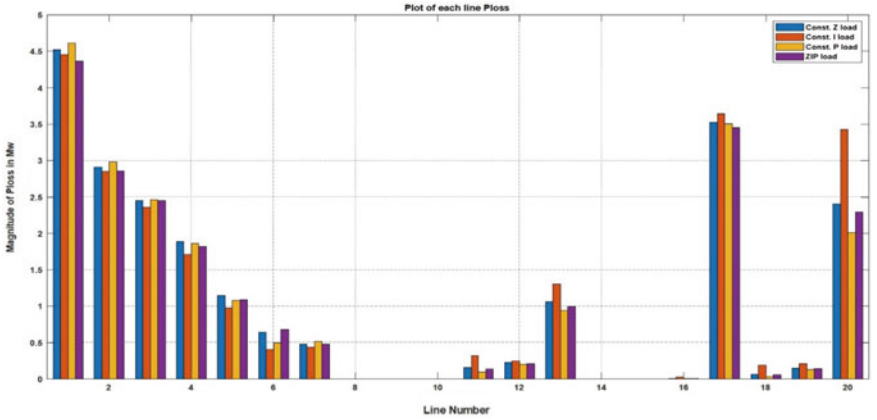

Fig. 4 Each line active power loss for various load models at large loading condition of weak bus

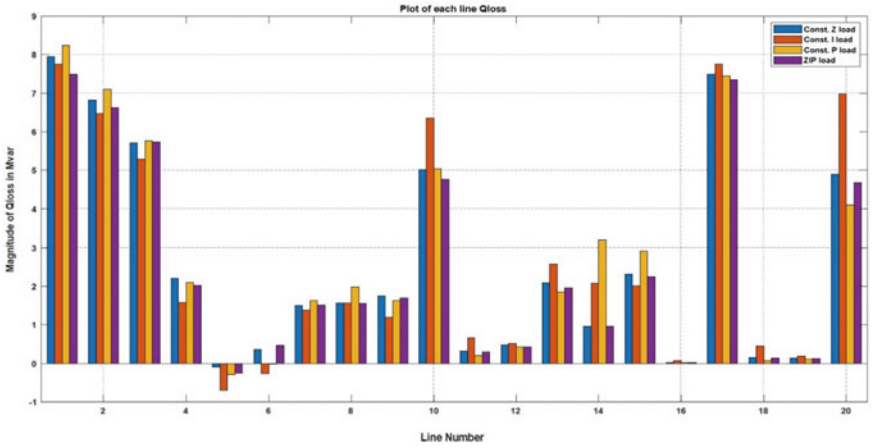

Fig. 5 Each line reactive power loss for various load models at large loading condition of weak bus

Table 1 Maximum load estimation at weak bus for various load models

Type of load	Maximum Q load in Mvar	L_{mn}	FVSI	VQI_{line}	NVSI	NLVSI
Constant Z load	99	1.0821	1.0311	1.0311	0.7449	0.9251
Constant I load	97.5	1.0275	0.9797	0.9797	0.6819	0.8757
Constant P load	69.5	1.0139	0.9771	0.9771	0.6872	0.8948
ZIP load	77.1	1.0588	1.0136	1.0136	0.7264	0.9172

Table 2 Total system active and reactive power loss at maximum loading of weak bus

Type of load	Total *P* loss (Mw)	Total *Q* loss (Mvar)
Constant *Z* load	21.64	51.714
Constant *I* load	22.575	53.936
Constant *P* load	20.963	53.614
ZIP load	21.044	49.874

6 Conclusions

Line voltage stability indices-based approach is used in this paper for identifying the effect of various load models on maximum load ability estimation of a load bus. From the result analysis, it is identified that constant current-type load model offered good voltage profile and constant power-type load models maintained good bus angle profile for the maximum load at a weak bus. From the each line losses point of view, constant current and constant power-type load models gave less losses. Constant impedance-type load model offered more reactive loading at a weak bus compared to other load models. From the above discussion, it can be understood that voltage-sensitive load models are better to use for getting more accurate results.

References

1. Kundur P, Balu NJ, Lauby MG (1994) Power system stability and control, vol 7. McGraw-hill, New York
2. Ajjarapu V, Christy C (1992) The continuation power flow: a tool for steady state voltage stability analysis. IEEE Trans Power Syst 7:416–423
3. Chakrabarti S (2009) Static load modelling and voltage stability indices. Int J Power Energy Syst 29
4. Mrudveeka JNS, Lalitha SVNL, Ramamoorty M (2016) Analysis of maximum loadability of a bus for different load models using new algorithms. Indian J Sci Technol 9:1–8
5. Concordia C, Ihara S (1982) Load representation in power system stability studies. IEEE Trans Power Apparat Syst 969–977
6. Lal NK, Mubeen SE (2015) Voltage dependent load in power flow analysis. Electr Electron Eng Int J (ELELIJ) 4:65–77
7. Moghavvemi M, Omar FM (1998) Technique for contingency monitoring and voltage collapse prediction. IEE Proc Generat Trans Distribut 145:634–640
8. Musirin I, Rahman TA (2002) Novel fast voltage stability index (FVSI) for voltage stability analysis in power transmission system. In: Student onference on research and development
9. Althowibi FA, Mustafa MW (2010) Line voltage stability calculations in power systems. In: 2010 IEEE International conference on power and energy
10. Kanimozhi R, Selvi K (2013) A novel line stability index for voltage stability analysis and contingency ranking in power system using fuzzy based load flow. J Electr Eng Technol (JEET) 8:694–703

11. Burle T, Chintapalli VBR, Thota P (2020) A new line voltage stability index (NLVSI) for voltage stability assessment,. In: Intelligent computing techniques for smart energy systems, pp 535–548. Springer
12. El-Hawary ME (1982) Power system load modeling and incorporation in load flow solutions. In: Proceedings of the third large systems symposium
13. Christie R (1993) Power systems test case archive-14 bus power flow test case

Impact of Ultra Capacitor on Automatic Load Frequency Control of Nonlinear Power System

Tulasichandra Sekhar Gorripotu, Ahmad Taher Azar, Ramana Pilla, and Nashwa Ahmad Kamal

Abstract This article focuses on the performance of an ultra capacitor in a two-area reheat thermal power system for automatic load frequency control (ALFC). Initially, the power system model is designed in MATLAB/SIMULINK environment. Then, differential evolution (DE) technique based on two degree of freedom tilt integral derivative (2-DOF-TID) controller is placed as secondary controller. In order to improve the system's transient reactions, ultra capacitors (UCs) are mounted in each region, and their output is observed. Finally, the sensitivity has been analyzed to demonstrate the effectiveness of the proposed concept.

Keywords Automatic load frequency control (ALFC) · Differential evolution (DE) · Two degree of freedom tilt integral derivative (2-DOF-TID) controller · Ultra capacitors (UC)

T. S. Gorripotu (✉)
Department of Electrical and Electronics Engineering, Sri Sivani College of Engineering, Srikakulam, Andhra Pradesh 532410, India
e-mail: gtchsekhar@gmail.com; gtchsekhar@srisivani.com

A. T. Azar
Robotics and Internet-of-Things Lab (RIOTU), Prince Sultan University, Riyadh 11586, Saudi Arabia
e-mail: aazar@psu.edu.sa; ahmad.azar@fci.bu.edu.eg

Faculty of Computers and Artificial Intelligence, Benha University, Benha, Egypt

R. Pilla
Department of Electrical and Electronics Engineering, GMR Institute of Technology, Rajam, Andhra Pradesh 532127, India
e-mail: ramana.pilla@gmrit.edu.in; pramana.gmrit@gmail.com

N. A. Kamal
Faculty of Engineering, Cairo University, Giza, Egypt
e-mail: nashwa.ahmad.kamal@gmail.com

G. T. C. Sekhar et al. (eds.), *Intelligent Computing in Control and Communication*, Lecture Notes in Electrical Engineering 702,
https://doi.org/10.1007/978-981-15-8439-8_27

1 Introduction

The demand for load is continuously changing in a power system [1]. The power input must also differ accordingly. A shift in frequency occurs if the input–output balance is not retained. Frequency control is mainly accomplished by means of a speed control system assisted by additional means for precise control [2]. When an effective power balance between generation and demand is achieved, the frequency specification is fulfilled automatically. The total real electricity generation is equivalent to the total demand for MW, plus actual power losses. A change in speed or frequency immediately shows some difference. Generators are fitted with varying speed controls: various sensitivities, dead bands, reaction times, and drooping characteristics. The input is balanced within their own limits to satisfy demand. The machine generators automatically absorb any changes to local demand within the permissible limits. The automatic generation control is aimed independently at rearranging generation changes for preselected machines in the network after load adjustments have been randomly changed by the governors [3, 4]. For proper control, new regulatory devices and governors are therefore required. The generation control is called the frequency load control [5, 6]. The main principle behind the concept of automatic load frequency control (ALFC) is to regulate the generation of active power from the output of the generator according to the frequency revision and the transfer of power between the connection lines [2]. If a minor digression occurs at the pre-planned load demand value, it results in frequency deviations and interpower change between the device-related areas. To regulate the generator loads, it is obligatory to use a secondary controller to facilitate the quality power supply. This controller plays a major role in the design of the power system operation. A power system is said to be well designed when it maintains its standards with high quality, frequency at nearly a stable value, and regulating the voltage in its specified limits. The ALFC will monitor the generator by automatically revising the settings of the speed changer to normalize the gap between the generations and load [7–9].

The remaining of this paper is ordered as follows. In Sect. 2, related work is presented, and methodology of the proposed work is discussed in Sect. 3. The details of results are presented in Sect. 4. Finally, in Sect. 5, conclusion is provided.

2 Related Work

Over the few decades, power engineers/researchers doing lots of work on the concept of ALFC. They have introduced computational control techniques to employ with ALFC concept [10–13]. Paliwal et al. [14] have discussed particle swarm optimization (PSO)-based classical controller for a single-area power system. They also compared the related transient responses with genetic algorithm (GA). Tripathy et al. [15] reviewed various TDOF based fractional-order controllers for a two-area and three-area power system by employing grasshopper optimization technique.

The authors also analyzed the systems with and without nonlinear elements for various load disturbances. Sahu et al. [16] have addressed Salp swarm technique-based fuzzy system for eco-AGC of a power system. Sahu et al. [17] implemented 2DOFPID controller with teaching-learning-based optimization technique for diverse sources of power system, and they also addressed the ability of 2DOFPID controller by comparing with other techniques. Having all the above techniques taken into consideration, DE based 2-DOF-TID controller is implemented in the present study.

3 Methodology

In this paper, a two-area thermal (reheat) power system is intended for analysis purpose which is shown in Fig. 1 [8]. It is well known that a secondary controller is always needed to reduce area frequencies and tie-line power during hasty load disturbances. Although two areas are equal in capacity, two different 2-DOF-TID controllers are included due to unequal disturbances in each area. The DE optimization technique is designed to tune the parameters of proposed 2-DOF-TID controller. The range of the parameters exist in 2-DOF-TID controller are taken as [0, 2]. The design of 2-DOF-TID controller [17, 18] and flowchart of DE technique [18, 19] are provided in Figs. 2 and 3 respectively.

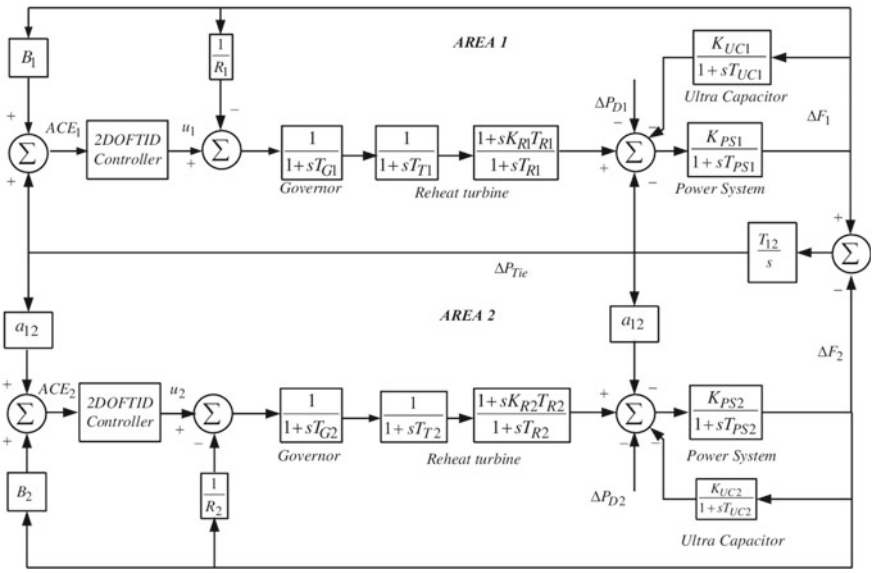

Fig. 1 Modeling of investigated system

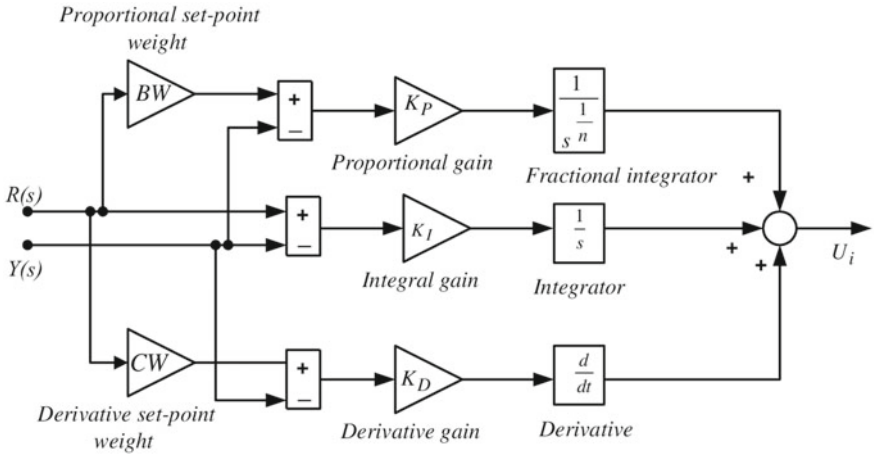

Fig. 2 Design of 2-DOF-TID controller

4 Result Analysis

In order to reveal the effect of inclusion of ultra capacitor units in the system, a step load perturbation (SLP) of 10% is applied in area 1 and 20% in area 2.

The optimal values of the 2-DOF-TID controllers are obtained for different cases as follows.

Case 1: Only with 2-DOF-TID controllers:

$K_{P1} = 1.2487;\ K_{I1} = 1.4510;\ K_{D1} = 1.0577;\ NC_1 = 2.1113;\ BW_1 = 1.4267;\ CW_1 = 1.3482;$
$K_{P2} = 1.8411;\ K_{I2} = 1.4761;\ K_{D2} = 0.7660;\ NC_2 = 2.1113;\ BW_2 = 1.5215;\ CW_2 = 1.7146$

Case 2: Inclusion of UC in area-1:

$K_{P1} = 1.4614;\ K_{I1} = 1.8899;\ K_{D1} = 0.9667;\ NC_1 = 2.0841;\ BW_1 = 0.6215;\ CW_1 = 1.9661;$
$K_{P2} = 1.3090;\ K_{I2} = 1.8347;\ K_{D2} = 1.6227;\ NC_2 = 2.0841;\ BW_2 = 1.1672;\ CW_2 = 0.5841$

Case 3: Inclusion of UCs in both areas:

$K_{P1} = 1.8768;\ K_{I1} = 1.2966;\ K_{D1} = 0.5539;\ NC_1 = 2.1241;\ BW_1 = 0.8894;\ CW_1 = 1.9191;$
$K_{P2} = 1.2250;\ K_{I2} = 1.2955;\ K_{D2} = 1.3127;\ NC_2 = 2.1241;\ BW_2 = 1.9217;\ CW_2 = 1.8591.$

The simulation results are observed when 10% SLP in area-1 and 20% SLP in area-2 are applied. Initially, the transient responses are observed for both the areas without any energy storage system like ultra capacitor. In the next step, UC is kept in area-1, and then UCs are kept in both the areas. The related dynamic responses

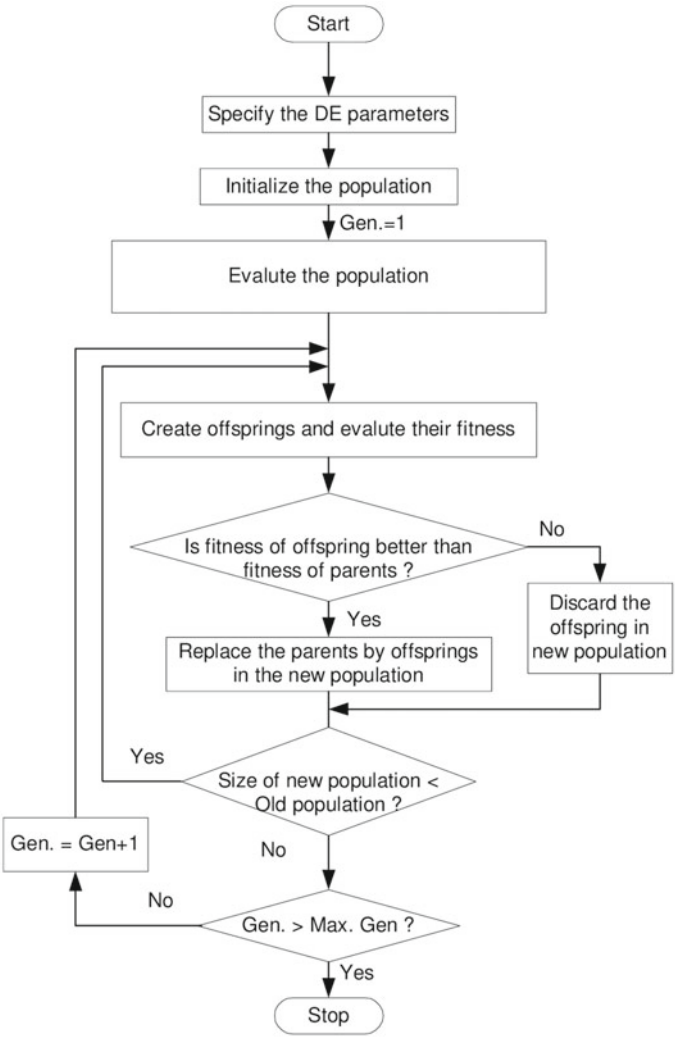

Fig. 3 DE technique flowchart

are revealed in Fig. 4a–c. The performance index values are also presented in Table 1. From Fig. 4a–c and Table 1, it is observed that the system with two UCs achieves good results than others. The integral time multiplied absolute error (ITAE) value is 0.3226 when two UCs are implemented in the system. The ITAE value is large in the remaining two cases: case 1 (ITAE = 0.5774) and case 2 (ITAE = 0.4328).

Sensitivity analysis test was carried out to show the capability of the DE based 2-DOF-TID controller. In this test, time constants are changed to −25% and +25%

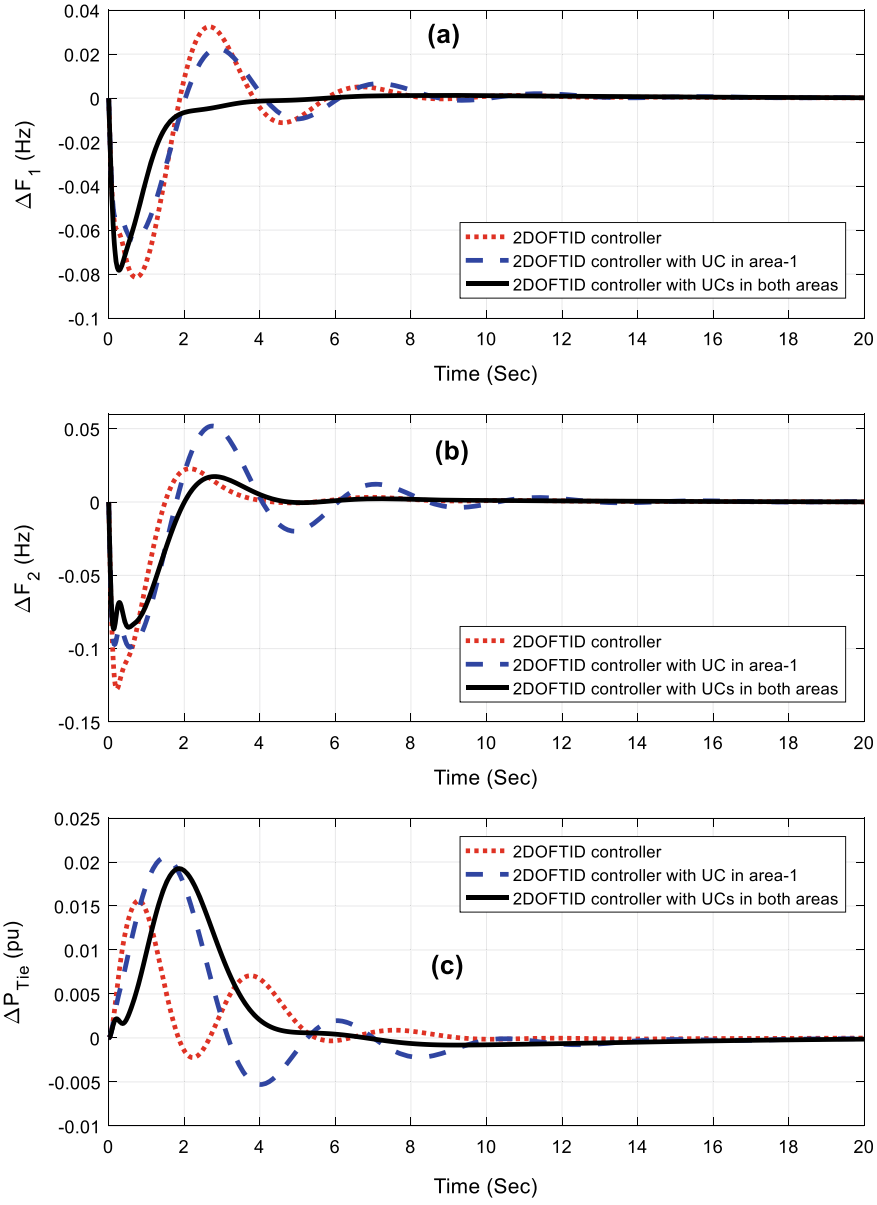

Fig. 4 **a–c** Transient responses

Table 1 Performance index values

Technique	ITAE	Peak overshoot			Peak undershoot (−ve)			Settling time (2% band) T_S (sec)		
		ΔF_1	ΔF_2	ΔP_{Tie}	ΔF_1	ΔF_2	ΔP_{Tie}	ΔF_1	ΔF_2	ΔP_{Tie}
DE tuned 2-DOF-TID	0.5774	0.0324	0.2227	0.0156	0.0815	0.1275	0.0022	2.74	2.70	1.89
DE tuned 2-DOF-TID with UC in area-1	0.4328	0.0225	0.0518	0.0205	0.0644	0.0990	0.0053	2.03	2.04	1.92
DE tuned 2-DOF-TID with UC in both areas	**0.3226**	**0.0012**	**0.0173**	**0.0192**	**0.0783**	**0.0866**	**0.0008**	**1.93**	**1.78**	**1.84**

Bold signifies best results in Table 1

Table 2 System parameters during sensitivity

Parameter variation	% Change	ITAE	Peak overshoot			Peak undershoot (−ve)			T_S (sec) (2% band)		
			ΔF_1	ΔF_2	ΔP_{Tie}	ΔF_1	ΔF_2	ΔP_{Tie}	ΔF_1	ΔF_2	ΔP_{Tie}
Nominal	0	**0.3226**	**0.0012**	**0.0173**	**0.0192**	**0.0783**	**0.0866**	**0.0008**	**1.93**	**1.78**	**1.84**
T_G	−25	0.3879	0.0012	0.0174	0.0192	0.0731	0.0836	0.0008	1.93	1.78	1.84
	+25	0.3790	0.0012	0.0173	0.0193	0.0836	0.0947	0.0008	1.93	1.78	1.84
T_T	−25	0.3960	0.0012	0.0170	0.0190	0.0672	0.0804	0.0008	1.94	1.79	1.85
	+25	0.3734	0.0012	0.0180	0.0190	0.0882	0.0979	0.0008	1.92	1.77	1.83
T_{I2}	−25	0.3047	0.0010	0.0183	0.0170	0.0776	0.0868	0.0006	1.95	1.74	1.89
	+25	0.3670	0.0013	0.0164	0.0209	0.0789	0.0869	0.0009	1.92	1.80	1.81

Bold signifies reference values in Table 2

of their actual values, and transient reactions are plotted without optimizing the 2-DOF-TID controller. The UC system in both areas achieved good reactions. The resulting parameters during sensitivity are given in Table 2 and, for example, the graphs for governor time-constant (T_G) variation are shown in Fig. 5a–c.

5 Conclusion

In this article, the DE based 2-DOF-TID controller is executed for a two-area system. In each region, UCs are monitored to have an effect. The result analyzes concluded that, by placing UCs in the both areas, the system received superior responses. For the system with two UCs, the ITAE value is small. For adjustments in system parameters, the proposed definition was robust. The research may be applied to deregulated and distributed power systems as a future direction.

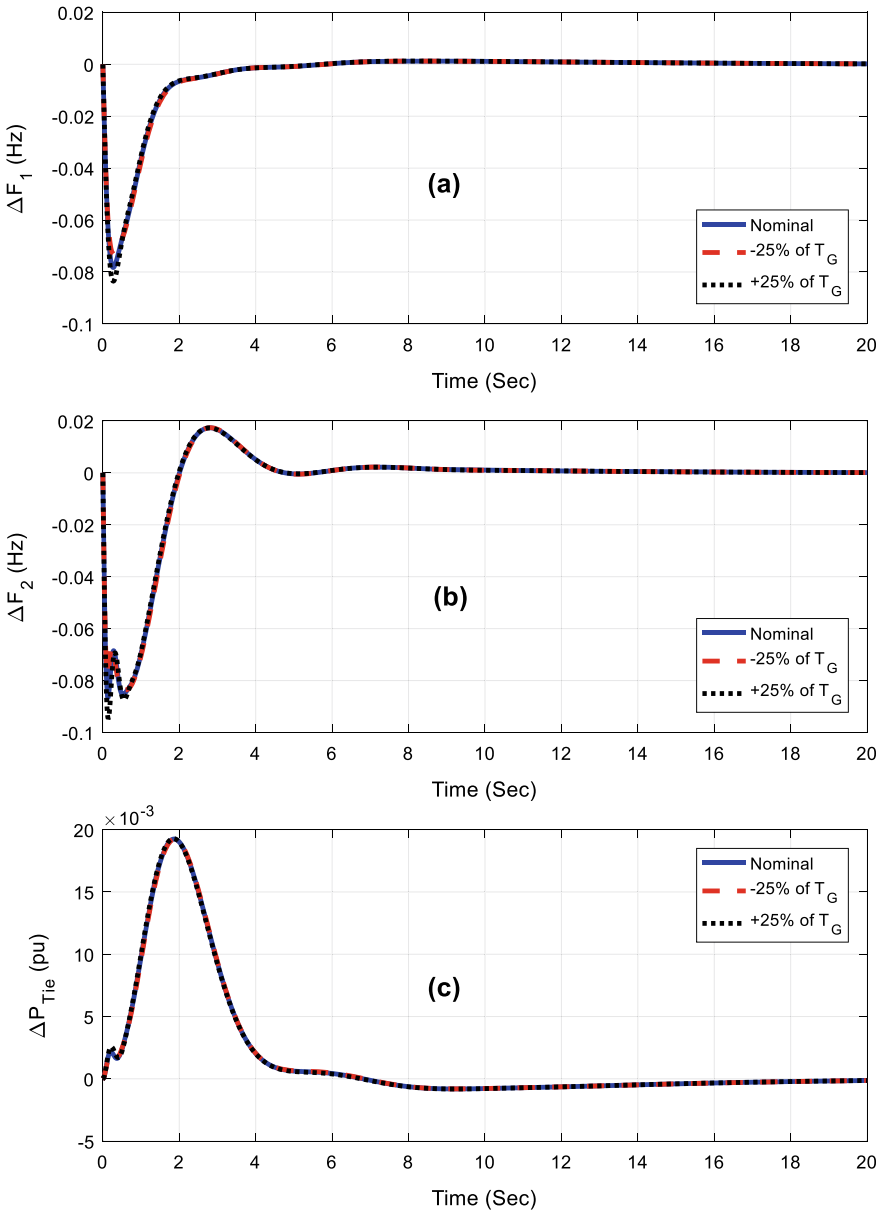

Fig. 5 **a–c** Responses for variation of T_G

References

1. Elgerd OI (2000) Electric energy systems theory–an introduction. Tata McGraw Hill, New Delhi
2. Bevrani H (2009) Robust power system frequency control. Springer
3. Pilla R, Botcha N, Gorripotu TS, Azar AT (2020) Fuzzy PID controller for automatic generation control of interconnected power system tuned by glow-worm swarm optimization. In: Nayak J, Balas V, Favorskaya M, Choudhury B, Rao S, Naik B (eds) Applications of robotics in industry using advanced mechanisms. ARIAM 2019. Learning and Analytics in Intelligent Systems, vol 5, pp 140–149. Springer, Cham
4. Gorripotu TS, Samalla H, Jagan Mohana Rao C, Azar AT, Pelusi D (2019) TLBO algorithm optimized fractional-order PID controller for AGC of interconnected power system. In: Nayak J, Abraham A, Krishna B, Chandra Sekhar G, Das A (eds) Soft computing in data analytics. Advances in intelligent systems and computing, vol 758. Springer, Singapore
5. Pappachen A, Fathima AP (2017) Critical research areas on load frequency control issues in a deregulated power system: astate-of-the-art-of-review. Renew Sustain Energy Rev 72:163–177
6. Tungadio DH, Sun Y (2019) Load frequency controllers considering renewable energy integration in power system. Energy Reports 5:436–453
7. Bervani H, Hiyama T (2011) Intelligent automatic generation control. CRC Press
8. Sahu RK, Panda S, Chandra Sekhar GT (2015) A novel hybrid PSO-PS optimized fuzzy PI controller for AGC in multi area interconnected power systems. Int J Electr Power Energy Syst vol 64, pp 880–893
9. Sahu RK, Panda S, Padhan S (2014) Optimal gravitational search algorithm for automatic generation control of interconnected power systems. Ain Shams Eng J 5(3):721–733
10. Chandra Sekhar GT, Kumar DV, Boddepalli MK, Pilla R (2018) Design and analysis of BFOA optimized PID controller with derivative filter for frequency regulation in distributed generation system. Int J Automat Control 12(2):291–323
11. Dash P, Saikia LC, Sinha N (2014) Comparison of performances of several Cuckoo search algorithm based 2DOF controllers in AGC of multi-area thermal system. Int J Electr Power Energy Syst 55:429–436
12. Taher SA, Fini MH, Aliabadi SF (2014) Fractional order PID controller design for LFC in electric power systems using imperialist competitive algorithm. Ain Shams Eng J 5(1):121–135
13. Padhy S, Panda S, Mahapatra S (2017) A modified GWO technique based cascade PI-PD controller for AGC of power systems in presence of Plug in electric vehicles. Eng Sci Technol Int J 20(2):427–442
14. Paliwal N, Srivastava L, Pandit M (2020) PSO-based PID controller designing for LFC of single area electrical power network. In: Pandit M, Dubey H, Bansal J (eds) Nature inspired optimization for electrical power system, algorithms for intelligent systems, pp 43–54. Springer, Singapore
15. Tripathy D, Dev Choudhury NB, Sahu BK (2020) Comparative performance assessment of several fractional order-two degree freedom controllers tuned using GOA for LFC. Procedia Comput Sci 167:2022–2032
16. Sahu PC, Prusty RC (2020) Frequency and tie-line power awareness in eco-AGC of multi-area power system with SSO-based fractional order controller. Int J Power Energy Conver 11(2):200–221
17. Sahu RK, Panda S, Rout UK, Sahoo DK (2016) Teaching learning based optimization algorithm for automatic generation control of power system using 2-DOF PID controller. Int J Electr Power Energy Syst 77:287–301
18. Sahu RK, Panda S, Biswal A, Chandra Sekhar GT (2016) Design and analysis of tilt integral derivative controller with filter for load frequency control of multi-area interconnected power systems. ISA Trans 61:251–2644
19. Stron R, Prince K (1995) Differential evolution-a simple and efficient adaptive scheme for global optimization over continuous spaces. J Global Optimizat 11:341–359

Support Vector Machine-Based Dynamic Cyber-Attack Detection in AGC System

Tummala S. L. V. Ayyarao, L. Venkata Sureshkumar, and D. Vijaya Kumar

Abstract This paper presents novel dynamic cyber-attack detection in automatic generation control (AGC) using support vector machine (SVM). The basic idea of attack detection is based on the pattern recognition of the residual signal of the linear observer designed to estimate the states of the AGC system. Features are extracted from the residual and its derivative signal and are trained using SVM. The proposed idea is tested for various types of attack signals

Keywords Cyber-attack · Load frequency control · Attack detection · SVM

1 Introduction

Smart grids are important for their increased versatility and efficiency [1]. However, due to the use of Internet connectivity, the power system is vulnerable to cyber-attacks. Attackers either steal sensitive network information or modify existing data. In the event of a cyber-attack, the data transmitted is either manipulated or blocked, resulting in huge financial losses and creating chaos in the system [2, 3]. Several cyber-attack events have been recorded in the history of the power system [4–6].

Automatic generation control (AGC) is a load frequency control mechanism in power systems. The working of the AGC requires the integration of information

T. S. L. V. Ayyarao · L. V. Sureshkumar (✉)
Department of Electrical and Electronics Engineering, GMR Institute of Technology, Rajam, Andhra Pradesh 532127, India
e-mail: lvenkatasureshkumar@gmail.com

T. S. L. V. Ayyarao
e-mail: ayyarao.tummala@gmail.com

D. Vijaya Kumar
Department of Electrical and Electronics Engineering, Aditya Institute of Technology and Management, Tekkali, Srikakulam, Andhra Pradesh 532201, India
e-mail: drdvk2010@gmail.com

G. T. C. Sekhar et al. (eds.), *Intelligent Computing in Control and Communication*, Lecture Notes in Electrical Engineering 702,
https://doi.org/10.1007/978-981-15-8439-8_28

communication and physical layers. The power outputs of the generators are regulated via AGC in order to balance a stochastic load changes by tracking area control error (ACE) and hold the grid frequency around the nominal value [7–9]. As this process involves data transfer through communication channels and thus vulnerable to cyber-attacks. Real time attack detection is essential as it enhances system stability and security. Most of the intrusion detection algorithms in the literature are inspired and extended from the fault detection methods. Outlier detection algorithms can be broadly generally categorized into three groups. The first one is a conventional method of attack detection, where rules are framed based on expertize of the system. However, the performance of this basic approach is not superior in the event of multiple attacks. The second type is model-based intrusion detection, where the existing model ratifies online data [10–13]. The third category is a pattern-based intrusion detection, where different machine learning algorithms are used to detect the attacks based on pattern recognition [14–17]. This paper proposes a hybrid method which is a combination of the last two methods. This method takes the advantages of the both the methods.

Rules are framed on the basis of the measured and predicted ACE difference for the detection of an attack in [11]. Attack can be detected, if the error of the regression model is above the threshold value [18]. Stochastic game theory-based attack detection is proposed in [19]. Multilayer perception classifier is applied for attack detection in [20]. Various attack detection algorithms based on statistics and machine learning algorithms are proposed in the literature. Such techniques are basically static detection methods, and the detection mechanism fails in the case of coordinated attacks. An unknown input observer is designed, and the residual function value of the observer is greater than the threshold, and then attack is detected [10]. The attack detection mechanism can be strengthened, if the attack detection is based on the pattern recognition instead of threshold setting.

This paper proposes a novel SVM-based dynamic outlier detection. In the proposed hybrid intrusion detection algorithm, the linear dynamic observer is used to generate the residual signal. Features are extracted using the evaluation functions and are used to build a model in offline.

Contributions

The major contributions of the paper are as follows: A linear observer is designed to estimate the states of the AGC system with output information, and the residual of the observer is examined to detect the attack on the system. Features of the residual signal are extracted using two evaluation functions of the residual and its time derivative signal. The features extracted are used to train and build a model in offline, and this model is used for attack detection in online. The performance of the proposed attack detection approach is evaluated for various attacks like FDI, DRA, and DoS. The simulation results show that this dynamic attack detection is a simple and an effective procedure for attack detection.

2 System Model

Power system load frequency mechanism is used to regulate the frequency and power exchange deviations with neighboring control areas. Frequency and tie-line power measurements are communicated to centralized monitoring and control system. Area control error (ACE), a linear combination of frequency and energy exchange deviations is created. ACE is communicated back to each area for frequency regulation as shown in Fig. 1. Frequency dynamics are slow, and thus, AGC system is developed based on the linearized model of power systems. The dynamics of ith area linearized power system model [7, 21, 22] are given as Eqs. (1)–(5):

$$\Delta \dot{f}_i(t) = -\frac{D_i}{2H_i}\Delta f_i(t) + \frac{1}{2H_i}\Delta P_{gi}(t) - \frac{1}{2H_i}u_i(t) - \frac{1}{2H_i}\Delta P_{ij}(t) \tag{1}$$

$$\Delta \dot{P}_{gi}(t) = -\frac{1}{T_{Ti}}\Delta P_{gi}(t) + \frac{1}{T_{Ti}}\Delta X_{gi}(t) \tag{2}$$

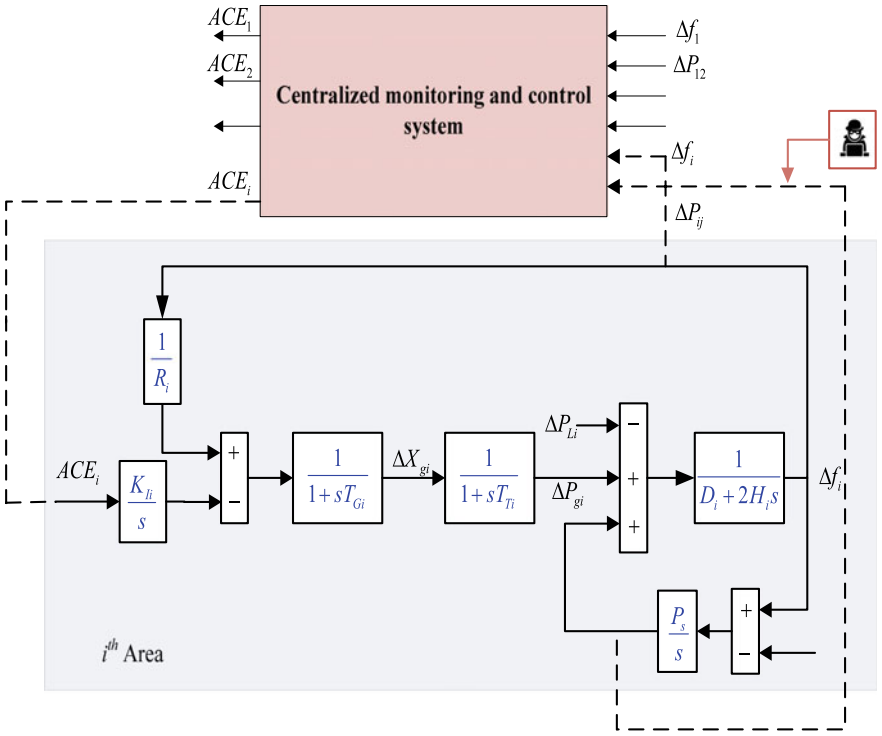

Fig. 1 AGC system

$$\Delta \dot{X}_{gi}(t) = -\frac{1}{R_i T_{Gi}} \Delta f_i(t) - \frac{1}{T_{Gi}} \Delta X_{gi}(t) + \frac{1}{T_{Gi}} ACE_i(t) \tag{3}$$

$$A\dot{C}E_i(t) = -K_{Ii} B_i \Delta f_i(t) - K_{Ii} \Delta P_{ij}(t) \tag{4}$$

$$\Delta \dot{P}_{ij}(t) = P_s \Delta f_i(t) - P_s \Delta f_j(t) \tag{5}$$

Now, the dynamics of n-area AGC system are represented in state space form as Eqs. (6)–(7):

$$\dot{x} = Ax + Bu + w \tag{6}$$

$$y = Cx + v \tag{7}$$

where

$$x = \left[x_1 \; x_2 \cdot \cdot \; x_n \right]^T$$

$$y = \left[\Delta f_1(t) \; \Delta f_2(t) \cdot \cdot \; \Delta f_n(t) \; \Delta P_{12}(t) \; \Delta P_{23}(t) \cdot \cdot \; \Delta P_{in}(t) \right]^T$$

$$u = \left[\Delta P_{L1}(t) \; \Delta P_{L2}(t) \cdot \cdot \; \Delta P_{Ln}(t) \right]^T$$

$$A = \begin{bmatrix} A_{11} & A_{12} \cdot \cdot & A_{1n} \\ A_{21} & A_{22} \cdot \cdot & \cdot \\ \cdot & \cdot \cdot \cdot & \cdot \\ \cdot & \cdot \cdot \cdot & \cdot \\ A_{n1} & \cdot \cdot \cdot & A_{nn} \end{bmatrix}$$

$$x_i = \left[\Delta f_i \; \Delta P_{gi} \; \Delta X_{gi} \; ACE_i \; \Delta P_{ij} \right]^T$$

3 Dynamic Attack Detection

Attack detection involves five major functions like data acquisition and residual generation, feature extraction, SVM-based model buildup, data acquisition, and residual generation as shown in Fig. 2. Centralized monitoring and control unit collect frequency, tie-line power, and load measurements from all control areas. These measurements are processed through a linear observer to generate residual signal.

Consider a linear invariant discrete system of form Eqs. (8)–(9):

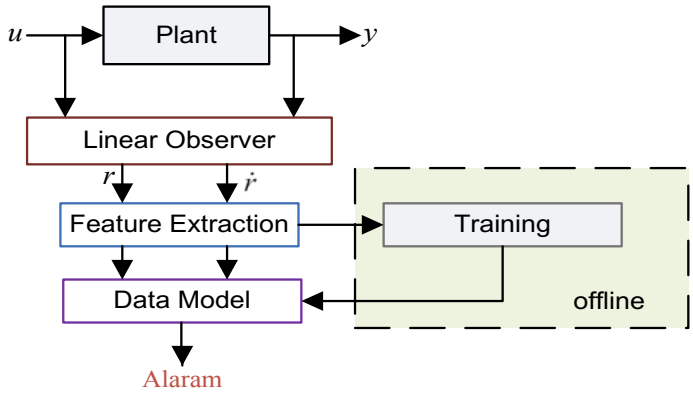

Fig. 2 SVM-based dynamic attack estimation

$$\dot{x} = Ax + Bu + Fb + w_k \tag{8}$$

$$y = Cx + Gb + v_k \tag{9}$$

where x is the state vector, u is the input vector, and b is the bias/attack vector at time t_0.

The states of the dynamic system can be estimated using a linear observer. The dynamics of the linear observer is given in this section as Eq. (10).

$$\dot{\hat{x}} = A\hat{x} + Bu + K\left(y - C\hat{x}\right) \tag{10}$$

The dynamics of the linear observer is given in this section.

Where $\hat{x}$ is the estimated state vector; K is the observer gain which can be obtained using pole placement technique.

The residual of the filter is obtained as Eq. (11):

$$r = R\left(y - C\hat{x}\right) \tag{11}$$

The derivative of the residual signal can be given as Eq. (12):

$$r_1 = \dot{r} \tag{12}$$

Most of the research on the attack/fault detection in the literature is focused on the threshold setting of the residual signal. Attack is detected, if the cumulative sum (cusum) of the residual is greater than the threshold. However, the residual depends to a large extent on the attack signal injected into the measurements, and therefore, attack detection is basically a problem of pattern recognition. The more detailed we get, the more accurate the outcome.

Feature Extraction: Machine learning algorithms require huge amount of raw data to generate a model. However, in many practical applications, the data availability may be an issue. The problem of attack detection can be addressed by converting raw SCADA data to a smaller set of features in order to differentiate between different classes in aggregate. The pattern of the residual signal can be extracted using a variety of statistical functions like norm, average, standard deviations, root mean square value, integral square, etc. Here, in this paper, we have considered two signals (r, r_1) for attack detection [23]. In this innovative approach, we have utilized the integral square function for feature extraction.

Two statistical functions used for attack detection are as depicted in Eqs. (13)–(14):

$$J_1 = \frac{1}{N}\sum_{k=1}^{N} r^T(k)r(k) \tag{13}$$

$$J_2 = \frac{1}{N}\sum_{k=1}^{N} r_1^T(k)r_1(k) \tag{14}$$

where N is the number of samples.

SVM-based Model Buildup: An SVM categorizes data by identifying the best hyperplane that separates every data point for one class from the other [24, 25]. The one-class SVM approach has been proposed in the literature to tackle the problem of lack of erroneous data during the training process. Let us assume that the SCADA data S used for classification contains N_1 samples of attack-free data and N_2 samples of attack data.

$$S = \left\{ (x_1, y_1)\ (x_2, y_2) \cdot \cdot (x_N, y_N) \right\} \tag{15}$$

where in Eq. (15), x_i represents the features of the data, and y_i represents the classes of data.

An ideal hyperplane is constructed as a decision surface through a support vector machine to maximize the separation margin between the two classes.

The hyperplane separating the two classes is represented mathematically as Eq. (16):

$$\beta^T x_i + b = 0 \tag{16}$$

The supporting vectors of each class are defined as:

$\beta^T x_i + b = +1$ for $y_i = +1$ (attack-free data points).

$\beta^T x_i + b = -1$ for $y_i = -1$ (attack data points).

Now, general support vector machine is now formulated as an optimization function, and including the slack vector ζ and penalty factor C, SVM generates a soft margin as given in Eq. (17).

$$\begin{aligned} &\min \frac{1}{2}\|\beta\|^2 + C\sum_{i=1}^{N}\zeta_i \\ &\text{s.t. } y_i\left(\beta^T x_i + b\right) > 1 - \zeta_i, \quad i = 1, 2, \ldots N \\ &\qquad \zeta_i > 0, \quad i = 1, 2, \ldots N \end{aligned} \tag{17}$$

In the case of linearly non-separable data, the binary classification does not have a simple hyperplane as a useful separating criterion. Using a non-linear transformation, kernel function $\Gamma\left(x_i, x_j\right)$ is used to solve the original feature problem as a regular linear separable problem. The kernel-based mathematical approach relies on the hyperplanes computational process. All hyperplane classification calculations use only dot products. Non-linear kernels can therefore use similar equations and solution algorithms to obtain non-linear classifications. For non-linear pattern classification, there are several kernel functionalities in the SVM, like linear, polynomial, sigmoid, radial basis, etc., as given in Eq. (18)

$$\begin{aligned} &\min \frac{1}{2}\sum_{i=1}^{N}\sum_{j=1}^{N}\alpha_i\alpha_j y_i y_j \Gamma\left(x_i, x_j\right) - \sum_{i=1}^{N}\alpha_i \\ &\text{s.t. } \sum_{i=1}^{N}\alpha_i y_i = 0 \\ &\qquad 0 < \alpha_i > 0, \quad i = 1, 2, \ldots N \end{aligned} \tag{18}$$

4 Applications for Attack Detection

As the frequency and tie-line measurements are prone to attacks, the dynamics of ACEs are affected. Now, the linearized model of AGC system represented in Eq. (16) is now modified, and attack signals are added as unknown input signals. The proposed idea of attack detection is applied for two-area and three-power system model. The implementation of attack detection is detailed in this section, and the same can be extended to *n*-area power system. The parameters of the two-area AGC power system dynamics represented in Eq. (16) are obtained as:

$$x = \left[\, \Delta f_1 \;\; \Delta P_{g1} \;\; \Delta X_{g1} \;\; ACE_1 \;\; \Delta f_2 \;\; \Delta P_{g2} \;\; \Delta X_{g2} \;\; ACE_2 \;\; \Delta P_{12} \,\right]^T$$

$$u = \left[\, u_1 \;\; u_2 \,\right]^T$$

$$y = \left[\, \Delta P_{12}(t) \;\; \Delta f_1(t) \;\; \Delta f_2(t) \,\right]^T$$

Attack detection involves two different stages. In the first stage named as training stage, SCADA data with and without attack are given to linear observer to generate the residual. The pattern is extracted from the residual signal, and the extracted features are given to SVM for model buildup. This model is used for attack detection in real time. In the second stage termed as testing stage, the model is tested for attack detection.

5 Simulation Results and Discussion

The proposed idea of state and bias/attack estimation is simulated for two-area and three-area power system models in MATLAB/SIMULINK for various cases of attacks. A zero mean white noise of 10^{-7}, 10^{-4} covariances is considered as process noise and measurement noise. The parameters of the two-area power system model are referred from [21]. The observer gain is designed using pole placement technique, and the pole locations are considered as

$$q = -0.01 \times \begin{bmatrix} 8 & 2.3 & 3 & 2.9 & 0.5 & 4 & 6 & 5 & 2 \end{bmatrix}$$

Initially, the system is simulated for 1200 s with and without attack injection. The injected attack signal in the tie-line measurements are shown in Fig. 3. Figure 4 shows the residual signal with and without outliers, and this clearly illustrates that residual signal pattern largely depends on the injected attack signal. The total measurements and the residual signal are divided into 600 groups so that time duration of each

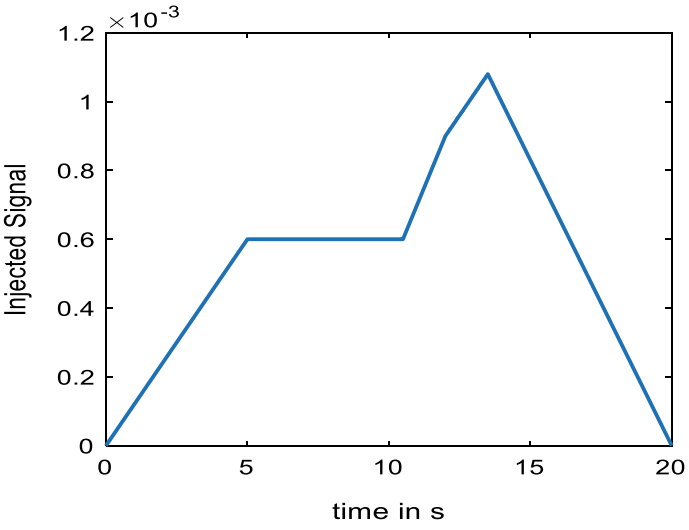

Fig. 3 Injected attack signal for training

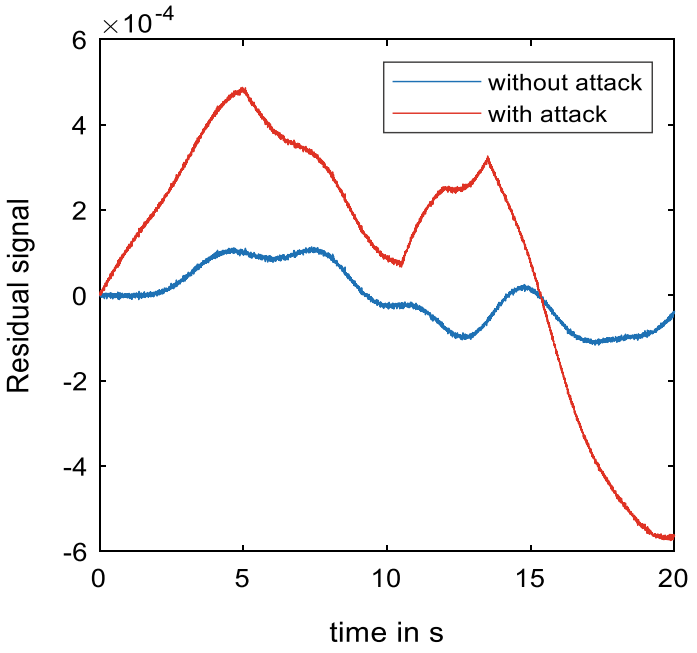

Fig. 4 Residual signal

group is two seconds. Reducing the time duration of each group will adversely affect performance of the attack detection. For each group, features are extracted using the evaluation functions. These features data are trained with support vector machine using the MATLAB command fitcsvm. Three different kernel classes are used during the training process, and the details are given in Table 1. The soft margin that separates the attack data with the non-attack data is visualized in Figs. 5, 6 and 7.

First, the proposed idea of attack detection with features is compared to that of raw data. The efficiency with features data is on an average is 90.45% when compared to 48.5% with raw data. The developed model after training process is tested with four types of cyber-attacks that are mentioned in Sect. 4. The results are recorded in Table 2.

Table 1 Different kernel functions

S. No.	Class	Kernel function
1.	Linear	$x^T x_i + \beta$
2.	Polynomial	$\left(x^T x_i + 1\right)^{\chi}$
3.	Radial-bias	$\mathrm{e}^{\left(-\frac{\|x-x_i\|^2}{2\sigma^2}\right)}$

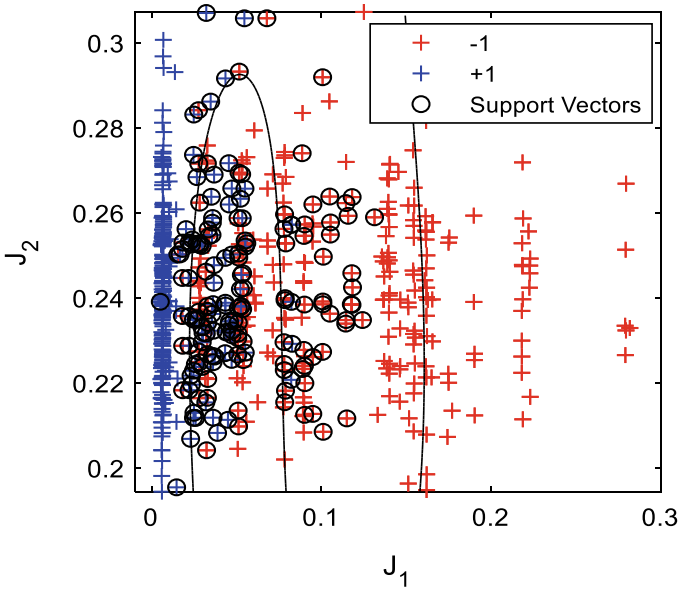

Fig. 5 Classification with RBF kernel

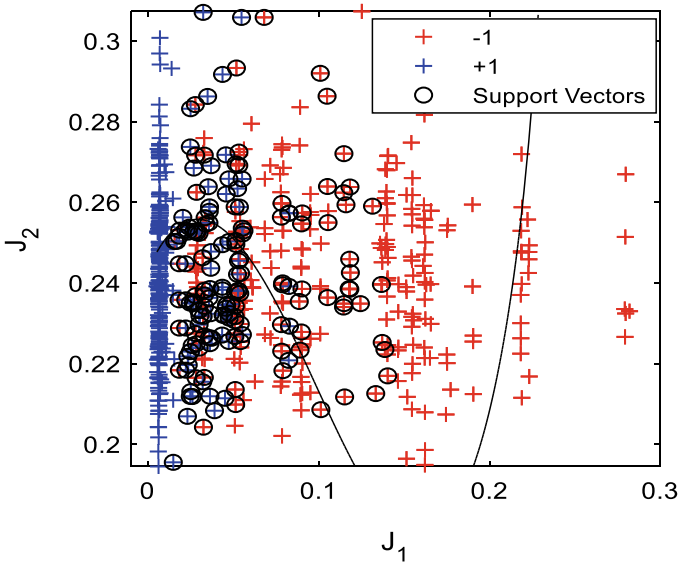

Fig. 6 Classification with polynomial kernel

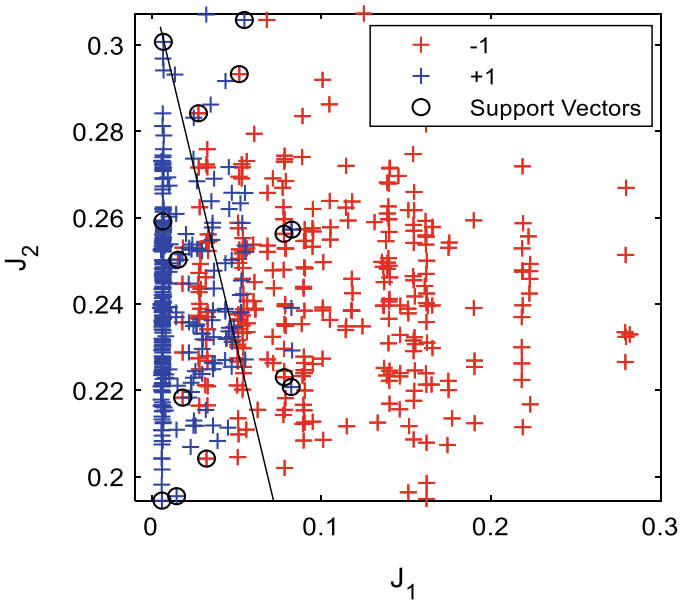

Fig. 7 Classification with linear kernel

Table 2 Performance of SVM with different kernel classes

Kernel class	False data injection	DoS attack	Data replay attack	Scaling attack
Linear	90.45	86.6	89.5	90.45
Polynomial	90.45	90.1	90.45	90.45
Radia1-bias	90.45	90.1	90.45	90.45

6 Conclusions

The performance of static attack detection schemes is uncertain in the case of coordinated cyber-attacks. To address this drawback, this paper proposes dynamic attack detection by extracting the features of the residual signal of linear observer for pattern identification. These features data are trained with SVM in offline to develop an attack detection model. This developed model is tested for various types of attacks like FDI, DRA, DoS, and scaling attack. The results show that proposed model is highly efficient in detection of attacks on frequency and tie-line measurements. This idea can be extended to classification of attack signals based on advanced machine learning algorithms.

References

1. Bou-Harb E, Fachkha C, Pourzandi M, Debbabi M, Assi C (2013) Communication security for smart grid distribution networks. IEEE Commun Mag 51:42–49. https://doi.org/10.1109/MCOM.2013.6400437
2. Barreto C, Giraldo J, Cardenas AA, Mojica-Nava E, Quijano N (2014) Control systems for the power grid and their resiliency to attacks. IEEE Secur Priv 12:15–23. https://doi.org/10.1109/MSP.2014.111
3. Liang G, Zhao J, Luo F, Weller SR, Dong ZY (2017) A review of false data injection attacks against modern power systems. IEEE Trans Smart Grid 8:1630–1638. https://doi.org/10.1109/TSG.2015.2495133
4. Case DU (2016) Analysis of the cyber attack on the Ukrainian power grid. Electr Inform Sharing Anal Cent (E-ISAC) 388
5. Li X, Liang X, Lu R, Shen X, Lin X, Zhu H (2012) Securing smart grid: cyber attacks, countermeasures, and challenges. IEEE Commun Mag 50:38–45. https://doi.org/10.1109/MCOM.2012.6257525
6. Liu C-C, Stefanov A, Hong J, Panciatici P (2012) Intruders in the grid. IEEE Power Energy Mag 10:58–66. https://doi.org/10.1109/MPE.2011.943114
7. Bevrani H (2014) Robust power system frequency control. Springer International Publishing, Cham. https://doi.org/10.1007/978-3-319-07278-4.
8. Taha AF, Qi J, Wang J, Panchal JH (2018) Risk mitigation for dynamic state estimation against cyber attacks and unknown inputs. IEEE Trans Smart Grid 9:886–899. https://doi.org/10.1109/TSG.2016.2570546
9. Sureshkumar, LV, Nagesh Kumar GV, Madichetty S (2017) Pattern search algorithm based automatic online parameter estimation for AGC with effects of wind power. Int J Electr Power Energy Syst 84:135–142
10. Ameli A, Hooshyar A, El-Saadany EF, Youssef AM (2018) Attack detection and identification for automatic generation control systems. IEEE Trans Power Syst 33:4760–4774. https://doi.org/10.1109/TPWRS.2018.2810161
11. Sridhar S, Govindarasu M (2014) Model-based attack detection and mitigation for automatic generation control. IEEE Trans Smart Grid 5:580–591. https://doi.org/10.1109/TSG.2014.2298195
12. Ameli A, Hooshyar A, Yazdavar AH, El-Saadany EF, Youssef A (2018) Attack detection for load frequency control systems using stochastic unknown input estimators. IEEE Trans Inf For Secur 13:2575–2590. https://doi.org/10.1109/TIFS.2018.2824253
13. Karimipour H, Dehghantanha A, Parizi RM, Choo K-KR, Leung H (2019) A deep and scalable unsupervised machine learning system for cyber-attack detection in large-scale smart grids. IEEE Access 7:80778–80788. https://doi.org/10.1109/ACCESS.2019.2920326
14. Ahmed S, Lee Y, Hyun S-H, Koo I (2019) Unsupervised machine learning-based detection of covert data integrity assault in smart grid networks utilizing isolation forest. IEEE Trans Inf For Secur 14:2765–2777. https://doi.org/10.1109/TIFS.2019.2902822
15. Wang H, Ruan J, Wang G, Zhou B, Liu Y, Fu X, Peng J (2018) Deep learning-based interval state estimation of AC smart grids against sparse cyber attacks. IEEE Trans Ind Inform 14:4766–4778. https://doi.org/10.1109/TII.2018.2804669
16. Esmalifalak M, Liu L, Nguyen N, Zheng R, Han Z (2017) Detecting stealthy false data injection using machine learning in smart grid. IEEE Syst J 11:1644–1652. https://doi.org/10.1109/JSYST.2014.2341597
17. Wang J, Shi D, Li Y, Chen J, Ding H, Duan X (2019) Distributed framework for detecting PMU data manipulation attacks with deep autoencoders. IEEE Trans Smart Grid 10:4401–4410. https://doi.org/10.1109/TSG.2018.2859339
18. Tan R, Nguyen HH, Foo EYS, Yau DKY, Kalbarczyk Z, Iyer RK, Gooi HB (2017) Modeling and mitigating impact of false data injection attacks on automatic generation control. IEEE Trans Inf For Secur 12:1609–1624. https://doi.org/10.1109/TIFS.2017.2676721

19. Law YW, Alpcan T, Palaniswami M (2015) Security games for risk minimization in automatic generation control. IEEE Trans Power Syst 30:223–232. https://doi.org/10.1109/TPWRS.2014.2326403
20. Chen C, Zhang K, Yuan K, Zhu L, Qian M (2018) Novel detection scheme design considering cyber attacks on load frequency control. IEEE Trans Ind Inform 14:1932–1941. https://doi.org/10.1109/TII.2017.2765313
21. Kundur P (2012) Power system stability and control. CRC Press
22. Tummala ASLV, Inapakurthi R, Ramanarao PV (2018) Observer based sliding mode frequency control for multi-machine power systems with high renewable energy. J Mod Power Syst Clean Energy. https://doi.org/10.1007/s40565-017-0363-3
23. Zhou J, Yang Y, Ding SX, Zi Y, Wei M (2018) A fault detection and health monitoring scheme for ship propulsion systems using SVM technique. IEEE Access 6:16207–16215. https://doi.org/10.1109/ACCESS.2018.2812207
24. Jan SU, Lee Y-D, Shin J, Koo I (2017) Sensor fault classification based on support vector machine and statistical time-domain features. IEEE Access 5:8682–8690. https://doi.org/10.1109/ACCESS.2017.2705644
25. Ahmed S, Lee Y, Hyun S-H, Koo I (2018) Feature selection-based detection of covert cyber deception assaults in smart grid communications networks using machine learning. IEEE Access 6:27518–27529. https://doi.org/10.1109/ACCESS.2018.2835527

Modelling and Design of Static Compensator and UPFC Based FACTS Devices for Power System Oscillations Damping and Voltage Compensation

D. V. N. Ananth, L. V. Sureshkumar, and Manmadhakumar Boddepalli

Abstract In this paper, four synchronous generators in a bi-area system generally known as Kundur system is considered for analysis of power oscillations and voltage dips. There are two parallel lines available for this network. Here, STATic COMpensator (STATCOM) which is a shunt device and Unified Power Flow Controller (UPFC) a hybrid shunt and series combination FACTS device is compared to identify better power oscillation damping and voltage compensating device when a grid disturbance is occurred. A very low impedance symmetrical fault occurs at the middle of the transmission network and these FACTS devices are kept near the fault but towards the second area. This fault creates surge currents that will flow in all lines, creating voltage dip across the lines, real and reactive power oscillations in the synchronous generators and quickly stability of the total system is influenced. These STATCOM and UPFC controller will act like low impedance path for the fault current and will divert the fault current which will in return stored in the converter capacitor is injected in the form of current by shunt device and voltage injection by the series device. Hence overall system profile and stability is improved. Results prove that the compensation in area-2 is better. These FACTS devices are kept after the fault and among these two devices, UPFC found better with effective compensation. The study is observed in two cases with first using a STATCOM, and second case with UPFC.

D. V. N. Ananth
Department of Electrical and Electronics Engineering, Raghu Institute of Technology, Visakhapatnam, Andhra Pradesh 531162, India
e-mail: nagaananth@gmail.com

L. V. Sureshkumar (✉)
Department of Electrical and Electronics Engineering, GMR Institute of Technology, Rajam, Andhra Pradesh 532127, India
e-mail: sureshkumar.lv@gmrit.edu.in

M. Boddepalli
Department of Electrical and Electronics Engineering, Aditya Institute of Technology and Management, Tekkali, Srikakulam, Andhra Pradesh 532201, India
e-mail: manmadhakumarboddepalli@gmail.com

G. T. C. Sekhar et al. (eds.), *Intelligent Computing in Control and Communication*, Lecture Notes in Electrical Engineering 702,
https://doi.org/10.1007/978-981-15-8439-8_29

Keywords Power oscillations · STATCOM · UPFC · Voltage compensation

1 Introduction

The main role of the transmission network is to have better reliability with lesser losses and higher stability margin. For attaining desired stability margin, the system must operate with reserve margin to overcome overloading or over current during load and fault transients [1]. But, this factor is not recommended for economical reason hence the transmission lines and generators will operate near its nominal rating. To ensure nominal power flow and also to attain high stability margin, FACTS technology is promising [2]. These FACTS devices capital cost is high but having very lesser running cost. Among these FACTS family Static Var Compensator, STATCOM and UPFC are better choice for voltage compensation, stability improvement and power flow improvement [3]. Static compensator (STATCOM) is a shunt device capable of voltage and reactive power regulation, and effective in power oscillation damping for a synchronous generator system under any transient conditions like switching and faults [4–6]. The series FACTS devices like Static Synchronous Series Compensator (SSSC) is a voltage injecting device and can be placed anywhere in the transmission network has advantages than STATCOM in terms of voltage compensation, stability improvement, power oscillations damping (POD) and operate at lower rating [7].

For high power electric generation, steam or hydro turbines are coupled to salient pole or cylindrical rotor synchronous generators. These FACTS devices must be losses-free, quicker in response, must not create new disturbance or aid to disturbance already in the system, but must compensate voltage and improve its profile [8–10]. In this paper, four synchronous generators in a bi- area system generally known as Kundur system is considered [11, 12]. The comparison of SVC and STATCTCOM in small signal stability for single machine infinite bus system (SMIB) using Eigen value and bifurcation methods and their effectiveness is studied in [13]. Nonlinear design of PSS and STATCOM using cuckoo search algorithm [14] and few authors observed POD is effective when advanced robust controllers like H-infinity ($H\infty$) controllers, fuzzy controllers, neural networks, meta-heuristic multi-objective controllers will be very helpful [15–19]. Among FACTS family STATCOM plays a major role in damping power system oscillations [17, 18]. These controllers will be faster, accurate and lesser parameter dependant and act according to the system and its fault behavior.

2 Configuration of the System

The equivalent Kundur power system test single line diagram is shown in Fig. 1. This system consists of four generators of equal rating. The impedances $Z1$ to $Z3$

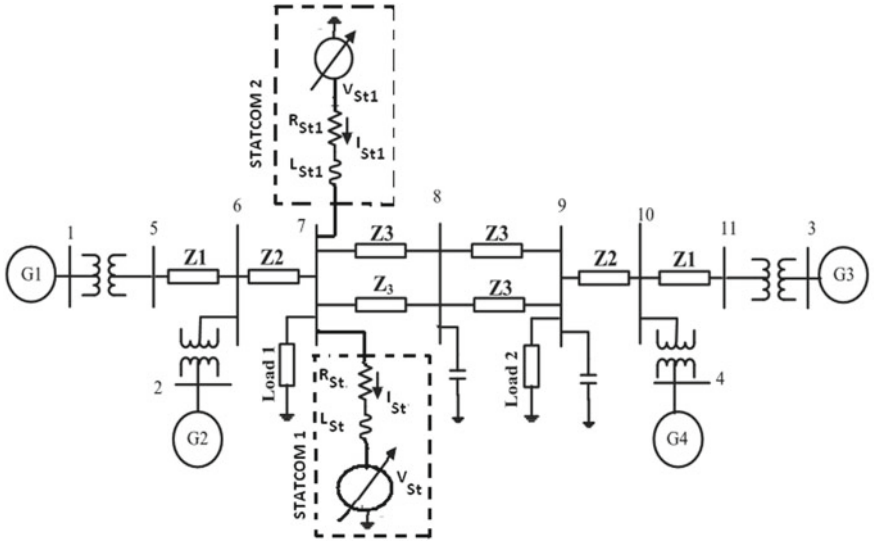

Fig. 1 Kundur four generators two area 11 bus system with STATCOM

represent transmission line passive components. The generator, line, transformer and load parameters are taken from [11].

2.1 Synchronous Generator Block Diagram

The synchronous block diagram is shown in Fig. 2. The system consists of governor, voltage controller and system stabilizer. The difference between desired and actual

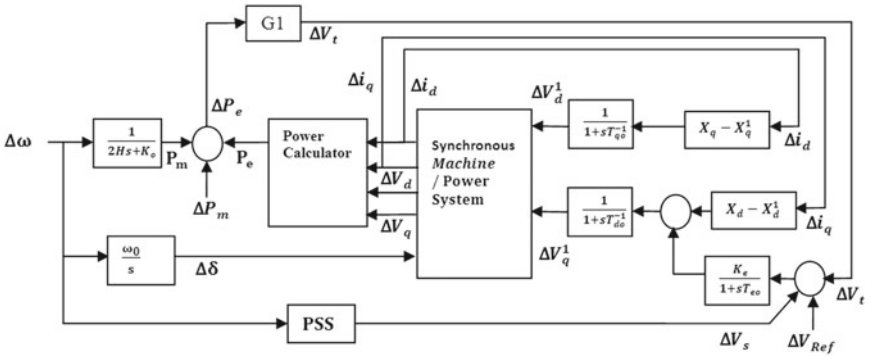

Fig. 2 The free body diagram of the synchronous generator with PSS and AVR

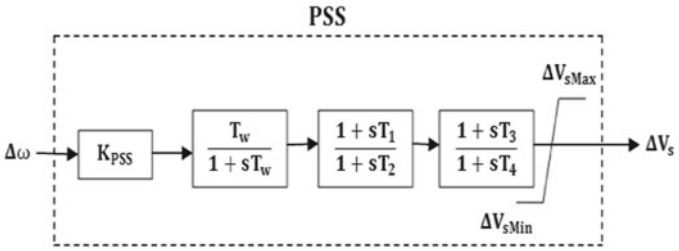

Fig. 3 The speed regulator based 5th order PSS representation

speed is said to be speed error, it is controlled by speed governor. Based on the difference in the speed ($\Delta\omega$), mechanical output (P_{m}) varies. From two space analysis, output power can be derived.

2.2 Power System Stabilizer (PSS)

The block diagram representation of 5th order PSS lead-lag compensator is shown in Fig. 3. If a disturbance occur to power system, if the system regains its pre-disturbance state is defined as stable. During or after disturbance, oscillations in generator parameters take place and if these oscillations are damped quickly then system comes to steady state operation. For oscillations damping PSS with lead-lag compensator type is used. K_{pss} is PSS gain constant; T_{w} is washout time constant, its value is about 30 s [15]. Lower than this value oscillations persist. For compensating excitation control system and also to maintain local phase lag, lead time constants are to be tuned and to improve stability lag time constants are used. For active power oscillations damping, the relationship with mechanical power flow change can be represented as in Eq. (1) as

$$\frac{2HS_B}{\omega_0}\frac{\mathrm{d}\omega_s}{\mathrm{d}t} = P_{\mathrm{turbine}} - P_{\mathrm{ref}} - K(\omega_1 - \omega_0) \tag{1}$$

Equation (1) is common representation of the synchronous generator under equilibrium with $\frac{\mathrm{d}\omega_1}{\mathrm{d}t}$ is zero when $P_{\mathrm{ref}} = P_{\mathrm{turbine}}$ and $\omega_s = \omega_1 = \omega_o$, where ω_1 is angular frequency of transmission lines in area-1 measured using phase locked loop (PLL).

2.3 Statcom

The static compensator is abbreviated as STATCOM which is a shunt connected voltage source converter (VSC) for a transmission line system connected where voltage and power flow profile improvement is necessary. The STATCOM is effective

than SVC in terms of compensation, stability improvement and can quickly control reactive power is damp power oscillations characteristics. The PSS and exciter control system are used to damp generator as well as inter-area oscillations to a maximum level and to enhance transient stability of complete power system.

2.4 UPFC-Unified Power Flow Controller

Among all FACTS devices, UPFC is said to be more versatile and robust [20]. It is due to the fact that it contains both series and shunt devices, disadvantages of any series or shunt can be compensated by the combination of the two. The advantages of UPFC are instantaneous control and can be designed with chatter-free characteristics, finite convergence time, smooth and faster control, effective to external disturbances.

3 Analytical Analysis of the System with STATCOM

The Dynamic equations of the power system with all parameters are taken from Fig. 4 and from [11]. The sub-script '*s*', '*st*' and '*r*' represents supply, STATCOM and receiving terminals. The voltage and current are represented with *V* and *I* and passive components like resistance, inductance and capacitance with *R*, *L* and *C*. STATCOM is having variable voltage, hence represented as shown in figure with variable mark Let δ_i is load angle and angular frequency of generator and STATCOM is represented as ω_i and ω_t at terminal "*t*" [11].

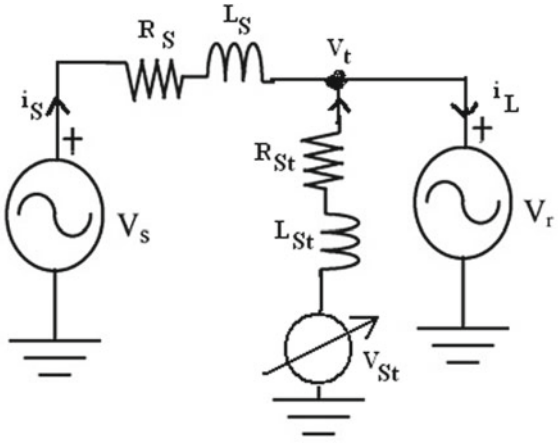

Fig. 4 Single line diagram of two area transmission and receiving system with a STATCOM at the midpoint

3.1 Generator Modelling

The dynamic equations of the alternator will be helpful in understanding the behavior under steady-state and transient conditions and also help in identifying and control the parameter dependency variables. The load angle in terms of angular speed change is shown in Eq. (2).

$$\frac{\mathrm{d}\delta_i}{\mathrm{d}t} = \omega_i - \omega_t \tag{2}$$

Similarly, the ith generator angular speed and its voltages are shown from Eqs. (3) to (8).

$$\frac{\mathrm{d}\omega_i}{\mathrm{d}t} = \frac{\omega_s}{2H_i}\left[T_{mi} - E^1_{qi} I_{qi} - (X^1_{di} - X^1_{qi}) I_{di} I_{qi} - E^1_{di} I_{di} - D_i(\omega_i - \omega_b)\right] \tag{3}$$

$$\frac{\mathrm{d}E_{qi}}{\mathrm{d}t} = \frac{1}{T^1_{doi}}\left[E_{fdi} - E^1_{qi} - (X_{di} - X^1_{di}) I_{di}\right] \tag{4}$$

$$\frac{\mathrm{d}E_{di}}{\mathrm{d}t} = \frac{1}{T^1_{qoi}}\left[-E_{di} + (X_{qi} - X^1_{qi}) I_{qi}\right] \tag{5}$$

$$\frac{\mathrm{d}E_{fdi}}{\mathrm{d}t} = \frac{1}{T_{Ei}}\left[-(S_{Ei}(E_{fdi} + K_{Ei}) E_{fdi} + V_{Ri}\right] \tag{6}$$

$$\frac{\mathrm{d}R_{fi}}{\mathrm{d}t} = \frac{1}{T_{Fi}}\left[\frac{K_{Fi}}{T_{Fi}} E_{fdi} - R_{fi}\right] \tag{7}$$

$$\frac{\mathrm{d}V_{Ri}}{\mathrm{d}t} = \frac{1}{T_{Ai}}\left[-V_{Ri} + K_{Ai} R_{fi} - \frac{K_{Fi} K_A}{T_{Fi}} E_{fdi} + K_{Ai}(V_{\mathrm{refi}} - V_i)\right] \tag{8}$$

Under equilibrium state, the voltage of direct and quadrature is represented as in Eqs. (9) and (10) as

$$E^{'}_{di} - V_i \mathrm{Sin}(\delta_i - \theta_i) - R_{si} I_{di} + X^{'}_{qi} I_{di} = 0 \tag{9}$$

$$E^{'}_{qi} - V_i \mathrm{Cos}(\delta_i - \theta_i) - R_{si} I_{qi} + X^{'}_{di} I_{qi} = 0 \tag{10}$$

Equations (9) and (10) are satisfactory under steady-state conditions, but in the transient state, they are not equal to zero.

3.2 Dynamic Modelling of STATCOM as Current Injecting Device

The STATCOM which is a shunt device will inject current at the point of coupling and is represented using Eqs. (11) and (12) as

$$\frac{\mathrm{d}I_{std}}{\mathrm{d}t} = \frac{-\omega_s R_{st}}{X_{st}} I_{std} + \omega_s I_{stq} - \omega_s \frac{\mathrm{Sin}(\alpha + \theta_s)}{X_{sr}} V_{dc} + \frac{\omega_s}{X_{st}} V_s \mathrm{Cos}(\theta_s) \tag{11}$$

$$\frac{\mathrm{d}I_{stq}}{\mathrm{d}t} = \frac{-\omega_s R_{st}}{X_{st}} I_{stq} + \omega_s I_{std} + \omega_s \frac{\mathrm{Cos}(\alpha + \theta_s)}{X_{sr}} V_{dc} + \frac{\omega_s}{X_{st}} V_s \sin(\theta_s) \tag{12}$$

If LHS of Eqs. (11) and (12) are negative, the STATCOM is defined to be injecting else absorbing that axis current. The difference in the DC link capacitance voltage, there will be change in current flow in or from STATCOM as in Eq. (13).

$$\frac{\mathrm{d}V_{dc}}{\mathrm{d}t} = -\sqrt{3}\omega_s X_{dc} \mathrm{Sin}(\alpha + \theta_s) I_{std} - \sqrt{3}\omega_s X_{dc} \mathrm{Cos}(\alpha + \theta_s) I_{stq} \tag{13}$$

The real and reactive power rating of STATCOM is decided by Eqs. (14)–(16) as

$$P_{st} + jQ_{st} = \frac{V_s V_{st} \mathrm{e}^{-j\alpha} - V_s^2}{R_{st} - jX_{st}} \tag{14}$$

$$P_{st} = \frac{V_s V_{dc} R_{st} \mathrm{Cos}\alpha + V_s V_{dc} X_{st} \mathrm{Sin}\alpha - R_{st} V_s^2}{R_{st}^2 + X_{st}^2} \tag{15}$$

$$Q_{st} = \frac{V_s V_{dc} X_{st} \mathrm{Cos}\alpha - V_s V_{dc} R_{st} \mathrm{Sin}\alpha - X_{st} V_s^2}{R_{st}^2 + X_{st}^2} \tag{16}$$

Equations (11) and (12) are simplified as decoupling current and voltage parameters is represented in Eqs. (17) and (18)

$$\frac{\mathrm{d}I_{std}}{\mathrm{d}t} = -\frac{R_{st}}{L_{st}} I_{std} - \omega I_{stq} + \frac{1}{L_{st}} (V_{std} - V_{td}) \tag{17}$$

$$\frac{\mathrm{d}I_{stq}}{\mathrm{d}t} = -\frac{R_{st}}{L_{st}} I_{stq} - \omega I_{std} + \frac{1}{L_{st}} \left(V_{stq} - V_{tq}\right) \tag{18}$$

The current flow in the STATCOM d and q axis is described in Eqs. (1) and (2) with supply current constant as assumption are simplified with the operation under the steady-state and rewritten as in Eqs. (17) and (18).

3.3 Analytical Analysis of STATCOM Converter Capacitor

Based on Equations from 11 to 18, the STATCOM power flow equation in terms of capacitor voltage, terminal voltage and STATCOM voltage and current as in Eq. (19)

$$\frac{3}{2}\left[-V_{std}I_{std} - V_{std}I_{stq}\right] = CV_{dc}\frac{\mathrm{d}V_{dc}}{\mathrm{d}t} + \frac{V_{dc}^2}{R_{dc}} + \frac{3}{2}\left(V_{td}I_{d1} + V_{tq}I_{q1}\right) \tag{19}$$

And hence the change in dc link voltage across the capacitor is given by Eq. (20)

$$V_{dc} = \frac{3}{2CV_{dc}}\left[-V_{std}I_{std} - V_{stq}I_{stq} - V_{td}I_{d1} - V_{tq}I_{q1}\right] - \frac{V_{dc}}{CR_{dc}} \tag{20}$$

Hence, the d-axis STATCOM current as shown in Eq. (21) gives the relation with the difference in the STATCOM and the PCC terminal voltage and the current injected into it. If there is no difference in voltage, the current injected will be small.

$$\frac{\mathrm{d}I_{sd}}{\mathrm{d}t} = -\frac{R_s}{L_s}I_{ds} - \omega I_{qs} + \frac{1}{L}(V_s - V_{td}) \tag{21}$$

4 Design and Analysis of Controller Circuit of STATCOM

The PQ control theory based STATCOM controller is in Fig. 5 with the reference voltage and current parameters taken from bus number 10. The reference real and reactive powers are derived at bus 10 in three axis form as in Eqs. (22) and (23).

$$P = V_aI_a + V_bI_b + V_cI_c \tag{22}$$

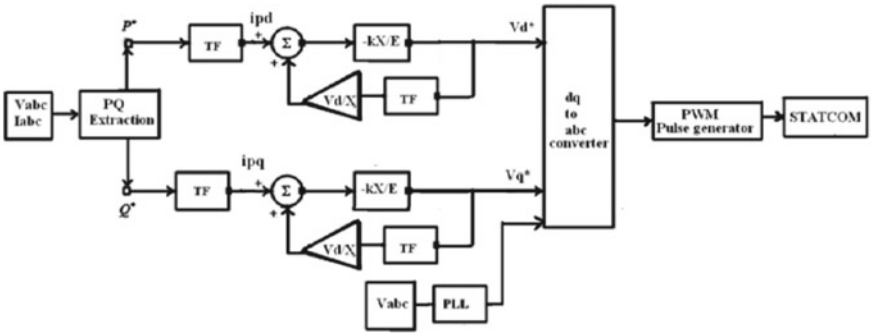

Fig. 5 Block Diagram of STATCOM controller

$$Q = \frac{[(V_a - V_b)I_c + (V_b - V_c)I_a + (V_c - V_a)I_b]}{\sqrt{3}} \tag{23}$$

Powers are also extractable from stationary two axis parameters as in Eqs. (24) and (25) as

$$P = V_d I_d + V_q I_q \tag{24}$$

$$Q = V_q I_d - V_d I_q \tag{25}$$

Equations (24) and (25) is represented in the matrix notation as in Eqs. (26) and (27) as

$$\begin{bmatrix} P \\ Q \end{bmatrix} = \begin{bmatrix} V_d & V_q \\ V_q & -V_d \end{bmatrix} \begin{bmatrix} I_d \\ I_q \end{bmatrix} \tag{26}$$

or

$$\begin{bmatrix} I_d \\ I_q \end{bmatrix} = \frac{1}{V_d^2 + V_q^2} \begin{bmatrix} V_d & -V_q \\ V_q & V_d \end{bmatrix} \begin{bmatrix} P \\ Q \end{bmatrix} \tag{27}$$

The voltages and the two powers P and Q in Eq. (27) are taken from the point where the STATCOM is connected, based on this equation the d and q axis current injections are obtained. Based on the requirement of real or reactive power, respective axis current flow parameter changes and will inject the current at the point of connection independently. The STATCOM bus voltage terminal point angle is given by 'α' refers and its phase angle measured by the PLL is represented as θ_s.

5 Time Domain Simulation

The test system shown in Fig. 1 is used for the analysis and the results are observed with STATCOM and with UPFC in two cases. Gen 1 and 2 represent generating stations in area 1 and Gen 3 and 4 in area 2. An equivalent nominal Π transmission line network is considered for analysis. The direct and quadrature axis currents will independently control the STATCOM real and the reactive power flow. The two phase to three phase voltage transformation by using inverse Park's transformation (dq to abc) and this reference voltage is fed to the STATCOM PWM converter. This PWM will control the current flow and the direction of STATCOM based on the voltage at reference terminal and at the STATCOM DC link capacitor terminal. If the voltage magnitude is higher at the reference point, the current will flow towards STATCOM capacitor terminal and will be charged otherwise, current flow from STATCOM to the reference injected point. The parameters values are specified in the Appendix at

the end of the conclusion section. Here, base voltage is 230 KV and the base current is 1600 A. The two case studies are discussed now:

5.1 Case-1: With STATCOM

The STATCOM connected two area power system for the test system shown in Fig. 1 is used here. A fault occurred at the bus 7 which is near the Area-1 and also the STATCOM is placed near this terminal. It is pragmatic from Fig. 6a (i) and (ii), the voltage and current in the area-2 is compensated completely, while in area-1 to a certain extent only due to the direction and location of fault and based on STATCOM reference point. In area-1, voltage dips from 1 to 0.45 p.u. and current raised from 0.5 to 0.95 p.u., whereas without STATCOM, the voltage dip is 0.1 p.u., and the and current rise is 18 p.u., (which is not shown here). Based on Fig. 6b (i) the voltage in *q*-axis in area-1 reached 0.85 p.u., during the fault and reached to normal pre-fault value once fault is cleared without any oscillations as they are damped effectively using the STATCOM. There is voltage dip or power oscillations observed in the area-2 as these are compensated successfully by the STATCOM. There are considerable oscillations in the real power in area-1 but are sustained and decreasing with time.

The area-2 synchronous generator (SG) parameters are shown in Fig. 6b (ii), the two dimensional voltages are almost constant during and after the fault and also no oscillations in the power are observed as these are efficiently mitigated by the STATCOM. The voltage at the STATCOM converter point and the current injected by it at bus number 7 is shown in Fig. 6c.

As the STATCOM behaves like a low impedance path when the current at the point of injection increases, will be diverted to its capacitor VSC terminal point and this current is reinjected to the same terminal, there by compensation is done effectively. This action will make sure, the surge current is decreased effectively in both the areas and mainly the area-2 as this is the reference point and the voltage being compensated during the fault. The post fault behaviour is also improved in both areas considerably.

5.2 Case-2: With UPFC

For the same test system, UPFC is placed in between buses 7 and 8. The advantage of UPFC over STATCOM is, it has both STATCOM and SSSC, which are shunt and series devices. The rating of system is higher than single STATCOM and hence has much higher and quicker capability to mitigate the voltage dip and power oscillations damping. SSSC is connected towards bus 7 and STATCOM in bus 8 in this study. Comparing Figs. 7a (i) and 6a (i), voltage compensation is higher with UPFC than STATCOM for Gen 1 in area 1. With UPFC the voltage decreased from 1 to 0.9 p.u., whereas with STATCOM, it is 0.5 p.u., but surge current is higher with UPFC. For

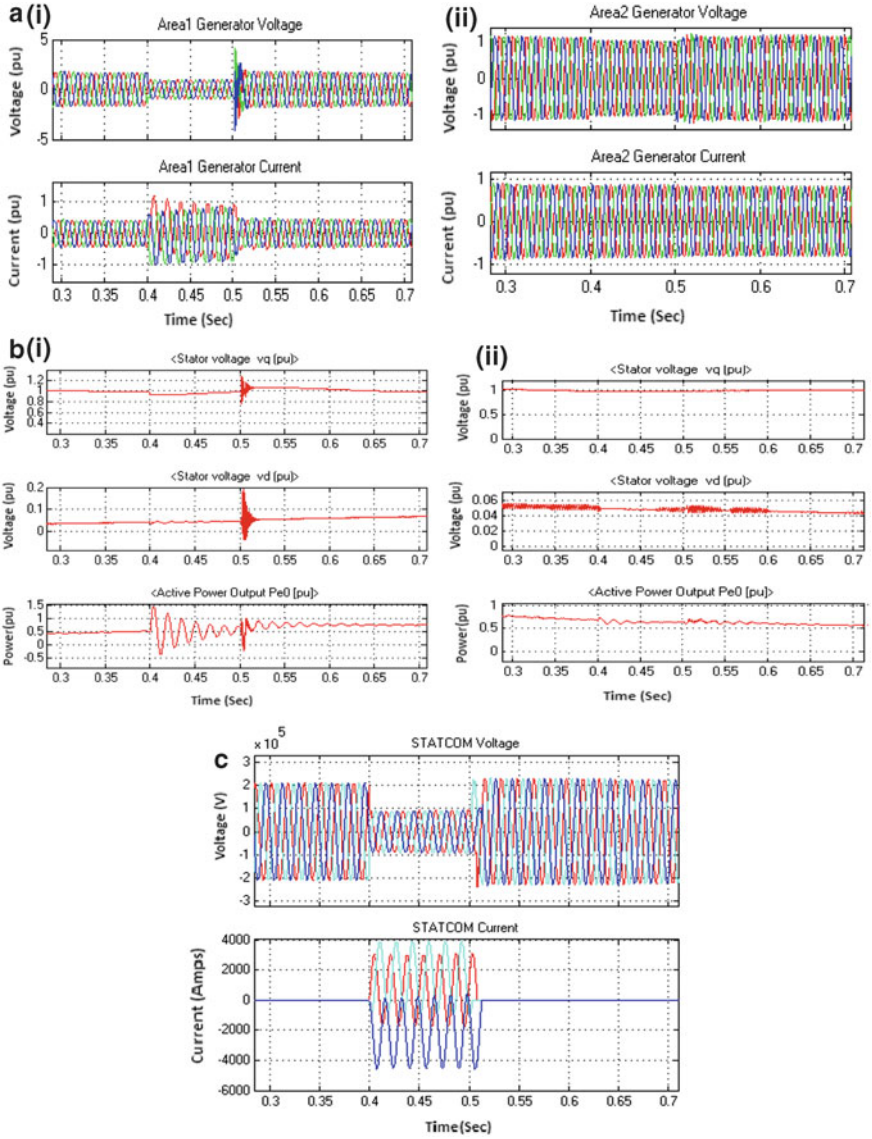

Fig. 6 **a** Terminal voltage and current in (i) area-1 (ii) in area2 with STATCOM connection. **b** SG parameters in (i) area-1 and (ii) in area2 using STATCOM converter. **c** STATCOM terminal Voltage and the current injection to the bus 7

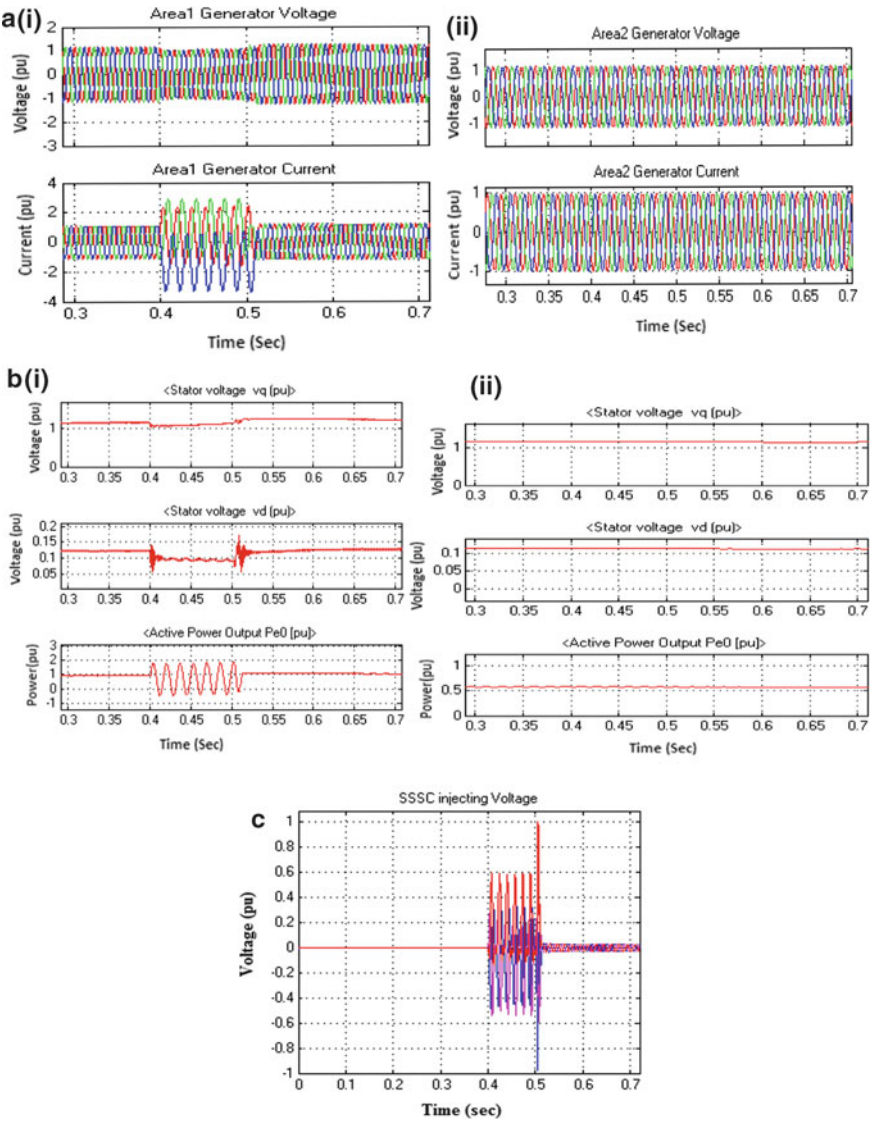

Fig. 7 **a** (i) Voltage and current in area 1 with UPFC (ii) Voltage and current in area 2 with UPFC. **b** (i) SG parameters in area 1 and the (ii) area 2 using UPFC based FACTS device. **c** DC voltage across capacitor link

area 2 shown in Fig. 7a (ii), the mitigation of voltage and current are same for both UPFC and STATCOM.

From Fig. 7b (i), the *q*-axis voltage decreased from 1 to 0.9 p.u. at the instant of fault and slowly regains to normal value even fault is not cleared. But when fault is cleared a surge voltage is produced due to sudden decrease in current flow and the oscillations were damped quickly due to UPFC. From Fig. 7b (ii), the system behaves normally with or without fault. The voltage injected by the SSSC during the fault is shown in Fig. 7c. It can be observed that voltage across capacitor is almost constant and can absorb huge inrush current entering into the circuit. But when fault is released voltage across capacitor is increased due to the influence of STATCOM.

However UPFC is an excellent device which can regulate power flow in the line, decrease losses, improve power factor, regulate voltage margin and can damp effectively power oscillations in the system. Disadvantages are design complexity, high capital investment for gate circuit, switches and high rating capacitors and transformer bank. If power oscillations can be damped quickly and mitigate voltage sag and limit surge current for UPFC, it can be a much better device.

6 Conclusion

A severe low impedance symmetrical ground fault occur in the midpoint of the two area Kundur system with four synchronous generators with two in each sides of two areas is considered. STATCOM is placed in area-1 and reference is taken in area-2. During this fault, the voltage in area-1 decreased to about half of its pre-fault value and area-2 voltage is almost constant with the STATCOM injection. The voltage dip or power oscillations are considerably very high when there is no STATCOM. It is also observed that voltage mitigation in area-1 is also improved using UPFC than with STATCOM. The power oscillations in both areas are efficiently damped, the *q*-axis voltage is maintained almost pre-fault value even during and after the fault using UPFC. Therefore, the STATCOM is better shunt device than other basic shunt FACTS devices, but UPFC as it is having both series and shunt compensating devices like STATCOM and SSSC, it is superior in performance. The advantages of proposed STATCOM controller are its simplicity in design and are applicable. In the controller, no decoupling components, hence so system parameters effect and dependency are minimised. No need to calculate voltage across DC link capacitance, but STATCOM three phase voltages and current parameter is required. The cost incurred to design is much cheaper than UPFC and complexity of designing series and shunt compensators can be eliminated. It is more effective than UPFC in voltage regulation, power factor correction and oscillations damping.

Appendix

Synchronous generator and its transformer: Nominal Power- 200 MW, nominal phase to phase voltage-13800 V, frequency-60 Hz, Xd-1.315, $Xd^1 = 0.286$, $Xd^{11} = 0.262$, $Xq = 0.484$, $Xq^1 = 0.253$, $Xq^{11} = 0.178$. Transformer nominal power rating 210 MW, voltage rating- 13.8/230 KV, internal resistance and reactance are 0.0027 and 0.08 per-unit.

Transmission line parameters: Nominal PI transmission line network is considered. Positive and zero sequence resistance is 0.01273 and 0.3864 ohms per kilometre.

STATCOM Parameters: Three winding, three phase transformer, 120 MVA, 230/230/20 KV for single STATCOM and 60 MVA, 230/230/20 KV.

References

1. Ananth D, Kumar GN, Deepak Chowdary D, Appala Naidu K (2017) Damping of Power System Oscillations and Control of Voltage Dip by Using STATCOM and UPFC. Int J Pure Appl Math 114(10):487–496
2. Behera B, Chandra Rout K (2018) Comparative performance analysis of SVC, Statcom & UPFC during three phase symmetrical fault. In: 2018 second international conference on inventive communication and computational technologies (ICICCT). IEEE, pp 1695–1700
3. Darabian M, Jalilvand A (2017) A power control strategy to improve power system stability in the presence of wind farms using FACTS devices and predictive control. Int J Electr Power Energy Syst 85:50–66
4. Sharma S, Narayan S (2017) Damping of low frequency oscillations using robust PSS and TCSC controllers. In: 2017 8th international conference on computing, communication and networking technologies (ICCCNT). IEEE, pp 1–7
5. Tossaporn S, Ngamroo I (2016) Hierarchical co-ordinated wide area and local controls of DFIG wind turbine and PSS for robust power oscillation damping. IEEE Trans Sustain Energy 7(3):943–955
6. Jolfaei MG, Sharaf AM, Shariatmadar SM, Poudeh MB (2016) A hybrid PSS–SSSC GA-stabilization scheme for damping power system small signal oscillations. Int J Electr Power Energy Syst 75:337–344
7. Tavakoli AR, Seifi AR, Arefi MM (2018) Fuzzy-PSS and fuzzy neural network non-linear PI controller-based SSSC for damping inter-area oscillations. Trans Inst Measur Control 40(3):733–745
8. Khezri R, Bevrani H (2015) Voltage performance enhancement of DFIG-based wind farms integrated in large-scale power systems: coordinated AVR and PSS. Int J Electr Power Energy Syst 73:400–410
9. Shayeghi H, Safari A, Shayanfar HA (2010) PSS and TCSC damping controller coordinated design using PSO in multi-machine power system. Energy Convers Manag 51(12):2930–2937
10. Baek S-M, Park J-W (2013) Nonlinear parameter optimization of FACTS controller via real-time digital simulator. IEEE Trans Ind Appl 49(5):2271–2278
11. Ananth DVN, Nagesh Kumar GV (2017) Mitigation of voltage dip and power system oscillations damping using dual STATCOM for grid connected DFIG. Ain Shams Eng J 8(4):581–592
12. Kundur PS (2017) Power system stability and control, power system stability. CRC Press, pp8–1

13. Yang L, Xu Z, Østergaard J, Dong ZY, Wong KP, Ma X (2011) Oscillatory stability and eigenvalue sensitivity analysis of a DFIG wind turbine system. IEEE Trans Energy Convers 26(1):328–339
14. Abd-Elazim SM, Ali ES (2016) Optimal location of STATCOM in multimachine power system for increasing loadability by Cuckoo Search algorithm. Int J Electr Power Energy Syst 80:240–251
15. Prasad, Sheetla, Shubhi Purwar, and Nand Kishor.:H-infinity based non-linear sliding mode controller for frequency regulation in interconnected power systems with constant and time-varying delays. IET GTD., 10(11), 2771–2784 (2016).
16. Mokhtari M, Aminifar F, Nazarpour D, Golshannavaz S (2012) Wide-area power oscillation damping with a fuzzy controller compensating the continuous communication delays. IEEE Trans Power Syst 28(2):1997–2005
17. Ananth DVN, Vineela KST (2019) A review of different optimisation techniques for solving single and multi-objective optimization problem in power system and mostly unit commitment problem. Int J Ambient Energy, 1–23
18. Sureshkumar LV, Nagesh Kumar GV, Madichetty S (2017) Pattern search algorithm based automatic online parameter estimation for AGC with effects of wind power. Int J Electr Power Energy Syst 84:135–142
19. Sureshkumar LV, Nagesh Kumar GV, Prasanna PS (2016) Differential evolution based tuning of proportional integral controller for modular multilevel converter STATCOM. In: Computational intelligence in data mining, vol 1. Springer, New Delhi, pp 439–446
20. Mohanty AK, Barik AK (2011) Power system stability improvement using FACTS devices. Int J Mod Eng Res (IJMER) 1(2):666–672

Validation of Real-Time Novel Voltage Instability Detection Index Using Real-Time Digital Simulator

Hemanthakumar Chappa and Tripta Thakur

Abstract Voltage instability detection in good time has become highly demanded in the recent power system operations. This work is a step towards the voltage instability detection using the reactive power loss-based voltage instability detection index SQLVIDI proposed by the authors. This index is validated under real time for Western System Coordinating Council (WSCC 9) bus test system by considering all the dynamic components responsible for voltage instability using real-time digital simulator (RTDS). The proposed index is also compared with synchrophasor technology-based voltage instability monitoring index VIMI in real time. The RTDS results show that the index SQLVIDI is fast in detecting the voltage instability and can be used to monitor voltage stability in real-time power system applications.

Keywords Voltage stability · Voltage collapse · Real-time digital simulator (RTDS) · Phasor measurement units (PMUs) · Reactive power losses

1 Introduction

Voltage stability is the ability of the system to maintain acceptable voltage at all the nodes before and after the occurrence of a disturbance [1, 2]. There are many methods proposed so far, in literature to identify the voltage instability before its occurrence. Most of the methodologies are usually based on formulating indices which are scalars and dimensionless quantities. Voltage stability indices proposed in [3–10] utilize the concept of either singularity of power flow Jacobian matrix or examination of roots of the discriminant of voltage quadratic equation to detect voltage instability.

H. Chappa (✉)
Department of Electrical and Electronics Engineering, GMR Institute of Technology, Rajam, Andhra Pradesh 532127, India
e-mail: hemanthkumar.ch@gmrit.edu.in

T. Thakur
Department of Electrical Engineering, MANIT, Bhopal 462003, India
e-mail: tripta_thakur@yahoo.co.in

G. T. C. Sekhar et al. (eds.), *Intelligent Computing in Control and Communication*, Lecture Notes in Electrical Engineering 702,
https://doi.org/10.1007/978-981-15-8439-8_30

These methodologies are developed with suitable approximations and are static in nature. These methodologies are very slow in detecting the instability and therefore not suitable for online monitoring. The indices proposed in [11–15] utilize local phasor measurement unit (PMU) to detect voltage instability at any bus of interest. These methodologies are devised based on the computation of Thevenin's parameters which are very difficult to estimate accurately. A few methodologies [16–18] are proposed to detect voltage instability using wide area measurements which may give the exact picture of voltage instability. However, these methodologies require either high computational ability or extensive offline study. One of the indices based on the wider area measurements is QLVIDI developed by authors [1, 19]. This index is computationally simple, does not require any offline studies and can be used for real-time monitoring of voltage stability in power systems.

In this paper, the effectiveness of the SQLVIDI's performance under real time is tested with RTDS which contains parallel processing hardware architecture. RTDS[1] has also been utilized for validation of various algorithms and methodologies to solve various significant problems in power system protection, renewable integration, microgrids, flexible AC transmission system (FACTS), power system state estimation, plug-in electric vehicles, etc. [20]. In this proposed work, an effort is made to validate voltage instability detection index so that the index could be used as an early warning to prevent voltage collapse in real-time environment.

Of late there are a few methodologies for fast detection of voltage instability in power systems by utilizing the global measurements. A large number of PMUs are required for global measurements. Rate of change of voltage and its accelerated change has been utilized using PMU measurements to detect the impending voltage instability [17]. However, this methodology requires extensive offline studies to fix the threshold values. By utilizing only pre-disturbance variables and disturbance severity from PMU measurements, an algorithm is devised to detect voltage instability using decision tree algorithm [21]. For preparing and analysing larger test

[1]RTDS hardware contains racks which are parallel processing modules (PB5 cards), Gigabit Transceiver Workstation Interface Card (GTWIF), Gigabit Transceiver Analogue Input (GTAI), Gigabit Transceiver Analogue output (GTAO), Gigabit Transceiver Digital Input (GTDI), Gigabit Transceiver Digital Output (GTDO), Gigabit Transceiver Synchronization (GTSYNC), Gigabit Transceiver Front Panel Interface (GTFPI), Global Bus Hub (GBH) and Gigabit Transceiver Network (GTNET) cards. PB5 cards have two identical RISC processors. Each PB5 card has 24 analog output channels with 12 bit digital to analog (D/A) converters. This means each PB5 card can handle up to 24 nodes (three phase) in the power system. The purpose of GTWIF is to communicate RTDS with host computer installed with RSCAD software. RSCAD is a user-friendly GUI software where all the simulation diagrams are designed. RSCAD contains different modules to assemble the network. The modules are Draft, Runtime, and Transmission line module. The draft module is used to develop the network to be simulated by assembling the components available in the library section. The run time module is to run the simulation and to visualize the graphical signals. Apart from viewing the signals it also allows dynamic control actions while the simulation is running. Transmission lines both underground and overhead lines data can be entered in Transmission line modules. GTWIF also provides inter rack synchronization with GBH. GTSYNC is used to synchronize the RTDS simulation time step to GPS clock and also used to synchronize devices such as PMUs. GBH is used to exchange synchronization signals between racks. GTNET provides real-time communication with other software or hardware to RTDS.

systems, decision trees become complex and time-consuming. Singular value decomposition (SVD) application to power flow Jacobian has been explored, which has an advantage of detecting instability with reduced set of measurements but is computationally rigorous [22]. To address this, set of critical nodes have been identified by developing suitable indices to consider the combined effect of voltage distance to collapse and load distance to collapse [23].

Various drawbacks like slow in detection, rigorous computation, complexity of the index, etc. have been overcome in the SQLVIDI index proposed by authors [1]. This index utilizes the PMU measurements to compute nodal reactive power losses [18]. The only limitation with above index was that it is prone to ill-conditioning if there is no change in system state between two sampling instants of the PMUs [18]. To overcome this ill-conditioning problem, the developed methodology [1] uses only nodal reactive power losses and its rate of change to detect exactly the initiation of sharp rise in reactive power losses. As the system is stressed, it is known that reactive power losses increase and there comes a time where the reactive power losses shoot up. The time at which reactive power losses shoots up suddenly is the collapse time. This index [1] detects successfully when the sharp rise in reactive power losses initiated and its continuance with respect to time. This proves that the index is very simple in computation and can detect voltage instability occurrence in good time.

The remaining paper is organized as follows. Brief description of the proposed methodology is explained in next section. In Sect. 3, RTDS simulation results are discussed followed by conclusions and future scope in Sect. 4.

2 Proposed Index

In this paper, a new methodology is used to compute the index in real time using both RTDS and MATLAB. The time series voltage measurements, phasor angles and power flows both active and reactive from RTDS were sent to a computer installed with MATLAB through open phasor data concentrator (open PDC). Open PDC is to streamline time series data and can be used to send and receive messages between open PDC and a host computer. In this computer, SQLVIDI algorithm is developed in MATLAB environment, and the algorithm receives the above-mentioned time series data and computes the nodal reactive power losses and QLVIDI between the time $t(k)$ and $t(k+1)$. It also computes SQLVIDI between the time $t(k-1)$ and $t(k)$. The entire setup is shown as a flow chart in Fig. 1.

The complete details of the proposed index are shown in [1]. The preliminary index is shown in [19], and this index has been evaluated without considering the reactive limits of the generators. The index's performance in the presence of noise signals has been presented in [23]. The index's performance with various load modes is shown in [24] and with STATCOM for voltage stability improvement in [1]. In all the above-mentioned works, the index is tested with either repetitive runs of Newton Raphson (NR) load flow technique or dynamic simulation in PSAT, a toolbox in MATLAB platform.

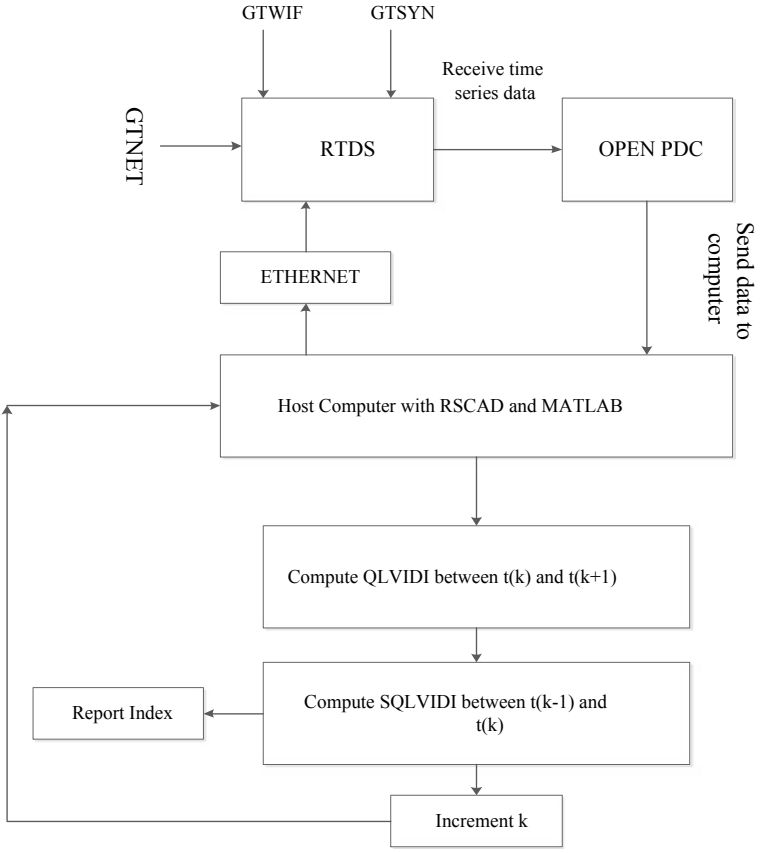

Fig. 1 Flow chart of the computation of SQLVIDI in RTDS and MATLAB

The flow chart for the computation of the index is given in Fig. 1. In the figure, computation of QLVIDI between $t(k)$ and $t(k+1)$ means the computation of QLVIDI for all the data points between $t(k)$ and $t(k+1)$ [25]. The time between $t(k)$ and $t(k+1)$ considered here is 1 s. In this one sec, 25 data points are obtained from PMUs (reporting rate is 25 frames/s). After computing QLVIDI for all the data points between $t(k)$ and $t(k+1)$, then SQLVIDI is computed for the same data points. While computing SQLVIDI between $t(k)$ and $t(k+1)$, QLVIDI is computed for the data between $t(k+1)$ and $t(k)$ and so on. This algorithm computes parallel both QLVIDI and SQLVIDI at a time difference of 1 s.

In this proposed work, the index is tested in real time using RTDS at IIT Kanpur. The RTDS at IIT Kanpur contains:

- Six Racks,
- PB5 cards,
- Gtnet,

- Gtwif,
- Gtio,
- Gtsync.

The PB5 cards have the following specifications:

- Freescale MC7448 RISC processor,
- Two processors per card,
- 1.7 GH clock frequency,
- 72 single-phase or 24 three-phase nodes,
- 24 number of 12 bit D/A converters,
- 2 network solutions per card,
- 2 I/O and 6 communication ports,
- 12 load units,

GTNET card protocols are as follow:

- GTNET-GSE (GOOSE 64 bit I/O),
- Gtnet-Sv(Iec61850-9–2),
- GTNET-Playback,
- Gtnet(Dnp 3.0),
- Gtnet Pmu(C37.118.2).

The front view of 6 rack RTDS at IIT Kanpur is shown in Fig. 2, its close-up view in Fig. 3 and its rear view in Fig. 4.

Fig. 2 RTDS front view at IIT Kanpur

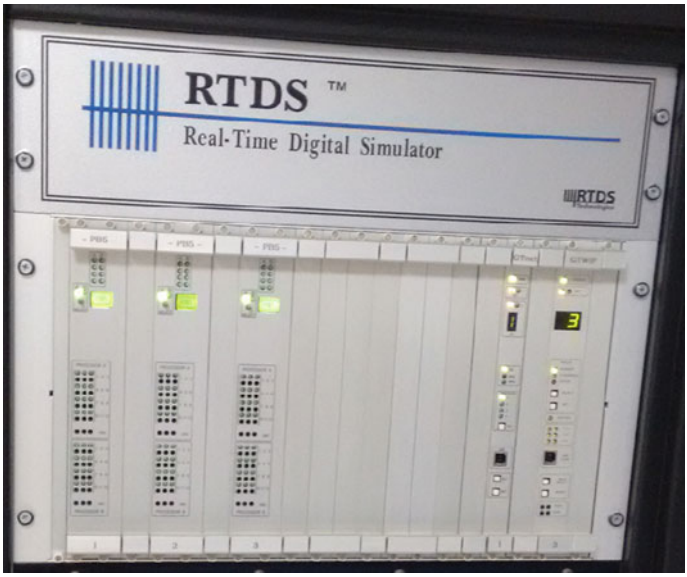

Fig. 3 Close-up front view of one rack

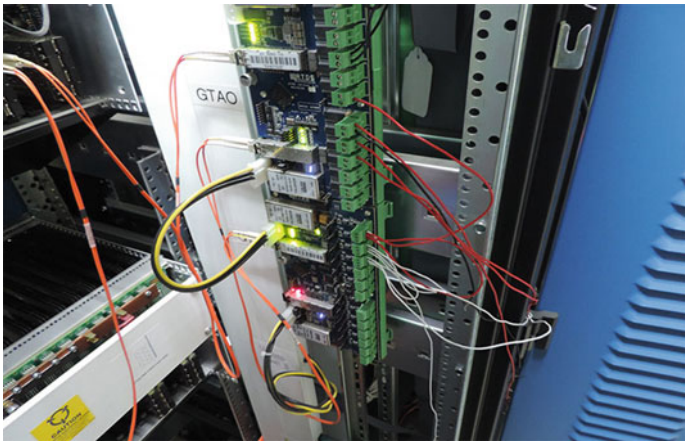

Fig. 4 Rear view of the rack

3 Simulation Results

In this work, WSCC 9 bus test system is considered to test the voltage instability detection in real time. The considered test system contains three load busses, nine branches and three generators. The test system data including generator models and IEEE Type-I DC Exciter is available in [26]. The nine bus system with all the dynamic

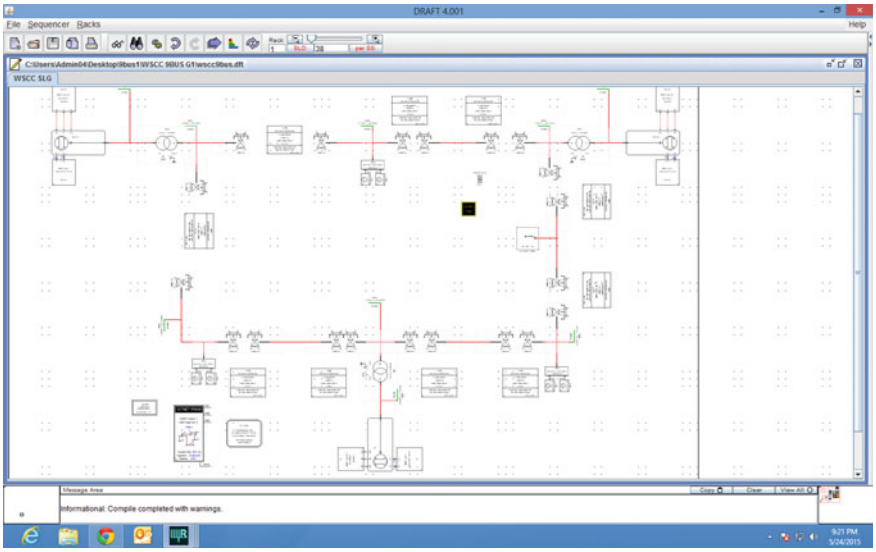

Fig. 5 Screenshot of the test system

components is developed in RSCAD software. The developed test system screenshot is shown in Fig. 5. In the considered test system, a load increment of 4% pu/s has been considered in all the load buses. This pattern of load increment is chosen to make the system transfer from a stable state to an unstable state in the long-term time frame. Apart from this reason, the voltage instability leading to blackout occurred in Japan [27] in the year 1997 is due to the continual increment of load at the rate of 400 Mw/min in the system. The load increment under real time is done using the scheduler in RSCAD. The sequencer may also be used for the same. PMU data from all the load nodes are utilized to compute active power flow in all the lines. The direction of active power flow in the lines and the reactive power losses in the lines are utilized to compute nodal reactive power losses.

The PMU voltages are shown in Fig. 6a, and it is clear that voltage instability occurs at 36 s. As load increases with time, voltage drops and at time $t = 36$ s, voltage is a sharp decline and goes beyond the acceptable limits. The index basically monitors the rate of change of reactive power losses in the system. The computed nodal reactive power losses in the system are shown in Fig. 6b. Initially, the losses are negative which means the system is loaded below surge impedance loading (SIL). If the rate of rising of reactive power loss goes up, it then indicates the stress on the system initiated. If there is a sudden large change in reactive power loss and such rate continuous, then the index becomes positive and gives early warning signal. Voltage instability detection index SQLVIDI is positive (Fig. 6c) for bus 6 at 17 s which is the early warning signal. The index maintains the positive value from time $t = 17$ s, which means the system load is much greater than SIL. The index plot is shown in Fig. 6c, and this shows that the index is initially negative when the load is very less

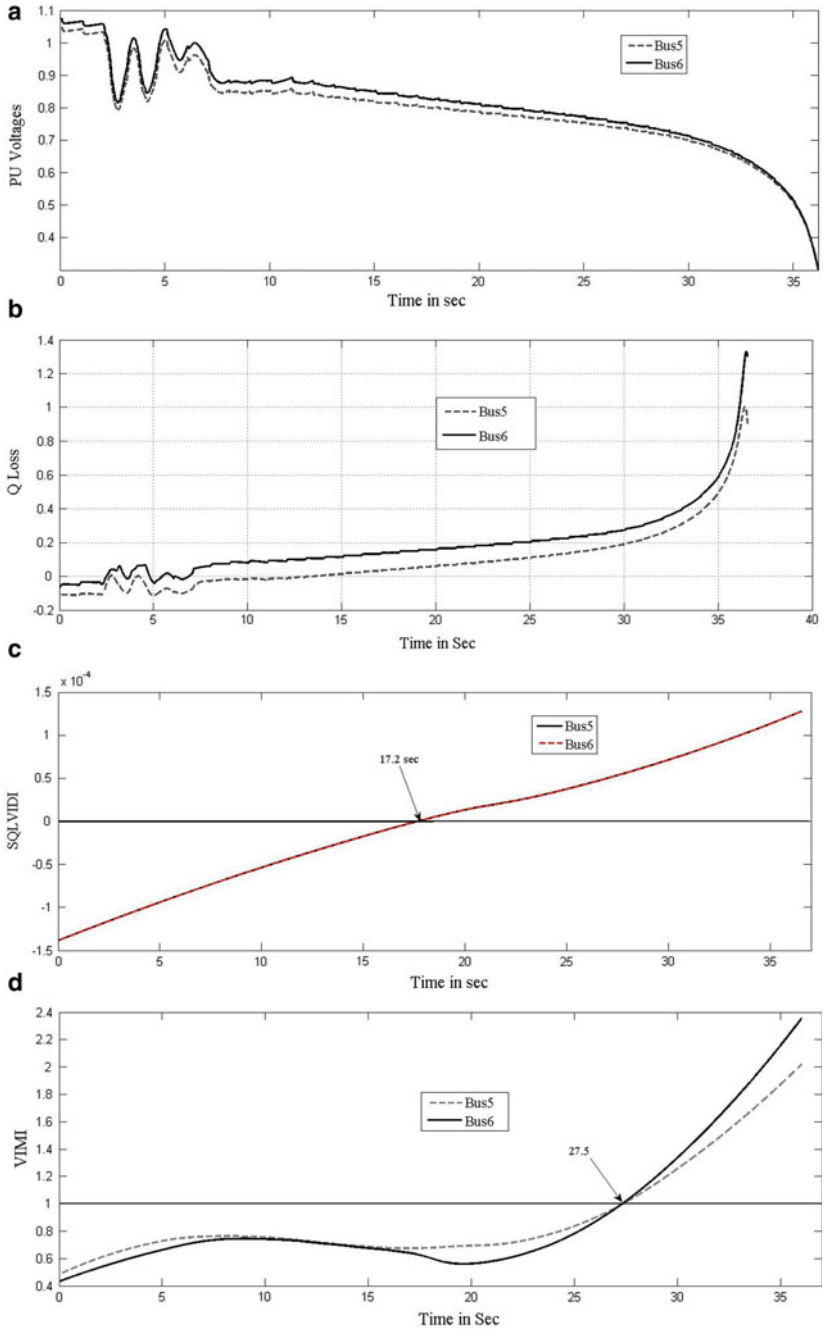

Fig. 6 **a** Voltages from PMUs. **b** Computed nodal reactive power losses. **c** Proposed index. **d** Plot of VIMI

on the system. Even though the index is derived from the nodal reactive power losses, the index will not follow the exact trend of nodal reactive power losses because of the weighting function in the algorithm. The weighting function makes the signal smooth; larger the number of outliers more will be the smoothness of the index due to assigned weights.

The proposed index is also been compared with the index VIMI [17]. This index considers only voltage magnitude measurements from PMUs at all the load busses. The measured voltages were then sent to the moving average filter to filter out the spurious signals. This index considers the change in voltage and accelerated change in voltage for detecting the voltage instability. However, this index needs setpoint values to be fixed which are obtained by offline studies, whereas SQLVIDI does not require any offline study or any setpoint adjustment. The computed VIMI is shown in Fig. 6d, and from the figure, it is clear that VIMI becomes unity at 26 s. If the value of VIMI is unity or above, it is an indication of voltage instability.

The comparison of the two indices shows that the index SQLVIDI gives an early warning and enables the power system operator with more time for decision-making and activating the preventive control measures. It is also advised that these two indices may also be used in conjunction with the power system. SQLVIDI may be used to activate the available reactive power reserves and VIMI can be used to activate load shedding. Effective utilization of these two indices may safeguard the system from voltage instability issues.

4 Conclusion and Future Scope

In this work, voltage instability detection index (SQLVIDI) has been tested under real time in RTDS. The computation of the index has been done in both RTDS and MATLAB. The brief description of RTDS along with its components is lucidly presented. The RTDS results show that the index is very fast in detecting voltage instability and thereby issues an alarm which will be the early warning signal for impending voltage instability. The proposed index has also been compared with VIMI. The real-time results show that SQLVIDI is faster in detecting voltage instability than VIMI. As this index proved to be fast in detecting voltage instability through time series nodal reactive power losses, this index may be used in real-time power systems for monitoring the long-term voltage instability. Apart from this, these two indices may also be used in parallel for taking the control actions. As future work, control actions may be devised and developed based on these two indices. SQLVIDI may be used for the activation of reactive power reserves and VIMI for developing a load shedding algorithm taking constraint as minimum load shedding without loss of voltage security.

Acknowledgements The authors wish to acknowledge the Commonwealth Commission, Dr. SC Srivastava, IIT Kanpur, India, for providing the laboratory facility to develop the preliminary index and to test the index in RTDS.

References

1. Chappa H, Thakur T (2019) A fast online voltage instability detection in power transmission system using wide area measurements. J Iran J Sci Technol Trans Electr Eng 47(1):427–438
2. Kundur P (1994) Power system stability and control. McGraw-Hill, New York
3. Mohamed A, Jasmon GB, Yousoff S (1989) A static voltage collapse indicator using line stability factors. J Ind Tech 7:73–85
4. Moghavvemi M, Omar FM (1998) Technique for contingency monitoring and voltage collapse prediction. IEE Proc Gener Trans Distrib 145(3):634–640
5. Chappa H, Thakur T (2020) Voltage instability detection using synchrophasor measurements: a review. In: International transactions on electrical energy systems. Wiley (2020)
6. Tiwari R, Niazi KR, Gupta V (2012) Line collapse proximity index for prediction of voltage collapse in power systems. Int J Electr Power Energy Syst 41:105–111
7. Kessel P, Glavitsch H (1986) Estimating the voltage stability of a power system. IEEE Trans Power Deliv 3:346–354
8. Balamourougan V, Sidhu TS, Sachdev MS (2004) Technique for online prediction of voltage collapse. IEE Proc Gen Trans Distrib 151(4):453–460
9. Perez-Londonoa S, Rodrigueza LF, Olivar G (2014) A simplified voltage stability index (SVSI). Int J Electr Power Energy Syst 63:806–813
10. Berizzi A, Finazzi P, Dosi D, Marannino P, Corsi S (1998) First and second order methods for voltage collapse assessment and security enhancement. IEEE Trans Power Syst 13:543–549
11. Wang Y, Li W, Lua J (2009) A new node voltage stability index based on local voltage phasers. Electr Power Syst Res 79:265–271
12. Smon I, Verbic G, Gubina F (2006) Local voltage-stability index using Tellegen's theorem. IEEE Trans Power Syst 21:1267–1275
13. Li W, Wang Y, Chen T (2010) Investigation on the Thevenin equivalent parameters for online estimation of maximum power transfer limits. IET Gen Trans Distrib 4:1180–1187
14. Jorge Esteba Tobon V, Gutierrez REC, Ramirez JM (2014) Voltage collapse detection based on local measurements. Int J Electr Power Syst Res 107:77–84
15. Vournas C, Van Cutsem T (2008) Local identification of voltage emergency situations. IEEE Trans Power Syst 23(3):1239–1248
16. Milosevic B, Begovic M (2003) Voltage-stability protection and control using a widearea network of phasor measurements. IEEE Trans Power Syst 18:121–127
17. Sodhe R, Srivastava SC, Singh SN (2012) A simple scheme for wide area detection of impending voltage instability. IEEE Trans Smart Grid 3(2):818–827
18. Gadiraju KVR, Kolwalkar A, Gurrala G (2013) Systems and methods for predicting power system instability. U.S. 0154614 A1, Jun. 2013 [Online]. Available: https://www.freepatentsonline.com/y2013/0154614.html
19. Chappa HK, Thakur T, Srivastava SC (2015) Reactive power loss based voltage instability detection using synchrophasor technology. In: IEEE PES Asia-Pacific power and energy engineering conference (APPEEC). Brisbane, QLD, Nov 2015, pp 1–5
20. Sharma A, Srivastava SC, Chakrabarti S (2016) Testing and validatation of power system dynamic state estimators using real time digital simulator (RTDS). IEEE Trans Power Syst 31(3)
21. Khoshkhoo H, Shahrtash SM (2014) Fast online dynamic voltage instability prediction and voltage stability classification. IET Gen Trans Distrib 8(5):957–965
22. Lim JM, DeMarco CL (2016) SVD-based voltage stability assessment from phasor measurement unit data. IEEE Trans. Power Syst 31(4):2557–2565
23. Lee DHA (2016) Voltage stability assessment using equivalent nodal analysis. IEEE Trans Power Syst 31(1):454–463
24. Chappa HK, Thakur T, Kazemtabrizi B (2016) A new voltage instability detection index based on real-time synchronophasor measurements. In: International conference on environment and electrical engineering. Florence

25. Cleveland WS (1979) Robust locally weighted regression and smoothing scatterplots. J Am Stat Assoc 74(368):829–836
26. Sauer PW, Pai MA (1998) Power system dynamics and stability. Prentice Hill, New Jersey
27. Atputharajah A, Saha TK (2009) Power system blackouts—literature review. In: Proceedings of the ICIIS, Dec 2009, pp 460–465

Improvement of Grid-Tied Hybrid System Reliability Using MPPT Techniques

Ijjada Ramesh and G. V. Siva Krishna Rao

Abstract In present scenario, the main problem of generation system is to meet the load requirement and maintenance of power management strategy. Consideration of environmental problems and greenhouse effect, renewable energy system is one of the alternate solutions to meet this requirement. So that DG systems become future energy sources due to the advantage of environmental conditions and energy costs linked with addition of existed energy systems. Out of all DG systems, PV and wind energy systems are alternative to each other to maintain the load supply reliability. This paper proposes a concept of hybrid system which consists of PV/wind and battery energy systems to improve reliability of system. A DC–DC converter with MPPT technique is used to regulate the DG systems. A cuckoo search algorithm is proposed as MPPT technique in this paper. This system is verified in Simulink environment and verified the results for various load conditions to meet the demand.

Keywords PV system · MPPT technique · Wind energy system · Cuckoo search algorithm and DC–DC converter

1 Introduction

The main problem of present power generation system is to meet the load demand and increases in environmental problems. A DG system can overcome these problems. In such situations, renewable power sources, together with solar photovoltaic and wind turbine generator, provide a practical alternative to supplement engine-pushed turbines for energy technology in off-grid areas. Therefore, the cost of many off-grid systems can be reduced with the help of these hybrid system configurations. Here, the

I. Ramesh (✉) · G. V. Siva Krishna Rao
Department of Electrical Engineering, Andhra University College of Engineering (A), Visakhapatnam, Andhra Pradesh 530003, India
e-mail: rameshijjada@gmail.com

G. V. Siva Krishna Rao
e-mail: gvskrishna_rao@yahoo.com

G. T. C. Sekhar et al. (eds.), *Intelligent Computing in Control and Communication*, Lecture Notes in Electrical Engineering 702,
https://doi.org/10.1007/978-981-15-8439-8_31

hybrid system is combination of PV, wind and also a battery energy storage system [1]. The concept of hybrid system is to maintain the cost-effective and reliable, and moreover, these are best suitable for the locations where the grid facility is difficult and also more expensive to build a transmission lines. Here, PV and wind energy systems are part of renewable energies. The solar energy is one of the non-polluting, site dependable sources available in environment. In order to extract maximum energy from the solar system, a maximum power transfer technique-based DC–DC boost converter is proposed. The duty cycle required for this boost converter is obtained with reference to MPPT signal and reference current signal from PV system.

In addition with PV system, the other alternative energy system is wind turbine. Wind turbine generates electrical energy from natural wind. There are two types of generators available in market, i.e., PMSG and induction generators. Like PV system, wind turbine also has combination of MPPT-based DC–DC converter to improve the voltage levels and to maintain constant power from the system.

To maintain synchronization between grid and hybrid PV-wind energy systems, a suitable PWM-based control diagram is designed for three-phase inverter [2].

2 Structure of PV-Wind Hybrid System

The hybrid PV-wind system is shown in Fig. 1. This hybrid system consists of combination of wind and PV energy systems. To improve the reliability and continuity of

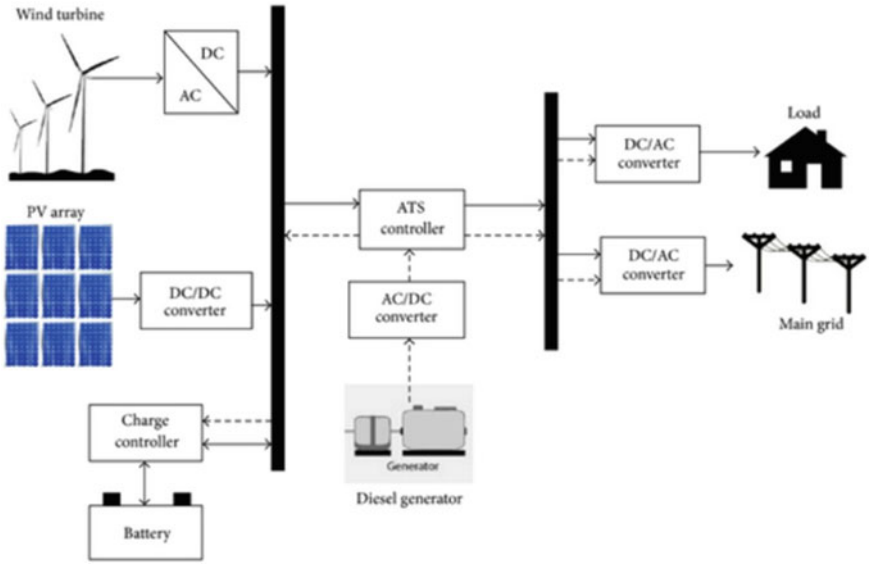

Fig. 1 Structure of grid interfaced hybrid system

supply to load demand, battery energy systems are also implemented in this structure. PV, wind and battery systems are interconnected at DC bus and converted to AC using PWM-based inverter [3]. The purpose of this PWM controller is to maintain synchronization between grid and hybrid system.

2.1 Solar System

PV system is one of the energy sources in renewable family, as compared to all DG systems it plays a key role in the present power generation systems because of it freely available in environment and its durability. The PV system converts sun irradiance into electrical current with photon effect. An equivalent circuit is designed to convert solar current into voltage. And a DC–DC MPPT converter is used to extract maximum output from the solar system [4]. Operational diagram for solar system is shown in Fig. 2.

The expression for photovoltaic system current is shown in Eq. (1)

$$I = I_{\text{ph}} - I_{\text{o}}\left[\text{e}^{\left(\frac{qV_{\text{D}}}{nKT}\right)}\right] - \left(\frac{V_{\text{D}}}{R_{\text{s}}}\right) \tag{1}$$

Figure 3 shows the characteristics of *P*–*V* and *I*–*V* of photovoltaic system. From this, the maximum power point of system is identified. The structure of closed loop control diagram from DC–DC converter using MPPT technique is shown in Fig. 4. Here, the reference signal obtained from MPPT is compared with PV system voltage and applied to PWM converter to generate duty cycle required for DC–DC converter [5].

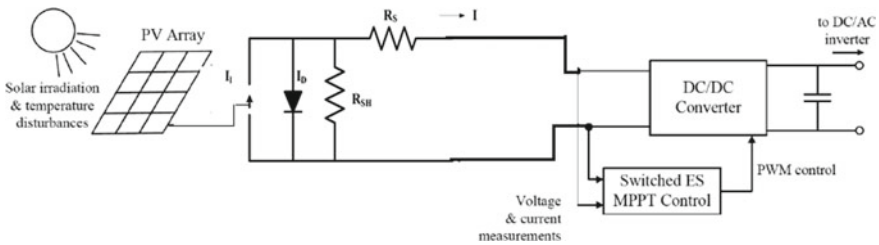

Fig. 2 Structure of solar energy system

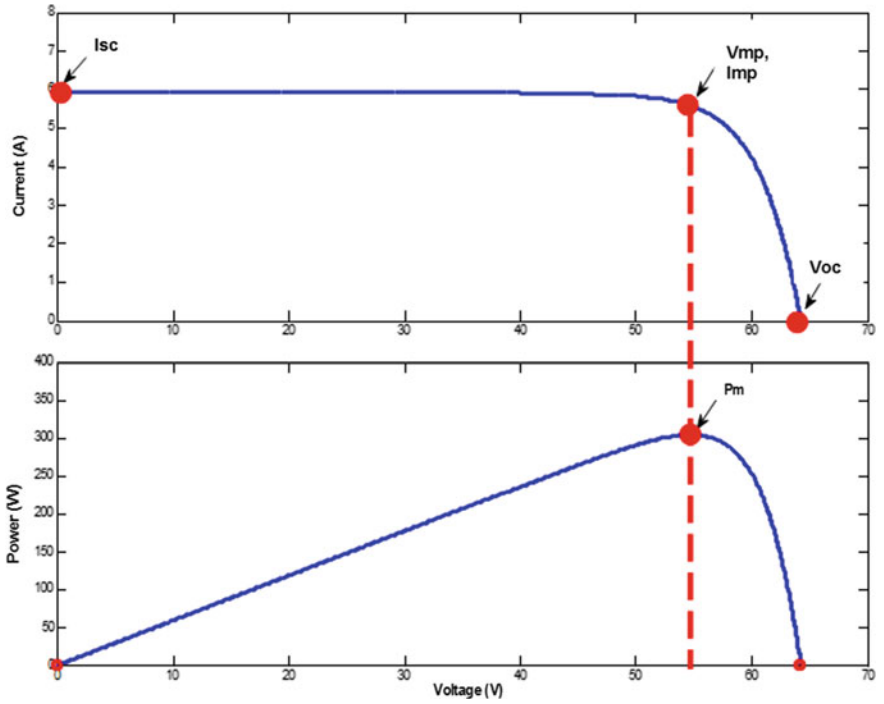

Fig. 3 *V–I* characteristics of PV system

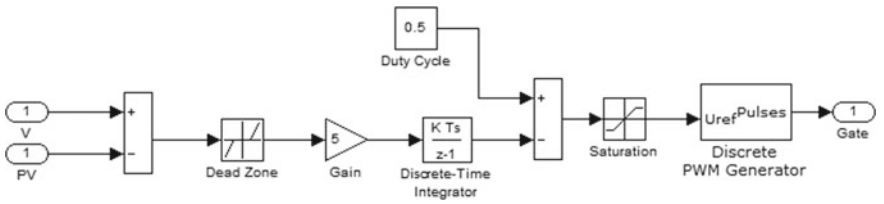

Fig. 4 MPPT-based PWM controller for DC–DC converter

2.2 Wind Turbine System

The mechanical turbine and generator are the main components of wind turbine system, the wind turbine converts wind energy to kinetic energy and is applied to gear mechanism to boost up speed, and the generator converts mechanical energy to electrical energy. The output from the generator is converted to DC energy with the help of rectifier unit as shown in Fig. 5. The synchronization between wind and grid system is obtained with local control unit (LCU). An MPPT-based DC–DC chopper circuit is proposed to the wind turbine to control wind power.

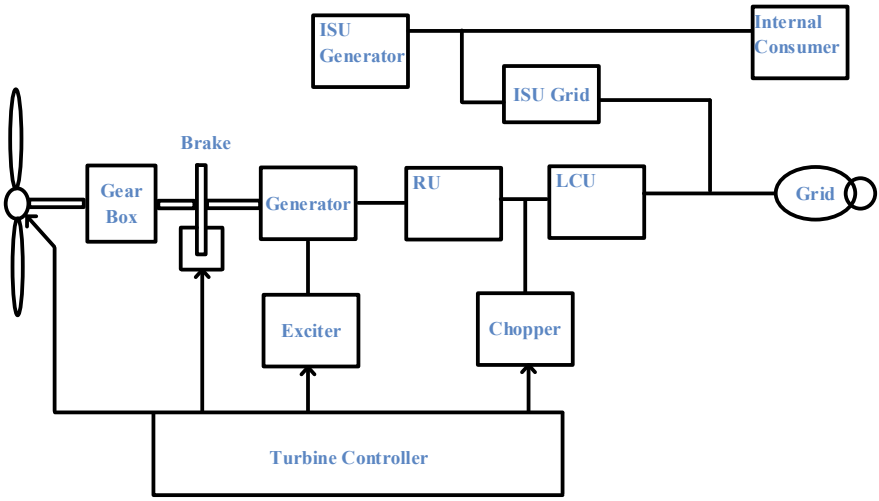

Fig. 5 Basic diagram of wind turbine

The mathematical analysis for wind energy system is expressed as below [7]. Wind turbine mechanical power is expressed in Eq. (2), and C_p is shown in Eq. (3)

$$P_{\text{mech}} = \frac{1}{2}\text{PAV}^3 C_{\text{P}} \tag{2}$$

where C_{P} is the coefficient of power

$$C_{\text{P}} = 0.53(\lambda - 0.2)(0.7 - \lambda) \tag{3}$$

3 MPPT Techniques

The purpose of MPPT technique is to design a suitable reference signal required for PWM of DC–DC converter. This MPPT technique increases the efficiency of DG system and battery charging controllers [8]. This paper proposes different MPPT controllers and compares the performances of each MPPT, and the chosen MPPT techniques are (a) perturb and observe, (b) LOA technique and (c) cuckoo search algorithm.

3.1 Cuckoo MPPT Algorithm

Due to its sound and aggressive reproduction strategies, cuckoos are fascinating birds. Generally, cuckoo birds lay their eggs in communal nests and may remove other eggs to increase hatching probability of their eggs [9]. The nature of female cuckoos is to identify the group of similar nests which suits their own egg characteristics and then choosing the best from them.

Cuckoo birds start looking for the best nest, and this is important step in cuckoo's reproduction method. To search for best nest and process of food, the Le'vy flight plays a key role. The step length or Le'vy flight distribution is shown in Eq. (4).

$$S = \alpha_{\mathrm{q}}(V_{\mathrm{bt}} - v_j) \oplus \mathrm{le}(\lambda) \tag{4}$$

Figure 6 shows the flowchart for Le'vy-based cuckoo search algorithm. In this, the random initial solution of the operating voltage and current of PV panel is selected. The fitness of power is calculated as shown $P = V * I$.

The expression for fitness function is expressed in Eq. (5)

$$V_i^{t+1} = V_i^t + \alpha \oplus \mathrm{levy}(\lambda) \tag{5}$$

3.2 LOA Optimization Technique

In this section described, the inspiration of the proposed meta-heuristic algorithm and its process are explained in detailed. Male cubs sleep in their birth to the planet pride until they reach early adulthood, whereupon they disregard the pride to meander as itinerant lions. Within the case of during their meandering, a roaming male experiences another pride, and it would challenge the pioneer for strength. If the itinerant male successes this experience, it turns into the new pioneer of the pride [10]. Within the lion's calculation, every lion speaks to a solution. The stream chart of the LOA is introduced in Fig. 7.

4 MATLAB Results

The proposed grid interconnected hybrid wind-PV system with different MPPT controllers is tested in MATLAB/Simulink environment under different loading conditions.

Figure 8, shows the simulation result for the proposed system to show the power management strategies. Here, the load sharing is chosen between PV, battery and grid system according to their generations. Here, the load variation is considered at

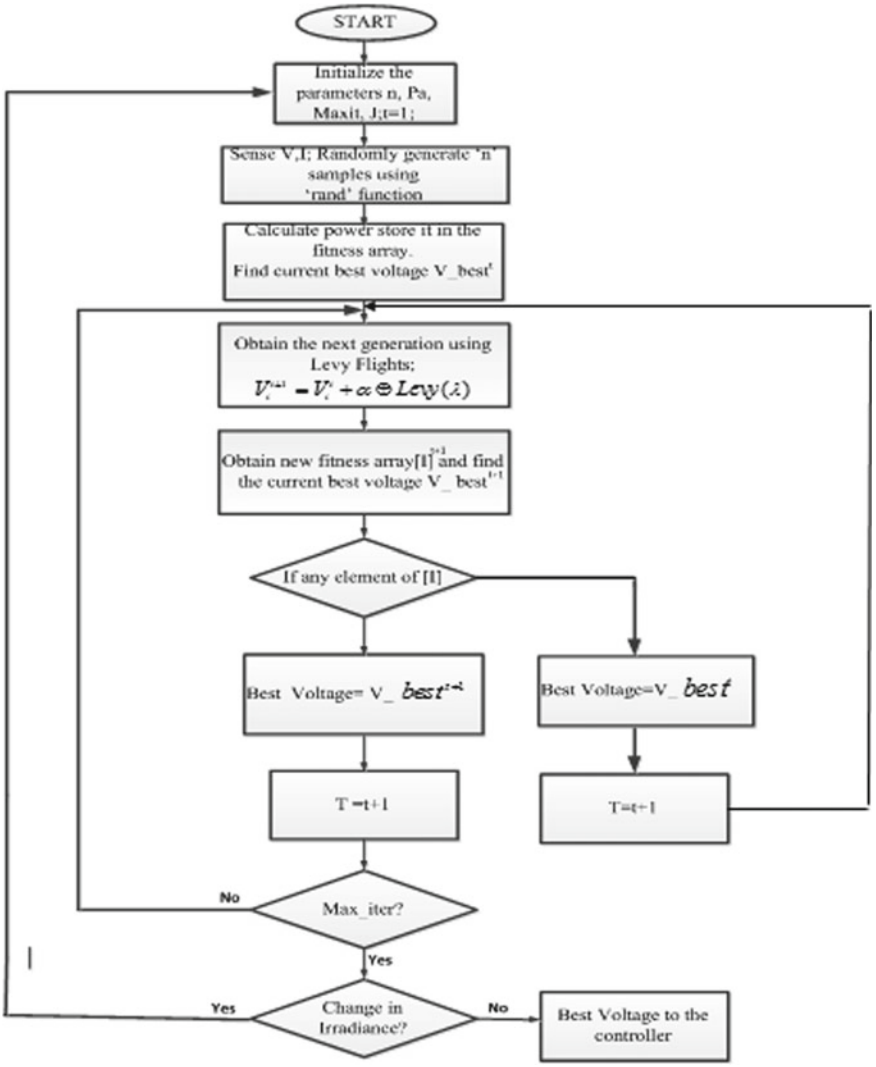

Fig. 6 Cuckoo search algorithm

3 and 6 s. During this period, the load is changed from 18 to 16 KW. During the period 0–2 s, the solar system generates 10 KW and wind system generates 1.1 KW. The excess of 18 KW is transferred to load.

Figure 9 shows the simulation result for the proposed system to show the power management strategy with cuckoo optimization technique. Here, the load sharing is chosen between PV, battery and grid system according to their generations. Here, the load variation is considered between 4 and 6 s from 18 to 20 KW. During this

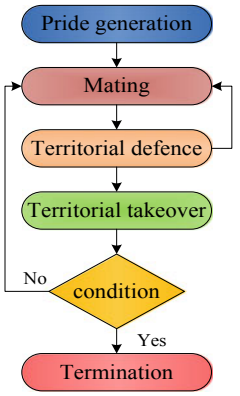

Fig. 7 LOA technique flowchart

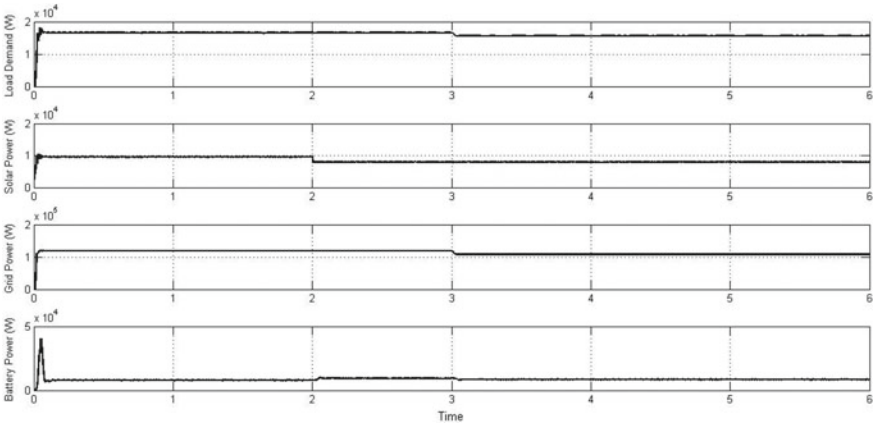

Fig. 8 Simulation result for **a** load demand, **b** solar power, **c** grid power and **d** battery power

period, the solar system generates 8 KW and wind system generates 20 KW. The excess power from these systems is transferred to battery.

Figure 10 shows the simulation result for the proposed system to show the power management strategy with LOA optimization technique. Here, the load sharing is chosen between PV, battery and grid system according to their generations. Here, the load variation is considered between 4 and 6 s from 18 to 20 KW. During this period, the solar system generates 10 KW and wind system generates 5 W. The remaining required power will take from battery system.

Figure 11 shows the comparative analysis between the PO, LOA and cuckoo search techniques. In this, case, the comparison analysis is done for hybrid system reliability (efficiency) with respect to power. As per the comparison, the cuckoo-based hybrid system produces better efficiency than LOA and PO algorithms.

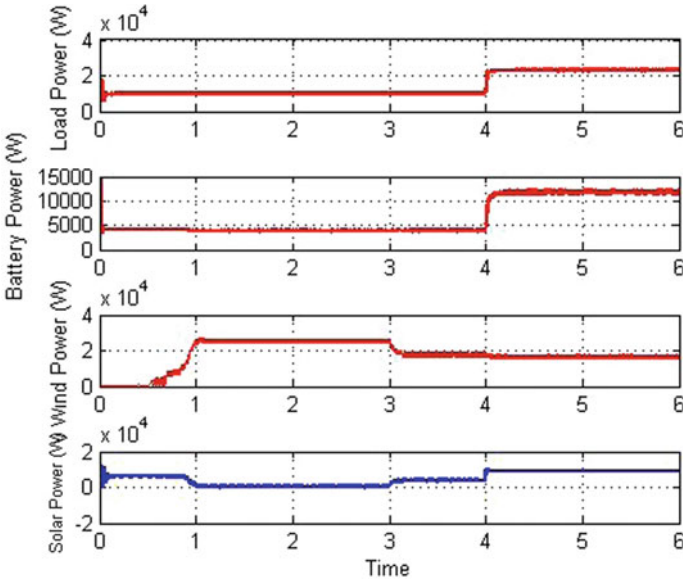

Fig. 9 Simulation result for **a** load demand, **b** solar power, **c** wind power and **d** battery power using cuckoo MPPT controller

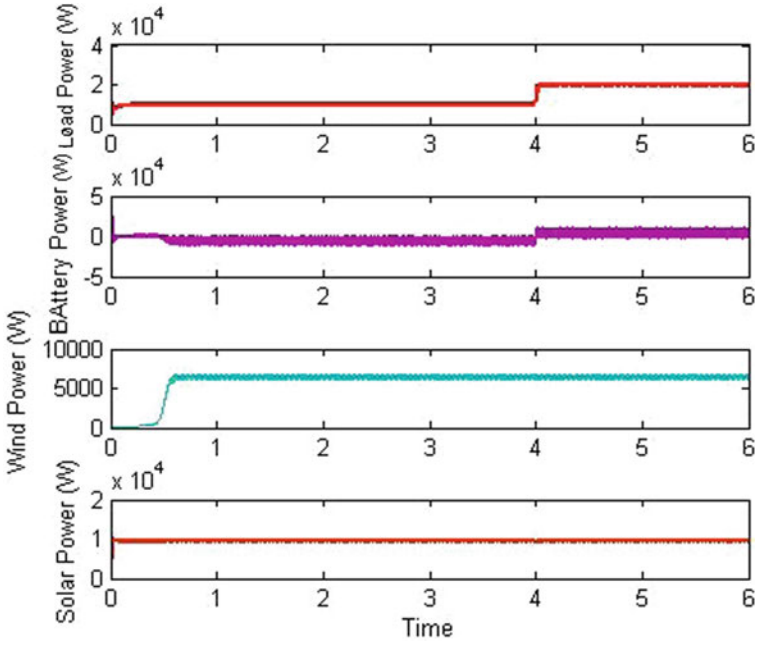

Fig. 10 Simulation result for **a** load demand, **b** solar power, **c** wind power and **d** battery power using LOA controller

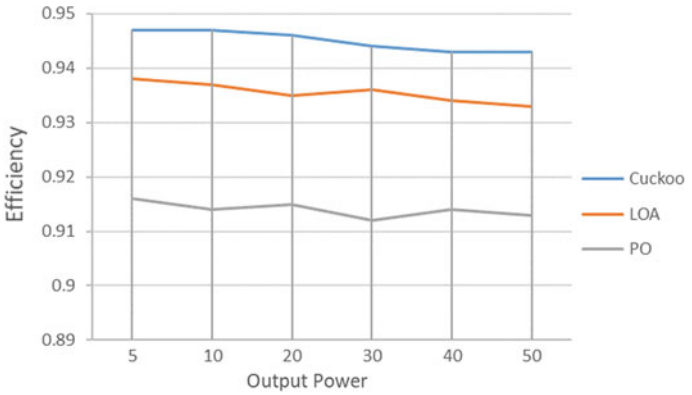

Fig. 11 Efficiency versus power curve

5 Conclusion

The PV-wind-battery-based hybrid system is implemented in this paper to meet the supply demand. Here, the PV system is designed for 10 kW, wind system for 15 kW, and load sharing capability between two systems has verified under the different load conditions. A PO, cuckoo and LOA MPPT techniques for DC–DC converter are implemented for both PV and wind systems to improve the reliability of hybrid system and their efficiency. These proposed techniques for system are tested in Simulink and compared the performance in terms of efficiency. From the following results, the cuckoo-based MPPT controller produces better results as compared to the remaining techniques.

References

1. Elkazazab M, Sumner M, Thomasa D (2020) Energy management system for hybrid PV-wind-battery microgrid using convex programming, model predictive and rolling horizon predictive control with experimental validation. Int J Electr Power Energy Syst 115:105483
2. Geem ZW (2012) Size optimization for a hybrid photovoltaic–wind energy system. Int J Electr Power Energy Syst 42(1):448–451
3. Eid A (2014) Utility integration of PV-wind-fuel cell hybrid distributed generation systems under variable load demands. Int J Electr Power Energy Syst 62:689–699
4. Chaib A, Achour D, Kesraoui M (2016) Control of a solar PV/wind hybrid energy system. Energy Proc 95:89–97
5. Kale M, Ozdemir E (2005) Harmonic and reactive power compensation with shunt active power filter under non-ideal mains voltage condition. J Electr Power Syst Res 74:363–370
6. Kaldellis JK (2010) Stand-alone and hybrid wind energy systems. In: Technology, energy storage and applications. Woodhead Publishing, 27 July 2010
7. Bhadra SN, Kastha D, Banerjee S (2009) Wind electrical systems. Oxford University Press, New Delhi

8. Wang F, Duarte JL, Hendrix MAM (2008) Reconfiguring grid interfacing converters for power quality improvement. In: Proceedings of the IEEE Benelux young researchers symposium in electrical power engineering, pp 1–6
9. Reyna AAC (2006) Applications of the differential evolution optimization algorithm in power systems planning, operation and control. Citeseer
10. Renuka TK, Sreedharan S (2018) An enhanced LOA algorithm for improving the RES penetration and small signal stability in power system. Renewables 5:6. https://doi.org/10.1186/s40807-018-0053-4

Implementation of Firefly Algorithm Employed PIDD Controller for an Interconnected Power System

Prema Kumar Navuri and Manmadha Kumar Boddepalli

Abstract Application of firefly algorithm (FA) tuned integral double derivative (IDD) and proportional integral double derivative (PIDD) controllers are addressed in this article. Two identical areas have been anticipated with a thermal unit as the first one, hydropower as a second system, and gas power plant as the third component in each area. At the outset, the IDD controller has been employed, and then, PIDD controller has been employed to exhibit its supremacy when evaluating against IDD controller in terms of dynamic responses. FA has been used to attain the gains of IDD and PIDD controllers. Robustness analysis has been accompanied to find the dominance of the PIDD controller through MATLAB simulation.

Keywords IDD controller · PIDD controller · Firefly algorithm · Automatic load frequency control

1 Introduction

An interconnected complex power system can be effectively worked when there is a set of scales in the generated power and the connected load including the losses. When a sudden digression in the load occurs in one of the areas of the integrated system, then the change in frequency appears in all areas. This revision can be minimized or controlled by a concept called automatic load frequency control (ALFC) [1, 2].

As the load in any power system revises momentarily and randomly, so balancing the generation and load is a big assignment. To fulfill this assignment, a controller is

P. K. Navuri
Department of Electrical Engineering, Andhra University College of Engineering (A), Andhra University, Visakhapatnam, Andhra Pradesh 530003, India
e-mail: preamnavuri@gmail.com

M. K. Boddepalli (✉)
Department of Electrical and Electronics Engineering, Aditya Institute of Technology and Management (A), Tekkali, Andhra Pradesh 532201, India
e-mail: manmadhakumarboddepalli@gmail.com

G. T. C. Sekhar et al. (eds.), *Intelligent Computing in Control and Communication*, Lecture Notes in Electrical Engineering 702,
https://doi.org/10.1007/978-981-15-8439-8_32

required to maintain variation in frequency and active power, practically a constant value. The ALFC system will always supervise and automatically revises the settings of the speed changer of the generator to normalize the gap between the generation and load incorporating the losses in the system [3, 4].

For both single-area and multi-area systems, the parameters of controller are designed by the expansion of controller transfer through Laurent series. The dynamics of power system are estimated by relay-based identification technique [5]. Its robustness has been tested with Kharitonov's theorem. A non-reheat two-area system has been acknowledged with the PID controller [6], and bacterial foraging optimization algorithm (BFOA) is used to obtain the controller constraints and also compared with Ziegler Nichols (ZN) and genetic algorithm (GA).

The conventional PID controller has been intended for a two-area hydropower system [7], GA has been exercised to facilitate the study of the effectiveness of the traditional controller has been judged against the integral derivative controller for the hydro system. Lozi map-based chaotic algorithm (LCOA) [8] has been conceded to study the two-area system. Its effectiveness has been addressed with a PID controller with GA-PID, simulated annealing PID controller, and pattern search-PID controller.

Firefly algorithm(FA)-based PID controller has been addressed for three different power systems [9] and also judged the working nature of the three areas when there is no controller in the loop. It also addressed the system with random load for all the three addressed systems. An imperialist competitive algorithm [10] has been projected for the ALFC problem in a multi-area system. Its supremacy has been judged against the PI controller.

2 System Under Study

For the present investigation, two identical areas have been anticipated with a thermal unit as a first one, hydropower as a second element, and gas power plant as the third component in each area. Power system understudy is displayed in Fig. 1.

In this paper initially, integral double derivate (IDD) controller has been acknowledged. In addition to the conventional proportional, integral, and derivative (PID) controller one more derivative controller has been added in parallel with the derivative control gain, to execute as the PIDD controller [11].

The main intend to keep an additional derivative controller is to increase the system stability and helps in stipulations of the settling time in a better way while judging against the traditional PID controller. The configuration of the anticipated PIDD controller is presented in Fig. 2.

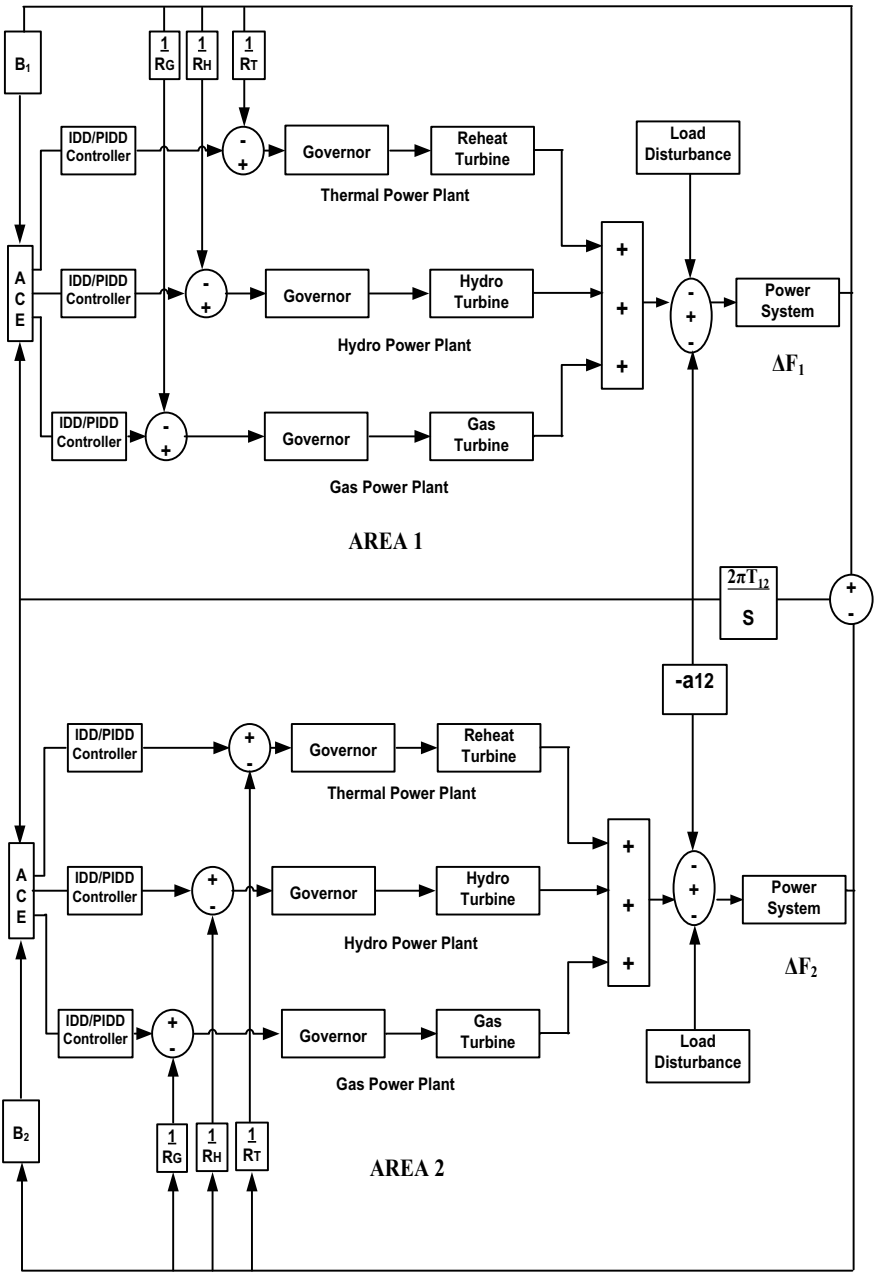

Fig. 1 Two-area system by means of IDD/PIDD controllers

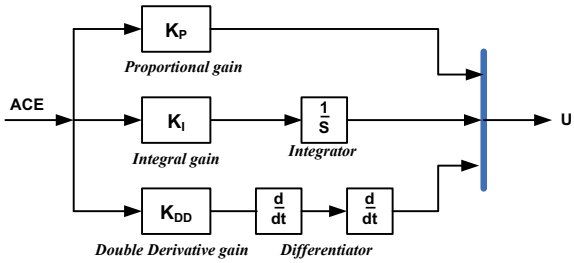

Fig. 2 PIDD controller structure

3 Results and Discussion

The IDD controller has been used to anticipate the proposed system. The index values are not good when the IDD controller is used so subsequent to IDD controller, the anticipated controller named PIDD has been practiced, and both the consequences were compared. The optimal values of both the implemented controllers were acquired by means of the firefly algorithm (FA) [12, 13]. The course of action of the optimization has been noticed in the reference [14, 15]. In the optimization randomization parameter, attractiveness and absorption coefficients correspondingly selected are 0.5, 0.4, and 0.5. Six fireflies have been used for the study. The number of generations exploited is 100 to tune the control parameters. Tables 1 and 2 illustrate the optimal values of the IDD and PIDD controllers correspondingly.

At the outset, 10% of disturbance has been imposed in area-1. The corresponding responses in a change of frequency within area-1, area-2 also tie-line are displayed correspondingly in Fig. 3a–c. It is very clear that PIDD furnishes a better response than the IDD controller.

In the current study, 2% of the band has been intended to obtain the settling time. The settling times, peak overshoot, and peak undershoots of the anticipated system have been tabulated in Table 3.

Table 1 Optimal values of IDD controller

$KI_1 =$ 0.9166	$KI_2 =$ 0.5122	$KI_3 =$ 0.1755	ITAE = 12.18048672
$KD_1 =$ -0.1924	$KD_2 =$ 0.1703	$KD_3 =$ -0.0176	

Table 2 Optimal values of PIDD controller

$KP_1 =$ 1.9439	$KP_2 =$ 1.3421	$KP_3 =$ 1.8209	ITAE = 1.43234190
$KI_1 =$ 0.5011	$KI_2 =$ 0.4337	$KI_3 =$ 1.5617	
$KD_1 =$ 0.0000	$KD_2 =$ 0.5694	$KD_3 =$ 1.2421	

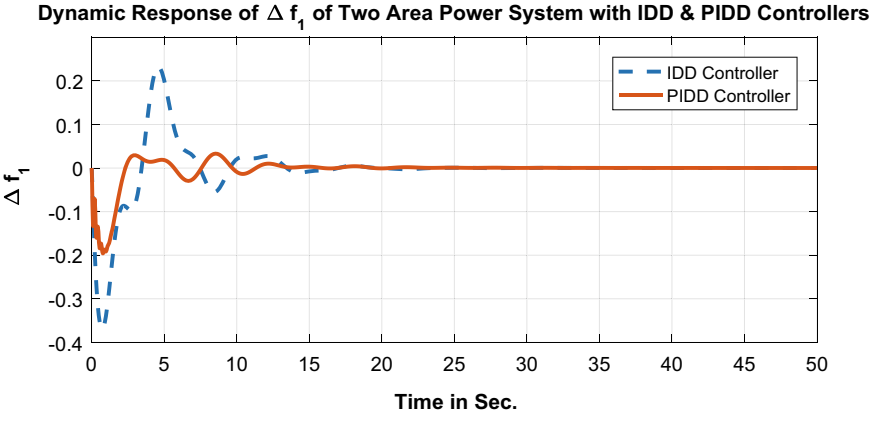

(a)

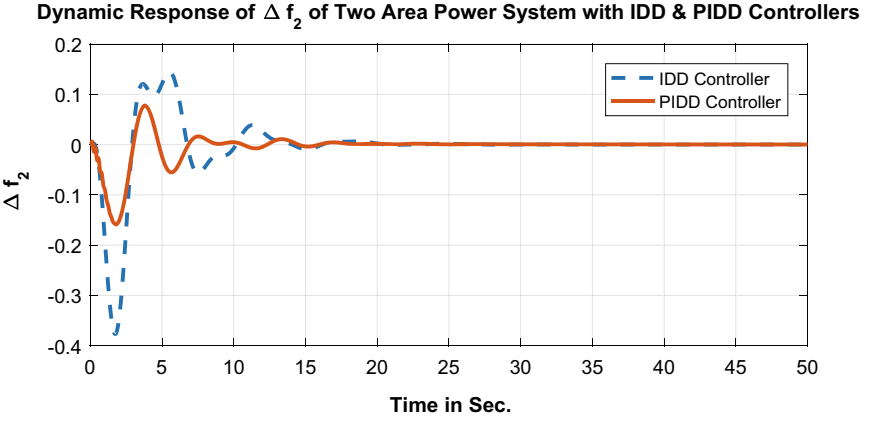

(b)

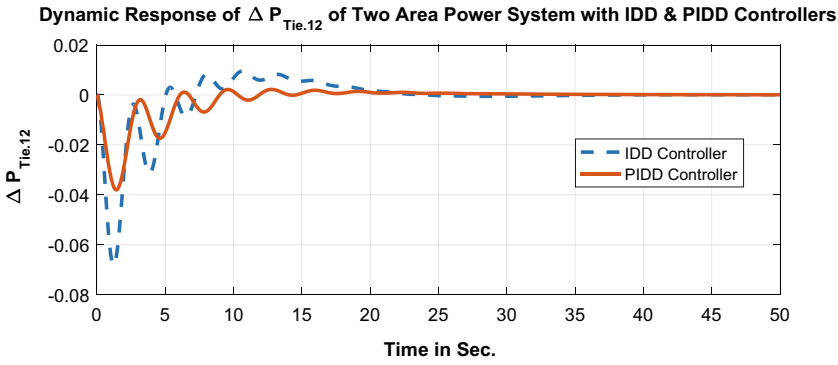

(c)

Fig. 3 **a**. Dynamic response of Δf_1 with IDD and PIDD controllers. **b**. Dynamic response of Δf_2 with IDD and PIDD controllers. **c**. Dynamic response of $\Delta P_{\text{Tie.12}}$ with IDD and PIDD controllers

Table 3 Performance index values

	Peak undershoot	Peak undershoot	Peak overshoot	Settling time (2% band) (S)
Δf_1	IDD controller	−0.37	0.23	22.4
	PIDD controller	−0.195	0.03	21.9
Δf_2	IDD controller	−0.376	0.145	20.0
	PIDD controller	−0.16	0.078	17.8
$\Delta P_{\text{Tie.12}}$	IDD controller	−0.068	−0.0037	19.7
	PIDD controller	−0.038	−0.0018	13.1

Here, the robustness of the anticipated controller has been executed [16–18]. The gas turbine compressor discharge volume-time constant (T_{CD}) has been varied in the range of +10 to −10% and simulated the model without retuning controller parameters. The responses associated with the above are presented in Figs. 4a–c. It has been perceived that the responses give the impression that they are similar even though there is a change in parametric values. All the parameter values are taken from reference [14].

4 Conclusion

Integral double derivative (IDD) and proportional integral double derivative (PIDD) controllers are proposed for two-area interconnected system. The firefly algorithm has been used to find the control parameter gains. Simulation consequences confirmed that the PIDD controller superior when judged against the IDD controller. Robust analysis has been done for the deviation in gas turbine compressor discharge volume-time constant (T_{CD}). In conclusion, the PIDD controller exhibits its supremacy when compared to the IDD controller.

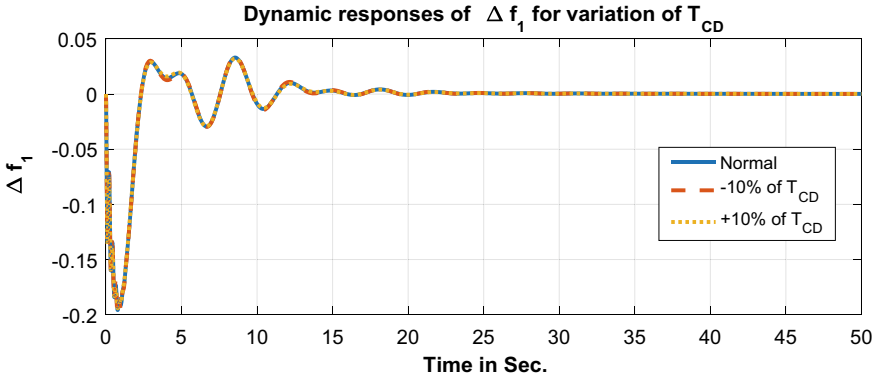

(a)

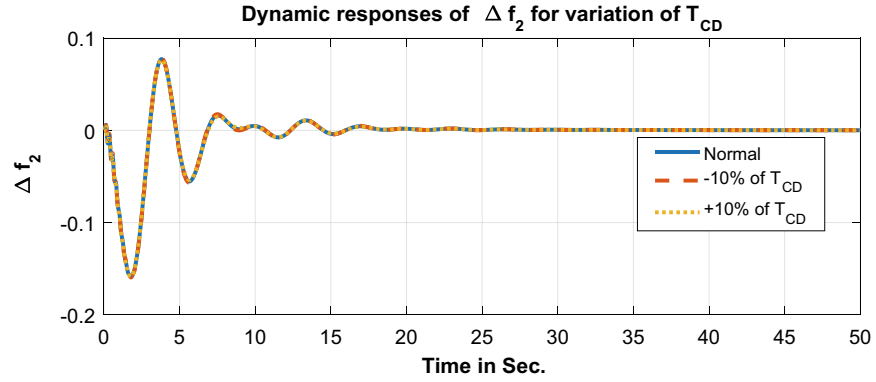

(b)

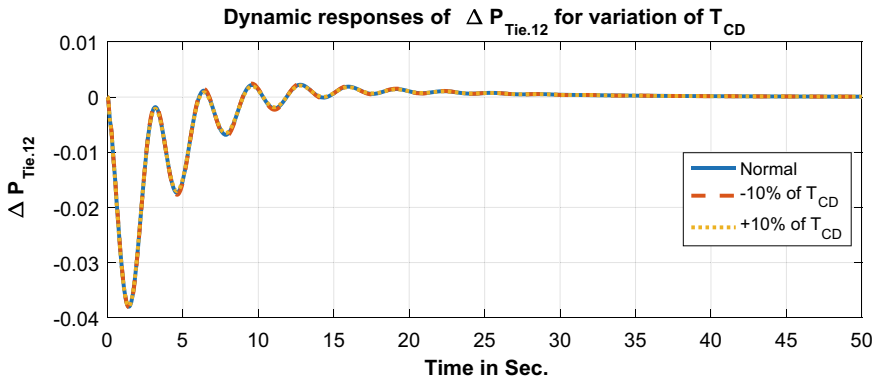

(c)

Fig. 4 **a–c**. Dynamic response of Δf_1, Δf_2, and $\Delta P_{\text{Tie.12}}$ for T_{CD} variation

References

1. Elgerd OI (2004) Electric energy systems theory: an introduction (Chapter 9), 2nd edn. Tata McGraw-Hill Publishing Company Ltd., New Delhi
2. Kundur P, Balu NJ, Lauby MG (1994) Power system stability and control, vol 7. McGraw-hill, New York
3. Saadat H (1999) Power system analysis. McGraw-Hill, USA
4. Kothari DP, Nagrath IJ (2003) Modern power system analysis (Chapter 8). Tata McGraw-Hill Publishing Company Ltd., New Delhi
5. Dola Gobinda P, Majhi S (2013) A new control scheme for PID load frequency controller of single-area and multi-area power systems.ISA Trans 52(2):242–251
6. Ali ES, Abd-Elazim SM (2013) BFOA based design of PID controller for two area load frequency control with nonlinearities. Int J Electr Power Energy Syst 51:224–231
7. Aditya (2003) Design of load frequency controllers using genetic algorithm for two area interconnected hydro power system. Elect Power Compon Syst 31(1):81–94
8. Farahani M, Ganjefar S, Alizadeh M (2012) PID controller adjustment using chaotic optimisation algorithm for multi-area load frequency control. IET Control Theory Appl 6(13):1984–1992
9. Boddepalli MK, Navuri PK (2019) Firefly algorithm based PID controllers for automatic load frequency control in different power systems. Int J Eng Adv Technol 8(6S3). ISSN: 2249–8958
10. Shabani H, Vahidi B, Ebrahimpour M (2013) A robust PID controller based on imperialist competitive algorithm for load-frequency control of power systems. ISA Trans 52(1):88–95
11. Sahu RK, Gorripotu TS, Panda S (2016) Automatic generation control of multi-area power systems with diverse energy sources using teaching learning based optimization algorithm. Eng Sci Technol Int J 19(1):113–134
12. Yang XS (2008) Nature-inspired metaheuristic algorithms. Luniver Press, UK, p 2008
13. Yang, X-S (2010) Firefly algorithm, stochastic test functions and design optimisation. arXiv preprint arXiv:1003.1409
14. Boddepalli MK, Navuri PK (2018) Design and analysis of firefly algorithm based PID controller for automatic load frequency control problem. In: 2018 technologies for smart-city energy security and power (ICSESP). IEEE
15. Boddepalli MK, PK Navuri (2020) Application of fuzzy controller for multi-area automatic load frequency control system. In: Innovative product design and intelligent manufacturing systems, pp 313–321. Springer, Singapore
16. Gorripotu TS, Sahu RK, Panda S (2015) Application of firefly algorithm for AGC under deregulated power system. In: Computational intelligence in data mining, vol 1, pp 677–687. Springer, New Delhi
17. Gorripotu TS et al (2019) TLBO algorithm optimized fractional-order PID controller for AGC of interconnected power system. In: Soft computing in data analytics, pp 847–855. Springer, Singapore
18. Gorripotu TS, Sahu RK, Panda S (2017) Firefly algorithm optimised PID controller for automatic generation control with redox flow battery. Int J Comput Syst Eng 3(1–2):48–57

Comparative Analysis of Different Types of Membership Functions for Fuzzy Logic Controller in Direct Torque Control of Induction Motor

Sudheer Hanumanthakari

Abstract Fuzzy logic controller performance depends upon fuzzy rule base. The control strategy is represented by a set of rules which explain basic characteristics of the controller. The fuzzy logic controllers' inputs and outputs are characterized by its membership function. Most of the researchers use triangular MFs for implementation of control algorithms. The basic objective of the paper is to evaluate the performance of fuzzy logic switching controller with different membership functions. The comparative analysis of different types of membership functions is carried out in direct torque control of induction motor. In DTC, speed control is achieved by selection of optimal voltage vector of voltage source inverter using switching logic table. Major disadvantages of DTC are high ripples in torque and flux and variable switching frequency due to hysteresis controllers. Use of fuzzy logic controller replaces the conventional switching table, and hysteresis controller exhibits reduction in torque and flux ripples. In this paper, fuzzy logic controllers are developed using different membership functions in MATLAB/Simulink Environment. Performance of speed control is evaluated and summarized.

Keywords Direct torque control (DTC) · Induction motor (IM) · Fuzzy logic · Membership function · Fuzzy logic controller

1 Introduction

Direct torque control (DTC) is an advance control algorithm used for high-performance industrial drive applications [1–2]. However, DTC have few advantages over vector control like absence of coordinate transformations and current regulators. However, DTC also have disadvantages: High torque ripples under steady-state, variable switching frequency owing to presence of hysteresis controller in torque and

S. Hanumanthakari (✉)
Faculty of Science and Technology, ICFAI Foundation for Higher Education, Shankarpally Road, Hyderabad 501203, India
e-mail: Sudheer_hraj@yahoo.co.in

G. T. C. Sekhar et al. (eds.), *Intelligent Computing in Control and Communication*, Lecture Notes in Electrical Engineering 702,
https://doi.org/10.1007/978-981-15-8439-8_33

flux loop and harmonics in stator current during perturbation of switching states in inverter. Several solutions are developed by researchers to overcome the disadvantages. Several modified DTC schemes like direct self control, indirect self control, and space vector modulated- direct torque control (SVM-DTC) are proposed to overcome the disadvantages of DTC [3–5]. The application of artificial intelligent (AI) techniques like artificial neural networks (ANN), fuzzy logic (FL), and neuro-fuzzy in control system application gained a momentum. Few solutions are use of fuzzy logic, ANN, and advanced met heuristic algorithms for tuning of PI controllers [6–7]. In DTC, the torque and flux ripples are reduced by employing fuzzy logic controller (FLC) in place of torque, flux hysteresis bands, and switching table for selection of optimal switching state of voltage source inverter (VSI) [8–11]. Most of the researcher will employ triangular membership functions for implementation of fuzzy logic controllers. Very less research is carried over in selection of membership functions (MFs) and comparative performance analysis with different membership functions. Performance evaluation of different MFs for indirect vector control induction motor is given in [12]. In [12], fuzzy logic PI controller using different MFs is implemented. Use of different MFs for SVM, ANFI, S, and AC voltage controller is proposed in [13–14]. In all previous works, fuzzy logic-based PI controllers are evaluated for different MFs. In this paper, fuzzy logic switching controller which embeds complete DTC control algorithm is implemented with different MFs. The general MFs considered are simple triangular and trapezoidal, Gaussian shaped, bell-shaped, sigmoid, and Z, S, and π shaped polynomial functions. The performance of fuzzy logic controller for DTC is evaluated with each type of MFs based on speed, torque, and flux response under transient and steady state.

2 DTC of Induction Motor with Fuzzy Logic Controller

In the DTC algorithm, the choice of an ideal switching state to control torque and flux is characterized by a switching table. The transition from one switching state to another relies upon torque error, flux error, and stator flux space sector. The complete knowledge of the selection of optimal switching state is developed using fuzzy logic controller (FLC).

2.1 Direct Torque Control with FLC

The basic block diagram of DTC with FLC is shown in Fig. 1. The switching table used for selection of optimal switching state of VSI. Selection and alteration of switching state are based on stator flux angle, torque, and flux errors. As shown in Fig. 1, the motor speed is compared with the reference speed which gives the speed error. The speed error acts as input to the speed PI controller which gives reference torque as output. The torque and flux are estimated using flux and torque estimator

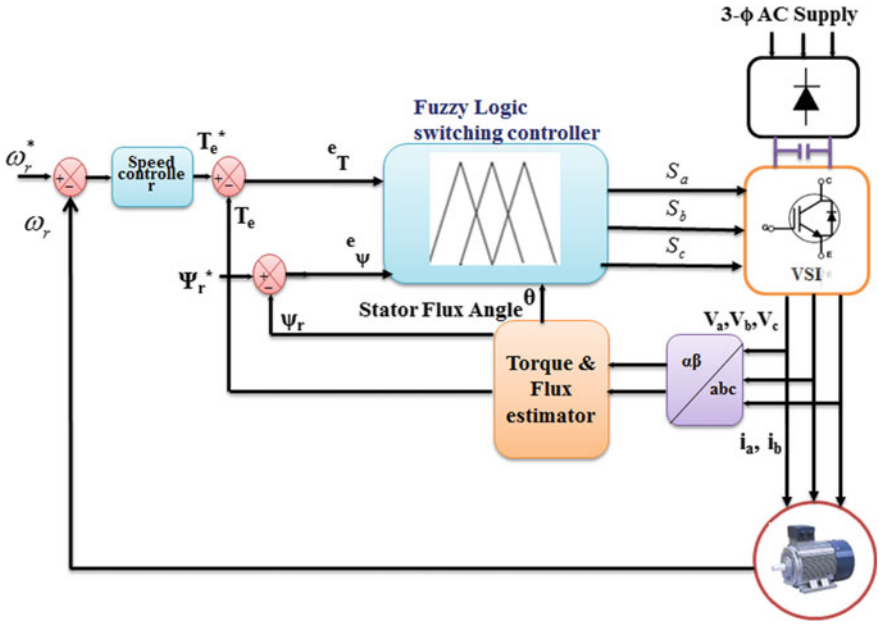

Fig. 1 Block diagram of DTC with FLC

from voltage and current feedback from IM parameters. As shown in Fig. 1, torque error, stator flux error, and flux angles are the inputs for FLC. The stator flux space is divided into 12 sectors of 6° each. The Flux and torque errors are fuzzified and fuzzy sets are defined using linguistic variables which indicate the where they are positive or negative with degree of positivity and negativity. The fuzzified inputs of torque and flux errors, stator flux angle respective switching state is selected to increase/decrease the flux and torque of the induction motor using fuzzy rule base. In fuzzy logic, the torque and flux errors can be categorized as fuzzy sets based on the magnitude of the errors, and the linguistic terms are assigned. In fuzzy logic, the fuzzy variables are assigned to membership value (0 and 1), and the errors are subdivided into multiple fuzzy sets. Using fuzzy logic controller, smooth control and best possible selection of the switching state is achieved.

2.2 Design of Fuzzy Logic Controller for DTC

Fuzzy logic controller is designed to implement conventional switching table logic. FLC implementation involves fuzzification, rule base, and defuzzification as shown in Fig. 2 [14]. The torque error, flux error, and stator flux angles are analog values that cannot be applied directly to FLC.

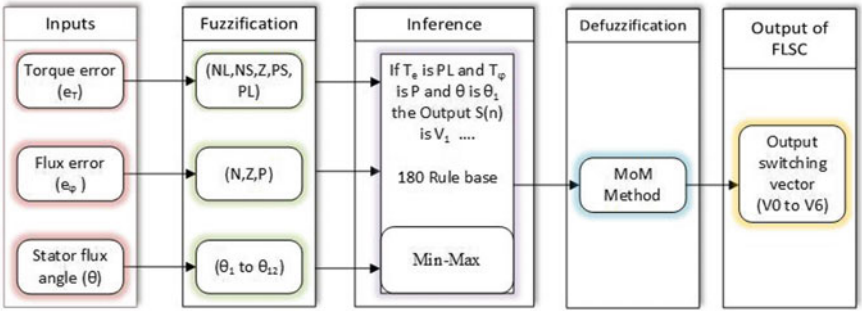

Fig. 2 Block diagram of fuzzy logic controller for DTC [14]

Each input is converted into a fuzzy variable using fuzzification process. The fuzzy variable is assigned a membership value in the universe of discourse, defined by linguistic terminology. Torque error (e_T) greater than +4 N-m is defined as positive large (PL), $0.01 < e_T < 4$ is defined as positive small (PS), $-0.01 < e_T < 0.01$ is defined as zero (Z), $-4 < e_T < -0.01$ is defined as negative small (NS), and less than −4 N-m is defined as negative large (NL). Similarly flux error (e_ψ) fuzzified using three linguistic terms are negative (N), zero (Z), and positive (P). The stator flux locus fuzzified variables (θ_1 to θ_{12}) dividing entire flux space into 12 sectors.

2.3 Different Types of MFs

The fuzzy sets with variable membership value are represented by membership functions. The MF is used to map each element of the universe of discourse "X" to a membership value "$\mu_A(x)$" ranges between 0 and 1. The different types of MFs used in fuzzy logic (FL) are "triangular, trapezoidal, gaussian, generalized bell, π shaped membership function, and S shaped membership functions." Fuzzy logic controller (FLC) is developed with different MFs of symmetrical shape for both inputs and outputs of FLC. The speed responses are evaluated and compared taking triangular MF as a reference.

The shape of the MF depends upon the knowledge representation of input in linguistic term of fuzzy sets. The shape of MF is generally decided based on simplicity in implementation, type of data, mathematical representation, and speed of evaluation. Different types of membership functions are shown in Fig. 3.

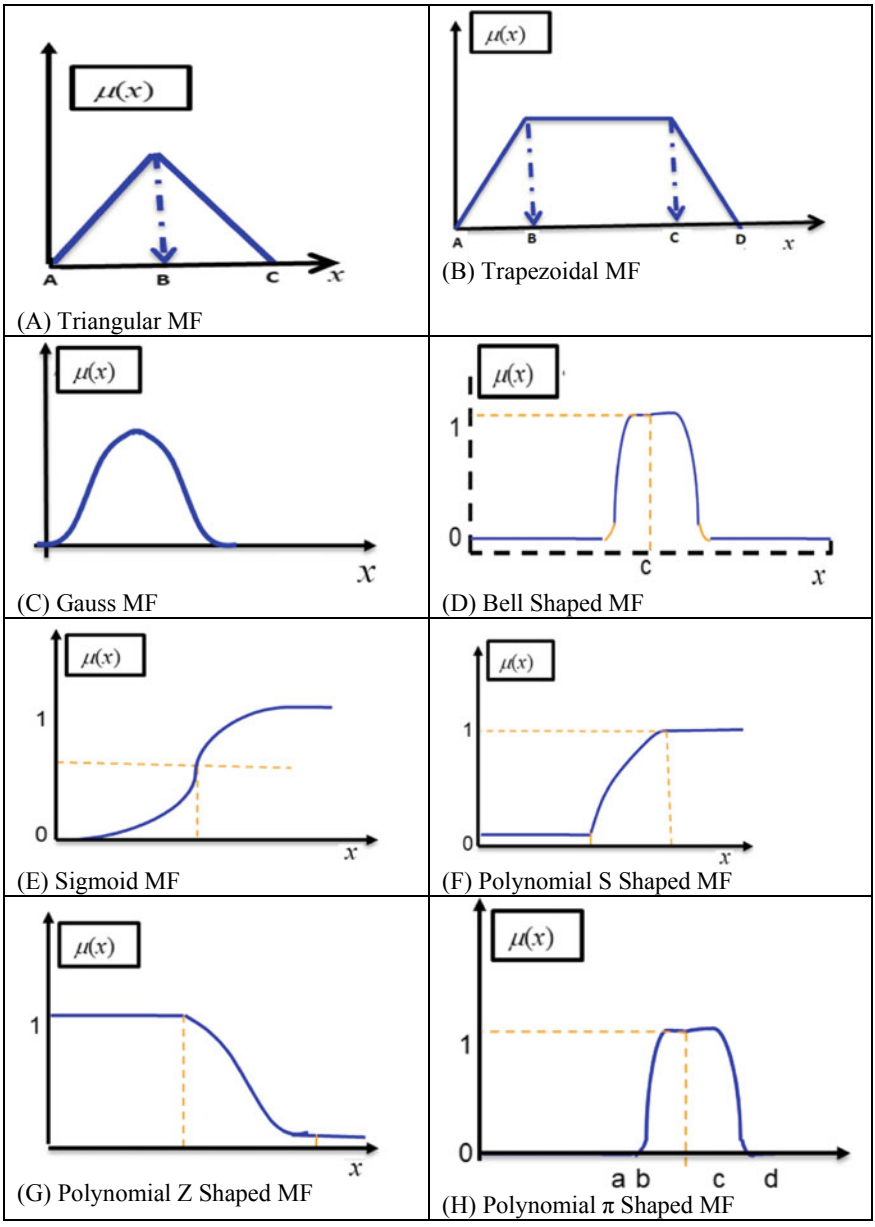

Fig. 3 Different types of membership functions

2.3.1 Triangular and Trapezoidal MFs

Triangular and trapezoidal MFs are popular and most commonly used MFs for majority of applications. These two MFs are simple to implement and take less computational time.

A membership function of a fuzzy set maps given input value to its suitable membership value. The trapezoidal MF is given by

$$f(x : A, B, C, D) = \max\left\{\min\left(\frac{x - A}{B - A}, 1, \frac{D - x}{D - C}\right), 0\right\} \tag{1}$$

The trapezoidal MF can be represented by algebraic given by Eq. (1), the shape of MF can easily modified by varying b and c. In Eq. (1), if $b = c$, then it will result into a special case of trapezoidal MF called as triangular MF given by Eq. (2)

$$f(x : A, B, C) = \max\left\{\min\left(\frac{x - A}{B - C}, 1, \frac{C - x}{C - B}\right), 0\right\} \tag{2}$$

2.3.2 Gaussian MFs

Gaussian MFs are smooth curves characterized by Gaussian distribution curve that is given by Eq. (3)

$$f(x; \sigma, a) = \mathrm{e}^{\frac{-(x-a)^2}{2\sigma^2}} \tag{3}$$

The Gaussian MF is defined by only two parameters "σ" and "a." Using just two parameters. it is difficult to design the symmetrical MF for wide range of inputs. Symmetrical Gaussian MF can be formed using two Gaussian MFs.

2.3.3 Bell-Shaped MFs

Bell-shaped MFs are also smooth and nonzero curves like Gaussian MF, but bell has additional parameter for designing of MF given by Eq. (4)

$$f(x; a, b, c) = \frac{1}{1 + \left|\frac{x-c}{a}\right|^{2b}} \tag{4}$$

2.3.4 Sigmoidal MFs

Gaussian and bell-shaped MFs cannot represent asymmetric nature of curves. Using sigmoid function with right open is more popular and generally used as activation function in artificial neural networks. Asymmetric and closed differential sigmoid function is formed using two sigmoid functions. Sigmoid function is given by Eq. (5)

$$f(x; a, b) = \frac{1}{1 + e^{-a(x-b)}} \tag{5}$$

2.3.5 Polynomial MFs

In general, three types of polynomial MFs used are S, Z, and π shaped polynomial curves. S is open end toward right, Z is open toward left, and π shaped is closed on both ends. S and Z shaped MFs are modified using two parameters "a" and "b," whereas π shaped MF is defined by a, b, c, and d parameters. The S shaped polynomial MF is given by Eq. (6)

$$y = smf(x, [ab]) = \begin{Bmatrix} 0, x \le a \\ 2\left(\frac{x-a}{b-a}\right)^2, a \le x \le \frac{a+b}{2} \\ 1 - 2\left(\frac{x-a}{b-a}\right)^2, \frac{a+b}{2} \le x \le b \\ 1, x \ge b \end{Bmatrix} \tag{6}$$

2.4 Fuzzy Rule Base

Based on the present stator flux position, torque and flux errors' respective switching state is selected to increase/decrease the flux and torque of induction motor. The fuzzy rules are developed based on conventional switching table and the movement of stator flux. For instance, if stator flux angle is in sector 1, VSI switching vector is k; if flux and torque increases, the voltage vector is increased by $K + 1$; if flux increase and torque decreases, voltage vector is $k - 1$. As there are three MFs for flux error, five MFs for torque error, and 12 MFs for stator flux space signals, a total of ($3 \times 5 \times 12 = 180$) fuzzy rules are listed [14]. "The fuzzy rule base of FLC is developed using "Min–Max" inference method" [7].

3 Performance Analysis of FLC with Different MFs in DTC of Induction Motor

The simulation model of DTC with FLC is developed in MATLAB/Simulink software. The fuzzy logic controllers with different MFs are developed using fuzzy logic toolbox in MATLAB software. The induction motor initially started on no-load with reference speed of 1000 rpm. To measure robustness of controller at $t = 0.2$ s, load torque is increased to 4 N-m, keeping reference speed at 1000 rpm. To measure the effectiveness of DTC closed loop controller at $t = 0.5$ s, the motor reference speed is subjected to step change from 1000 to 1400 rpm. The effect of change in MFs in fuzzy logic controller is measured based on speed and torque response of DTC.

The sensitivity of different MFs in performance of FLC for DTC is analyzed based on the torque and speed response of the induction motor. Eight different types of FLCs are applied to DTC of IM for the same transient and steady-state conditions. Figure 4 shows the torque response with different types of MFs subjected to the same loading conditions. From Fig. 4, it is observed that triangular, trapezoidal, bell-shaped, sigmoid, and polynomial π type MFs based FLC shows satisfactory results.

Figure 5 shows the speed response with different types of MFs subjected to the same perturbation in reference speed. From Fig. 5, it is observed that using triangular, trapezoidal, bell-shaped, sigmoid, polynomial π type MFs based FLC is able to follow the reference speed. Comparative effect of different MFs on performance is given in Table 1.

4 Conclusion

Different types of MFs are considered for designing of FLC. Same type of MFs is used for designing inputs using the Mamdani-type fuzzy logic controller. From the results, it is evident that symmetrical MFs like triangular, trapezoidal, bell-shaped, differential sigmoid, and π shaped polynomial are suitable for DTC implementation. Of the available MFs, triangular and trapezoidal MFs are mostly used in control implementation as they are simple, flexible, and represented by simple algebraic equations. In general, triangular membership functions are employed in control algorithms implemented using DSP, microcontroller, and FPGA. The Gaussian and other MFs are generally used in pattern recognition and complex data problems. So, triangular MFs in combination with trapezoidal MFs at extreme membership value are best suitable for implementation of DTC of induction motor.

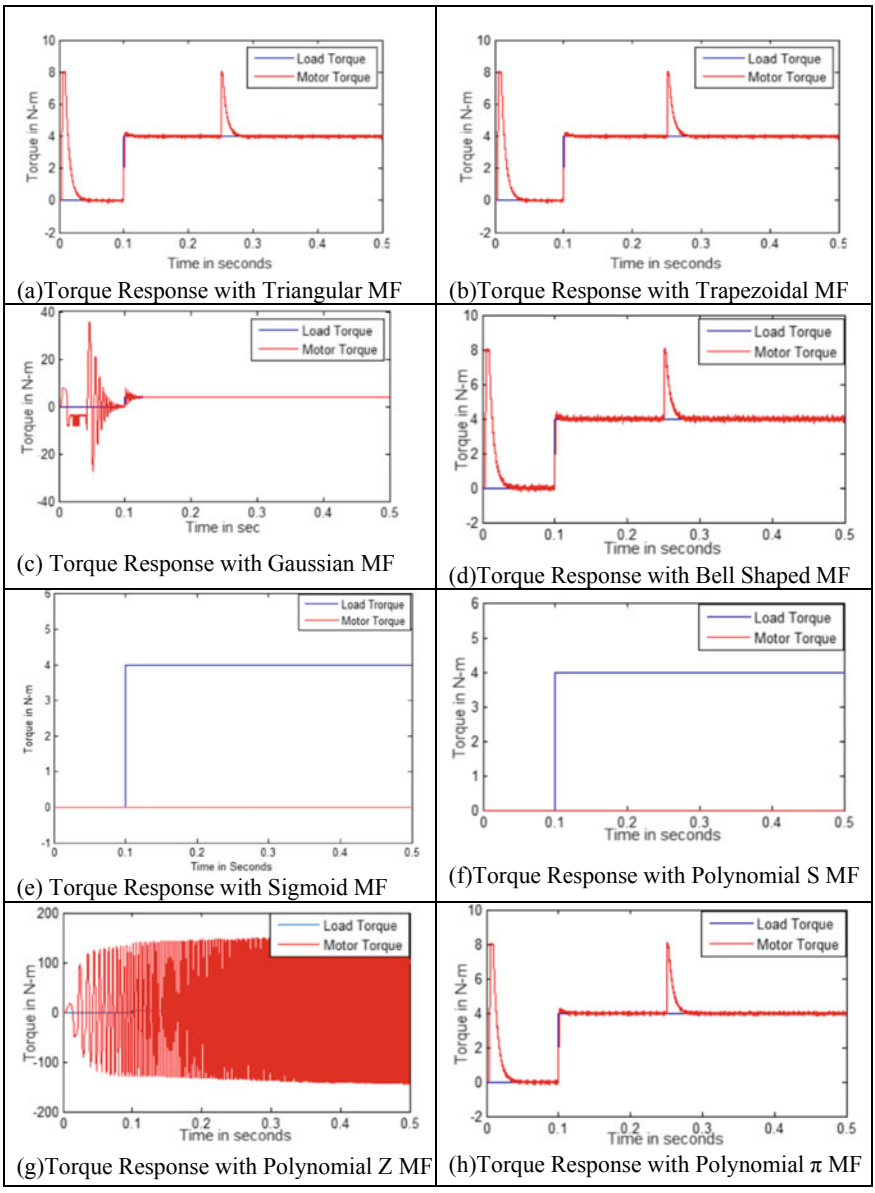

(a)Torque Response with Triangular MF

(b)Torque Response with Trapezoidal MF

(c) Torque Response with Gaussian MF

(d)Torque Response with Bell Shaped MF

(e) Torque Response with Sigmoid MF

(f)Torque Response with Polynomial S MF

(g)Torque Response with Polynomial Z MF

(h)Torque Response with Polynomial π MF

Fig. 4 Torque response of DTC of induction motor using FLC with different MFs

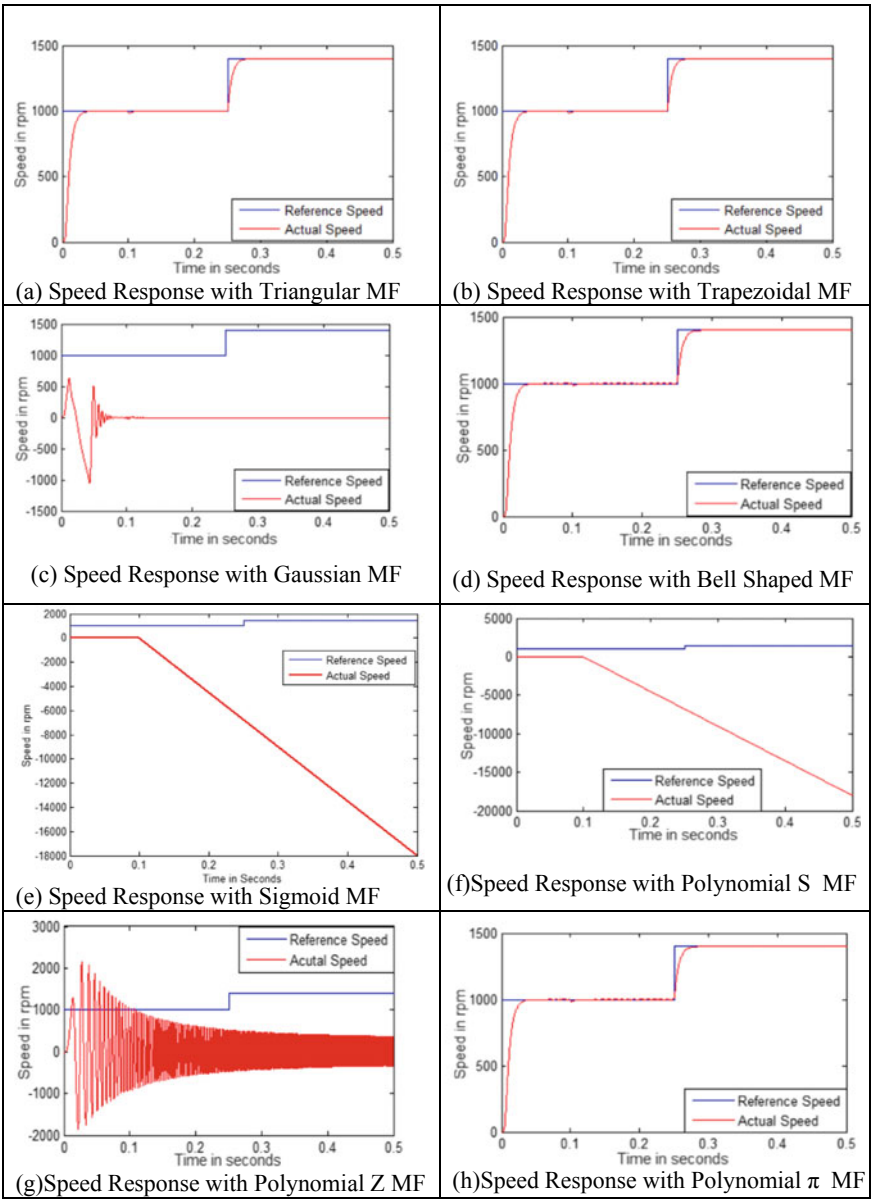

(a) Speed Response with Triangular MF

(b) Speed Response with Trapezoidal MF

(c) Speed Response with Gaussian MF

(d) Speed Response with Bell Shaped MF

(e) Speed Response with Sigmoid MF

(f)Speed Response with Polynomial S MF

(g)Speed Response with Polynomial Z MF

(h)Speed Response with Polynomial π MF

Fig. 5 Speed response of DTC of induction motor using FLC with different MFs

Table 1 Comparative analysis of FLC with different MFs

Types of MFs	Performance	Conclusion
Triangular	Very good	To implement switching table, both triangular and trapezoidal exhibit better selection switching vector for DTC
Trapezoidal	Very good	
Gaussian	Unstable operation, no control action provided	In Gaussian, MF is characterized with just two variables, which makes it difficult to design the MFs of torque error and flux error MFs which are symmetrical around positive and negative errors
Bell shaped	Stable operation with ripples	Gauss bell will give the freedom of third variable to design the MF. Thereby, stable control operation can be achieved using these MFs, but have small ripples
Sigmoid	Unstable operation	As sigmoid is *S* shaped MF with open at the right end, so implementation of switching table with sigmoid cannot select the optimal switching vector. Differential or product of two sigmoid results in better control action, and stable operation is achieved compared to sigmoid
S shaped	No control action	As *S* shaped and *Z* shaped MF are open at the right end and left end that cannot implement torque error, flux error, and uniform distribution of stator flux linkage space vector angles of each 30°, which results in unstable operation, no control action is provided by FLC
Z shaped	Unstable operation	
π shaped	Stable operation slight ripples	The drawback of *S* and *Z* shaped MFs can be overcome by π shaped MFs which allows the distribution of torque and flux error symmetrical over positive and negative values. So, control action is provided, and stable output response is achieved

References

1. Takahashi I, Ohmori Y (1989) High-performance direct torque control of an induction motor. IEEE Trans Ind Appl 25(2):257–264
2. Kazmierkowski MP, Kasprowicz AB (1995) Improved direct torque and flux vector control of PWM inverter-fed induction motor drives. IEEE Trans Indus Electron 42(4):344–350
3. Habetler TG, Profumo F, Pastorelli M, Tolbert LM (1992) Direct torque control of induction machines using space vector modulation. IEEE Trans Indus Appl 28(5):1045–1053
4. Buja GS, Kazmierkowski MP (2004) Direct torque control of PWM inverter-fed AC motors—a survey. IEEE Trans Indus Electron 51(4):744–757

5. Ibrahim Z, Levi E (2002) A comparative analysis of fuzzy logic and PI speed control in high performance ac drives using experimental approach. IEEE Trans Indus Appl 38:1210–1218
6. Hafeez M, Uddin MN, Rahim NA, Ping HW (2014) Self-tuned NFC and adaptive torque hysteresis-based DTC scheme for IM drive. IEEE Trans Indus Appl 50(2):1410–1420
7. Sudheer H, Sarvesh B, Kodad SF (2016) Improved Fuzzy Logic based DTC of Induction machine for wide range of speed control using AI based controllers. J Electr Syst 12(2):301–314
8. Gdaim S, Mtibaa A, Mimouni MF (2015) Design and experimental implementation of DTC of an induction motor based on fuzzy logic control on FPGA. IEEE Trans Fuzzy Syst 23(3):644–655
9. IvicaKuric MZ (2005) Direct Torque and flux control of Induction machine and fuzzy controller. J Electr Eng 56(9–10):278–280
10. Cruz PP, Paredes JPS (2003) Artificial intelligence applications in direct torque control. In: 5th international conference on power electronics and drive systems, vol 2, pp 1208–1212
11. Zhao J, Bose BK (2002) Evaluation of membership functions for fuzzy logic controlled induction motor drive. In: 28th annual conference of the industrial electronics society, vol 1, pp 229–234. IECON 02, Sevilla
12. Orsenigo C, Vercellis C (2007) Evaluating membership functions for fuzzy discrete SVM. In: Masulli F, Mitra S, Pasi G (eds) Applications of fuzzy sets theory. WILF 2007. Lecture notes in computer science, vol 4578. Springer, Berlin, Heidelberg
13. Monicka JG, Sekhar NG, Kumar KR (2011) Performance evaluation of membership functions on fuzzy logic controlled ac voltage controller for speed control of induction motor drive. Int J Comput Appl 13(5):8–12
14. Sudheer H, Kodad SF (2018) Sarvesh B: Improvements in direct torque control of induction motor for wide range of speed operation using fuzzy logic. J Electr Syst Inf Technol 5(3):813–828

Modified Triangular Microstrip Monopole Design Employing Meandered Edge-Cut and Partial Ground Configuration for UWB Applications

G. Viswanadh Raviteja and Perla Devi

Abstract This paper deals with a novel UWB antenna. A triangular microstrip antenna is considered initially and improved structurally to suit the conditions of using it for 3.1–10.6 GHz frequency range. A novel edge-cut is proposed in this design, where the use of the meandered line is implemented along the edges which resulted in improved S11 and gain. To this basic design which uses meandered line edge-cut, structural improvements were carried in which the concept of partial ground and ground slots are added stage by stage, making the final monopole design to be able to work for UWB applications. The proposed antenna structure exhibits a bandwidth range of 8.4 GHz (125.74%) with frequency ranging from 2.48 to 10.88 GHz. The peak gain observed was about 7.23 dB. Comparisons were also drawn with respect to antenna parameters for the initial, intermediate, and final stage UWB monopole antenna design. Finally, the proposed antenna is fabricated and tested where a good agreement is found between simulated and measured results.

Keywords Triangular monopole · Meandered line · UWB applications · Partial ground

1 Introduction

In view of the extensive growth in the field of wireless communication systems, there is a huge demand for developing novel wireless applications. This led to the design of broadband wireless systems. This trend continued to a point where the spectrum reached its maximum usage. In view of providing services over wide frequency ranges, ultra-wideband (UWB) systems are designed [1]. For these UWB systems,

G. V. Raviteja (✉) · P. Devi
Department of Electronics and Communication Engineering, Anil Neerukonda Institute of Technology and Sciences-ANITS, Visakhapatnam, Andhra Pradesh 531162, India
e-mail: tejar512@gmail.com

P. Devi
e-mail: devi.ece@anits.edu.in

G. T. C. Sekhar et al. (eds.), *Intelligent Computing in Control and Communication*, Lecture Notes in Electrical Engineering 702,
https://doi.org/10.1007/978-981-15-8439-8_34

it is necessary to develop antennas which can cover a wide range of frequencies with high gain. It is a major challenge to design an efficient UWB antenna. Microstrip patch antennas are highly used mainly for their low profile and easy fabrication with less cost and its ease of deployment wherever it finds its application. But, microstrip antennas possess a disadvantage of narrow bandwidth which constitutes only 5% around the center frequency [2].

In order to overcome the limitations associated with microstrip antenna, a number of methodologies were proposed. *E*-shaped wideband microstrip antenna is proposed in [3], a triband *H*-shaped antenna with frequency selectivity feature is discussed in [4], and spear-shaped antenna for UWB applications is seen in [5]. The concept of using symmetrical *U*-slots is introduced in [6]. Here, the *U*-slots are cut in a symmetrical distribution on the ground plane. A triple-band antenna with toothbrush-shaped, meander line and inverted *U*-shaped patch structure is discussed in [7]. Defected ground structures are another way of increasing the antenna performance. Impedance bandwidth is one of the parameters to show betterment with the use of defected ground structures. A wideband antenna employing cambered shaped ground plane with a rectangular slot cut defected ground structure is discussed in [8], and the use of stacked microstrip patch antenna with DGS to improve the compactness is shown in [9]. More recently, application of meander line concept to the modern antenna designs gained much attention. Meander line design on an antenna is preferred as it provides better miniaturization, and also the efficiency is improved [10].

The application of meander line antenna design with AMC ground for wearable applications is discussed in [11]. In this, the overall compactness of the antenna is increased, and also the efficiency is improved. More recently, meander line structures are used in for UHF RFID tags and also the GPS applications and wireless local area network applications. These are shown in [12, 13]. SAR reduction with the use of meander line antenna for wearable applications is also discussed in [14]. This paper deals with the meander edge cut modified triangular patch antenna which would be the conventional antenna in this case. Thereby, the antenna is modified structurally with respect to the ground specifications, so that the design structure is suitable for its working for ultra-wideband (UWB) applications.

2 Antenna Design Structure

An initial design of triangular microstrip antenna is considered. To this initial design, modifications are carried out with respect to radiating edges of the triangular patch. This is done on purpose to study the characteristics the antenna exhibit with respect to multiple sharp edges along the entire length of the side arms of a triangle. The third side which constitutes the base of the triangle is set undisturbed. Meander line structure cut is implemented along the side arms defining sharp edge-cuts along its entire length of the sides. The ground configuration in this case is a full ground with dimensions set to be 60 $\times$ 60 (in mm) along the $W \times L$ (in mm). The substrate used is FR4 epoxy with dielectric constant 4.3 and loss tangent of 0.02. The antenna

discussed is seen in Fig. 1 designated as Antenna 1. The resonant frequency "f_{mn}" for the triangular patch is calculated using the standard formula discussed in [15].

Meander line structures are utilized in the antenna design considerations as they provide miniaturization. This is an important aspect as the compactness of the antenna also plays a vital role as far as future wireless communications are concerned. The meander line edge-cut for the Antenna 1 is shown in Fig. 2.

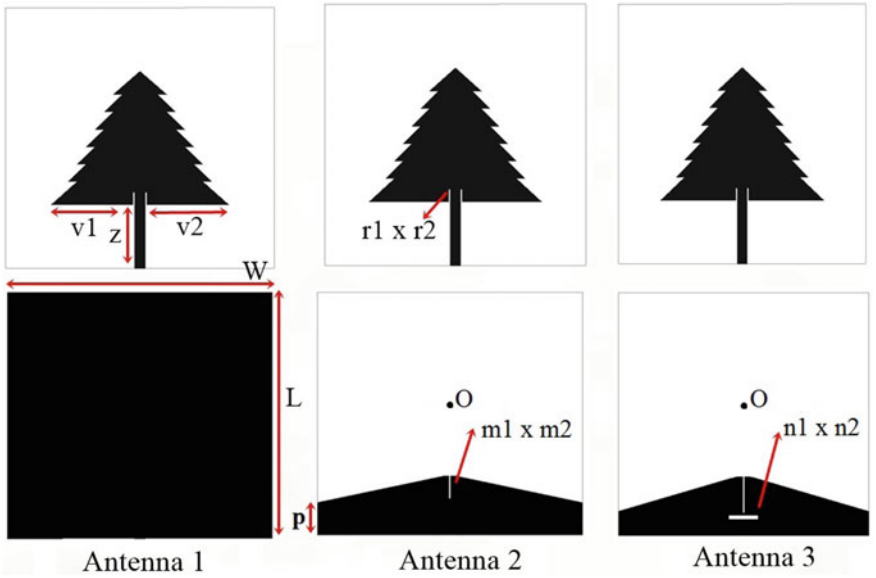

Fig. 1 Structural modifications of the given antenna stage by stage

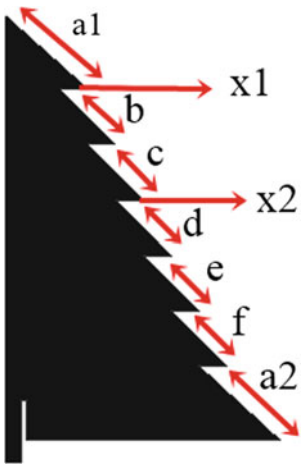

Fig. 2 Meander line edge-cut configuration

The triangular patch is modified in terms of its radiating edges. Seven step cuts are proposed in a particular configuration such that the length of the first and seventh slant edges a_1 and a_2 are of a constant value "5.36 mm." The rest all five slant cuts are maintained at a same value $b = c = d = e = f = 4$ mm each. The step cut followed for each slant edges is the same throughout the entire sidearm. This is given as $x_1 = x_2 = 2$ mm each. The purpose of these defined cuts and slants is to maintain a symmetrical distribution pertaining to the radiating edges. Therefore, the left sidearm of the triangle is also maintained with the same configuration similar to as reported on the right side. The antenna is fed with the inset-fed technique with a length of the feed line "$z = 14.63$ mm" in order to provide better impedance matching. Two slots are cut, so that the feed line stretches into the geometry of the patch. The slots dimensions are specified to be $r_1 \times r_2 = 0.35 \times 2.86$ mm ($W \times L$). All the parameters discussed are optimized so as to achieve desired results.

3 Discussions with Respect to Antenna 1

Simulations are carried out for Antenna 1. The simulated S11 plot shows a return loss of −19.66 dB with center frequency of 2.45 GHz. The gain, in this case, is found out to be 3.26 dB. The S11 and gain values obtained are concerning the triangular microstrip monopole design with meandered edge-cut. Comparison is drawn with respect to triangular microstrip without meandered edge-cut, where the S11 is found out to be 11.01 dB and the gain being 1.42 dB for the center frequency of 2.51 GHz. On taking these low values into consideration, structural modifications are performed with respect to radiating edges. The meandered edge-cut is performed along the two sides of the antenna. This modification enables the fringing fields to add up at the sharp edges formed by the meandered cut, which improves the radiation properties of the antenna. The improved S11 is seen in Fig. 3, and the 3D gain plots are mentioned in Fig. 4.

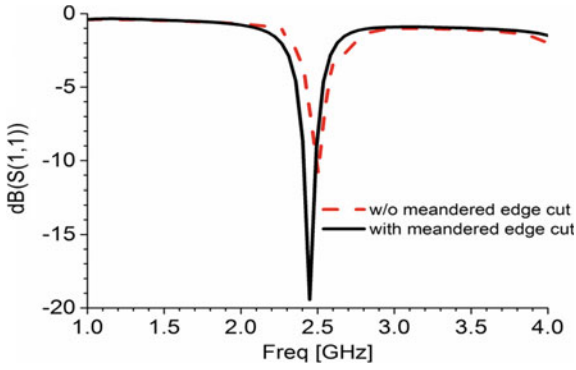

Fig. 3 S11 comparison plot for Antenna 1 with and without meandered edge-cut

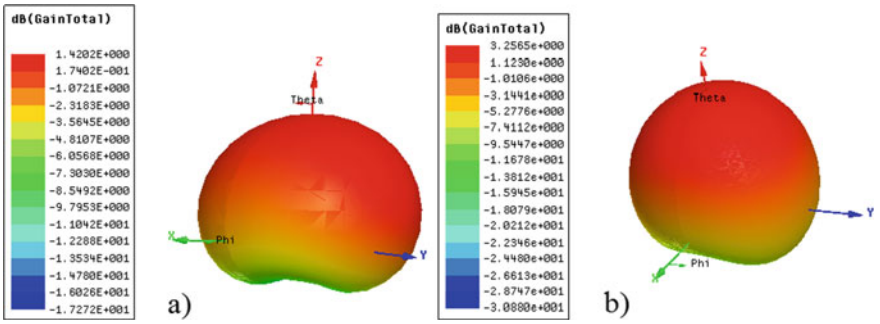

Fig. 4. 3D radiation plot for Antenna 1 **a** without meandered edge-cut **b** with meandered edge-cut

4 Discussions with Respect to Antenna 2

On observing the improved gain and S11, the antenna with meandered edge-cut is taken into final consideration. In the next stage, in order to achieve wideband characteristics, the use of partial ground is considered. The optimized dimensions considered were 60 × 08 mm ($W \times L$). In addition to the reduction of the ground plane, a minor rectangular slot is cut in a vertical position right at the center of the modified ground plane at a distance of 15 mm from *y*-axis with respect to origin '*O*.' The rectangular slot is 5.63 × 0.4 mm ($m_1 \times m_2$). When the original ground plane is cut into the partial ground, the electrical length of the antenna is increased which in turn decreases the resonant frequency. Therefore, in order to maintain the wideband characteristics and to restrict mismatch to a minimum level, the vertical rectangular slot is incorporated within the partial ground plane design. The result is a modified S11 plot with an improved bandwidth of 4.01 GHz (64.10%) with frequency ranging from 4.25 to 8.26 GHz. This is shown in Fig. 5.

With respect to gain, Antenna 2 exhibited a peak gain of 4.21 dB at 4.6 GHz. The gain was observed to be over 3 dB for the frequency range covering 4.5–6.8 GHz with a gain of 4.17 dB at 6.06 GHz, 2.68 dB at 6.5 GHz, and 3.38 dB at 7.5 GHz.

The VSWR is also observed to be less than 2 for the entire bandwidth range obtained. On an overall note, the gain of the Antenna 2 showed up above 2 dB on the entire bandwidth region with gain being over 3 dB till 6.8 GHz frequency, where a gain of 3.38 was seen at 7.5 GHz. Figures 6 and 7 deal with the VSWR and gain plots for Antenna 2.

5 Discussion with Respect to Antenna 3

In order to achieve bandwidth applicable for UWB applications, the rectangular slot etched in the Antenna 2 is furthermore cut into the ground plane with respect to length. The width of the slot is maintained the same with respect to Antenna 2. The

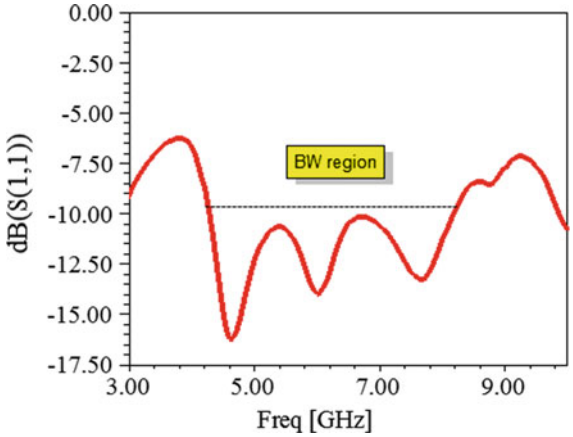

Fig. 5 S11 plot for Antenna 2

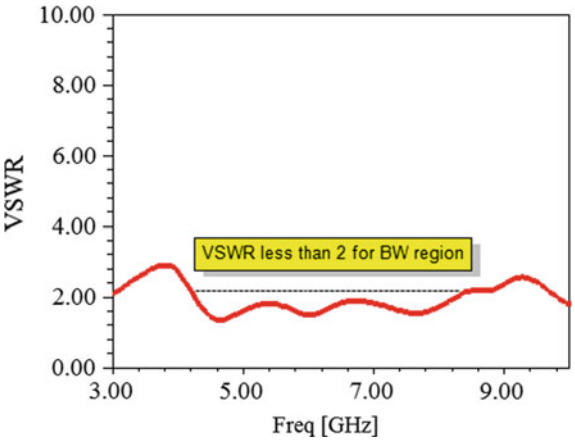

Fig. 6 VSWR plot for Antenna 2

modified rectangular slot dimensions are 9 × 0.4 mm ($L \times W$). In addition to the vertical slot, another rectangular slot is etched in the horizontal direction. *This new slot is cut away at a distance of 25 mm from the center of the origin along the y-axis. It is positioned at a distance of 4 mm from the bottom boundary of the ground plane.* The dimensions are optimized to be set at 1 × 7 mm ($n_1 \times n_2$). This combination of vertical and horizontal slots makes it possible to combine two different modes exciting from the antenna to realize wider bandwidths. The end result is an increase in bandwidth which was found out to be 8.4 GHz with frequency ranging from 2.48 to 10.88 GHz. The realized bandwidth is more than the FCC recommended range which was 3.1–10.6 GHz. The fabricated prototype of Antenna 3 and the return loss S11 plot is seen in Figs. 8 and 9.

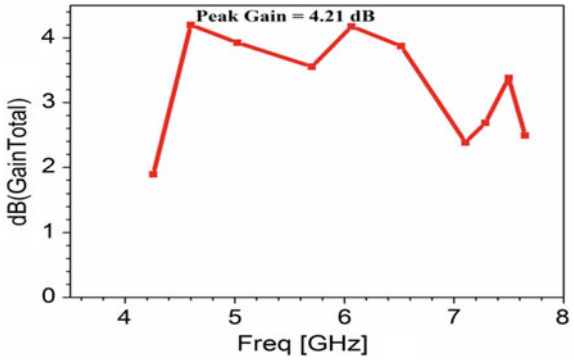

Fig. 7. 2D gain plot for Antenna 2

Fig. 8 Fabricated prototype of Antenna 3

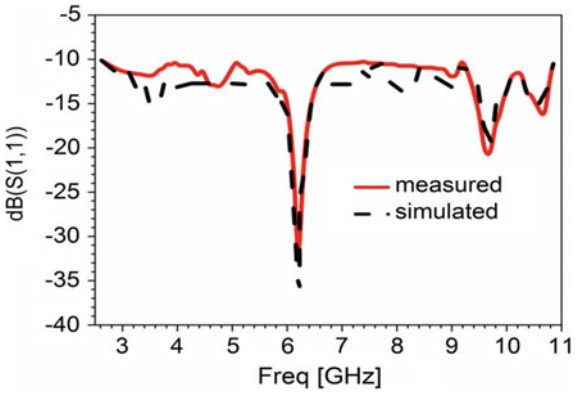

Fig. 9 S11 plot for Antenna 3

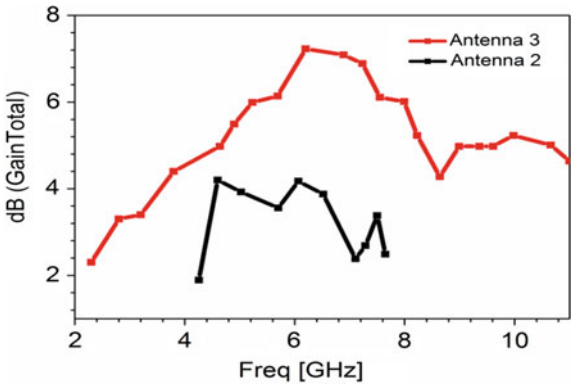

Fig. 10. 2D gain comparison plot for Antenna 2 and Antenna 3

From the results, it is evident that UWB characteristics are achieved with a center frequency of 6.22 GHz. Comparisons are drawn in accordance with measured and simulated S11 plot, and a good agreement is seen between the two. The peak gain for Antenna 3 is observed to be 7.23 dB at the center frequency. Overall gain was found out to be above 3 dB mark from frequencies 2.89–10.88 GHz which is appreciable. From frequency range 4 GHz up to the center 10.88 GHz, the gain was observed to be above 4.5 dB. The gain plot comparison for Antenna 2 and Antenna 3 is given in Fig. 10.

Reflections arise out of antenna if the impedance is not properly matched. Therefore, standing waves will be seen along the transmission line which is an unwanted factor. For an antenna to work efficiently, its radiated power should be very large when compared to reflected power. The results indicated that in both the cases of antennas 2 and 3, the reflected power is less than 10%. The mismatch loss on the other hand shows that the amount of loss (in dB) with respect to mismatch is found to be less than 0.5 dB which is appreciable.

6 Group Delay Discussions

The distortion state of the transmitted pulses should be studied which is deduced using group delay plot. This parameter is necessary when considering UWB systems. Constant group delay indicates the proper transmission of pulses. For a UWB system, this parameter is analyzed for the entire bandwidth region considered. Therefore, group delay is computed for the proposed monopole design, Antenna 3. From Fig. 11, it is seen that the group delay is almost constant for the entire bandwidth region specified. At 6.2–6.3 GHz, a spike is observed with maximum value of the spike being less than 3 ns. Therefore, on an overall note, the pulse transmission is acceptable for

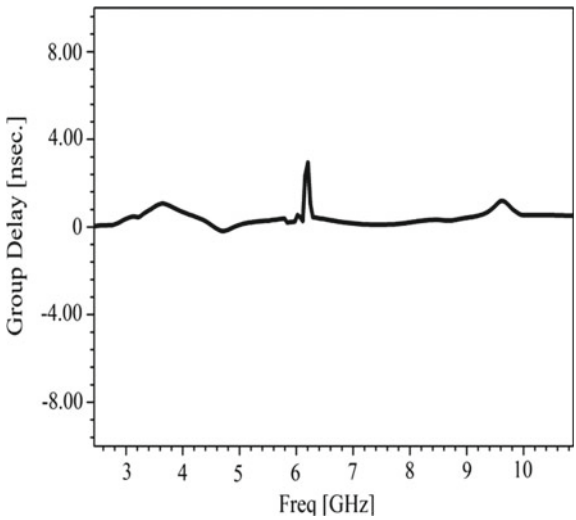

Fig. 11 Group delay versus frequency plot for Antenna 3

the antenna taken into consideration. The group delay versus frequency plot is given in Fig. 11.

7 Conclusion

A new triangular microstrip antenna is discussed, in which structural modifications are carried stage by stage arriving at the monopole design at the last stage to meet the requirements of UWB characteristics. The final version of the proposed monopole antenna with meander edge-cut employing partial ground, vertical, and horizontally etched ground slots provided a bandwidth of 8.4 GHz (125.74%) covering the frequency ranges of 2.48–10.88 GHz with a peak gain of 7.23 dB at 6.22 GHz. The bandwidth achieved is almost double when compared to Antenna 2 which achieved a bandwidth of 64.10%. The performance in terms of mismatch loss and reflected power was also calculated which was found to be less than 10% and less than 0.5 dB. Group delay is computed which is found to be almost constant for the entire UWB range. Comparisons were discussed with respect to implementations carried out structurally. The final version of Antenna 3 is also fabricated and tested. The results were found to be in good agreement with the simulated results. Therefore, the proposed monopole antenna can be extensively considered for its usage in UWB applications.

References

1. Islam MT, Shakib MN, Misran N (2009) Design analysis of high gain wideband L-probe fed microstrip patch antenna. Prog Electromagnet Res 95:397–407
2. Ramadan A, Kabalan KY, El-Hajj A, Khoury S, Al-Husseini M (2009) A reconfigurable U-Koch microstrip antenna for wireless applications. Prog Electromagnet Res 93:355–367
3. Ang BK, Chung BK (2007) A wideband E-shaped microstrip patch antenna for 5–6 GHz wireless communications. Prog Electromagnet Res 75:397–407
4. AbuTarboush HF, Nilavalan R, Nasr KM, Cheung SW, Peter T, Al-Raweshidy HS, Budimir D (2011) Reconfigurable tri-band H-shaped antenna with frequency selectivity feature for compact wireless communication systems. IET Microwaves Antennas Propag 5(14):1675–1682
5. Reddy NS, Naidu KS, Kumar SA (2018) Performance and design of spear shaped antenna for UWB band applications. Alexandria Eng J 57(2):719–722
6. Toshniwal S, Sharma S, Rawat S, Singh P, Ray K (2016) Compact design of rectangular patch antenna with symmetrical U slots on partial ground for UWB applications. In: Innovations in bio-inspired computing and applications. Springer, Cham, pp 535–542
7. Li Y, Yu W (2015) A miniaturized triple band monopole antenna for WLAN and WiMAX applications. Int J Antennas Propag 2015
8. Gautam AK, Bisht A, Kanaujia BK (2016) A wideband antenna with defected ground plane for WLAN/WiMAX applications. AEU-Int J Electron Commun 70(3):354–358
9. Khandelwal MK, Kanaujia BK, Dwari S, Kumar S, Gautam AK (2015) Analysis and design of dual band compact stacked microstrip patch antenna with defected ground structure for WLAN/WiMax applications. AEU-Int J Electron Commun 69(1):39–47
10. Mokhtar NHM, Malek NA, Jusoh AZ, Ali K, Isa FNM, Rahman FDA (2019) Design and comparison of printed antennas using meander line technique. Bull Electr Eng Inf 8(2):596–603
11. Bhattacharjee S, Midya M, Mitra M, Chaudhuri SRB (2016) Performance enhancement of meander line antenna with AMC ground for wearable applications. In: 2016 Asia-Pacific microwave conference (APMC). IEEE, pp 1–4
12. Rokunuzzaman M, Islam MT, Rowe WS, Kibria S, Singh MJ, Misran N (2016) Design of a miniaturized meandered line antenna for UHF RFID tags. PLoS ONE 11(8):e0161293
13. Bartwal P, Gautam AK, Singh AK, Kanaujia BK, Rambabu K (2016) Design of compact multi-band meander-line antenna for global positioning system/wireless local area network/worldwide interoperability for microwave access band applications in laptops/tablets. IET Microwaves Antennas Propag 10(15):1618–1624
14. Bhattacharjee S, Mitra M, BhadraChaudhuri SR (2017) An effective SAR reduction technique of a compact meander line antenna for wearable applications. Prog Electromagnet Res 55:143–152
15. Bhattachaijee S, Teja S, Chaudhuri SB, Mitra M (2017) Wearable triangular patch antenna for ON/OFF body communication. In: 2017 IEEE applied electromagnetics conference (AEMC). IEEE, pp 1–2

Automatic Generation Control with Renewable Energy Sources Optimized by TLBO Algorithm

P. Venkatesh and K. Sri Kumar

Abstract In interconnected power system, frequency control problem is much more complex with variations in size and load. Two different areas are taken in which area 1 consists of three thermal reheat turbines with renewable energy sources, i.e., DFIG wind turbine, Photovoltaic generation system, fuel cell, battery storage system, and aqua electrolyzer. Area 2 consist of three non-reheat turbines with renewable energy sources, i.e., DFIG wind turbine, Photovoltaic generation system, fuel cell, battery storage system, and aqua electrolyzer. In this, three controllers are used, namely PID, PIDF, and cascaded PD-PI controllers. The controller parameters are effectively tuned by the "Teaching Learning Based Optimization" technique. 1% step load disturbance is applied in area 1 for analyzing the performance of the system. The performance of the power system with and without renewable energy sources is done in MATLAB software. The dynamic response of the considered system is compared in terms of undershoots, overshoots, and settling times.

Keywords Automatic Generation Control (AGC) · Proportional Integral Derivative with Filter (PIDF) · Renewable Energy Sources · Teacher learning based optimization (TLBO) algorithm

1 Introduction

As Power demand grows rapidly, hence essential to maintain secure power to the utilities, for that basic control loops function accordingly to sustain the load demand with nominal voltage and frequency. The basic control loops generally preferred to balance the active and reactive powers with the load. If load increases with respect to

P. Venkatesh (✉)
Electrical and Electronics Engineering, V R Siddhartha Engineering College, Vijayawada, Andhra Pradesh 520007, India
e-mail: venki249@gmail.com

K. Sri Kumar
Electrical and Electronics Engineering, JNTUK, Kakinada, Andhra Pradesh 533003, India

G. T. C. Sekhar et al. (eds.), *Intelligent Computing in Control and Communication*, Lecture Notes in Electrical Engineering 702,
https://doi.org/10.1007/978-981-15-8439-8_35

the generation, the frequency starts drooping below its nominal value. Correspondingly, as load decreases, frequency rises above its nominal value. In a power system network, Automatic Generation Control is the basic primary loop which is utilized for controlling the frequency [1, 2]. Thus AGC is mostly utilized for matching load demand with generation of electric power. If there is extra load on the power system network than that of the actual load, then speed of the turbine starts decreasing and leads to decrease in the nominal frequency. Objectives of using AGC are maintaining frequency within permissible range and to schedule the changes in Tie-line power interchanges. Two area multi-unit power system with renewable energy sources is considered for observing the dynamic behavior of the system [3]. The area 1 consists of three reheat turbine units and area 2 consists of three non-reheat turbine units with renewable energy sources. In this paper three different controllers are used, namely PID, PIDF, and cascaded PD-PI controllers to control the parameters [4]. These parameters are effectively tuned by the "Teaching Learning Based Optimization" technique [5, 6].

In this paper, effect of renewable sources on AGC in multi area power system is analyzed. It is seen that renewable energy sources in multi-area power improve the performance of the system in all aspects under load disturbances.

2 Power System Investigated

Here, two different areas are taken in which area 1 consists of three thermal reheat turbines with renewable energy sources and Area 2 consisting of three non-reheat turbines with renewable energy sources as shown in Fig. 1 and TLBO is implemented for optimum values of PID and cascaded PD-PI controller parameters. All parameters of two area thermal power systems data are given in Table 7. All area participation Factors are taken as 0.33, such that $a_{11} + a_{12} + a_{13} = 1$ for area 1 and $a_{14} + a_{15} + a_{16} = 1$ for Area 2. All gains of controllers are tuned to reduce the Area Control Error to zero; these are represented in Eqs. 1 and 2.

$$\mathrm{ACE}_1 = \Delta \mathrm{P}_{12} + B_1 \Delta f_1 \tag{1}$$

$$\mathrm{ACE}_2 = \Delta \mathrm{P}_{21} + B_2 \Delta f \tag{2}$$

where $\Delta \mathrm{P}_{12}$ and $\Delta \mathrm{P}_{21}$ are deviations of tie line powers in Area 1 and Area 2, respectively. B_1 and B_2 are frequency bias factors for both areas. These two areas are connected to wind energy with Doubly Fed Induction Generator.

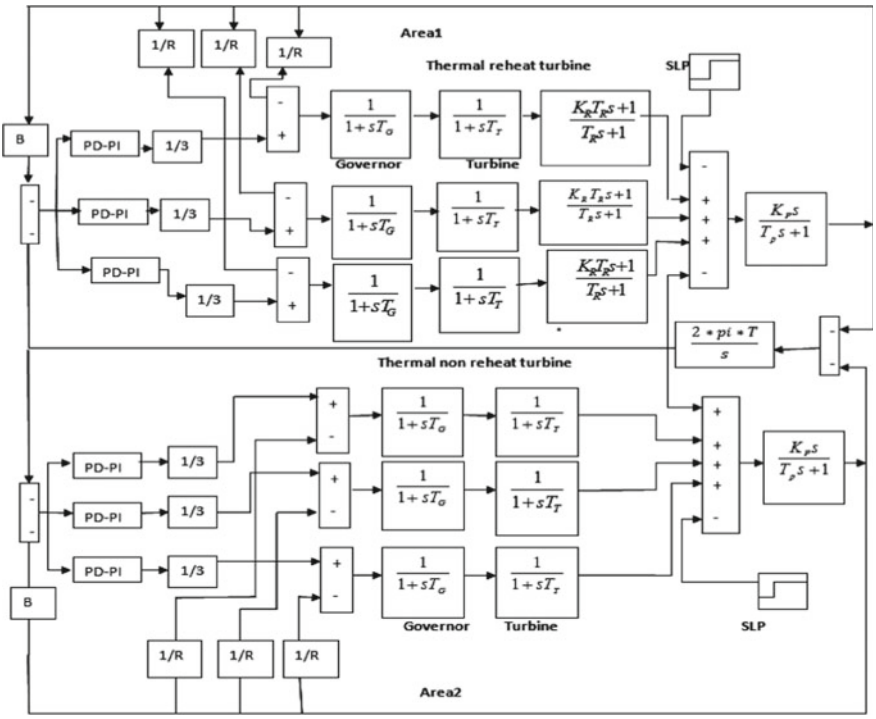

Fig. 1 Simulation diagram of two area power system without renewable energy sources

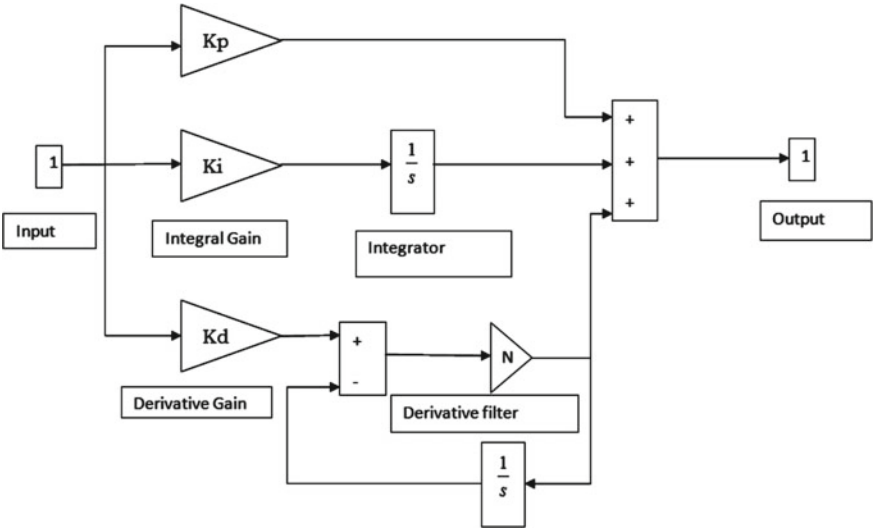

Fig. 2 Structure of PIDF controller

2.1 Structure of Controllers

In this section, two different controllers names as PIDF and cascaded PD-PI controllers are used to control the parameters and these controllers are described below.

2.1.1 Tuning of PIDF Controllers

PID controller does not give satisfactory operation due to the presence of noise and harmonics in the input signal. This effect is minimized by adding filter to the PID controller, which is named as PIDF controller. The parameters of PIDF controller are optimized by TLBO. The proposed PIDF controller transfer function is written in Eq. 3 and structure of PIDF controller is given in Fig. 2.

$$\mathrm{TF}_{\mathrm{PIDF}} = \left[K_p + \frac{K_i}{s} + K_d\left[\frac{N_s}{s+N}\right]\right] \tag{3}$$

where K_p, K_i, K_d and N_s are constants.

2.1.2 Cascaded PD-PI Controller

Cascaded PD-PI controller is the two combinational process, it is inner process supplied to output to the outer process. Cascaded PD-PI controller decreases the settling time, undershoot and overshoot times [8–11]. Cascaded PD-PI controller transfer function is written in Eq. 4 and the structure of Cascaded PD-PI controller is shown in Fig. 3.

$$\mathrm{TF}_{\mathrm{PD-PI}} = K_p + K_d s \times K_p + \frac{K_i}{s} \tag{4}$$

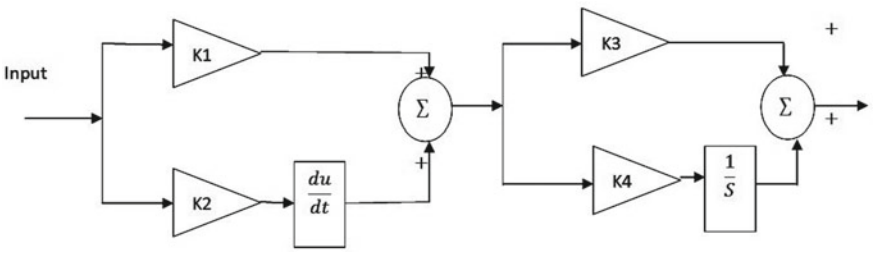

Fig. 3 Structure of cascaded PD-PI controller

3 Renewable Energy Sources

In this section, Different renewable energy sources are described which are used in AGC multiarea power system. All parameters of renewable energy sources are given in Table 6. Different renewable energy sources are described below.

3.1 Aqua Electrolyzer

Wind turbine generators are used in the aqua electrolyzer to produce hydrogen. It is supplied to fuel cells for generation of electrical power. Aqua Electrolyzer transfer function is represented in Eq. 5

$$G_{\mathrm{AE}} = \frac{K_{\mathrm{AE}}}{1 + sT_{\mathrm{AE}}} \tag{5}$$

3.2 Fuel Cell

Fuel cell converts the chemical energy into electrical energy and it uses hydrogen gas (H_2) and oxygen gas (O_2) as fuel. The transfer function for the fuel cell is represented in Eq. 6

$$G_{\mathrm{FC}}(s) = \frac{K_{\mathrm{FC}}}{1 + sT_{\mathrm{FC}}} \tag{6}$$

3.3 Battery Energy Storage System

Energy Storage Systems are needed to help the grid to balance the load. BESS transfer function is represented in Eq. 7

$$G_{\mathrm{BESS}} = \frac{K_{\mathrm{BESS}}}{1 + sT_{\mathrm{BESS}}} \tag{7}$$

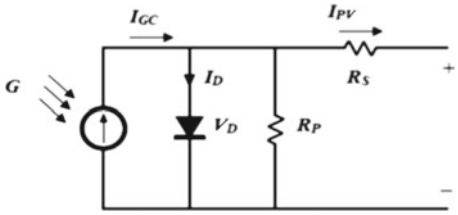

Fig. 4 Electric circuit of PV module

3.4 Photovoltaic Power Generation System

Photovoltaic modules are used to improve the dynamic response. The output current of PV module is given in Eq. 8 and Electrical circuit of PV module is shown in Fig. 4.

$$I_{\mathrm{A}} = N_{\mathrm{P}} I_{\mathrm{SC}} - N_{\mathrm{P}} I_0 \exp\left(\left[\frac{V_{\mathrm{A}} + I_{\mathrm{A}} P_{\mathrm{S}}}{n N_{\mathrm{S}} V_{\mathrm{T}}}\right]\right) \tag{8}$$

where

I_0 is the diode saturation of current.
R_{s} is the series resistor.
N is the diode ideal constant.
V_{T} is the PV module thermal potential.
V_{A} is the PV array terminal voltage.

PV module transfer function is represented in Eq. 9

$$G_{\mathrm{PV}}(s) = \frac{K_{\mathrm{PV}}}{1 + sT_{\mathrm{PV}}} \tag{9}$$

3.5 DFIG Wind Turbine

Wind turbine converts the electrical energy from kinetic energy and it is added to DFIG wind turbine to maintain the constant frequency. When wind turbines participate to regulate the frequency, it prevents themselves to take care of frequency. The parameters of DFIG wind turbine is given in Table 5. Figure 5 shows the simulation model for active power control with DFIG based wind generators [7]. In DFIG rotor is connected to the grid through a back-to-back voltage source converter that controls both slip rings and both rotor and grid streams. So the rotation frequency is different.

Under disturbance active power injected by wind turbine is ΔP_{NC}. The power injected by the wind turbine is compared with the $\Delta P_{\mathrm{NC1ref}}$ to get the maximum output; it is obtained by reference rotor speed. The controllers will control the speed of turbine to supply maximum power. It responds to frequency change during load

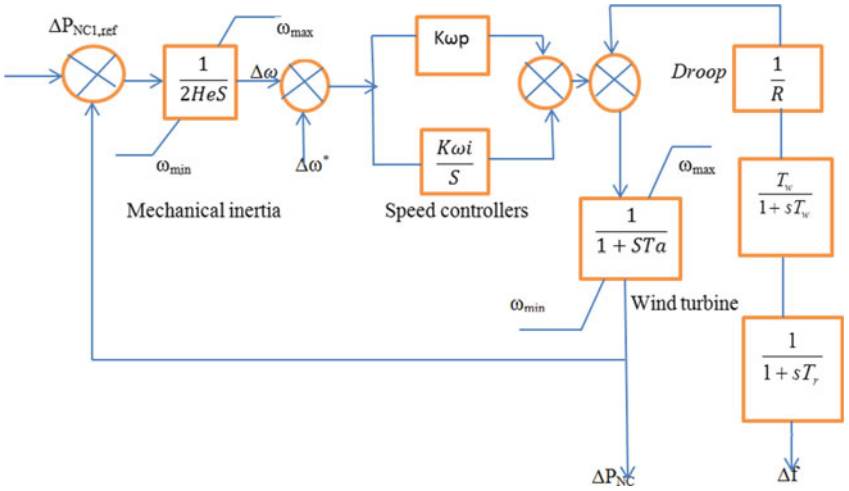

Fig. 5 Block diagram of DFIG wind turbine

disturbance using stored Kinetic energy. Complete block diagram of DFIG wind turbine is shown in Fig. 5.

4 Teacher Learning Based Optimization

This is the population-based algorithm, it is teaching-learning process. In this algorithm, group of students are learners and subjects offered considered as design variables. The first phase of this algorithm is called as learner phase and second phase as learner phase. Flowchart of TLBO is shown in Fig. 6.

4.1 Teacher Phase

Teacher improves the mean result in the class. Teacher identifies the highly learned person in the class named as best learner. Difference mean is calculated from the Eq. 10

$$\text{Diff\_mean} = r_i(X_{\text{best}} - T_F M_i) \tag{10}$$

where

X_{best} is the best learner in the result

T_F nnis the teaching factor and these values randomly assumed with equal probability

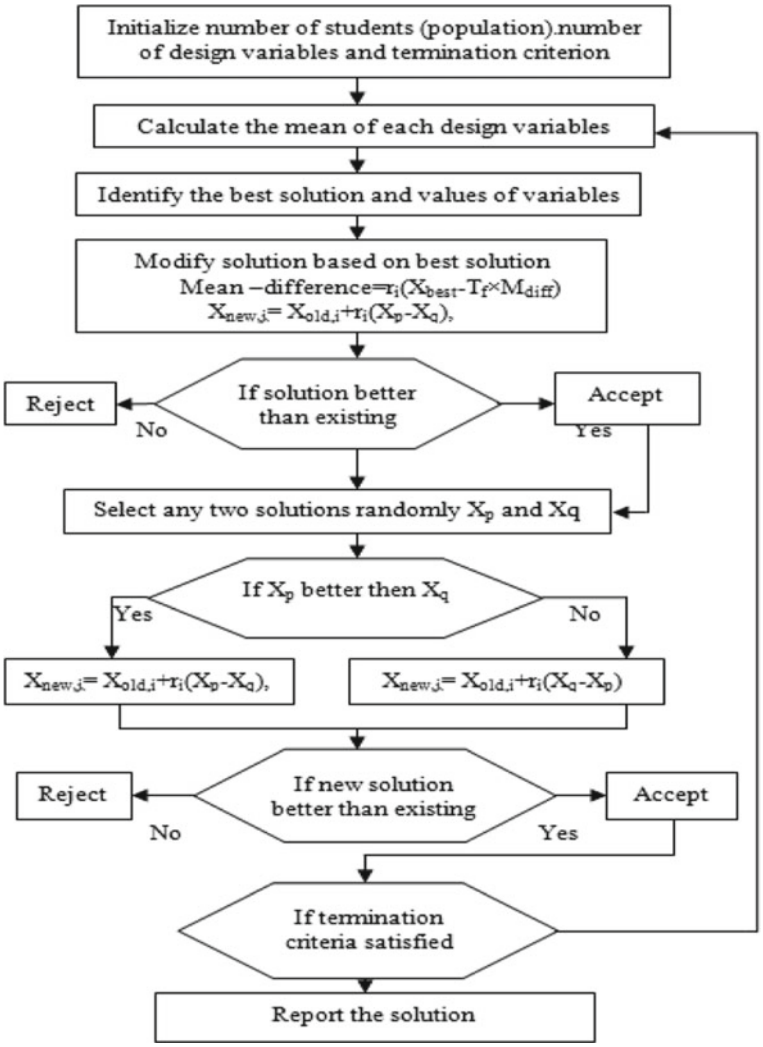

Fig. 6 Flowchart of TLBO

Teaching factor is given in Eq. 11

$$T_F = \text{round}[1 + r_2] \tag{11}$$

r_2 is assumed between 0 and 1. Modify the solution using Eq. 12, Which gives the new solution, i.e., better value in the TLBO algorithm. Modify solution formula given in Eq. 12

$$X' = X + \text{Diff\_mean} \tag{12}$$

where

X' nnis the new solution and X is the old value.

4.2 Learner Phase

In which every learner interacts with the other learners randomly for improving the knowledge using Eqs. 13 and 14. Two learners X_1 and X_2 continuously interact with each other, until p is not equal to q.

$$X'' = X' + r_i(X'_p - X'_q) \text{ if } p \leq q \tag{13}$$

$$X'' = X' + r_i(X'_q - X'_p) \text{ if } q \leq p \tag{14}$$

Gain values of cascaded PD-PI, PID, and PIDF for different controllers with and without renewable energy sources which are tuned by TLBO are represented in Tables 1, 2 and 3 respectively.

Table 1 Gains of Cascaded PD-PI controller for different units

Gains	Area 1 for PD-PI			Area 2 for PD-PI		
	Unit 1	Unit 2	Unit 3	Unit 1	Unit 2	Unit 3
K_1	1.6026	1.7117	2.8517	1.6026	1.7117	2.8517
K_2	1.5911	2.6955	2.1502	1.5911	2.6955	2.1502
K_3	1.6659	2.1656	1.0200	1.6659	2.1656	1.0200
K_4	1.9341	2.1724	2.6188	1.9341	2.1724	2.6188

Table 2 Gains of PID, PIDF, and PD-PI controllers

Controller	Area 1			Area 2		
	PID	PIDF	PD-PI	PID	PIDF	PD-PI
K_1	2.1712	2.4848	1.7117	2.3232	2.2362	2.8517
K_2	2.5258	2.6623	2.6955	2.0340	2.8644	2.1502
K_3	1.1659	1.3130	2.1656	1.3421	2.6702	1.0200
K_4	–	–	2.1724	2.1724	–	2.6188
N	–	183.466	–	–	358.27	–

Table 3 Gains of PD-PI controller with renewable energy sources optimized by TLBO

	Area 1 for PD-PI			Area 2 for PD-PI		
	Unit 1	Unit 2	Unit 3	Unit 1	Unit 2	Unit 3
K_1	1.6026	2.2964	2.7082	1.6026	2.2964	2.7082
K_2	1.5911	1.0505	1.6958	1.5911	1.0505	1.6958
K_3	1.6659	2.6844	1.8921	1.6659	2.6844	1.8921
K_4	1.9341	2.1181	1.1085	1.9341	2.1181	1.1085

5 Simulation Results

In the modeling of the system, the time constants and gains of the respective units will play a key role. So, the given data used in the simulation model are $T_{g1,}$ T_{g2} are the time constants of governor in sec and $T_{t1,}$ T_{t2} are the time constants of turbine in sec T_{p1}, T_{p2} are the power system time constants in sec and respective loop gains like power system $K_{p1,}$ K_{p2}, re heater $K_{r1,}$ K_{r2} are in Hz/P.U.MW and the deviation coefficients of governor. $R_{1,}$ R_2 are in Hz/P.U and B_1, B_2 are frequency biased constants.

Simulation results of Frequency Deviation in two areas and Tie line power deviation without renewable energy sources for different controllers are represented in Figs. 7, 8 and 9 respectively, from this, it is observed that out of all controllers cascaded PD-PI controller is best in all aspects.

Two different areas are taken in which area 1 consists of three thermal reheat turbines with renewable energy sources, i.e., DFIG wind turbine, Photovoltaic generation system, fuel cell, battery storage system, and aqua electrolyzer. Comparison of settling times with and without renewable energy sources is given in Table 4. It is

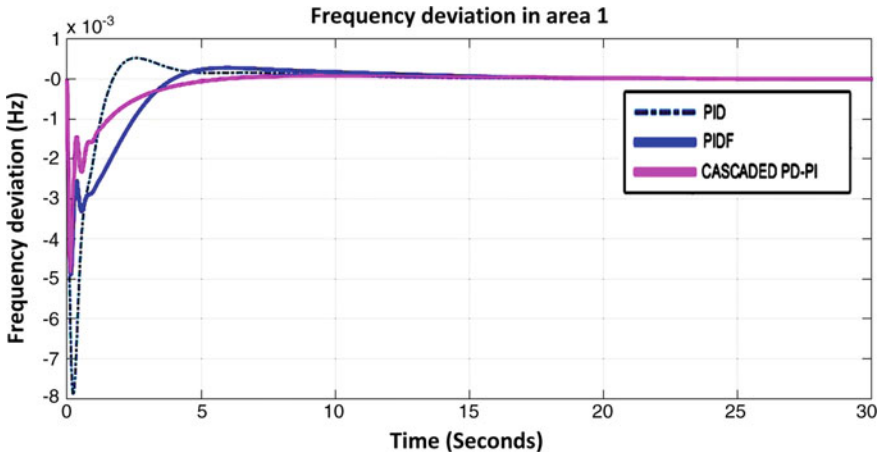

Fig. 7 Frequency deviation in area 1 without renewable energy sources for different controllers

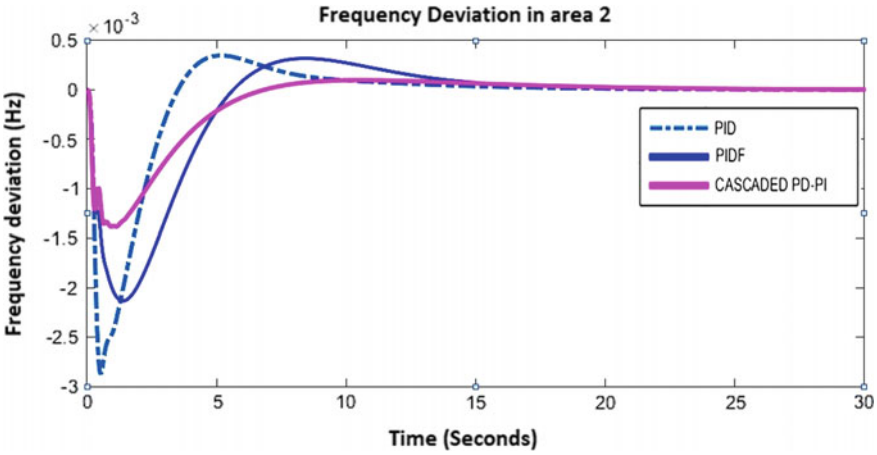

Fig. 8 Frequency Deviation in area 2 without renewable energy sources for different controllers

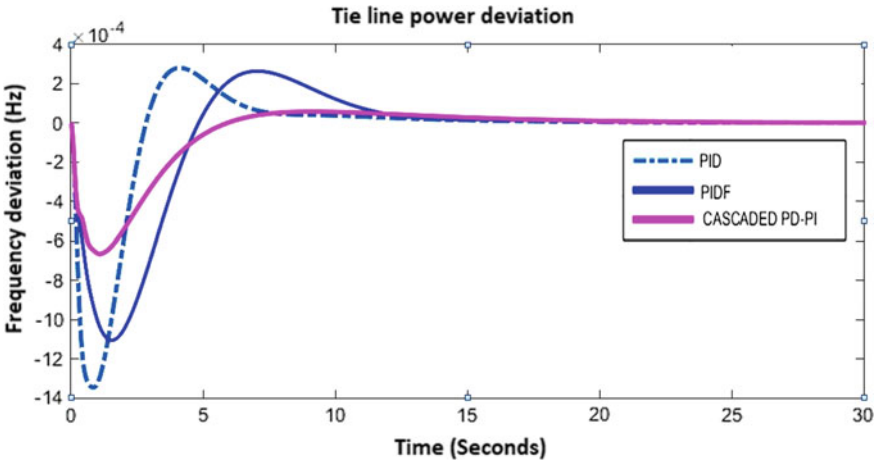

Fig. 9 Tie line power deviation without renewable energy sources

Table 4 Comparison of settling times (seconds) for without and with renewable energy sources

	Settling times (s) Without renewable energy sources		Settling times (s) With renewable energy sources	
	PIDF	PD-PI	PIDF	PD-PI
Area 1	10.8	5.79	5.6	4.3
Area 2	10.4	10.2	9.9	4.9
Tie line power	9.8	5.2	5.9	5.1

observed that settling times are improved with renewable energy sources in frequency deviations in area 1 and 2 and tie line power deviations.

6 Conclusion

Two area multi-unit power system with renewable energy sources is considered for observing the dynamic behavior of the system. Cascaded PD-PI controller gives better results over PID and PIDF controllers of deviations in frequency and the scheduled tie line powers. The overall performance of two area multi-unit interconnected power system is improved with renewable energy sources in terms of undershoot, overshoot, and settling times.

Appendix

See Tables 5, 6 and 7.

Table 5 DFIG wind turbine parameters

Parameter	Area 1	Area 2	Value
Wind turbine inertia	H_{e1}	H_{e2}	3.5
DFIG proportional controller gain	$K_{\omega p1}$	$K_{\omega p2}$	1
DFIG turbine	T_{a1}	T_{a2}	0.2
Transducer time constant	T_{r1}	T_{r2}	15
Wish out filter time constant	$T_{\omega 1}$	$T_{\omega 2}$	6
Regulation	R_1	R_2	2.4

Table 6 Renewable energy sources

Parameters	Symbol	Value (s)
Aqua electrolyzer	T_{AE}	0.2
Fuel cell	T_{FC}	4
PV	T_{PV}	1.8
Battery energy storage system	T_{BESS}	4
All gain values	K_{AE}, K_{FC}, K_{PV} and K_{BESS}	1

Table 7 Two area thermal power system data

Parameter	Symbol	Value
Frequency bias factor	B	0.4249
Governor time constant	T_{G}	0.08
Turbine time constant	T_{T}	0.3
Reheat time constant	T_{R}	10
Control area gain	K_{P}	120
Regulation	R	2.4
Synchronous time constant	T	0.0866
Reheat gain	K_{R}	0.5
Area participation factors	APF	0.33
Control area time constant	T_{P}	20

References

1. Kundur P, Balu NJ, Lauby MG (1994) Power system stability and control, vol 7. McGraw-Hill, New york (1994)
2. Kothari DP, Nagrath U (2003) Modern power system analysis. Tata McGraw-Hili, India
3. Garg K, Kaur J (2014) Particle swarm optimization based automatic generation control of two area interconnected power system. Int J Sci Res Publ 4(1)
4. Panda S, Patidar NP, Kolhe M (2016) Cascaded PD-PI controller for active power frequency control of two-area multi-units power system. In: IEEE international conference on power and renewable energy, Shanghai, China
5. Manoj Kumar D, Patel N, Ranjan Kumar M (2016) Automatic generation control of a two area multi-unit interconnected power system with proportional-integral-derivative controller with filter (PIDF) optimized by TLBO algorithm. In: International conference on circuit, power and computing technologies, pp 1–6
6. Sahu BK, Pati TK, Nayak JR, Panda S, Kar SK (2016) A novel hybrid LUS–TLBO optimized fuzzy-PID controller for load frequency control of multi-source power system. Int J Electr Power Energy Syst 74:58–69
7. Ibraheem, Nazi KR, Sharma G (2015) Study on dynamic participation of wind turbines in automatic generation control of power system, electric power components and system. Taylor and Francis, pp 44–55
8. Kaur R, Prakash S (2017) Load frequency control of hybrid power system using intelligent controllers. In: 7th International conference on recent development in engineering science, humanities and management ESHM-17, pp 227–289
9. Sahu Bk, Pati S, Panda S (2014) Hybrid differential evolution particle swarm optimisation optimised fuzzy proportional–integral derivative controller for automatic generation control of interconnected power system. IET Gener Trans Distrib (2014)
10. Debnath MK, Jena T, Mallick RK (2016) Novel PD-PID cascaded controller for automatic generation control of a multi-area interconnected power system optimized by Grey Wolf Optimization (GWO). In: 1st IEEE international conference on power electronics, intelligent control and energy systems, Delhi, India, pp 1–6
11. Nilaykumar N, Kotwal D (2016) The State space modeling of single, two and three a LFC of power system using integral control and optimal LQR control method. IOSR J Eng 2(3):501–510

Ten Bus Closed Loop Distribution System Using Sliding Mode Controlled Distributed Unified Power Quality Conditioner

S. K. Abdul Pasha and N. Prema kumar

Abstract Distributed Unified Power Quality Conditioner (DUPQC) has been identified as a good FACTS controller between feeding end and far end of distribution system. The goal of the recommended closed loop DUPQC system is to enhance the dynamic response utilizing proportional resonant (PR), hysteresis controller (HC) and sliding mode (SM) controllers. Simulink models are designed for PR, HC and SMC controlled distributed UPQC-based ten bus systems. Computer results for three different reference values are presented for PRC, HC and SMC with reactive power. The results of PRC-, HC- and SMC-based DUPQC ten bus system indicate that voltage response with SMC is exceptional to PR and HC controlled DUPQC systems. Hence, SMC is proposed for the control of closed loop distribution system (CLDS) using DUPQC. SMC makes the CLDS to track the reference voltage with minimum steady-state error and settling time.

Keywords Proportional resonant controller (PRC) · Sliding mode control (SMC) · Hysteresis controller (HC) · Ten bus distribution system (TBDS)

1 Introduction

Quality of power is the essential parameter for the two degrees of sending and circulation. It is especially fundamental to deal with the proper limits of power quality. Hingorani [1] had provided an essential idea for value benefited power. It accords the unwavering quality-stream power. Solid form of breakers, static compensators

S. K. Abdul Pasha (✉)
Department of Electrical & Electronics Engineering, Anurag Engineering College (Autonomous), Kodad 508206, India
e-mail: abdulpsh@gmail.com

N. Prema kumar
Department of Electrical Engineering, Andhra University College of Engineering (A), Andhra University, Visakhapatnam 530003, India
e-mail: premnavuri@gmail.com

G. T. C. Sekhar et al. (eds.), *Intelligent Computing in Control and Communication*, Lecture Notes in Electrical Engineering 702,
https://doi.org/10.1007/978-981-15-8439-8_36

and condensers give out premise from value-added power. Benacaiba and Ferdi [2] depicted dynamic voltage restorer, convincing value-added power device as directing potential growth and list. Additionally, it makes the strategy for voltage reclamation under the CCP & DVR. For example, the common coupling point, DVR standards, furthermore depicted concern to various strategies of voltage infusion.

Voltage restorers deal with two unequal, adjusted circumstances viably. Ucar and Ozdemir [2] suggested a PQ hypothesis likewise entitled immediate responsive hypothesis power, and some other regulated counts become recommended to 3stage-4wire and 4legparallel-dynamic-power-channel, in view of this proposition, for compensation of receptive power, symphonious flows concealments and adjusting of the heap flows towards un-immaculate supply voltage circumstances, lopsided un-straight burden. Kamran and Habetlar [3] had intended another strategy considering the pulse restrained that accosts UPQCS-inverter relationship into a single set. Entire idea had displayed using three-stage series and shunt dynamic channel which additionally utilized a full-request-prescient state onlooker.

Displaying the framework as a singular multi-input, multi-yield structure had numerous points of interest. It showed quicker powerful reaction and consistent state accuracy and subsequently giving upgraded control execution. Kwan et al. [4] proposed MPC structure in regard to UPQC. Considering Kalman proposed systems channels becomes simple to undertake and retrieve head and symphonious pieces of burden. Singh et al. [5] contemplated a technique to the restorer, for example, it has to beat issues in terms of intensity nature and control over mains voltage. Khadikar et al. [6] presented a novel strategy for UPQC.

Unfaltering state examination and scientific investigation of UPQC was given. The I&V harmonics will be reimbursed capably by means of control framework. Pal et al. [7] presented a suitable procedure for 3S-4 W-UPQC. VSI was utilized towards PAPF/SAPF and 3S-3L-VSI to acknowledge SDP channel. Das [8] suggested two control plot schemes for conditioner. Such two control plans are dependent on to the potential sort pay methodology, which are UPQC-Q & P. Sufficiency for two control models was tried [9]. Conditioner successfully exchanges reactive volt-amps among two compensators. Chandra and Khadikar [10] recommended new strategy as PAC scheme of conditioner with the goal; such arrangement was utilized to farthest point. From this idea by altering point among the source burden voltages appropriately, these parallel arrangement inverters appropriately distribute heap response.

2 Research Gap

It is required to enhance the power quality of ten bus distribution system. Hence, this work deals with the comparison responses of ten bus distribution system using PR/HC/SM controller. This work proposes SMC for the control of DUPQC. It is required to perform load flow study for closed loop DUPQC-based TBDS using PR, HC and SM controllers.

3 System Configuration

The one-line diagram of TBDS with DUPQCs is shown in Fig. 1. The DUPQCs are located near buses 5 and 8.

Block diagram of DUPQC-TBS with PR, HC and SMC is represented in Fig. 2. Potential of bus 10 will be perceived and evaluated with the ref voltage to get voltage lapse. The VL is given to PR, HC and SM controllers. The yield of PR, HC and SMC is utilized to update the pulse width.

3.1 Design of DUPQC System

The design is suggested for obtaining the values of V_1, I_1 and frequency of MOSFET. Based on output capacitor voltage, the duty ratio is analyzed by utilizing Eq. (1). Efficiency is calculated using Eq. (2).

$$V_0 = \frac{V_1}{(1-a)} \tag{1}$$

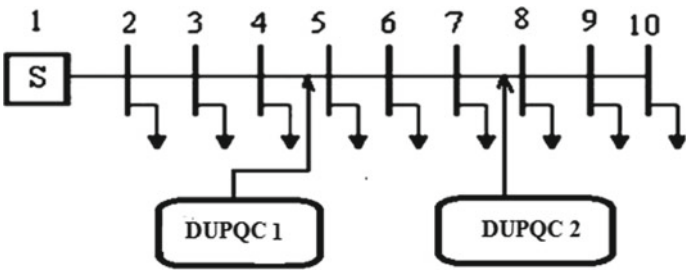

Fig. 1 One-line diagram of TBDS with DUPQCs

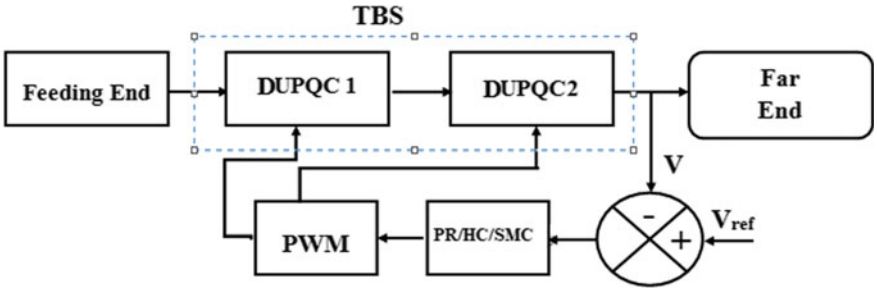

Fig. 2 Block diagram of TBS with PR, HC and SMC

Efficiency of the converter to evaluate the yield current is

$$\eta = \frac{V_a I_a}{V_1 I_a} \tag{2}$$

The values of L and C are calculated by assuming ΔI and ΔV in Eqs. 3 and 4

$$\Delta V = \frac{V_1 D}{f L} \tag{3}$$

$$\Delta I = \frac{I_a D}{f C} \tag{4}$$

Voltage to be infused is identical to IZ. The AF is planned to provide fifth harmonic. The value of C_5 is presumed, and L_5 is evaluated with formula given in (Eq. 5).

$$f_5 = \frac{1}{2\pi (L_5 C_5)^{\frac{1}{2}}} \tag{5}$$

Pulse width for switches of DVR inverter is $\frac{T_0}{2}$. Pulse width for switches of AF inverter is $\frac{T_5}{2}$.

3.2 *Slide Mode Controller*

The block diagram of slide mode controller is appeared in Fig. 3. The majority of the controllers comprise fault of one or numerous states of the structure in the sliding surface (e.g., inductor current or capacitor voltage).

Herein, the sliding surface can be symbolized as a second-order differential equation for which wide numerical study is needed to assure system steadiness. An additional surface is characterized for the recovery in the steady-state error and settling

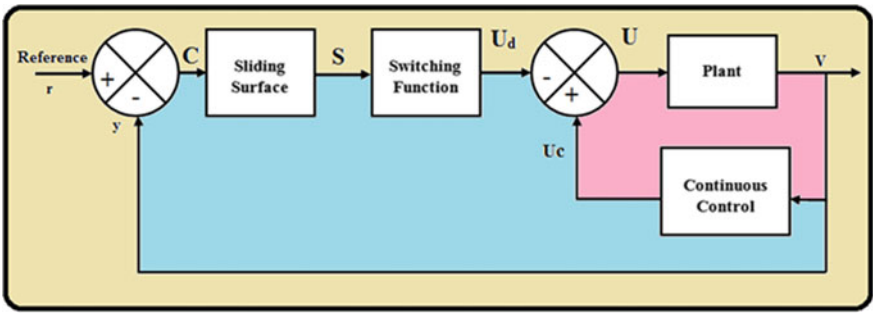

Fig. 3 "Slide mode controller" block diagram

time which comprises voltage blunder. The output of plant (Y) is the control voltage for PWM generator.

4 Results and Discussions

The simulation results of closed loop TBDS with PR, HC and SMC are presented below.

4.1 Closed Loop TBDS with PR Controller

Circuit diagram of the "closed loop TBD system" (CLTBDS) and 'PR controller' is shown in Fig. 4. Now Bus 10 voltage will be sensed and rectified by referring to 'V' for obtaining 'error of voltage'. It is directed PRC. Yield of PR is utilized for updating pulses. The RMS voltage at Bus 10 f CLTBDS with PR is shown in Fig. 5, and its value is 2900 V, and it is found to be stable. The real power at Bus 10 of CLTBDS with PR is shown in Fig. 6, and its real power value is $9.20 * 10^4$ W. Reactive power at Bus 10 of CLTBDS with PR is shown in Fig. 7, and its reactive power value is $3.1 * 10^4$ VAR.

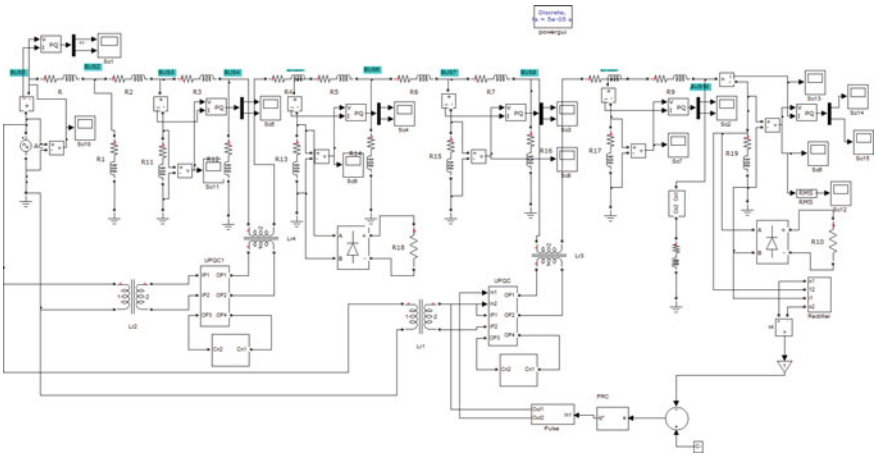

Fig. 4 Circuit diagram of CLTBDS with PR controller

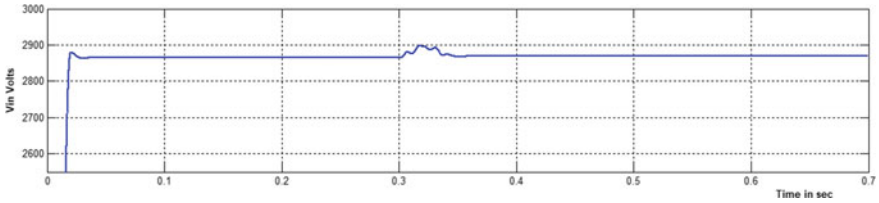

Fig. 5 RMS voltage at bus 10 of CLTBDS with PR controller

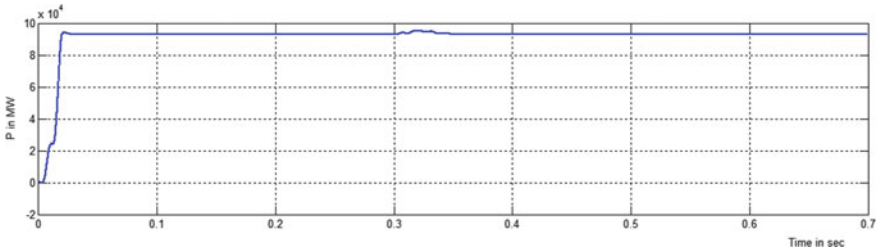

Fig. 6 Real power at bus 10 of CLTBDS with PR controller

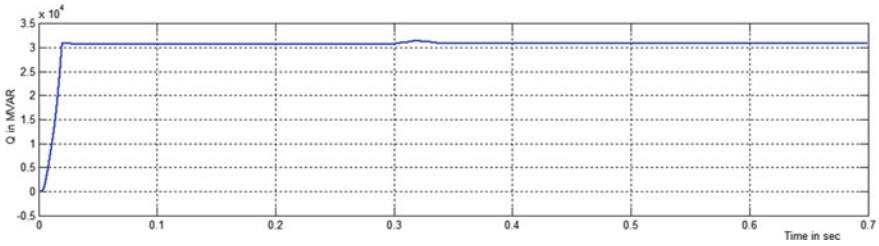

Fig. 7 Reactive power at bus 10 of CLTBDS with PR controller

4.2 Closed Loop TBDS with HC Controller

Circuit diagram of the CLTBDS with HC is located in Fig. 8. Bus 10 is sensed, rectified and matched through ref V for obtaining VE. EV is directed to HC controller. The RMS voltage at bus 10 of CLTBDS with HC controller is shown in Fig. 9, and its magnitude is 2800 V. The real power at bus 10 of CLTBDS with HC controller seems in Fig. 10, and its magnitude is $9.20 * 10^4$ W. Q at bus 10 of CLTBDS with HC controller is shown in Fig. 11, and its value is $3.1 * 10^4$ VAR.

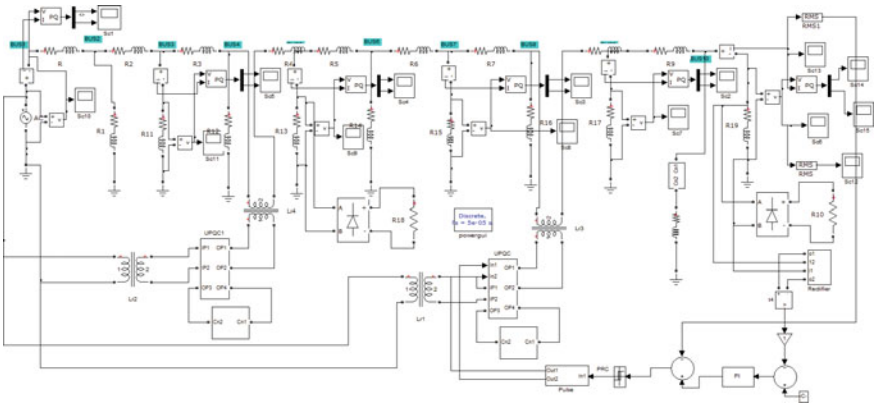

Fig. 8 Circuit diagram of the CLTBDS with HC controller

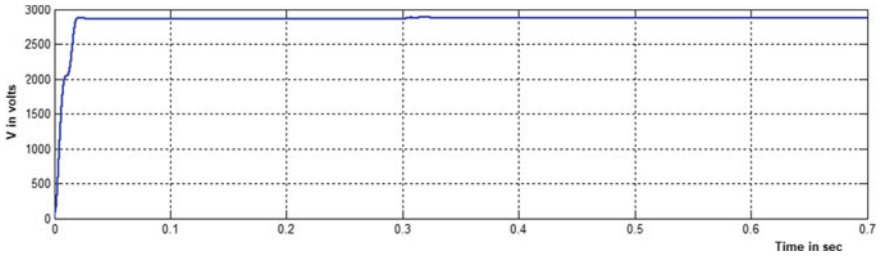

Fig. 9 RMS voltage at bus 10 of CLTBDS with HC controller

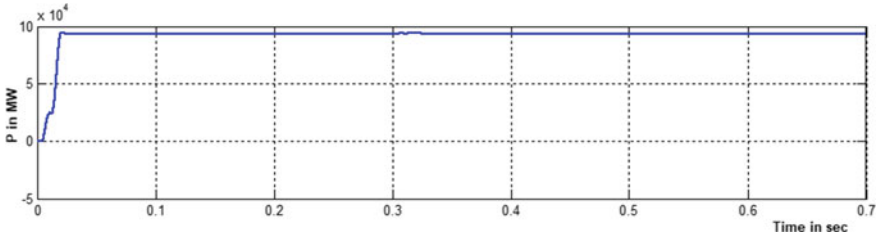

Fig. 10 Real power at bus 10 of CLTBDS with HC controller

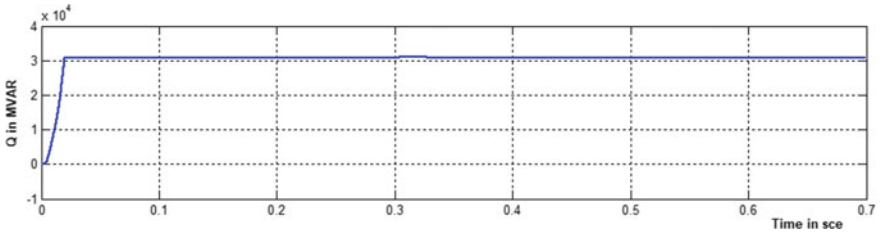

Fig. 11 Reactive power at bus 10 of CLTBDS with HC controller

4.3 Closed Loop TBDS with SM Controller

Circuit diagram of the CLTBDS with SM is located in Fig. 12. At bus 10, the voltage is sensed, rectified and summarized for V referral for obtaining EV. VE is directed at SMC. Response near SMC with ramp is compared to generate pulses required by the UPQC. The SMC acts such that the sliding surface is made zero. SMC is chosen due to non-linearity of loads at the far end. The RMS voltage at bus 10 of CLTBDS with SM controller is shown in Fig. 13, whose magnitude be 2800 V. The P of bus 10 for CLTBDS with SM controller shown in Fig. 14 ranges to 9.21 * 10^4 W. Q at bus 10 of CLTBDS with SM controller is shown in Fig. 15, and its magnitude is 3.1 * 10^4 VAR.

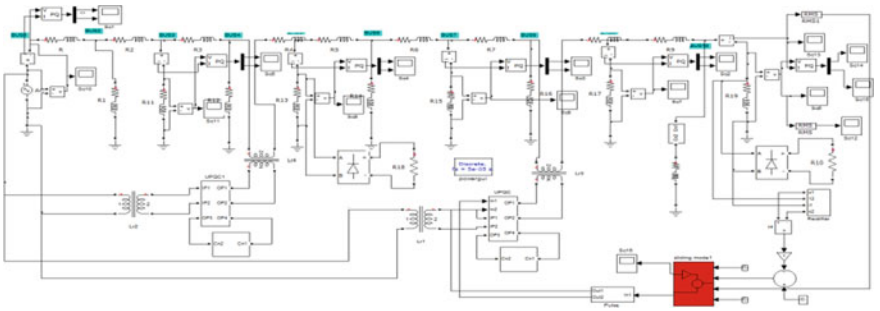

Fig. 12 Circuit diagram of the CLTBDS with SM controller

Fig. 13 RMS voltage at bus 10 of CLTBDS with SM controller

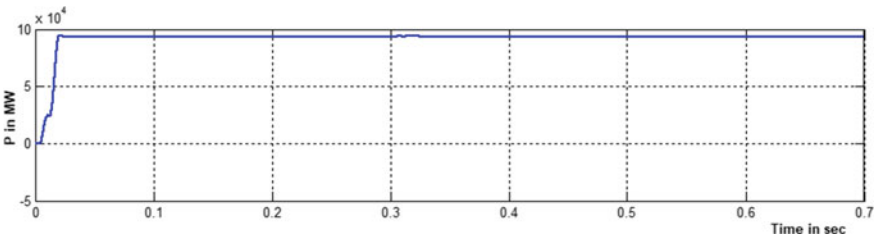

Fig. 14 Real power at bus 10 of CLTBDS with SM controller

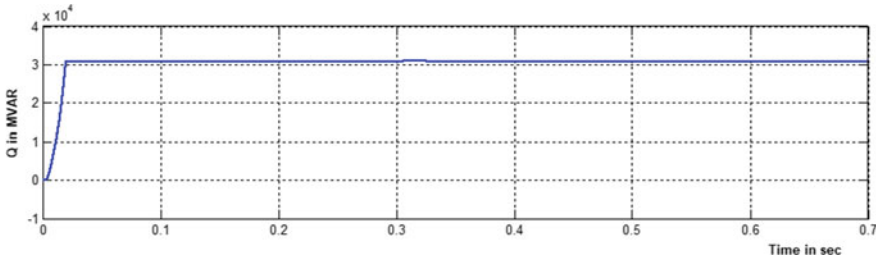

Fig. 15 Reactive power at bus 10 of CLTBDS with SM controller

Comparison of time domain parameters of CLTBDS ($V_{ref} = 3900$ V) using PR, HC and SMC is given in Table 1. By using SMC, the rise time is reduced from 0.34 to 0.32 s; peak time is reduced from 0.36 to 0.34 s; settling time is reduced from 0.37 to 0.35 s; steady-state error is reduced from 2.3 to 1.7 V.

Comparison of time domain parameters of CLTBDS ($V_{ref} = 3950$ V) using PR, HC and SMC is reflected in Table 2. Considering SMC, the time rise lowered from 00.33 to 00.31 s; time peak goes from 0.35 to 0.33 s; time settle goes from 0.36 to 0.34 s; steady-state error drops from 1.9 to 00.9 V.

Comparison of time domain parameters of CLTBDS ($V_{ref} = 4000$ V) using PR, HC and SMC strikes in Table 3. Considering SMC, the T_r is lapsed from 00.32 to 00.30 s; peak time is reduced from 0.33 to 0.32 s; time setting downs from 00.34 to 00.31 s; E_{ss} decreases from 1.80 to 00.70 V. Figure 16 delineates the bar chart comparison of real and reactive powers of PR, HC and SM controller.

Table 4 represents the analysis of PQR through PR, HC and SM controller

Table 1 Comparison of time domain parameters of CLTBDS ($V_{ref} = 3900$ V) using PR HC and SMC

Type of controller	$T_{r\,(s)}$	$T_{p\,(s)}$	$T_{s\,(s)}$	$E_{ss\,(V)}$
PR	0.34	0.36	0.37	2.3
HC	0.33	0.35	0.36	1.9
SMC	0.32	0.34	0.35	1.7

Table 2 Comparison of time domain parameters of CLTBDS ($V_{ref} = 3950$ V) using PR, HC and SMC

Type of controller	$T_{r\,(s)}$	$T_{p\,(s)}$	$T_{s\,(s)}$	$E_{ss\,(V)}$
PR	0.33	0.35	0.36	1.9
HC	0.32	0.34	0.35	1.5
SMC	0.31	0.33	0.34	0.9

Table 3 Comparison of time domain parameters of CLTBDS ($V_{ref} = 4000$ V) using PR, HC and SMC

Type of controller	$T_{r\,(s)}$	$T_{p\,(s)}$	$T_{s\,(s)}$	$E_{ss\,(V)}$
PR	0.32	0.33	0.34	1.8
HC	0.31	0.32	0.33	1.4
SMC	0.30	0.32	0.31	0.7

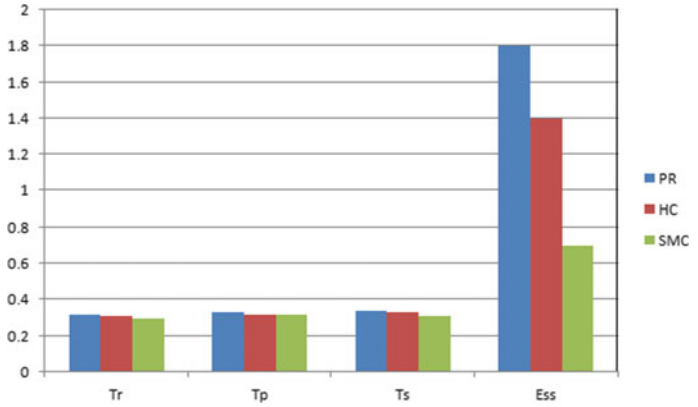

Fig. 16 Bar chart for P-Q analysis with PR, HC and SM controller

5 Conclusion

The real power and reactive powers with SMC are higher than those of PR controlled TB system. TBDS with DUPQCs is successfully designed, modeled and simulated using MATLAB Simulink. The comparison outcomes of CL-TBDS with PR, HC and SMC are presented. By using SMC, settling time is reduced to 0.34–0.31 s, and the steady-state error is low as 0.7 V. The outcome indicates that the voltage response is improved using SM controller. The results prove that the voltage of TBDS can be effectively controlled with the help of SM controller than PR/HC controller. Hence, closed loop TBDS with SMC is superior to closed loop TBDS with PR and closed loop TBDS with HC controller. The merits of CLTBDS minimized steady-state error and settling time. Drawback for DUPQC is that inverters operate at different frequencies. The contributions of the present work are as follows: Multiple DUPQCs are proposed for distribution system. SMC is proposed for TBDS to improve the dynamic response.

Table 4 Analysis for P&Q through PR, HC and SM controller

Bus No	Real power (MW)with UPQC (PRC)	Real power (MW)with UPQC (HC)	Real power (MW)with UPQC (SMC)	Reactive power(MVAR)with UPQC(PRC)	Reactive power(MVAR)with UPQC(HC)	Reactive power(MVAR)with UPQC(SMC)
Bus 1	2.253	2.254	0.254	0.896	0.896	0.898
Bus 2	1.678	1.679	1.683	0.440	0.442	0.445
Bus 3	0.489	0.491	0.496	0.238	0.239	0.243
Bus 4	0.245	0.247	0.250	0.139	0.141	0.142
Bus 5	0.199	0.201	0.204	0.068	0.069	0.071
Bus 6	0.183	0.186	0.190	0.083	0.085	0.087
Bus 7	0.166	0.170	0.173	0.068	0.070	0.072
Bus 8	0.158	0.163	0.166	0.067	0.071	0.075
Bus 9	0.148	0.150	0.152	0.058	0.062	0.069
Bus 10	0.153	0.154	0.155	0.061	0.065	0.073

References

1. Hingorani N (1995) Introducing custom power. IEEE Spectr 32(6):41–48
2. Benacaiba C, Ferdi B (2008) Voltage quality improvement using DVR. Electr Power Qual Util XIV(1):30–46
3. Ucar M, Ozdemir E (2008) Control of a 3 phase 4 leg active power filter under non ideal mains voltage condition. Electr Power Syst Res 78:58–73
4. Kamran F, Habetler TG (1995) Combined deadbeat control of a series parallel converter combination used as a universal power filter. In: Proceedings of power electronics special conference, vol 1, 196–201
5. Zhang X, Zhang W, Lv Y, Liu W, Wang Q (2010) Unified power quality conditioner with model predictive control. In: Proceedings of 5th international conference on computer science & education, pp 1239–1244
6. Singh B, Jayaprakash P, Kothari DP, Chandra A, Al Haddad K (2011) New control algorithm for capacitor supported dynamic voltage restorer. Electromagn Anal Appl 3:277–286
7. Khadkikar V, Agarwal P, Chandra A, Bany AO, Nguyen TD (2004) A simple new control technique for unified power quality conditioner (U.P.Q.C). In: IEEE international conference on harmonics and quality of power, pp 289–293
8. Pal Y, Swarup A, Singh B (2011) A control strategy based on UTT and Icosϕ theory of three phase, four wire U.P.Q.C for power quality improvement. Int J Eng Sci Technol 3(1):30–40
9. Basu M, Das S, Dubey GK (2007) Comparative evaluation of two models of U.P.Q.C for suitable interface to enhance power quality. Electric Power Syst Res 77(7):821–830
10. Khadkikar V, Chandra A, A new control philosophy for a unified power quality conditioner (U.P.Q.C) to coordinate load reactive power demand between shunt and series inverters. IEEE Trans Power Del 23(4):2522–2534

Frequency Regulation of Hybrid Power Systems with Robust Higher-Order Sliding Mode Control

L. V. Suresh Kumar, Tummala S. L. V. Ayyarao, and Tulasichandra Sekhar Gorripotu

Abstract Increased renewable energy additions and load fluctuations in the power system lead to large frequency fluctuations due to intermittent nature of renewable energy systems. The main scope of this paper is to regulate the frequency deviations in the power system by automatically controlling speed governor of thermal power plant. A nonlinear disturbance observer (NDO) has been used to find the net disturbance as well as those results of the frequency deviation are estimated with same method NDO. For controlling the system frequency of a new approach, control method is developed with higher-order sliding mode control (HOSMC). This proposed idea of frequency regulation is evaluated for single-area hybrid power system for various working methods. System output characteristics are shows the superior performance of the HOSMC for better power system operation.

Keywords Frequency regulation · Nonlinear disturbance observer · Sliding mode control · Thermal power plant

1 Introduction

With increased energy demand, change in government policies (carbon reduction), increased revenue resulted in renewable energy additions in power systems. In US, the wind energy additions are raised up to 8.6 GW in 2015 [1]. According to Navigant

L. V. Suresh Kumar · T. S. L. V. Ayyarao
Department of Electrical & Eletronics Engineering, GMR Institute of Technology, Rajam, Andhra Pradesh 532127, India
e-mail: lvenkatasureshkumar@gmail.com

T. S. L. V. Ayyarao
e-mail: ayyarao.tslv@gmrit.edu.in

T. S. Gorripotu (✉)
Department of Electrical & Eletronics Engineering, Sri Sivani College of Engineering, Chilakapalem, Srikakulam, Andhra Pradesh 532410, India
e-mail: gtchsekhar@gmail.com; gtchsekhar@srisivani.com

G. T. C. Sekhar et al. (eds.), *Intelligent Computing in Control and Communication*, Lecture Notes in Electrical Engineering 702,
https://doi.org/10.1007/978-981-15-8439-8_37

Research, the predicted mounted capacity of the mini, small, micro, and medium wind turbines will surge to 446 MW in the year 2026 [2]. As the renewable energy systems are highly intermittent in nature, the gap between energy demand and supply fluctuates with time, and thus, these energy additions leads to large frequency deviations in power grid [3].

In practical power systems, frequency is regulated by controlling the speed governor of thermal power plant. This automatic generation control is achieved by employing linear controllers like PI, PID, etc. As parameters of PID control greatly affect the stability as well as system performance, several tuning methods are proposed in the literature. These tuning methods include conventional methods like Ziegler–Nichols, Tyreus–Luyben, etc., and several other advanced optimization algorithms [4–9]. A combination of PID controller and low-pass filter is developed for robust frequency control in the region [10]. Even though PID control is simple and industry adopted, these controllers are not robust to uncertainties and disturbances. Robust control methods like sliding mode control, model predictive control, H_∞ control, active disturbance rejection control, adaptive learning method, etc., are proposed in the literature for handling the uncertainties [11–17]. One of the major drawbacks of modern robust controllers is the design in complexity.

In the control methods, the sliding mode method is another powerful control technique to compensate the disturbances on the system. Sliding mode methods are applied to power systems which was initiated in early 1980s [18]. Sliding based method used frequency control of multi-machine power systems is proposed in [19–22]. The nominal behavior of the controller method is dominated by greater disturbance rejection. The controller performance can be superior by estimating the suffering conditions and compensate by using a control law [22–24]. This novel idea of disturbance observer-based frequency regulation is proposed in [25]. But the major drawback with sliding mode method is suffers with chattering. Another issue with sliding mode method is that the regulation of high frequency signal may not be practically realizable. The above drawbacks of sliding mode method can be minimized exhausting a higher-order sliding mode regulator [26–31]. Another major hurdle in the design of HOSMC is compensating the mismatched disturbance.

In this paper, a novel method for frequency regulation to the hybrid power systems using HOSMC is proposed. The occurring disturbance, which will affect the system output, is estimated by using NDO. This estimated disturbance is used to derive the sliding variables [23]. A higher-order robust sliding mode regulator law depends on the sliding variables which is developed to compensate the disturbances on the output frequency.

In this paper, the remaining sections are ordered as following: power system small signal circuit is given in Sect. 2. The novel method of HOSMC with NDO is accessible in Sect. 3. Outlines of the frequency regulation by means of the novel method given in Sect. 4. The enactment of the modified frequency regulation to single-area hybrid power systems are evaluated with simulation results are given in Sect. 5. The conclusions are given for proposed method in the final section.

2 Small Signal Model of Hybrid Power System

Power system is a distributed system that consists of generating stations, transformers, transmission lines, etc., and the dynamics are highly nonlinear in nature. For regulating the frequency, the system dynamics should always move around the fixed operating point. The small signal model of power system with wind integration is given in this section.

2.1 Dynamics of Thermal Power Plant

The thermal power system dynamics are represented as follows in Eqs. (1)–(3)

$$\Delta \dot{f}(t) = -\frac{1}{T_{\mathrm{P}}}\Delta f(t) + \frac{K_{\mathrm{P}}}{T_{\mathrm{P}}}\Delta P_g(t) - \frac{K_{\mathrm{P}}}{T_{\mathrm{P}}}\Delta P_{\mathrm{d}}(t) + \frac{K_{\mathrm{P}}}{T_{\mathrm{P}}}\Delta P_{\mathrm{w}}(t) \tag{1}$$

$$\Delta \dot{P}_{\mathrm{g}}(t) = -\frac{1}{T_{\mathrm{T}}}\Delta P_{\mathrm{g}}(t) + \frac{1}{T_{\mathrm{T}}}\Delta X_{\mathrm{g}}(t) \tag{2}$$

$$\Delta \dot{X}_{\mathrm{g}}(t) = -\frac{1}{RT_{\mathrm{G}}}\Delta f(t) - \frac{1}{T_{\mathrm{G}}}\Delta X_{\mathrm{g}}(t) - \frac{1}{T_{\mathrm{G}}}u(t) \tag{3}$$

where

Δf is the variation of the frequency;
ΔP_{g} is the variation of the generator output power;
ΔP_{d} is the variation of the load demand;
ΔP_{w} is the variation of input wind power;
K_{P} is gain of the power system;
T_{P} is time constant of the power system;
K_{T} is time constant of the turbine;
ΔX_{g} is position of governor valve change;
T_{G} is time constant of the governor;
R is regulation coefficient of the speed;
u is input of the control.

In this system, lumped parameter variations and renewable energy changes are treated as a lumped disturbance on the system.

The Eq. (1) can be modified as Eq. (4)

$$\Delta \dot{f}(t) = -\frac{1}{T_{\mathrm{P}}}\Delta f(t) + \frac{K_{\mathrm{P}}}{T_{\mathrm{P}}}\Delta P_{\mathrm{g}}(t) + d \tag{4}$$

where

$$d = -\frac{K_P}{T_P}\Delta P_d(t) + \frac{K_P}{T_P}\Delta P_w(t) \tag{5}$$

The Eq. (5) represents the lumped disturbance on the system.

2.2 Wind Turbine Model

The output power of wind turbine $P_T$is a function of wind speed v_w and is given in Eq. (6)

$$P_T = \frac{1}{2}\sigma A v_w^3 c_p(\lambda, \beta) \tag{6}$$

where

σ is the air density;
A is the area swept by the turbines;
c_p is the Performance coefficient of the turbine;
λ is tip speed ratio
β is the pitch angle.

The wind turbine output changes with change in environmental conditions (Fig. 1).

3 Proposed Method

The small signal model of hybrid power systems is represented in the state space model as Eqs. (7) and (8)

$$\dot{x} = Ax + B_u u + B_d d \tag{7}$$

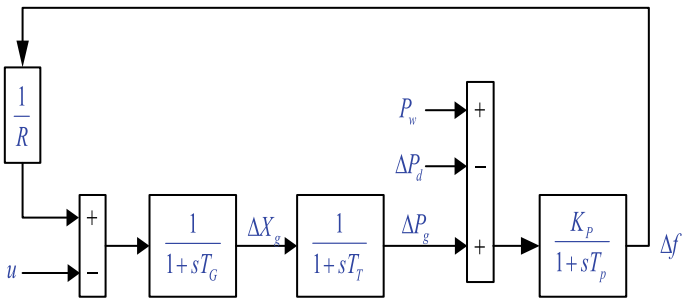

Fig. 1 Small signal model of power systems

Fig. 2 Proposed HOSMC

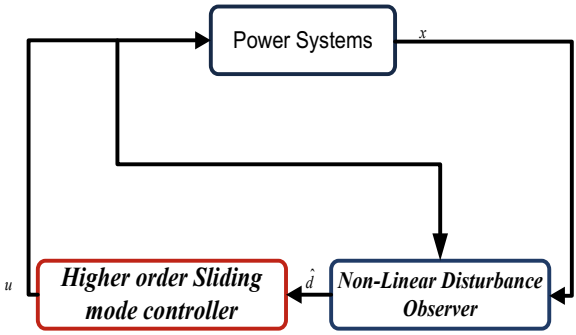

$$y = Cx \tag{8}$$

where $x \in R_n$ is the state vector, $u \in R$ is the control vector, d is the disturbance on the system, and y is the output of the system. This disturbance is mismatched type as the control and disturbance does not appear in the same channel, i.e., $B_\mathrm{u} \neq B_\mathrm{d}$.

The objective of the proposed method is to compensate the effect of the disturbance on the output of the system. The following assumptions are considered during the design.

Assumptions The pair (A, B) is controllable. All the states of the system are measurable. The system was bounded with disturbance. i.e., $\|d\| \leq \chi$. Here, χ value is a positive.

The proposed method includes two steps: First step deals with design of nonlinear disturbance observer for estimating the disturbance, and second one deals with the design of HOSMC, and this is depicted as shown in Fig. 2.

3.1 Nonlinear Disturbance Observer Design

The disturbance on the system can be estimated in several methods like NDO, extended state disturbance observer, perturbation observer, etc. Refer this paper for more information on disturbance observer-based control [32]. In this paper, the net disturbance on the system is estimated using NDO [23, 33]. To estimate the net disturbance $\hat{d}$ on the system, a virtual state β is considered during the design process whose dynamics are given in Eq. (9).

$$\dot{\beta} = -GB_\mathrm{d}\hat{d} - G(Ax + B_\mathrm{u}u) \tag{9}$$

$$\hat{d} = \beta + Gx \tag{10}$$

Taking the derivative of Eq. (10)

$$\dot{\hat{d}} = -GB_{\mathrm{d}}(\hat{d} - d)$$

If $GB_{\mathrm{d}} > 0$, then $\lim_{t \to \infty} (d - \hat{d}) = 0$.
Thus, the stability of the NDO can be proved.

3.2 *Higher-Order Sliding Mode Control*

Compensating the matched disturbances is simple. By including the estimated disturbance in the control law, the matched disturbances can be suppressed. But compensating the unmatched disturbances is little bit difficult. As the main objective of this paper is load frequency regulate of the hybrid power system, Δf is selected as the sliding variable s. The control law for HOSMC depends on the relative degree of the system. Similarly, in order to find the relative degree of the system, differentiate sliding variable consecutively until the control appears in the equation.

As a first step, transform the system represented in Eq. (6) to controllable canonical form using the transformation matrix as shown in Eq. (11),

$$T_{\mathrm{c}} = \begin{bmatrix} C & CA & CA^2 \end{bmatrix}^{\mathrm{T}} \tag{11}$$

This transformation modifies the system into a new state model given by Eq. (12)

$$\dot{\xi} = A_{\mathrm{C}}\xi + B_{\mathrm{C}}u + \theta \tag{12}$$

where

$$\xi = T_{\mathrm{c}}x;\ A_{\mathrm{C}} = T_{\mathrm{c}}AT_{\mathrm{c}}^{-1};\ B_{\mathrm{C}} = T_{\mathrm{c}}B_{\mathrm{u}};\ \theta = T_{\mathrm{c}}B_{\mathrm{d}}$$

The new state vector for the design of controller is represented as shown in Eq. (13)

$$\xi = \begin{bmatrix} \xi_1 & \xi_2 & \xi_3 \end{bmatrix}^{T} \tag{13}$$

, and the system dynamics are modified as Eqs. (14)–(16)

$$\dot{\xi}_1 = \xi_2 + \theta_1 \tag{14}$$

$$\dot{\xi}_2 = \xi_3 + \theta_2 \tag{15}$$

$$\dot{\xi}_3 = f(\xi) + bu + \theta_3 \tag{16}$$

Now, the sliding mode variables are chosen as provided in Eqs. (17)–(20)

$$s = \xi_1 \tag{17}$$

$$\dot{s} = \xi_2 + \theta_1 \tag{18}$$

$$\ddot{s} = \xi_3 + \theta_2 \tag{19}$$

$$\dddot{s} = f(\xi) + bu \tag{20}$$

Thus, the absolute degree of the power system is three as the control appears in the third derivative of s.

A quasi higher-order sliding mode control law is designed for compensating the mismatched disturbances on the output. The control input is a function of sliding mode variables as given in Eq. (21).

$$u = \psi(s, \dot{s}, \ddot{s}) \tag{21}$$

The control is chosen as [30]

$$u = \alpha \frac{\ddot{s} + 2\gamma^{3/2}\left(|\dot{s}| + \gamma|s|^{2/3}\right)^{-1/2}\left(\dot{s} + \gamma|s|^{2/3}\text{sign}(s)\right)}{|\ddot{s}| + 2\gamma^{3/2}\left(|\dot{s}| + \gamma|s|^{2/3}\right)^{1/2}} \tag{22}$$

In Eq. (22), γ and α are the design parameters. Large α value results in large control effort, but a small α may worsen the settling time. Thus, α value is selected to trade-off between control effort and performance. Parameter γ decides the rate of convergence. The parameter selection for the proposed hybrid power system is explained in Sect. 5. Stability of higher-order sliding mode control is already established in the literature.

4 Frequency Regulation Using the Proposed Method

The hybrid power system is represent in generalized state space model in given Eq. (7), and let the state vector is selected as Eq. (23)

$$x = \begin{bmatrix} \Delta f & \Delta P_g & \Delta X_g \end{bmatrix}^T \tag{23}$$

and the matrices are computed as

$$A = \begin{bmatrix} -\frac{1}{T_P} & \frac{K_P}{T_P} & 0 \\ 0 & -\frac{1}{T_T} & \frac{1}{T_T} \\ -\frac{1}{RT_G} & 0 & -\frac{1}{T_G} \end{bmatrix}; B_u = \begin{bmatrix} 0 & 0 & -\frac{1}{T_G} \end{bmatrix}^T; C = \begin{bmatrix} 1 & 0 & 0 \end{bmatrix}$$

These matrices are useful in design of NDO and HOSMC.

4.1 Design of Disturbance Observer

The demand mismatch is considered as a net disturbance on the system. This mismatched disturbance is estimated using NDO.

4.2 Design of HOSMC

From Eqs. (14)-(16), the unknown disturbances $\theta_1, \theta_2, \theta_3$ are function of net disturbance d. These are calculated from the estimated disturbance $\hat{d}$. As sliding variables are the function of these disturbances, estimated disturbance and state variables are used for obtaining the sliding variables. When compared to higher-order differentiator for estimating the disturbances, this is a simplified method. These sliding variables are useful for deriving the control law Eq. (22).

5 Simulation Results and Discussion

The proposed method is applied on single-area hybrid power system. The system parameters for hybrid energy systems are referred from [25]. The proposed method of HOSMC is simulated in MATLAB using ode4 solver with a sampling time of 10^{-3} s. HOSMC with NDO is implemented using embedded MATLAB function. The proposed method is evaluated for two different cases

1. **Case-1: Sudden change in load**

The design parameter for NDO is selected as $G = (4 \quad 0 \quad 1)$.

To assess the performance of the developed method, the load on the hybrid power system is suddenly improved by 0.1 p.u. The NDO evaluate the net disturbance on the system as shown in Fig. 3,and it clearly shows that estimated disturbance tracks the true value with in 0.1 s.

The performance of HOSMC largely depends on the design parameters. The performance of the controller is verified with different α values, and this is shown in Figs. 4 and 5. System performance with different γ values is shown in Fig. 6. It is observed that for $\alpha = 0.5$, the peak overshoot of $|\Delta f|$ is more when compared to $\alpha = 1, 1.5$. But for $\alpha = 1.5$, the control effort is more. Thus, the value of α is chosen as 1.

Convergence of HOSMC is slow with low values of γ. Even the convergence of the system is almost similar for $\gamma = 3$ and 4, but the control effort is high with $\gamma =$

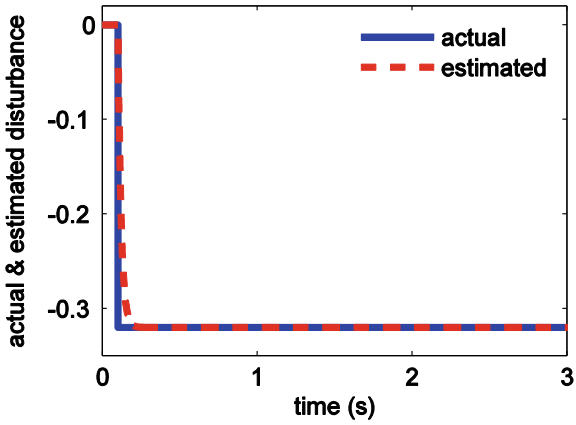

Fig. 3 Actual disturbance and estimated disturbance

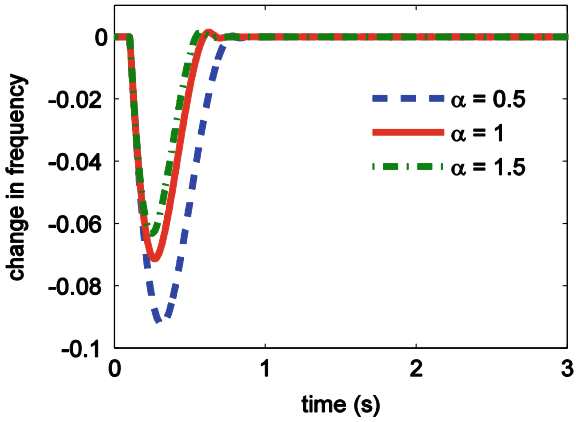

Fig. 4 Change in frequency for different values of α

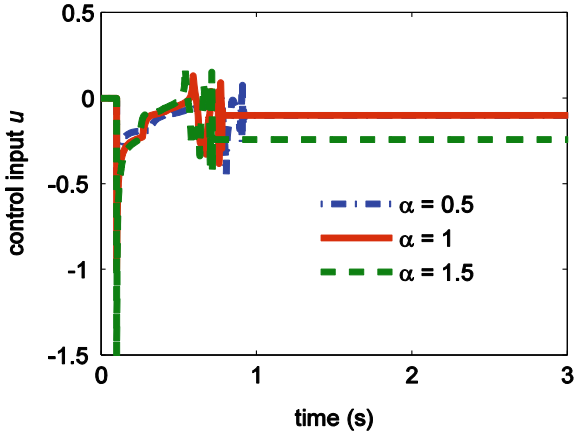

Fig. 5 Control input with change in α

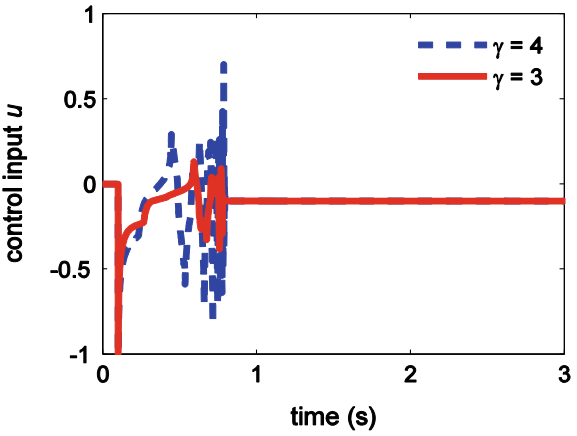

Fig. 6 Control input for different values of γ

4. Thus, the optimum value γ is chosen as 3. Another alternate method of choosing the parameters is minimizing the objective function as depicted in Eq. (24).

$$F = \int \left(\Delta f^2 + u^2\right) \mathrm{d}\tau \tag{24}$$

Sliding variables are shown in Fig. 7, and it can be observed that these variables reach zero after the disturbances.

2. **Case-2**

The performance of the above system is tested for variable wind conditions. To reflect the practical conditions, the wind speed is modeled as a random number with mean

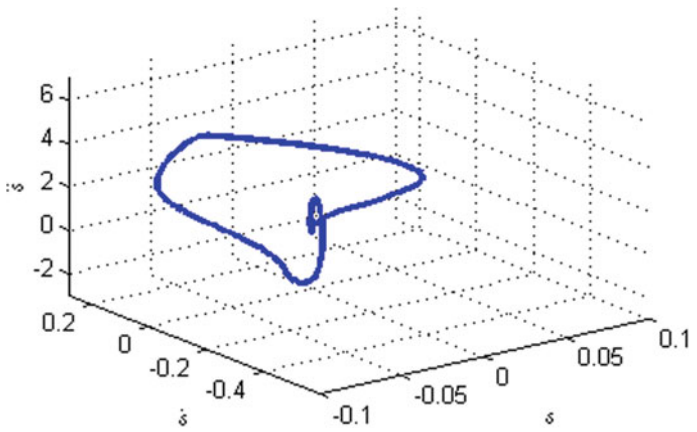

Fig. 7 Sliding variables

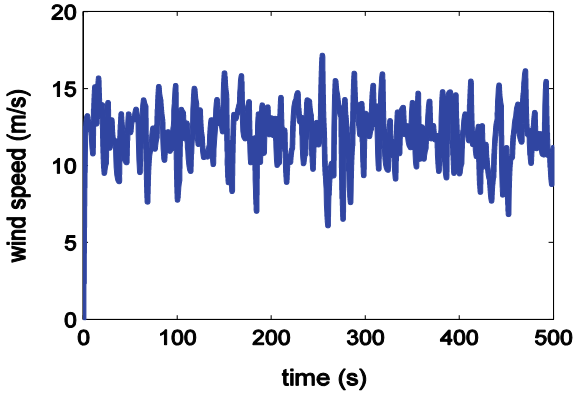

Fig. 8 Wind speed in m/s

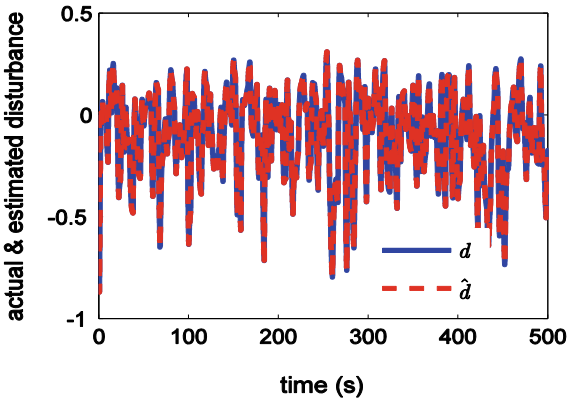

Fig. 9 Actual disturbance and estimated disturbance in case-2

value of 12 m/s and variance of 6 m/s in MATLAB. The wind speed variations are shown in Fig. 8.

The complete simulation results are given in Figs. 9 and 10

6 Conclusion

This paper proposed a robust HOSMC based on the estimates of NDO and also addressed the wide frequency deviations in power system. The nonlinear disturbance observer estimates the net disturbance on the system, and these estimates along with system states are useful in design of sliding variables. A suitable higher-order control law that tracks the system frequency to the desired value is designed based on the sliding variables. This proposed method is evaluated on a hybrid power system model under two different operating conditions. The simulation results show the robustness of the proposed approach even under large wind power deviations. The

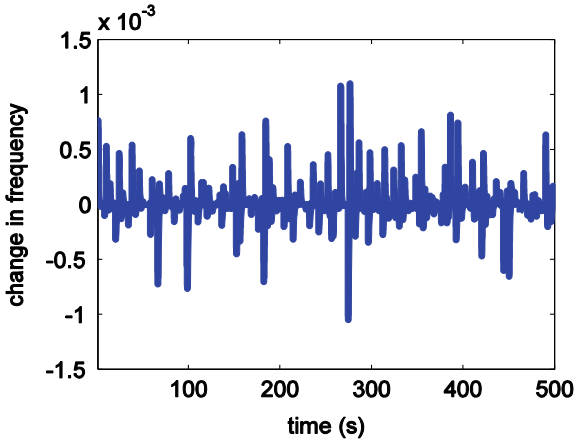

Fig. 10 Change in frequency for case-2

proposed method can be extended to large-scale power systems with high penetration of wind energy.

References

1. Wiser R, L.B.N.L., Bolinger M, L.B.N.L.W (2016) 2015 Wind technologies market report
2. Wilson A, Broehl J (2017) Executive summary : market data : small and medium wind turbines demand drivers, market trends and challenges, and global market forecasts
3. Tummala A, Bharani Chandra KP, Pulipaka VRR (2017) A decentralised nonlinear SDRE observer-controller scheme for large scale power systems. IET Gener. Trans. Distrib. https://doi.org/10.1049/iet-gtd.2017.0691
4. Sahu RK, Panda S, Padhan S (2015) A hybrid firefly algorithm and pattern search technique for automatic generation control of multi area power systems. Int J Electr Power Energy Syst 64:9–23. https://doi.org/10.1016/j.ijepes.2014.07.013
5. Ali ES, Abd-Elazim SM (2011) Bacteria foraging optimization algorithm based load frequency controller for interconnected power system. Int J Electr Power Energy Syst 33:633–638. https://doi.org/10.1016/j.ijepes.2010.12.022
6. Gozde H, Taplamacioglu MC (2011) Automatic generation control application with craziness based particle swarm optimization in a thermal power system. Int J Electr Power Energy Syst 33:8–16. https://doi.org/10.1016/j.ijepes.2010.08.010
7. Panda S, Mohanty B, Hota PK (2013) Hybrid BFOA–PSO algorithm for automatic generation control of linear and nonlinear interconnected power systems. Appl Soft Comput 13:4718–4730. https://doi.org/10.1016/j.asoc.2013.07.021
8. Pilla R, Tummala AS, Chintala MR (2016) Tuning of extended Kalman filter using self-adaptive differential evolution algorithm for sensorless permanent magnet synchronous motor drive. Int J Eng Trans A Basics 29. https://doi.org/10.5829/idosi.ije.2016.29.11b.00.
9. Suresh Kumar LV, Nagesh Kumar GV, Madichetty S (2017) Pattern search algorithm based automatic online parameter estimation for AGC with effects of wind power. Int J Electr Power Energy Syst 84:135–142. https://doi.org/10.1016/j.ijepes.2016.05.009
10. Shabani H, Vahidi B, Ebrahimpour M (2013) A robust PID controller based on imperialist competitive algorithm for load-frequency control of power systems. ISA Trans. 52:88–95. https://doi.org/10.1016/j.isatra.2012.09.008

11. Chuang N (2016) Robust H_∞ load-frequency control in interconnected power systems. IET Control Theory Appl. 10:67–75. https://doi.org/10.1049/iet-cta.2015.0412
12. Zheng Y, Zhou J, Xu Y, Zhang Y, Qian Z (2017) A distributed model predictive control based load frequency control scheme for multi-area interconnected power system using discrete-time Laguerre functions. ISA Trans. https://doi.org/10.1016/j.isatra.2017.03.009
13. Liu F, Li Y, Cao Y, She J, Wu M (2016) A two-layer active disturbance rejection controller design for load frequency control of interconnected power system. IEEE Trans Power Syst. 31:3320–3321. https://doi.org/10.1109/TPWRS.2015.2480005
14. Cai L, He Z, Hu H (2017) A new load frequency control method of multi-area power system via the viewpoints of Port-Hamiltonian system and cascade system. IEEE Trans. Power Syst. 32:1689–1700. https://doi.org/10.1109/TPWRS.2016.2605007
15. Mu C, Tang Y, He H (2017) Improved sliding mode design for load frequency control of power system integrated an adaptive learning strategy. IEEE Trans Ind Electron 0046:1–1. https://doi.org/10.1109/TIE.2017.2694396
16. Dong L, Tang Y, He H, Sun C (2017) An event-triggered approach for load frequency control with supplementary ADP. IEEE Trans Power Syst 32:581–589. https://doi.org/10.1109/TPWRS.2016.2537984
17. Benysek G, Bojarski J, Smolenski R, Jarnut M, Werminski S (2016) Application of stochastic decentralized active demand response (DADR) System For Load Frequency Control. IEEE Trans Smart Grid 3053:1–1. https://doi.org/10.1109/TSG.2016.2574891
18. Bengiamin NN, W.C. (1992) Variable structure control of, electric power generation. IEEE Trans Power Syst 2:376–380
19. Huerta H, Loukianov AG, Cañedo JM (2010) Decentralized sliding mode block control of multimachine power systems. Int J Electr Power Energy Syst 32:1–11. https://doi.org/10.1016/j.ijepes.2009.06.016
20. Vrdoljak K, Perić N, Petrović I (2010) Sliding mode based load-frequency control in power systems. Electr Power Syst Res 80:514–527. https://doi.org/10.1016/j.epsr.2009.10.026
21. Mi Y, Fu Y, Wang C, Wang P (2013) Decentralized sliding mode load frequency control for multi-area power systems. IEEE Trans Power Syst 28:4301–4309. https://doi.org/10.1109/TPWRS.2013.2277131
22. Tummala ASLV, Inapakurthi R, Ramanarao PV (2018) Observer based sliding mode frequency control for multi-machine power systems with high renewable energy. J Mod Power Syst Clean Energy. https://doi.org/10.1007/s40565-017-0363-3
23. Yang J, Li S, Yu X (2013) Sliding-mode control for systems with mismatched uncertainties via a disturbance observer. IEEE Trans Ind Electron 60:160–169. https://doi.org/10.1109/TIE.2012.2183841
24. Yang J, Su J, Li S, Yu X (2014) High-order mismatched disturbance compensation for motion control systems via a continuous dynamic sliding-mode approach. IEEE Trans Ind Inf 10:604–614. https://doi.org/10.1109/TII.2013.2279232
25. Mi Y, Fu Y, Li D, Wang C, Loh PC, Wang P (2016) The sliding mode load frequency control for hybrid power system based on disturbance observer. Int J Electr Power Energy Syst 74:446–452. https://doi.org/10.1016/j.ijepes.2015.07.014
26. Tummala ASLV, Alluri HKR, Ramanarao PV (2018) Optimal control of DFIG wind energy system in multi-machine power system using advanced differential evolution. IETE J Res 1–12 (2018) https://doi.org/10.1080/03772063.2018.1466732
27. Ayyarao TSLV (2019) Modified vector controlled DFIG wind energy system based on barrier function adaptive sliding mode control. Prot Control Mod Power Syst 4:4. https://doi.org/10.1186/s41601-019-0119-3
28. Levant A (2003) Higher-order sliding modes, differentiation and output-feedback control. Int J Control 76:924–941. https://doi.org/10.1080/0020717031000099029
29. Ding S, Levant A, Li S (2016) Simple homogeneous sliding-mode controller. Automatica 67:22–32. https://doi.org/10.1016/j.automatica.2016.01.017
30. Shtessel Y, Edwards C, Fridman L, Levant A (2014) Sliding mode control and observation. Springer, New York, New York, NY. https://doi.org/10.1007/978-0-8176-4893-0

31. Ding S, Li S (2017) Second-order sliding mode controller design subject to mismatched term. Automatica 77:388–392. https://doi.org/10.1016/j.automatica.2016.07.038
32. Chen W-H, Yang J, Guo L, Li S (2016) Disturbance-observer-based control and related methods—An overview. IEEE Trans. Ind. Electron. 63:1083–1095. https://doi.org/10.1109/TIE.2015.2478397
33. Li SH, Sun HB, Yang J, Yu XH (2015) Continuous finite-time output regulation for disturbed systems under mismatching condition. IEEE Trans Autom Contr 60:277–282. https://doi.org/10.1109/Tac.2014.2324212

Diabetic Retinopathy Detection at Early Stage Using a Set of Morphological Operations

N. Ramakrishna and Vinayadatt V. Kohir

Abstract Diabetic retinopathy is one of the major causes of blindness in the world. The computer-based approaches play a vital role in early detection and diagnosis to avoid future complications and loss of vision. This paper discusses techniques to localize microaneurysms and exudates, the early signs of the disease. The retina fundus images are pre-processed to eliminate blood vessels and optic disk to detect lesions present in the retina. A set of morphological operations are carried out, to identify microaneurysms and exudates. The results are compared with ground truth images. The proposed work achieved an average sensitivity of 85.68% for exudate detection and 96.41% for microaneurysms detection.

Keywords Diabetic retinopathy · Exudates · Microaneurysms

1 Introduction

Diabetic retinopathy (DR) is observed in diabetic patients and is one of the significant reasons for visual deficiency among individuals [1]. DR is a progressive disease that occurs due to retinal blood vessel damages. Ophthalmologists concur that early discovery and treatment are the best solutions for this disease. Hence, to prevent vision loss due to DR, the people with diabetics must go through regular checkups. If not appropriately treated, it leads to loss of vision. We propose an easy and early detection computer-based diagnostics aid to reduce the load on ophthalmologists in mass screening of DR disease. DR is classified into two stages as non-proliferative DR (NPDR) and proliferative DR (PDR) [2]. Figure 1 shows a healthy retina image. Figure 2 shows images of NPDR and PDR retina. Further, NPDRs can be classified

N. Ramakrishna
Department of ETE, GNITS, Hyderabad 500104, India
e-mail: ramakn@gmail.com

V. V. Kohir (✉)
Department of E&CE, PDACE, Kalaburagi 585102, India
e-mail: vvkohir@yahoo.com

G. T. C. Sekhar et al. (eds.), *Intelligent Computing in Control and Communication*,
Lecture Notes in Electrical Engineering 702,
https://doi.org/10.1007/978-981-15-8439-8_38

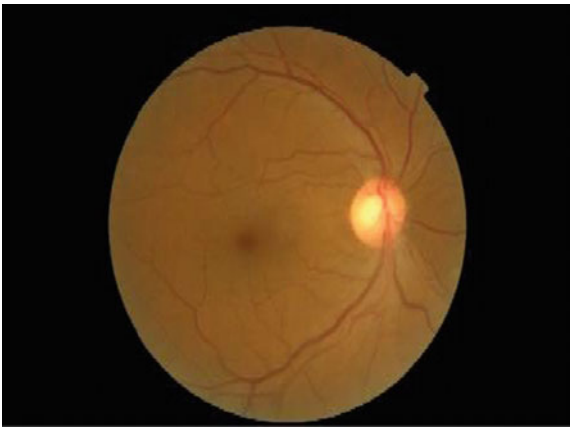

Fig. 1 Healthy retina image

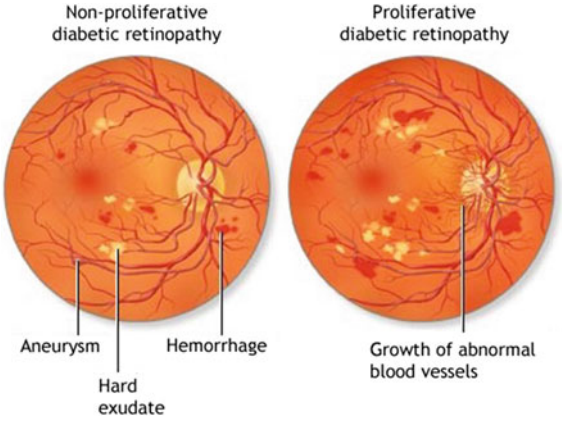

Fig. 2 Signs of DR image

into mild, moderate and severe NPDR. In mild NPDR, blood vessels swell in the retina and result in blood leakages. The small red dots, microaneurysms (MAs), are the first clinical signs of DR. The MAs show up as disconnected small groups of red spots. The size of the MAs ranges from 10 to 100 microns. The disease in the mild stage may not lead to vision loss, but as DR progresses, the hemorrhages are formed due to rapture of MAs in the retina and exudates are observed as small yellowish lipid deposits in the retina. This stage of the disease is known as a moderate stage. Table 1 shows the different stages of DR and their corresponding signs.

The proposed work aims to detect MAs and exudates. The MAs are detected by eliminating blood vessels. To detect the exudates, first optic disk is removed from a retina image and a set of morphological operations and filtering techniques are performed. This paper is organized into five sections: In Sect. 1, the introduction of the proposed work is discussed. In Sect. 2, the literature survey on DR detection is

Table 1 Different stages of DR

S. No.	Diabetic retinopathy stage	Signs
1	Mild NPDR	Few microaneurysms
2	Moderate NPDR	The number of microaneurysms increases. Hemorrhages and exudates are appears
3	Severe NPDR	Blood vessels are blocked, and cotton wool spots will appear
4	PDR	Growth of new, abnormal and fragile blood vessels

presented. The methodology of the proposed work is discussed in Sect. 3. The results are discussed in Sect. 4 followed by Sect. 5 of conclusions.

2 Literature Review

Eadgahi and Pourreza [3] propose segmentation of exudates using morphological procedures. The optic disk and the blood vessels are eliminated from the image to get exudates. Zhang et al. [4] used a framework of automatic exudate detection using mathematical morphology, top hat and bottom hat transform along with random forest algorithm. Shahin et al. [5] also use morphology techniques to detect blood vessels, exudates and MAs. The area of blood vessels, exudates and MAs is calculated. Usman Akram et al. [6] implemented a process that finds MAs in the retinal image. A vector is prepared using shape, color and intensity properties and is fed to a hybrid classifier consisting of the Gaussian mixture model (GMM) and support vector machine (SVM). Sehirli et al. [7] described a fast and efficient prototype for MA detection based on pixel classification and connected component analysis. Sopharak et al. [8, 9] presented the detection of both MAs and exudates using morphological operators. The MAs are detected by removing vessels and exudate from fundus images. The proposed work intends to achieve higher sensitivity value on heterogeneous image database.

3 Methodology

The MAs, the dark red spots, are detected by removing brighter blood vessels from fundus image. The exudates are bright yellowish lesions and are obtained by removing the optic disk. The proposed work is divided into two parts: The first part deals with the detection of exudates and the second one performs detection of MAs.

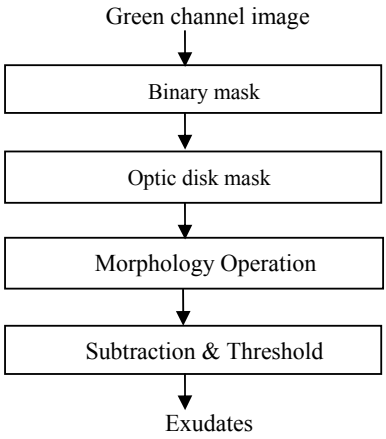

Fig. 3 Block diagram of exudate detection

3.1 Detection of Exudates

The exudate detection process consists of sequences of operations presented in the block diagram shown in Fig. 3.

The green channel has good contrast compared with red and blue channels of the RGB image, and therefore, a green channel of retina image is used for exudate detection. To remove the outer ring of the fundus image, a binary mask is created by image inversion and then the binary mask is subtracted from the input image. The optic disk is seen as the bright yellowish circular region of the retinal image. The exudates have similar intensity values as of optic disk, and therefore, it is necessary to remove the optic disk from the image to get exudate in the final image. The brightest part is extracted using Gaussian filter, and its dimensions are used to optic disk mask. Morphological dilation of the contrast-enhanced image is performed with a square structuring element to make exudates bigger or thicker. This dilated image is subtracted from the optical mask, and Otsu threshold [10] is applied to get a binary image with valid exudates as shown in Fig. 5.

3.2 Detection of MAs

The MA detection process steps are shown in the process flow diagram shown in Fig. 4. To guarantee better segmentation of MAs, the fundus image is enhanced by passing the green channel image through contrast-limited adaptive histogram equalization (CLAHE) [11] filter.

In this contrast enhancement technique, small regions are enhanced instead of the whole image, and all small regions are combined using bilinear interpolation to obtain the contrast-enhanced image. The closing operation is performed on the CLAHE filter output image. The closing operation, by definition, is dilation ($\oplus$)

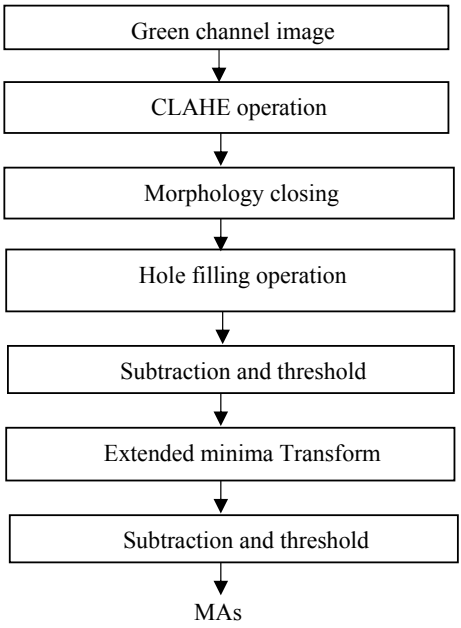

Fig. 4 Detection of MAs process flow

followed by erosion (⊖) as given by Eq. (1).

$$C \bullet S = (C \oplus S) \ominus S \tag{1}$$

Here, C (green channel), S (structuring element) and symbol (●) represent a morphological closing operation. The closing operations fill the tiny dark spot or gap between the bright spot into the same intensity as a bright spot whereas large bright areas remain unaltered. The MAs, the small dark spots, can be assumed as holes in the image. The hole filling operation fills these dark spots with background pixels in the CLAHE image. The closed image is subtracted from the hole filled image. The subtraction operation removes spots smaller than MAs. The image contains blood vessels as well as MAs. Now, the blood vessels are to be removed to identify MAs in the final image. This image is converted to a binary image using the Otsu threshold technique, and the inverted extended minima transform (EMT) [11] is applied. This process extracts all possible bright regions representing blood vessels and MAs. The blood vessels are brighter regions represented by connected pixels, and MAs are brighter and isolated regions constituting of small number of pixels. The subtraction is performed to keep isolated brighter spots MAs, and finally, Otsu threshold is applied to get valid MAs.

4 Results and Discussion

The proposed algorithm experimented on 80 retinal images from a clinical heterogeneous database. The e-ophtha image database provides images with MAs and exudates along with ground truth images [12]. The detection algorithm enables the ophthalmologists to detect DR signs at an early stage more quickly especially in mass screening. The performance of the proposed algorithm was evaluated quantitatively by comparing output images with the ground truth images to measure its effectiveness. The sensitivity [13] was chosen as a performance metric whose value indicates the degree of the trueness of the DR signs in the images and is obtained using Eq. (2).

$$\text{sensitivity} = \text{TP}/(\text{TP} + \text{FN}) \times 100 \tag{2}$$

where true positive (TP) is the number of pixels representing DR signs accurately, false positive (FP) is the number of pixels recognized erroneously as pixels belonging to DR signs, false negative (FN) is the number of pixels identified dishonestly as healthy, and true negative(TN) is a number of pixels representing no DR-related information. The higher the sensitivity value, the better the exudates and MA detection. Table 2 shows TP, FP, FN, TN and sensitivity values of exudates detected

Table 2 Performance of the exudate detection algorithm

Image	True positive (TP)	False negative (FN)	False positive (FP)	True negative (TN)	Sensitivity (S)
1	1236	106	6955	1,374,103	92.10
2	93	0	90,196	1,292,111	100
3	1800	663	2817	1,498,720	73.08
4	318	45	49,248	1,454,389	87.60
5	1568	221	83,130	2,700,361	87.65
6	16,561	1895	147,561	2,619,263	89.73
7	2786	242	148,932	2,633,320	92.01
8	7396	2654	72,817	2,702,413	73.59
9	681	2	302,421	2,482,176	99.71
10	2556	1	282,305	2,500,418	99.96
11	3274	0	159,471	4,151,879	100
12	10,567	706	116,120	4,187,231	93.74
13	312	4	8682	4,305,626	98.73
14	2327	621	119,054	4,192,622	78.93
15	4421	1407	66,253	4,242,543	7586
16	97	1	40,905	4,273,621	98.98

(continued)

Table 2 (continued)

Image	True positive (TP)	False negative (FN)	False positive (FP)	True negative (TN)	Sensitivity (S)
17	3302	782	161,256	4,149,284	80.85
18	5296	261	2,659,137	9,547,530	95.30
19	5969	2317	334,373	11,869,565	72.04
20	43,526	15,527	82,679	12,070,492	73.71
21	246,219	44,904	483,263	11,437,838	84.58
22	6480	146	1,145,494	11,060,104	97.80
23	169,789	31,527	695,696	11,315,212	84.34
24	92,762	13,519	488,315	11,617,628	87.28
25	13,763	3668	252,277	11,942,516	78.96
26	140,155	43,577	210,787	11,817,705	76.28
27	11,723	3089	398,727	11,798,685	79.15
28	3305	1420	542,680	11,664,819	69.95
29	71,467	13,508	482,427	11,644,822	84.10
30	54,706	3523	1,086,869	11,067,126	93.95
31	18,208	1665	591,094	11,601,257	91.62
32	5197	696	562,155	11,644,176	88.19
33	22,257	3502	415,295	11,771,170	86.40
34	11,123	1428	567,344	11,632,329	88.62
35	17,528	1205	875,225	11,318,266	93.57
36	5997	1782	319,373	11,885,072	77.09
37	17,913	6885	384,072	11,803,354	72.24
38	17,604	3587	200,367	11,990,666	83.07
39	29,641	8941	737,272	11,436,370	76.83
40	6602	2848	320,477	11,882,297	69.86
					85.68

images. Table 4 shows TP, FP, FN, TN and sensitivity values of MAs detected images. Table 3 and 5 show the comparison of proposed work with results obtained by various researchers. The average sensitivity value achieved with exudate detection is 85.68%. The average sensitivity value achieved with MA detection is 96.41%. The simulation results of the proposed work are present in Figs. 5 and 6, respectively.

Table 3 Comparison of exudate detection results

S. NO	Methods	Average sensitivity (%)
1	Zhang et al	83
2	Sopharak et al	80
3	Proposed work	85.68

Table 4 Performance values of MA detection

Image	True positive (TP)	False positive (FP)	False negative (FN)	True negative (TN)	Sensitivity (S)
1	33	11,040	2	1,492,925	94.29
2	112	11,382	1	1,370,905	99.12
3	146	10,266	3	1,371,985	97.99
4	961	42,179	33	4,271,451	96.68
5	419	32,079	0	4,282,126	100
6	455	51,208	7	4,262,954	98.48
7	309	45,599	26	4,268,690	92.24
8	280	49,230	0	4,265,114	100
9	140	28,591	0	4,285,893	100
10	44	19,291	0	4,295,289	100
11	229	36,300	7	4,278,088	97.03
12	63	46,723	0	4,267,838	100
13	175	41,537	11	4,272,901	94.09
14	310	34,776	37	4,279,501	89.34
15	310	67,583	2	4,246,729	99.36
16	149	48,761	0	4,265,714	100
17	487	76,193	65	4,237,879	88.22
18	255	59,418	0	4,254,951	100
19	134	71,259	1	4,243,230	99.26
20	523	44,622	42	4,269,437	92.57
21	1249	48,397	144	4,264,834	89.66
22	1362	58,754	65	4,254,443	95.44
23	313	48,318	3	4,265,990	99.05
24	249	47,126	27	4,267,222	90.22
25	767	19,471	57	4,294,329	93.08
26	894	36,302	36	4,277,392	96.13
27	370	37,140	4	4,277,110	98.93
28	497	36,248	34	4,277,845	93.60
29	212	72,021	2	4,242,389	99.07
30	238	59,978	1	4,254,407	99.58
31	252	58,238	8	4,256,126	96.92
32	1320	30,791	76	4,282,437	94.56
33	446	31,728	6	4,282,444	98.67
34	132	48,269	0	4,266,223	100
35	212	28,477	0	4,285,935	100

(continued)

Table 4 (continued)

Image	True positive (TP)	False positive (FP)	False negative (FN)	True negative (TN)	Sensitivity (S)
36	68	39,499	0	2,745,713	100
37	181	25,437	20	2,759,642	90.05
38	271	18,563	12	2,766,434	95.76
39	133	21,770	13	2,763,364	91.10
40	740	30,291	31	2,754,218	95.98
					96.41

Table 5 Comparison of MA detection results

S. NO	Methods	Average sensitivity (%)
1	Sopharak et al	81.61
2	Eftal Sehirl et al	69.1
3	Proposed work	96.41

Figure 5a–f shows output images of exudate detection. The RGB and green channel images are shown in Fig. 5a, b. The binary mask is shown in Fig. 5c. The optic disk could make erroneous result in detecting exudates as they both share similar color intensity. Therefore, the optic disk is removed using an optical mask before exudates detected as shown in Fig. 5d. Finally, exudates are shown in Fig. 5e. The detected exudates are superimposed on green channel image as shown in Fig. 5f.

It is observed from Table 2 that sensitivity values of some images are low (about 69–80%), and in these images, the true positive pixels are detected incorrectly due to the artifacts that are similar to exudates, the artifacts from noise in the image acquisition process. The success of exudate detection depends on the elimination of optic disk as well as other artifacts present in the image.

Figure 6a–h shows output images of MA detection. To get better detection of MAs, the contrast of the green channel is improved by using the CLAHE filter as shown in Fig. 6c. Figure 6d shows image obtained after closing operation. The MAs (dark spots) hole filled as shown in Fig. 6e is subtracted from Fig. 6d, and Otsu threshold is applied to remove small spots in the fundus image as shown in Fig. 6f. The inverted extended minima transform detects bright areas in the retina image as shown in Fig. 6g. The detected MAs are shown in Fig. 6(h).

5 Conclusion

The DR lesion detection algorithm was developed in the proposed work. The proposed work detects exudates and MAs using morphological operations along with Otsu threshold techniques. The results obtained from the proposed method are

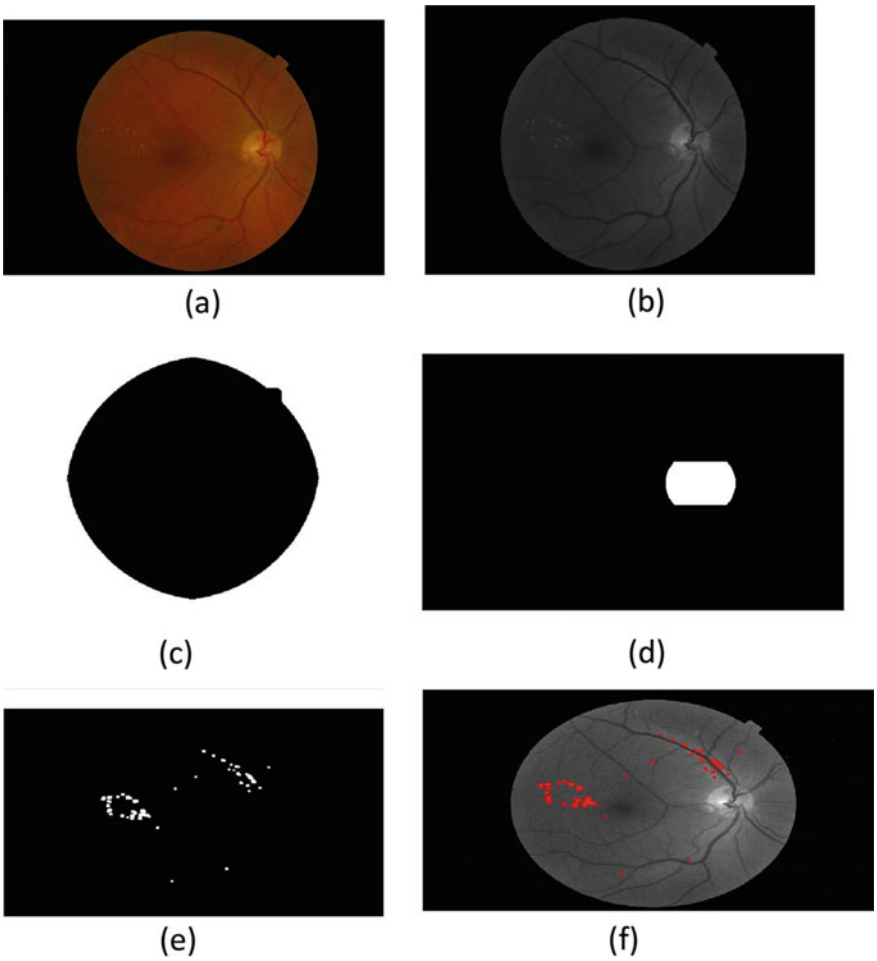

Fig. 5 **a** RGB image, **b** green channel image, **c** binary mask, **d** optic disk mask, **e** exudates detected, **f** exudates overlay green channel image

compared with ground truth images. The average sensitivity of exudate detection is 85.68%. The average sensitivity achieved with MA detection is 96.41%. In a mass screening of eye examination, the proposed algorithm can be used as a preliminary diagnostic tool.

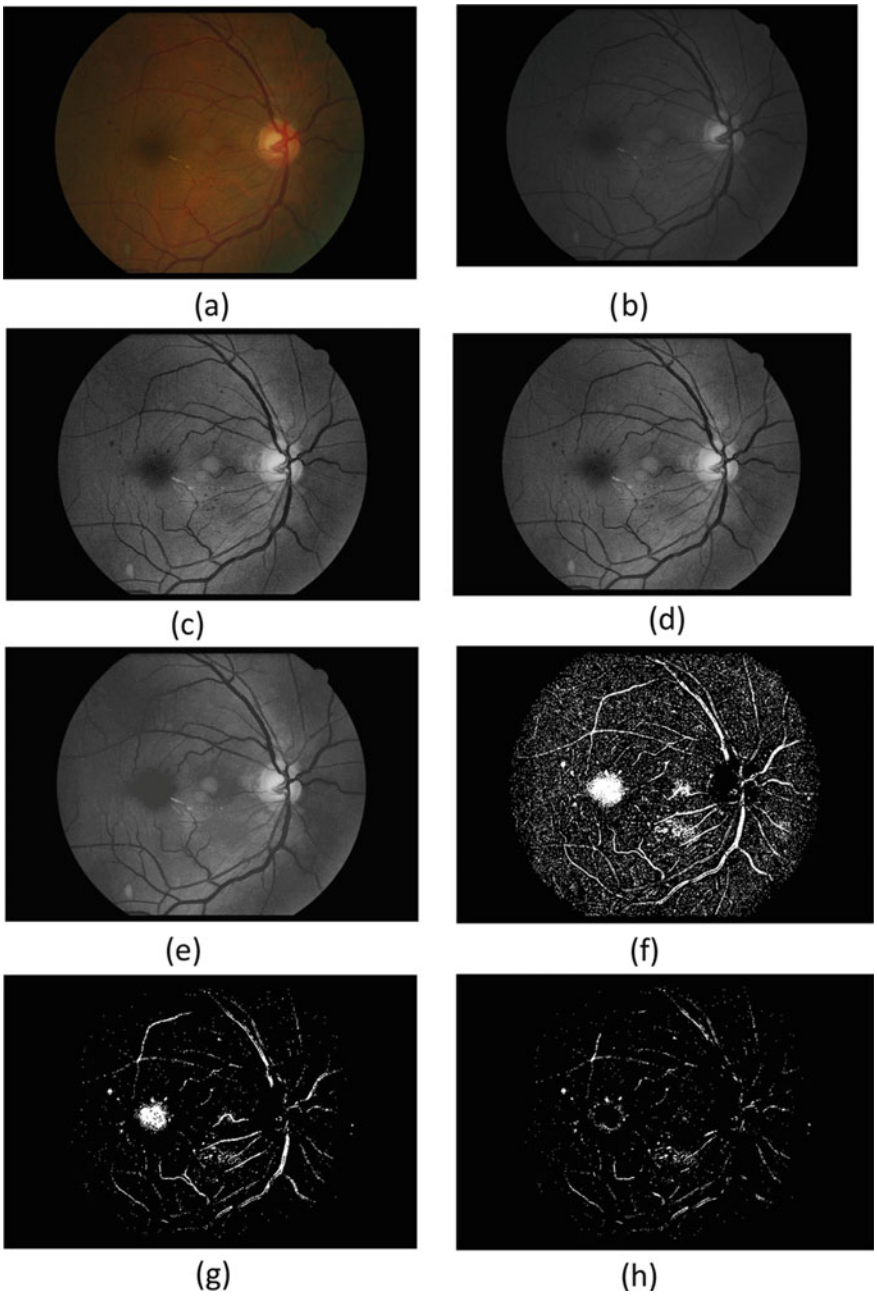

Fig. 6 **a** RGB image, **b** green channel, **c** CLAHE image, **d** closed image, **e** hole filled, **f** threshold image, **g** extended minima image, **h** final image with MAs

References

1. Vislisel J, Oetting T (2010) Diabetic retinopathy: from one medical student to another. EyeRounds.org
2. Abramoff MD, Garvin MK, Sonka M (2010) Retinal imaging and image analysis. IEEE Rev Biomed Eng 3:169–208
3. Eadgahi MGF, Pourreza H (2012) Localization of hard EXs in retinal fundus image by mathematical morphology operations. In: 2nd International econference on computer and knowledge engineering (ICCKE), Mashhad, 18–19 Oct 2012, pp 185–189
4. Zhang X et al (2014) Exudate detection in colour retinal images for mass screening of DR. Medical Image Anal 18(7):1026–1043. ISSN:1361-8423
5. Shahin EM, Taha TE, Al-Nuaimy W, El Rabaie S, Zahran OF, El-Samie FEA (2012) Automated detection of DR in blurred digital fundus images. In: 8th International computer engineering conference (ICENCO), Cairo, pp 20–25
6. Usman Akram M et al (2013) Identification and classification of MA for early detection of DR. Pattern Recogn 46(1):107–116. ISSN 0031-3203
7. Şehirli E, Turan M, Dietzel A (2015) Automatic detection of microaneurysms in RGB retinal fundus images. Int J Sci Technol Res 1:1–8
8. Sopharak A et al. Automatic detection of diabetic retinopathy exudates from non-dilated retinal images using mathematical morphology methods. Comput. Med. Imaging Graph: Off J Comput Med Imaging Soc 32:720–727. https://doi.org/10.1016/j.compmedimag.2008.08.009
9. Sopharak A et al (2013) Simple hybrid method for fine microaneurysm detection from non-dilated diabetic retinopathy retinal images. Comput. Med. Imaging Graph: Off J Comput Med Imaging Soc 37:5–6:394–402
10. Otsu N (1979) A threshold selection method from gray-level histograms. IEEE Trans Syst Man Cybern 9(1):62–66
11. Gonzalez RCW (2010) Digital image processing using Matlab. 2nd edn., pp 62–63
12. Decencière E et al (2013) TeleOphta: machine learning and image processing methods for teleophthalmology. IRBM. https://doi.org/10.1016/j.irbm.2013.01.010,2013-RetinalImagedatabase
13. Sridhar (2011) Digital image processing, 1st edn., pp 483–487

Global Solar Radiation Estimation Modeling Using Artificial Neural Network: A Case Study on Metro Cities of India

Amar Choudhary, Deependra Pandey, and Saurabh Bhardwaj

Abstract The environmental constraints and limited availability of traditional energy resources have made the twenty-first century for the optimization of renewable energy resources. Solar energy is solely related to the quantity of solar radiation to be received by solar panel/devices. Optimization of solar energy is best possible when solar radiation is estimated well before. To overcome the availability of solar radiation measuring devices at the location of interest, solar radiation estimation models are developed. In the present study, four metro cities (Bombay-Colaba, Calcutta-Alipore, Madras-Meenambakkam, and New Delhi-Safdarjung) of India have been selected. The data are downloaded from CROPWAT 8.0. The solar radiation is taken as output whereas latitude, longitude, altitude, months of a year, maximum temperature, minimum temperature, humidity, wind velocity, and the sunshine hour are considered as input. Simulation is executed with MATLAB R2016a with MLP and LM algorithm. The proposed model shows an overall regression value of 0.99178, and RMSE for training is 0.0961, for validation 0.3102, and for testing 0.5727.

Keywords Artificial intelligence · Machine learning · Artificial neural network · Solar radiation · Renewable energy

A. Choudhary (✉) · D. Pandey
Electronics and Communication Engineering Department, Amity School of Engineering and Technology, Amity University, Lucknow, Uttar Pradesh 226010, India
e-mail: amar.giet.ece@gmail.com

D. Pandey
e-mail: dpandey@lko.amity.edu

S. Bhardwaj
Electronics and Instrumentation Engineering Department, Thapar Institute of Engineering and Technology, Thapar University, Patiala, Punjab 147001, India
e-mail: saurabh.bhardwaj@thapar.edu

G. T. C. Sekhar et al. (eds.), *Intelligent Computing in Control and Communication*, Lecture Notes in Electrical Engineering 702,
https://doi.org/10.1007/978-981-15-8439-8_39

1 Introduction

Energy is the most integral part of human life since ancient times. People were using fuels like kerosene oil, petrol, diesel, wood, etc. to meet their energy requirements. These sources of energy were non-renewable. Also they were pollutants and limited availability. So, since the twentieth-century people started the exploration of renewable energy resources like wind energy, solar energy, etc. In the twentieth/twenty-first century, people started optimizing them. Among all other types of renewable energy, solar energy takes great lead over others due to its abundance [1]. The amount of energy released by the sun in an hour is more than required to meet the energy demand across the globe for the whole year [2, 3]. Solar radiation can be categorized as extraterrestrial solar radiation and global solar radiation. The first one is the radiation received above the atmosphere, and the second one is below the atmosphere. Again, global solar radiation is the integration of direct normal radiation and diffuse horizontal radiation. In the present study, global solar radiation is considered. Solar devices/panel receives solar radiation and converts it to electrical energy. As much and as for proper they receive radiation, electrical energy is generated. If the amount/intensity of radiation to be known well in advance at the station of interest, then the devices may be customized in such a way that they would be able to utilize maximum solar radiation for electrical energy generation. Devices like solarimeter, pyranometer, pyrheliometer, radiometer, etc. are used to measure solar radiation. These devices are of high cost, and they are generally installed at the meteorological stations only. They are limited, and they may not be the station of interest for researchers/developers [4]. To meet this difficulty, solar radiation estimation models are developed since 1924. Some of them are mathematical models, and some are soft computing like ANN, fuzzy logic, SVM, etc. based models. This paper is dedicated to an artificial neural network-based solar radiation estimation model. India's status in solar energy is well explained in [5]. Due to the unparalleled advantages of ANN over other soft computing techniques, a lot of models have been developed using ANN, especially for Indian locations [6–8].

Section 2 of this paper shall give an idea of ANN. In Sect. 3, various steps of the development of a solar radiation model are elaborated. Sections 4 and 5 are for results and conclusions.

2 Artificial Neural Network-Based Approach

This is an important modeling technique to estimate solar radiation. Different ANN-based solar radiation estimation model may be obtained in the literature [9–20]. ANN is a branch of artificial intelligence. It ensures an efficient way of establishing a nonlinear relationship between input and output. ANN is a more accurate tool for determining solar radiation in comparison with nonlinear, fuzzy, conventional, Angstrom, etc. models [11].

A mathematical representation of ANN is shown in Fig. 1. It consists of inputs, weights, transfer function, threshold/bias, and activation function. The output of ANN is well determined by Eq. 1.

$$O_j = \sum_{j=1}^{n} x_j.w_j + \varphi.\theta_j \tag{1}$$

Here, O_j denotes the output of ANN, x denotes the input of ANN, w denotes the corresponding weights of ANN, θ_j denotes the threshold, and ϕ denotes the activation function.

Several researchers have developed/studied the number of ANN-based solar radiation estimation models [9–14].

3 Global Solar Radiation Estimation Modeling

Solar radiation has two parts, namely extraterrestrial radiation which is above the atmosphere and global solar radiation which is below the atmosphere. This section is dedicated for development of global solar radiation estimation model, its methodology, and statistical testing through various subsections.

3.1 Geographical and Meteorological Data

In the present analysis, four metro cities (Bombay-Colaba, Calcutta-Alipore, Madras-Meenambakkam, and New Delhi-Safdarjung) of India of the different climatic zone are selected for the study. The selected stations are represented on the map of India in Fig. 2. Table 1 shows the geographical properties of selected stations. The stations are selected from CLIMWAT 2.0 software, and CLI (.cli) and PEN (.pen) are downloaded. The downloaded files are imported to CROPWAT 8.0 and geographical, meteorological, and radiation data are downloaded for selected stations. The data contained altitude, latitude, longitude, months, maximum temperature, minimum temperature, humidity, wind velocity, sunshine hour, and monthly solar radiation.

Climatic plots have also been observed for study from CROPWAT 8.0 of respective stations. These are 2D/3D plots between minimum temperature, maximum temperature, humidity, wind velocity, sunshine hour, and solar radiation. Simple observation of all plots depicts that wind velocity and humidity have less correlation with solar radiation as compared to others.

Since downloaded data are in different scales and ranges. So, min-max normalization of data is executed as per Eq. (2):

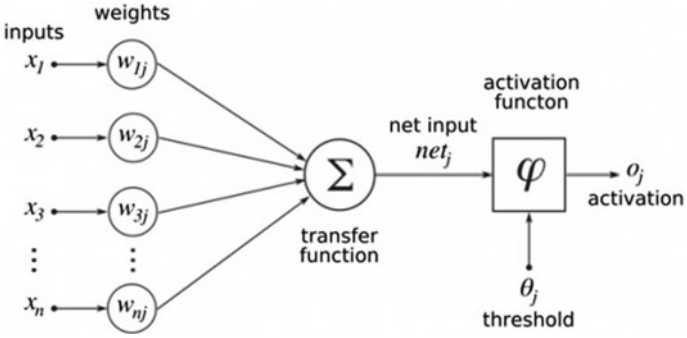

Fig. 1 Artificial neural network mathematical representation

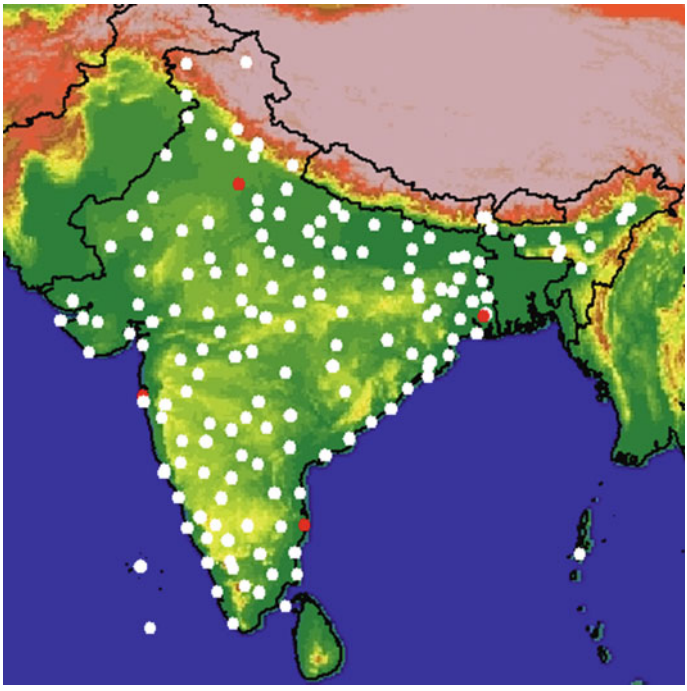

Fig. 2 Metro city stations of India for study

Table 1 Geographical definition of selected stations along with solar radiation

Stations	Latitude (°N)	Longitude (°E)	Altitude (m)
Bombay-Colaba	18.90	72.81	11
Calcutta-Alipore	22.53	88.33	6
Madras-Meenambakkam	13.00	80.18	16
New Delhi-Safdarjung	28.50	77.20	216

$$x_{\text{normalized}} = \frac{x - x_{\text{minimum}}}{x_{\text{maximum}} - x_{\text{minimum}}} \tag{2}$$

3.2 Methodology

A computer program is performed under MATLAB-R2016a using neural fitting tool, configured as detailed in Table 2. The number of neurons determines the perfectness of iterations in backpropagation. If excess neurons are used, then the network will attempt to record the problem and hence got generalize well later. If the number of neurons is below required, then they are used by the network to simplify good but may not have sufficient ability to acquire from the patterns properly. Therefore, getting the correct number of neurons is a trial and error approach. Presently, the following empirical relation (Eq. 3) is used to determine the required number of

Table 2 Customization of neural fitting tool

S. No.	Particulars	Configuration details
1	Network type	Feedforward backpropagation
2	Training algorithm	TRAINLM
3	Error function	MSE
4	Number of hidden layers	02
5	Transfer function	TANSIG
6	No. of neurons	11
7	Training parameters	Epochs: 1000, max_fail: 6
8	Data division	Random (dividerand)
9	Training	Levenberg–Marquardt (trainlm)
10	Performance	Mean squared error (MSE)
11	Calculation	MEX
12	Plot interval	1 epoch

neurons for proper learning and memorizing as well.

$$\text{Number of Neurons} = \left[\left(\frac{\text{Input} + \text{Output}}{2} \right) . (\text{Sample})^{1/2} \right] \tag{3}$$

In this study, there are nine inputs and one output. The total number of samples is 48. As per Eq. 3, the number of neurons required becomes 11.

This model is validated by root mean square error (RMSE) used for error calculation by Eq. (4):

$$\text{RMSE} = \left[\left(\frac{1}{n} \right) \sum_{i=1}^{n} \left(\text{SR}_{i\,(\text{predicted})} - \text{SR}_{i\,(\text{actual})} \right)^2 \right]^{1/2} \tag{4}$$

Here, n is the number of input, and SR is the solar radiation.

4 Results

As per Table 2 and Eq. 3, neural network fitting tool is customized. Normalized input and output have been provided to network for training, testing, and validation. The simulation environment is shown in Fig. 3.

After training and retraining of the network, a maximum validation check of 2 is achieved with 08 iterations. After this, performance, training state, error histogram, and regression plots are obtained, and they are shown in Figs. 4, 5, 6, and 7.

Performance plot is a plot between epochs and mean squared error (MSE). In this, the best validation performance of 0.00052548 is obtained at epoch 6. The plot depicts that mean squared error is becoming smaller as the number of epochs increases.

Training state plot consists of three subplots, between epochs vs. gradient, epochs vs. mu (training gain), and epochs vs. Val Fail. Best gradient of 0.0006, best mu of 0.00004, and best validation checks of 2 have been obtained at epoch 8.

Figure 6 is the error histogram for training data. It is a plot between errors and instances. It is essential for additional verification of network performance. Out of 20 number of errors, 9 are above the axis and 12 are not present, and this signifies that 12 data are completely different from others. The histogram is overall in support of the network performance, especially test performance.

Figure 7 is a regression plot with four subplots of regression for training, validation, testing, and overall. The plots are between target and output. These plots between target and output measures of how well the variations in the output are explained by the targets. For training, validation, testing, and overall, the value of R is 0.099997, 0.099577, 0.96679, and 0.99178 which are obtained, respectively. Overall R-value is 0.99178 (99.17%) for total response. Slope (m) and intercept (b) values for overall are 1 and 0.013 respectively which justifies the fitness of simulation.

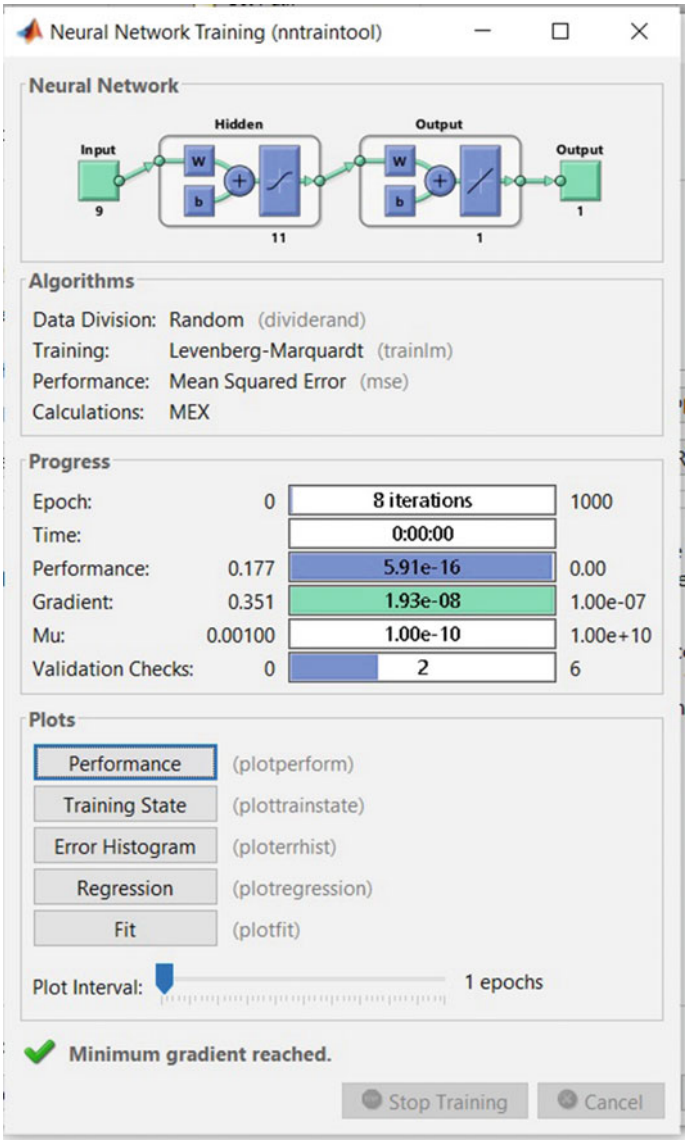

Fig. 3 Training environment

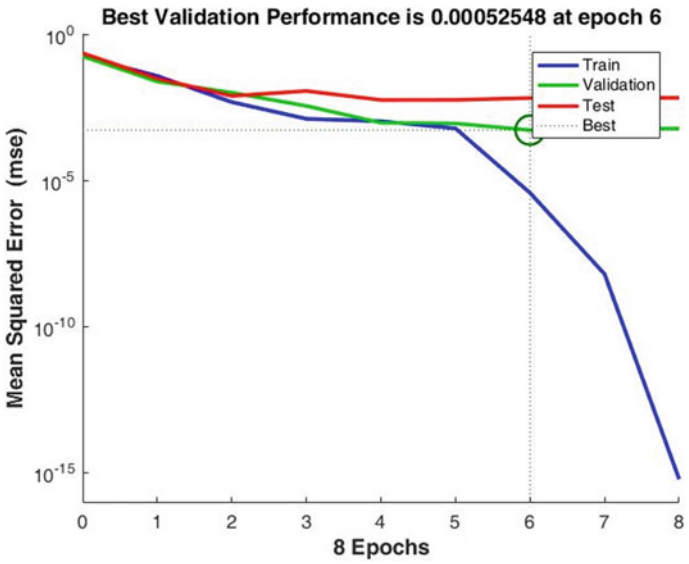

Fig. 4 Performance plot

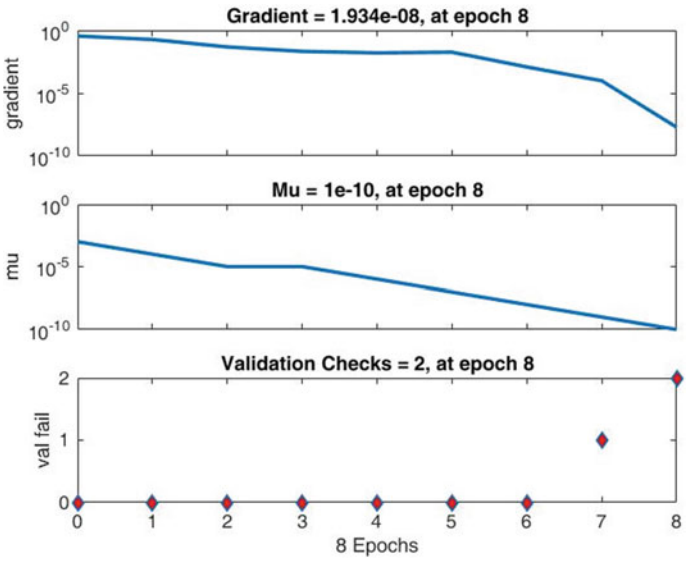

Fig. 5 Training state plot

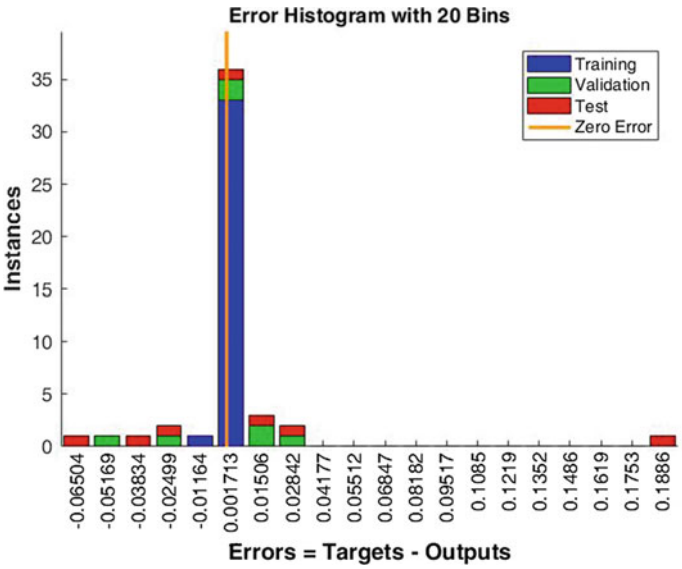

Fig. 6 Error histogram

After obtaining these plots/results, the RMSE value of training, validation, and testing is recorded which is shown in Table 3.

5 Conclusion

With the justification of the newly developed model, paper gives an ANN-based approach of solar radiation estimation using the Levenberg–Marquardt feedforward backpropagation algorithm. This model involved different geographical and atmospheric parameters as input, and solar radiation is predicted at output. The overall regression is 0.99 (approx.), and RMSE for training, validation, and testing is 0.0961, 0.3102, and 0.5727, respectively. These results advocate the correctness of the developed model. This model may be implemented for the estimation of global solar radiation in the far-flung areas where the availability of solar radiation measuring devices is scarce.

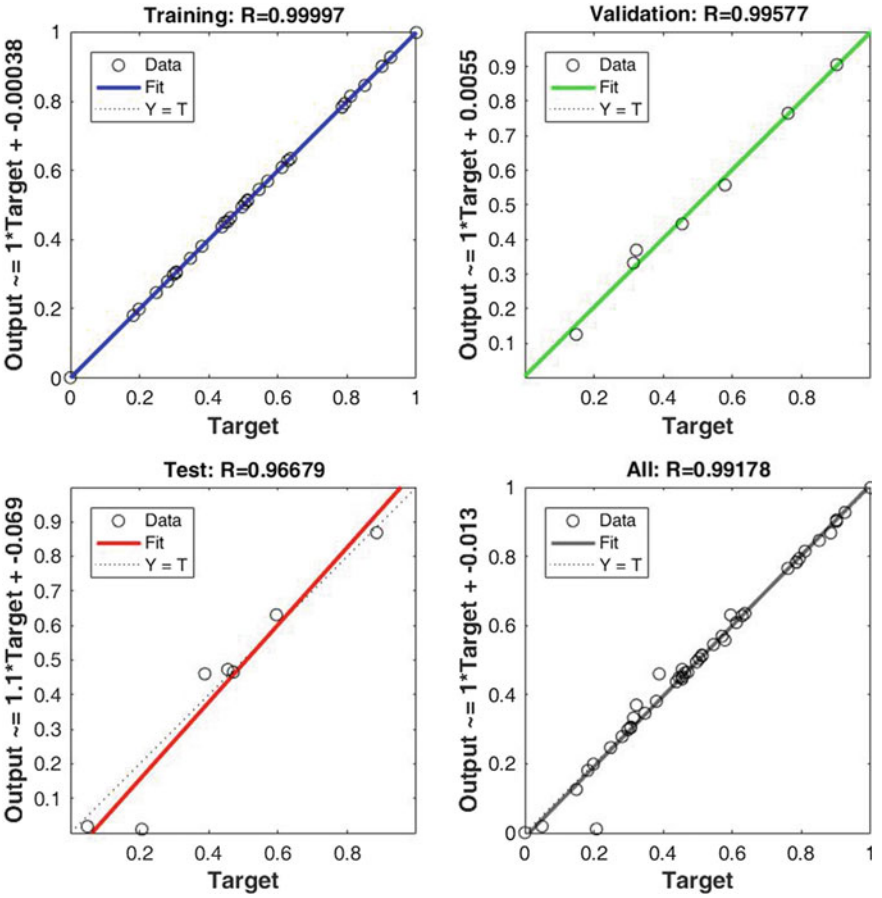

Fig. 7 Regression plot

Table 3 RMSE

Results	Samples	RMSE
Training	34	0.0961
Validation	7	0.3102
Testing	7	0.5727

References

1. Pandey D, Choudhary A (2018) A review of potential, generation and factors of solar energy. J Thermal Eng Appl STM J 5(3). ISSN 2349-8994 (Online)
2. Kapoor K, Pandey KK, Jain AK, Nandan A (2014) Evolution of solar energy in India: a review. Renew Sustain Rev 40:475–485

3. Jemaa ABEN, Rafa S, Essounbouli N, Hamzaoui A, Hnaien F, Yalaoui F (2013) Estimation of global solar radiation using three simple methods. Energy Procedia 42:406–415 (Elsevier ScienceDirect)
4. Mubiru J, Banda EJKB (2008) Estimation of monthly average daily global solar irradiation using ANN. Sol Energy 82:181–187 (ScienceDirect (Elsevier))
5. Rizwan M, Jamil M, Kothari DP (2012) Generalized neural network approach for global solar energy estimation in India. IEEE Trans Sustain Energy 3(3)
6. Yadav AK, Chandel SS (2012) Artificial neural network based prediction of solar radiation for Indian stations. Int J Comput Appl (0975-8887) 50(9)
7. Malik H, Garg S (2019) Long-term solar irradiance forecast using artificial neural network: application for performance prediction of Indian cities. Adv Intell Syst Comput 697. https://doi.org/10.1007/978-981-13-18221-1_26
8. Kumar A, Khatri R (2019) Solar energy prediction using backpropagation in artificial neural networks. In: International conference on advanced computing networking and informatics, advances in intelligent systems and computing, vol 870. https://doi.org/10.1007/978-981-13-2673-8_4
9. Benghanem M, Mellit A, Alamri SN (2009) ANN-based modeling and estimation of daily global solar radiation data: A case study. Energy Convers Manage (Elsevier) 50:1644–1655
10. Dorvlo ASS, Jervase JA, Lawati AI A (2002) Solar radiation estimation using artificial neural networks. Appl Energy 307–319
11. Yadav AK, Chandel SS (2013) Solar radiation prediction using artificial neural network techniques: a review. Renew Sustain Energy Rev. https://doi.org/10.1016/j.rser.2013.08.055
12. Kumar R, Aggarwal RK, Sharma JD (2012) Solar radiation estimation using artificial neural network: a review. Asian J Contemp Sci 1:12–17
13. Kalgirou SA (2001) Artificial neural networks in renewable energy systems applications: a review. Renew Sustain Energy Rev 5:373–401
14. Choudhary A, Pandey D, Kumar A (2001) A review of various techniques for solar radiation estimation. In: 3rd International conference on recent developments in control, automation & power engineering (RDCAPE), Noida, India, pp 169–174
15. Ozgoren M, Bilgili M, Sahin B (2012) Estimation of global solar radiation using ANN over Turkey. Expert Syst Appl 39(5):5043–5051
16. Sfetsos A, Coonick AH (2000) Univariate and multivariate forecasting of hourly solar radiation with artificial intelligence techniques. Sol Energy 68(2):169–178
17. Behrang MA, Assareh E, Ghanbarzadeh A, Noghrehabadi AR (2010) The potential of different artificial neural network(ANN) techniques in daily global solar radiation modeling based on meteorological data. Sol Energy 84(8):1468–1480
18. Mohandes M, Rehman S, Halawani TO (1998) Estimation of global solar radiation using artificial neural networks. Renew Energy 14(1–4):179–184
19. Cao J, Lin X (2008) Study of hourly and daily solar irradiation forecast using diagonal recurrent wavelet neural networks. Energy Convers Manage 49(6):1396–1406
20. Benghanem M, Mellit A, Alamria SN (2009) ANN-based modeling and estimation of daily global solar radiation data: a case study. Energy Convers Manage 50(7):1644–1655

Analysis of a Transient Lightning Current Flowing Through the Horizontal Grounding Conductor

G. Ramarao, Ch. Prasad, Ch. Upendhra, S. Prasanthi, and G. Manikanta

Abstract Analysis of transient response of current along the horizontal buried conductor due to the excitation of standard lightning impulse current in lossy grounding conditions is an important objective for designing the proper grounding system. In this paper, the transient analysis of current along the buried conductor is performed and reported due to the application of standard lightning current of 100 kA, 1.2/50 μs under different grounding conditions (i.e., $\sigma = 0.01, 0.001, 0.0001, 0.00001$ s/m) by using transmission line (TL) approach. This is the first of its kind attempt that the standard lightning current is considered as an exciting current. It is observed from the reported results that the conductivity of ground much effects on peak of transient current along the buried conductor. Further, this approach will be helpful in order to design proper grounding system to diminish the peak current along the horizontal buried conductor.

Keywords Conductivity · Lightning current · Transmission line approach

G. Ramarao (✉) · Ch. Prasad · Ch. Upendhra · S. Prasanthi · G. Manikanta
Department of EEE, Aditya Institute of Technology and Management, Tekkali, Srikakulam, Andhrapradesh 532201, India
e-mail: grr231@gmail.com

Ch. Prasad
e-mail: prasadchongala58@gmail.com

Ch. Upendhra
e-mail: upendhra009@gmail.com

S. Prasanthi
e-mail: prasanthisusarapu@gmail.com

G. Manikanta
e-mail: maggi33246@gmail.com

G. T. C. Sekhar et al. (eds.), *Intelligent Computing in Control and Communication*, Lecture Notes in Electrical Engineering 702,
https://doi.org/10.1007/978-981-15-8439-8_40

1 Introduction

The knowledge of lightning impulse or surge voltages plays an important role in economical designs of insulation of high voltage power apparatus. The transient behavior of the current along the thin wire configurations has subject of significant notice of many prominent researchers over the years. These types of studies can be seen in various applications of antenna theory and electromagnetic compatibility (EMC) in buried power conductors and telecommunication wires [1, 2].

Grounding system is the most important objective for protecting the underground cable from lightning and switching over voltages and currents. Whenever the lightning discharge occurs on the ground where the power conductor is buried, if the ground is non-perfect, then a large amount of impulse current flows in buried conductor and develops the transient currents and voltages into it. These transient induced voltages may damage the insulation of such buried power conductor so that the continuity of power supply cannot be achieved. So, the analysis of transient behavior of currents and voltages and the study of coupling between electromagnetic fields produced by the lightning impulse currents and the horizontal grounding conductor are the basic objectives that are significant in the designing of proper grounding system [3–5]. The transient response of lightning current along the grounding conductor applied by non-standard lightning currents is illustrated in [6–8].

There are basically two models to analyze the transient behavior of voltages and currents along horizontal buried conductor. One is antenna theory (AT) model, and another one is transmission line (TL) model [9]. The solution of aforementioned models is achieved in frequency domain as well as in time domain.

AT approach has quite complexity in nature and requires much computational time compared to the TL approach. The transient response of wire AT model is performed in frequency domain in the horizontal grounding conductor as illustrated in [10]. The transient analysis of buried conductor was reported based on the excitation of non-standard lightning impulse current waveform in [11]. In general, the over and underground cables mainly suffer from standard and non-standard lightning impulse waveforms. Thus, there is a scope of considering standard lightning impulse current waveform as exciting current to analyze the transient behavior of the current along the horizontal buried conductor by using TL model.

In this paper, the telegrapher's equations (TEs) are solved firstly by finite difference time domain (FDTD) method, and later, the standard lightning impulse current is applied as an exciting current to buried conductor and at different conductivities of the ground. Finally, the analysis of the results is performed and reported.

2 Horizontal Grounding Conductor Phenomenon

The geometry related to a straight thin conductor is buried horizontally in non-perfect grounding conditions as illustrated in Fig. 1. The length and diameter of the horizontal conductor are respectively L and $2a$ which is buried in a lossy medium at a depth of d. Here, it is assumed that the lossy ground has a permittivity of ε and the conductivity of σ exists at a depth d as illustrated in Fig. 1. The buried conductor is excited by the current source which is equivalent to standard lightning impulse waveform with peak of 100 kA.

In general, the analysis of transient impulse currents and voltages in horizontal conductor buried in lossy medium is significant for the protection of insulation of power conductor during the real-time operation so that the proper operation of power system can be achieved. An approximate transmission line (TL) approach can be used for assessing the transient current along the horizontal grounding conductor buried in lossy medium. In TL approach, the transient voltage and current through the horizontal buried conductor can be achieved by solving the TEs [12] which are illustrated as Eqs. (1) and (2):

$$\frac{\partial v(x,t)}{\partial x} + Ri(x,t) + L\frac{\partial i(x,t)}{\partial t} = 0 \tag{1}$$

$$\frac{\partial i(x,t)}{\partial x} + Gv(x,t) + C\frac{\partial v(x,t)}{\partial t} = 0 \tag{2}$$

Wherein (1) and (2), $v(x,t)$ and $i(x,t)$ are the spatio-temporal variation of induced voltage and current along the conductor, respectively. Also, R, L, G, and C are the per-unit length series resistance, inductance, conductance, and capacitance of the conductor, respectively.

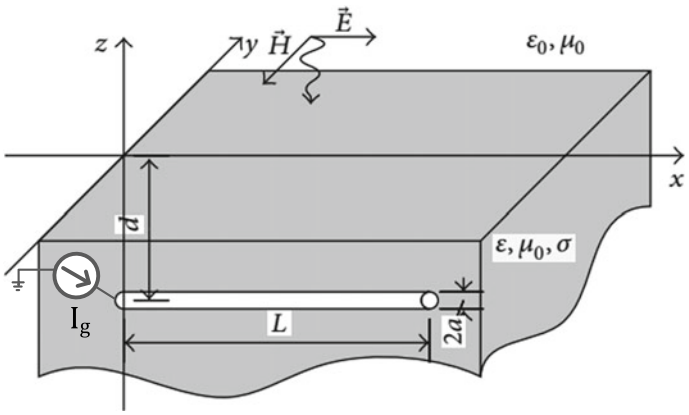

Fig. 1 Horizontal conductor buried in lossy grounding conditions

Besides, the per-unit values of L, G, and C of the buried conductor can be calculated by using the equations given in [13] which are illustrated as Eq. (3)

$$\begin{aligned} L &= \frac{\mu_0}{2\pi} \ln\left(\frac{2l}{\sqrt{2ad}} - 1\right) \\ G &= \frac{2\pi\sigma}{\ln\left(\frac{2l}{\sqrt{2ad}} - 1\right)} \\ C &= \frac{2\pi\varepsilon_0\varepsilon_r}{\ln\left(\frac{2l}{\sqrt{2ad}} - 1\right)} \end{aligned} \tag{3}$$

Finally, the resistance R value can be obtained by conductivity of different groundings. If the ground assumed to be perfect means $R = 0$, if the ground is not perfectly conducting means that there is existence of resistance R.

In Eq. (3), the values of L, G, and C can be obtained majorly by physical parameters as illustrated in Fig. 1. The l, a, and d are respectively the length, radius, and depth of the buried conductor. Furthermore, the permeability of air, the relative permittivity, and the conductivity of the ground are represented as μ_0, ε_r, and σ, respectively. The solution of Eqs. (1) and (2) must be carried out to assess the transient current and voltage along the buried conductor. Thus, the finite difference time domain (FDTD) method is used in this work to find the solution of the TEs given by Eqs. (1) and (2).

3 Exciting Lightning Impulse Current

In order to analyze the transient current along the buried conductor, the excitation current is essential. In this work, excitation current is taken which is equivalent to standard lightning current of peak of 100 kA, rise time of 1.2 μs, and tail time of 50 μs.

In order to represent the standard lightning impulse current, the double exponential (DEXP) function is utilized in this work and it is given in [14] as Eq. (4)

$$I_g(t) = I_0 K\left(e^{-\alpha t} - e^{-\beta t}\right) \tag{4}$$

wherein (4), I_0 is amplitude of lightning current, and α and β are the DEXP function parameters. To keep the pulse positive polarity, the DEXP function parameters α and β should satisfy the condition that $\beta > \alpha > 0$, $t \geq 0$ [15]. K is the amplitude modifying factor [16]. The impulse current or voltage waveforms generated by the DEXP function mimic the actual properties of the standard lightning impulse waveform. Thus, DEXP function is utilized in our work to generate the standard LI current waveform.

The determination of DEXP function constants is significant in order to generate the standard lightning impulse current waveform with required waveshape. Thus, the

Nelder-Mead algorithm and liner regression method [17, 18] are used here to achieve I_0, K, α, and β for approximating standard lightning impulse waveform.

The obtained values of I_0, K, α, and β are illustrated below.

$I_0 = 100$ kA,
$K = 0.9493$,
$\alpha = 1.4912 \times 10^4$ s^{-1},
$\beta = 1.6335 \times 10^6$ s^{-1}.

4 Solution of Telegrapher's Equations Using FDTD Method

In this section, the TEs are solved by implementing the MATLAB code based on FDTD method [18, 19]. This approach is an efficient numerical solution technique proposed by YEE in 1966. Moreover, the FDTD method is widespread method for evaluating the transient response lightning current along the transmission line or buried conductor. The derivatives presented in Eq. (1) are implemented by finite difference of voltage and current between future and past values. In this approach, the time and position variables are discretized as Δt and Δx, respectively.

In general, Maxwell's equations (MEs) can be used to explain the concept of FDTD method [20], there the differentiation is taken as a finite difference that means that the time differentiation is equal to the difference of time between previous and next values, and the space differentiation is equal to the difference of space between the previous and next values. These MEs are consisting of time and space differentiation. Thus, the electromagnetic fields are interdependent with each other. This means that in order to evaluate the next step value of electric field, there is a necessity to have present values of magnetic field and vice versa [21].

The space and time discretization of buried conductor is illustrated in Fig. 2. It is clearly observed from Fig. 2 that there is a possibility to take the finite differences of voltages and current as given in [22] which are illustrated by Eq. (5)

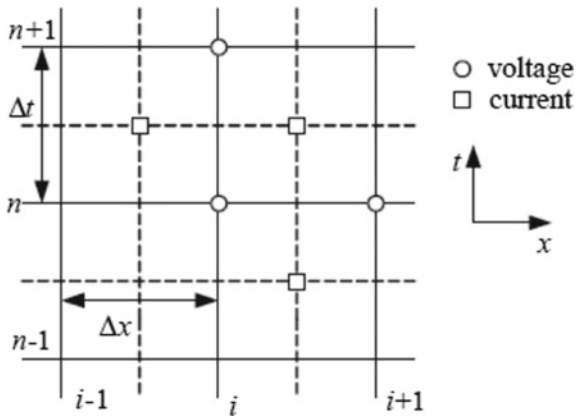

Fig. 2 Space and time discretization of the conductor

$$\frac{\partial v(x,t)}{dx} = \frac{v_{k+1}^{n} - v_{k}^{n}}{\Delta x}$$
$$\frac{\partial i(x,t)}{dt} = \frac{i_{k+1/2}^{n+1/2} - i_{k+1/2}^{n-1/2}}{\Delta t} \tag{5}$$

By substituting Eq. (5) in Eq. (1), then Eq. (1) is modified as Eq. (6) as follows

$$\frac{v_{k+1}^{n} - v_{k}^{n}}{\Delta x} + R\frac{i_{k+1/2}^{n+1/2} + i_{k+1/2}^{n-1/2}}{2} + L\frac{i_{k+1/2}^{n+1/2} - i_{k+1/2}^{n-1/2}}{\Delta t} = 0 \tag{6}$$

By simplifying Eq. (6), then the final equation for the spatio-temporal variation of current along the buried conductor is illustrated by Eq. (7)

$$i_{k}^{n+3/2} = A\left[Bi_{k}^{n+1/2} - \left(v_{k+1}^{n+1} - v_{k}^{n+1}\right)\right] \quad \text{for } k = 2, 3 \ldots, N \tag{7}$$

wherein Eq. (7),

$$A = \left(\frac{\Delta x}{\Delta t}L + \Delta x\frac{R}{2}\right)^{-1} \quad \text{and} \quad B = \left(\frac{\Delta x}{\Delta t}L - \Delta x\frac{R}{2}\right)^{-1}$$

Again, it is from Fig. 2 that the following Eq. (8) can be formed as follows

$$\frac{\partial i(x,t)}{dx} = \frac{i_{k+1/2}^{n+1/2} - i_{i-1/2}^{n+1/2}}{\Delta x}$$
$$\frac{\partial v(x,t)}{dt} = \frac{v_{k}^{n+1} - v_{k}^{n}}{\Delta t} \tag{8}$$

By substituting Eq. (8) in Eq. (2), then Eq. (2) is modified as Eq. (9) as follows

$$\frac{i_{k+1/2}^{n+1/2} - i_{i-1/2}^{n+1/2}}{\Delta x} + G\frac{v_{k}^{n+1} + v_{k}^{n}}{2} + C\frac{v_{k}^{n+1} - v_{k}^{n}}{\Delta t} = 0 \tag{9}$$

By simplifying Eq. (9), then the final equation for the spatio-temporal variation of voltage at different distances along the buried conductor is illustrated by Eq. (10) as

$$v_{k}^{n+1} = D\left[Ev_{k}^{n} - \left(i_{k}^{n+1/2} - i_{k-1}^{n+1/2}\right)\right] \quad \text{for } k = 2, 3 \ldots, N \tag{10}$$

wherein Eq. (10),

$$D = \left(\frac{\Delta x}{\Delta t}C + \Delta x\frac{G}{2}\right)^{-1} \quad \text{and} \quad E = \left(\frac{\Delta x}{\Delta t}C - \Delta x\frac{G}{2}\right)^{-1}$$

The excitation current equivalent to standard lightning impulse is applied at the starting point of the buried conductor as shown in Fig. 1, and then it is possible to observe the transient current and voltages at the different distances along the conductor based on Eqs. (7) and (10), respectively.

5 Results and Discussion

One example case has been taken to analyze the current along the conductor buried with depth of $d = 0.5$ m and the radius of $a = 5$ mm with relative permittivity of $\varepsilon_r = 10$. The length of buried conductor is taken as 10 m. This buried conductor is excited by lightning impulse current waveform of 100 kA, 1.2/50 μs generated by the DEXP function as illustrated by Eq. (4). The transient current is derived from TEs [(1) and (2)] by using FDTD and is illustrated as Eq. (7). These equations are developed in MATLAB and excited the buried horizontal conductor with DEXP function with peak of 100 kA, 1.2/50 μs. The analytical results have been taken at different conductivities of the ground ($\sigma = 0.01, 0.001, 0.0001, 0.00001$ s/m). The results related to the peak of transient lightning current have taken at different points (at 2, 4, 6, 8, and 10 m) along the buried horizontal conductor and reported in Table 1. The input current to the buried horizontal conductor of 100 kA, 1.2/50 μs is developed and illustrated in Fig. 3, which is applied to horizontal buried conductor for observing the transient behavior of the current along the conductor. In order to get exciting current with required waveshape (i.e., 1.2/50 μs), the data of DEXP function constants is given as follows

$$\alpha = 1.4912 \times 10^4 \text{ s}^{-1}$$
$$\beta = 1.6335 \times 10^6 \text{ s}^{-1}$$

The change in space and time is taken as Δx and Δt, respectively. The length of the conductor is taken as 10, and it is divided into 10 equal parts. Where Δx is taken as 1 m and Δt is taken as 0.4×10^{-8} (in general, the value of Δt should be less than 1×10^{-8}).

Table 1 Transient response of current at different distances at different conductivities of the ground when 100 kA, 1.2/50 μs impulse current is excited

Conductivity of the ground (s/m)	Peak value of current at 2 m (A)	Peak value of current at 4 m (A)	Peak value of current at 6 m (A)	Peak value of current at 8 m (μA)	Peak value of current at 10 m (μA)
0.01	153.3	0.9221	0.005545	33.65	0.2377
0.001	1298	10.34	0.08245	657.1	5.75
0.0001	4754	39.05	0.3209	2636	23.82
0.00001	7857	64.75	0.5336	4395	39.86

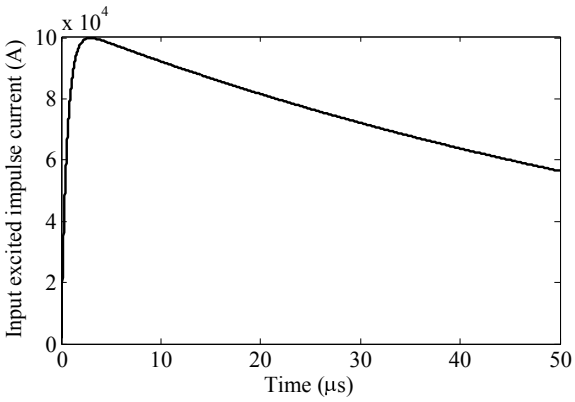

Fig. 3 Input excited impulse current waveform of 1.2/50 μs with peak of 100 kA

The transient response of current at a distance of 2 m along the buried conductor with respect to time is plotted and illustrated in Fig. 4. This response is obtained at different conductivities of the lossy ground, i.e., $\sigma = 0.01, 0.001, 0.0001, 0.00001$ s/m. It is observed from Fig. 4 that there is an increment nature observed in peak current and peak time when the conductance of the ground decreases.

The transient response of current at a distance of 4 m along the buried conductor with respect to time is plotted and illustrated in Fig. 5. This response is obtained at different conductivities of the lossy ground as mentioned earlier. It is observed from Fig. 5 that there is an increment nature observed in peak current and peak time when the conductance of the ground decreases.

The transient response of current at a distance of 6 m along the buried conductor with respect to time is plotted and illustrated in Fig. 6. This response is obtained at different conductivities of the lossy ground as mentioned earlier. It is observed from

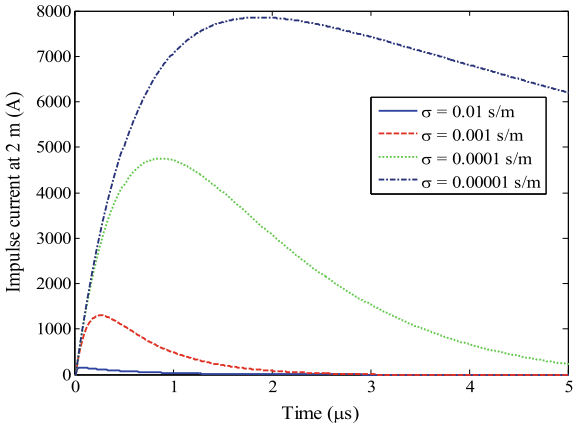

Fig. 4 Impulse current at 2 m with at different ground conductivities

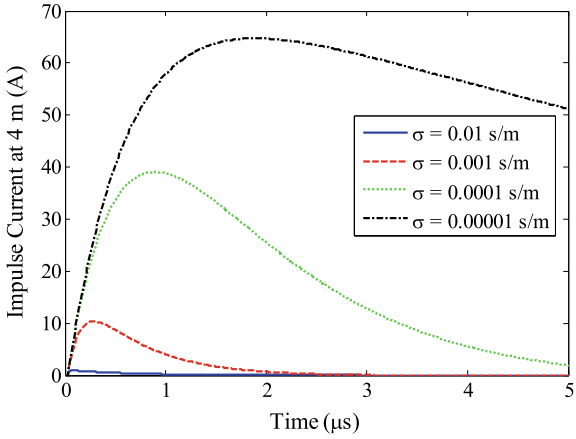

Fig. 5 Impulse current at 4 m with at different ground conductivities

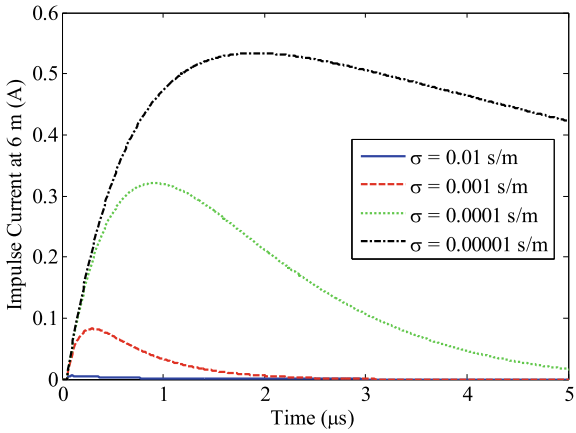

Fig. 6 Exciting current at 6 m for various ground conductivities

Fig. 6 that there is an increment nature observed in peak current and peak time when the conductance of the ground decreases.

The transient response of current at a distance of 8 m along the buried conductor with respect to time is plotted and illustrated in Fig. 7. This response is obtained at different conductivities of the lossy ground as mentioned earlier. It is observed from Fig. 7 that there is an increment nature observed in peak current and peak time when the conductance of the ground decreases.

The transient response of current at a distance of 10 m along the buried conductor with respect to time is plotted and illustrated in Fig. 8. This response is obtained at different conductivities of the lossy ground as mentioned earlier. It is observed from Fig. 8 that there is an increment nature observed in peak current and peak time when the conductance of the ground decreases.

Finally, it is observed from Figs. 4, 5, 6, 7, and 8 that there is a large variation of the peak current is observed at same peak time when the conductance of lossy

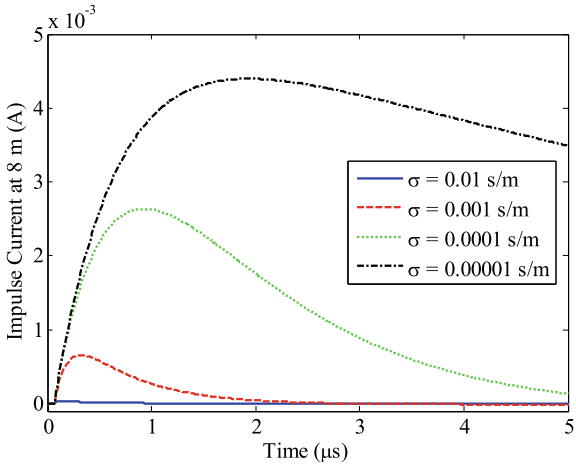

Fig. 7 Exciting current at 8 m for various ground conductivities

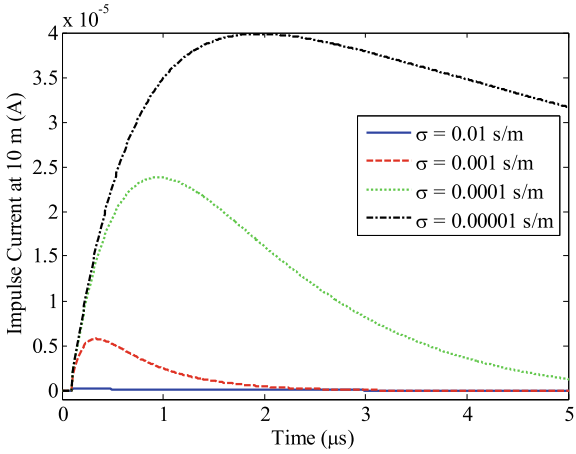

Fig. 8 Exciting current at 10 m for various ground conductivities

ground decreases. This type of analysis will be helpful in order to design the proper grounding to reduce the effect due to lightning impulse current.

6 Conclusion

The transient behavior of the lightning impulse current along the horizontal conductor buried in lossy medium is discussed and analyzed in this paper based on the transmission line (TL) approach. The TEs of buried conductor are solved by using finite difference time domain (FDTD) method to analyze the transient lightning current at different points along the conductor at various conductivities of lossy medium.

The peak currents are calculated at 2, 4, 6, 8, and 10 m along the buried conductor at the ground conductivities of $\sigma = 0.01, 0.001, 0.0001, 0.00001$ s/m and reported. It is observed from the results that the peak of current decreases when the observation point moves towards end from the starting or exciting point. Moreover, the peak current increases with the decreases of ground conductance. This means that the obtained peak current is inversely proportional to the ground conductivity. Thus, this type of analysis will be helpful in order to design proper grounding system to diminish the peak current along the horizontal buried conductor.

References

1. Jin X, Ali M (2010) Embedded antennas in dry and saturated concrete for application in wireless sensors. Progr Electromagn Res 102:197–211
2. Poljak D, Doric V (2006) Wire antenna model for transient analysis of simple grounding systems, part II: the horizontal grounding electrode. Progr Electromagn Res 64:167–189
3. Leonid GD, Menter FE (1996) Transient electromagnetic fields near large earthing systems. IEEE Trans Magn 32(3):1525–1528
4. Liu Y, Zitnik M, Thottappillil R (2001) An improved transmission-line model of grounding system. IEEE Trans Electromagn Compat 43(3):348–355
5. Ala G, Silvestre MLD (2002) A simulation model for electromagnetic transients in lightning protection systems. IEEE Trans Electromagn Compat 44(4):539–554
6. Suflis SA et al (1998) Transient behavior of a horizontal grounding rod under impulse current. In: Recent advances in circuits and systems, Word Scientific Publishing Company, Singapore, pp 61–64
7. Gonos IF et al (2003) Transient behavior of a horizontal electrode under impulse current. In: XIIIth International symposium on high voltage engineering
8. Masanobu T et al (2006) FDTD simulation of a horizontal grounding electrode and modeling of its equivalent circuit. IEEE Trans Electromagn Compat 48(4):817–825
9. Tesche FM et al (1997) EMC analysis methods and computational models. Wiley
10. Poljak D et al (2008) Comparison of wire antenna and modified transmission line approach to the assessment of frequency response of horizontal grounding electrodes. Eng Anal Boundary Elem 32(8):676–681
11. Poljak D et al (2016) Transient electromagnetic field coupling to buried thin wire configurations: antenna model versus transmission line approach in the time domain. Int J Antennas Propag
12. Paul CR (2008) Analysis of multiconductor transmission lines. Wiley, New York, NY, USA
13. Sunde ED (1968) Earth Conduction effects in transmission systems. Dover Publications, New York, NY, USA
14. Naidu MS, Kamaraju V (1995) High voltage engineering. Tata McGraw-Hill, New Delhi
15. Qin F, Mao C, Wu G, Zhou H (2016) Characteristic parameter estimation of EMP energy spectrum. In: 7th Asia Pacific international symposium on electromagnetic compatibility, pp 11–13
16. Camp M, Garbe H (2004) Parameter estimation of double exponential pulse (EMP, UWB) with least squares and Nelder Mead algorithm. IEEE Trans Electromagn Compat. 46(4):675–678
17. Ramarao G, Chandrasekaran K (2017) Calculation of multistage impulse circuit and its analytical function parameters. Int J Pure Appl Math 114(12):583–592
18. Ramarao G, Chandrasekaran K (2017) Evaluation of circuit and its analytical function parameters for lightning and switching impulse. In: 2017 International conference on innovations in electrical, electronics, instrumentation and media technology, Coimbatore, India, pp 302–305
19. Song J, Liu Y, Yu Y (2012) Numerical analysis of transmission line telegraph equation based on FDTD method. JCIT 7(20):258–265

20. Nagel JR (2010) The finite-difference time-domain (FDTD) algorithm. Department of Electrical and Computer Engineering, University of Utah
21. Gedney SD (1996) The application of the finite-difference time domain method to EMC analysis. In: Proceedings of symposium on electromagnetic compatibility. IEEE
22. Sullivan DM (2013) Electromagnetic simulation using the FDTD method. Wiley

Design of Smart Socket for Monitoring of IoT-Based Intelligent Smart Energy Management System

Challa Krishna Rao, Sarat Kumar Sahoo, M. Balamurugan, and Franco Fernando Yanine

Abstract Smart socket is designed for collecting and sending the data from the various nodes in one field to other fields. Smart socket consists of the Arduino_Uno, XBee, sensors, gateway, computer, USB, and IDE. This works emphasis on design and development of smart socket with wireless capability, this can be used to collect the data from each electrical device by using sensors. An XBee transmitter and receiver node are used for data communication in wireless networks. Real-time data gathered at the central node can be used to prioritize and schedule the appliances. Then, the system analyzes the data to generate control commands to turn the devices attached to the smart socket on or off. This paper presents the operation and functions of smart socket in different sensor network topologies. The results show that the proposed smart socket can correctly read the data from the various nodes and also send it to different nodes of different parameters.

Keywords Smart socket · IoT · Energy management

C. K. Rao (✉) · S. K. Sahoo
Parala Maharaja Engineering College, Sitallapalli, Berhampur, Odisha 761003, India
e-mail: krishnarao.challa@gmail.com

S. K. Sahoo
e-mail: sksahoo.ee@pmec.ac.in

C. K. Rao
Biju Patnaik University of Technology, Rourkela, Odisha 760010, India

M. Balamurugan
Jain Deemed to be University, Bengaluru, Karnataka 560041, India
e-mail: m.balamurugan@jainuniversity.ac.in

F. F. Yanine
School of Engineering, Universidad Finis Terrae, 1509 Santiago, Providencia, Chile
e-mail: fyanine@uc.cl

G. T. C. Sekhar et al. (eds.), *Intelligent Computing in Control and Communication*, Lecture Notes in Electrical Engineering 702,
https://doi.org/10.1007/978-981-15-8439-8_41

1 Introduction

Most of the technologies are dependent on the internet, and operation of devices through the internet is called the Internet of Things (IoT). It gives the improved solution to environmental issues. In the renewable energy system, the updating of smart grid gives several investigating issues similar to a prerequisite for technology-based metering, self-healing, etc. [1]. This improving end product includes products such as smart socket, smart receptacles, plus ordinary applications as domestic devices, smart grid, and automation. Internet of things based system will process work development, prioritizing duties plus assignments based on continuing assessment at a point of time, so the type of the organization can be monitored and efficient at regular intervals [2]. It is adaptable to domestic devices like lighting and thermal system, electrical and electronic gadgets, turning ON and OFF from local and remote location [3].

A different analysis was completed to estimate the energy price savings to the customer's absence of turning off the electric lamps and remain domestic appliances. Monitoring plus control of electrical devices based on time and possession can be considerably reducing energy expenditure cost. Hall Effect sensors are widely used as proximity sensors, position sensors, automotive sensors, voltage and current sensors, etc. The features of Hall effect sensors are high-speed operation, long life, no moving parts, and operated for wide temperature range (−40 to +150 °C). Hall Effect sensors can be used to measure both DC as well as AC because of the static and dynamic measuring capability [4].

Sensors are used to detect the magnetic field around the measuring terminals and there is no electrical contact between them which will consider as an additional advantage because it provides more safety to the device as well as sensors and it has very low-temperature dissipation compared to other sensors [4].

A smart socket is a device that is used to communicate data from an individual application in the environment to a gateway node. It consists of a microcontroller, sensor, XBee, ZigBee unit, and relay [1]. The smart socket is used to collect the utilization data from each device node and send it to the gateway node. The collected information is processed and appropriate resolution is received based on the constraints used by the parameter.

2 Smart Socket Model

A smart socket is the hardware device in an electrical system. A smart socket reads the power utilization of any appliance close to it. The data transmitted in real-time into the main controller to operate as inputs to the management algorithm. The socket can control the attached electrical device by turning it on or off. Figure 1 shows the design of the smart socket [3].

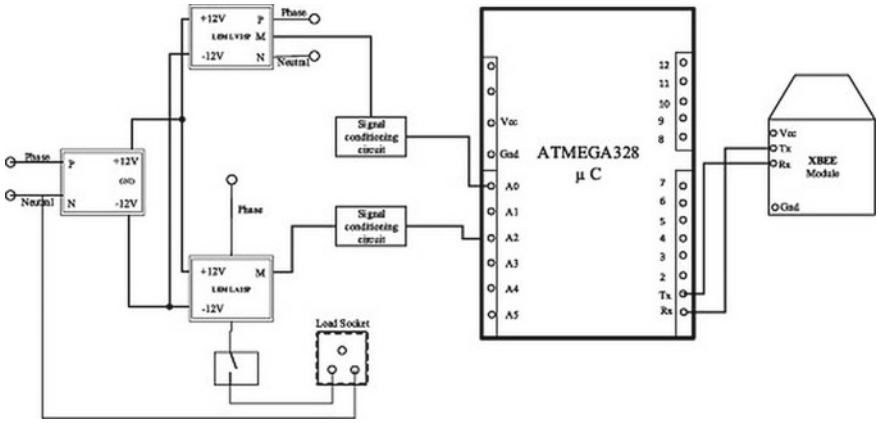

Fig. 1 The smart socket model [3]

Different methodologies are followed in the plan of the functionalities of a smart socket. The different protocols are used to collect the data from the sensors in the fields. This collected data transmitted to the gateway location with the help of communication techniques. Naturally, smart sockets carry out wireless communication by the main controller.

3 Smart Socket Components

This section describes the different components of smart socket and its functional operations.

3.1 Arduino_Uno

Arduino_Uno is integrated with different type's sensors, relays, and actuators and also allows monitoring and controlling different devices as shown in Fig. 2. It is used to collect information from different nodes deployed in the fields and also send information to different nodes in other fields. Arduino_Uno has functional libraries and can be downloaded from open-source and have different programming statements like other programming languages. It is used in many IoT based applications. Table 1 represents the specifications of Arduino_UNO.

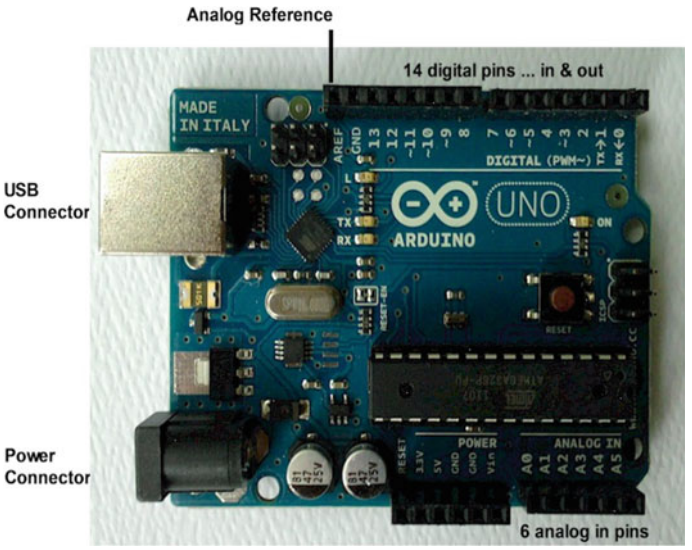

Fig. 2 Arduino_Uno pin diagram [5]

Table 1 Arduino_UNO specifications [5]

Parameter	Rating
Operating voltage	5 V
Clock speed	16 MHz
Digital input-output pins	14
Analog input pins	6
PWM pins	6
UART	1
Universal asynchronous receiver and transmitter	Dependent

3.2 XBee Module

This is a communication module, which is used to communicate data between two points. Figure 3 depicts the block diagram of XBee module and its pin configuration. Its operation can be divided into two main series, first one series is used for point-to-point communication, and second series used for different network topologies like star, tree, and mesh topologies. It is also an embedded system and provides the communication path with XBee protocol [1]. The parameters used in the XBee module is illustrated in Table 2.

Table 3 represents the comparison analysis of various communication protocols used.

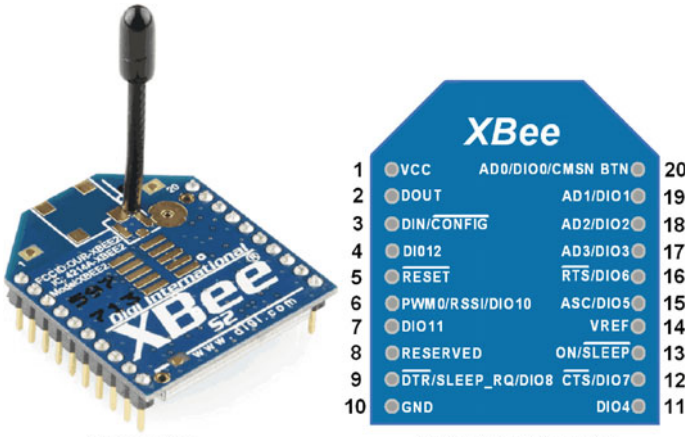

Fig. 3 XBee series [6]

Table 2 Parameters of XBee

Parameter	Rating
Working voltage	3.3 V
I/P pins	20
Digital I/O pins	12
Analog I/P pins	4
Clock speed	2.4 GHz
UART	1
Universal asynchronous receiver and transmitter	Dependent

Table 3 Comparison of wireless communication protocols [5]

	XBee	Bluetooth	Wi-Fi
Price	Low	High	High
Coverage (m)	10.0–100.0	10.0	100.0
Network topologies	Point–point, star, mesh, and tree	Piconet	Service set
Power required (mW)	63.0	100.0	0–500

3.3 Gateway

The gateway is a component, which is used to communication between different devices like smart socket, seniors, actuators, and web server. It is combination of Ethernet, XBee radio, an Arduino_Uno and power source, and interconnection between components as shown in Fig. 4.

Fig. 4 Gateway module [7]

3.4 Voltage Sensor

Hall-effect voltage sensors are extensively used in power electronic applications as an important element of a control loop in industrial systems. Due to inherent galvanic isolation, the measuring capability of the sensor has a very high bandwidth compared to the other sensing techniques [8]. In Hall effect voltage sensors the voltage can be measured by inserting a resistor across the terminals of the primary coil of measuring device. The magnetic flux around the primary coil is balanced by secondary coil. Therefore the balanced voltage can be measured by using this sensor [8].

Figure 5 shows the connection diagram for LEM LV 25-P Hall effect voltage sensors which consists of resistor R, the input voltage ($+V$, $-V$), Is is the secondary coil current, Rm is the tunable resistor (trim pot) and output voltage ($+U$, 0, $-U$). It can sense the voltage up to 500 V (AC or DC). The features of Hall Effect Voltage sensors are excellent accuracy, linearity, isolation. A safe environment is provided for device safety, temperature drift is low and measurement can be done for high

Fig. 5 LEM LV 25-P voltage sensor [8]

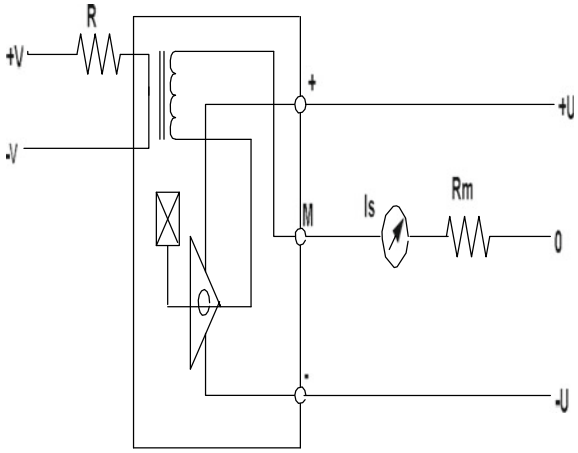

voltage in networks. The applications of Hall-effect sensors in electrical systems are to detect, monitor, and regulate voltages of the different systems.

3.5 Current Sensor

The current sensor is used to measure the continuously changing current in order to afford feedback for the control systems which will pave the way for correct and smooth operation of the converter. In order to detect the transient response, inductor waveform is required [4]. The features of the current sensor are response time is fast, excellent accuracy, temperature drift is low, no insertion losses, excellent linearity, and it have also been operated in wide frequency range [4].

Figure 6 shows the connection diagram for LEM LA55-P Hall Effect current sensors, here, Ip is the primary coil current, Is is the secondary coil current, Rm is the tunable resistor (trimpot) and output voltage ($+U$, 0, $-U$). It can sense the current up to 50 A (AC or DC) and generate the output signal in the range of (0–10 V) by adjusting the gain of Trim pot (Rm). To protect the circuit against overloading conditions the current rating of the system should be monitored which will seriously affect the system and it will lead to short circuit, failure, or malfunction of a device if some appropriate measures are not taken. So, sensors play a vital role to detect the fault and to minimize its effect. The utilizations of current sensor will also improve the transient response and efficiency of the system and it is also used to detect the ground fault.

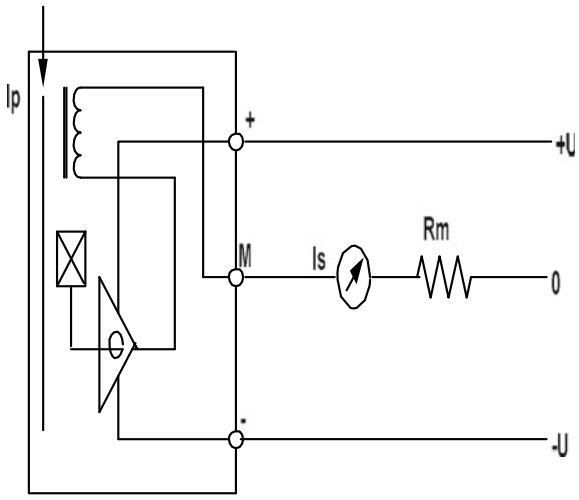

Fig. 6 LEM LA 55-P current sensor [4]

3.6 Breadboard

This is one of a kind board, which is used to integrate all components with the Arduino_Uno.

3.7 Relay Box

This box can be used to control the various tasks of the smart socket.

3.8 Ethernet Module

The Ethernet board as shown in Fig. 7. It is provided with the internet connection to the Arduino_Uno board and supports four-socket terminal points for external connection.

4 Implementation and Result

This section describes the implementation and result of the different components of smart socket and its performance.

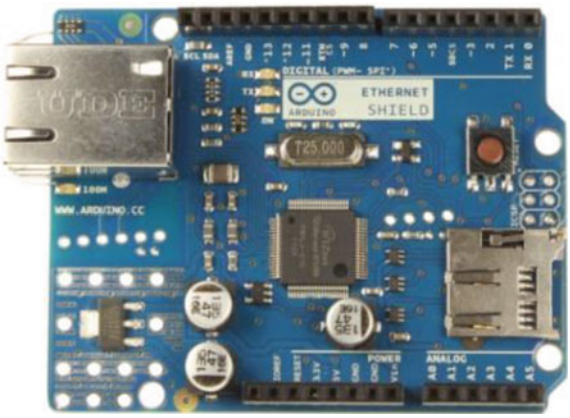

Fig. 7 Ethernet shield module [6]

4.1 The Block Diagram Model of Smart Socket

The smart socket is the main component of the system; its function is both controlling and monitoring of electrical devices. It is one kind of a socket linked to power source and to which the user connects the electrical devices. The smart socket consists of an Arduino_Uno, a microcontroller, sensors, XBee, plus relays. The smart socket diagram representation is shown in Fig. 8. The operation of Hall Effect based voltage and current sensor has described in the previous section with diagrammatic representation. The voltage rating of Arduino_Uno microcontroller is positive voltage with magnitude range (0–5 V). If the magnitude of input voltage is more than 5 V, it may get damaged. This problem can be solved by using a Zener diode with cut-off voltage of 4.70 V. The function of relay unit is the ability to turn the choosing device ON/OFF, i.e., depending on the information given by the controlling unit. The relay unit has a common pin which is connected to the other socket pin.

Figure 9 shows the various steps involved in the operations of the smart socket. It is based on developing programming code and uploading it to a board and getting results on the computer by program execution.

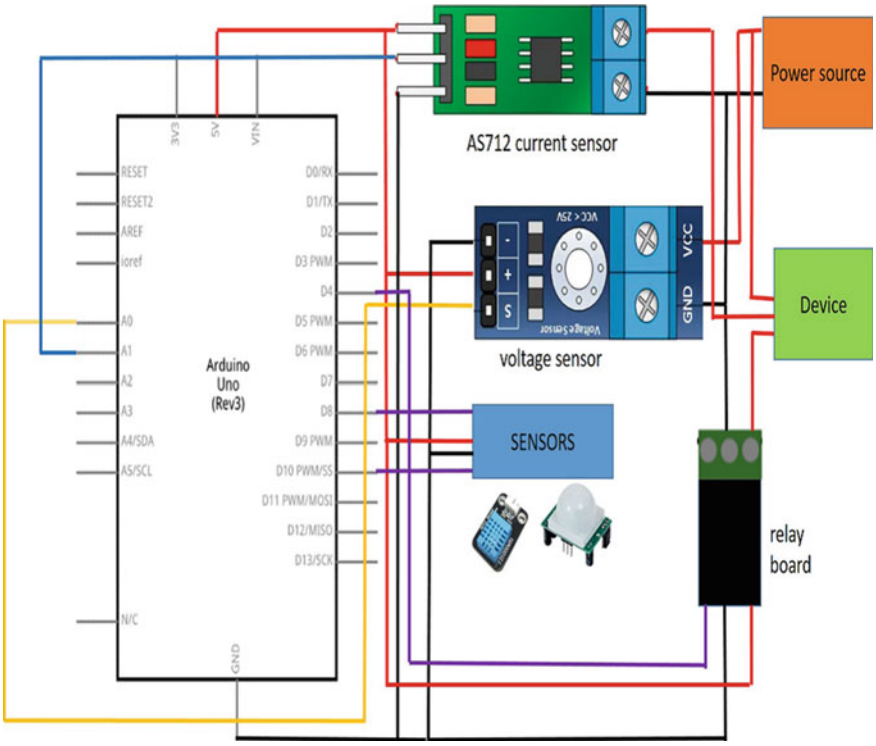

Fig. 8 Hardware setup block diagram of the smart socket [9]

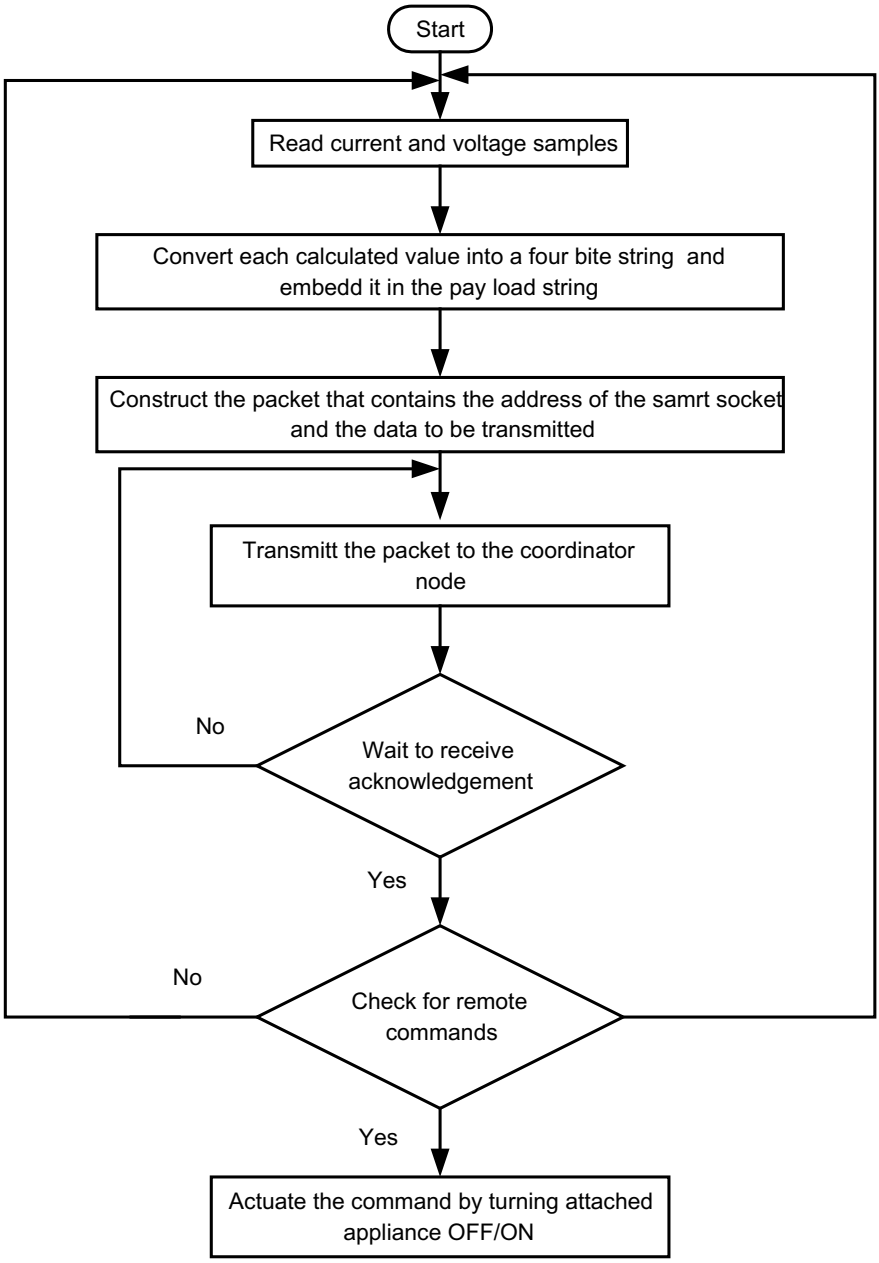

Fig. 9 Data processing in the smart socket [10]

4.2 Software Implementation of the Arduino_Uno

Nowadays, Arduino_Uno has become popular and an open-source programmable device in IoT. It is built with ATMEGA328 base microcontroller and IDE software. Figure 10 shows details of code uploaded to Arduino_Uno for the data receiving by serial communication. The function of the Arduino_Uno code is the collection of data from various sensors remotely. Second one is different coding for sending and receiving data from or to different components of the system.

Figure 10 shows the information collected from sensors and sent to both smart socket and gateway and two-way communication between them. The main aim of this test is to show information flow on a computer is by serial communication and the data is collected from the sensors. Figure 10 shows the Arduino_Uno connected to sensors by analog pins. It displays the information with serial communication on a computer screen.

Result: The development of programming code on the basis of the above flowchart is done by using IDE software. It is used for collecting data from various sensors, uploading the developed code into Arduino_Uno, and getting data from various sensors on the computer.

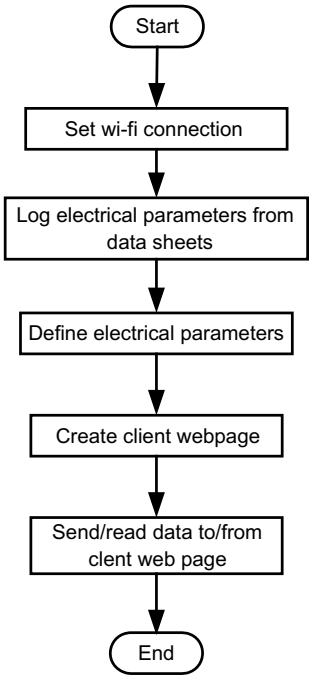

Fig. 10 Programming step of Arduino_Uno [11]

4.3 Implementing XBee-Arduino_Uno Interface

The XBee Series 2 unit has communication information device in the coordinator unit, based on the commands given by Arduino_Uno from various Router units via XBee unit and also collects the data that was obtained from the data uploaded to the local server using the Ethernet unit of the Arduino_Uno. The architecture of the XBee and Arduino_Uno interface is depicted in Fig. 11.

4.3.1 Router Node or End Node

This section describes the different components of Router node and its functional operations as shown in Table 4.

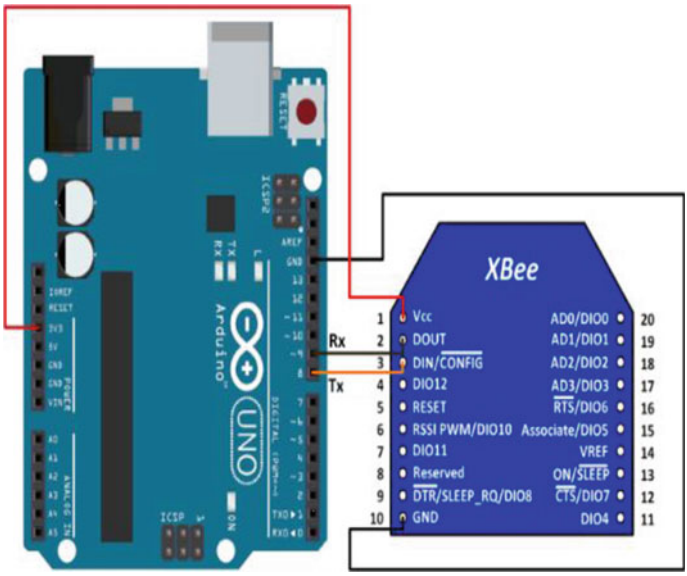

Fig. 11 XBee and Arduino_Uno interface [6]

Table 4 Components and its function [12]

Component	Function
XBee shield	Connecting the XBee and the Arduino
XBee series 2	Received sensing information from the Arduino plus sending the information to the coordinator node
Arduino_Uno	The program that collects the ongoing output used as communication link between the XBee and the sensors
Sensors' circuit	Receive information from the fields

Table 5 Components and its function [12]

Component	Function
XBee shield	A message link between the XBee and the Arduino
XBee series 2	Collect sensing data sent from the radio of the router node
Arduino_Uno	Communication link between the Bee and the computer
Ethernet shield	Message link between the coordinator and the database

4.3.2 Coordinator Node or Base Station

Table 5 describes the different components of coordinator node and its functional operations.

4.4 Programming the XBee-Arduino_Uno Interface

Arduino_Uno has a simple programming language and easy to use and flexible. It is open-source programming software and used to collects data from sensors deployed in the field. It is similar to other programming languages and based on processing. Using XBee protocol, to send data collected from sensors remotely from one to other station.

4.4.1 Programming XBee Coordinator or Router Node-Arduino_Uno Interface as Receiver

The router was collected information from the same field in environment as the coordinator and the programming was writing based on IDE software and the following flow chart shows the implementation steps.

Figure 12 shows, the connection details of an Arduino_Uno, XBee, USB to a computer, the sensor networks, and the router station and the programming code of coordinator node is shown in Fig. 13.

Result: When the router sending a message to the coordinator and that message received by the coordinator, it collects the data from the sensor as shown in serial monitor of the Arduino_Uno interface.

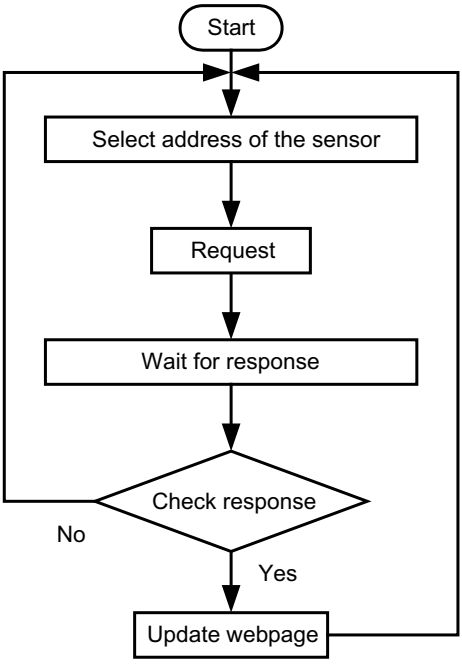

Fig. 12 Programming ladder of coordinator node [12]

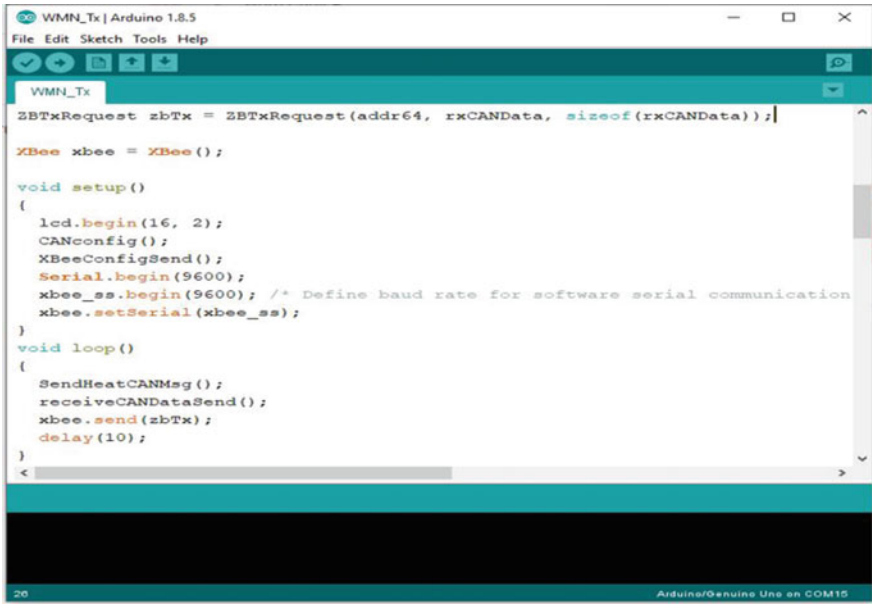

Fig. 13 Programming of coordinator node [5]

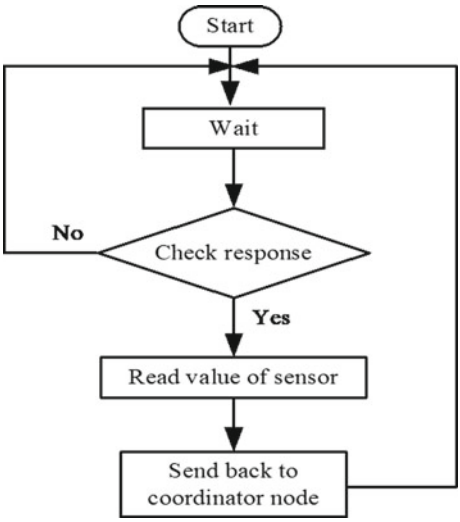

Fig. 14 Programming ladder of the coordinator node [12]

4.4.2 Programming XBee End-Device-Arduino_Uno Interface as Transmitter

The IDE software programmed end devices act as the transmitter connected to the sensor and received information from it and send the information via the router in the same field to the base station. The steps for programming method is shown in Fig. 14.

Result: When the router sending a message to the coordinator and that message received by the coordinator, it collects the data from the sensor as shown in serial monitor of the Arduino_Uno interface. The sensor output of the Coordinator node is depicted in Fig. 15.

5 Conclusion

This paper presents the design and software implementation of smart socket for IoT based smart energy systems. In addition to that, the characteristic feature of Hall Effect voltage and the current sensor has been presented in detail along with its application. The implementation of the smart socket based on Arduino_Uno, XBee, gateway, sensors, and software IDE. From the discussions, it has been conveyed that the socket is used to collect the data from various sensors and sending data to different fields. It is understood that this paper will afford a valuable source of information for researchers in the field of smart energy management systems.

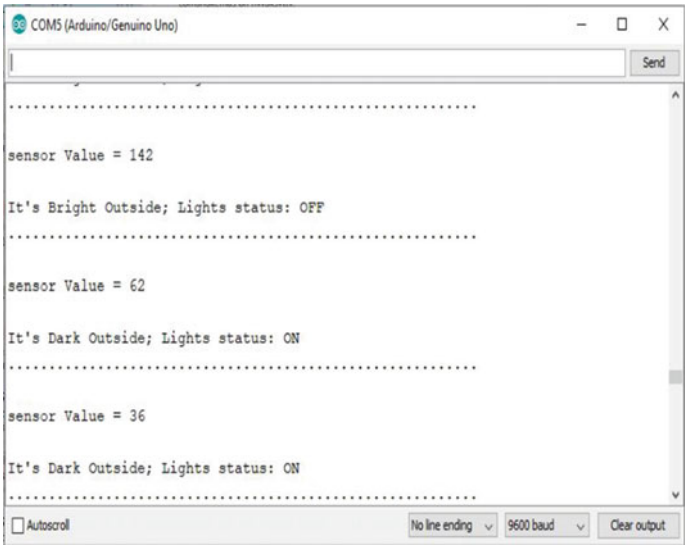

Fig. 15 Sensor output of the coordinator node [5]

References

1. Lem (2013) Voltage transducer LV 25-P I PN = 10 mA V PN = 10–500 V, data sheet. 18–20
2. Ziegler S, Woodward RC, Ho H, Iu C, Borle LJ (2009) Current sensing techniques: a review. IEEE Sens J 9
3. Pawar P, TarunKumar M, Vittal PK (2019) An IoT based intelligent smart energy management system with accurate forecasting and load strategy for renewable generation. Measurement
4. Rao CK, Sahoo SK, Balamurugan M, Satapathy SR, Patnaik A, Yanine FF (2020) Applications of sensors in solar energy systems. In: ICREISG-2020, Bhubaneswar, 14–15 Feb 2020
5. Tutorials point (2018) Arduino program structure. Available online: https://www.tutorialspoint.com/arduino/arduino_program_structure.htm
6. XBee 2 mW antena de PCB Serie 2. Available on https://5hertz.com/index.php?_page=product_info&products_id=324
7. Smart home energy management system monitoring and control of appliances using an Arduino based network in the context of a micro-grid. Available on https://www.aui.ma/sse-capstone-repository/pdf/Smart-Home-Energy-Management-System
8. Management system using rule-based controller on https://scholarworks.uaeu.ac
9. Lee S-H, Yang C-S (2017) An intelligent power monitoring and analysis system for distributed smart plugs sensor networks. Int J Distrib Sens Netw 13(7)
10. Al-Hassan E, Shareef H, Islam MM, Wahyudie A, Abdrabou AA (2018) Improved smart power socket for monitoring and controlling electrical home appliances. In: 2018 IEEE conference
11. Monzer KM, Tariq YM, Farouq A-T (2019) New design of socket modules for smart home applications. Instrum Mesure Metrol 18(1):43–48
12. DIGI International (2019) Zigbee wireless mesh networking. Available online: https://www.digi.com/resources/standards-and-technologies/zigbee-wireless-standard

WOA Optimized 2DOF TIDF Controller for Automatic Generation Control of Hydro-Thermal System

Kumaraswamy Simhadri, B. V. S. Acharyulu, Banaja Mohanty, and K. Suneel Goutham

Abstract In this competitive world, the growth rate of one nation majorly depends on electrical power, automatic generation control is one of the key factors for supplying standard and continuous power supply to all the consumers. An automatic generation control (AGC) system needs excellent control techniques to establish power system stability. This paper proposes a new two degree of freedom tilt integral derivative with filter (2DOF TIDF) controller to regulate AGC problems of two areas hydrothermal system. The modern proposed whale optimization algorithm (WOA) is used to obtain the optimal controller parameters. The comparative results with other techniques and controllers prove the advantage of the suggested 2DOF TIDF regulator with WOA. The sturdiness analysis of the controller shows the strength of the controller.

Keywords AGC · Fractional controllers · WOA technique

1 Introduction

The major goal of power system is to uphold system frequency and interarea power variation within the acceptable range even during usual and unusual conditions.

K. Simhadri (✉) · K. S. Goutham
EEE Department, Aditya Institute of Technology and Management (AITAM), Tekkali, Andhra Pradesh 532201, India
e-mail: kumar.simhadri@gmail.com

K. S. Goutham
e-mail: goutham.suneel@gmail.com

B. V. S. Acharyulu
EEE Department, Lendi Institute of Engineering and Technology, Vizianagaram 535005, India
e-mail: acharyulu201@yahoo.com

B. Mohanty
EE Department, Veer Surendra Sai University of Technology (VSSUT), Burla, Odisha 768018, India
e-mail: banaja_m@yahoo.com

G. T. C. Sekhar et al. (eds.), *Intelligent Computing in Control and Communication*, Lecture Notes in Electrical Engineering 702,
https://doi.org/10.1007/978-981-15-8439-8_42

All ways equilibrium is maintained between power demand and power generation, otherwise it will cause either rise or lessen the system frequency. This will create the improper operation of the electrical appliances. The AGC will take care alteration in system frequency and improves the system solidity [1]. Consequently, innovative methods are to be incorporated along with AGC to lessen the frequency errors and to maintain good interarea power interchange.

Elgerd and Fosha established finest regulation of frequency in a multi area power system (MAPS) [2]. Due to the simplicity and reliability of the classical controllers like PI, PID are used to minimize frequency variations [3]. To investigate finest gains of the classical controllers for AGC, there are various optimization techniques introduced by different authors. The PID controller gains are optimized by PSO for AGC [4]. Gozde et al. [5] proposed craziness based PSO to reduce the frequency variations in a multiarea thermal power system. The multiarea multisource (MAMS) power system stability can be improved by differential evolution (DE) tuned PID controller parameters [6]. The hybridization of two algorithms proves the finest improvement of MAMS power system [7]. Recently many authors used 2DOF structure to many of the controllers to trace the set point and regulate the system in the occurrence of disturbance. Sahu et al. proposed DE optimized 2DOFPID for AGC to maintain system stability also stated that 2DOFPID offers better performance even under the presence non-linearities [8]. In recent days, an attempt has been made towards the use of 2DOF fractional controllers for AGC [9]. It is motivated from the above literature, a new 2DOF TIDF regulator is proposed for AGC of two area hydrothermal power system (TAHTPS), and WOA is applied to tune K_{p}, K_{i}, K_{d}, K_{p1}, K_{d1}, dw, N, n to strengthen the system performance in terms of settling time, overshoot, and under shoot.

The noticeable significances of current work are abridged as follows:

- To project and implement a new 2DOF TIDF regulator for AGC of TAHTPS.
- To optimize the controller parameters using WOA.
- To validate the advantage of 2DOF TIDF over GA based PI, hFA-PS based PI/PID.
- To study the robustness of the controller under parameter varied conditions.

2 Power System Model

The examined system during this study is TAHTPS is shown in Fig. 1 [7]. "Each control area consists of non-reheat thermal system and a governor based hydro system. The rating of each control area is 2000 MW and a load 1000 MW is applied. T_{g1}, T_{g2} are called governor time constants at area-1 and 2; T_{t1}, T_{t2} are turbine time constants; Δf_1, Δf_2 are the frequency deviations at area-1 and 2; B_1, B_2 are the frequency bias constants; R_1, R_2 are the regulation constants; ΔP_{D} is the load disturbance. The nominal parameters of the system are represented in Appendix".

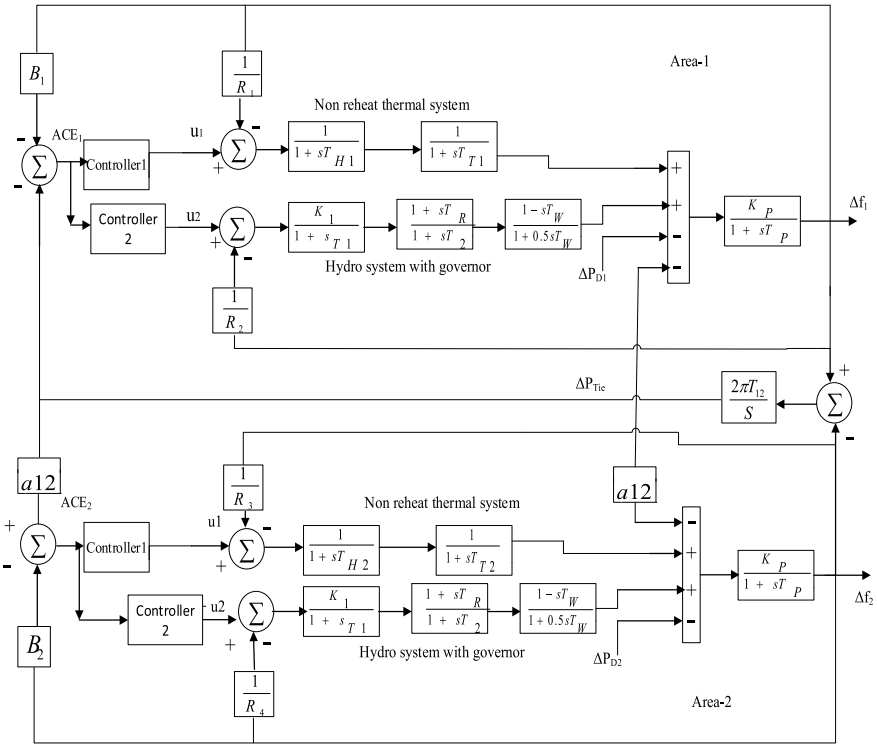

Fig. 1 Two area hydro thermal system [7]

3 2DOF TIDF Control Structure

The combination of 2DOF structure and TIDF controller is called 2DOF TIDF is suggested for AGC. The 2DOF structure will improve system regulation and performance during disturbances. TIDF controller can be formed by including a tilted component in series to the proportional gain. The derivative mode of this regulator will enhance the steadiness of the system and also speed up the system response even under abnormal conditions [10]. TIDF structure is taken from FOMCON toolbox [11]. Figure 2 shows block diagram of 2DOF TIDF controller.

4 Whale Optimization Algorithm

It was a nature motivated algorithm suggested by Mirjalili and Lewis [12]. The no. of iterations are divided into two sections. In the first section of repetitions, half of the whales move arbitrarily which causes high exploration, second section of iterations the whales move themselves about best location.

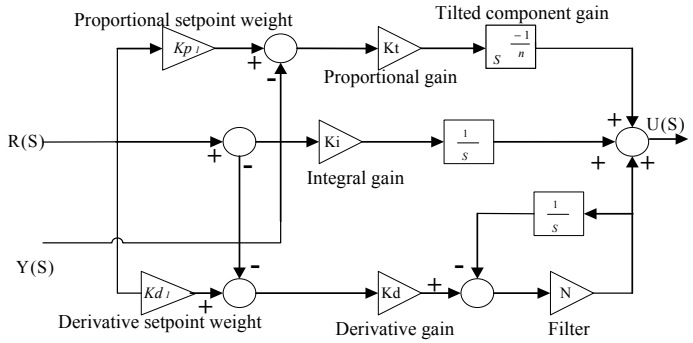

Fig. 2 Structure of 2DOF TIDF controller

WOA comprises three approaches

1. Encircling prey
2. Searching prey
3. Bubble net feeding method.

4.1 Encircling Prey

In this section, whales recognize the position of target and surrounding them. The initialization of control variables is totally arbitrary in the search space as shown in Eqs. (1) and (2). Hence WOA considers the present best position as location of target prey [12]

$$\vec{E} = \left| \vec{D} \cdot \underset{\text{best}}{\vec{y}}(k) - \vec{y}(k) \right| \tag{1}$$

$$\vec{y}(k+1) = \underset{\text{best}}{\vec{y}}(k) - \vec{B} \cdot \vec{E} \tag{2}$$

where $\vec{y}$ is the population, $\underset{\text{best}}{\vec{y}}$ is best solution calculated, k is the current iteration, the values of $\vec{B}$ and $\vec{D}$ are calculated using Eqs. (3) and (4) [12]

$$\vec{B} = 2\vec{b}\vec{s}_1 - \vec{b} \tag{3}$$

$$\vec{D} = 2\vec{s}_2 \tag{4}$$

$\vec{s}_1$ and $\vec{s}_2$ are two random vectors selected between the range of (0, 1); $\vec{b}$ is search direction linearly increasing matrix.

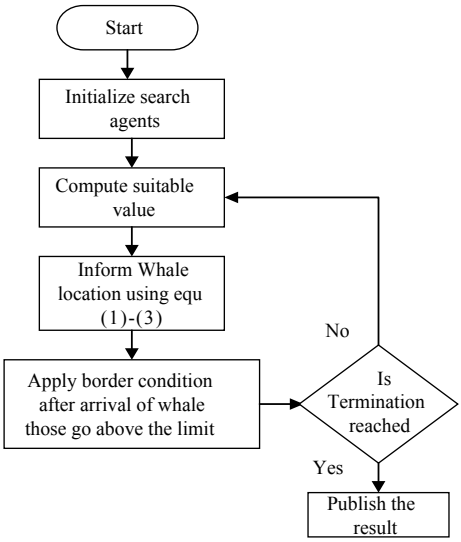

Fig. 3 Flow chart of WOA

4.2 Searching Prey

The location of whales is restructured based on arbitrarily selected whale instead of best whale computed so far. Flowchart of WOA is represented in Fig. 3.

5 Results and Analysis

The performance of 2DOF TIDF is tested for TAHTPS. WOA is used to obtain the optimal parameters of 2DOF TIDF controller. A load disturbance of 1.5% SLP is applied at area-1. WOA algorithm is run for 50 iterations to obtain optimal parameters. The optimal controller parameters are mentioned as follows: $K_{\mathrm{P1}} = 1.4825$; $K_{\mathrm{d1}} = 1.0529$; $K_{\mathrm{t}} = 0.9578$; $K_{\mathrm{i}} = 1.9719$; $K_{\mathrm{d}} = 0.7984$; $n = 7.2725$; $N_1 = 31.2773$; $K_{\mathrm{P11}} = 1.6980$; $K_{\mathrm{d11}} = 0.1031$; $K_{\mathrm{t1}} = 0.6443$; $K_{\mathrm{i1}} = 0.8838$; $K_{\mathrm{d1}} = 0.0133$; $n_1 = 1.4804$; $N_2 = 123.5880$; $K_{\mathrm{P12}} = 1.8673$; $K_{\mathrm{d12}} = 1.2772$; $K_{\mathrm{t2}} = 0.9199$; $K_{\mathrm{i2}} = 1.4816$; $K_{\mathrm{d2}} = 0.3787$; $n_2 = 3.6141$; $N_3 = 185.3321$; $K_{\mathrm{P13}} = 0.8159$; $K_{\mathrm{d13}} = 0.0322$; $K_{\mathrm{t3}} = 0.0880$; $K_{\mathrm{i3}} = 1.4118$; $K_{\mathrm{d3}} = 0.8994$; $n_3 = 8.2993$; $N_4 = 97.0070$; Corresponding system performance is mentioned in Fig. 4a–c. The frequency deviations at area-1 and 2, interarea power variation of WOA optimized 2DOF TIDF compared to hFA-PS PI/PID are represented in Table 1.

It is observed from Table 1 that lowest value of ITAE is attained with WOA tuned 2DOF TIDF regulator than the hFA-PS tuned PI and PID and GA and ZN tuned PI controller [7]. It is also observed from Table 1 that, the settling time (ST) for ΔF_1, ΔF_2, ΔP_{tie} is improved by 14.89, 59.61, 26.02% with suggested WOA optimized

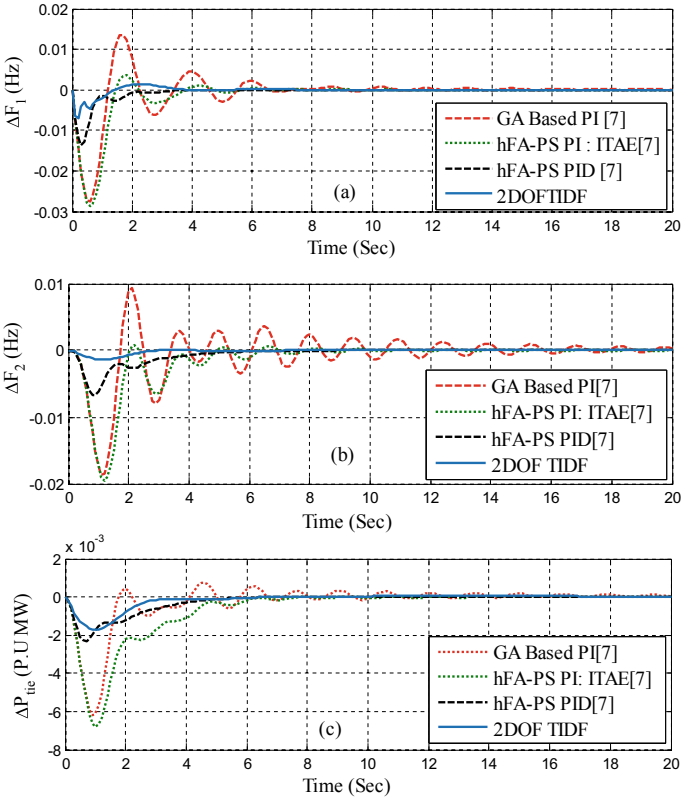

Fig. 4 **a–c** Simulation analysis of 2DOF TIDF controller for two area hydro thermal systems. **a** ΔF_1 versus time in s. **b** ΔF_2 versus time in s. **c** ΔP_{tie} (P.U MW) versus time in s

Table 1 Evaluation of dynamic performance of 2DOF TIDF controller compared to hFA-PS PID

Optimized controller	Settling times (T_s) in s			Performance index
	ΔF_1	ΔF_2	ΔP_{tie}	ITAE $\times 10^{-3}$
GA tuned PI [7]	16.03	25.72	9.84	625.8
hFA–PS tuned PI [7]	6.43	8.60	5.98	228.5
hFA–PS tuned PID [7]	3.29	5.20	3.92	87.0
WOA tuned 2DOF TIDF	2.8	2.1	2.9	28.1

2DOF TIDF regulator contrasted to hFA-PS optimized PID controller, 56.45, 75.58, 51.50% compared to hFA-PS optimized PI controller and 82.53, 91.83, 70.52% compared to GA tuned PI controller.

Therefore, it is perceived that the suggested WOA optimized 2DOF TIDF controller will reduce the frequency errors and interarea power deviation in both areas.

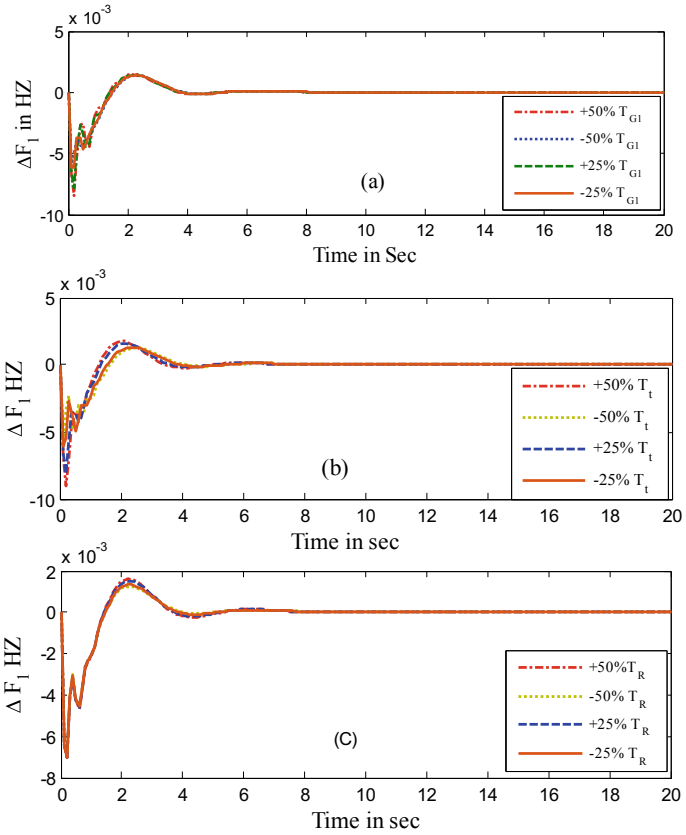

Fig. 5 **a–c** Robustness analysis of proposed controller for AGC

The sturdiness analysis of proposed controller is shown in Fig. 5a–c. The parameters such as T_{G1}, T_t and T_R are varied from +50 to −50% and from +25 to −25% for the considered system, the corresponding STs, overshoots are mentioned in Table 2. The simulations results of frequency variation at area-1 show the strength of the proposed controller.

6 Conclusion

The proposed 2DOF TIDF regulator is tested for AGC of TAHTPS to lessen the frequency variations and to improve interarea power transactions. The proposed recent WOA algorithm is used to achieve the optimal gains of the controller. The comparative results show the superiority of the controller over hFA-PS PID/PI controller. The robustness analysis proves the strength of the controller. Hence it

Table 2 Frequency variation of hydro-thermal system for parameter varied condition

Parameter variation	% Change	Settling times			Overshoot[a]			Obj[a]
		ΔF_1 (Hz)	ΔF_2 (Hz)	ΔP_{tie}	ΔF_1 (Hz)	ΔF_2 (Hz)	ΔP_{tie}	
T_{G1} at area-1	+50	2.8	2.1	2.8	1.5	0.027	0.017	27.6
	−50	2.9	2.2	2.9	1.4	0.029	0.017	28.7
	+25	2.8	2.1	2.9	1.4	0.027	0.017	27.8
	−25	2.8	2.1	2.9	1.4	0.028	0.017	28.4
T_t at area-1	+50	2.8	2.2	2.9	1.4	0.028	0.017	28.6
	−50	2.8	2.1	2.9	1.4	0.026	0.017	26.8
	+25	2.9	2.1	2.9	1.4	0.028	0.017	27.8
	−25	2.7	2.1	2.9	1.5	0.026	0.017	28.4
T_R at area-1	+50	2.8	2.1	2.8	1.4	0.026	0.017	28.5
	−50	2.8	2.2	2.9	1.4	0.028	0.017	28.6
	+25	2.9	2.1	2.9	1.3	0.027	0.017	28.6
	−25	2.9	2.2	2.9	1.5	0.028	0.017	28.6

[a]Indicates overshoots and objective function values are multiplied by 10^{-3}

is suggested that with the combination fuzzy this controller can be used for different types of engineering problems.

Appendix

Multi-area multi-source system [7]: $f = 50$ Hz, B_1, $B_2 = 0.410$ p.u. MW/Hz; $R_1 = 1.99.0$ Hz/p.u.; $R_2 = 2.39$ Hz/p.u.; $T_{G1} = 0.079$ s; $T_{t1} = 0.29$ s; $K_P = 99.99$ Hz/p.u.; $T_P = 19.99$ s; $K_1 = 0.99$; $T_1 = 46.99$ s; $T_w = 1.0$ s; $T_2 = 0.511$ s; $T_R = 4.99$ s; $T_{12} = 0.0707$ p.u.; $a_{12} = -0.99$.

References

1. Cohn N (1956) Some aspects of tie-line bias control on interconnected power systems. IEEE Trans Power Appar Syst 75:1415–1436
2. Elgerd OI, Fosha CE (1970) Optimum megawatt-frequency control of multi-area electric energy systems. IEEE Trans Power Appar Syst 89:556–563
3. Saikia LC, Nanda J, Mishra S (2011) Performance comparison of several classical controllers in AGC for multi-area interconnected thermal system. Int J Electr Power Energy Syst 33:394–401
4. Ghoshal SP (2004) Optimizations of PID gains by particle swarm optimizations in fuzzy based automatic generation control. Electr Power Syst Res 72(3):203–212
5. Gozde H, Taplamacioglu MC (2011) Automatic generation control application with craziness based particle swarm optimization in a thermal power system. Int J Electr Power Energy Syst 33(1):8–16

6. Mohanty B, Panda S, Hota PK (2014) Controller parameters tuning of differential evolution algorithm and its application to load frequency control of multi-source power system. Int J Electr Power Energy Syst 54:77–85
7. Sahu RK, Panda S, Padhan S (2015) A hybrid firefly algorithm and pattern search technique for automatic generation control of multi area power systems. Int J Electr Power Energy Syst 64:9–23
8. Sahu RK, Panda S, Rout UK (2013) DE optimized parallel 2-DOF PID controller for load frequency control of power system with governor dead-band nonlinearity. Int J Electr Power Energy Syst 49:19–33
9. Mohapatra TK, Dey AK, Sahu BK (2020) Employment of quasi oppositional SSA-based two degree of freedom fractional order PID controller for AGC of assorted sources of generation. IET Gener Transm Distrib. https://doi/org/10.1049/iet-gtd.2019.0284
10. Sahu RK, Panda S, Biswal A, Chandra Sekhar GT (2016) Design and analysis of tilt integral derivative controller with filter for load frequency control of multi-area inter connected power systems. ISA Trans 61:251–264
11. Tepljakov A, Petlenkov E, Belikov J (2011) FOMCON: a MATLAB toolbox for fractional-order system identification and control. Int J Microelectron Comput Sci 2(2):51–62
12. Mirjalili S, Lewis A (2016) The whale optimization algorithm. Adv Eng Softw 95:51–67

Characterization of Yttrium-Doped NiAl Fabricated at Different Substrate Temperatures Using EBPVD for Bond Coat in Thermal Barrier Coatings

Hemalatha Kandi, Ramji Koona, and G. M. J. Raju

Abstract A film has been developed by electron beam physical vapor deposition (EBPVD) method on Inconel 625 substrate with substrate temperature of 873 K for bond coat in thermal barrier application. For this coating, a composition of Ni-49.8Al-0.2Y material formed into a pellet which is prepared by using a hydraulic press. The structural information, roughness, and morphology of coating have been characterized by using X-ray diffraction (XRD), atomic force microscopy (AFM), and field emission scanning electron microscopy (FESEM), respectively. The obtained results show that the crystallinity size is 29.43 nm, the average roughness is 88.14 nm in 2D and 3D topography, and the film is coated uniformly.

Keywords EBPVD technique · AFM · FESEM

1 Introduction

Thermal barrier coatings (TBC) are widely used to protect a substrate, against the thermal affected environments. TBC systems basically consist of topcoat, bond coat, and thermally grown oxide (TGO) deposited on substrate for the application of gas turbine engines [1]. The Ni based super alloy such as Hastalloys and Inconel 625 contains significant amounts of alloying elements such as Cr, Mo, Al, Ti, Fe, and C, and these have been used as a substrate for TBC applications [2–4]. These alloys

H. Kandi (✉) · R. Koona
Department of Mechanical Engineering, Andhra University College of Engineering (A), Visakhapatnam 530003, India
e-mail: hemalathakandi2014@gmail.com

R. Koona
e-mail: ramjidme@yahoo.co.in

G. M. J. Raju
Department of Chemical Engineering, Andhra University College of Engineering (A), Visakhapatnam 530003, India
e-mail: gmjraju@gmail.com

G. T. C. Sekhar et al. (eds.), *Intelligent Computing in Control and Communication*, Lecture Notes in Electrical Engineering 702,
https://doi.org/10.1007/978-981-15-8439-8_43

possess excellent corrosion, oxidation, and erosion resistance at high temperatures and have good mechanical strength. The major purpose of the bond coat is used to improve the adhesion and reduction of thermal strain aids in improvement of oxidation resistance between the ceramic topcoat and substrate. Currently, MCrAlY (M is Ni or/and Co) coatings are used as a bond coat, and depending on the chemical composition of the substrate, these can exhibit an excellent protection against high temperature oxidation and corrosion. Intended for a MCrAlY bond coat, the Al diffusion in the composition is the foremost element causing the microstructural changes because of the change in Al to β-Al_2O_3. For comparison, NiCoCrAlY bond coat presents better characteristics of oxidation and crack resistance than CoNiCrAlY with a higher Al content which is due to the lower β-depletion rate and smaller Al inter-diffusion coefficient [5].

During the thermal cycling process, the TGO formed on NiAl will spall which may obstruct its application due to poor adherence. To overcome these obstructions, additional reactive elements (0.05–0.5%) such as Hf, Zr, Dy, and Y in the composition will improve the TGO adherence as a doping element [6].

The main objective of this paper is to develop Ni-49.8Al-0.2Y bond coat on Inconel 625 substrate using EBPVD method. An investigation has been done on how the substrate temperature (873 K) influences the phase evaluation and surface properties of the deposited film. Study is carried by analyzing the average roughness and surface morphology by using X-ray diffractometer (Model XPERT-PRO), atomic force microscopy (AFM), and field emission electron scanning microscopy (FESEM), respectively.

2 Experimentation

High-purity pellet with composition of Ni-49.8Al-0.2Y is prepared by using hydraulic press and after that annealed at temperature of 1050 ºC for 2 h. Before deposition, the substrate was preheated at temperatures of 873 K for around 1 h. EBPVD consists of one electron gun and substrate holder which holds the substrate, bond coat pellet was placed in the curable which was placed beneath the substrate holder, coating was developed by applying a voltage 4 kV, and 50 mAps is applied for E-beam. At first, the chamber is evacuated with 8 X 10^{-4} millibar base pressure. Bond coating was deposited in vacuum under 9 X 10^{-6} millibar working pressure to avoid contaminations. To achieve uniform deposition coating, the target was kept at 8 cm away from the substrate which was placed in the substrate holder, and sustained deposition time is 1:30 min. The substrates were heated with a heater and monitored by a thermocouple. After coating, coated samples were annealed at 1000 ºC. The phase evaluation of a coating was investigated at a room temperature by X-ray diffractometer (Model XPERT-PRO) to validate the result. The obtained graph was loaded in Match! Software. Scherrer's equation is used to calculate crystallite size. Surface topology and roughness of the bond coating are measured by atomic force

microscopy (AFM) (XEI's Park System). Surface morphology was analyzed by field emission scanning electron microscopy (FE-SEM) (JEOL).

3 Results with Discussions

This section describes the analysis and results of XRD, AFM, and FESEM of bond coat surface.

3.1 XRD Analysis

XRD pattern of bond coat deposited on Inconel 625 substrate with substrate temperature at an 873 K done by EBPVD technique is shown in Fig. 1. From the results, coating curves contain the highest peak [7] at 45.669º, and peak positions are in good agreement with a PDF number 96-210-0949 in match software phase analysis. The average crystallite size has been estimated from projecting diffraction peaks by using Debye–Scherer's equation.

$$D(\text{nm}) = k\lambda/\beta\text{Cos}\theta \tag{1}$$

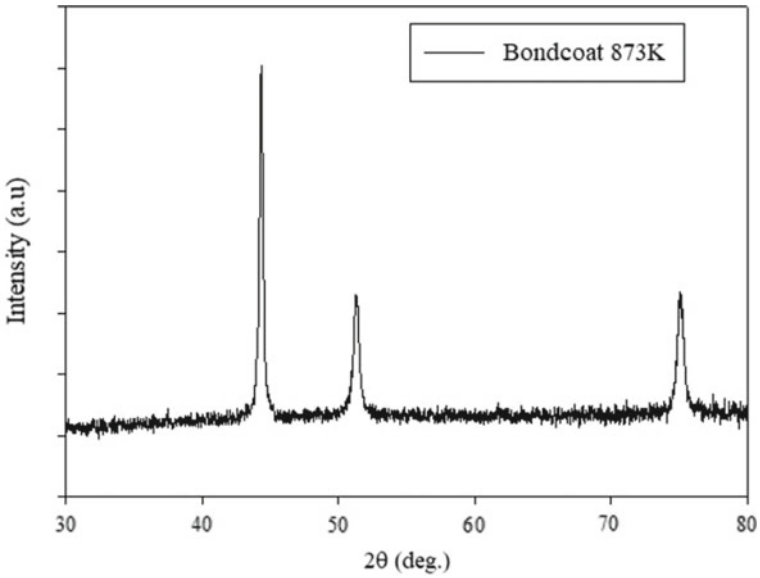

Fig. 1 XRD pattern of bond coat at 873 K substrate temperature

Table 1 From XRD analysis crystallite size and lattice strain

Substrate temperature (K)	Crystallite size (±1) (nm)	Lattice strain
873	29.43	0.0032

The representation notations of Eq. (1) are 'D'—Average crystallite cize, 'k'—Shape factor ($k = 0.89$), 'λ—Wavelength of X-rays ($\lambda = 1.54\text{A}^{\circ}$), '$\beta$'—Full width at half maxima, and 'θ'—Braggs angle.

Due to higher substrate temperature, the crystallinity size was increased to 29.43 nm, and lattice strain is 0.0032 as given in Table1.

3.2 AFM Analysis of Bond Coat Surface

The bond coat surface roughness is the significant parameter for the thermal barrier applications. The roughness parameters are determined by scanning the surface sample followed by analyzing the topography of the sample. Figures 2 and 3a, b represent the 2D and 3D topography diagram of coated samples which are coated at 873 K substrate temperature by EBPVD. Data collected from AFM imagery topography are given in Table2 in which average surface roughness (Ra) value is 88.14. These results are significant that the surface roughness are applicable because of asperity height distribution of these surfaces that are approximately Gaussian asperity [8].

These results concluded that bond coating at 873 K substrate temperature exhibits more bumpy texture on the surface.

3.3 FESEM Analyis of Bondcoat Surface

Bond coating deposition was done by EBPVD method with substrate temperature of 873 K. The bond coat surface morphology was characterized by FESEM. From these observations, Fig. 3 illustrates the surface morphology of bond coat which was formed with few blowholes. This happens due to insufficient burning and impurities present.

4 Conclusion

In this paper, the effect of substrate temperature on Yttrium-doped NiAl bond coat which was deposited by EBPVD method on Inconel 625 is studied.

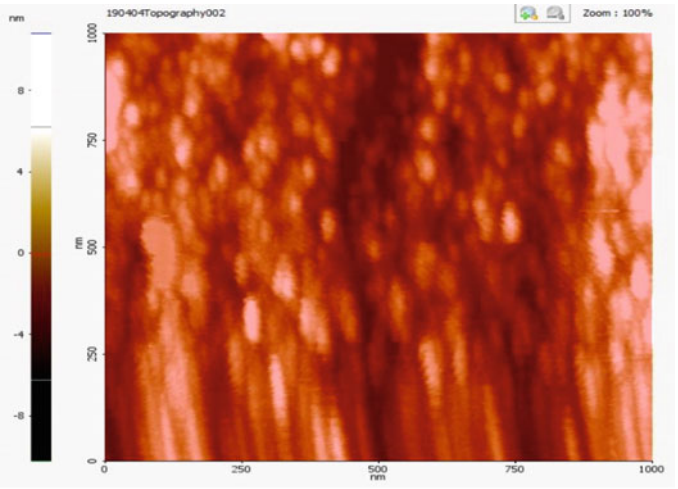

(a) 2D

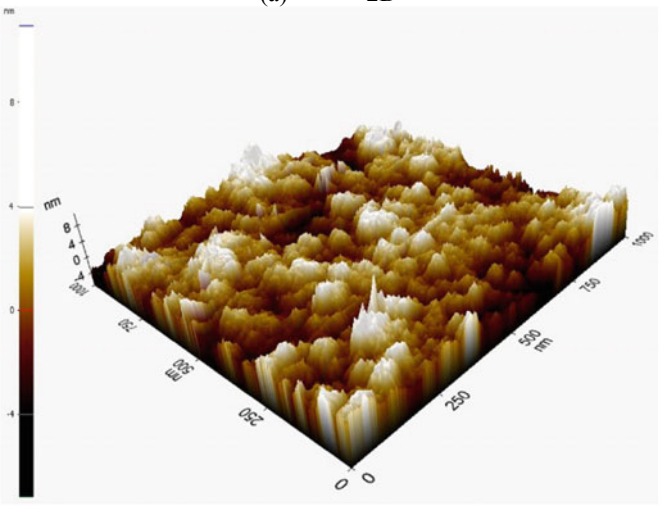

(b) 3D

Fig. 2 **a**–**b** AFM (2D and 3D) diagrams of coated sample at 873 K

Table 2 Roughness parameters of bond coat at 873 K substrate temperature

Substrate temperature (K)	Ra (nm)
873	88.14

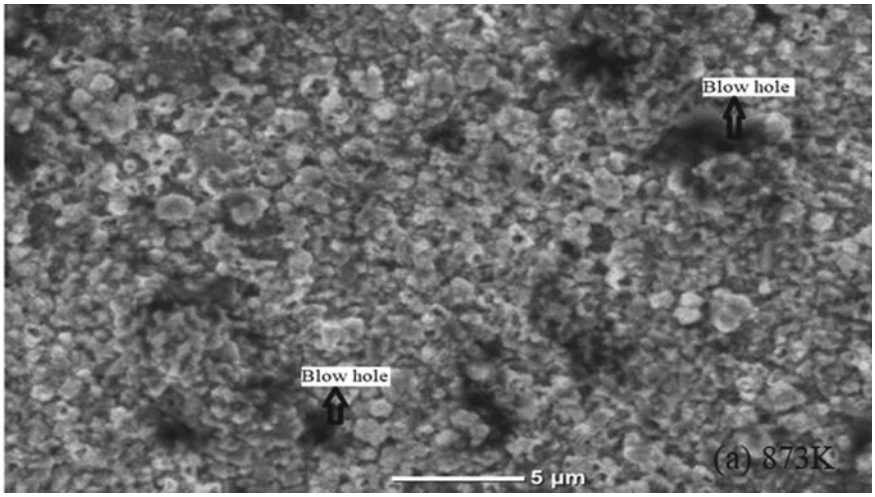

Fig. 3 Surface morphology of bond coating with a substrate temperature (873 K)

- The crystallinity was formed with 29.43 nm with the lattice strain of 0.0032 by XRD analysis.
- The average surface roughness is 88.14 nm and shown that there are bumpy depositions on the surface when deposited at substrate temperature of 823 K by AFM analysis.
- Surface morphology was observed by FESEM, and by this, few blows are seen on the coated surface at substrate temperature (873 K) which is not suitable for bond coating by EBPVD method.

The future scope of this work is to check the properties at higher temperatures substrate depositions.

Acknowledgements The authors thankfully acknowledge the financial support from TEQIP-II through Ministry of Human Resource Development, Government of India, and greatly appreciated Andhra University College of Engineering (A), Andhra University, Visakhapatnam, Andhra Pradesh, India.

References

1. Miller RA (1987) Current status of thermal barrier coatings- An overview. Surf Coat Technol 30(1):1–11. https://doi.org/10.1016/0257-8972(87)90003-x
2. Rai SK, Kumar A, Shankar V, Jayakumar TB, Sankara Rao K, Raj B (2004) Characterization of microstructures in Inconel 625 using X-ray diffraction peak broadening and lattice parameter measurements. ScriptaMaterialia 51(1):59–63. https://doi.org/10.1016/j.scriptamat.2004.03.017

3. Zhao J-C, Larsen M, Ravikumar V (2000) Phase precipitation and time–temperature-transformation diagram of Hastelloy X. Mater Sci Eng: A 293(1–2):112–119. https://doi.org/10.1016/s0921-5093(00)01049-2
4. Juliand O, Alejandro T (2012) Thermal barrier coatings for gas turbine applications: failure mechanisums and key microstructural features, pp 149–158, No 176. ISSN 0012–7353
5. Weng W-X, Wang Y-M, Liao Y-M, Li C-C, Li Q (2018) Comparison of microstructural evolution and oxidation behaviour of NiCoCrAlY and CoNiCrAlY as bond coats used for thermal barrier coatings. Surf Coat Technol 352:285–294. https://doi.org/10.1016/j.surfcoat.2018.08.024
6. Wang D, Peng H, Gong S, Guo H (2014) NiAlHf/Ru: Promising bond coat materials in thermal barrier coatings for advanced single crystal superalloys. Corros Sci 78:304–312. https://doi.org/10.1016/j.corsci.2013.10.013
7. Moskal G, Jasik A (2016) Thermal diffusivity characterization of bond-coat materials used for thermal barrier coatings. J Therm Anal Calorim 126(1):9–17. https://doi.org/10.1007/s10973-016-5785-z
8. Rajesh Kumar B, Subbarao T (2012) AFM studies on surface morphology, topography and texture of nanostructured zinc aluminium oxide thin films 7(4):1881–18889

Implementation of Particle Swarm Optimization to Evaluate Single-Stage Impulse Generator Circuit Parameters

G. Ramarao, N. Jayaram, P. Ram Mohan Naidu, A. Vamsi, M. Krishna Prasad, and D. Jagadeesh

Abstract In this paper, a new approach based on particle swarm optimization (PSO) algorithm is used to evaluate the single-stage impulse generator (SSIG) circuit parameters (R_1, R_2, C_1, and C_2) from the known values of rise and tail times. The results reported in this paper provide the standard lightning impulse (LI) signals which meticulously matches with those waveforms illustrated in the IEEE 4-2013, and IEC-62305-1, 2010 standards. This is the first of its kind attempt to use PSO as a tool to evaluate the SSIG circuit parameters. This approach helps to overcome the practice of conventional trial and error methods for finding the impulse circuit parameters. These results are verified by the impulse circuit developed in MATLAB.

Keywords Lightning impulse · Impulse circuit · Particle swarm optimization

G. Ramarao (✉) · N. Jayaram · P. Ram Mohan Naidu · A. Vamsi · M. Krishna Prasad · D. Jagadeesh
Department of Electrical and Electronics Engineering, Aditya Institute of Technology and Management, Tekkali, Srikakulam 532201, Andhra pradesh, India
e-mail: grr231@gmail.com

N. Jayaram
e-mail: jayaram7893@gmail.com

P. Ram Mohan Naidu
e-mail: rammohan6199@gmail.com

A. Vamsi
e-mail: avamsi6463@gmail.com

M. Krishna Prasad
e-mail: Mallipamulakrishna143@gmail.com

D. Jagadeesh
e-mail: jagadeesharjun44@gmail.com

G. T. C. Sekhar et al. (eds.), *Intelligent Computing in Control and Communication*, Lecture Notes in Electrical Engineering 702,
https://doi.org/10.1007/978-981-15-8439-8_44

1 Introduction

The design of insulation against overvoltages in the power system is significant task in order to ensure the continuity of power supply without interruptions. These overvoltages mainly occur because of the lightning impulse (LI) voltages. Thus, for preserving the reliability of power system against such aforementioned said voltages, it is necessary to identify the breakdown strength of apparatus used in the power transmission network before installing them into its network [1–4]. This means that the apparatus should be tested with standard LI voltage signals. Moreover, the IEC 60,060-1, 2010 [5] and IEEE 4–2013 [6] standards illustrate that the LI voltage tests were basically done on insulation of apparatus used in the power system for examining the breakdown strength. As per the aforementioned standards, 1.2/50 μs impulse is represented as the standard LI and its waveform is given in Fig. 1. Hence, for checking the breakdown strength of power apparatus, it is important to generate an LI voltage signals in the laboratory with proper wave shaping properties [7].

Standard LI waveform illustrated in Fig. 1 is categorized mainly by three basic parameters. Those are peak value of the voltage (V_{peak}), rise time (t_{rise}), and tail time (t_{tail}). As per the IEC-62305-1, 2010 and IEEE std 4-2013 standards, the LI waveform should have t_{rise} of 1.2 μs and t_{tail} of 50 μs. The tolerances are also provided for t_{rise} which is ±30% and for t_{tail} which is ±20% [8, 9]. The rise and tail times will be treated as the physical parameters since they usually accessed from the impulse waveform itself.

Theoretically, it is possible to generate the standard LI waveform based on mathematical expression (i.e., double exponential (DEXP) function) which is illustrated by Eq. (1).

$$V(t) = V_0 K\left(\mathrm{e}^{-\alpha t} - \mathrm{e}^{-\beta t}\right) \tag{1}$$

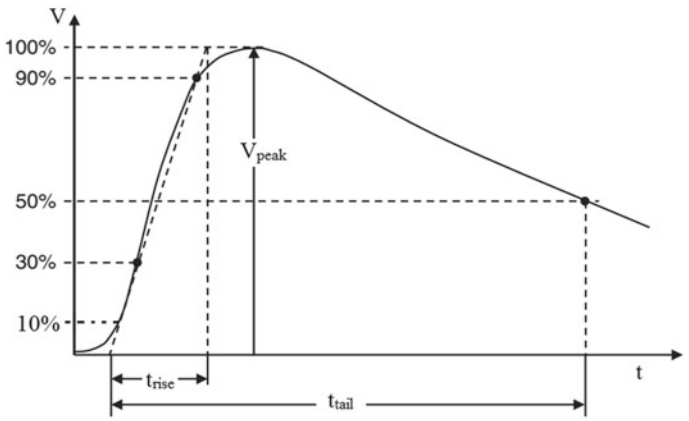

Fig. 1 Standard LI voltage waveform (1.2/50 μs)

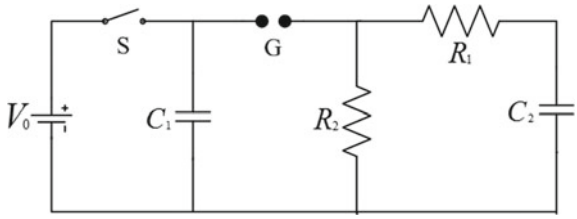

Fig. 2 Single-stage impulse generation circuit

where V_0 is peak value of voltage, and α and β are the DEXP function constants. In order to maintain the wave positive polarity, DEXP function constants (α and β) must obey $\beta > \alpha > 0$ [10]. K is the peak voltage correcting factor [11]. Practically, it is possible to generate the standard LI waveform through the impulse circuit which is illustrated in Fig. 2. The appropriate values of the parameters (R_1, R_2, C_1, and C_2) must be chosen in order to provide the standard LI voltage signals as given in the IEC and IEEE standards. Thus, the Nelder-Mead algorithm and linear regression method are used to determine single-stage impulse generator (SSIG) circuit parameters [12, 13]. In continuation of this, a new approach based on the particle swarm optimization (PSO) is used in this work to evaluate SSIG circuit parameters.

2 PSO and Its Application in Evaluation of Single-Stage Impulse Circuit Parameters

PSO is a metaheuristic algorithm which could solve any type of problem in various engineering applications. It can solve any problem by performing three activities, i.e., personal best (*Pbest*), global best (*Gbest*), and the movement of the particles. The movement of these particles is depending on acceleration coefficients (c_1, c_2), random vectors (r_1, r_2), inertia factor (w), etc. The comprehensive steps in the PSO algorithm are illustrated in [14]. In this paper, the SSIG circuit parameters (R_1, R_2, C_1, and C_2) are evaluated by application of PSO. Here, the objective function (fitness) is derived from rise time (t_{rise}) and tail time (t_{rise}) of the standard LI voltage waveform. MATLAB code is implemented based on an objective function and taken to evaluate the unknown SSIG circuit parameters. The objective function is developed and illustrated by Eq. (2) to minimize the error between rise and tail times of computed and standard impulse waveforms.

$$f = \left| \frac{t_{\text{rised}} - t_{\text{risec}}}{t_{\text{rised}}} \right| + \left| \frac{\text{t}_{\text{taild}} - \text{t}_{\text{tailc}}}{\text{t}_{\text{taild}}} \right| \tag{2}$$

where f is the objective function, t_{rised} is the rise time of desired or standard impulse waveform, t_{risec} is the rise time of the computed impulse waveform, t_{taild} is the tail time of desired or standard impulse waveform, and t_{tailc} is the tail time of the computed

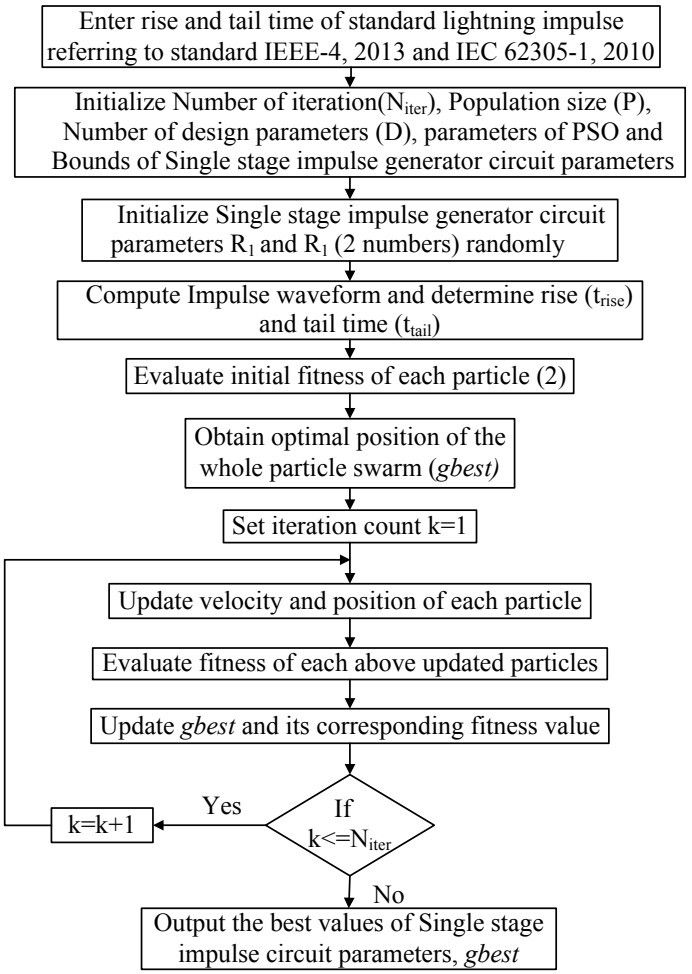

Fig. 3 PSO flowchart to find SSIG circuit parameters to generate the standard LI waveform

impulse waveform. In this work, the population size and total number of iterations are 50 and 200, respectively. The total steps involved in order to evaluate the SSIG circuit parameters are clearly explained with the help of flowchart which is illustrated in Fig. 3.

3 Results from Proposed Technique

The SSIG circuit parameters, i.e., C_1, C_2, R_1, and R_2, for producing the standard LI voltage waveform obtained from Sect. 2 are reported in Table 1 verified by using

Table 1 SSIG circuit parameters for generating standard full LI voltage waveform

Standard LI waveform (rise and tail time) (μs)	Result of circuit parameters obtained from PSO algorithm			
	C_1 (μF)	C_2 (μF)	R_1 (Ω)	R_2 (Ω)
1.2/50	0.1	0.001	608.62	678.5

the simulation impulse circuit developed in MATLAB. The data of SSIG circuit parameters which is reported in this work can able to generate the standard LI voltage signals as illustrated in IEEE-4, 2013 with rise and tail times of 1.2 μs and 50 μs respectively from the PSO algorithm.

4 Results Validation and Discussion

The SSIG circuit implemented in MATLAB shown in Fig. 4 is taken for validating the results obtained from the PSO algorithm. The SSIG circuit parameters (C_1, C_2, R_1, and R_2) illustrated in Table 1 are placed in the respective places in Fig. 4 for generating the standard LI voltage waveform, and its results are reported in Fig. 5 with the black solid line. The standard LI waveform (i.e., 1.2/50 μs) is also illustrated in Fig. 5 with red dashed line, and it is compared to the LI waveform obtained from simulated impulse circuit (Fig. 4). The percentage error in rise time, tail time, and peak voltage is calculated between impulse voltage waveform generated by the impulse circuit parameters obtained from PSO and standard LI voltage waveform and is illustrated in Table 2.

Finally, it is observed from Fig. 5 that the impulse voltage waveform generated by the PSO-based impulse circuit parameters is closely matched with the standard LI voltage waveform illustrated in IEEE and IEC standards. Also, it is observed

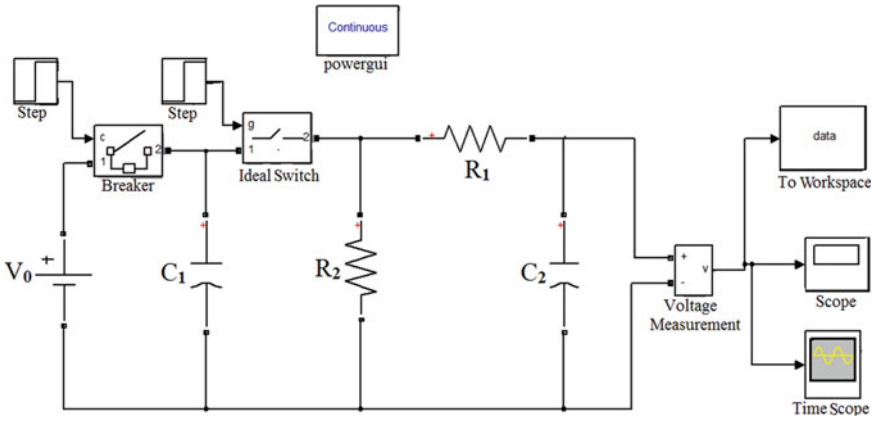

Fig. 4 SSIG circuit implemented in MATLAB

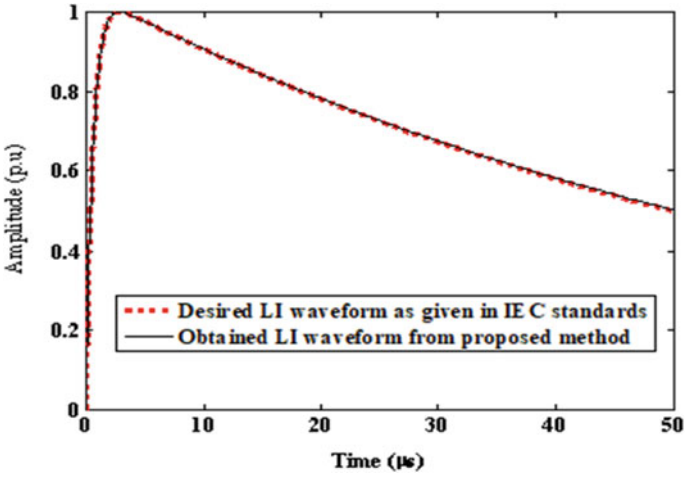

Fig. 5 Comparison of standard LI waveform with obtained waveform

Table 2 Percentage error in rise time, tail time, and peak voltage between impulse waveform generated by the impulse circuit parameters obtained from PSO and standard LI waveform

Comparison between Standard LI waveform and obtained waveform		
Rise time (%)	Tail time (%)	Peak voltage (normalized) (%)
0.44	−0.24	0.00

from Table 2 that the percentage error in rise time, tail time, and peak voltage is less than 0.5%. Hence, it is concluded from the above two statements that the SSIG circuit parameters in this paper will be helpful in order to generate the standard LI voltage waveforms for testing the dielectric strength of insulation of power apparatus efficiently.

5 Conclusion

Particle swarm optimization (PSO) algorithm is used in this paper to determine the single-stage impulse generator (SSIG) circuit parameters. The results of SSIG circuit parameters are reported and are verified by using the simulation circuit developed in MATLAB. The percentage error is calculated in rise time, tail time, peak time, and peak voltage between the lightning impulse (LI) voltage waveform generated by the PSO-based impulse circuit parameters and standard LI voltage waveform. The error detected in between the LI voltage waveform obtained by PSO-based SSIG circuit parameters and standard LI waveform is less than 0.5%. Thus, the SSIG

circuit parameters generated in this paper will be helpful for providing the standard LI voltage waveforms for testing the breakdown strength of power apparatus.

References

1. Fitch RA (1971) Marx-and marx-like-high-voltage generators. IEEE Trans Nucl Sci 18(4):190–198
2. Liang J, Zhang L, Li J, Li Y (2014) Study on oscillating switching impulse voltage generation for power transformer onsite test. IEEE Trans Power Del 29(5):2223–2230
3. Yutthagowith P, Pattanadech N (2016) Improved least-square prony analysis technique for parameter evaluation of lightning impulse voltage and current. IEEE Trans Power Del 31(1):271–277
4. Satish L, Gururaj BI (2001) Wavelet analysis for estimation of mean-curve of impulse waveforms superimposed by noise oscillations and overshoot. IEEE Trans Power Del 16(1):16–121
5. High-Voltage Test Techniques Part 1: General Definitions and Test Requirement, IEC Standard 60060–1 (2010)
6. IEEE Standard Technique for High-Voltage Testing (2013) IEEE Standard 4
7. Wu G (2014) Shape properties of pulses described by double exponential function and its modified forms. IEEE Trans Electromagn Compat 56(4):923–931
8. Li YM, Kuffel J, Janischewskyj W (1993) Exponential fitting algorithms for digitally recorded HV impulse parameter evaluation. IEEE Trans Power Del 8(4):1727–1735
9. Perez J, Martinez J (1998) Digitally recorded lightning impulse with overshoot parameter evaluation by using the Kalman Filtering method. IEEE Trans Power Del 13(14):1005–1014
10. Qin F,Mao C, Wu G, Zhou H (2016) Characteristic parameter estimation of EMP energy spectrum. In: 7th Asia Pacific international symposium on electromagnetic compatibility, pp 11–13
11. Camp M, Garbe H (2004) Parameter estimation of double exponential pulse (EMP, UWB) with least squares and nelder mead algorithm. IEEE Trans Electromagn Compat 46(4):675–678
12. Ramarao G, Chandrasekaran K (2017) Calculation of multistage impulse circuit and its analytical function parameters. Int J Pure Appl Math 114(12):583–592
13. Ramarao G, Chandrasekaran K (2017) Evaluation of circuit and its analytical function parameters for lightning and switching impulse. In: International conference on innovations in electrical, electronics, instrumentation and media technology, pp 302–305. Coimbatore, India
14. Eberhart R, Shi Y (2001) Particle swarm optimization: developments, applications, and resources. Proc 2001 Congr Evol Comput 81–86

Particle Swarm Optimization Based Intelligent Controller for Maximum Power Point Tracking of a Standalone Solar Photovoltaic Power System

Bibhuti Bhusan Rath, Manoj Kumar Panda, Bhola Jha, and Swati Rawat

Abstract Photovoltaic (PV) system is a green and nonconventional energy source. The prime goal is to draw the highest energy to satisfy the demand by using the PV cell at the peak or maximum powerpoint. This study suggests a particle swarm optimization (PSO) based proportional-integral-differential (PID) controller to track the maximum power point (MPP) of a photovoltaic (PV) system. The PSO-PID controller minimized the fluctuations in the equilibrium state, transients, and the response is found to be quicker as compared to the perturb and observe (P&O) assisted fuzzy logic controller (FLC) as the maximum power point tracker. The suggested PSO-PID MPPT based solar PV energy system is shaped and the outcomes are verified in MATLAB/SIMULINK.

Keywords Particle swarm optimization (PSO) · PID controller · Fuzzy logic controller (FLC) · Perturb and observe (P&O) · PV system · Maximum power point tracking (MPPT)

B. B. Rath (✉)
Department of Electrical and Electronics Engineering, Aditya Institute of Technology and Management (AITAM), Tekkali, Andhra Pradesh 532201, India
e-mail: bibhutibhusanrath2007@gmail.com

M. K. Panda · B. Jha · S. Rawat
Department of Electrical Engineering, G. B. Pant Engineering College, Pauri-Garhwal 246194, India
e-mail: pandagbpec@gmail.com

B. Jha
e-mail: bholajhaeee@gmail.com

S. Rawat
e-mail: rawat.swatieee@gmail.com

G. T. C. Sekhar et al. (eds.), *Intelligent Computing in Control and Communication*, Lecture Notes in Electrical Engineering 702,
https://doi.org/10.1007/978-981-15-8439-8_45

1 Introduction

Photovoltaic cell converts solar radiation into electrical energy directly. This effect is known as photovoltaic effect. Industries across the globe started large scale production of solar panels for harvesting electrical energy to meet the increased demand. Solar PV plants are available in standalone and grid-tied forms. The power-voltage (P-V) characteristic is nonlinear. For a given irradiation a single maximum power point exists and that is fixed. The PV system has to be regulated at that particular point to draw the maximum power under changing atmospheric conditions and to have the highest possible efficiency. The disadvantages of PV systems are poor efficiency of around 20% [1]. The MPPT algorithm makes the system fit to draw and allow the highest power to flow to the burden, to regulate the duty cycle of dc-dc converter [2].

MPPT is a key part of PV energy structure. The conventional and soft computing based MPPT methods are the key approaches found in the literature [2–4]. The popular old approaches are Perturb and Observe (P&O) or Hill-Climbing (HC) [5] Incremental Conductance (InC) [6, 7]. Each of the abovementioned methods has a common drawback of continuous fluctuation about the MPP. This fluctuation leads to more power damage during equilibrium state.

To overcome these problems, intelligent controllers such as fuzzy logic controllers, neural controllers [8–11] and controllers based on nature-inspired search algorithms which are also known as soft computing approaches are reported in the literature. Some of the soft computing based MPPT methods such as particle swarm optimization algorithm, cuckoo search algorithm, fireflies algorithm, grey wolf optimization technique, flower pollination algorithm, intelligent monkey king evolution algorithm, whale optimization with differential evolution (WODE), human psychology optimization have been reported in the literature [12–22].

This work is in the following order. Section 2 explains designing of Solar PV cell, Sect. 3 presents system description, Sect. 4 briefly describes the MPPT control algorithms used here, and Sect. 5 briefs results and discussion. Section 6 concludes this paper.

2 Designing of Solar PV Cell

A one diode model of a PV cell is represented by the saturation current I given by Eq. (1) as,

$$I = I_{\mathrm{pv}} - I_0\left[\exp\left(\frac{qV + qR_{\mathrm{s}}I}{N_{\mathrm{s}}k_{\mathrm{s}}Ta} - 1\right) - \frac{V + R_{\mathrm{s}}I}{R_{\mathrm{p}}}\right] \tag{1}$$

The physical quantities are given above in the expression for current I are mentioned below:

I_{pv}: Photovoltaic current source; D: a diode joined in parallel to the current source; I_D: The diode current;

R_p: parallel resistance which is expected to be large;

R_s: the addition of resistances (also known series resistance) because of all the elements which are in the way of current which should be too small;

Saturation current, I is the difference between the photovoltaic current source and the diode current which is given by Eq. (2) as,

$$I = I_{pv} - I_D \tag{2}$$

where I = saturation current, a = diode ideality factor, q = charge of electron, T = temperature in Kelvin, N_s = the number of cells in series, k_s = Boltzmann's constant.

Here, the diode is in anti-parallel with the current source to regulate the voltage of the PV cell.

3 System Description

This work deals with a solar PV energy system with a PV array, DC-DC buck converter, DC link capacitor, a three-phase PWM inverter, LC-filter, and resistive load of 50 W as shown in Fig. 1. Here the MPPT controller is driving the gate of IGBT present in the DC-DC buck converter to extract the maximum power from the PV array. The inverter converts the DC into AC, the PWM technique is used with

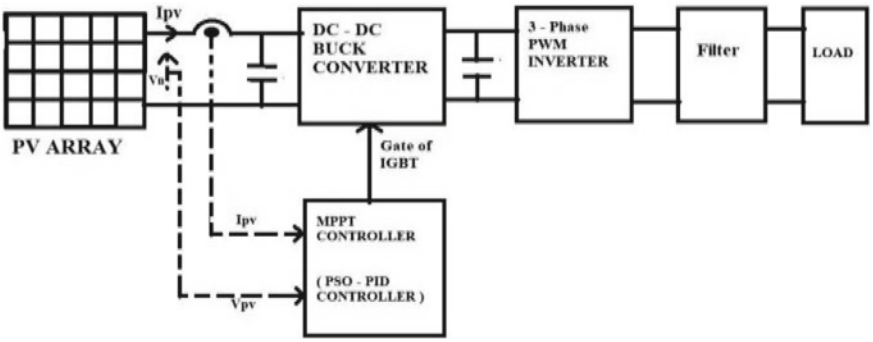

Fig. 1 Schematic diagram of an individual photovoltaic schemes

inverter to minimize the harmonics in the output of the inverter. The LC filter is used to minimize the harmonics in the load.

Parameters of the PV Panel
$I_{sc} = 8.01$ A, $V_{oc} = 36.90$ Current at $P_{max} = 7.10$ A Voltage at $P_{max} = 30.30$ V, number of modules connected in cascade in PV panel = 22.

PWM Inverter
Three-arm bridge (6-pulses), carrier frequency = 4000 Hz, frequency of output voltage = 50 Hz, modulation index = 0.96, Sample time = 20×10^{-6} s.

LC Filter
$L = 2$ mH, $C = 8.49 \times 10^{-6}$ F.

4 MPPT Control Algorithms

The maximum power point changes if the irradiation changes. Due to the use of MPPT algorithm the highest power is drawn from the PV structure as per the availability of the solar irradiation. There are many MPPT algorithms reported in the literature which are already mentioned in introduction. In this work, P&O algorithm assists fuzzy logic controller to enhance the searching ability of the fuzzy logic controller. The flow chart of the P&O algorithm is given below.

4.1 Perturb and Observe Algorithm

As the name implies, it works on the principle of perturbation and observation to have maximum power. The reference voltage is being generated from this algorithm. The important challenge is to draw peak power from PV array under changing atmospheric states and variable loads. This could be made possible only when a power converter/IGBT is connected that can progressively vary the impedance of the system by applying the P&O method, whose flow chart is shown in Fig. 2a.

4.2 Fuzzy Logic Controller

A fuzzy logic controller deals with uncertain inputs, it doesn't require exact mathematical model and deals with nonlinearity [9–11]. A fuzzy logic controller has three steps such as fuzzification, rule base, and defuzzification. The basic structure of a fuzzy logic controller is depicted in Fig. 2b.

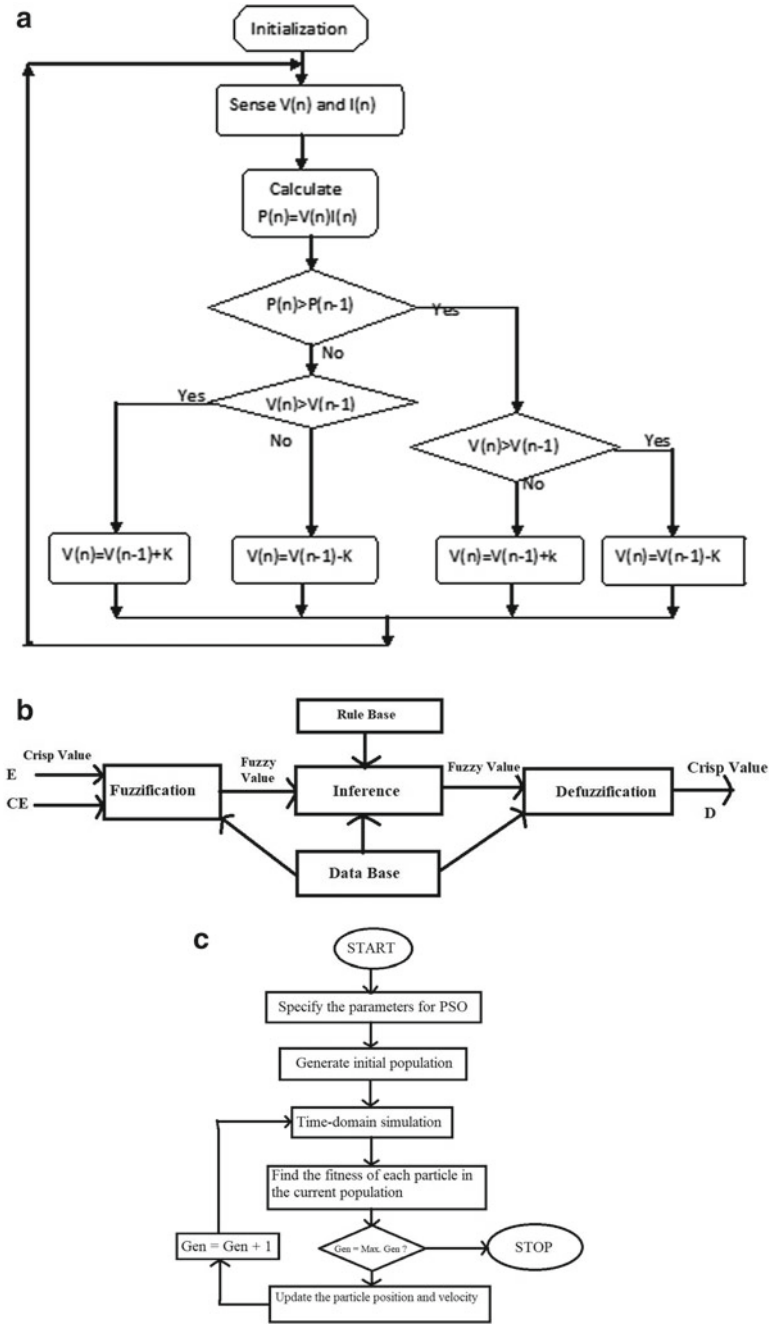

Fig. 2 **a** Flow chart for perturbing and observe method. **b** General structure of a fuzzy logic controller. **c** Flow chart of PSO algorithm

Table 1 Fuzzy rule base

E/CE	NS	PM	NB
NS	NM	NS	NM
PM	NB	NB	PM
NB	NS	PM	NM

4.2.1 Fuzzification

Fuzzification deals with changing crisp values into linguistic values depending on a membership function shown in Table 1. In this work, triangular membership functions are used. Normally a fuzzy logic controller is applied with two inputs namely error (E) and change in error (CE).E and CE are expressed by Eqs. (3) and (4) as

$$E(k) = \frac{P_{\text{pv}}(k) - P_{\text{pv}}(k-1)}{I_{\text{pv}}(k) - I_{\text{pv}}(k-1)} \tag{3}$$

$$\text{CE}(k) = E(k) - E(k-1) \tag{4}$$

After finding the error and change in error, the error and change in error are further changed to linguistic values. The output of the fuzzy logic controller is controlling the duty cycle D of the dc-dc power conditioner in use. The linguistic values are bringing a change in duty cycle for various blending of error and change in error which is decided by the power converter utilized by the system and the expertise of the researcher.

4.2.2 Rule Base

The goal of the rule base is to regulate the output specifications. The rule base is an If-then rule with a proper action and finish, identified by a Table 1.E and CE are two specifications and the conclusions are kept in Table 1. The output of the membership function in the rule base is properly specified as minimum and maximum operative. The fuzzy rule base is essentially computed by the variation in input. The input and output constants are given in linguistic designations namely, negative small (NS), negative medium (NM), negative big (NB). The rule base is kept inside the inference system. Here Mamdani's method has been utilized. The fuzzy rule base for this work has been shown in Table 1.

4.2.3 Defuzzification

In this level of defuzzification, the response of FLC is changed from linguistic value to crisp value by utilizing the membership function to apply a control signal to the

gate of IGBT present in the dc-dc power buck converter to draw the largest power from the PV array.

4.3 PSO-PID Controller

Particle swarm optimization [13] exists since 1995. PSO is a heuristic search optimization algorithm. PSO algorithm is inspired by the action of creatures like a group of insects, fishes, animals on land, and birds moving (flying) along a particular direction which uses a population-based exploration. A group of birds search food by foraging. As per the assumption, every information is shared in the group. This is the fundamental idea behind PSO. The key features of PSO are: it is easy to apply, there are less parameters to adjust, and fast convergence. Every particle in PSO acts as a single solution. In PSO every particle sails over the exploration area with an adjustable speed which is potentially changed as per its self-searching expertise and the expertise of different members as well. Every member tries for enhancing itself by emulating its stronger associates. Every particle is capable of recollecting its best place ever occupied in the area of exploration. Pbest is the place analogous to the best fitness, gbest is the finest among entire members in the group. The velocity and position update equations are given by Eqs. (5) and (6) respectively.

$$v_{i,j}^{(t+1)} = w * v_{i,j}^{(t)} + C_1 r_1()\left(\text{pbest}_{i,j} - x_{i,j}^{(t)}\right) + C_2 r_2()\left(\text{gbest}_j - x_{i,j}^{(t)}\right) \tag{5}$$

$$x_{i,j}^{(t+1)} = x_{i,j}^{(t)} + v_{i,j}^{(t+1)} \tag{6}$$

where

$i = 1, 2, 3 \ldots k$;

$j = 1, 2, 3 \ldots f$;

$k =$ Number of members in the swarm;

$f =$ Dimension of the exploration area;

$t =$ Number of repetitions;

$v_{i,j}^{(t)} =$ Velocity of member i at repetition t;

$w =$ inertia weight factor;

$r_1, r_2 =$ arbitrary numbers between 0 and 1;

$C_1, C_2 =$ acceleration factors;

$\text{pbest}_i =$ finest past location of the member;

gbest = finest member amidst all the members in the group.

Here the exploration area is having a dimension of three because here we have to find out the optimal Values of K_p, K_i and K_d (the gains of a PID controller) by using the particle swarm optimization. Here optimal means to minimize the objective function. For maximum power point, the objective function is the voltage error. This work presents integral squared error (ISE) as the objective function, which is given by Eq. (7).

$$\text{ISE} = \int e^2 \mathrm{d}t \tag{7}$$

Here 'e' stands for error. The particle moves with velocity and position for each iteration and checks for the optimization of fitness function in order to have an ideal proportional-integral-derivative controller. The computational step-by-step diagram of particle swarm optimization algorithm is displayed in Fig. 2c. In our PSO-PID controller [13] design the following parameters are chosen.

Population size = 10, No. of iterations 15, $C_1 = C_2 = 1$, $W_{max} = 0.75$, $W_{min} = 0.2$, $r_1 = 0.7$ and $r_2 = 0.7$ and the best value of the tuning parameters are found as $K_p = 370$, $K_i = 0.045$ and $K_d = 0.32$ [16, 17] by using particle swarm optimization.

5 Results and Discussion

The simulation of the solar photovoltaic power structure was conducted by using MATLAB/SIMULINK 2013a software for both fuzzy logic and particle swarm optimization tuned proportional-integral-derivative controllers for maximum power point tracking.

Figures 3 and 4 show the power-voltage and current-voltage curves respectively of the photovoltaic array under various irradiations. These curves confirm that the power increases as the irradiance increase.

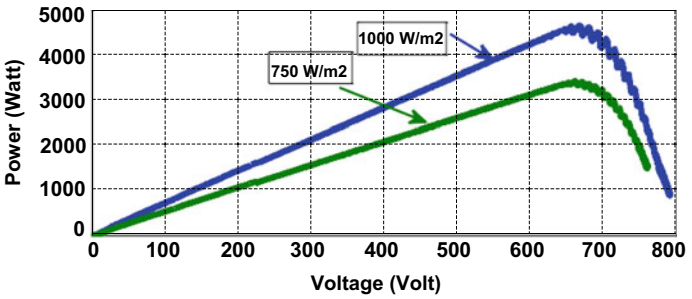

Fig. 3 P-V curves of PV array at different environmental conditions (irradiance 1000 and 750 W/m^2)

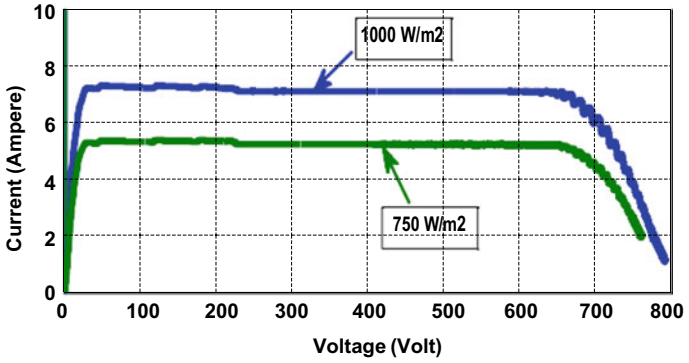

Fig. 4 I-V curves of PV array at different atmospheric state (irradiance 1000 and 750 W/m^2)

Figures 5, 6 and 7 show that higher voltage is found to appear across the output of photovoltaic array, the power outputs remain almost same for both the controllers.

Figures 5, 6 and 7 show the comparison of the output powers, current, and voltage, respectively for the irradiance of 750 W/m^2. This is obvious from these figures that the performance of PSO-PID is found good. To validate the dynamic performance of maximum power point tracking, a constant irradiance is changed from 1000 to 750 W/m^2 at 2 s. Dynamic performance comparison of power outputs of PV system with proposed PSO-PID and Fuzzy Logic controllers is shown in Fig. 8. This is

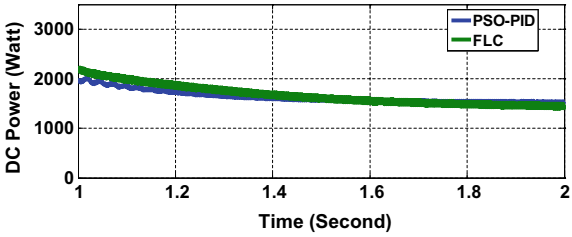

Fig. 5 Comparison of power outputs of PV system using PSO-PID and FLC

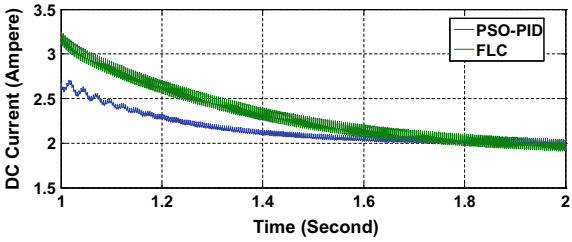

Fig. 6 Comparison of DC currents of PV system using PSO-PID and FLC

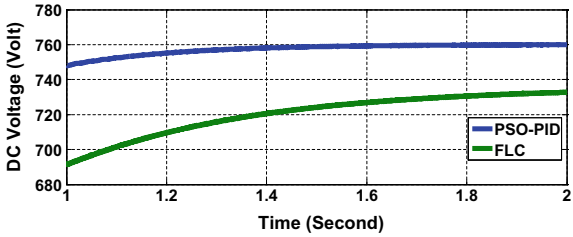

Fig. 7 Comparison of DC voltages of PV panel using PSO-PID and FLC

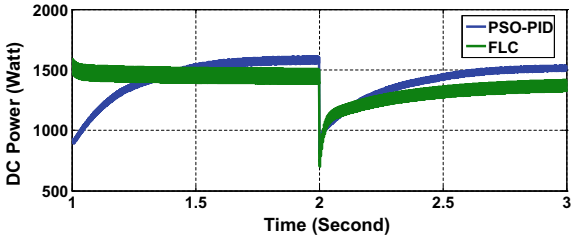

Fig. 8 Dynamic performance comparison of power outputs of PV system with proposed PSO-PID and fuzzy logic controllers

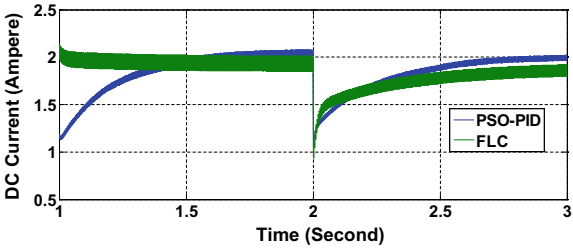

Fig. 9 Dynamic performance comparison of DC currents of PV system with proposed PSO-PID and fuzzy logic controllers

observed from Figs. 9, 10 and 11 that the performance of PSO-PID is comparatively better because the power, current, and voltage all are on higher side.

Figures 11, 12, 13 and 14 validate the DC to AC conversion using inverter.

6 Conclusion

Intelligent MPPT controllers are of more interest due to the properties such as quick merging, better performance, and insignificant fluctuations during equilibrium state. In the present study, the two controllers are intelligent in nature. The suggested PSO-PID controller exhibited lot more achievement. Greatly it has minimized the

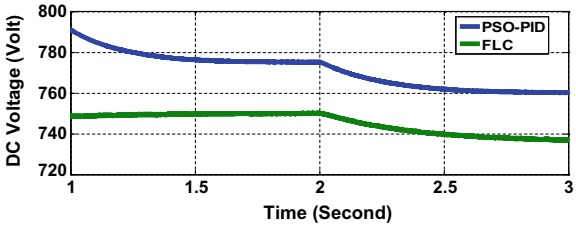

Fig. 10 Dynamic performance comparison of DC voltages across the PV panel with proposed PSO-PID and fuzzy logic controllers

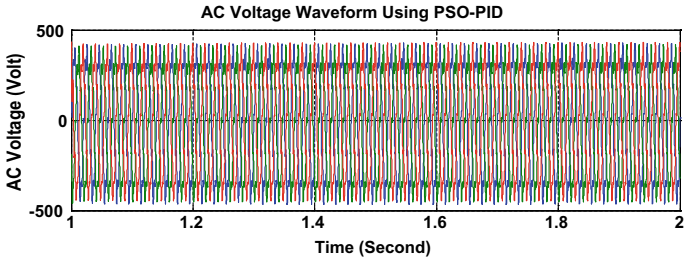

Fig. 11 AC voltage versus time using PSO-PID

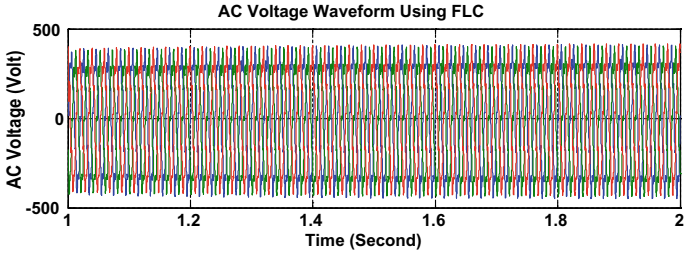

Fig. 12 AC voltage versus time using FLC

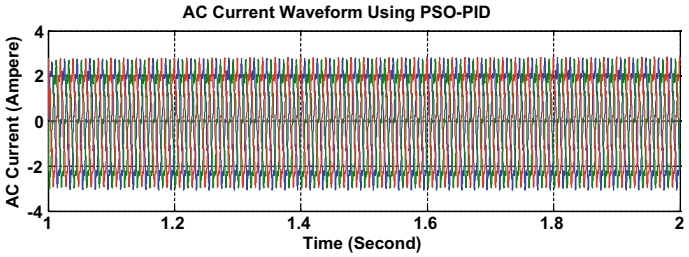

Fig. 13 AC current versus time using PSO-PID

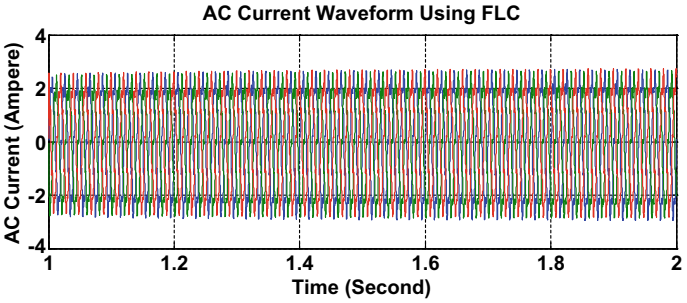

Fig. 14 AC current versus time using FLC

oscillations in the state of equilibrium. The dynamic performance of the proposed MPPT technique is admirable. Conversion from DC to AC voltage and AC current is also verified. Continuing investigation will need an execution of the suggested controllers on dSPACE or FPGA to quicken farther the operation to substantiate them analytically.

References

1. Rath BB, Panda MK, Jha B (2019) Centroid analogy-based MPPT technique for uniformly shaded solar photovoltaic array. Iran J Sci Technol Trans Electr Eng
2. Esram T, Chapman PL (2007) Comparison of photovoltaic array maximum power point tracking technique. IEEE Trans Energy Convers 22(2):439–449
3. Subudhi B, Pradhan R (2013) A comparative study on maximum power point tracking for photovoltaic power systems. IEEE Trans Sustain Energy 4(1):89–98
4. Salam Z, Ahmad J, Merugu BS (2013) The application of soft computing methods for MPPT of PV system: a technological status review. Appl Energy 107:135–148
5. Femia N, Petrone G, Spagnuola G, Vitelli M (2005) Optimization of perturb and observe maximum power point tracking methods. IEEE Trans Power Electron 20:963–973
6. Safari A, Mekhilef S (2011) Implementation of incremental conductance method with direct control. In: IEEE TENCON, pp 944–948
7. Lin CH, Huang CH, Du YC, Chen JL (2011) Maximum photovoltaic power for the PV array using the fractional order incremental conductance method. Appl Energy 88:4840–4847
8. Veerachary M, Yadaiah N (2000) ANN based peak power tracking for PV supplied DC motors. Sol Energy 69:343–350
9. Kottas TL, Boutalis YS, Karlis AD (2006) New maximum power point tracker for PV arrays using fuzzy controller in close cooperation with fuzzy cognitive networks. IEEE Trans Energy Convers 21:793–803
10. Rawat S, Jha B, Panda MK, Rath BB (2016) Load frequency control of a renewable hybrid power system with simple fuzzy logic controller. In: International conference on computing, communication and automation (ICCCA2016), pp 918–923. ISBN 978-1-5090-1666-2/16
11. Won CY, Kim DH, Kim SC, Kim WS, Kim HS (1994) A new maximum power point tracker of photovoltaic arrays using fuzzy controller. In: 25 Annual IEEE PESC, vol 1, 20–25 Jun 1994, pp 396–403
12. Kennedy J, Eberhart R (1995) Particle swarm optimization. In: Proceedings of IEEE international conference on neural networks, vol 1, Perth, pp 1942–1948

13. Gaing ZL (2004) A particle swarm optimization approach for optimum design of PID controller in AVR system. IEEE Trans Energy Convers 19:384–391
14. Ishaque K, Salam Z, Amzad M, Mekhilef S (2012) An improved particle swarm optimization (PSO)-based MPPT for PV with reduced steady state oscillation. IEEE Trans Power Electron 27:3627–3638
15. Taheri H, Salam Z, Ishaque K (2010) A novel maximum power point tracking control of photovoltaic system under partial and rapidly fluctuating shadow conditions using differential evolution. IEEE Sym Ind Electron Appl (ISIEA) 7
16. Ahed J, Salam Z (2014) A maximum power point tracking for PV system using cuckoo search with partial shading capability. Appl Energy 119:118–130
17. Sundareswaran K, Sankar P, Sankaran P (2014) MPPT of PV systems under partial shaded conditions through a colony of flashing fireflies. IEEE Trans Energy Convers 29(2):463–472
18. Mohanty S, Subudhi B, Ray PK (2016) A new MPPT design using grey wolf optimization technique for photovoltaic system under partial shading condition. IEEE Trans Sustain Energy 7(1)
19. Prasanth Ram J, Rajasekar N (2016) A novel flower pollination based global maximum power point method for solar maximum power point tracking. IEEE Trans Power Electron
20. Kumar N, Hussain I, Singh B, Panigrahi BK (2017) Maximum power peak detection of partially shaded PV panel using intelligent monkey king evolution algorithm. IEEE Trans Ind Appl 53(6):5734–5743
21. Kumar N, Hussain I, Singh B, Panigrahy BK (2017a) MPPT in dynamic condition of partially shaded PV system by WODE technique. IEEE Trans Sustain Energy 8(3):1204–1214
22. Kumar N, Hussain I, Singh B, Panigrahy BK (2017b) Single sensor based MPPT for partially shaded solar photovoltaic by using human psychology optimization algorithm. IET Gener Transm Distrib 11(10):2562–2574

Observation and Control of Smart Grid Using IoT and Cloud Technology

Salil Tiwari, Vatsal Agrawal, Sanjiv Kumar Jain, and Piyush Kumar Shrivastava

Abstract The traditional electrical grids deals with generation, transmission and distribution have one-way communication and are centered around the distributor. They also lack in routing and interconnection of different types of generations which lead to a reduction in the reliability of supply. Hence to overcome this issue we propose the comprehensive architecture of Smart Grid and it's Observation and control using the Internet of Things (IoT) and Cloud Technology. We have Integrated the different sources of energy (thermal and renewable) in a system and introduces the automatic routing of electric power according to peak and low demand. It also incorporates the smart metering facility using IoT and Cloud Technology. It can gather, send and receive the real-time data, which provide two-way communication of data of power being consumed at customer's end to the service producer. The whole data can be stored, accessed and analyzed on the very secured and customized API platform. We have built and thoroughly tested demonstration model of our project having Wi-Fi-based smart meter, which helped us to monitor and control the electric power and to enhance the reliability of the system.

Keywords Smart grid · Smart meter · Internet of Things (IoT) · Cloud technology · Application programming interface (API)

S. Tiwari (✉) · V. Agrawal · S. K. Jain · P. K. Shrivastava
Department of Electrical Engineering, Medi-Caps University, Rau, Indore, Madhya Pradesh 453331, India
e-mail: tsalil779@gmail.com

V. Agrawal
e-mail: vatsalagrawal98@gmail.com

S. K. Jain
e-mail: sanjivkumar.jain@medicaps.ac.in

P. K. Shrivastava
e-mail: piyushkumarshrivastava000@gmail.com

G. T. C. Sekhar et al. (eds.), *Intelligent Computing in Control and Communication*, Lecture Notes in Electrical Engineering 702,
https://doi.org/10.1007/978-981-15-8439-8_46

1 Introduction

The electricity demand globally is expected to increase more than two-thirds by the year 2035 according to the International Energy Agency. In the last few decades, more and more stress is put on the electricity supply and infrastructure to accommodate future demands. It is much more than the expected demand in earlier studies. Electricity is mostly dependent on fossil fuel which is inefficient to supply the growing demands. Rural areas are more prone to power outages in India as it depends on "mood" of power industries [1]. These industries not only generate power but also debt which is the result of inefficient infrastructure. As of today, electricity usage is increasing significantly and became very fluctuating as current system is unable to bear fluctuating demands. Fluctuating power requirement has to be generated and transmitted. The grid refers to the electric grid, a widespread network of transmission lines, substations, transformers and more for delivering electricity from the power sources to consumers. It powers lights and computers on which modern life is dependent. There is communication infrastructure present between energy generation, transmission, and distribution and consumption having partly two-way communications called power line communication. Communication between substation and consumers is negligible. Today, there is requirement of infrastructure facilitating two-way communications, inter-operability between advanced applications which is safe, reliable and redundant [2]. Digital technology which supports two-way communication between the service provider and its customers, and sensing along the distribution network makes normal grid a smart grid. Smart Grid will provide control and communication using computers the control is driven by data received from sensors the computer can be autonomous with support of new technologies and equipment working together with the electrical grid to respond quickly to sudden peak in electric demand. A smart grid technology is need of the hour to support integrated and reliable performance for electricity delivery. It is a self-sufficient system based on modern autonomous devices for control and analysis within the network. Problems can be rectified very quickly in smart system and will reduce the manpower significantly as of now there are supervisors who look at the physical condition of wires, switchgears to perform maintenance. When the grid will be updated using the smart devices there will be least human interference and the condition of devices will be automatically monitored, point of failure will be easily located and detailed report and history of failures will be generated automatically for future references. If the whole process is automated as proposed making grid smart it will become possible to provide sustainable, reliable and good quality electricity [3].

Basic applications of smart grids are:

- Automatic recovery from faults in grid.
- Adaptability of grid network is increased.
- Stress on one system is shared during peak demands.
- They are capable of being integrated with renewable energy sources on a large scale to share load during peak demand.
- Cost Reduction.

Many technologies to be adopted by smart grid have already been used in other industrial applications, in manufacturing industry, there are sensors integrated to monitor and control every process and quality of product in assembly line. Wireless communication extensively used in mobile telecommunications industry for transmitting and receiving data. Wired broadband is also part of this industry. Smart grid technologies mainly belong to the following groups advanced devices, sensing, decision support and communication.

Data of IoT is processed using Cloud Computing as it is now widely used for hosting web platforms and services because it is proven model for industries to scale their operations. Many industries use special connectivity to transfer data called Direct Link because services of cloud are available based on software as a service model which means charges as per usage. Direct link into the cloud ensures the privacy of data as protection of IoT data is an emerging challenge in smart devices. A web-based interface is implemented according to the business requirement. The networks can be managed and administrative rights can also be shared according to the role, Amazon is already providing this facility in their SaaS platform (Amazon Web Services) [4].

1.1 Cloud Computing

Cloud computing is service on demand. Computer resources such as data storage and processing power are achieved without direct access from the user. It is generally accessing computer over the internet. Large clouds host multiple servers in different location. If the location of user is relatively close, it may be designated as edge server. Edge computing is part of cloud computing many industries which use IoT devices use their own servers to pre-process data to reduce cost and latency. It just like accessing some other computer with more processing power situated at another corner of world which is possible because of internet. Cloud is a physical computer system especially designed to be used remotely. Cloud computing uses pay as usage model. This makes cloud computing scalable for user with different needs. User can simply use their service on rental basis and increase or decrease the usage depending on business needs [5].

Companies like Google and Microsoft aiming for zero-latency servers for clients worldwide, even in the scenario of local power outage. It is cheap because its maintenance is automatic and capacity can be increased effortlessly. Let's understand it using common example if normal person requires more data storage they purchase an external drive and plug it in their computer. In the same way, processing can be improved by employing more RAM in certain cases.

Amazon is the biggest player in Cloud industry according to report their platform is used most, it's mainly because they have multiple services integrated into one platform into very reasonable price and scalability, which means incorporating large numbers of sensors, actuators and customers, also an ability to run on large numbers of lightweight, inexpensive servers within a data center.

The idea of Smart Grid is very raw and is a possibility in near future. It is not so that it has never been done many electric companies like Schneider Electric and Huawei have already installed smart grid in many region but not to the extent expected. In this paper, we have discussed a possibility using a model which is unique idea in its own. In reality this model will employ a lot of different sensors and actuators which will make systems more complex and will need robust cloud platform [6]. Traditional systems are very simple and, that is one of the reasons the Smart Grid is still not reality. In recent innovation, home appliances can automatically communicate to service provider for maintenance and some can make purchases from store according to availability of items and they can also track usage pattern. Society is appreciating "virtual smartness" hence smart society, as society is extensively using sensors for security and household work there is immense possibility of smart grid will make lives better in near future [7].

1.2 Application Program Interface

It is program written to facilitate communication with software which runs in front end and user interacts with software and API runs in backend. It is extensively used to integrate multiple software in single software. This also makes possible communication between software. It can integrate new function to the existing architecture. An API may portray the manners by which a specific errand is performed. In procedural dialects like C language, the activity is typically intervened by a capacity call. Subsequently, the API as a rule incorporates a portrayal of the considerable number of capacities/schedules it gives. For example, the math.h incorporate record for the C language contains the meaning of the capacity models of the numerical capacities accessible in the C language library for scientific preparing (ordinarily called libm).

1.3 Processor

Most IoT applications require something beyond adding a sensor to a physical item. At the point when individuals talk about 'keen articles' they are normally discussing the expansion of an Internet-associated microcontroller (otherwise called a MCU). Microcontrollers can be thought of as little PCs that are added to any physical article or space to give it a 'mind'. They contain at least one PC processors, alongside memory and programmable information/yield peripherals all in a solitary coordinated circuit. MCUs are not the same as the chip that is found in PCs since they are explicitly intended for inserted applications where figuring isn't the sole reason for the application. While MCUs have less ability than a standard PC processor, their minimal effort makes them an increasingly pragmatic choice for adding figuring capacities to an item, space, or procedure that doesn't have them. A minimal effort, low-power framework from a chip (SoC) arrangement that has been made by Espressif Systems,

ESP32 accompanies Wi-Fi and double mode Bluetooth capacities. One of the key highlights is its double center or single-center TensilicaXtensa LX106 chip with a clock pace of up to 240 MHz. Profoundly incorporated with worked in reception apparatus switches, RF, power intensifier, low-commotion get enhancer, channels, power the board modules, contact touchy pins, worked in corridor impact sensor and temperature sensor, ESP32 has been designed for cell phones, wearable hardware, and IoT applications.

2 Current Scenario of Smart Grid

Many countries are exploring the opportunity for implementing smart grid and driving research, in this field, in very fast pace. World's biggest economies like United States of America have already laid the foundation of successful smart grid infrastructure and allocate separate fund for smart grid in millions of dollars in budgets. India in recent budget allocated funds for procurement of 1 Million Smart Meters. Meters with advanced metering infrastructure is minimum requirement.

However, looking at current scenario provision for renewable sources such as routing should be considered as implemented in this paper.

2.1 United States of America

The smart grid market is going to reach US$ 86.6 billion by 2024, as per a report published by Research Cosmos. The report says that the market which was previously valued at US$ 32.4 billion in 2015, is expected to grow at a Compound Annual Growth Rate (CAGR) of 13.15% during the forecast period of 2016–2024. Research Cosmos is a syndicated and personalized aggregator of market research, consulting services, business intelligence.

The rise in the demand of conservation of energy has emphasized the development of the smart grids across the world. The continuous development of smart cities and reliable infrastructure is also pushing the development of smart grids. The existing grid infrastructure is traditional in most electrical networks around the world and needs to be upgraded. The growing need for renewable energy could fuel the smart grids market. The Internet of Things (IoT), too, can boost smart grid demand. These are some prominent projects. Advanced Grid Intelligence and Security (AGIS) initiative implemented by the Public Service of Colorado to make the electric distribution system more secure and efficient [8].

Honeywell has implemented this with the help of Entergy Services Inc. in order to provide the profit to the utility companies in many different locations like Louisiana, Texas etc.

2.2 European Union

A recent Pike Research report predicts that increasing investment in Smart Grid technology in European nations will extend upto 56.5 billion euro over the period of 2010–2020, having 37% of total amount of transmission. The study further indicates that nearly 240 million smart meters will be installed in Europe by 2020. A report suggests that there is a requirement of big investment of around 1500 billion euro over the period of 2007–2030 for the maintenance, expansion and renewal of the current electrical grids of Europe into the new smart grids [9].

2.3 India

India's vision of enhancing the output of its power sector can be accomplished by the modernization of its currently available grids through incorporating the Smart Grid concept. India's Vision for the development of Smart Grid is "Transform the Indian power sector into a secure, adaptive, sustainable and digitally-enabled ecosystem that provides reliable and quality energy for all with active participation of stakeholders" [10]. For technology demonstration Ministry of power under the government of India has made the Indian Smart Grid Task Force which has selected 14 Smart Grid pilot projects lying all across India. Govt. of India will provide funds of 50% of the project costs as the grant and balance costs must be borne by the respective government utilities.

A pioneering initiative has taken by the POWERGRID through open coordination effort together with Electricity Department for the development of Smart Grid Pilot Project at Puducherry. Puducherry Govt. provide insight into the standardization and interoperability process of different technologies, policy advocacy and regulatory system for tariff design and net metering, introduction of electric vehicles with renewable charging, etc. to demonstrate technical efficiency.

Various Smart Grid features have already been introduced under this initiative, and are being slowly scaled up. More than 1600 smart meters at customer site, along with various units for concentration of data and meter framework for handling the data have now been incorporated into single platform at the Puducherry Smart Grid Control Centre [11].

Advanced Metering Infrastructure has also installed in the city. This AMI system have made possible the monitoring of real-time data of different patterns of energy consumption and their alarms. Different communication technology meters including broadband and narrow band PLC have been deployed. A wise energy audit of Real-Time Transformer is also possible. In addition, systems for various outage management, monitoring of distribution transformers and faulty passage indication have also been installed with control center for Smart Grid to reduce the outage hours and to ensure the reliable power supply to the customers.

2.4 China

The major organization for building the nationwide smart grid in China is State Grid Corporation of China (SGCC). For the period 2009–2020, SGCC plans to invest a total of $601 (€ 423) billion in a national transmission network with $101 (€ 71) billion of those funds for the implementation of Smart Grid technology [12].

Smart Grids made by Chinese people is currently focusing on designing and building the interconnected transmission system having huge capacity to manage and to transmit the power which helps them to accommodate the rapidly increasing demand for electricity. The grids currently available in China is not much advanced as that of grids that are present in many developed nations and the access to small scale renewable suppliers are currently limited [13]. According to the report of an Innovation Observatory survey, Chinese government is planning to install around 36 crore of smart meters in different locations by the year 2030 and they have also planned to invest heavily in modern and reliable distribution transformers.

3 Components Used in the Present Work

In present work, the components employed are readily available in market and are generic. The power rating of some components is not appropriate for high power applications but can serve domestic load easily. For high power applications, components can be replaced with suitable power rating.

3.1 Current Sensor (ACS712)

Sensing of flow of current and its regulation is a basic requirement in a large number of applications, including over current protection circuits, reprogrammable current sources, power supplies for switching mode, optical watt meters, battery chargers etc. ACS712 is a device that offers a cost-effective and accurate way of sensing DC and AC currents based on Hall Effect. Current sensor ACS712 is based on the Hall-effect principle. This principle states that when the current-carrying conductor is placed in a magnetic field then the voltage will generate perpendicular to the direction of both current and magnetic field across the edges of the conductor.

This current sensor module consists of two ports one is “wire in” and another is “wireout” these are the current-carrying wires whose current is to be measured. It consists of three pins: Vcc, output, and ground. Vcc pin is used for providing input voltage of +5 V for various applications while Output pin gives us the analog voltage proportional to the current to be measured and Ground pin is used for providing ground connection to the circuit. It is furnished in a small SOIC8 surface mount package. It has an accurate and Hall sensor circuit with a conduction path made

of copper that is present close to the die surface. When the current flows through the copper conductor a magnetic field is produced, the magnetic field strength of this magnetic field is proportional to the applied current. This produces the output voltage proportional to the input current, which is having linear relationship. The filter circuit and signal conditioner provided on the chip stabilizes and increases the produced Hall voltage to a suitable level to be measured by a microcontroller's ADC channel.

3.2 NodeMCU (ESP8266-12E)

NodeMCU is an open-source firmware which offers board designs for open source prototyping. The name "NodeMCU" combines "micro-controller unit" and "node". The term "NodeMCU" applies solely to the firmware and not to the associated development kits. ESP8266EX is embedded with a 32-bit Micro Controller (MCU). The speed of the CPU clock is 80 MHz. A maximum frequency of 160 MHz can also be achieved. The microcontroller series of ESP8266 provides comprehensive and inbuilt Wi-Fi module which provides us two-way data communication facility in a single module. If the application is hosted by ESP8266EX it boots up directly from an external flash. It has inbuilt cache to enhance system performance in such applications (see Figs. 1 and 2).

Specifications of NodeMCU (ESP8266-12E):

- TensilicaXtensa 32bitLX106
- Its frequency of operation is between 80 and 160 MHz
- 128 kb internal RAM
- It offers 4 MB of external flash memory.

3.3 PCB Relay

It is an electromechanical switch which operates on principle of electromagnetic induction. It opens and closes circuit when coil is magnetized or demagnetized. It is now employed in every smart gadget to enable remote operation. The structure may not be big or small according to rating the principle is always same. In electrical grid, the relays are already in use and they serve the same purpose as in this project switching of buses or in our case switching of sources. The relays in grid are powered using dc source as we do in our project. The difference in relay is that it is operated by a processor and program and switches automatically as programmed. The relay we used has two contacts one is normally open (N/O) and other is normally closed (N/C) (see Fig. 3).

This also has a spring contact mechanism which is in contact with N/C when inactive, if activated it contacts with N/O point. If the relay loop is stimulated by offering supply to the coil terminals at 'C', at that point the mobile contact of the

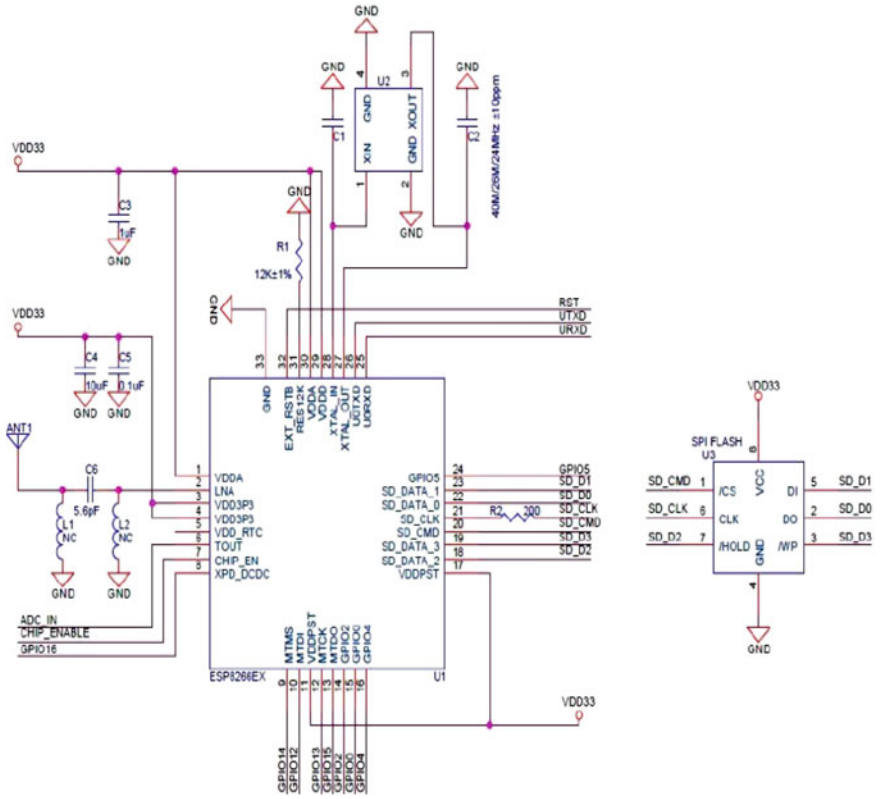

Fig. 1 Schematics of Esp-12E WiFi module. Schematic obtained from AI-Thinker datasheet of Esp-12E present at https://components101.com/sites/default/files/component_datasheet/ESP12E%20Datasheet.pdf

hand-off is pulled in towards the fixed contact. In this manner, the transfer turns on and the supply is connected with the load as appeared in Fig. 3.

3.4 Inverter 12 V DC to 230 V AC

It is an inverter circuit which is used to convert the 12 V dc to 230 V ac which is supplied to the load as load is mostly ac and renewable supply is dc.

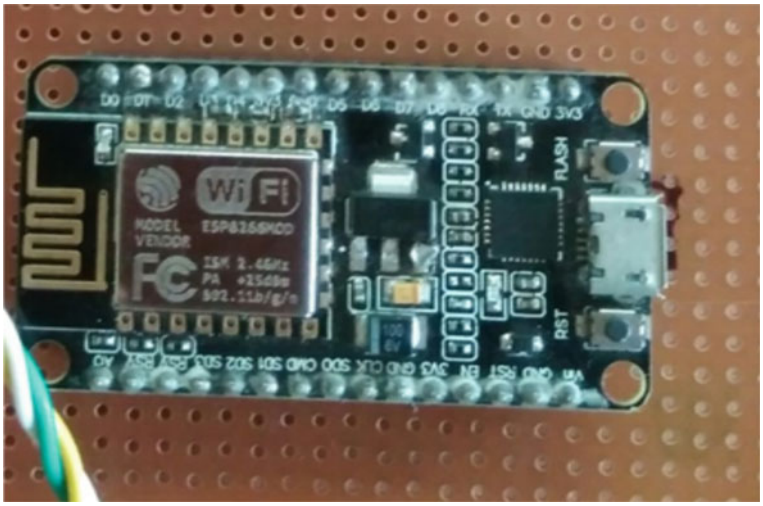

Fig. 2 Figure of ESP8266-12E module

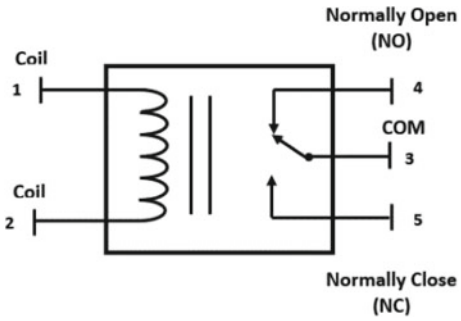

Fig. 3 PCB mounted sugar cube relay and its different pins [14]

3.5 Power Supply Board (230 V AC to 5 V DC)

It is a board which convert the 230 V ac to 5 V dc which is here in this project is used to give the supply to relay which will provide the operating voltage to relay. This is a low cost and simple circuit used to power small electronic devices. The power is tapped directly via resistor from the mains. Diode rectifies voltage, and the output is filtered using the two capacitors. The Zener diode controls the filtered DC and keeps the voltage at 5 V stable (see Fig. 4).

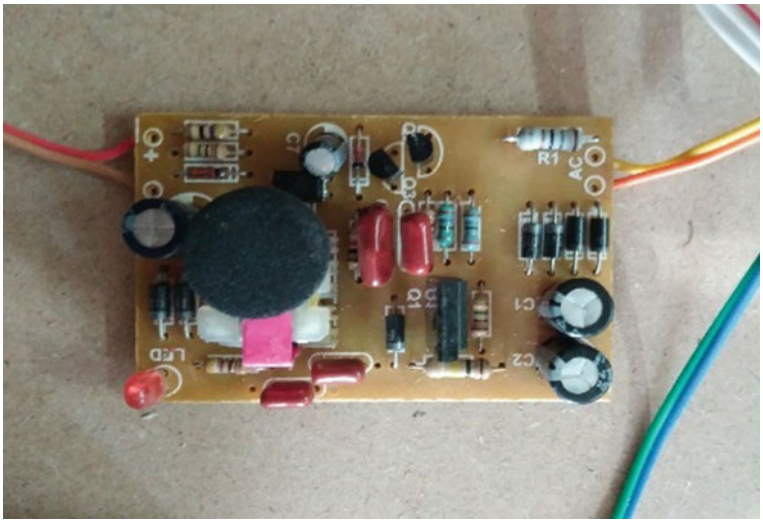

Fig. 4 Power supply board (230 V AC to 5 V DC)

3.6 LM358 OP AMP IC

This series of operational amplifiers are uniquely engineered in such a way they have to two separate op amps, which are internally frequency compensation and have large gain [15]. The process of split power supply current drain is independent of the magnitude of power supply voltage.

3.7 EX-OR Gate IC7486

The IC7486 is a high-speed CMOS Logic Quad 2-input XOR Gate. 74HCT86 contains four independent EOR gates in one package [16]. Logic gates use CMOS technology from the silicone gate to achieve operating speeds similar to low power consumption LSTTL gates. It is typically used in buffer circuits, inverter circuits with sensors etc.

3.8 Voltage Sensor Module 25 V

This is a basic yet extremely useful and convenient module that uses a potential divider to lower by a factor of 5 any voltage input. By using this microcontroller's analog input to monitor voltages sensors can detect far higher voltage. It can measure

a voltage up to maximum 25 V. The package also includes convenient screw terminals for fast and safe wire fit.

3.9 TA12 Current Sensor

It provides the analog output of around 5 mA for 5 A. It consists of sampling resistor on-board and precision transformer with microcurrent performing accurate sampling for signal and correct compensation, including several different functions. Within 5 A current communication, the module can be measured, which can be adjusted according to the analog output quantity.

4 Framework of Smart Grid

The system is designed for maximum efficiency and renewable energy usage. The model has two types of sources connected to it one is non-renewable such as thermal plant and other is renewable such as solar plant. There are three sugar cube relays, 2 current sensors and one voltage sensor. These sensors are connected to respective pins of Esp8266. Inverter is integrated into model to convert the dc provided from solar panel into usable 230 V ac. When supply is provided to the circuit the Esp8266 checks for the availability of WiFi connection if suitable WiFi connection is found it status is changed to connected and it requests for current sensor reading and converts it into RMS value then Esp8266 requests for API client using the API key which is already provided in the program of Esp8266 (see Figs. 5 and 6).

The current sensor and voltage sensor takes reading in microsecond period and this reading is converted into power using the formula. The Esp8266 is programmed such that if the power consumption exceeds the predefined limit or production of power from solar panel it sends signal to relay to switch supply from solar panel to thermal plant to supply extra power demand. This ensures that most of time the power is used from renewable source so to save money and environment.

Process of sensing and updating is continuous till the system is connected to Wi-Fi. ThingSpeak API is designed such that to show graphical representation of these parameters in different fields. In graphs X axis is for time and Y axis for parameter. In this API there are four fields field one for voltage, field two for current, field three for power consumption and field four for power factor.

Each field is updated automatically as programmed in Esp8266 and these fields can be monitored remotely from any corner of the world either using Mobile phone or Computer. ThingSpeak API also provides data in tabular form which can be easily downloaded and stored locally.

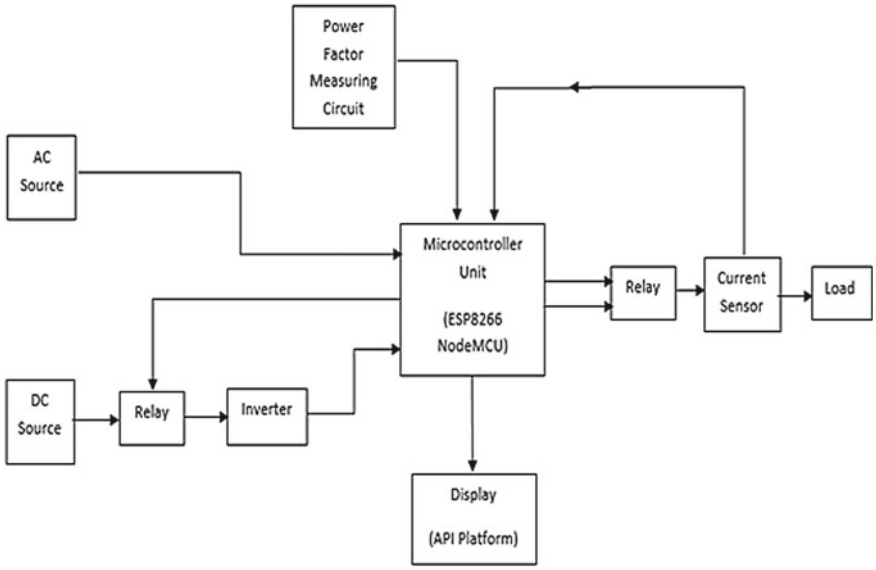

Fig. 5 Block diagram of prototype of smart grid system using IoT and cloud technology

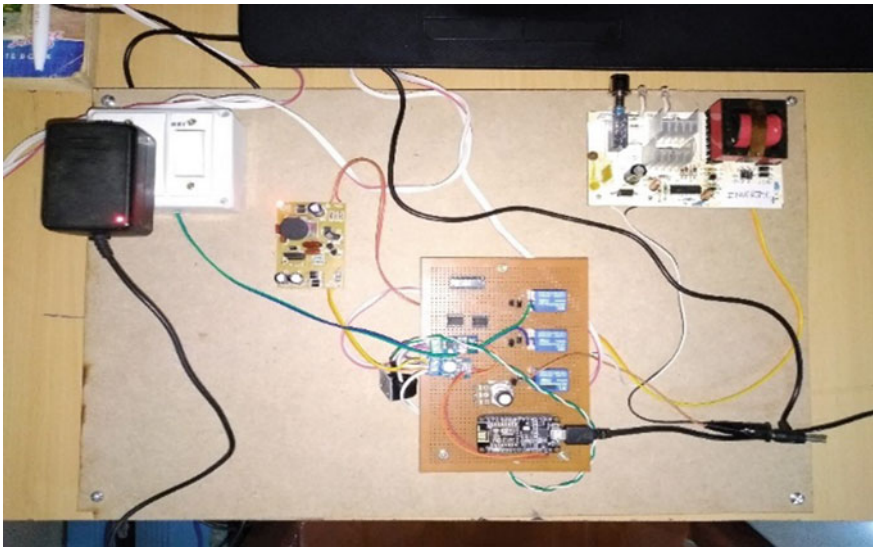

Fig. 6 Figure of smart grid model

5 Various Parameters and It's Tabular Representation

Voltage in volts will be sensed by the voltage sensor and it will be sent to the ThingSpeak API. In ThingSpeak, we see the readings and the graph of the voltage with respect to the time.

Current in amps is sensed by the TA12 Current Sensor Module which will directly update the value of the current in ThingSpeak API through WiFi Module. Here, we can see the value of current (in Amps) with respect to the time.

Power in watts is calculated with the help of current and voltage values obtained from respective sensors. Since, $P = V * I$ by using this formula in ThingSpeak API power is easily calculated.

Power factor is very important for the determining the power loss and efficiency of the system since power factor needs to be calculated (see Figs. 7 and 8). Power Factor is calculated by the method that current sensor and voltage sensor will sense the current and voltage and send it to their respective LM358 op amp and this is then given to EX-OR Gate IC7486 which makes the comparison between the current and voltage waveforms and give the difference in time Δt.

We know that phase angle $(\theta) = 2 * \text{pi} * f * \Delta t$ we also know the "f" frequency is 50 Hz and Δt is will be calculated by EX-OR gate and pi value is 3.14, so by this phase angle (θ) will be calculated and after taking cosine of phase angle (θ) by using coding done on NodeMCU we will get power factor.

$\text{PF} = \cos(\theta)$, hence this power factor will appear on ThingSpeak API in the form of graph or value. In Table 1 all the parameters are saved in cloud database as it is shown.

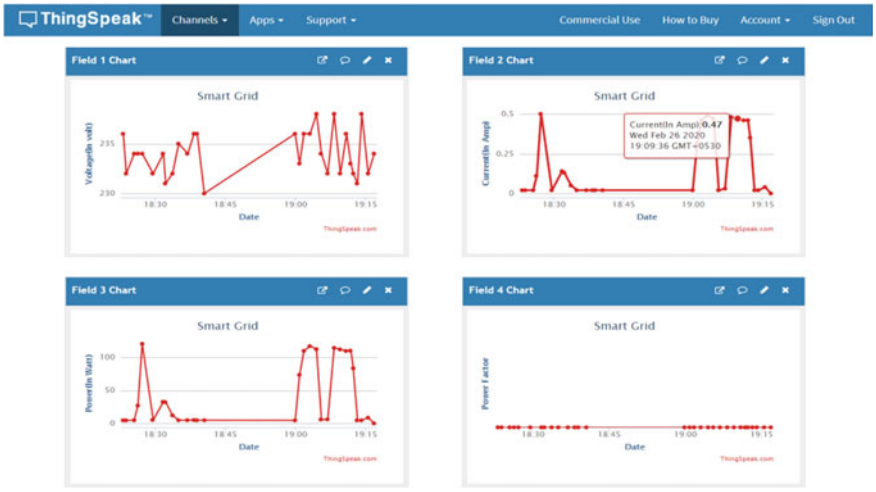

Fig. 7 Figure representing four parameters with respect to time on ThingSpeak API

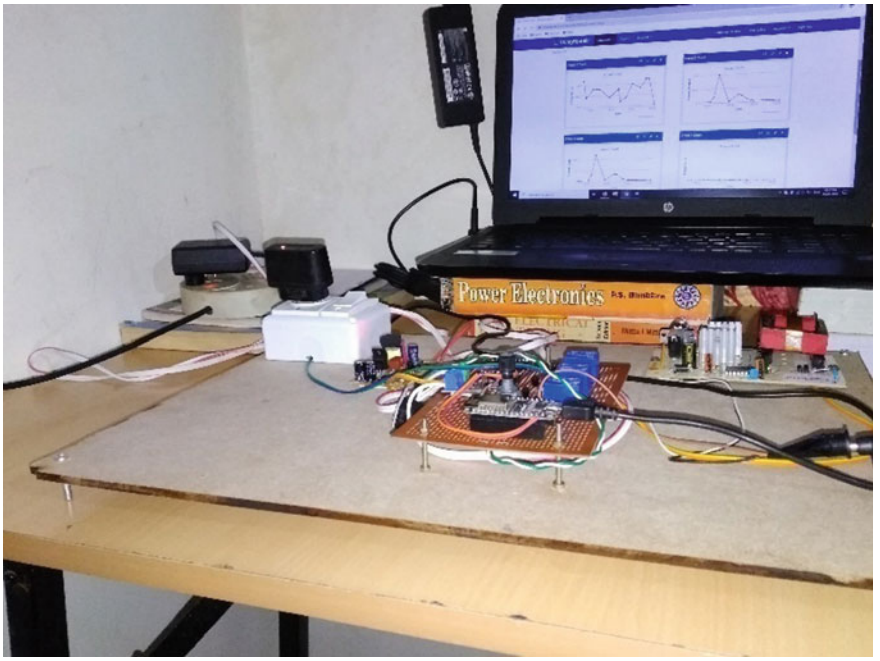

Fig. 8 Figure of model representing the various parameters

Table 1 Tabular representation of obtained data

Created_at	Entry_id	Field1	Field2	Field3	Field4
2020-02-26 12:53:10 UTC	1	236	0.02	4.67	0.96
2020-02-26 12:53:49 UTC	2	232	0.02	4.53	0.96
2020-02-26 12:55:30 UTC	3	234	0.02	4.75	0.96
2020-02-26 12:56:17 UTC	4	234	0.11	26.98	0.96
2020-02-26 12:57:13 UTC	5	234	0.5	120.45	0.96
2020-02-26 12:59:34 UTC	6	232	0.02	5.24	0.96
2020-02-26 13:01:45 UTC	7	234	0.14	32.54	0.96
2020-02-26 13:02:15 UTC	8	231	0.13	32.17	0.96
2020-02-26 13:03:41 UTC	9	232	0.05	12.09	0.96
2020-02-26 13:05:02 UTC	10	235	0.02	4.87	0.96
2020-02-26 13:06:58 UTC	11	234	0.02	4.83	0.96
2020-02-26 13:08:17 UTC	12	236	0.02	5.08	0.96
2020-02-26 13:08:59 UTC	13	236	0.02	4.72	0.96
2020-02-26 13:10:30 UTC	14	230	0.03	4.8	0.96

6 Conclusion

In this paper, we have discussed the future of smart grid having routing and smart metering capabilities using the wireless communication and cloud technology. As compared with traditional grid smart grid overcomes the challenges of power management. The data can be availed remotely after logging in with credentials. We made the demonstration model having MCU unit with clock frequency of 160 MHz which is enough for a house. Routing of power made system very redundant and efficient. If thermal system turns off the solar power supplies the source. The API platform is fed with data every second which is gathered from different sensors. The API platform converts the data into graphical representation after processing which made understanding of the trends easier. In India, government wants to procure smart meter which costs around INR 2000. The most important factor is cost, this system is very basic after doing the cost analysis of the smart meter, it needs a processor and some basic sensors which are readily available for cheap price and does not have very specific requirements. If the system is produced in mass the cost can be further brought down. As our model is very basic demonstration, its "power" is limited but possibilities are unlimited.

7 Future Scope

This model is scalable and has a great scope for future works. In this project work, we have considered two sources one is thermal and second one is a solar power source (renewable) integrated into a system equipped with the routing feature that can be extended by adding more sources in a system for increasing the redundancy of the system. Instead of using Wi-Fi, we can use 4G module so the system gets automatically connected to nearest cell tower as Wi-Fi has range issues. The whole data of various parameters could be seen on the API platform, so this can be extended by adding pricing feature which may be static or dynamic pricing as per the government norms for various types of loads (industrial and household) etc. It can further enhance the redundancy and reliability of the system, ease the working of producer and resulting in good quality and uninterrupted power supply to the consumer.

References

1. Kenneth PB, Lakshmi G, Robbert VR (2011) Running smart grid control software on cloud computing architectures. In: Workshop on computational needs for the next generation electric grid. Cornell University, New York, pp 1–27
2. Vehbi CG, Dilan S, Taskin K, Salih E, Concettina B, Carlo C, Gerhard PH (2011) Smart grid technologies: communication technologies and standards. IEEE Trans Ind Inf 7(4):1–8
3. Xi F, Satyajayant M (2012) Smart grid—the new and improved power grid: a survey. IEEE Commun Surv Tutor 14(4):944–980

4. Elisa S, Luca N, Stefano DP, Giuseppe I (2015) Last-meter smart grid embedded in an internet-of-things platform. IEEE Trans Smart Grid 6(1):468–476
5. Zhang Q, Cheng L, Boutaba R (2010) Cloud computing: state-of-the-art and research challenges. J Internet Serv Appl 1:7–18
6. Dragan SM, Dejan Z, Irina B, Ranko P, Dragan C (2013) Smart power grid and cloud computing. Renew Sustain Energy Rev 24:566–577
7. Yuichi K, Hiroki N, Naoko Y, Shinichi Y (2014) Internet of things (IoT): present state and future prospects. IEICE Trans Inf Syst 97(10):2568–2575
8. Smart grid economy. https://www.tdworld.com/grid-innovations/smart-grid/article/20972252/smart-grid-market-to-touch-us866-billion-by-2024. Accessed 2020/04/10
9. EIA Article. https://www.iea.org/topics/world-energy-outlook. Accessed 2020/04/10
10. Government of India Document. https://www.nsgm.gov.in/sites/default/files/India-Smart-Grid-Vision-and-Roadmap-Full-Document.pdf. Accessed 2020/04/10
11. Jha IS, Subir S, Rajesh K (2014) Smart grid development in India—a case study. In: Eighteenth national power systems conference (NPSC). IEEE, Guwahati, pp 1–6
12. China's largest utility plans a national power grid integrating Internet of Things technologies. https://www.scmp.com/news/china/society/article/3034684/chinas-largest-utility-plans-national-power-grid-integrating. Accessed 2020/04/10
13. Smart Grid System Article. https://www.energy.gov/sites/prod/files/2019/02/f59/Smart_Grid_System_Report_November_2018_1.pdf. Accessed 2020/04/10
14. Sugar Cube Relay. https://circuitdigest.com/article/relay-working-types-operation-applications. Accessed 2020/04/10
15. LM358. https://www.diodes.com/part/view/LM358. Accessed 2020/04/10
16. IC7486. https://www.solic.in/product/ic-7486-quad-2-input-exclusive-or-gate. Accessed 2020/04/10

Fabrication and Characterization of CZTS for Solar Cell Application

Kaza Jasmitha, Mallikarjuna Rao Pasumarthi, and P. S. Avadhani

Abstract This article is about, the description of the topography, compositional, optical band structural characteristics of a cost-effective and toxic-free CZTS thin film deposition using SILAR method as an absorbing layer in a solar cell. The specimens were defined by the various instrumentation techniques such as X-Ray diffraction (XRD), UV-VIS-NIS spectrometry, Field Emission Scanning Electron Microscope (FESEM) attached with Elemental Analysis (EDX). XRD results indicated perfect polycrystalline phase CZTS. UV Spectrophotometer measurements of CZTS thin film stated that the Bandgap of the film is 1.3 eV. At a glance, the Morphology of the film by FESEM showed the deposited film is crack-free and deposited uniformly. The stoichiometry of CZTS is perfectly matched with the literature.

Keywords SILAR · CZTS · Solar cell · Band gap energy · Morphology

1 Introduction

Generally, thin-film solar cells are being fabricated by taking Cadmium Telluride (CdTe) or else Copper Indium Gallium Selenide (CIGS) as an absorbing layer for absorbing light. But these materials are highly toxic and non-economical. Research is now in a forward step to replace these materials with widely available, non-toxic and which can absorb light. Copper Zinc Tin Sulphate (CZTS) is the material which

K. Jasmitha (✉) · M. R. Pasumarthi
Department of EE, Andhra University, Andhra University College of Engineering (A), Visakhapatnam 530003, India
e-mail: kaza.jasmitha@gmail.com

M. R. Pasumarthi
e-mail: electricalprofessor@gmail.com

P. S. Avadhani
Department of CS & SE, Andhra University, Andhra University College of Engineering (A), Visakhapatnam 530003, India
e-mail: psavadhani@yahoo.com

G. T. C. Sekhar et al. (eds.), *Intelligent Computing in Control and Communication*, Lecture Notes in Electrical Engineering 702,
https://doi.org/10.1007/978-981-15-8439-8_47

satisfies all the requirements like high absorption coefficient, direct bandgap in solar energy utilization [1]. Taking a non-toxic material like CZTS as an absorbing layer fulfills the requirement of researchers [2]. CZTS is one among the quaternary semiconductors with optical bandgap of 1.5 eV, absorption coefficient 104 cm^{-1} for solar cell application [3]. Development of the CZTS thin film is widely investigated to fabricate viz., pulsed laser deposition, electrochemical technique, sputtering, evaporation, SILAR and CBD. Due to the limitations and disadvantages in fabricating in physical methods, researchers adopted a chemical route to fabricate CZTS [4–10]. All the chemical technique approaches for producing standardized products including wide-area thin film fabrication are been processed by the Successive Ionic Layer Adsorption and Reaction (SILAR) process. This process is based on dipping (immersion) of the substrates into separately located cations and anions solution. For several metal sulfides, selenides, tellurides, and oxides, the SILAR process was employed effectively. Compared to many other film fabrication techniques, SILAR's distinctive qualities are used to fabricate deposition temperature low, the applications of aqueous solvents, is by increasing layer upon layer functionality, the different anionic and cationic origins. To synthesize a technically significant CZTS substance a basic solution-based SILAR approach has not yet been employed.

In this work, the novelty is about reporting the synthesis and fabrication of CZTS's thin film using a uncomplicated wet chemical technique, namely SILAR method, this helps in facilitates in development of CZTS's thin film by sequential dipping of these substrates in the cationic and anionic solutions. These deposited films are characterized by XRD, UV-VIS-NIR spectrometry, FESEM, EDX and J-V to find structural, optical bandgap, compositional and the electrical properties of synthesized CZTS film.

2 Experimentation

CZTS thin film is deposited by using SILAR process which majorly consists of dipping of substrates into cation and anionic precursor solution further then washing with double DI water to get rid of lossy bonded ions.

Firstly, to develop CZTS thin film on FTO substrate is cleaned with acetone methanol and DI water. These substrates are dipped in a beaker filled with cationic solution (0.02 M $CuCl_2$, 0.02 M $SnCl_2$ and 0.01 M $ZnCl_2$) to form CZT layer on the FTO substrate for 30 s. Then these substrates are rinsed using DI water. Now, these substrates are being dipped in a beaker filled with anionic solution consists of 0.2 M Na_2S solution for 30 s. To form S-layer which finally to form CZTS layer. Finally, these layers are rinsed in DI water to get rid of the lossly bonded ions. This process is repeated for 50 times. This helps in the formation of CZTS layer.

Final thin films are been investigated by X-Ray Diffraction (XRD) with the help of Philips X'pert diffraction spectra, generated setting at 40 mA, 45 kV using Ni filtered Cu-Kα radiation at a step range of 0.0080 [Å] $- 2\theta$ and a count time of 40 s counted per angular abscissa in the measured in range of 10–89.9962 °C.

UV-Vis-NIR Spectra were measured by Ocean Optical UV-1800 Spectrometry. The powder specimens were dispersed in methanol and the optical absorbance valve was measured in the wavelength ranges with nanometer step size.

For analyzing particle size and elemental composition was done by JEOL FESEM with EDX. The specimen is affixed on copper tape with emission current 96 microamps, accelerating voltage 10 kV. Working distance 4 mm for film.

3 Results with Discussions

This section describes the analysis and analysis of XRD, Bandgap, FESEM and EDX.

3.1 XRD Analyzation

XRD plot for CZTS film is represented in Fig. 1 and Table 1 gives the Crystalline size for CZTS film. From the XRD data the notified peak positions are at 23.32°, 28.48°, 29.41°, 32.54°, 33.16°, 35.11°, 38.17°, 45.1°, 47.13°, and 48.98° these peaks

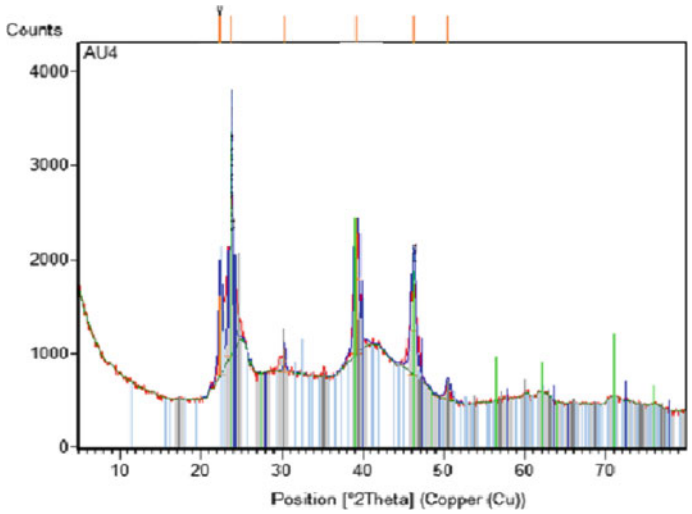

Fig. 1 XRD plot for CZTS film

Table 1 Crystalline size for CZTS film

Peak position (θ)	Crystalline size (nm)	Lattice strain
28.48	35	0.0034

are matching with JCPDS data no—26-0575 with *h k l* valves (1 1 2) (1 0 1) (2 0 0) (2 2 0) (3 1 2) (0 2 0) (1 1 5) (0 2 3) (2 0 7) (3 3 1). From it is clearly determined that the film is in polycrystalline with 35 nm crystalline size.

3.2 Bandgap Analysis

A perfect CZTS film has a significant impact on the absorption of light which further implies optical bandgap. The number of SILAR cycle is directly proportional to thickness deposited on the film. Increase in thickness of the film aids in the decrease of bandgap of the film. The cutoff in the absorbed wavelength is being expended in the visible areas with increases in the number of cycles. Using Kubelkae Munk function, the band-gap of the CZTS film is also calculated by the absorption edge position by the formula given below in Eq. (1)

$$E_g = \frac{1240}{\lambda\,(\text{nm})} \tag{1}$$

In this Eq. (1), is being obtained by drawing a tangent along with the absorption edge. In Fig. 2, the maximum peak intersected to zero of wavelength axis is denoted by λ. This result proves that Bandgap decreases with increase in SILAR cycles. From Eq. (1) the bandgap observed is 1.3 eV. Table 2 represents the bandgap of CZTS, corresponding to the wavelength of the maximum peak.

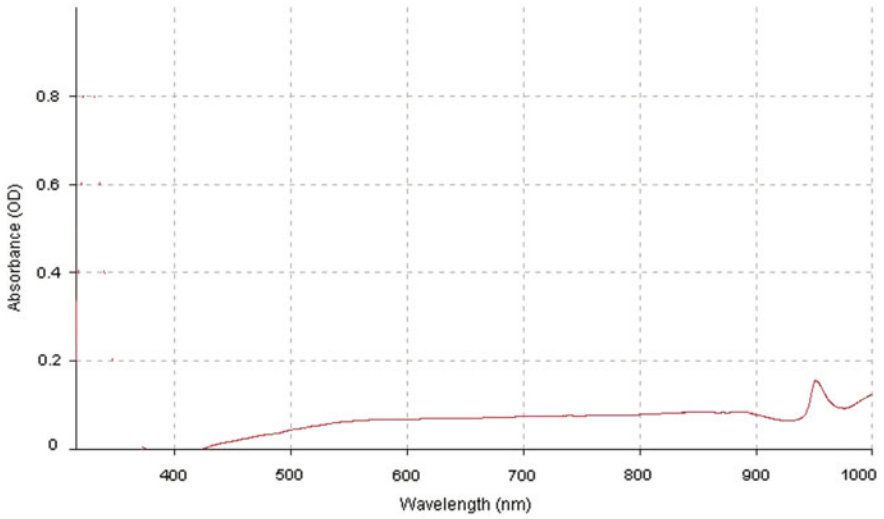

Fig. 2 UV-visible result for CZTS deposited film

Table 2 CZTS thin film bandgap value is 1.3 eV

Parameter	CZTS
Band gap (eV)	1.3
Wavelength (nm)	953.8

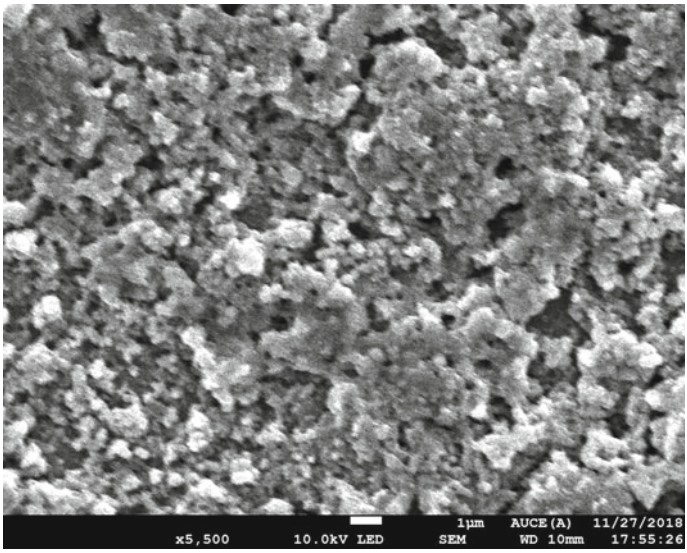

Fig. 3 FESEM image of CZTS by SILAR technique

3.3 FESEM Analysis

Figure 3 shows the morphological properties of CZTS's thin film, which are deposited by the SILAR method with cycles 50, the characterizations were done at a magnification of 5500 at a working distance of 10 mm. By seeing the film morphology, at a glance of the film topology, it can be clearly said that there is no agglomeration while transmitting from solution to film. There is no nonuniformity in the distribution of the particles and we can also observe the crystal grains are large in size. The average particle size observed is around 100 nm.

3.4 EDX Analysis

Figure 4 show the EDS image of CZTS's thin film fabricated by SILAR technique. From the data, it was observed that they are very strong peak of Copper, Zinc, Tin and Sulfate of concern range of keV. The atomic percentage of each individual element in the CZTS's thin film is calculated by the peak strengths. The stoichiometry of CZTS

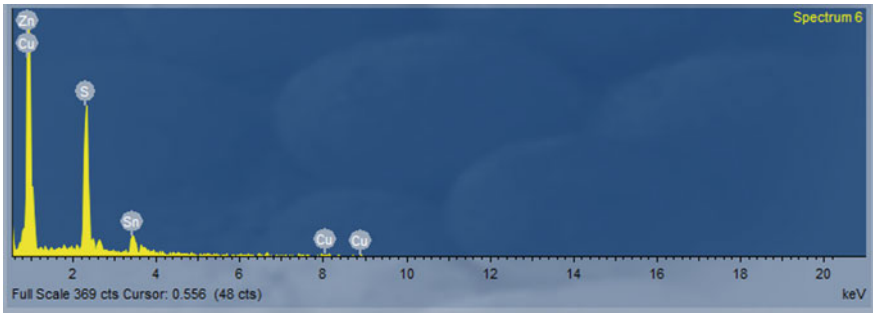

Fig. 4 EDS image of CZTS thin film by SILAR method

thin film measured was 26.17%, 11.14%, 13.01%, and 49.68% of Copper, Zinc, Tin and Sulfate, respectively, which was approximately equal to 2:1:1:4. From the data, it was observed that copper is poor compare to sulfate and Zinc is rich enough which aids in conversion efficiency.

4 Conclusion

In this work, a low cost and nontoxic CZTS thin are deposited using SILAR method for an absorbing layer in solar cell application and the topography, compositional, optical and structural properties of CZTS's thin film is described. The specimens were defined by various electronics characterization methods such as X-Ray diffraction (XRD), UV-VIS-NIS spectrometry, Field Emission Scanning Electron Microscope (FESEM) attached with Elemental Analysis (EDX). XRD results indicated perfect polycrystalline phase CZTS. UV Spectrophotometer measurements of CZTS thin film stated that the Bandgap of the film is 1.3 eV. At a glance the Morphology of the film by FESEM showed the deposited film is crack-free and deposited uniformly. The stoichiometry of CZTS is perfectly matched with the literature. The further scope of this work is to check for the efficiency of the film by varying the annealing temperature and check the efficiency of the CZTS thin film.

References

1. Miles RW, Hynes KM, Forbes I (2005) Photovoltaic solar cells: an overview of state of-the-art cell development and environmental issues. Prog Cryst Growth Charact Mater 51:1–42
2. Shin SW, Pawar SM, Park CY, Yun JH, Moon JH, Kim JH et al (2011) Studies on Cu_2ZnSnS_4 (CZTS) absorber layer using different stacking orders in precursor thin films. Sol Energy Mater Sol Cells 95:3202–3206
3. Pawar SM, Inamdar AI, Gurav KV, Shin SW, Jo Y, Kim J et al (2014) Growth of void free Cu_2ZnSnS_4 (CZTS) thin films by sulfurization of stacked metallic precursor films. Vacuum

104:57–60
4. Sarswat PK, Snure M, Free ML, Tiwari A (2012) CZTS thin films on transparent conducting electrodes by electrochemical technique. Thin Solid Films 520:1694–1697
5. Vanalakar SA, Agawane GL, Shin SW, Suryawanshi MP, Gurav KV, Jeon KS et al (2015) A review on pulsed laser deposited CZTS thin films for solar cell applications. J Alloys Compd 619:109–121
6. Lu Y, Wang S, Li Z, Jiang Z, Yang M, Li Q (2017) Effects of sputtering period on the performance of Cu_2ZnSnS_4 solar cells. Phys B 507:35–40
7. Tombak A, Ocak YS, Genisel MF, Kilicoglu T (2014) Electrical and optical properties of Cu_2ZnSnS_4 grown by a thermal co-evaporation method and its diode application. Mater Sci Semicond Process 28:98–102
8. Ansari MZ, Khare N (2014) Structural and optical properties of CZTS thin films deposited by ultrasonically assisted chemical vapour deposition. J Phys D Appl Phys 47:185101–185106
9. Rana TR, Shinde NM, Kim JH (2016) Novel chemical route for chemical bath deposition of Cu_2ZnSnS_4 (CZTS) thin films with stacked precursor thin films. Mater Lett 162:40–43
10. Su Z, Yan C, Sun K, Han Z, Liu F, Liu J et al (2012) Preparation of Cu_2ZnSnS_4 thin films by sulfurizing stacked precursor thin films via successive ionic layer adsorption and reaction method. Appl Surf Sci 258:7678–7682

Implementation of Anti-windup Techniques for the Improvement of PID Performance

Bevara Srikanth and Matta Mani Sankar

Abstract The PID algorithm is the most popular feedback controller used within the process industries despite the varied dynamic characteristics of process plant. But the performance of PID control can be deteriorated due to integrator windup phenomenon. Conditional integration, back calculation and combined approaches are implemented to avoid windup phenomenon. This paper presents an application of the above-mentioned approaches to different order process plants with normalized dead times and illustrates the performance of different methodologies.

Keywords PID · Windup · Back calculation · Conditional integration

1 Introduction

One of the major problems arise in PID control is saturation of actuators within the process industries. The consequence of actuator saturation leads to windup phenomenon. When an input is saturated, the integral controller will continue its operation and reaches a very high value which is undesirable. The transient response of the system will be deteriorated due to unacceptable value of the integrator. This phenomenon is known as windup. To keep away from windup various techniques are developed. Out of those techniques back calculation and conditional integration are found to be the best. But these techniques need additional effort of tuning if the process having an existence of dead times. In order to overcome this drawback, a combination of the earlier mentioned techniques is adopted. The aim of this paper

B. Srikanth (✉)
Department of EEE, Aditya Institute of Technology and Management (AITAM), Tekkali, Andhra Pradesh 532201, India
e-mail: sreekanthbevara@gmail.com

M. M. Sankar
Department of Electrical Engineering, BIT Sindri, Dhanbad, Jharkhand 828123, India
e-mail: che.shankar@gmail.com

G. T. C. Sekhar et al. (eds.), *Intelligent Computing in Control and Communication*, Lecture Notes in Electrical Engineering 702,
https://doi.org/10.1007/978-981-15-8439-8_48

is to illustrate the application of these techniques to process plants and compare the performance of PID control [1–4].

2 Back Calculation

The integral operation is hold back if the saturation of output is taken place. It means the value of integral is computed again which will give an output at this instant of saturation. As the integrator reset is done dynamically (through T_t), it seems to be more advantageous [3, 5, 6].

The input to the integrator is represented in Eq. (1)

$$\frac{1}{T_t} e_s + \frac{k_p}{T_i} e \tag{1}$$

where e is the control error and e_s is the error signal. Hence, in the steady state, it is expressed in Eq. (2)

$$e_s = -\frac{k_p T_t}{T_i} e \tag{2}$$

Since $e_s = U_s - U$, the output of the controller is expressed in Eq. (3)

$$u = u_{lim} + \frac{k_p T_t}{T_i} e \tag{3}$$

where U_{lim} is the saturating value of the control variable.

3 Conditional Integration

The integral operation is stopped if control is no way nearer to the steady state. The integral operation will be active if only if few conditions are satisfied, else it is treated as constant [2, 3, 5, 6].

4 Combinational Scheme

The combination of earlier mentioned techniques is expressed through Eq. (4) as follows

$$e_i = \begin{cases} \frac{k_p}{T_i} e + \frac{1}{T_t}(u_s - u) & \text{if } u \neq u_s \text{ and } u \times e \succ 0 \\ & \text{and} \begin{cases} y \succ y_0 \text{ if } y_1 \succ y_0 \\ y \prec y_0 \text{ if } y_1 \prec y_0 \end{cases} \\ \frac{k_p}{T_i} e & \text{otherwise} \end{cases} \tag{4}$$

The objective of Eq. (4) is to increase the integral as long as the transient response of process output is delayed due to the existence of dead time [5, 6].

5 Results and Discussions

The performance of back calculation, conditional integration and combinational approaches was illustrated by implementing them for the following process plants.

5.1 First-Order Process Plant

Let a process of first-order with normalized dead time is considered in Eq. (5)

$$P_1(S) = \frac{1}{10s + 1} e^{-2s} \tag{5}$$

The PID parameters are tuned based on Ziegler-Nichols methodology [3, 4, 7–11]. The application of conventional PID controller to the process $P_1(s)$ is shown in Fig. 1.

The results of back calculation, conditional integration and combinational approaches were reported in Figs. 2, 3 and 4, respectively.

The performance of different approaches for the application of first-order process plant was compared and tabulated in Table 1.

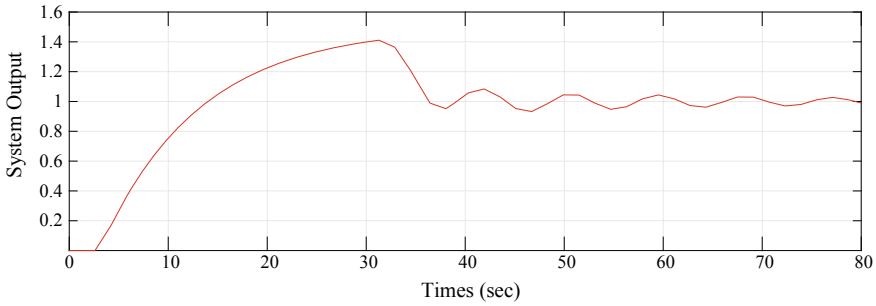

Fig. 1 System response of P_1(s) with conventional PID controller

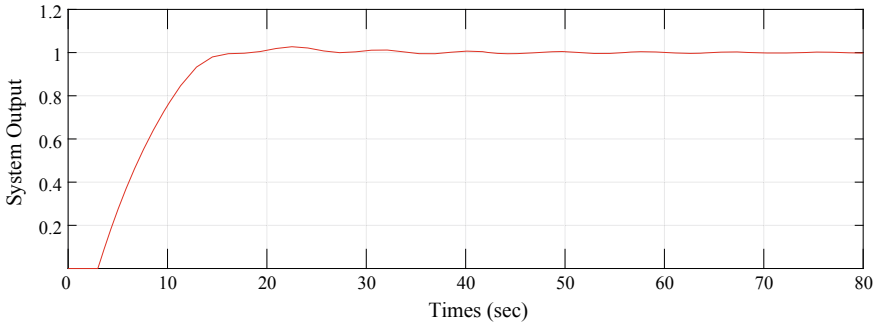

Fig. 2 System response of $P_1(s)$ with back calculation approach

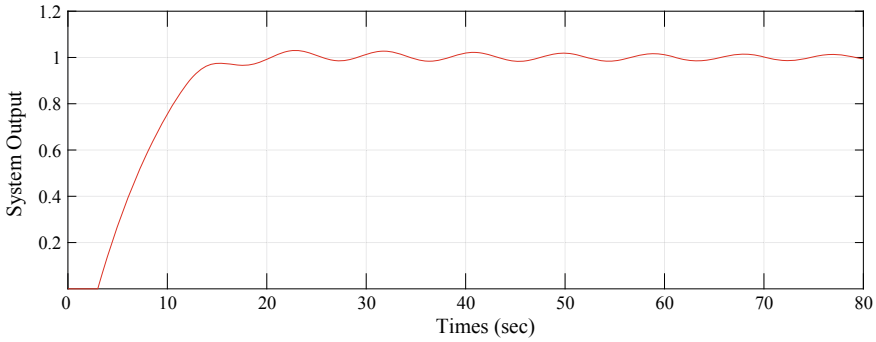

Fig. 3 System response of $P_1(s)$ with conditional integration approach

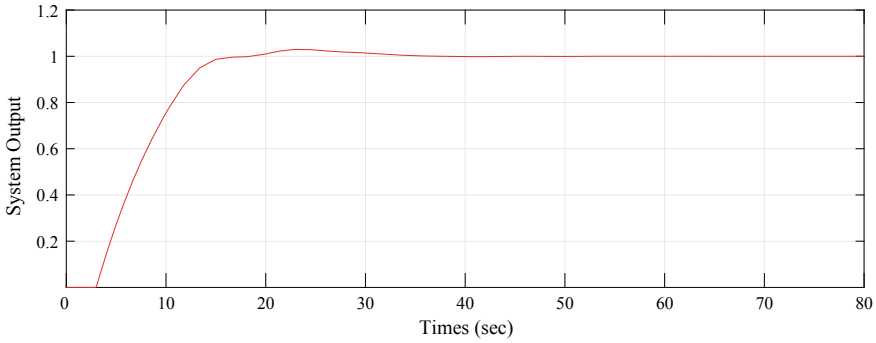

Fig. 4 System response of $P_1(s)$ with combinational scheme approach

Table 1 Comparison of different approaches for the application of first-order process $P_1(s)$

Approach	Percentage overshoot (%)	Settling time (s)
Conventional PID	40	Not settled
Back calculation	2.5	40
Conditional integration	3	Not settled
Combinational approach	2.6	30

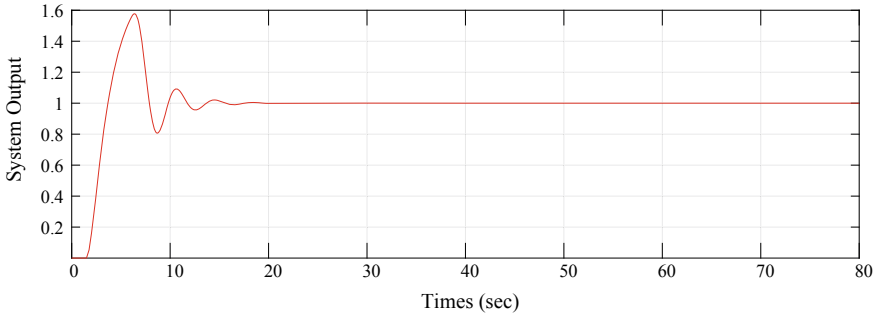

Fig. 5 System response of $P_2(s)$ with conventional PID controller

5.2 *Second-Order Process Plant*

Let a process of second-order with normalized dead time is considered in Eq. (6)

$$p_2(s) = \frac{1.2}{s^2 + 2.5s + 1} e^{-0.5s} \tag{6}$$

The application of conventional PID, back calculation, conditional integration and combinational approaches to the second-order process $P_2(s)$ were plotted in Figs. 5, 6, 7 and 8, respectively [3, 8, 10, 12].

The performance of different approaches for the application of second-order process plant were compared and tabulated in Table 2.

5.3 *Third-Order Process Plant*

Let a process of third-order with normalized dead time is considered in Eq. (7)

$$p_3(s) = \frac{1}{s^3 + 3s^2 + 3s + 1} e^{-0.3s} \tag{7}$$

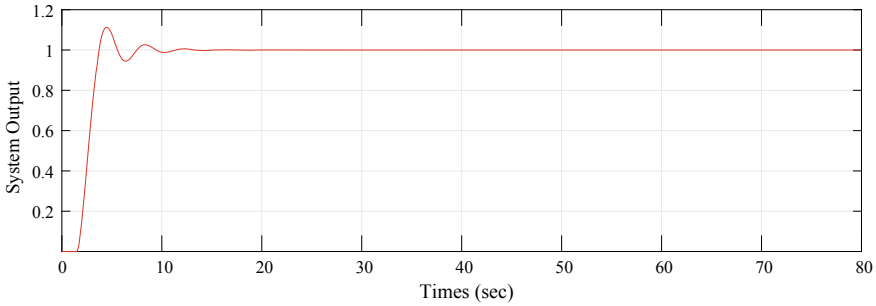

Fig. 6 System response of $P_2(s)$ with back calculation approach

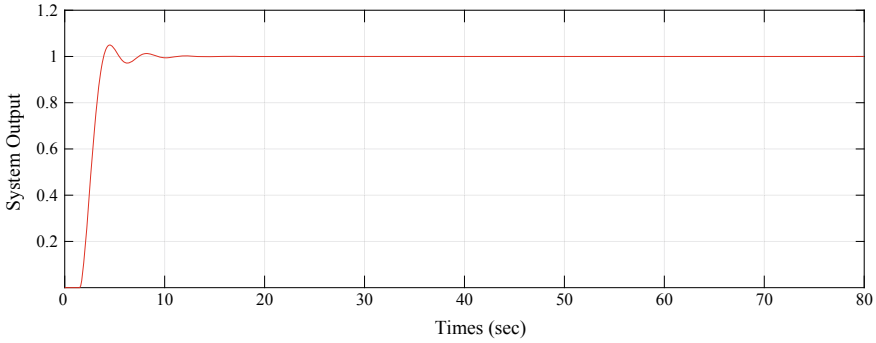

Fig. 7 System response of $P_2(s)$ with conditional integration approach

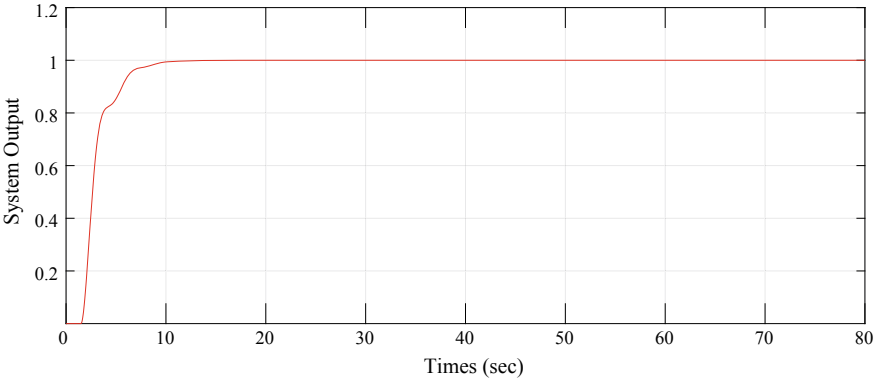

Fig. 8 System response of $P_2(s)$ with combinational scheme approach

Table 2 Comparison of different approaches for the application of second-order process $P_2(s)$

Approach	Percentage overshoot (%)	Settling time (s)
Conventional PID	57.5	21
Back calculation	11	15
Conditional integration	6	15
Combinational approach	0	10

The application of conventional PID, back calculation, conditional integration and combinational approaches to the second-order process $P_2(s)$ were plotted in Figs. 9, 10, 11 and 12, respectively [3, 5, 6, 8, 10].

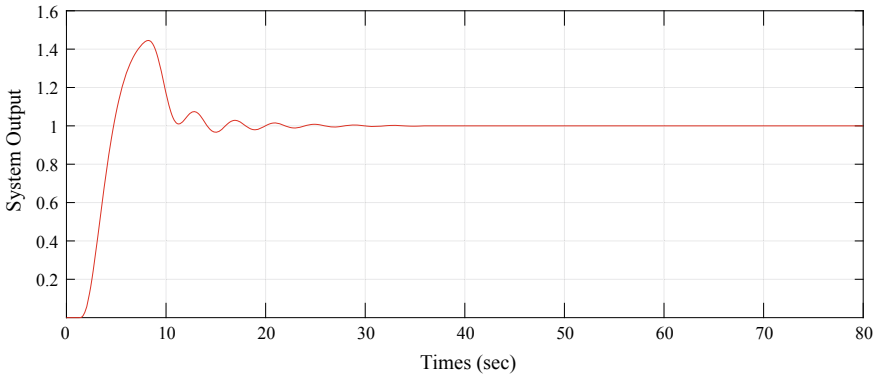

Fig. 9 System response of $P_3(s)$ with conventional PID controller

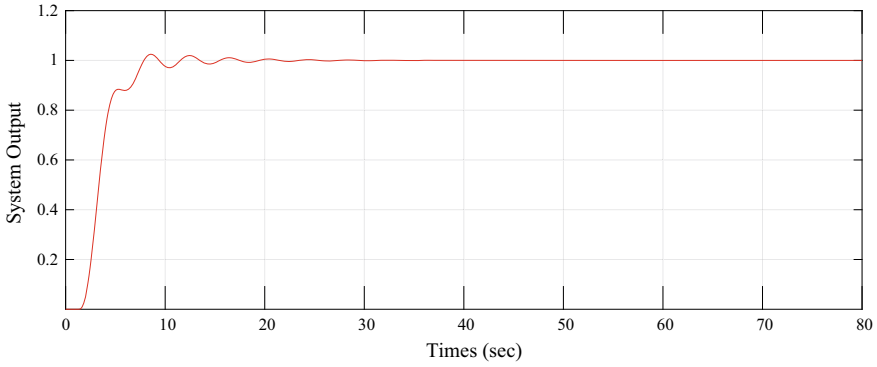

Fig. 10 System response of $P_3(s)$ with back calculation approach

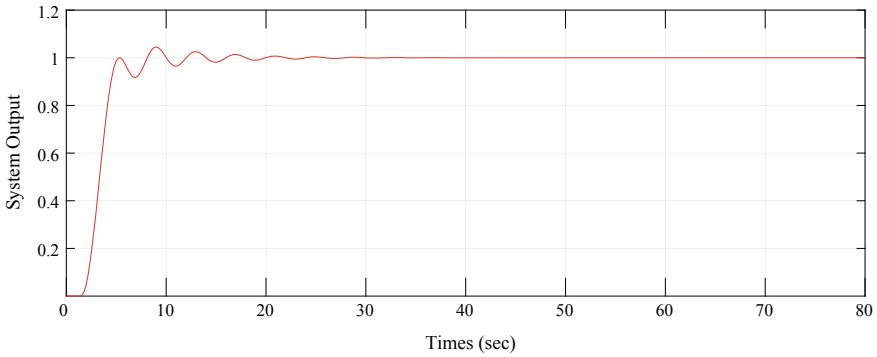

Fig. 11 System response of $P_3(s)$ with conditional integration approach

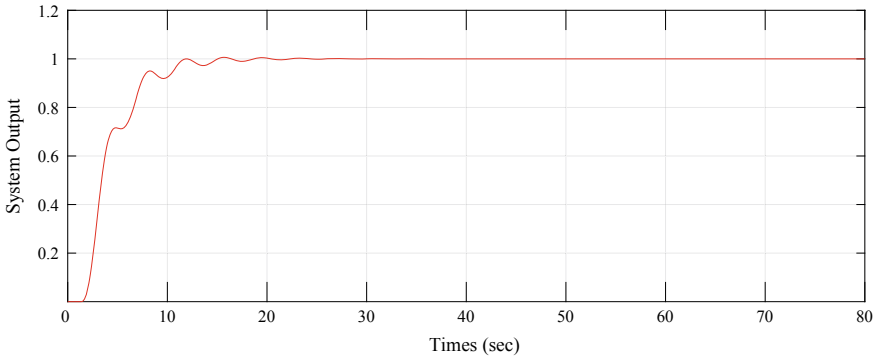

Fig. 12 System response of $P_3(s)$ with combinational scheme approach

The performance of different approaches for the application of third-order process plant were compared and tabulated in Table 3.

The application of combinational approach has given better results than that of the remaining two approaches in all the three cases. And it performs even better

Table 3 Comparison of different approaches for the application of third-order process $P_3(s)$

Approach	Percentage overshoot (%)	Settling time (s)
Conventional PID	45	30
Back calculation	2.5	30
Conditional integration	4.5	32
Combinational approach	0.6	22

for second- (no overshoot and settled at 10 s) and third-order process (negligible overshoot and settled at 22 s) when compared to first-order process (overshoot of 2.6% and settled at 30 s).

6 Conclusion

In this paper, windup phenomena are discussed and anti-windup approaches are implemented in MATLAB, and system performance is measured for different process systems. The severe effect of windup phenomenon on the conventional PID controller leads to large overshoots and high settling times are observed through the results. The simulation results have shown that the application of combinational approach for different order process has reduced the overshoot and settling time when compared to backcalculation and conditional integration approaches which are desirable for industrial process systems.

References

1. Scottedward Hodel A, Hall CE (2001) Variable-structure PID control to prevent integrator windup. IEEE Trans Ind Electron 48(2):442–451
2. Hanus R, Kinnaert M, Henrotte JL (1987) Conditioning technique, a general anti-windup and bumpless transfer method. Automatica 23(6):729–739
3. Astrom K, Hagglund T (1995) PID controllers theory, design and tuning. ISA Press, Research Triangle Park
4. Bi Q, Cai W-J, Lee E-L, Wang Q-G, Hang C-C, Zhang Y (1999) Robust identification of first order plus dead-time model from step response. Control Eng Pract 7:71–77
5. Visioli A, Branze V (2003) Modified anti windup scheme for PID controllers. IEE Proc Control Theory Appl 150(1):49–54
6. Luyben WL (1996) Tuning proportional-integral-derivative controllers for integrator/dead time processes. Ind Eng Chem Res 35:3480–3483
7. Cominos P, Munro N (2002) PID controllers: recent tuning methods and design to specification. IEE Proc Control Theory Appl 149(1):46–53
8. Bequette BW (2003) Process control: modeling, design and simulation. Pearson Education, Upper Saddle River
9. Johnson MA (2005) PID control technology. In: Johnson MA, Moradi MH (eds) PID control—new identification and design methods. Springer, London, pp 1–46
10. Åström KJ, Hägglund T (2006) Advanced PID control. ISA Press, Research Triangle Park
11. Ibrahim K, Nusret T, Atherton DP (2003) A simple procedure for improving performance of PID controllers. IEEE Trans Control Syst Mag 882–885
12. Shen J-C, Chiang H-K (2004) PID tuning rules for the second order systems. In: Asian control conference, pp 472–477

Analysis on Movement of Conducting Particle by Varying the Particle Dimensions in Gas Insulated Busduct Using Numerical Methods

A. Giriprasad, B. Shruthi, Poonam Upadhyay, and T. Nireekshana

Abstract Particles like copper and aluminium has four phases.They are produced in manufacturing, transportation, installation and the last one is operation in Gas Insulated Substation (GIS). In the cylinder, the smaller particles will be cleaned or removed using vacuum cleaners. Cylinder will always gets filled up with SF_6 gas. But after cleaning, some particles will present in that and these particles will affects the working of the circuit breaker. The conductor and the enclosure are made up of copper and aluminium particles. This enclosure will give the place to the particle to lie on it and inside the duct to move freely. Because of this, the serious problems of arcing and other failures will arise inside the duct. Out of these, one of the major problems is particle contamination. This particle movement will be observed by changing Radius, Length, coating thickness and SF_6 gas pressure. By coating the inner surface, this problem can be overcomes. By doing this, the particles take less charge and there will be change in the movement of the particle. The paper deals with the observation of particle movement by using Charge Simulation and Finite-difference Methods. Results are compared and analyzed.

Keywords Charge simulation method (C.S.M) · Finite difference method (F.D.M) · Gas-insulated substations (GIS) · Sulphur hexafluoride (SF_6) · Gas-insulated busduct (GIB) · Air-insulated substations (AIS)

A. Giriprasad · B. Shruthi (✉) · P. Upadhyay · T. Nireekshana
Department of EEE, VNR Vignana Jyothi Institute of Engineering and Technology, Hyderabad 500090, India
e-mail: billasruthi0185@gmail.com

A. Giriprasad
e-mail: giriprasad_a@vnrvjiet.in

P. Upadhyay
e-mail: upadhyay_p@vnrvjiet.in

T. Nireekshana
e-mail: nireekshana_t@vnrvjiet.in

G. T. C. Sekhar et al. (eds.), *Intelligent Computing in Control and Communication*, Lecture Notes in Electrical Engineering 702,
https://doi.org/10.1007/978-981-15-8439-8_49

1 Introduction

One of the best ways of reliable electricity transmission is through Air Insulated Substations (AIS). But it is not preferable to use where there is insufficiency in land availability. Even so, it has more reliability. In such cases, the most preferable one is Gas-Insulated Substations (GIS) [1]. The capacity is about 800 kV. These GISs have been working successfully for 30 years and are having very few long run buses. The circuit breakers and GISs are using 80% of worldwide SF_6 gas. It is very satisfactory in the reliability and availability. For maintaining the GIS, it requires the approach which is highly integrated and of good quality control for both the manufacturers and users. Everything must be planned carefully for the life cycle of GIS [2]. It should be from design and to the end, i.e., decommissioning. One of the main factors for the GIS is high reliability, which is of worldwide use. Future trends like compact design of the switchgear, Optimization of GIS design for maintenance are used in the development. There are some other main problems that industries are facing are effective management and some of the strategies for developing the older equipment for reuse.

As SF_6 gas history was started in 1900, it is the only gas that is used for the GIS for their non-toxic and good cooling characteristics, and it also has the highest dielectric strength, good physical, electrical and chemical properties. Generally, this SF_6 gas is filled in the cylinders at a pressure ranging from 20 to 30 bars in the form of liquid. It can be withdrawn either gaseous or in liquid form. Depending upon the position of the cylinder, the forms of the SF_6 gas are released. Depending on the standard specifications like IEC 60376-1971 [3], the quality of SF_6 gas will be observed. The preferable method for checking the quality of SF_6 gas is by burning the paper and then inserting it into the container [4]. If it is SF_6 gas, the flame will be extinguished. When there will be an electrical discharge, the gas will get decomposed. SF_6 is a green house gas [5]. It will absorb the infrared radiation.

This paper discusses the particle moment in Gas Insulated Busduct (GIB) using Charge Simulation and Finite Difference Methods. The parameters that we considered for the analysis are length of the particle, radius of the particle and coating thickness inside the conductor.

In this paper, the voltage of 145 kV is considered with zero enclosure potential. The radius of the conductor and enclosure will be 27.5 and 76 mm. The relative permittivity of 7.32 for SF_6 gas and 4 bar for gas pressure and the cylindrical are taken in this paper [6].

2 Mathematical Modelling of GIB

In this paper, a single-phase GIB is taken. The enclosure diameter will be with in the conductor diameter. In this paper, at the surface of the enclosure, the particle is at rest and will be assumed until the voltage that applied will get the capacity to lift

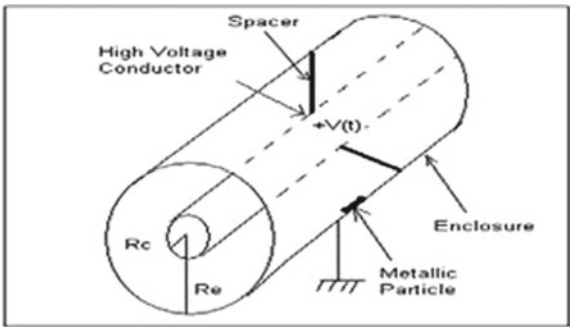

Fig. 1 Overview of gas-insulated bus duct

the particle. Whenever the particle gets the particular charge, then the particle will get lifted and travels in the same field [7]. The overview of the Gas-Insulated Bus duct is shown in Fig. 1 with conductor and enclosure radius.

$$F_{\mathrm{g}} = mg \tag{1}$$

F_{g} is the Gravitational Force

g is the acceleration due to gravity.

Whenever the particle is placed at enclosure surface, only image charges are to be considered [8]. Then, by considering correction factor (K) in Eq. (1), we get

$$F_{\mathrm{e}} = KQE \tag{2}$$

Then
E = electric field
Q = charge of the particle
K = correction factor.
The electric field can be expressed as

$$E(t) = \frac{V \sin \omega t}{[R_0 - y(t)] \ln\left[\frac{R_0}{R_i}\right]} \tag{3}$$

Substitute Eq. (3) in Eq. (2),
R_i = Radius of inner conductor
R_0 = Radius of the enclosure
$V\sin\omega t$ = supply voltage of electrode
$Y(t)$ = position of the moving particle in upward direction.
The particle motion equation will be

$$m\frac{\mathrm{d}^2 y}{\mathrm{d}t^2} = F_{\mathrm{e}} - F_{\mathrm{g}} - F_{\mathrm{d}} \tag{4}$$

F_d = drag force

Y = direction of motion.

The charge acquired by the particle will be:

$$Q_{net} = \frac{\Pi \varepsilon_0 l^2 E(t_0)}{\ln\left(\frac{2l}{r}\right) - 1} \tag{5}$$

Substitute Eq. (5) in Eq. (2)

Q_{net} = particle charge

l = Length of the particle

r = Radius of the particle.

The drag force equation will be

$$F_d = y\Pi r\left(6\mu K_d(y) + 2.656\left[\mu\rho_g l y\right]^{0.5}\right) \tag{6}$$

where

Y is the particle velocity

R is the radius of the particle

ρ_g is the density of the gas

l is the length of the particle

$K_d(y)$ is drag coefficient.

By substituting Eqs. (1), (2) and (6) in Eq. (4), the equation of motion will be

$$m\frac{d^2y}{dt^2} = \left[\frac{\Pi \varepsilon_0 l^2 E(t_0)}{\ln\left(\frac{2l}{r}\right) - 1} \times E(t)\right] - \rho l \Pi r^2 g - \dot{y}\,\Pi r(6\mu K_d(\dot{y}) + 2.656(\mu\rho_g l\,\dot{y})^{0.5}) \tag{7}$$

All these equations are calculated for finding the electrostatic force $E(t_0)$ from Eq. (7).

3 Numerical Methods

This paper deals with two methods. They are Charge Simulation and the Finite Difference Methods. The variation in the parameters and the particle contamination is determined by using the above said two methods [9].

3.1 Charge Simulation Method

From Fig. 2, it is clearly known that the charges that are distributed on the electrode surface will be replaced with N number of charges for calculating the electric fields. The charges positions can be predetermined but the magnitudes are not known. So for finding those charge magnitudes, some points will get selected on the electrode surface [10].

In this method, the points are selected depending on the charges. Based on the superposition principle the points and the charges are made equal. So according to the superposition principle, the expression can be written as:

$$\sum_{j=1}^{N} P_{ij} Q_j = V \tag{8}$$

where P_{ij} = potential coefficient and this will be calculated by using laplace equation.

For suppose when Eq. (8) is appealed to 'N' number of points then the resultant will be N fictitious charges that are not known.

$$[P]_{N\times N}[Q]_N = [V]_N \tag{9}$$

whereas from Eq. (9) $[P]$, coefficient matrix $[Q]$, column matrix and $[V]$, unknown charges. The above equation is for solving fictitious unknown charges [11]. After calculating the charge, the field intensity and the potential at any point is calculated outside the electrode. In this paper, single phase product at point P is evaluated by

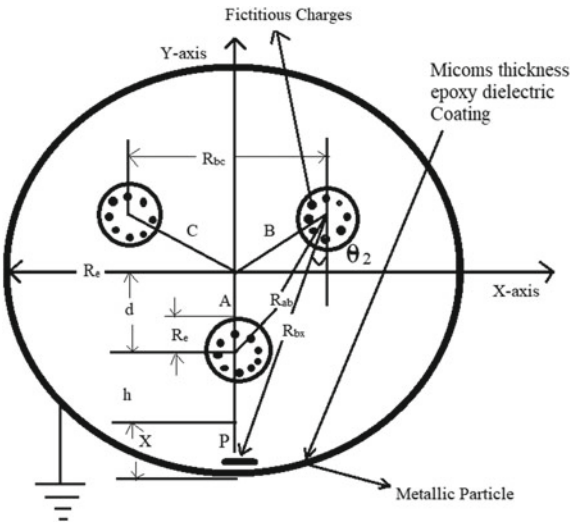

Fig. 2 The view of charge simulation method

using,

$$E = \frac{V}{R_{\mathrm{p}} \log\left[\frac{R_{\mathrm{e}}}{R_{\mathrm{c}}}\right]} \tag{10}$$

where

From Eq. (10), V is the bus duct voltage, R_{p} is the distance between point P and conductor R_{e}, enclosure radius and R_{c}, conductor radius.

By using Eqs. (11) and (12) the field coefficient at point $P(x, y)$ are determined.

$$E_x(t) = \sum_{i=1}^{3n} \frac{\lambda_i}{2\pi\varepsilon}\left[\frac{x - x_i}{\sqrt[3]{(x - x_i)^2 + (y - y_i)^2}}\right] \sin \omega t \tag{11}$$

$$E_y(t) = \sum_{i=1}^{3n} \frac{\lambda_i}{2\pi\varepsilon}\left[\frac{y - y_i}{\sqrt[3]{(x - x_i)^2 + (y - y_i)^2}}\right] \sin \omega t \tag{12}$$

where,

$E_x(t)$ = field component along x-axis,

$E_y(t)$ = field component along y-axis,

X_i, y_i = fictitious charge coordinates of ith component,

X_i = line charge density,

N = number of fictitious charges.

From Eqs. (11), (12) we will find the electric field at two different points.

3.2 Finite Difference Method

From Fig. 3, it is said that a particular section is divided accordingly and for certain points, FDM method is applied as shown in the below procedure [12].

This is one of the simple numerical techniques for solving any problem analytically. Any problem will be uniquely defined as three ways. Those are Laplace's equation, a solution region with initial or boundary conditions. The main objective of this method is to approximate the small differences to the Poisson's equation, which will use the approximation for finding these potential points at every point which are free. Poisson's equation is

$$\nabla^2 V = \frac{-\rho_{\mathrm{v}}}{\varepsilon} \tag{13}$$

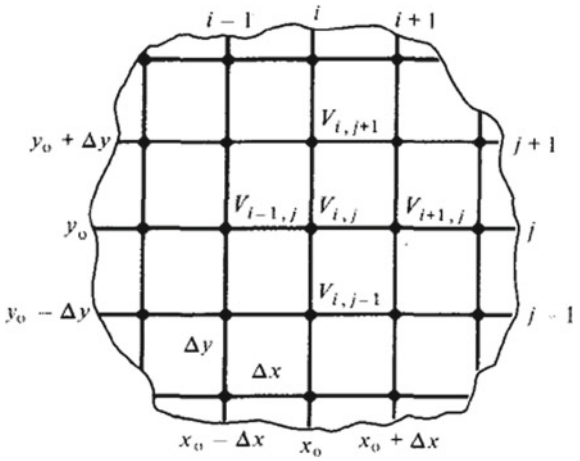

Fig. 3 Schematic view of FDM

When Eq. (13) is modified it becomes two-dimensional region then it becomes,

$$\frac{\partial^2 v}{\partial x^2} + \frac{\partial^2 v}{\partial y^2} = \frac{-\rho_s}{\varepsilon} \tag{14}$$

When the solution region is free and applied to Eq. (14), then the Laplace equation becomes as:

$$\nabla^2 V = \frac{\partial^2 v}{\partial x^2} + \frac{\partial^2 v}{\partial y^2} = 0 \tag{15}$$

Equation (15) is a 5-node approximation and for the potential at centre of the mesh, which is of square shape as shown in Fig. 4.

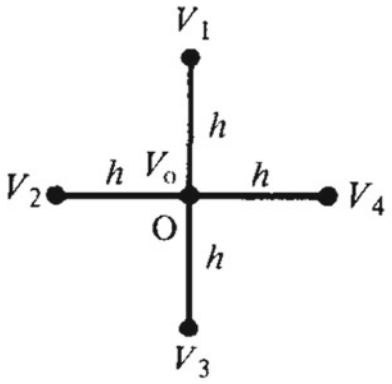

Fig. 4 5-node approximation

$$V_0 = \frac{1}{4}(V_1 + V_2 + V_3 + V_4) \tag{16}$$

From Eq. (16) it is clearly showing that it is the average of all the Laplace equation.

4 Effect of Change in Parameter

In this paper, we will observe the particle moment by changing the parameters. So for finding the change in these parameters, we use the numerical methods. The parameters that are considered in this paper are Radius, Length and Coating thickness.

4.1 By Changing the Particle Length, the Effect in the Movement of the Particle Will be Explained below

From this paper, we are assuming the particle shape will be cylindrical, and the particle will be of metallic. Then the particle movement observed will be as follows:

$$m\frac{\mathrm{d}^2 y}{\mathrm{d}t^2} = F_\mathrm{e} - F_\mathrm{g} - F_\mathrm{d} \tag{17}$$

$$F_\mathrm{g} = \pi r^2 g l \tag{18}$$

$$F_\mathrm{d} = 1.328(2\pi r)\left[\mu\rho_\mathrm{g} l\right]^{0.5} y^{0.5} \tag{19}$$

From Eqs. (17), (18), (19) we will observe the changes in the results. So by changing the length, there is a change in the gravitational and drag force and electrostatic force remains unchanged.

4.2 By Changing the Particle Radius, the Effect in the Movement of the Particle Will be Explained below

The particle movement is given by

$$F_\mathrm{g} \propto r^2 \tag{20}$$

$$F_\mathrm{d} \propto r \tag{21}$$

By changing the length and keeping the coating thickness and radius as constant, we will observe the changes in the results. By changing the radius all the three forces will change. From Eqs. (20) and (21) the radius changes depending upon the forces. Electrostatic force will also change, but it is negligible as the change is very small.

4.3 By Changing the Coating Thickness of the Particle, the Effect in the Particle Movement Will be Explained below

If the particle is not moving properly, it leads to the effect in the GIS safety and in its work. We will neglect the gap between the enclosure, with and without coating thickness which is of dielectric. The results are analysed.

5 Results and Discussions

In this section, the observation of change in length, radius and coating thickness on movement of particles is discussed.

5.1 Observation of Change in Length on the Movement of Particles

The busduct dimensions are:

Radius of the conductor: 27.5 mm.
Radius of the enclosure: 16 mm.
The space between enclosure and conductor: 48.5 mm.
Radius of the particle: 0.25 mm.
The range of varying particle length: 8–15 mm.
Applied Voltage: 145 kv.
Coating Thickness: 200 μm.

From Tables 1 and 2, we have used two methods. They are CSM and FDM. The lengths we are taken from 8 to 15 mm. From Table 1 we can clearly observe that the values of FDM are less compared to CSM. The movement that we considered here is radial. From Table 2 the FDM values are more compared to CSM, i.e., without charge image. The movement that we considered is Axial. Here the movement is more in FDM when there is a change in particle length. For better understanding, we are considering only radial movements. From Fig. 5, it is clearly seen that the particle movement is more in FDM compared to CSM. We use these values for both with and without dielectric coating thickness.

Table 1 The maximum radial movement of the aluminum particle for various lengths of the particle at 145 kv using CSM and FDM

S. No.	Length of particle (mm)	Maximum radial movements in Al particle (mm)	
		CSM	FDM
1	8	8.54	6.82
2	10	8.73	6.94
3	12	8.84	7.03
4	15	9.03	7.13

Table 2 The maximum axial movement of the aluminium particle at variable lengths of the particle at 145 kv using CSM and FDM

S. No.	Length of particle (mm)	Axial movements in Al particle (mm)	
		Without image charge (mm)	FDM
1	8	75.25	102.29
2	10	81.45	56.99
3	12	84.77	88.98
4	15	69.39	62.54

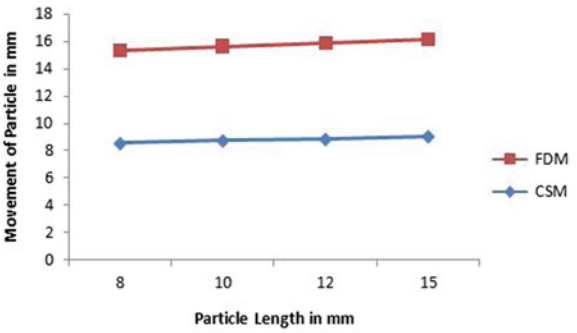

Fig. 5 Particle movement at different lengths with dielectric coating

For any method either it is CSM or FDM, we will observe the movement of the particle inside the conductor. All the results are done internally by using mathematical modeling. All the obtained values are calculated and we came to the conclusion that charge simulation method has less effect in the movement of the particle, whenever it is contaminated. Here the length of the particle will change the forces like gravitational and the drag force and there is negligible effect in the electrostatic force. By considering all the values from the three forces, we will observe the electric field inside the duct. And from the graph, it is clearly shown that particle movement is more in FDM compared to CSM. From this paper, it is only explained about particle movement for the electric field.

5.2 Observation of Change in Radius on Particle Movement

The busduct dimensions are:

Radius of conductor: 27.5 mm.
Radius of enclosure: 16 mm.
The space between the enclosure and conductor: 48.5 mm.
Particle Length: 12 mm.
The range of radius of the particle: 0.10–0.40 mm.
Applied Voltage: 145 kv.
Coating Thickness: 200 μm.

From Table 3. It is observed about the movement of the aluminium particle in Radial. In Table 4. It is explained only by Axial movement. But by finding the particular movement of the particle we will only consider the radial movements. From the below said two tables, the movement is calculated by using CSM and FDM. By changing the radius, the drag and gravitational forces will change.

For finding the particle movement by changing the particle radius is mentioned above. The bus duct dimensions are also given. From Table 3 it clearly observed that by changing the particle radius the particle movement will be less in FDM compared to CSM in Radial movement whereas in Axial movement FDM values are more compared to CSM. The movement keeps on decreasing by changing the radius of the particle.

Figure 6 shows the particle movement is more in FDM compared to CSM. We can consider the same values for with and without dielectric coating thickness. For proper

Table 3 The maximum radial movement of the aluminium particle at variable radius of the particle at 145 kv using CSM and FDM

S. No.	Radius of particle (mm)	Radial movements of Al particle (mm)	
		CSM	FDM
1	0.01	8.84	7.03
2	0.02	5.38	4.04
3	0.03	3.61	2.74
4	0.04	2.98	2.35

Table 4 The maximum axial movement of the Al particle at variable radius of the particle at 145 kv using CSM and FDM

S. No.	Radius of particle (mm)	Radial movements of Al particle (mm)	
		Without image charge (mm)	FDM
1	0.01	84.77	88.98
2	0.02	86.87	55.78
3	0.03	54.71	47.81
4	0.04	55.93	51.16

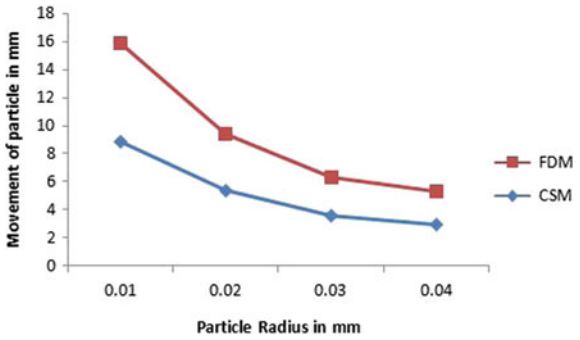

Fig. 6 Radial movements at different radius with dielectric coating

understanding, we only consider the radial movements instead of axial movements. From Fig. 6, it is clearly shown that the movement in CSM is less when compared to FDM. Here also there is more particle movement in FDM because of the change in the radius of the particle inside the bus duct.

5.3 Observation of Change in Coating Thickness on Particle Movement

The following are the observations identified

Applied voltage: 400 kv.
Coating Thickness: 100–400 μm.
Length of particle: 12 mm.
Radius of particle: 0.25 mm.

Coating thickness will play a vital role in the particle movement [13]. Whenever the particle is contaminated, the best method to overcome that contamination is coating thickness. But that should be within the limits. If the coating exceeds the limits, that will effect the insulation of the cylinder and also working of the GIS. So for proper given coating thickness, we will observe the movement of the particle by using the above given two methods. Table 5 gives clear values about the movement

Table 5 The maximum radial movement of the aluminium particle at variable coating thickness of the particle at 400 kv using CSM and FDM

S. No.	Coating thickness (μm)	Radial movements of Al particle (mm)	
		CSM	FDM
1	100	3.74	30.81
2	200	3.67	20.28
3	300	3.58	20.11
4	400	3.53	20.08

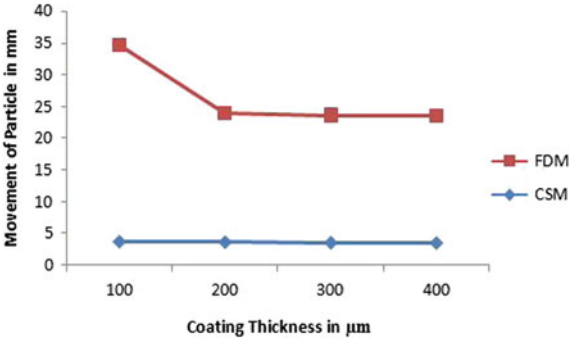

Fig. 7 Particle movement with different coating thickness values

of the particle for particular change in the coating thickness.

We are observing the particle movement by changing the coating thickness from Table 5. There is drastic change in the values of Table 5. By changing the coating thickness the movement in FDM is very much higher than the CSM.

Figure 7 shows the change in FDM values by comparing the CSM. The movement that we are considered in coating thickness is Radial. The voltage that we applied in this method is 400 kv. So here from Fig. 7, by changing the coating thickness particle movement remains same and to some extent, it keeps on decreasing and came to the constant state after some time in FDM.

To change the shape of the particle from cylindrical to spherical, the values of particle lengths and Radius should be changed. It is clearly observed that by changing both the length and radius of the particle, movement depends or changes. So, the particle movement will be more in cylindrical shape compared to spherical shape. For more analysis in particle movement of the cylindrical shape, it should be coated to the conductor. As a result, the distance between the conductor of the GIB and enclosure will gets decreased.

6 Conclusion

This paper clearly discuss about the particle movement by varying the length, Radius and coating Thickness by using different numerical Methods like CSM and FDM. We will find the electrical field intensity and observe the changes in the particle movement by using those Numerical Methods. This paper also clearly explains the CSM and FDM methods. We have also observed the changes using with and without dielectric coating thickness. We can reduce the failure rate of GIS by changing the particle dimensions and also the cost of the GIB. We should not change the radius of the enclosure for better reliability. Overall, this paper clearly explains that particle movement will be acceptable in CSM mostly. CSM is one of the most reliable methods for finding the electric field intensity.

References

1. Fujimoto N, Boggs SA, Chu FY (1985) Gas insulated substations—technology and practice. Pergamon press, New York
2. Kindsen O, Menon KV (1995) Future development trends in GIS technology. In: 3rd workshop and conference on EHV technology, Indian Institute of Science, Bangalore, 2–4 Aug 1995
3. Arora A, Koch H (2005) Design features of GIS. In: IEEE power engineering society general meeting, vol 1, 12–16 June 2005, pp 927–929
4. Christophorou LG, Olthoff JK, Van Brunt RJ (1997) SF_6 and the electric power industry. IEEE Electr Insul Mag 20–24
5. Radwan RM, Morsi R, Abd-Allah MA (1994) Motion of free conducting particles in SF_6 insulated systems under dc switching voltages. IEEE Trans Dielectr Electr Insul 1:25–30
6. Chu FY (1986) SF_6 decomposition in gas insulated equipments. IEEE Trans Electr Insul E-21(5)
7. Anis H, Srivastava KD (1981) Free conducting particles in compressed gas insulation. IEEE Trans Electr Insul E1–16:327–338
8. Macros MM, Ward SA, Anis H (1999) Particle initiated breakdown with spacer involvement in compressed gas and its mixtures. In: IEEE conference on electrical insulation and dielectric phenomenon
9. Naidu MS (2008) Gas insulated substations. IK International
10. Malik NH (1989) A review of charge simulation method and its applications. IEEE Trans Electr Insul 24(1):3–19
11. Singer H, Steinbigler H, Weiss P (1974) A charge simulation method for the calculation of high voltage fields. IEEE Trans Power Appar Syst PAS-93:1660–1668
12. Saidiku MNO (2001) Elements of electromagnetics, 3rd edn. Oxford University Press, pp 660–716
13. Nagesh Kumar GV, Amarnath J, Singh BP (2008) Behavior of metallic particles in a single phase gas insulated system with dielectric coated electrodes. In: International conference on condition monitoring and diagnosis, Beijing, 21–24 Apr 2008. ISSN 978-1-4244-1622-6/08

Intelligent Liver Disease Prediction (ILDP) System Using Machine Learning Models

A. Durga Praveen, T. PanduRanga Vital, D. Jayaram, and L. Venkata Satyanarayana

Abstract Liver disease (LD) is a common disease in the world. The functionality of the liver is very crucial in the human body where it impacts much physical functionality like the manufacture of protein, Metabolism of iron and sugar, and blood clotting. In the present decade, the research on prediction and prevention of LD with Data Mining and artificial intelligence concepts is very important. For this, artificial inelegancy concepts play a vital role. Many researchers have to utilize machine learning (ML) models for predictions of diseases. In this paper, we present the empirical statistical analysis to prevent the LD and apply efficient ML models for predictions of liver diseases in early with low cost. The data set is collected from hospital and reputed clinical centers of Andhra Pradesh, India during 2018–2020. The data set contains personal and clinical information. We apply reputed 5 ML models that are KNN, SVM, RF, Naïve Bayes, and AdaBoost. As per performance analysis, the KNN and AdaBoost models perform highly than other experimental models with accuracy 1 (100%) for predicting LDs. The remaining also performs well, where their accuracy values are above 0.86 (86%).

Keywords Liver disease · Machine learning · Andhra Pradesh · Prediction

A. D. Praveen
Department of IT, Anil Neerukonda Institute of Technology and Sciences (ANITS), Visakhapatnam 530003, India
e-mail: adurgapraveen@gmail.com

T. P. Vital (✉) · L. V. Satyanarayana
Department of CSE, Aditya Institute of Technology and Management (AITAM), Tekkali, Srikakulam, Andhra Pradesh 532201, India
e-mail: vital2927@gmail.com

L. V. Satyanarayana
e-mail: satyacse2005@gmail.com

D. Jayaram
Department of MCA, CBIT, Hyderabad, Telangana 500075, India
e-mail: jayaramcbit1974@gmail.com

G. T. C. Sekhar et al. (eds.), *Intelligent Computing in Control and Communication*, Lecture Notes in Electrical Engineering 702,
https://doi.org/10.1007/978-981-15-8439-8_50

1 Introduction

Liver is one of the significant major organs in human body. The normal liver occupies the right upper quadrant, extending from the fifth inter-costal space in the mid clavicular line down to the right costal margin. The lower margin descends below the costal margin during inspiration [1]. The average weight of liver is 1800 g in men and 1400 g in women. The liver is the second largest and the heaviest organ in the body and serves a key role in critical metabolic pathways and synthetic functions [2]. The liver is the biggest organ of the body encased inside the correct lower rib confine underneath the stomach. It is totally secured by instinctive peritoneum just as totally secured by a thick unpredictable connective tissue layer that lies profound to the peritoneum. Liver is partitioned into two head projections, a huge right flap, and a little left projection isolated by falciform tendon. The correct flap is considered by numerous anatomists to incorporate a second rate quadrate projection and a back quadrate flap. Liver has five surfaces as Anterior, back, prevalent, mediocre, and right [3, 4].

Acute liver disorder most regularly effects from acute huge liver cell corruption made by toxic drugs and viral hepatitis and harmful medications and substance additionally it follows the acute greasy difference in the liver Acute liver disappointment is portrayed by Hypoglycemia, Jaundice, Electrolyte and AST, LDH, ALT. There are three sorts of acute liver disorder that are FHF, Acute or CHF and Sub-acute HF. FHF is a symptom, described by serious encephalopathy ensuing on monstrous Carcinoma of the liver. The subsequent one is Acute or CHF; this may result from protein over-burden sepsis or intercession with medications or medical procedures. The third one is Sub-acute Hepatic Failure—It is characterized as an acute disappointment happening in patients without previous liver ailment, in whom the indications of encephalopathy grow over about two months after the beginning of the sickness [5–7].

ML is one of the parts of artificial intelligence (AI). It provides tools and methods that can solve diagnostic and prognosticative problems in various medical domains. It is being used for the investigation of the significance of clinical parameters and of their mixes for forecast, for the extraction of clinical information for examining, for treatment arranging, and for generally speaking patient administration. The fruitful fortunate execution of ML models can encourage the combination of system based frameworks in the clinical space giving chances to improve the work of clinical specialists and in this way improve the productivity and adequacy of clinical consideration [8, 9].

Early detection of disease is most important for saving life and money. Detection and forecasting of liver diseases (LD) with ML models and neural networks are very crucial for the researchers and analysts. Dhingra et al. [10] analyzed UCI ML repository Indian liver dataset with ML models like SVM, logistic regression, NB, and ANN. In this, they found that ANN model is the better-performed model with 80.7% of accuracy than other experimental models. El-Shafeiy et al. [11] researched on Egyptian LD data set with hybrid ML models that it describes as an ensemble

(C5.0 + NB + SVM) classifier. This is proposed to classify the data with combination of Boosted C5.0, SVM and NB ML algorithms chosen rules. Their proposed model performs 97.2% of accuracy. Książek et al. [12] proposed novel methodology to identification of HCC (Hepatocellular carcinoma). In this, they used C-SVC type SVM with 2 level GA optimizer and get the 88.49% of accuracy. Abdar et al. [13] applied new DT model on UCI ILPD and they also applied CHAID and C5.0 models for creating the rules in LD. They conclude that C5.0 via Boosting model had an accuracy of 93.75% and CHAID model performed 65.00% of accuracy. Gatos et al. [1] studied on CLD (Chronic liver disease) utilizing SWE images along with CAD system. In this work, they focused on 5 cluster segmentation of 35 features. They analyzed total 126 patients data that 70 CLD and 56 non-CLD. As per classification analysis, the highest accuracy was found in SVM model with 87.3% comparative other experimental setup models.

Fatty liver disease (FLD) is a very complicated disease in clinical level; it is related to mortality. Wu et al. [14] researched on FLD with noble ML methods like NB, RF, LR and ANN models. In this, they found ANN model was very accurate than other ML algorithms. LD is one of the significant ailments on the planet, liver is one of the immense strong organs in the human body; and is likewise viewed as an organ in light of the fact that, among its numerous capacities, it makes and secretes bile. The liver auditoriums are indispensable job in numerous physical capacities from protein assembling and blood thickening to fat, sugar and iron digestion. Liver issue infections are any issue of liver reason that purpose behind disorders. Ansari et al. [15] exhibits an ANN-based methodology for the analysis of hepatitis infection. The dataset utilized for this reason for existing is taken from the UCI ML database. Both supervised and neural models have been dissected with various structures, learning and enactment capacities. It is presumed that the regulated model performed superior to the unaided one. The paper compares the consequences of the past examinations on the analysis of hepatitis which utilize the equivalent dataset. Lee et al. [3] separate the characterization of liver malady into progressive multiclass clustering. The SVM includes state-of-the-art ML. The classifier is a piece of CADx, which helps radiologists in precisely diagnosing liver sickness. They figure separating between cysts, hematoma, cavernous hemangioma (CH), and normal tissue and apply SVM to ordering the sicknesses.

2 Proposal Model

Figure 1 shows the proposed model for Liver Disease Identification using Machine Learning (ML) Algorithms. In this, we collected the Liver Disease (LD) and non-LD patients' data from state of Andhra Pradesh, India. The whole information stored in the secondary storage section. In this process, avoid unnecessary information for the experiment. For this, we choose cleaning and preprocess the information and get the pure data set. This data set stored into the secondary storage section as *.csv format. As per dataset, we want to conduct the statistical analysis and fit the ML model for

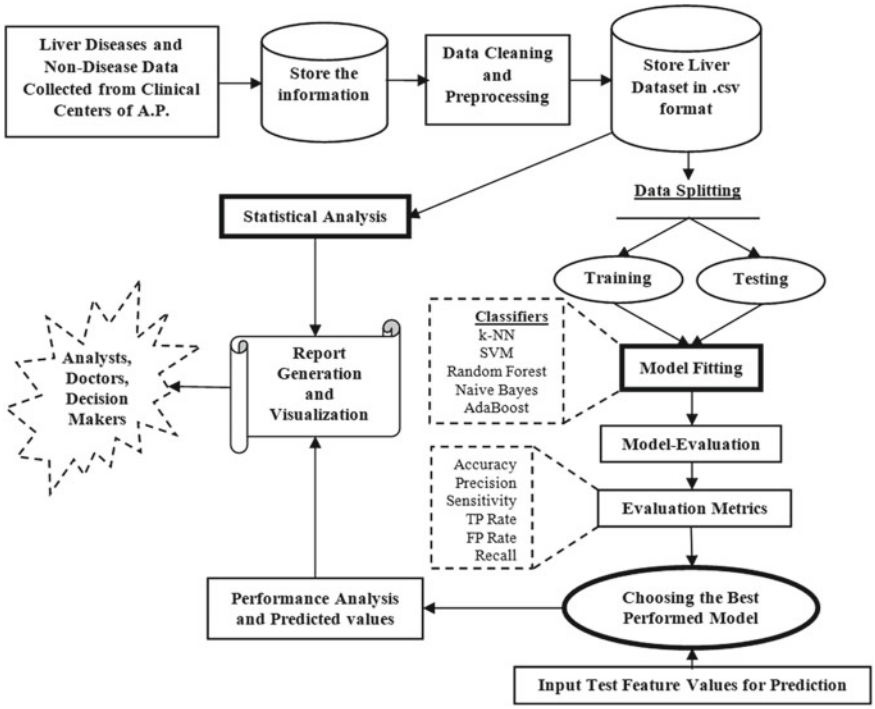

Fig. 1 Proposal model for liver disease identification

predicting LD. The statistical reports are very useful for the doctors, analytics and decision-makers for the preventions about LD. We evaluate the ML models utilizing performance parameters.

2.1 Description of Liver Data Set

Table 1 shows the description of the Liver Data set collected from Andhra Pradesh during 2018 March to 2020 February with 16 features attributes and one 2 classes (Diseased and non-Diseased) attribute. We choose 1640 instances for the experiment. In this, 586 attributes are related to non-liver disease and 874 instances are related to liver disease. The detailed information about attributes described in Table 1. It describes attribute name, Type and description of attributes with values and ranges.

Table 1 Description of Andhra Pradesh liver (APL) data set

S. No.	Attribute	Type	Description
1	Age	Continuous	Age of the individual range is 6–99
2	Gender	Categorical	Sex of individual Female—0 Male—1
3	Smoke	Categorical	Habit of smoke, values are NO—0 YES—1
4	Drink	Categorical	Habit of smoke, values are NO—0 YES—1
5	Vomiting	Categorical	Vomiting sensation, values are Absent—0 Present—1
6	Headache/bone ache	Categorical	Headache or bone ache, Absent—0 Present—1
7	Fever	Categorical	Fever, Absent—0 Present—1
8	BP	Categorical	Blood pressure, Normal—0 Low—1 High—2
9	Total_Bilirubin	Continuous	Total_Bilirubin range is 0.4–75
10	Direct_Bilirubin	Continuous	Direct_Bilirubin range is 0.1–19.7
11	Alkaline_Phosphotase	Continuous	Alkaline phosphates range is 10–4929
12	Alamine_Aminotransferase	Continuous	Alamine aminotransferase—range 10–2000
13	Aspartate_Aminotransferase	Continuous	Aspartate aminotransferase—range 5–4929
14	Total_Proteins	Continuous	Total_Proteins—range is 0.9–7.7
15	Albumin	Continuous	Albumin-range—range is 0.9–7.7
16	A-G_Ratio	Continuous	Albumin_and_Globulin_Ratio—range is 0.3–4.0
17	Diagnosis (Class)	Categorical	Non-liver disease (Class 0) and liver disease (Class 1)

2.2 Naïve Bayes (NB) Model

It expects that the presence of an unambiguous aspect of a class is autonomous of every other aspect. As per Bayes theorem, the contingent probability is given by Eqs. (1) and (2).

$$P(A|B) = \frac{P(A \cap B)}{P(B)} \tag{1}$$

$$P(A|B) = \frac{P(B|A)P(A)}{P(B)} \tag{2}$$

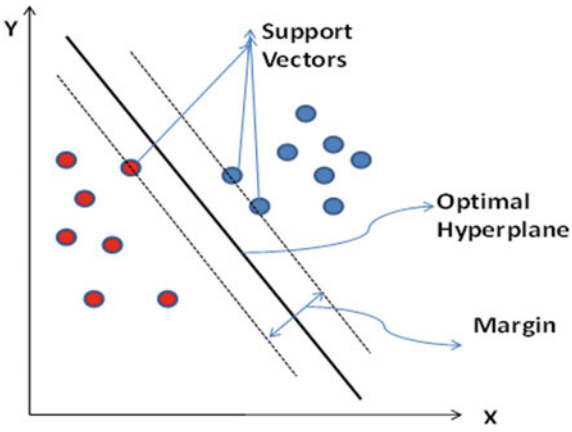

Fig. 2 SVM classifier analysis

2.3 SVM Model

An additional fantastic ML model is support vector (SVM) machine that can be utilized for both regression problems as well as classification. In this, '*n*' features are addressed on the *n*-dimensional plane spaces with every segment described by the assessment of a particular coordinate. A data segment containing n qualities is plotted on this *n*-dimensional space [16]. The fact of the matter is to discover a hyper-plane which orders and builds the edge in an *n*-dimensional space (shown in Fig. 2).

2.4 K-Nearest Neighbors' (k-NN) Classification

The k-NN is a nonparametric statistic technique fitted for regression problems as well as classification. It conceives the k nearest points of data in the preparation models. The yield contrasts dependent on the way that KNN is utilized for regression problems as well as classification. The yield predicts the class to which an information point has a place dependent on how intently it matches with the k closest neighbors. This is one of the case-based learning, or sluggish learning calculations, on the grounds that the capacity considers the nearby information focuses and all calculation is conceded until arrangement. This calculation utilizes separation capacity to ascertain the nearby inexact with the K Nearest Neighbors [17]. For uninterrupted factors, Minkowski (Eq. 5), Euclidean (Eq. 3) Manhattan (Eq. 4) and measures of outdistancing are utilized and hamming outdistance for straight out factors appeared in conditional Eqs. (3), (4), (5).

$$\text{Euclidean Distance} = \sqrt{\sum_{i=1}^{k} (x_i - y_i)^2} \tag{3}$$

Table 2 Analysis of confusion matrix structure

	Predicted values		
Actual values	Classes	Non-liver disease (0)	Liver disease (1)
	Non-liver disease (0)	(0, 0)	(0, 1)
	Liver disease (1)	(1, 0)	(1, 1)

$$\text{Mahattan Distance} = \sum_{i=1}^{k} |x_i - y_i| \tag{4}$$

$$\text{Minkowski Distance} = \left(\sum_{i=1}^{k} (|x_i - y_i|)^q \right)^{1/q} \tag{5}$$

2.5 *Confusion Matrix*

In this, we express the AP Liver Disease Confusion Matrix analysis structure for each ML model. Table 2 depicts a problem with 2 classes that are 0 specifies NLD and 1 specifies LD. It is construed with True positive, True Negative, False Negative and False positive that are specified with cells like (0, 0), (0, 1), (1, 0) and (1, 1) relatively. The diagonal values of the matrix represent the correctly classified instances by that ML model and non-diagonal values have represented the incorrectly classified instances. Confusion matrix is very curial for calculations of performance parameters like accuracy of model, recall, precision, $F1$-value and so on [18].

2.6 *Performance Parameters*

Performance specifies the working model efficiency. We will measure this with many parametric measures like classification accuracy, rates and ratios of truly and falsely classified instance and so on. Equations (6)–(17) describe the parameters like TPR, FNR, FPR, $F1$ Score and etc. These equations are clearly specified with their parametric values of the model performance. Every parameter specifies their individual behavioral value reflects the particular data set with particular ML model.

$$\text{TPR} = \frac{\sum \text{True Positive}}{\sum \text{Condition Positive}} \tag{6}$$

$$\text{FNR} = \frac{\sum \text{False Negative}}{\sum \text{Condition Positive}} \tag{7}$$

$$\text{FPR} = \frac{\sum \text{False Positive}}{\sum \text{Condition Negative}} \tag{8}$$

$$\text{SPC or TNR} = \frac{\sum \text{True Negative}}{\sum \text{Condition Negative}} \tag{9}$$

$$\text{Prevalence} = \frac{\sum \text{Condition Positive}}{\sum \text{Total Population}}. \tag{10}$$

$$\text{PPV or PRC} = \frac{\sum \text{True Positive}}{\sum \text{Predicted Condition Positive}} \tag{11}$$

$$\text{FOR} = \frac{\sum \text{False Negative}}{\sum \text{Predicted Condition Negative}} \tag{12}$$

$$\text{Accuracy (ACC)} = \frac{\sum \text{True Positive} + \sum \text{True Negative}}{\sum \text{Total Population}} \tag{13}$$

$$\text{FDR} = \frac{\sum \text{False Positive}}{\sum \text{Predicted Condition Positive}} \tag{14}$$

$$\text{NPV} = \frac{\sum \text{True Negative}}{\sum \text{Predicted Condition Negative}} \tag{15}$$

$$\text{DOR} = \frac{\text{LR}+}{\text{LR}-} \tag{16}$$

$$F_1 \text{ score} = 2 * \frac{\text{Precision} * \text{Recall}}{\text{Precision} + \text{Recall}} \tag{17}$$

3 Results and Discussions

In this section, we promote necessary simulation results that are correlation feature attributes of LD on class attribute (LD Patients (1) and non-LD patients (0)), statistical analysis reports and results, and MLs performance analysis and predicted values.

3.1 Correlation Feature Attributes Analysis

Figure 3 shows correlation Liver attribute analyzing with values between −1 and + 1, and colors (Red and Blue). As per correlation values analysis, the value is one that it specifies highly correlated attributes (indicated dark red) and minus values are declared as under correlated attributes (indicated blue color). Neutral correlated attribute values are zero or very nearer to zero (specified color is light blue).

The 'BP' attribute is correlated with the feature attribute 'Age' that the value is 0.64. Some of the feature attributes like 'Total-Bilirubin', Direct-Bilirubin, 'Alkaline-Phosphatases' and 'Alanine–Aminotransferase' are correlated to each other where the correlation value is greater than 0.49. Some other attributes also correlated to other that are 'Total-Proteins', 'Albumin' and 'Albumin_and_Globulin_Ratio' that Albumin_and_Globulin_Ratio is correlated to Albumin with 0.61 correlation value and 'Total-Proteins' attribute is correlated with 'Albumin' with 0.49 correlated value.

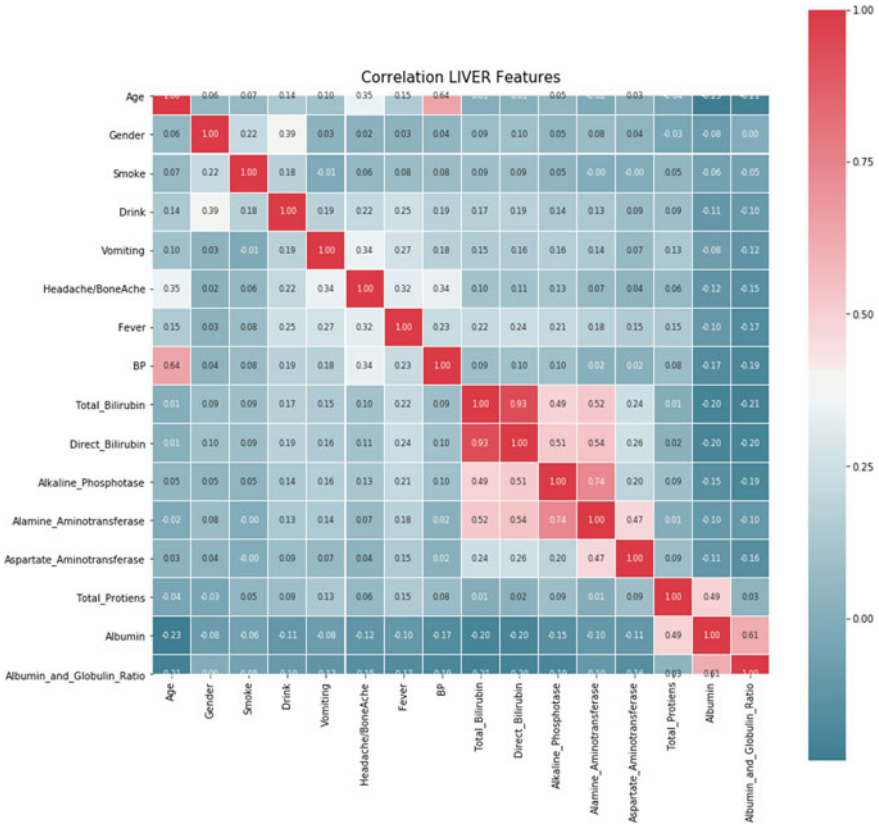

Fig. 3 Correlation feature attributes of A.P. liver (APL) data set

3.2 Statistical Analysis

Table 3 describes about Categorical (nominal) attributes of APL data set. As per ratio of gender, most of the instances are male than female that there are 685 male instances and only 191 female belonging to the LD instances set (total 876) because of habits, lifestyle or work environment. The more number of smokers and drinkers instances are in LD set than non-LD. The detailed analysis is shown in Table 3 about symptoms of liver disease patients like vomiting, head and bone ache, fever, and BP.

Table 4 projects the mean and median values of the attribute age and clinical result attributes. As per observations of clinical results, the mean and median LD values of the attributes like 'Total-Bilirubin', Direct-Bilirubin, 'Alkaline-Phosphatases' and 'Alanine–Aminotransferase' are very high than the Non-LD. The values of Aspartate-Aminotransferase and Total-Proteins are also some high mean and median values in LD comparative Non-LD.

Table 3 Categorical attribute statistical nominal values

Attribute statistical counting values				
Attributes	Attribute value	Non-liver disease (NLD)	Liver disease (LD)	Total dataset (TD)
Gender	Male	414	685	1099
	Female	174	191	365
Smoke	No (0)	318	412	730
	Yes (1)	270	464	734
Drink	No (0)	500	418	918
	Yes (1)	88	458	546
Vomiting	Absent (0)	472	245	717
	Present (1)	116	631	747
Headache/bone ache	Absent (0)	444	293	737
	Present (1)	144	583	727
Fever	Absent (0)	470	210	680
	Present (1)	118	666	784
BP	Normal (0)	398	368	766
	Low BP (1)	91	182	273
	High BP (2)	100	327	427

Table 4 Integral attributes statistical values

Mean and median attributes statistics						
Attributes	Mean values			Median		
	Non-liver disease (0)	Liver disease (1)	Total	Non-liver disease (0)	Liver disease (1)	Total
Age	41.75427	45.63616	44.07808	40	46	45
TB	1.219283	4.65389	3.275342	0.9	1.8	1.3
DB	0.384642	2.199199	1.47089	0.2	0.8	0.3
AP	96.87884	325.1705	233.5411	49	194	151
AA	36.3686	186.4611	126.2185	28	74	48
AAT	114.6672	213.7586	173.9863	93	168	126
TP	5.312799	6.237071	5.866096	5.5	6.4	6.2
Albumin	3.268601	3.071739	3.150753	3.2	3	3.1
AG_Ratio	1.074198	0.922197	0.983205	1	0.9	1

3.3 Experimental Set Up for Machine Learning (ML) Models on APLD Dataset

For the experiment, we apply 5 ML algorithms that are SVM, k-NN, Naive Bayes (NB), AdaBoost (AB) and Random Forest (RF) on APLD data set. In this, we analyze the confusion matrices of ML models, parameters of performance like classification accuracy, AUC, $F1$-score, precision and recall, and ROC analysis. Finally, we compare the ML models' accuracy for predicting the LD.

3.3.1 Confusion Matrices Analysis

Figure 4 depicts the confusion matrices of experimental ML models. The confusion matrix is constructed with combination of true and predicted elements of LD and NLD. In this, the '0' indicates the NLD and LD are specified with '1'. In other words, it is combination of true positive, true negative, false positive and false negative values. The model SVM with RBF kernel classifies correctly of LD and N-LD out of 1460 total instances, and incorrectly classified instances are 198. The confusion matrix of SVM is shown in Fig. 4A in detail. Figure 4B describes about confusion matrix of k-NN model. 1460 (586 + 874) instances are classified correctly by k-NN with 100% accuracy. The model Naive Bayes is classified 1296 correctly out of 1460 instances. The confusion matrix of NB is shown in Fig. 4C in detail. Figure 4D describes about confusion matrix of AdaBoost model and Fig. 4E describes Random Forest Tree (RF Tree).

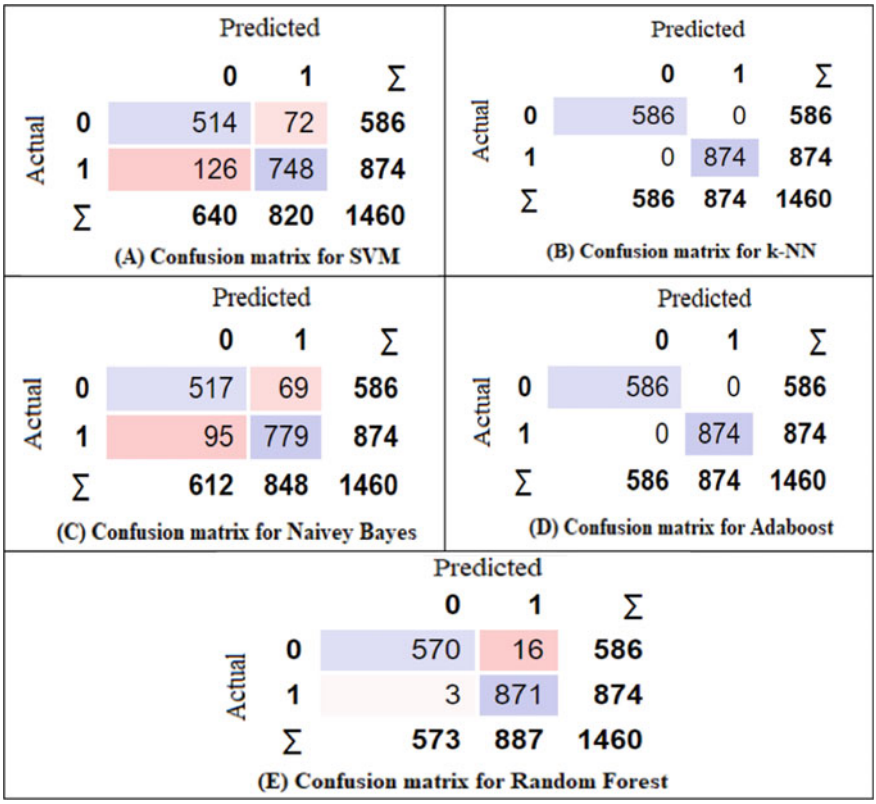

Fig. 4 Confusion matrices for experimental ML models

3.3.2 Accuracy Analysis

In this, we want to analyze the Non-Liver Diseases (NLD), LD and average weighted classes NLD and LD.

Target Class NLD Classification Analysis

Table 5 shows the class NLD performance parameters analysis. In this, the class NLD classifies 100% by the k-NN and AdaBoost algorithms where CA (classification accuracy) and AUC values are 1. The random forest model also performs better way where the CA value is 0.987 and AUC value is 0.999 (nearer to 1). Remaining models SVM with RBF kernel and Naïve Byes perform below 0.887 value of accuracy. The detailed analysis is shown in Table 5.

Table 5 Accuracy specifies for the APLD dataset on target class NLD

Model	AUC	CA	*F*1-score	Precision	Recall
k-NN	1	1	1	1	1
SVM	0.950791	0.864384	0.838499	0.803125	0.877133
Random Forest	0.999195	0.986986	0.983607	0.994764	0.972696
Naive Bayes	0.959648	0.887671	0.863105	0.844771	0.882253
AdaBoost	1	1	1	1	1

Table 6 Accuracy specifies for the APLD dataset on target class LD

Model	AUC	CA	*F*1-score	Precision	Recall
k-NN	1	1	1	1	1
SVM	0.950791	0.864384	0.883117	0.912195	0.855835
Random Forest	0.999194	0.986986	0.989211	0.981962	0.996568
Naive Bayes	0.959648	0.887671	0.904762	0.918632	0.891304
AdaBoost	1	1	1	1	1

Table 7 Accuracy specifies for the APLD dataset on average target classes LD and NLD

Model	AUC	CA	*F*1-score	Precision	Recall
k-NN	1	1	1	1	1
SVM	0.950791	0.864384	0.865209	0.868418	0.864384
Random Forest	0.999194	0.986986	0.986961	0.9871	0.986986
Naive Bayes	0.959648	0.887671	0.888042	0.888987	0.887671
AdaBoost	1	1	1	1	1

Target Class LD Classification Analysis

Table 6 shows the class LD performance parameters analysis. In this, the class LD classifies 100% by the k-NN and AdaBoost algorithms where CA (classification accuracy) and AUC values are 1. The random forest model also performs better way where the CA value is 0.987 and AUC value is 0.999 (nearer to 1). Remaining models SVM with RBF kernel and Naïve Byes perform below 0.887 value of accuracy. The detailed analysis is shown in Table 6.

Average Classes LD and NLD Classification Analysis

Table 7 shows the average classes of LD and NLD performance parameters analysis. In this, the average of classes LD and NLD classifies 100% by the k-NN and AdaBoost algorithms where CA (classification accuracy) and AUC values are 1. The random forest model also performs better way where the CA value is 0.986 and AUC value

is 0.999 (nearer to 1). Remaining models SVM with RBF kernel and Naïve Byes perform below 0.887 value of accuracy.

3.4 Receive Operator Characteristic (ROC) Curves

Figure 5 shows the ROC curves of the experimental ML Models on target class 0 (Non-Liver Disease). Each ML model ROC specified with different colors. The AdaBoost and k-NN model's AUC values are one and indication colors are dark green and orange. The Random Forest Tree specified with pink color and the AUC value is 0.999195 nearer to one. The Naïve Bayes model indicated with violet color and AUC values are 0.959648 better than SVM model (AUC value is 0.95079).

Figure 6 shows the ROC curves of the experimental ML Models on target class 1 (Liver Disease). Each ML model ROC specified with different colors. The AdaBoost and k-NN model's AUC values are one and indication colors are dark green and orange. The Random Forest Tree specified with pink color and the AUC value is

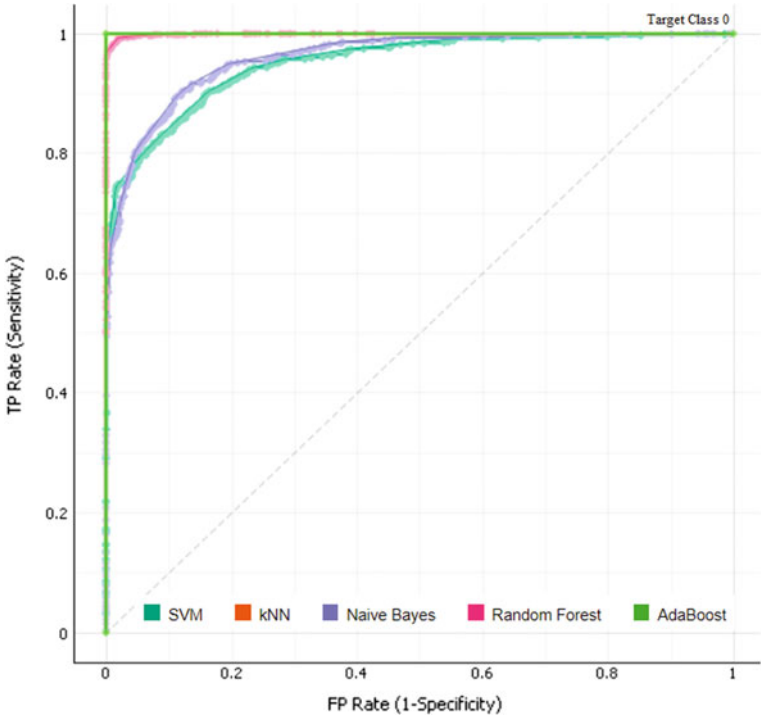

Fig. 5 ROC curves for the experimental ML models SVM, k-NN, Naïve Bayes, Random Forest, and AdaBoost on target class 0

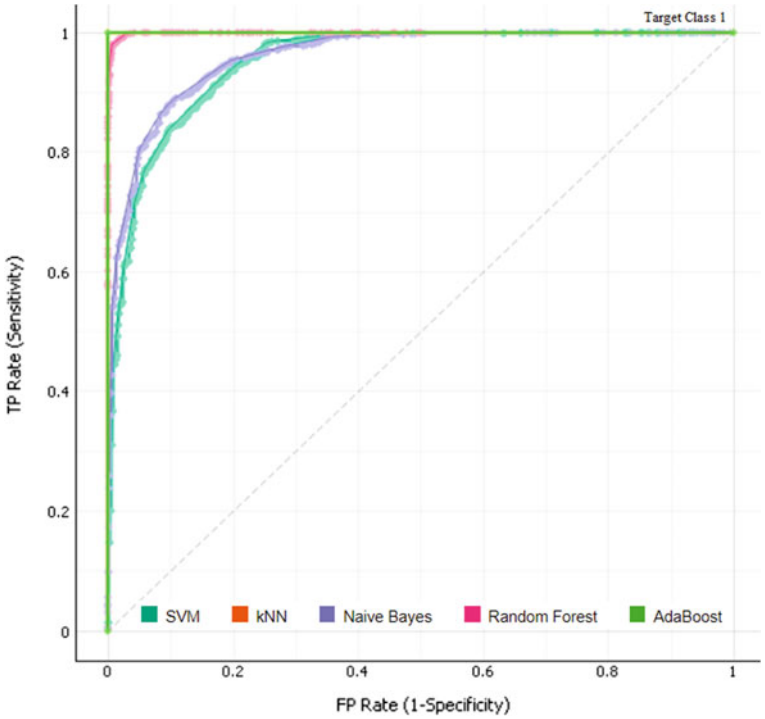

Fig. 6 ROC curves for the experimental ML models SVM, k-NN, Naïve Bayes, Random Forest and AdaBoost on target class 1

0.999194 nearer to one. The Naïve Bayes model indicated with violet color and AUC values are 0.959648 better than SVM model (AUC value is 0.95079).

3.5 ML Models Comparative Analysis

Figure 7 shows the comparative accuracy analysis of the experimental ML models. As per analysis, the k-NN and AdaBoost algorithms are very accurate to predict the Liver Diseases where the classification accuracy (CA) and AUC values are one. All experimental models are performed well with above 0.86 CA and 0.95 AUC values. The random forest algorithm is also well noted with 0.986 CA and 0.999 AUC value.

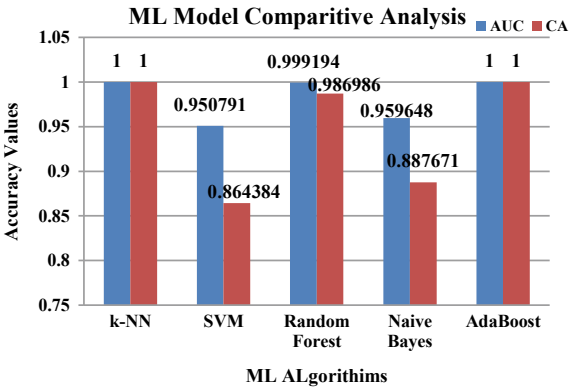

Fig. 7 Comparative analysis of experimental ML algorithms

4 Conclusion

Protection, prediction and preventions are very necessary for any health care system. Liver disease (LD) is a common disease in the world. For the protection and preventions, statistical analysis role is very crucial. In this research, empirical statistical analysis about LD patients is in detail with personal as well as clinical information. As per observation, we found that lifestyle of patient and habits are main factors for occurring LD. We also observed some symptoms like vomiting, fever and head/bone ache indication of LD. In clinical tests of patients, most correlated attributes were Total Bilirubin, Direct Bilirubin, Alkaline Phosphotase, and Alanine Aminotransferase for prediction of LD. As per ML performance analysis, the K-NN and AdaBoost models were very accurate. So, this model will very useful to predict the LD with APLD data set. Further, we will research on LD with Deep Learning models for identification of LD with scanning and CAD images.

References

1. Gatos I, Tsantis S, Spiliopoulos S, Karnabatidis D, Theotokas I, Zoumpoulis P, Kagadis GC (2017) A machine-learning algorithm toward color analysis for chronic liver disease classification, employing ultrasound shear wave elastography. Ultrasound Med Biol 43(9):1797–1810
2. Bean RB, Baker W (1919) Some racial characteristics of the liver weight in man. Am J Phys Anthropol 2(2):167–173
3. Lee CC, Chen SH, Chiang YC (2007) Classification of liver disease from CT images using a support vector machine. J Adv Comput Intell Intell Inform 11(4):396–402
4. Sinnatamby CS (2011) Last's anatomy e-book: regional and applied. Elsevier Health Sciences
5. Bernal W, Auzinger G, Dhawan A, Wendon J (2010) Acute liver failure. Lancet 376(9736):190–201
6. Rueff B, Benhamou JP (1973) Acute hepatic necrosis and fulminant hepatic failure. Gut 14(10):805
7. Lee WM (1993) Acute liver failure. N Engl J Med 329(25):1862–1872

8. Iyyanki M, Jayanthi P (2020) Machine learning for health data analytics: a few case studies of application of regression. In: Challenges and applications for implementing machine learning in computer vision. IGI Global, pp 241–270
9. Das S, Sanyal MK (2020) Application of AI and soft computing in healthcare: a review and speculation. Int J Sci Technol Res 8:21
10. Dhingra S, Singh I, Subburaj R, Diwakar S (2020) ANN model for liver disorder detection. In: Advances in data sciences, security and applications. Springer, Singapore, pp 161–167
11. El-Shafeiy EA, El-Desouky AI, Elghamrawy SM (2018) Prediction of liver diseases based on machine learning technique for big data. In: International conference on advanced machine learning technologies and applications, Feb 2018. Springer, Cham, pp 362–374
12. Książek W, Abdar M, Acharya UR, Pławiak P (2019) A novel machine learning approach for early detection of hepatocellular carcinoma patients. Cogn Syst Res 54:116–127
13. Abdar M, Zomorodi-Moghadam M, Das R, Ting IH (2017) Performance analysis of classification algorithms on early detection of liver disease. Expert Syst Appl 67:239–251
14. Wu CC, Yeh WC, Hsu WD, Islam MM, Nguyen PAA, Poly TN, Li YCJ (2019) Prediction of fatty liver disease using machine learning algorithms. Comput Methods Programs Biomed 170:23–29
15. Ansari S, Shafi I, Ansari A, Ahmad J, Shah SI (2011) Diagnosis of liver disease induced by hepatitis virus using artificial neural networks. In: 2011 IEEE 14th international multitopic conference, Dec 2011. IEEE, pp 8–12
16. Kim HC, Pang S, Je HM, Kim D, Bang SY (2003) Constructing support vector machine ensemble. Pattern Recogn 36(12):2757–2767
17. Kozma L (2008) k nearest neighbors algorithm (kNN). Helsinki University of Technology
18. Visa S, Ramsay B, Ralescu AL, Van Der Knaap E (2011) Confusion matrix-based feature selection. MAICS 710:120–127

Sliding Mode Based Modified Reference Voltage Control Aided Maximum Power Point Tracking for Photovoltaic Fed Brushless DC Motor System

N. K. Rayaguru, Pramod Kumar Gouda, Raghvendraprasad Deshpande, and P. K. Dhal

Abstract Maximum Power Point Tracking has been a proven technology to enhance power delivering capability of PV by making the PV system operating at maximum power for the offered temperature and irradiation. In this work, the MPPT method for Solar PV system using Sliding Mode Control (SMC) under standard test conditions has been proposed. The proposed controller strategy is robust technology in steady-state and also in inconsistent environmental conditions. A DC/DC buck-boost converter has been considered as a control actuator using PWM control on the switches for the MPP tracking. In this work, for a BLDC motor, an SMC scheme has been implemented for obtaining better tracking by receiving ripple-free torque using the inner loop current control.

Keywords Photovoltaic (PV) · Sliding mode controller (SMC) · Maximum power point tracking (MPPT) · Incremental conductance MPPT · Brushless DC motor

N. K. Rayaguru (✉) · P. K. Dhal
Department of EEE, Vel Tech Rangarajan Dr. Sagunthala R&D Institute of Science and Technology, Chennai 600062, India
e-mail: rayagurunk@veltech.edu.in

P. K. Dhal
e-mail: kdhalp@veltech.edu.in

P. K. Gouda
Department of EEE, Aditya Institute of Technology and Management (AITAM), Tekkli, Srikakulam, Andhra Pradesh 532201, India
e-mail: pk_gouda@gmail.com

R. Deshpande
Department of E & E Engineering, GSSIETW, Mysuru, Karnataka 570016, India
e-mail: raagu.deshpande@gmail.com

G. T. C. Sekhar et al. (eds.), *Intelligent Computing in Control and Communication*, Lecture Notes in Electrical Engineering 702,
https://doi.org/10.1007/978-981-15-8439-8_51

1 Introduction

The maximum power point tracking (MPPT) command used is a blend of two efficient and robust controls commands. First one, a neuron network-based control (ANN) to resolve the voltage at which the power of the system PV is maximum. The next command is the integral sliding mode control (ISMC), it takes the voltage generated by the first command as reference and later tries to diminish the error between the *V*ref and the voltage of the panel as presented by Ahmed et al. [1].

The existing algorithms such as perturb and observe and incremental conductance respond erroneously when solar irradiation is augmented. For that a modified incremental conductance algorithm is presented, the later can retort accurately when solar irradiation is increased and trim down the steady-state oscillations as worked out by Motahhir et al. [2]. BLDC motor phase current sensors can be omitted. No supplementary control is related to the speed control of motor-pump and it's soft starting. A DC-DC conversion stage is usually necessary for solar PV fed water pumping which is driven by a brushless DC (BLDC) motor, as presented by Kumar and Singh [3].

Research performance in terms of optimal transfer of energy from a photovoltaic generator to a permanent magnet synchronous motor using a centrifuge pump driver and stability analysis for the proposed MPPT is developed for a photovoltaic (PV) pumping system is done by Farhat [4]. Hahm et al. explained the integrated photovoltaic (PV) and proton exchange membrane fuel cell (PEMFC) system for continuous energy harvesting under various operating conditions for use with a brushless DC motor [5].

Kolluru et al. has explained the thought about Sliding Mode Controller (SMC) realization to a DC-DC boost converter with three criteria, i.e., Hitting, Sliding Mode (SM) Existence, and Stability [6]. In [7] various MPPT algorithms, i.e., perturb and observe (P&O), hill climbing, incremental conductance and neural networks (ANN) have been presented. The optimum photovoltaic (PV) water pumping system using maximum power point tracking technique (MPPT) with optimum chopping ratio of buck–boost converter for water pumping was explained by Kassem [8]. In [9] the authors made a relative study linking two control methods, i.e., the fuzzy logic controller (FLC) and the sliding mode controller (SMC).

This research paper renders a unique approach of suggesting a sliding mode MPPT control for PV fed BLDC motor system application and that uses P&O MPPT along with SMC and buck-boost converter by making the PV system more reliable. The rest of the paper has been outlined in the following way, Sect. 2 gives the overall description of the proposed work and also modeling of PV, buck-boost converter, and brush less DC motor. Section 3 presents the perturbation and observation application for the SMC-based MPPT controller. The speed control techniques for BLDC drive are explained in Sect. 4. Further, the outcome results and the discussions are dealt in Sect. 5. As the final point, Sect. 6 presents the conclusions and the future works.

2 System Description

The overall system comprising of various sections as shown in Fig. 1. The PV panels are arranged in series fashion to shape the PV array. In this work, six PV panels each of 43 W ($18.6 = V_{mp}$, $I_{mp} = 5.63$) are connected to constitute 258 W PV source. Since the PV panels are series-connected, the maximum practical obtainable voltage will be in the range of 100 V and this voltage is regulated through an SMC controller aided by buck-boost converter to charge battery bank (3×12 V $= 36$ V).

2.1 Modeling of PV Array

The Mathematical modeling of PV is crucial for simulation of any PV system and it is executed with reference to the data sheet of Kirloskar solar as shown in Table 1.

The different irradiation from 200 to 1000 W/m^2 in a step size of 200 W/m^2 [5, 10, 11].

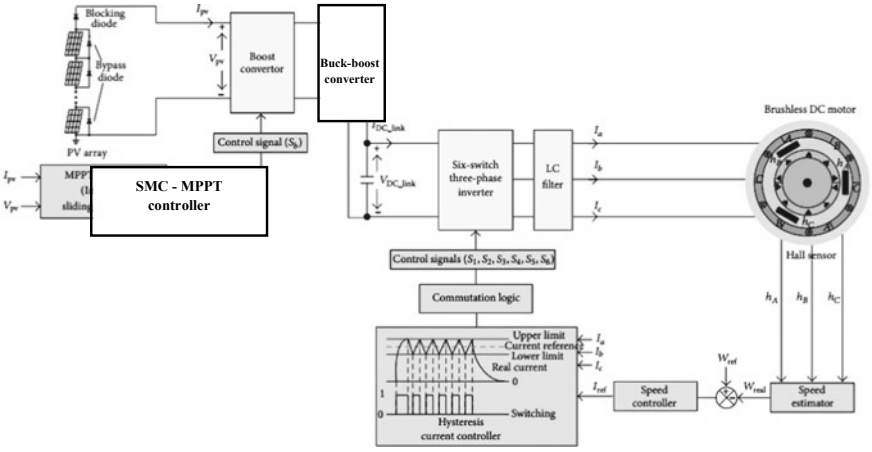

Fig. 1 Diagram of SMC based BLDC motor system

Table 1 System measurements (PV panel specifications SPS—105 W—sharp solar with STC)

Power (P_{max})	105 W
Voltage in open circuit (V_{oc})	22.8 V
Current in short circuit (I_{sc})	5.9 A
Current maximum (I_{mp})	5.63 A
Voltage maximum (V_{mp})	18.6 V

2.2 Mathematical Modeling of Buck-Boost Converter

Averaged modeling approach can be used to approximate the non-linear models of switching power converters. The simulation of the buck-boost DC-DC converter is done in MATLAB by considering the status of switch as on state and diode as off, (i.e.), $S = \text{ON}$; $D = \text{OFF}$; duty cycle $= d(t)$ as in Fig. 2 [3].

While the switch gets ON and the diode remains OFF, the form of state-space equation is as given in Eq. (1)

$$\dot{x} = A_{01}x + B_{01}u \tag{1}$$

When the status of switch is OFF and the diode remains ON, the form of state-space equation as provided in Eq. (2)

$$\dot{x} = A_{02}x + B_{02}u \tag{2}$$

Finally, the system model is represented as in Eq. (3),

$$\dot{x} = f(x_1, t) + g(x_1, t)d(t)$$

$$\begin{bmatrix} \frac{\partial i_L}{\partial t} \\ \frac{\partial v_C}{\partial t} \end{bmatrix} = \begin{bmatrix} -\frac{1}{L} & 0 \\ \frac{1}{C} & -\frac{1}{RC} \end{bmatrix} \begin{bmatrix} i_L \\ v_C \end{bmatrix} + \begin{bmatrix} \frac{i_L}{L} + \frac{V_{PV}}{L} \\ \frac{-i_L}{C} \end{bmatrix} \mathrm{d}(t) \tag{3}$$

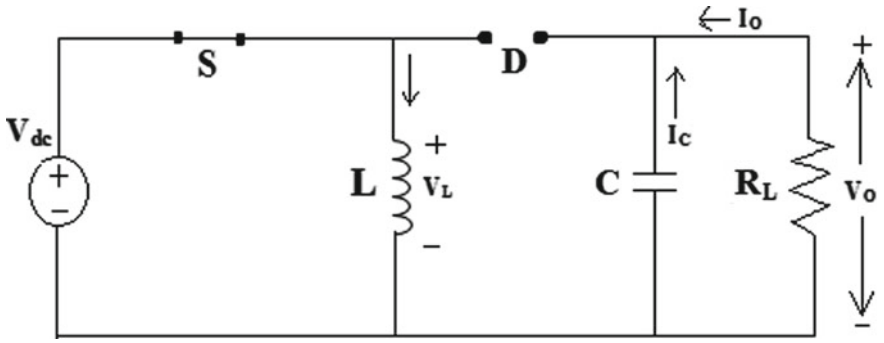

Fig. 2 Buck-Boost when $S = \text{ON}$

2.3 Modeling of BLDC Motor

Because of several drawbacks of DC and Permanent Magnet DC (PMDC) motors, BLDC motors are widely used in various applications. BLDC drive system has been deployed in the proposed work. In the modeling

V_{in} = DC Source voltage (V)
L_m = Motor inductance (H)
R_m = Motor Resistance (Ω)
$E_m = K_b\omega$ = Motor back EMF
K_b = EMF constant (V/rad/s)
ω_m = Motor Speed (rad/s)
T_m = Motor Torque in Nm
J_m = Moment of inertia in kg/ms
T_{Load} = Load Disturbance input
B = Coefficient of motor friction in kg/ms
i_m = Motor Current in A
K_t = Motor Torque constant.

The differential equations maybe written in state-space model along with output equation are provided in Eqs. (4) and (5):

$$\begin{bmatrix} \dot{i}_m \\ \dot{\omega}_m \\ \dot{\theta}_m \end{bmatrix} = \begin{bmatrix} -\frac{R_m}{L_m} & -\frac{K_n}{L_m} & 0 \\ \frac{K_t}{J_m} & -\frac{B}{J_m} & 0 \\ 0 & 1 & 0 \end{bmatrix} \begin{bmatrix} i_m \\ \omega_m \\ \theta_m \end{bmatrix} + \begin{bmatrix} \frac{1}{L_m} & 0 \\ 0 & -\frac{1}{J_m} \\ 0 & 0 \end{bmatrix} \begin{bmatrix} V_{in} \\ T_{Load} \end{bmatrix} \tag{4}$$

$$\begin{bmatrix} i_m \\ \omega_m \\ \theta_m \\ T \end{bmatrix} = \begin{bmatrix} 1 & 0 & 0 \\ 0 & 1 & 0 \\ 0 & 0 & 1 \\ 0 & K_t & 0 \end{bmatrix} \begin{bmatrix} i_m \\ \omega_m \\ \theta_m \end{bmatrix} \tag{5}$$

The specification of the BLDC is shown in Table 2.

Table 2 Specification of BLDC drive

Parameters	Value
Connection type	Star
Rated current	4.52 A
Rated voltage	36 Vdc
Rated speed	2500 rpm
Electromechanical torque	2.2 Nm
Pole	4

3 MPPT Techniques

In this section, the description of Perturb and Observe MPPT Algorithm and Design of sliding mode based MPPT controller has been presented.

3.1 Perturb and Observe MPPT Algorithm

Perturb and observe (P&O) mechanism being traditional is much uncomplicated to realize and has the disadvantage of slow response, fails in tracking voltage during varying atmospheric conditions [6].

3.2 Design of Sliding Mode Based MPPT Controller

Sliding regimes are generated by determining the sliding surface. Now, there are two modes for the SMC action; first one is the reachability mode through this infinite time, state of the system converges to pre-set surface and the second one is sliding mode which ensures that the system state is limited to the sliding surface. The system reaches the sliding mode surface of the trajectories driven by the equivalent control signal.

The general state-space equation for non-linear system is represented as Eq. (6):

$$\dot{x} = f(x) + b(x)u + d \tag{6}$$

Here d is a disturbance.

The MPPT can be determined as Eqs. (7) and (8), when;

$$\frac{\partial P_{\text{pv}}}{\partial V_{\text{pv}}} = 0 \tag{7}$$

$$\frac{\partial P_{\text{pv}}}{\partial V_{\text{pv}}} = \frac{\partial I_{\text{pv}}^2 R_{\text{pv}}}{\partial V_{\text{pv}}} = \frac{I_{\text{pv}}}{R_{\text{pv}}}\left(2R_{\text{pv}} + I_{\text{pv}}\frac{\partial R_{\text{pv}}}{\partial I_{\text{pv}}}\right) \tag{8}$$

where $R_{\text{pv}} = \frac{V_{\text{pv}}}{I_{\text{pv}}}$ is the PV array resistance.

$$2R_{\text{pv}} + I_{\text{pv}}\frac{\partial R_{\text{pv}}}{\partial I_{\text{pv}}} = 0 \tag{9}$$

Hence, the sliding mode surface can be written as

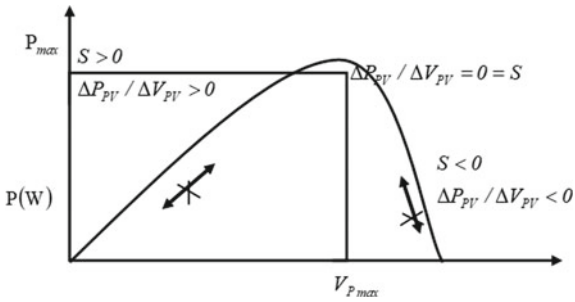

Fig. 3 Sign of the sliding surface at different points of the graph P-V

$$S = 2R_{\text{pv}} + I_{\text{pv}} \frac{\partial R_{\text{pv}}}{\partial I_{\text{pv}}} \tag{10}$$

With respect to Eqs. (9) and (10) the concept of SMC action can be represented as shown in Fig. 3 with the output control respectively in order to have different surface limit $s = 0$, $s > 0$ and $s < 0$ [12].

The control input of duty cycle is $D = d(t)$. By assuming continuous conduction mode of process, $D = u$ and $D_{\text{eq}} = u_{\text{eq}}$ (Eqs. 11 and 12)

$$D = \begin{cases} D - \Delta D & \text{for } S < 0 \\ D + \Delta D & \text{for } S > 0 \\ 0 & \text{for } S = 0 \end{cases} \tag{11}$$

With,

$$\Delta D = u - u_{\text{eq}} \tag{12}$$

Here u is actual input and u_{eq} is desired input.

The equivalent control suggested by Zhang et al. [12] has been determined from the following condition, i.e., Eq. (13):

$$\dot{S} = \left[\frac{\partial S}{\partial x}\right]^T \dot{x} = \left[\frac{\partial S}{\partial x}\right]^T (f(x) + b(x)u + d) = 0 \tag{13}$$

The equivalent control is given as Eq. (14):

$$D_{\text{eq}} = \frac{\left[\frac{\partial S}{\partial x}\right]^T f(x)}{\left[\frac{\partial S}{\partial x}\right]^T b(x)} \tag{14}$$

Since the range of control input for duty cycle should lie between $0 \leq D_{\text{eq}} \leq 1$, the real input control signal has been projected as Eq. (15):

$$D = \begin{cases} 0 & \text{for } D_{eq} - \lambda * \text{sign}(S) \leq 0 \\ D_{eq} - \lambda * \text{sign}(S) & \text{for } 0 < D_{eq} - \lambda * \text{sign}(S) < 1 \\ 1 & \text{for } D_{eq} - \lambda * \text{sign}(S) \geq 1 \end{cases} \quad (15)$$

where λ is a positive constant and as a consequence, the surface converges towards zero in order to track the reference point.

4 Speed Control Techniques

Various speed controls techniques for BLDC motor are described in this section.

4.1 Design of Proportional Integral (PI) Controller for BLDC Motor

The BLDC motor is operated by a PI controller. The PI controller gain parameters $K_p = 15$ and $K_i = 0.15$ are chosen [13]. Moreover, the speed of the BLDC motor is compared with the motor reference speed. Then, the error (speed) is processed by the PI controller [14] and torque is represented as Eq. (16)

$$T_e = \left(K_p + \frac{K_i}{s}\right)(\omega_{ref} - \omega_r) \quad (16)$$

where, T_e: Electromagnetic Torque.

4.2 Design of Sliding Mode Control for BLDC Motor

The system is controlled with the assistance of SMC, as the error speed in the BLDC motor all the time moves towards a sliding surface [13–15]. The surface of sliding is measured related with respect to the tracking speed error of the motor as well as it's rate of change of speed (ω). To device, the control input to the motor, the distance of the speed error trajectory from the surface of SMC and it's rate of convergence are utilized. The symbol of the control input will vary during the intersection of the tracking speed error trajectory on the surface of SMC. Thus, the error trajectory is at all times insisted to forward towards the sliding surface.

Equation (17) is rewritten as:

$$\frac{d\omega}{dt} = (a + \Delta a)\omega + (b + \Delta b)I_a + (c + \Delta c)T_L \quad (17)$$

where $a = -B/J$, $b = K_t/J$, $c = -1/J$.

Δa, Δb and Δc, demonstrate the transient or value of disturbance for the machine parameters, J, B and K_t respectively. The variable of state has been presented as Eq. (18)

$$y = \omega - \omega_{ref} \tag{18}$$

For set point changes in speed reference, Eq. (17) is substituted into Eq. (18). Then, it becomes as Eq. (19)

$$\dot{y} = ay + bI_a + a\omega_{ref} \tag{19}$$

5 Results and Discussion

In this section, all results are discussed. Generally, the standard irradiation 1000 W/m^2 is rendered for the PV array. Whereas in the present work, the power output is almost equal to the rated capacity of the PV array, i.e., ($6 \times 22.3V_{oc} = 133.8V_{oc}$, $133.8V_{oc} \times 2.3\, I_{sc} = 307.74$ W). Hence, the irradiation power of 400 W/m^2 is enough to satisfy the power need from PV system. Figure 4 shows the comparison of P&O MPP and SMC MPPT mechanisms for a single panel and it is observed that the SMC with MPPT has a clear edge over its P&O MPPT counterpart

5.1 Response of Proportional—Integral Controller

The performance of the PI controller performance of the BLDC motor with buck-boost converter is shown from Figs. 5, 6, 7 and 8. The variables such as the stator

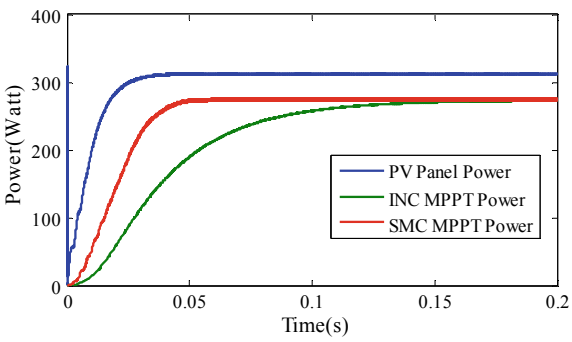

Fig. 4 PV power SMC MPPT and P&O MPPT techniques

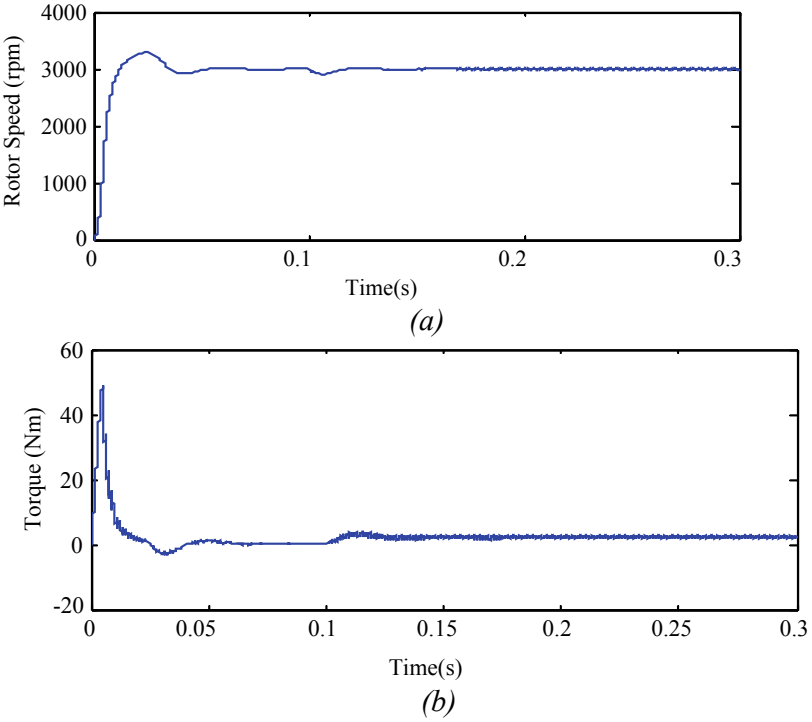

Fig. 5 **a** Rotor speed, **b** electromagnetic torque under no-load condition

current, the back EMF, the rotor speed, the electromagnetic torque are clearly observed from the presented results. The motor speed is directly proportional to the input voltage. Speed is a function of applied voltage. Speed of the BLDC motor can be controlled by the applied voltage. The Back EMF waveform is shown in Fig. 7a. From this response is shown that the commutation can be done at the same instant of zero-crossing detection. Similar concept holds good for SMC concept shown in Fig. 10a.

The BLDC motor stator back EMF is shown in Fig. 9a. This waveform presents the zero-crossing point at regular intervals. It remains almost unchanged with respect to Fig. 7a. The stator current under load condition is shown in Fig. 8b. But the same reached to zero at no load condition as shown in Fig. 7b.

5.2 Response of Sliding Mode Controller

The rotor speed dynamic responses are simulated under no-load condition. By using the exponential reaching law approach which is mentioned in Sect. 4.2, the sliding mode controllers are designed. For inner current loop, the SMC law can be used

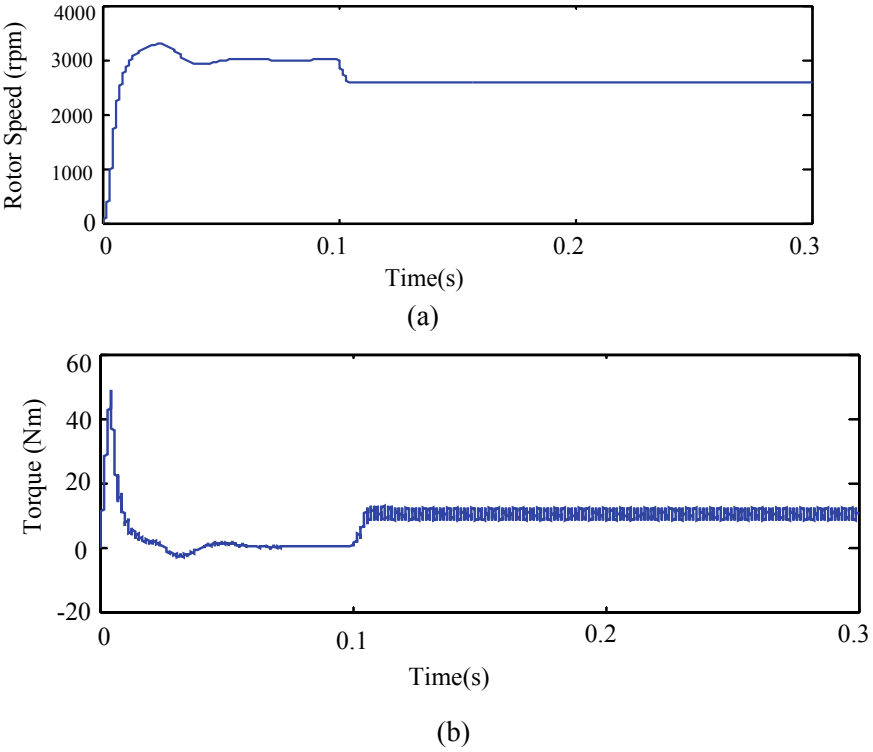

Fig. 6 **a** Rotor speed, **b** electromagnetic torque under load condition

because, it has been proved with the results of rotor speed, stator back EMF, stator current, electromagnetic torque of BLDC motor. They are shown in Figs. 9, 10, 11, 12 and 13.

The BLDC stator back-EMF waveform is depicted in Fig. 12a. The BLDC stator current waveform is shown in Fig. 12b which shows the stator current is reached to 10 A at load condition. The speed responses of the BLDC motor, PI, and SMC controllers, can be inferred from Figs. 5, 6, 7, 8, 9, 10, 11, 12 and 13, and it's comparison results are shown in Table 3.

So far rotor speed performance is concerned, it is clear that SMC exhibits better time-domain parameters as compared to PI as shown in Table 3. Hence, it is evident from the obtained results that the settling time and the peak overshoot are reduced in SMC method compared to PI control. The speed error waveform is shown in Fig. 14 shows that control error is reached to zero. The stator back EMF and stator current under load conditions are also provided in Fig. 15a, b.

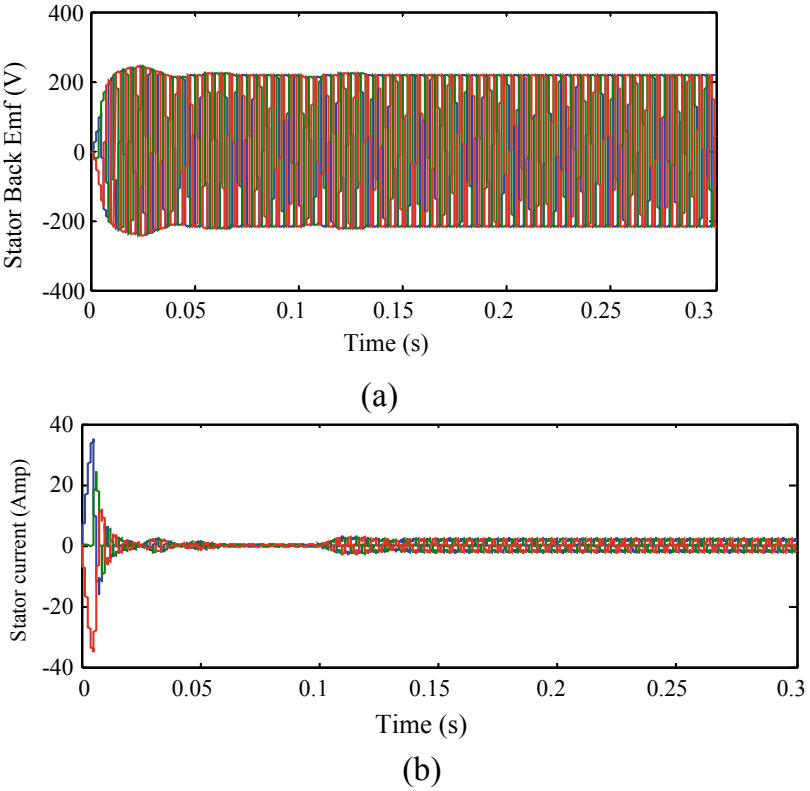

Fig. 7 **a** Stator back EMF, **b** stator current no-load condition

6 Conclusion

The results present the performance of the planned controller. The planned controller achieves rapid and smooth convergence. Furthermore, we find that the tracking accuracy of SMC MPPT is higher than that of P&O MPPT. Furthermore, this research also highlights the stability of the SMC approach to control the speed of the BLDC motor. The SMC approach offers a smooth controller action. When SMC and PI results are compared in terms of speed, current, and torque, SMC has higher performance than the PI controller. Furthermore, it has been shown that SMC offers better performance in all aspects. Since the BLDC motor has intrinsic compatibility with the photovoltaic system, in the future conventional induction (IM) units can be replaced by applications controlled by BLDC powered by photovoltaic energy.

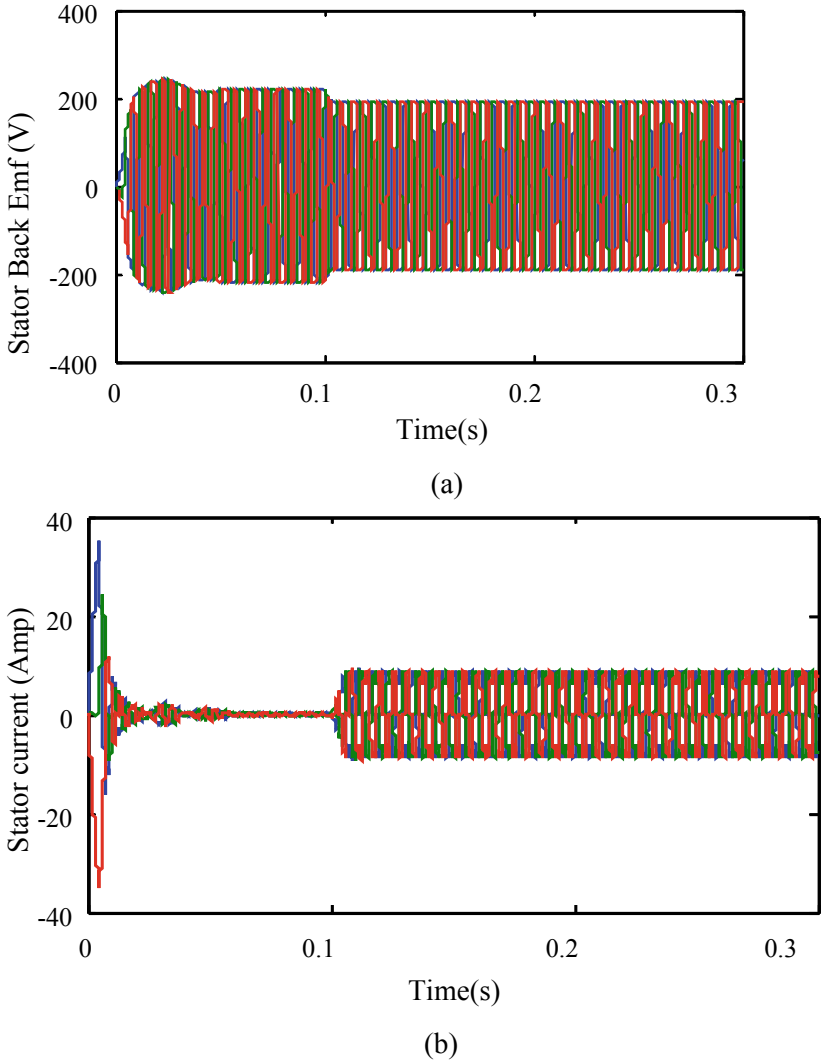

Fig. 8 **a** Stator back EMF, **b** stator current under load condition

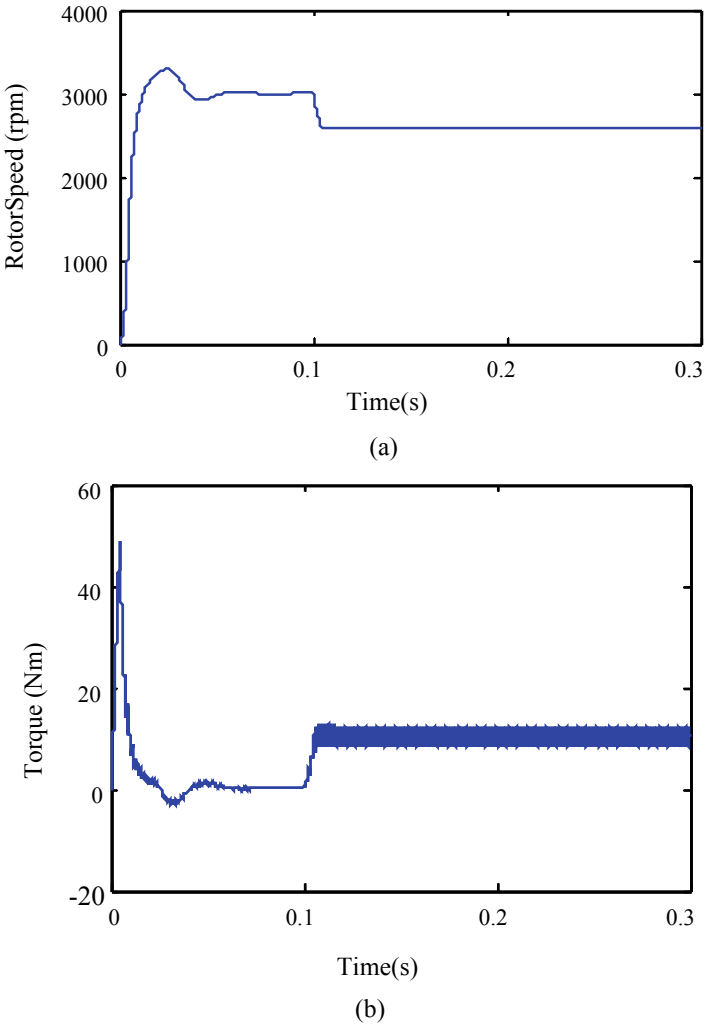

Fig. 9 **a** Rotor speed, **b** electromagnetic torque under load condition

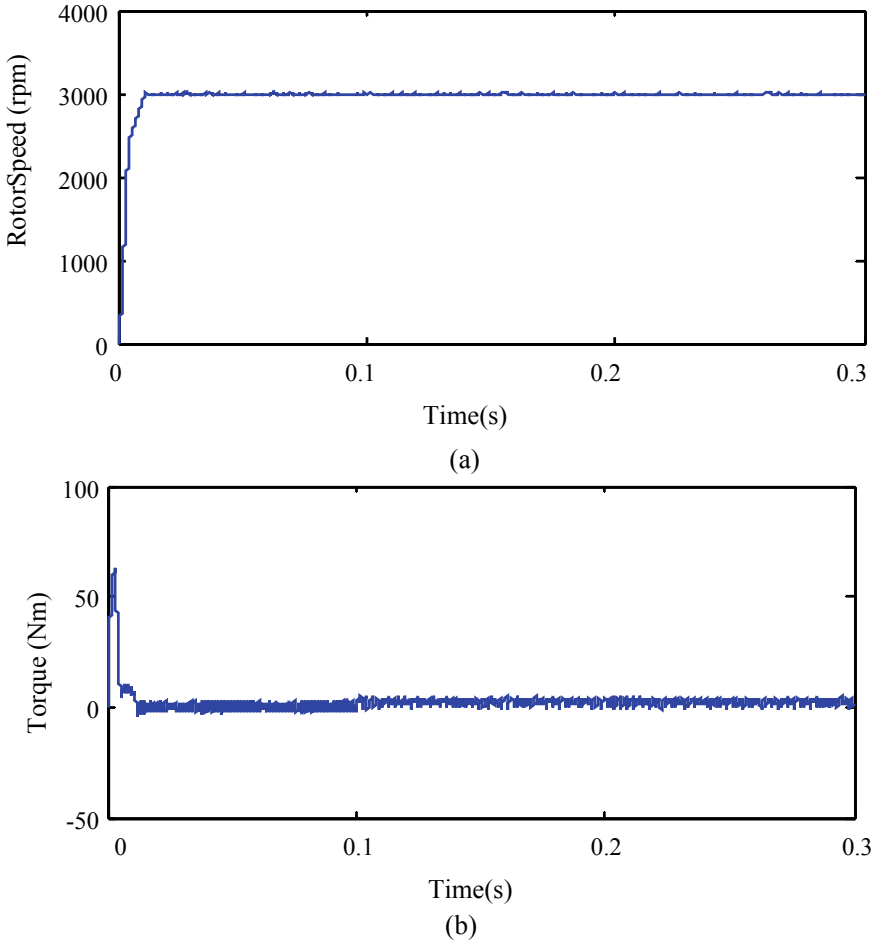

Fig. 10 **a** Rotor speed, **b** electromagnetic torque under no-load condition

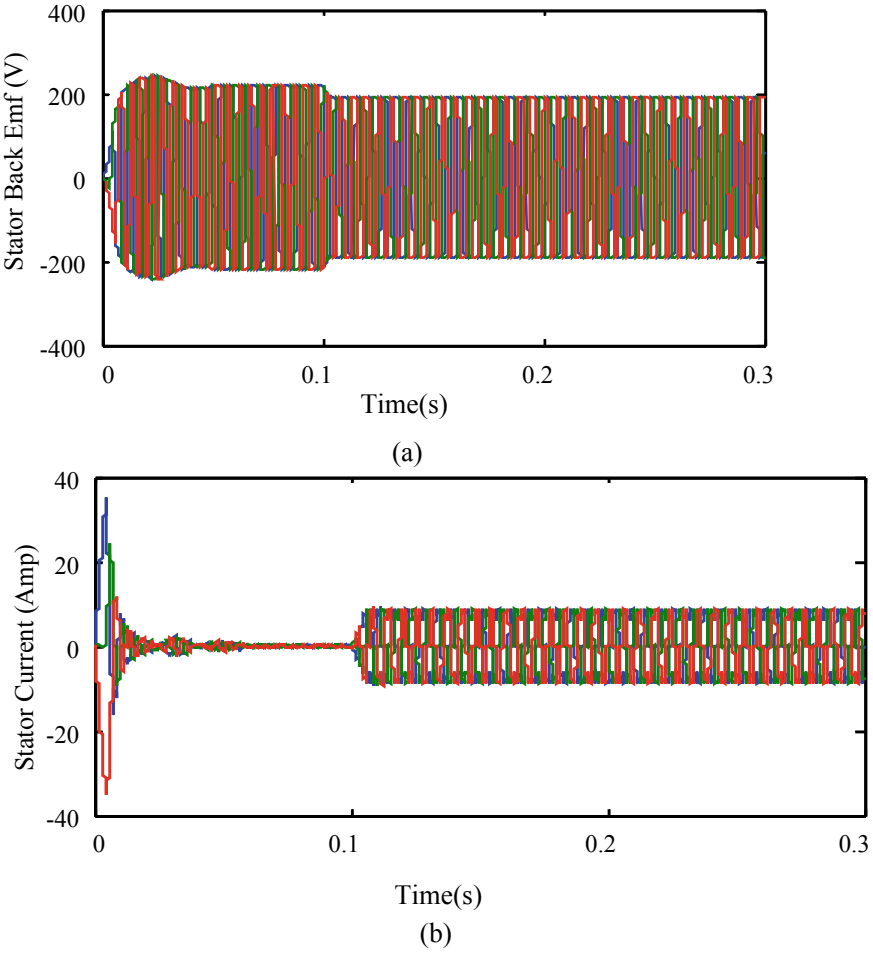

Fig. 11 **a** Stator back EMF, **b** stator current under load condition

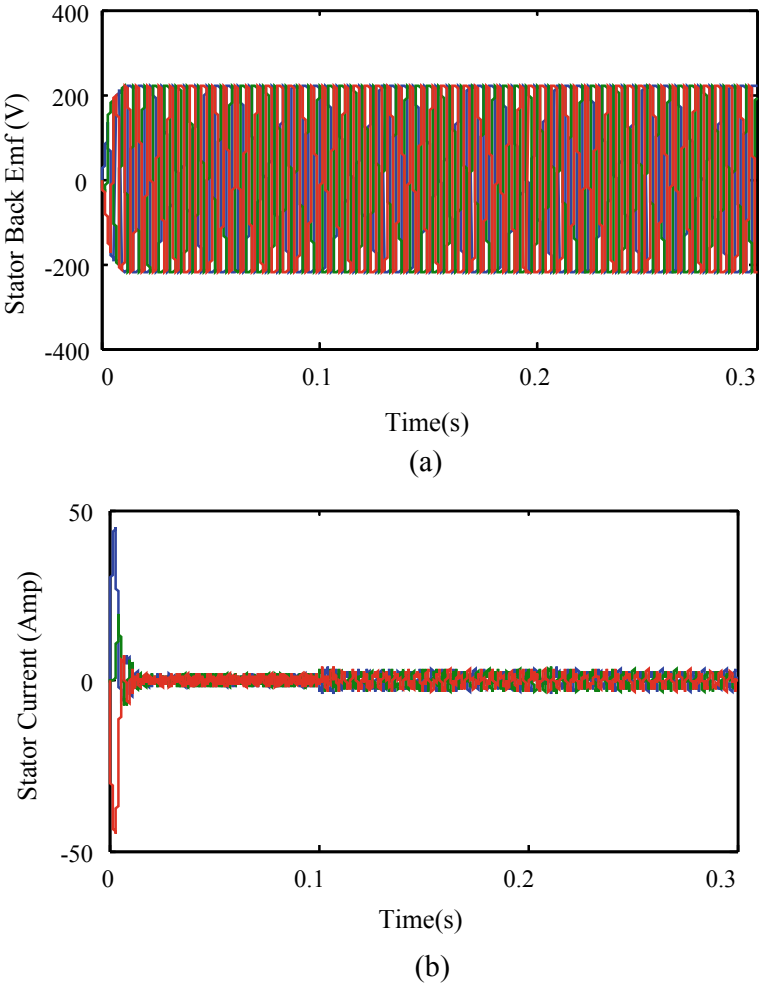

Fig. 12 **a** Stator back EMF, **b** stator current no-load condition

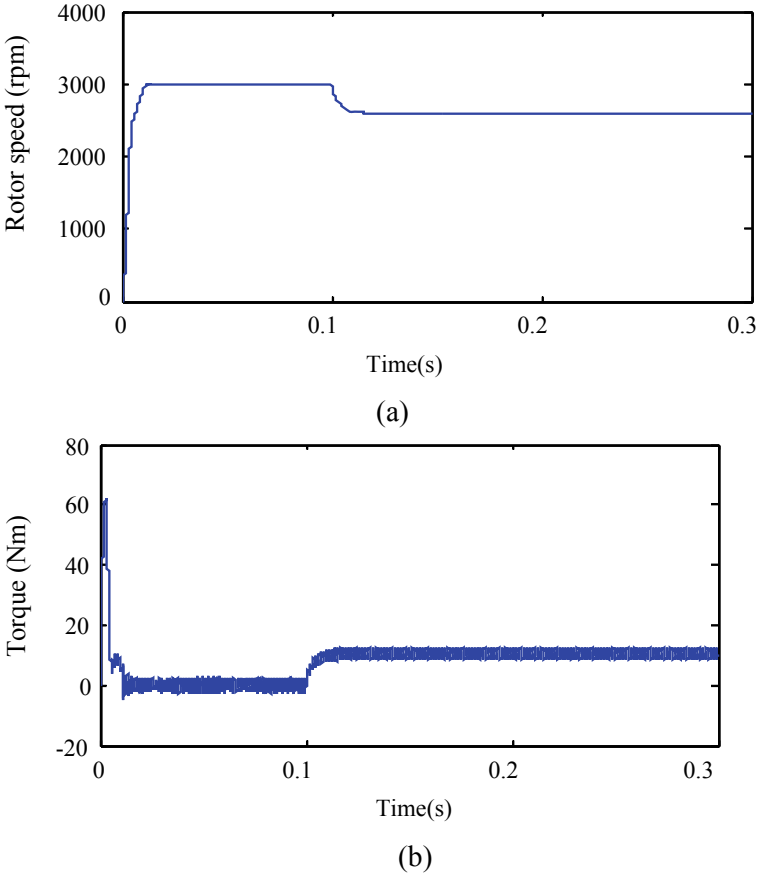

Fig. 13 **a** Rotor speed, **b** electromagnetic torque under load condition

Table 3 Comparison of PI controller with sliding mode controller for speed response obtained from Figs. 6a, 8a, 10a and 12a

Time-domain specifications (s)	PI controller with no-load condition	SMC controller—no load condition	PI controller—load condition (10 Nm)	SMC controller with load condition (10 Nm)
Rise time (R_t)	0.0069	0.0100	0.0055	0.0034
Peak time (P_t)	0.0247	0.0499	0.0186	0.0108
Settling time (S_t)	0.1273	0.0260	0.2445	0.0117
Peak over shoot ($\%M_p$)	9.8473	2.0083	5.0110	0.7435

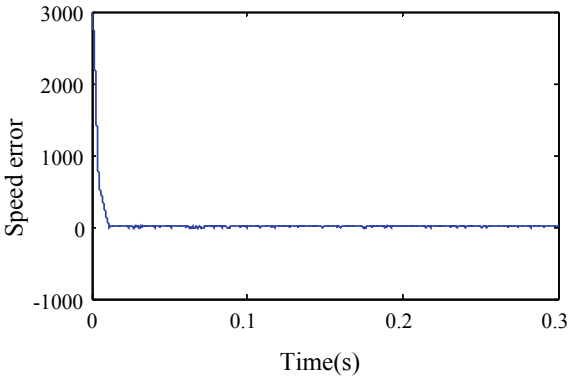

Fig. 14 Speed error

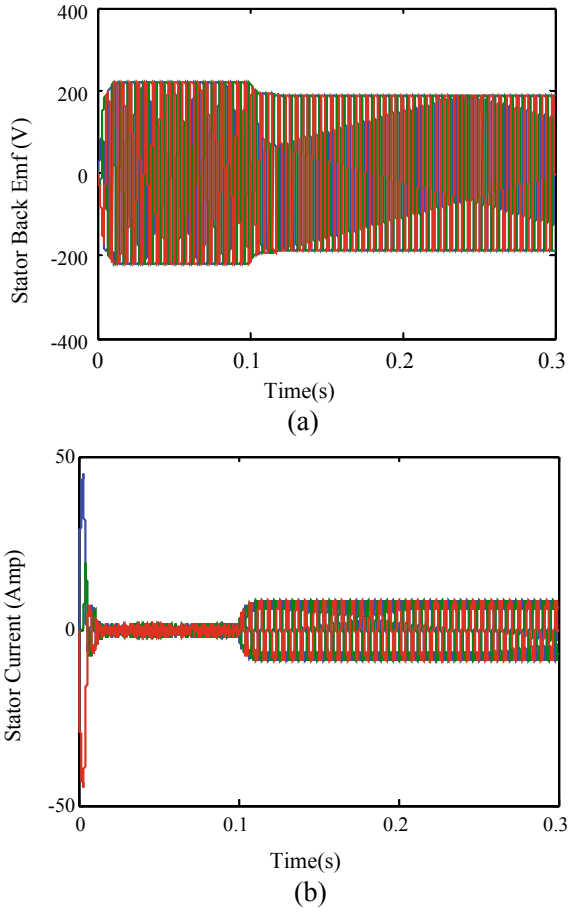

Fig. 15 **a** Stator back EMF, **b** stator current under load condition

References

1. Ahmed CC, Cherkaoui M, Mokhlis M (2019) MPPT control for photovoltaic system using hybrid method under variant weather condition. In: International conference on wireless technologies, embedded and intelligent systems (WITS), Fez
2. Motahhir S, El Hammoumi A, El Ghzizal A (2018) Photovoltaic system with quantitative comparative between an improved MPPT and existing INC and P&O methods under fast varying of solar irradiation. Energy Rep 4:341–350
3. Kumar R, Singh B (2017) Single stage solar PV fed brushless DC motor driven water pump. IEEE J Emerg Sel Top Power Electron 5(3):1377–1385
4. Farhat M, Barambones O, Fleh A, Sbita L (2016) Variable structure MPP controller for photovoltaic pumping system. Trans Inst Meas Control 39(9):1283–1292s
5. Hahm J et al (2015) Design of incremental conductance sliding mode MPPT control applied by integrated photovoltaic and proton exchange membrane fuel cell system under various operating conditions for BLDC motor. Int J Photo Energy 1–14. Article ID 828129
6. Kolluru VR, Sahu G, Mahapatra K, Subudhi B (2015) Design and simulation of a modified sliding mode controller evaluated with a conventional P&O MPPT controller for solar applications. In: IEEE international conference on signal processing, informatics, communication and energy systems (SPICES), Kozhikode, pp 1–5
7. Kwan TH, Wu X (2016) Maximum power point tracking using a variable antecedent fuzzy logic controller. Sol Energy 137:189–200
8. Kassem AM (2012) MPPT control design and performance improvements of a PV generator powered DC motor-pump system based on artificial neural networks. Int J Electr Power Energy Syst 43(1):90–98
9. Garraoui R, Ben Hamed M, Sbita L (2017) Chapter 12: MPPT controllers based on sliding-mode control theory and fuzzy logic in photovoltaic power systems: a comparative study. Springer Science Business Media, Singapore
10. Choi H-S, Park Y-H, Cho Y, Lee M (2001) Global sliding-mode control. Improved design for a brushless DC motor. IEEE Control Syst 21(3):27–35
11. Tey KS, Mekhilef S (2014) Modified incremental conductance algorithm for photovoltaic system under partial shading conditions and load variation. IEEE Trans Ind Electron 61(10):5384–5392
12. Zhang F, Maddy J, Premier G, Guwy A (2015) Novel current sensing photovoltaic maximum power point tracking based on sliding mode control strategy. J Sol Energy 118:80–86
13. Vázquez N, Azaf Y, Cervantes I, Vázquez E, Hernández C (2015) Maximum power point tracking based on sliding mode control. Int J Photoenergy. Article ID 380684, 8 pages
14. Lee B-K, Kim T-H, Ehsani M (2003) On the feasibility of four switch three-phase BLDC motor drives for cost commercial applications: topology and control. IEEE Trans Power Electron 18(1):164–172
15. Xia CL (2012) Permanent magnet brushless DC motor drives and controls. Wiley, Hoboken

Ensemble Bagging Approach for IoT Sensor Based Anomaly Detection

Dukka Karun Kumar Reddy, H. S. Behera, G. M. Sai Pratyusha, and Ravikiran Karri

Abstract The IoT is the next age of communication, as the rapidity of connecting physical objects around us to the internet is mounting swiftly. The inanimate physical devices can be empowered to create, receive, and exchange data into information networks to provide highly developed intelligent services without any human intervention. The future IoT applications are extremely promising with an enhanced level of automation, efficiency, and comfort for the users. To actualize such a world in an ever-developing mold requires enhanced user privacy, authentication, and high information security from attacks. This paper presents a characteristic examination of an anomaly detection system for successfully classifying hostile events by distinguishing them from normal activities within the Distributed Smart Space Orchestration System (DS2OS) traffic pattern associated with network operations. We presented a supervised meta algorithm-based approach known as Bagging (Bootstrap Aggregation) for classifying and handling various malicious operations on the network. This paper describes most affluent machine learning classifiers k-Nearest Neighbor(k-NN), Decision Tree(DT), Random Forest(RF), and Extra Trees Classifier(ETC) to progress the efficiency of the DS2OS dataset by acquiring through a proper training phase for the static idealization of normal and anomalous

D. K. K. Reddy (✉) · H. S. Behera
Department of Information Technology, Veer Surendra Sai University of Technology (VSSUT), Burla, Odisha 768018, India
e-mail: karun.redy@gmail.com

H. S. Behera
e-mail: hsbehera_india@yahoo.com

G. M. S. Pratyusha
Department of Computer Science and Technology, Dr. Lankapalli Bullayya College of Engineering (for Women), Resapuvanipalem, Visakhapatnam, Andhra Pradesh 530013, India
e-mail: saipratyushagm@gmail.com

R. Karri
Department of Computer Science, Sanketika Institute of Technology and Management, Pothinamallayya Palem, Visakhapatnam, Andhra Pradesh 530041, India
e-mail: ravikirankrr@gmail.com

G. T. C. Sekhar et al. (eds.), *Intelligent Computing in Control and Communication*, Lecture Notes in Electrical Engineering 702,
https://doi.org/10.1007/978-981-15-8439-8_52

network behavior. This paper estimates the overall experimentation performance and evaluation of the simulation model through accuracy, precision, recall, and $F1$-score.

Keywords Internet of Things (IoT) · Anomaly detection · Machine learning · Bagging classifier

1 Introduction

The accustomed data-driven infrastructures by human beings led a path for increasing the growth and demand for a network-based automated system. The 'stay-connected' aspect of the wireless network allows users to connect anytime and anywhere. The system of smart devices (IoT) which are organized and capable of transferring information over the network avoiding the need for human-human or human-computer interaction has made the interaction of humans with the virtual environment easy [1]. IoT is found to be a decisive infrastructure module due to its economic benefits and enormous impact. The exchange of data through wireless networks with various application platforms and protocols is increasing rapidly, due to the heterogeneity nature of IoT devices. IoT has gained a significant consideration within past years as it has enhanced the state of the art performance for many vital applications including security related application in critical structures such as intrusion detection, access control, malware detection, and anomaly detection. The mounting dependency of the decisive infrastructure of IoT technologies made vulnerable to attacks through the communication channels such as amputation, information disclosure, replacement, network disability, and interception of information has become the customary security issue. Therefore, the security issue of IoT has been fallen to critical concern. The security framework of IoT mainly consists of the perception layer, transportation layer, and application layer [2]. The data acquisition by the perception layer possesses with controller nodes, sensor nodes, etc. used for data attainment. In addition to this, insubstantial authentication and secure communications between nodes are the foremost security issues of this layer. The transportation layer offers ubiquitous information access for the perception layer using ad-hoc and wireless networks, etc. Consequently, several attacks such as network disability, information disclosure, DoS attack, and other vulnerabilities became the customary security issues that originate in this layer. To prevail over these problems, early attack detection, and prevention systems must be deployed before they make a huge loss in the entire layer.

So, an intelligent system that can detect and repeal any malevolent behavior within the network is materialized by employing an intrusion detection mechanism [3]. Surfeit techniques are proposed to progress the accuracy of the intrusion detection mechanism. The novel attacks are constantly escalating and sophisticated. The anomaly-based detection system is one of the intrusion detection mechanism that can be utilized to become aware of significant network patterns attacks [4]. In this study, classifier based anomaly detection is trained to construct a classification model

from the intrusion data and to predict the system by identifying whenever it is in an abnormal state. The primary aim is to develop a smart and secure system that is much reliable in categorizing the attacks efficiently.

The main contribution of this paper

1. *Design and implementation of bagging approach with different machine learning classifiers as base estimators.*
2. *Understanding the influencing characteristics of DS2OS traffic traces dataset and preprocessing, to recognize the feasible consequences and making it competent to detect categorical attacks.*
3. *Evaluating the performance using accuracy, precision, recall, and F1-score values.*

The proposed model has an enduring effect on the accuracy of the solution compared to existing models. This paper is organized as follows: Section 2 provides a brief study of major-related work in this area. Section 3 summarizes the proposed bagging classifier with machine learning algorithms. Section 4 provides the dataset description and preprocessing work. Section 5 illustrates the experimental setup and result analysis. Section 6 concludes the paper.

2 Related Work

The proposed system aims to predict the anomaly detection in the IoT network. Numerous techniques have developed so far as to predict the anomaly detection. Many researchers have focused on anomaly detection based system with machine learning techniques. Here, we are presenting some of the methodologies proposed by various researchers.

Hasan et al. [5] have proposed a computationally proficient RF technique on the DS2OS dataset for solving cyber-attacks in IoT network. The RF classifier is predicted precisely for Data-probing, Malicious-control, Malicious-operation, Scan, Spying, and Wrong-setup classes. The Normal and DoS attack classes are predicted more accurately than other classifier techniques. From the RF confusion matrix, except Normal and DoS classes, the RF classified each class precisely. The DoS class is misclassified with 403 samples as Normal, from a total of 1178 DoS testing samples. The Normal class is misclassified with 18 samples as DoS, from a total of 69,571 Normal testing samples. The RF results with accuracy of 99.4% whereas precision, recall, and $F1$-score with 99%.

The performance of the projected classifier is designed by applying F-means, K-means and proposed imputation methods by Vangipuram et al. [6]. For the experimental research, an open-source DS2OS dataset is considered, which is accessible from Kaggle. The projected approach is better performed using F-means and K-means imputation technique when compared to existing classifiers. It is observed that by the proposed imputation technique 100% accuracy is achieved for the

classes Scan, Malicious-operation, DoS, Spying, Data-probing, and Wrong-setup. The Malicious-control and Normal class are projected with 98% accuracy.

Akter et al. [7] has projected a model for attacks in IoT through a prehensile intrusion detection system. The anomaly detection using the deep learning approach of the proposed model is successful in detecting anomalies and different types of attack flood, i.e., Probe, DoS, DDoS, R2L, and U2L on the NSL-KDD dataset. The evaluation metrics that are taken into consideration are precision, recall, and F-measure. The precision score for Normal, Probe, DoS classes is 99%, for DDoS is 87.21%, for U2R is 80.01% and for R2L it is 76.70%.

Ullah and Mahmoud [8] have developed a model, a two-level flow-based anomalous activity detection system for IoT networks. The flow-based detection methodologies only examine packet headers to classify the network traffic. The flow-based features extracted from the IoT Botnet dataset and various machine learning classifiers are studied. The RF classifier shaped the maximum predictive results for level-2. The proposed model with accuracy, precision, recall, and *F*-score was measured as 99.99% and 99.90% for level-2.

The proposed model by Yin et al. [9], is an integrated model of the convolution neural network and recurrent auto-encoder for anomaly detection. A two-stage sliding window is implemented for data preprocessing for better representations, based on Yahoo Web scope S5 dataset, and raw time series. The proposed anomaly detection model for time series predicts the results with accuracy 99.62%, precision 98.78%, recall 97.20%, and *F*1-Score 97.98%.

In this paper, an ensemble learning technique with Bagging Classifier(BC) approach has been proposed for classification problems. In data science, BC is one of the most effectively utilized algorithmic calculations. BC bestows machine learning models with the capacity to advance their prediction accuracy. Dataset collection is the initial procedure framework, where the collected dataset is studied strictly to discover the types of data. Data preprocessing is executed on the required dataset through data cleaning and data visualization measures. These measures transform the data into meaningful attribute vectors with 80:20 ratios for training and testing. The proposed bagging algorithm is trained with a base estimator as machine learning classifiers. The simulated DS2OS is a multi-classification dataset from the Kaggle machine learning repository. These scenarios were experimented and predicted, to validate the performance of our proposed method with different machine learning classifiers.

3 Proposed Methodology

The proposed model framework is an integration of many independent processes. The framework represents the overall system process as shown in Fig. 1. Dataset collection is the initial procedure framework, where the collected dataset is studied strictly to discover the types of data. Data preprocessing is executed on the required

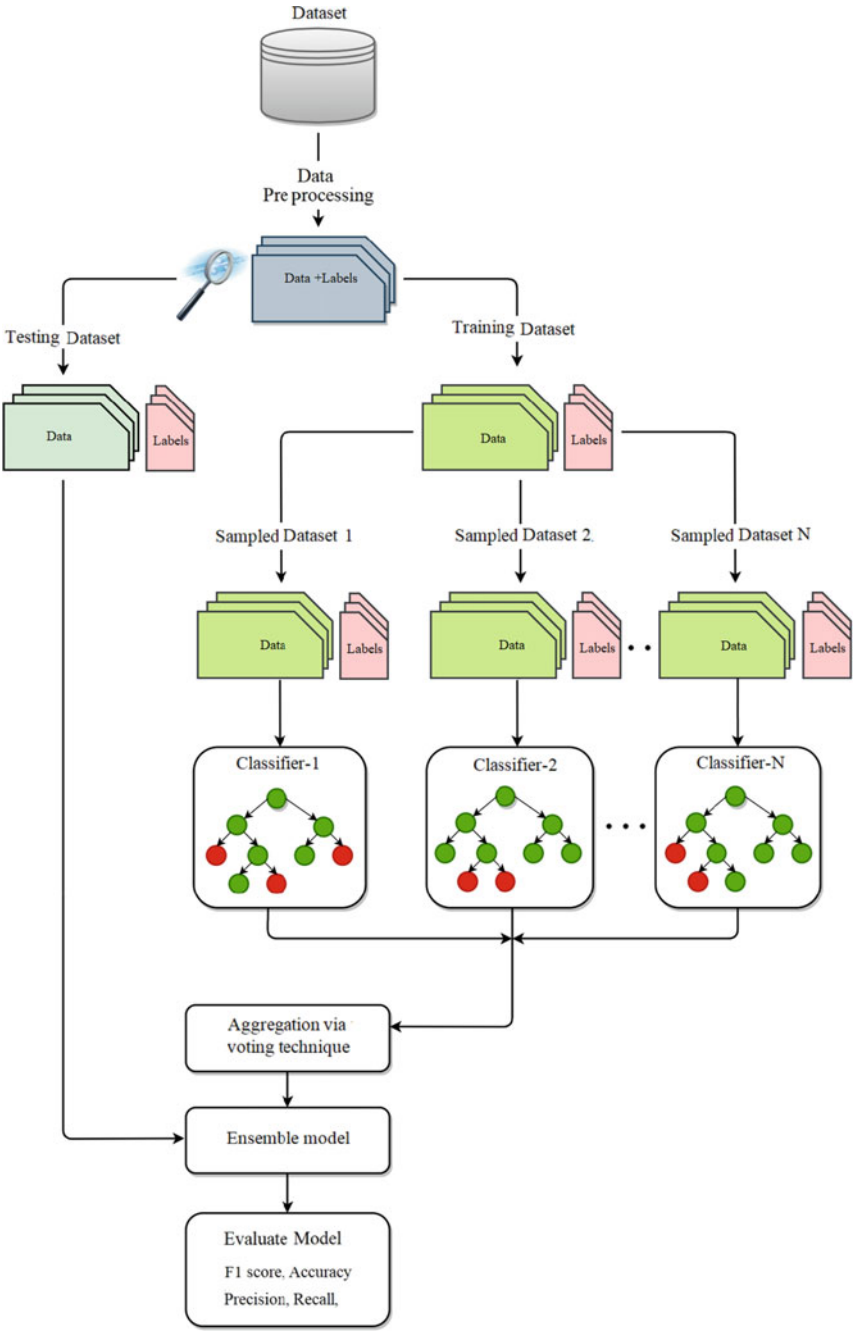

Fig. 1 Overall framework of the proposed model

dataset through data cleaning and data visualization measures. These measures transform the data into meaningful attribute vectors. These attribute vectors are then sliced into an 80:20 ratio for training and testing.

3.1 Ensemble Bagging Classifier

In this work, an ensemble BC (also called as Bootstrap aggregation classifier) has been proposed for the examination of anomaly detection systems within the DS2OS traffic pattern. Bagging is one of the ensemble meta-estimator learning technique proposed in [10]. In this method, it will consider multiple predictors, from which it will calculate the aggregated predictor. It is a procedure that will create classifiers in an ensemble way by considering random samples that are replaced from the dataset and then construct a classifier for every bootstrap sample. The decision is done by voting or aggregating from the bootstrap classifier that will reduce the variance over the class labels built by classifiers. In other words, we can say bagging builds classification trees by considering bootstrap samples that are taken from training data and combine all the predictions to get a finalized meta-predictor. The advantage of using this classifier is, it can approximate the variance of our ensemble model in obliging to estimate the uncertainty with which the classifier makes a prediction.

The procedure of the proposed BC is as follows:

Algorithm: Bagging classifier

Input:
'D' represents training data with labels $l_i = \{l_1, l_2, \ldots l_c\}$.
'C' represents classes.
Weak learning algorithm WeakLearners
'N' represents number of iterations.
'F' represents fraction to create bootstrapped training data
Begin $n = 1, 2, 3 \ldots, N$
1. Take a bootstrapped replica D_n by randomly drawing F percent of D.
2. Call Weak Learners with D_n and receive the classifier E_n.
3. Add E_n to the ensemble E.
End
Test: Simple majority voting by given unlabeled instance X.
1. Calculate the ensemble $E = \{E_1, \ldots, E_N\}$ on X.
2. Let $V_{n,j} = \begin{cases} 1, & \text{if } E_n \text{ picksclass} l_j \\ 0, & \text{otherwise} \end{cases}$ be the vote given to class l_j by classifier E_n.
3. Obtaining the total vote received by each class $V_j = \sum_{n=1}^{N} v_{n,j} \quad j = 1, 2, \ldots, C$
4. Choose the class that receives the highest total vote as the final classification.

4 Data Preprocessing

The data preprocessing is an important task for addressing and prioritizing the features because data preprocessing increases productivity through enhanced decisions. The analyzed data is preprocessed for building a confident decision-making classifier. Exploratory data observation and analysis are the major criteria required for machine learning research. Feeding data with an appropriate methodology is the foremost task for a classification model. The IoT DS2OS dataset is considered from the Kaggle website and provided by [11] and it contains 357,952 data samples of categorical data with 13 features Source ID, Source Address, Source Type, Source Location, Destination Service Address, Destination Service Type, Destination Location, Access Node Address, Access Node Type, Operation, Value, Timestamp, and Normality. The Value feature is continuous and all other features are nominal except Timestamp which is discrete, so this feature is excluded.

The IoT DS2OS dataset with the features Timestamp, Value, and Accessed Node Type are preprocessed accordingly because missing data is the initial step to deal with. The Timestamp feature is discrete by nature and this feature is not considered during the process and the columns with Value and Accessed Node Type hold missing values (null values), where the 'Value' feature contains continuous values and the Accessed Node Type feature contain categorical values. The attribute 'Access Node Type' contains 148 missing values and 'Value' contains 2050 missing values. The Access Node Type and Value features with missing values are processed into considerable continuous values, to facilitate the classifiers for better accuracy. The Value feature contains False with 25,966 instances are replaced with 0, True with 14,460 instances are replaced with 1, Twenty with 200 instances are replaced with 20, 'none' with 106 instances are replaced with 1, 'org.ds2os.vsl.core.utils.AddressParameters' with 11 instances are replaced by 1 and the missing values are also replaced with 1. These are preprocessed and during the process, the categorical data is encoded into numeric data. The frequency distribution of anomalous attacks from Normality feature is given in Table 1.

Table 1 Percentage distribution and occurrences of attacks

Attacks	Occurrences in data	% of aggregated data	% of anomalous data
DOS	5780	1.61	57.70
Scan	1547	0.43	15.44
Malicious control	889	0.24	8.87
Malicious operation	805	0.22	8.03
Spying	532	0.14	5.31
Data probing	342	0.09	3.41
Wrong setup	122	0.03	1.21

The dataset after preprocessing is further partitioned into training and testing datasets in the ratio of 80%:20%, respectively. Here 80% data i.e. 286,361 instances are considered for training purpose and the other 20% data i.e. 71,591 instances are considered for testing purposes.

5 Experimental Setup and Result Analysis

To test the effectiveness of the study and visualization for the dataset, it is imperative that the process is tested since any dataset would not demonstrate the appropriateness under variability and realistic noise structures. The experimental setup and results analysis disclose undetected phenomenon cases from the dataset. The experimental setup utilized LENOVO (IdeaPad 330) laptop where the operating system was Windows 10 Enterprise 64-bit, processor was Intel(R) Core(TM) i5-8250U CPU @ 3.10 GHz (4 CPUs). The laptop memory contains 8 GB RAM. For data preprocessing NumPy framework and Pandas framework are used. For data analysis Scikit-learn framework and for information visualization Matplotlib framework were utilized through Spyder integrated development environment.

This section represents the result analysis of the proposed bagging algorithm with base estimators as DT, ETC, k-NN, and RF classifiers. Table 2 shows the fine-tuned parameter setting of machine learning classifiers for better prediction results. The IoT traffic traces DS2OS consists of 357,952 instances with multi-classification, where 286,361 instances are used for training and 71,591 instances are used for testing purposes. To validate the performance of our proposed method we considered performance measures such as confusion matrix, true positive, true negative, false

Table 2 Parameter setting for machine learning classifiers

Dataset	Machine learning classifiers	Parameter setting
DS2OS dataset	ETC	criterion: gini
		n_estimators: 5
		max_depth: none
	DT	criterion: entropy
		splitter: best
		max_depth: 10
		n_estimators: 30
	RF	max_depth: 20
		n_estimators: 20
	k-NN	n_neighbors: 2
		algorithm: kd_tree
		n_estimators: 5

positive, false negative, true positive rate(TPR/Recall), false positive rate(FPR), $F1$-score, precision, individual class accuracy, and overall accuracy.

Tables 3, 4, 5, and 6 show the evaluation factors of BC with DT, ET, k-NN, and RF as base estimators. From Tables 3 and 4, the TPR and FPR values for all the classes

Table 3 Evaluation factors using BC(DT)

Metrics	DoS	Data probing	Malicious control	Malicious operation	Scan	Spying	Wrong setup	Normal
True positive	1160	81	176	153	313	90	29	69,518
True negative	70,360	71,510	71,415	71,438	71,278	71,501	71,562	2002
False positive	71	0	0	0	0	0	0	0
False negative	0	0	0	0	0	0	0	71
TPR/recall	1	1	1	1	1	1	1	1
FPR	0.001	0	0	0	0	0	0	0
$F1$ score	0.97	1	1	1	1	1	1	1
Precision	0.94	1	1	1	1	1	1	1
Accuracy	0.99	1	1	1	1	1	1	0.99
Overall accuracy	99.9							

Table 4 Evaluation factors using BC(ET)

Metrics	DoS	Data probing	Malicious control	Malicious operation	Scan	Spying	Wrong setup	Normal
True positive	1114	69	162	166	301	113	22	69,568
True negative	70,401	71,522	71,429	71,425	71,290	71,478	71,569	1947
False positive	76	0	0	0	0	0	0	0
False negative	0	0	0	0	0	0	0	76
TPR/recall	1	1	1	1	1	1	1	1
FPR	0.001	0	0	0	0	0	0	0
$F1$ score	0.97	1	1	1	1	1	1	1
Precision	0.94	1	1	1	1	1	1	1
Accuracy	0.99	1	1	1	1	1	1	0.99
Overall accuracy	99.89							

Table 5 Evaluation factors using BC(k-NN)

Metrics	DoS	Data probing	Malicious control	Malicious operation	Scan	Spying	Wrong setup	Normal
True positive	1117	86	183	162	318	104	21	69,489
True negative	70,371	71,505	71,408	71,429	71,265	71,487	71,570	2021
False positive	73	0	0	0	8	0	0	0
False negative	0	0	0	0	0	0	0	81
TPR/recall	1	1	1	1	1	1	1	1
FPR	0.001	0	0	0	0	0	0	0
$F1$ score	0.97	1	1	1	0.99	1	1	1
Precision	0.94	1	1	1	0.98	1	1	1
Accuracy	0.99	1	1	1	0.99	1	1	0.99
Overall accuracy	99.88							

Table 6 Evaluation factors using BC(RF)

Metrics	DoS	Data probing	Malicious control	Malicious operation	Scan	Spying	Wrong setup	Normal
True positive	1193	70	171	167	268	124	20	69,509
True negative	70,330	71,521	71,420	71,424	71,322	71,467	71,571	2013
False positive	68	0	0	0	8	0	0	0
False negative	0	0	0	0	0	0	0	69
TPR/recall	1	1	1	1	1	1	1	1
FPR	0	0	0	0	0	0	0	0
$F1$ score	0.97	1	1	1	1	1	1	1
Precision	0.95	1	1	1	1	1	1	1
Accuracy	0.99	1	1	1	0.99	1	1	0.99
Overall accuracy	99.9							

are 1 and 0. The $F1$-score and precision for all the classes are 1, except for the 'DoS' class the $F1$-score is 0.97 and precision is 0.94. The individual accuracies for all the classes are 1 except for 'DoS' and 'Normal' it is 0.99, whereas the overall accuracy of BC(DT) model is 99.9% and BC(ET) model is 99.89%. In Table 5, the TPR and FPR values for all the classes are 1 and 0, whereas the 'DoS' class with $F1$-score is 0.97 and precision is 0.94. The individual accuracies for 'DoS' 'Scan' and 'Normal' are 0.99 and all other classes are 1. The overall accuracy of this proposed model is 99.88%. Table 6 also shows TPR and FPR result values for all the classes as 1 and 0, whereas the 'DoS' class with $F1$-score is 0.97 and precision is 0.95. The individual accuracies for 'DoS' 'Scan' and 'Normal' are 0.99 and all other classes are 1. The overall accuracy of this proposed model is 99.9%.

The BC(DT) confusion matrix Fig. 2 illustrates that 71 'Normal' classes were predicted as 'DoS' class and remaining all the classes are classified correctly. Figure 3 confusion matrix for BC(ET) shows that only 76 'Normal' classes are predicted as 'DoS' class, and remaining all the classes are classified exactly. Figure 4 illustrates the confusion matrix of BC(k-NN) with 76 'Normal' class are predicted as 'DoS' class and 8 'Normal' class values are predicted as 'Scan' class. Figure 5 illustrates the confusion matrix of BC(RF) with 68 'Normal' class are predicted as 'DoS' class and 1 'Normal' class values is predicted as 'Scan' class. The remaining classes are classified correctly.

Figures 6, 7, 8 and 9 shows the ROC curves for BC with DT, ET, k-NN, and RF as base estimators.

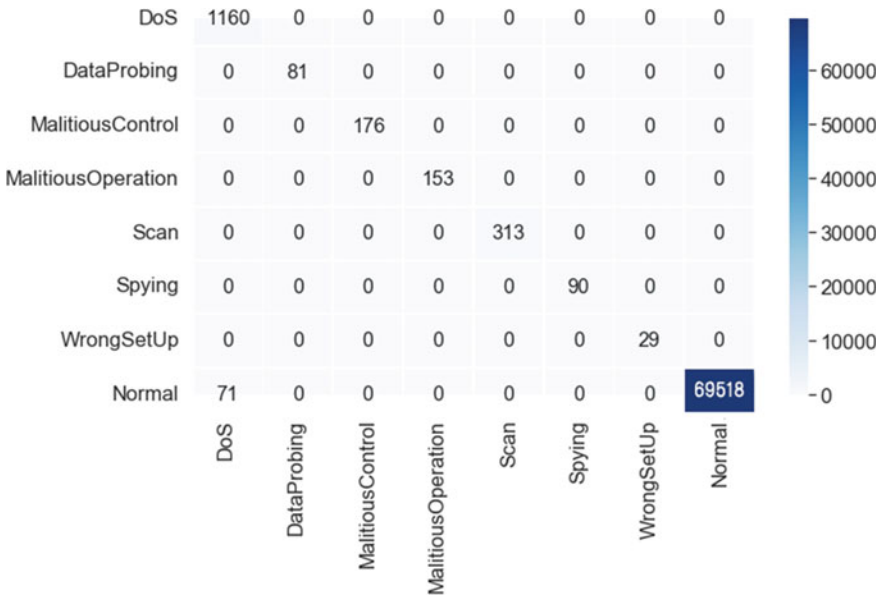

Fig. 2 Confusion matrix for BC(DT)

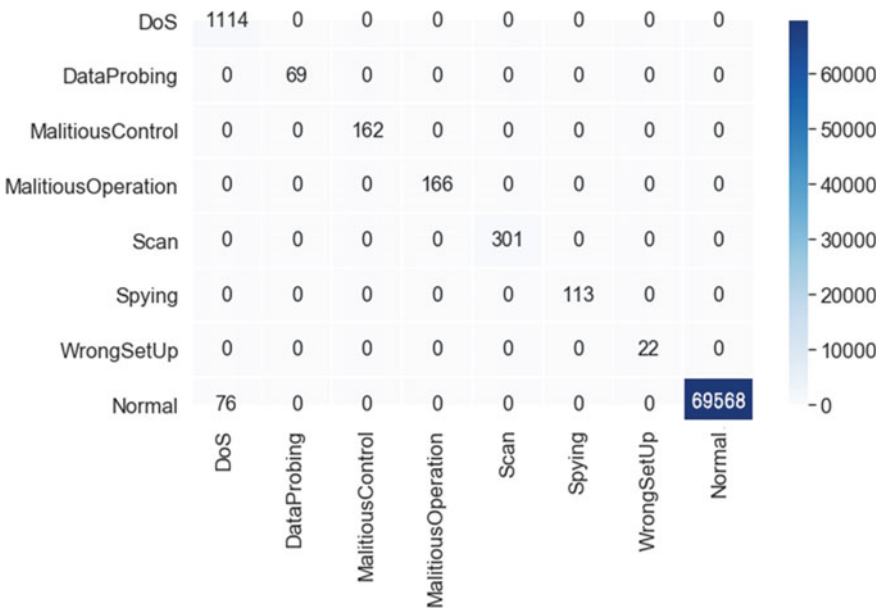

Fig. 3 Confusion matrix for BC(ET)

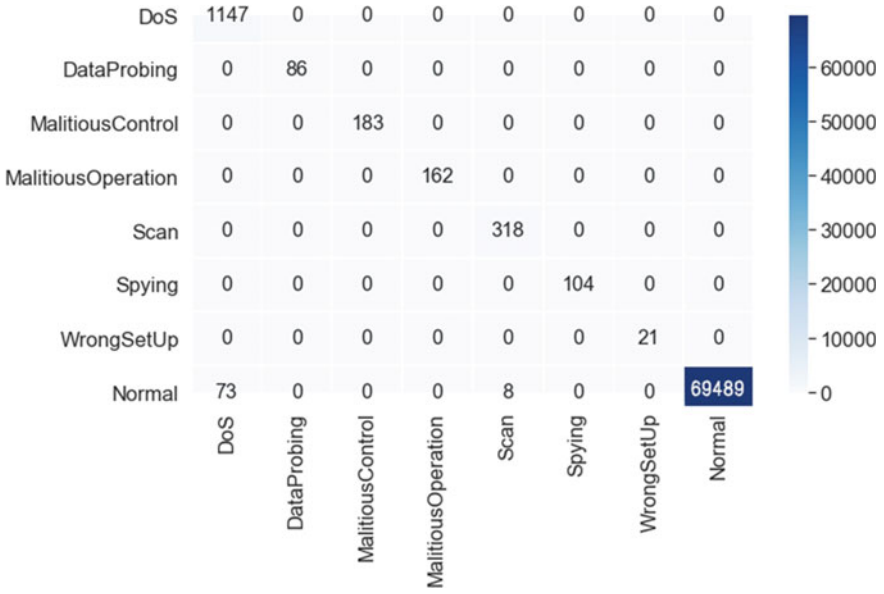

Fig. 4 Confusion matrix for BC(k-NN)

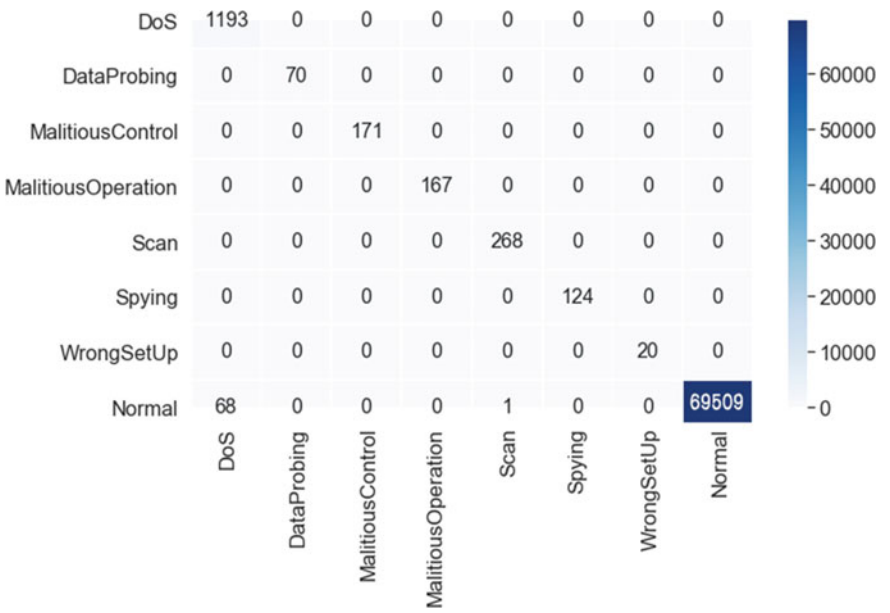

Fig. 5 Confusion matrix for BC(RF)

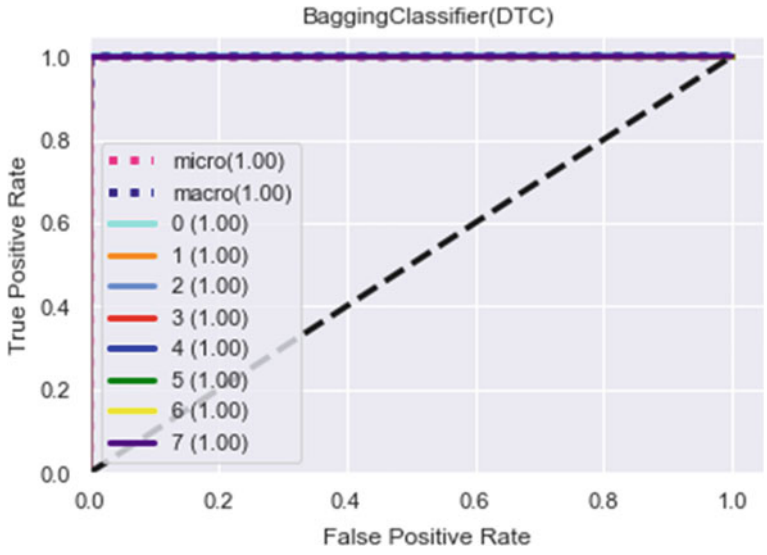

Fig. 6 ROC curve of BC(DT)

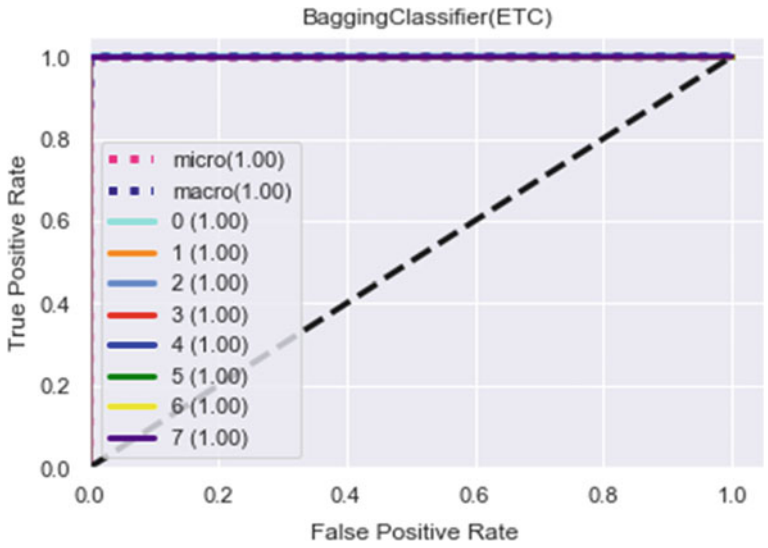

Fig. 7 ROC curve of BC(ET)

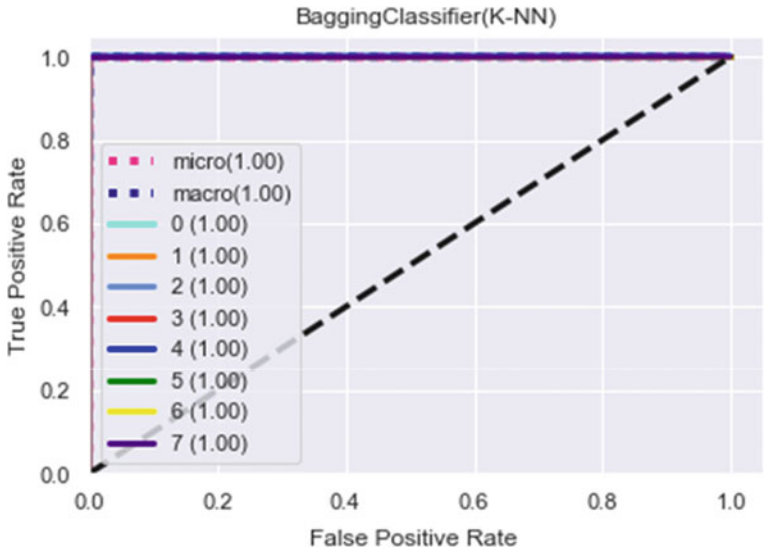

Fig. 8 ROC curve of BC(k-NN)

The in-depth analysis of target class study is analyzed on the basis of evaluation factors with respect to the proposed models. Figure 10 shows cent percent TPR for all the target classes with proposed models and the BC(DT), BC(ET), and BC(k-NN) FPR for 'DoS' class is 0.001 as shown in Fig. 11. The precision values given

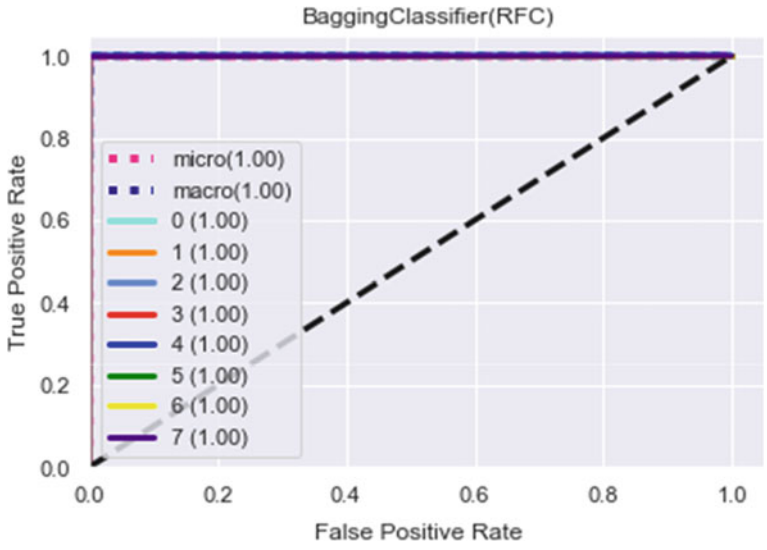

Fig. 9 ROC curve of BC(RF)

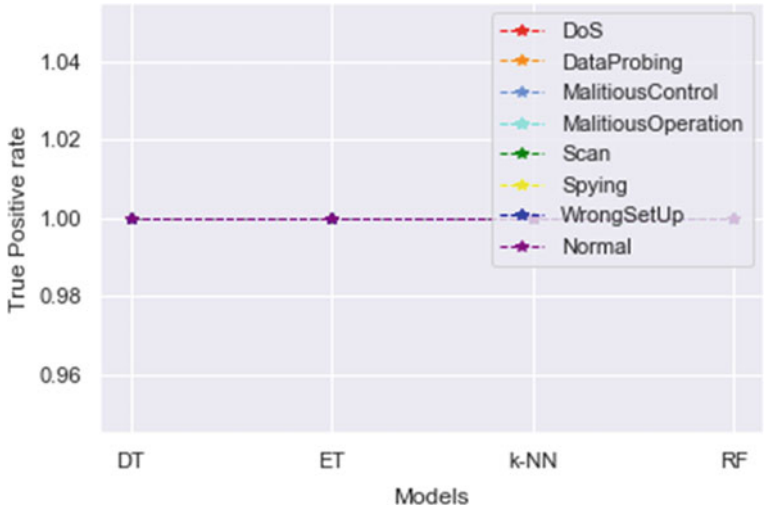

Fig. 10 TPR vs. BC (estimators)

in Fig. 12 shows that, all the classes are correctly full-filled except for 'DoS' it shows better (0.95) with random forest estimator, and 'Scan' with k-NN gives 0.98. Figure 13 shows all the target classes weighted average is 1 and the class 'DoS' is 0.97 and 'Scan' is 0.99 for BC(k-NN). Coming to individual class accuracies as shown in Fig. 14, the 'DoS' and 'Normal' classes give 99% accuracy for all the models, 'Scan'

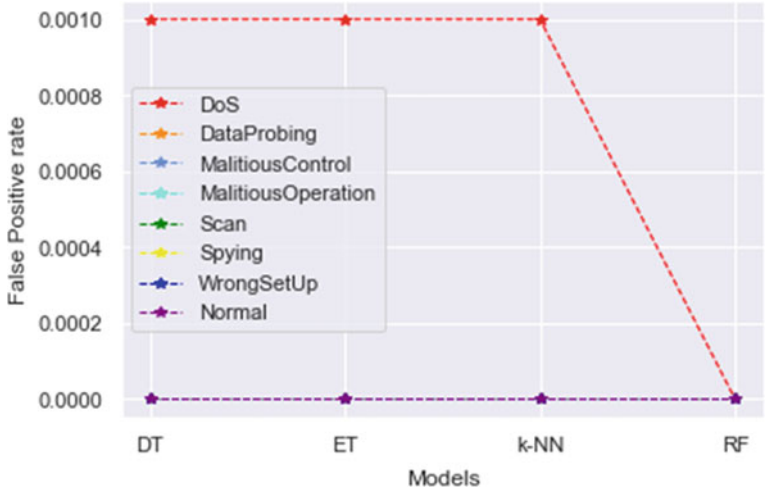

Fig. 11 FPR vs. BC (estimators)

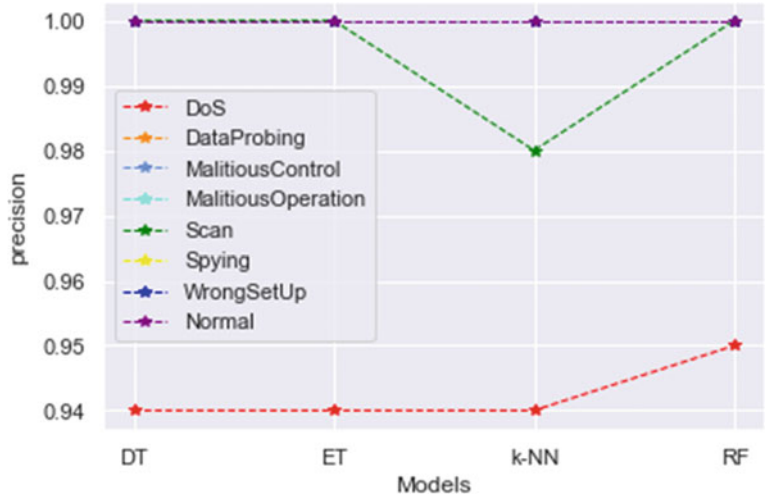

Fig. 12 Precision vs. BC (estimators)

for BC(k-NN) gives 99% and remaining all the classes are determined with 100% accuracy. The proposed model accuracies from Fig. 15, shows BC(RF), BC(DT) shows 99.90% accuracy, BC(ET) shows 99.89% and BC(k-NN) gives 99.88%.

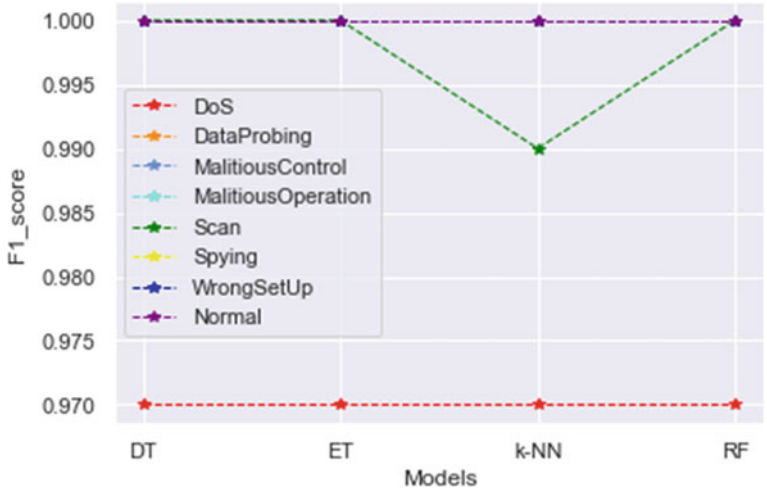

Fig. 13 *F*1-score vs. BC (estimators)

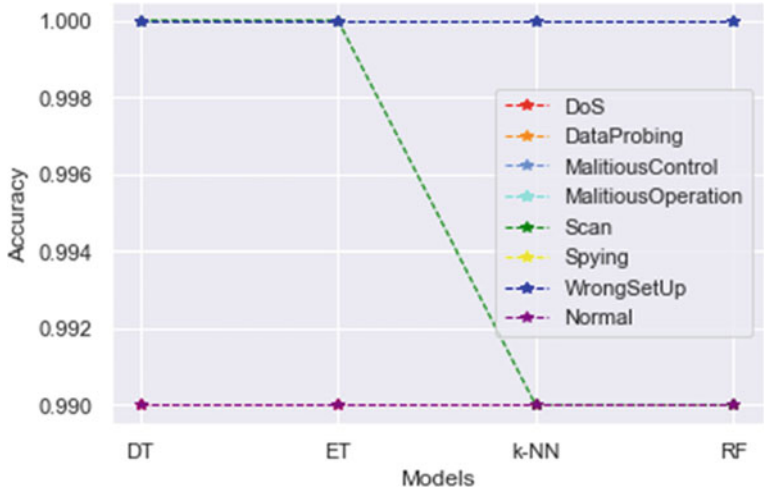

Fig. 14 Accuracy vs. BC (estimators)

6 Conclusion

This paper proposes an anomaly exposure system by analyzing the attack and anomaly classification in the IoT network. The proposed meta algorithm bagging performance is evaluated by using classifiers as base estimators. We conducted different combination search to determine the best learning parameters for four classifiers on novel benchmark datasets, i.e., DS2OS. With the base estimators as DT and

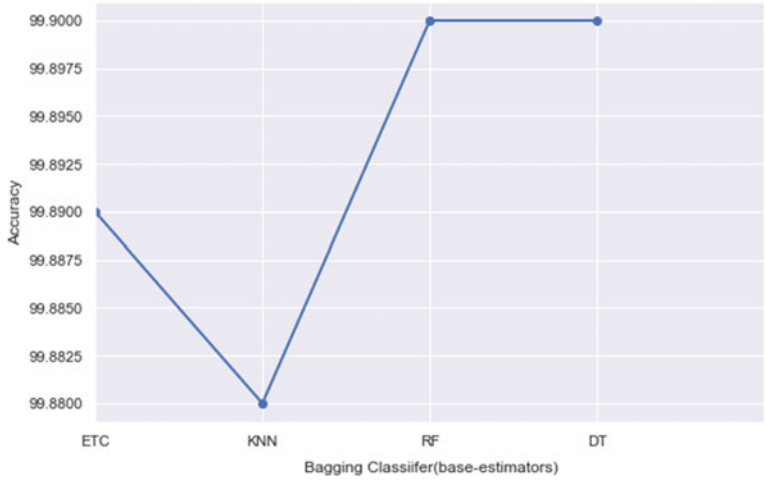

Fig. 15 BC accuracies with base-estimators

RF classifiers, it gave an outstanding performance comparative to ETC and k-NN, in particular to attack and anomaly detection performance in the IoT environment. The overall accuracy of BC with DT and RF is 99.9%, whereas the BC with ETC, k-NN is 99.89 and 99.88%. The BC(RF) predicted all the classes exactly, but 69 'Normal' class instances are classified as 68 'DoS' and one 'Scan' class, BC(DT) for 71 'Normal' class instances are classified as 'DoS' class. As the work is found on virtual environment data, there may have various issues with data in real-time. So, an experimental study on real-time data is required for this problem because IoT micro-services can causes deviation in normal behavior differently at different times in IoT service performance, thus creating an anomaly. To deduce such issues an in-depth analysis of the further study is needed.

References

1. Borgohain T, Kumar U, Sanyal S (2015) Survey of security and privacy issues of internet of things. Cryptogr Secur 10:1–178
2. Jing Q, Vasilakos AV, Wan J, Lu J, Qiu D (2014) Security of the internet of things: perspectives and challenges. Wirel Netw 20(8):2481–2501
3. Tama BA, Rhee K-H (2017) Attack classification analysis of IoT network via deep learning approach. Res Briefs Inf Commun Technol Evol 3(15):1–9
4. Hodo E et al (2016) Threat analysis of IoT networks using artificial neural network intrusion detection system. In: 2016 international symposium on networks, computers and communications (ISNCC), pp 1–6
5. Hasan M, Islam MM, Zarif MII, Hashem MMA (2019) Attack and anomaly detection in IoT sensors in IoT sites using machine learning approaches. Internet Things 7:100059
6. Vangipuram R, Gunupudi RK, Puligadda VK, Vinjamuri J (2020) A machine learning approach for imputation and anomaly detection in IoT environment. Expert Syst e12556

7. Akter M, Das Dip G, Mira MS, Abdul Hamid M, Mridha MF (2020) Construing attacks of internet of things (IoT) and a prehensile intrusion detection system for anomaly detection using deep learning approach, vol 2, pp 427–438
8. Ullah I, Mahmoud QH (2020) A two-level flow-based anomalous activity detection system for IoT networks. Electronics 9(3):530
9. Yin C, Zhang S, Wang J, Xiong NN (2020) Anomaly detection based on convolutional recurrent autoencoder for IoT time series. IEEE Trans Syst Man Cybern Syst 1–11
10. Breiman L (1996) Bagging predictors. Mach Learn 24(2):123–140
11. Pahl M-O, Aubet F-X (2018) DS2OS traffic traces. [Online]. Available: https://www.kaggle.com/francoisxa/ds2ostraffictraces

Deep Learning for COVID-19 Prognosis: A Systematic Review

H. Swapna Rekha, Himansu Sekhar Behera, Janmenjoy Nayak, and Bighnaraj Naik

Abstract In the twenty-first century, the novel coronavirus (COVID-19) with its origin in the city of Wuhan has been spreading expeditiously and infecting more than 4.9 million population of the world as of May 19, 2020. As it is inducing serious threat to the global health, it is necessary to develop accurate prediction models and early diagnosis tools of COVID-19 to empower healthcare specialist and government authorities to control the spread of the pandemic. The latest advances in the intelligent computing particularly deep learning approaches are providing a wide range of efficient methods, paradigms and tools in the interpretation and prophecy of COVID-19. In this paper, a perspective research on the ongoing deep learning approaches has been carried out. In this study, an analysis of the different approaches of deep learning techniques in the forecasting, classification and detection of COVID-19 has been performed. The main motive of this research is to facilitate the researchers and technocrats with some critical research briefing that may further assist in developing more adequate prototypes for the analysis and diagnosis of COVID-19.

Keywords COVID-19 · Deep learning · Coronavirus

H. S. Rekha (✉) · H. S. Behera
Department of Information Technology, Veer Surendra Sai University of Technology (VSSUT), Burla, Sambalpur, Odisha 768018, India
e-mail: swapnarekha23@gmail.com

H. S. Behera
e-mail: hsbehera_india@yahoo.com

J. Nayak
Department of Computer Science and Engineering, Aditya Institute of Technology and Management (AITAM), Tekkali, Andhra Pradesh 532201, India
e-mail: mailforjnayak@gmail.com

B. Naik
Department of Computer Application, Veer Surendra Sai University of Technology, Burla, Sambalpur, Odisha 768018, India
e-mail: mailtobnaik@gmail.com

G. T. C. Sekhar et al. (eds.), *Intelligent Computing in Control and Communication*, Lecture Notes in Electrical Engineering 702,
https://doi.org/10.1007/978-981-15-8439-8_53

1 Introduction

Over the past, several epidemics have been emerging and causing a serious threat to the public health all over the world. The outbreak of small pox has slayed approximately 500 million population all over the world over 3000 years ago [1]. An approximate of 17–100 million populations has been assassinated due to the surge of Spanish influenza in the year 1918 [2]. In the twenty-first century, human coronaviruses such as SARS and MERS coronavirus that have developed from the repositories of animals have induced world-wide epidemic with high fatality rate as per the World Health Organization (WHO). In December 2019, another outbreak was recognized when the local hospitals in the city of Wuhan in South China were reported with unidentified pneumonia-infected cases [3]. Most of the infected patients were associated to the Wuhan merchandise which is renowned for selling collection of distinct animals and seafoods such as poultry, bats, snakes [4]. The reason behind the unidentified cases was not identified in its early period as its symptoms are similar to the common pneumonia. But, on January 7, 2020, after making an analysis of the throat swab, the virus was declared as novel coronavirus pneumonia (NCP) by center for disease control (CDC) authorities [5]. Later, it was renamed as Severe Acute Respiratory Syndrome Coronavirus 2 (SARS-CoV-2) by the International Committee on Taxonomy of Viruses [6, 7]. On February 11, 2020, the disease was named as novel COVID-19 by the WHO [8]. On January 30, 2020, the outbreak was declared as Public Health Emergency of International Concern (PHEIC) by the WHO when the coronavirus infection disseminated to 18 countries of the world through person-to-person transmission. On March 11, 2020, the WHO declared the outbreak as pandemic when the number of cases other than china has raised 13 times imposing a serious threat to public health globally. Since March, the virus is spreading rapidly resulting in total of 4,951,752 confirmed cases and 322,948 deaths all over the world as on May 19, 2020. Figure 1 depicts the number of confirmed cases in top 15 countries of the world as on May 19, 2020.

The standard approach utilized for the detection of novel coronavirus is Reverse Transcription Polymerase Chain Reaction (RT-PCR). The limitations of RT-PCR are low sensitivity, more time and limited number of available kits. To conquer the limitations of RT-PCR, rapid screening can be performed through the interpretation of medical images such as X-ray and computer tomography. Therefore, the spread of the pandemic can be controlled by developing appropriate forecasting and prediction models. From the past decade, as computer intelligence techniques are vastly used in preventing the spread of diseases, the present global emergency is also exploring the support of intelligent computing approaches in developing more accurate forecasting and prediction models to control the dynamics of COVID-19. The assessment of human loss and the prophecy of mortality for a particular period of time or up to the finish of the pandemic can be performed using mathematical models and statistical models. As mathematical model does not include all aspects of the pandemic, these models cannot generate more accurate predictions. Due to the advancement of intelligent computing approaches in healthcare, these approaches have been widely

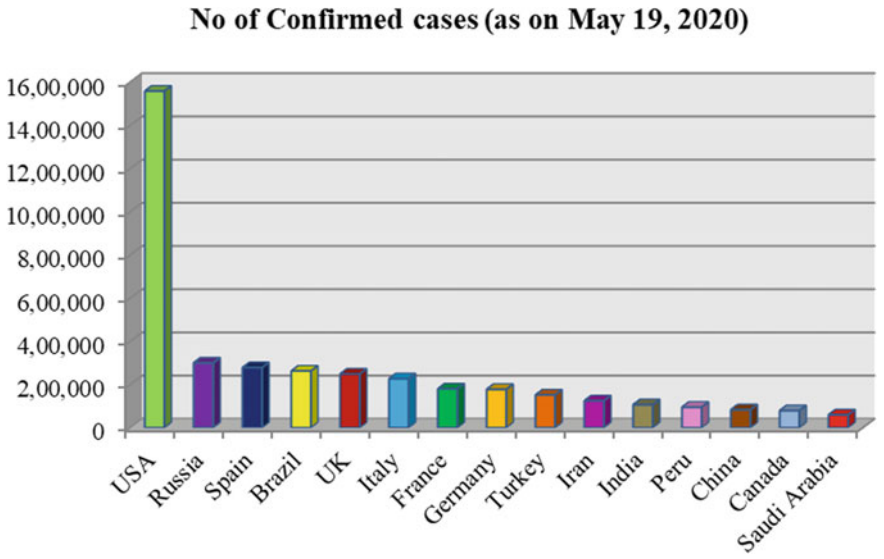

Fig. 1 Number of confirmed cases in top 15 countries as on May 19, 2020

used by the researchers and modeling developers to develop appropriate models and tools that help the physicians in diagnosing the COVID-19 infection and the government for taking appropriate actions to avoid the spread of the COVID-19 pandemic. Therefore, the present nCOVID-19 pandemic can be efficiently tackled by using distinct techniques of machine learning. Batista et al. [9] have suggested the usage of different approaches of machine learning in the prognosis of novel coronavirus. Further, the performance of various approaches of machine leaning has been evaluated by training these models using 70% of sample data and 30% of new data. From the results, it is identified that support vector machine achieves better performance with 0.68 sensitivity, 0.85 specificity, 0.85 AUC and 0.16 Brier score over random forests, logistic regression and gradient boosting trees techniques. There still exist some constraints with machine learning approaches such as exhaustive usage of medical data, inconsistency, dependency on temporal data, paucity, discrepancy and owing to high dimensionality for not generating the accurate forecastings and predictions [10–12].

Nowadays, deep learning approaches (DL) have exhibited excellence over the machine learning methods in the medical image analysis due to the availability of sufficient number of annotated images [13]. In addition, deep learning approaches have proven to be the best precise models for analyzing the medical datasets such as finding the abnormalities of brain, categorization of biomedical images, identification of tumors because of its deep architectural design [14–17]. The features of deep learning approaches such as superior performance, capability of handling composite and multimodal data, end-to-end learning along with feature learning, etc. has made the deep learning approaches to provide advanced facilities in the domain

of biomedical informatics. Because of its powerful feature learning capacity, deep learning approaches can automatically mine clinical features from CT images which are somewhat troublesome for the humans to sense. Several studies reveal the importance of deep learning paradigms in the effective segmentation and identification of pneumonia from other infections on radiography. In recent years, prototypes of deep learning have been employed in the segmentation and recognition of pneumonia from radiography images [18]. The model performs pixel-wise segmentation by utilizing both global and local characteristics. The durability of the system has been obtained with the alteration of training process and post-processing step. Moreover, results also indicate that the proposed model achieves better performance in the detection of pneumonitis from radiography images. Benefiting from the features such as excellent accomplishment, capability of feature derivation without human interference, lack of engineering benefit in training phase, the prototypes of deep learning approaches have also been extensively utilized in the forecasting and prediction of present COVID-19 outbreak.

The main intention of this article is to emphasize the importance of distinct deep learning approaches in the recognition, categorization and forecasting of novel COVID-19. Initially, a study on the applicability of different deep learning methods along with its applications in the categorization, forecasting and identification of COVID-19 has been represented. Further, an investigation on number of publications published using various approaches in the estimation, identification and categorization of COVID-19 depending on input data and contribution of articles on the current outbreak has been presented. Lastly, some of the issues in the ongoing research are highlighted at the end of the paper to provide further scope of research for the researchers. The rest of the paper is organized as specified. Section 1 describes about the cause of SARS-CoV-2 and its effect on public health and the advantages of deep learning approaches in the analysis of COVID-19. The applicability of different techniques of deep learning in the recognition, categorization and forecasting of nCOVID-19 is described in Sects. 2 and 3. Section 4 describes the analytical investigation of different types of DL methods used in the forecasting and detection of coronavirus depending on data type and growth of publications. Section 5 describes the challenges that need to be addressed for the advancement of precise models. Finally, conclusion along with further scope of research is represented in Sect. 6.

2 Application of Deep Learning Techniques in the Prophecy of nCOVID-19

Deep learning is a branch of machine learning (ML) that tries to learn top-level abstractions in data by exploiting hierarchical frameworks. Deep learning can be used to solve complicated artificial intelligent problems because of its multiple processing layers. The main aspect of the deep learning technique is that the layers of deep learning are not created by human techies instead they are created from data

by applying a learning procedure. Relevant clinical success has been achieved in the healthcare because of its advantages such as higher accomplishment, combined feature learning along with end-to-end learning scheme, ability to control composite intelligence problems. Due to the significant use of DL techniques in the analysis of medical images, presently, these approaches have also been applied in the recognition and screening of coronavirus pandemic. Several researchers and modeling developers have applied autoencoders, convolutional neural network (CNN), generative adversarial networks (GAN) and long short-term memory (LSTM), in the visualization, forecasting and analysis of the coronavirus pandemic.

2.1 Convolutional Neural Network (CNN)

Convolutional neural network is a deep learning approach that has been successfully enforced in the study of medical images. Basically, CNN consists of input, convolutional, pooling, fully connected and output layers. The basic advantage of CNN is its capability to extract features automatically from the images of specific domain without human interference. To optimize the medical resources and to perform early detection of COVID-19, a fully automated DL scheme has been recommended by Wang et al. [19]. The proposed system makes use of DenseNet129-FPN for performing the lung segmentation and COVID-19Net for performing the prognostic and symptomatic analysis of COVID-19. Initially, the proposed model was pre-trained with CT images and gene information of 4106 patients. Then the model was evaluated using CT images of 1266 patients of which 924 belong to COVID-19, 471 CT images have follow-up for more than five days and 342 of other pneumonia cases. From the findings, it has been observed that the proposed method attains better accomplishment with AUC of 0.87 and 0.88 for COVID-19 and AUC of 0.86 for other viral pneumonia. Moreover, the proposed deep learning scheme is also useful in classifying the infected patients into groups of high-risk and low-risk patients. To accurately identify the COVID-19 infection without annotating, a weakly supervised deep learning system that makes use of 3D CT volumes has been developed by Zheng et al. [20]. In the proposed system, pre-trained UNet was used to classify the lung region and the possibility of COVID-19 infection was identified using 3D deep neural network. Initially, the proposed system has been evaluated using 499 CT images and then validated using 131 CT images. The results show that the proposed system achieves an ROC AUC of 0.959 and PR AUC of 0.976 with 0.907 and 0.959 sensitivity and specificity in the ROC curve. Moreover, the algorithm has also achieved 0.901 accuracy, 0.840 positive predictive value and a very high 0.982 negative predictive value. To perform an efficient analysis of COVID-19 infection, pre-trained deep learning systems have been suggested by Razzak et al. [21]. The vigorous features of the images can be extracted automatically using these pre-trained models. Further, the effectiveness of the different CNN frameworks has been assessed using evaluative measures such as true positive, true negative, false positive, false negative and accuracy. In addition, using the pre-trained models, the

Table 1 Applicability of convolutional neural network in the diagnosis of nCOVID-19

Approach	Input data	Outcome	References
Tailored CNN models	145 COVID-19-infected chest X-ray images	DenseNet169 average classification accuracy = 95.72%	[22]
Custom CNN and pre-trained CNN models	Pediatric CXR, RSNACXR, Twitter COVID-19 CXR, Montreal COVID-19 CXR dataset	Accuracy = 99.01% AUC = 0.9972	[23]
Deep convolutional neural network ResNet50	135 COVID-19 X-ray and 320 other pneumonia X-ray images	Accuracy = 94.4% AUC = 0.99	[24]
Multiple 3D CNN models	618 CT samples	Overall accuracy = 86.7%	[25]
Mobile net using CNN framework	3905 diseases	Accuracy = 99.18% Sensitivity = 97.36% Specificity = 99.42%	[26]
CNN based COVIDX-Net model	50 images of chest X-ray with 25 X-ray images of confirmed COVID-19 cases	VGG19 f1-score = 0.89 DenseNet f1-score = 0.91	[27]
ResNet50, InceptionV3 and Inception-ResNetV2 pre-models	50 cases of COVID-19 and 50 images of normal chest X-ray	ResNet50 classification of accuracy = 95%	[28]

system has obtained an overall accuracy of 98.75% in distinguishing novel coronavirus from other bacterial pneumonia and 98.51% accuracy to identify coronavirus from other viral pneumonia. The appropriateness of convolutional neural networks in the diagnosis of nCOVID-19 infection has been represented in Table 1.

2.2 Long Short-Term Memory Network (LSTM)

LSTM network is a special kind of the recurrent neural network (RNN) that consists of a cell, an input and output gate and forget gate. As LSTM can be successfully utilized in training heavy architectures, they have been employed in deep learning approaches. Because LSTM can retain knowledge of earlier states, these are the best models for training the networks that requires memory. In time series analysis, LSTM is one of the excellent models used for performing more accurate forecasting of the outcome [29]. To predict the future trend of coronavirus cases in Iran, different models have been analyzed by the Kafieh et al. [30]. Initially, the models were trained with SARS data and then they were re-trained using COVID-19. The performance of the models has been evaluated using MAPE metrics. From these results, it can

be concluded that M-LSTM has achieved better performance with 0.81% MAPE value when compared with other models in predicting the future trend of coronavirus cases. To determine best therapeutic options, LSTM model was suggested by Patankar [31]. Initially, the model was pre-trained using IC50 binding data from PDB database and 310,000 drug-like compounds from the ZINC. Further, the generative semi-supervised variational autoencoder (SSVAE) has been trained with 310,000 molecules along with their identified IC50s values. Moreover, it has been observed that new molecules generated by the proposed model produce the lower binding energies when compared to the binding energies of the prior drugs. To identify meaningful topics and sentiment classification of comments on COVID-19 from healthcare symposium, a novel NLP based on LSTM model has been recommended by Jelodar et al. [32]. Further, the findings illustrate that the model proposed may assist in enhancing the practical scenarios of healthcare services related to COVID-19. Other analysis on the prediction of COVID-19 using LSTM approach has been represented in Table 2.

Table 2 Diagnosis of novel COVID-19 using LSTM

Approach	Input data	Results	References
LSTM and curve fitting model	Time series data from COVID-19 in data source	To forecast the number of cases in India for one month and the effect of prevention measures	[33]
Modified SEIR and LSTM model	Daily COVID-19 cases reported by National Health Commission of China	Prediction of the COVID-19 epidemic peaks and sizes	[34]
LSTM	Time series data from Worldometer	LSTM model generated an RMSE value of 27.187	[35]
Variational LSTM-autoencoder	Data of COVID-19 cases published by John Hopkins University	Short-term and long-term forecast of the coronavirus around the world	[36]
ConvLSTM	Time series data of new cases in different regions along with some spatiotemporal features	Achieved 5.57 and 0.3% mean absolute percentage error for total no of predicted cases for five days in USA and Italy	[37]
RNN with LSTM	Datasets of World Health Organization and Johns Hopkins University	Generated low root mean squared logarithmic error between predicted and validated data and trends	[38]
LSTM-GRU-RNN	Time series data from Kaggle	Generated an accuracy of 87, 67.8, 62 and 40.5% for confirmed, negative, deceased and released cases	[39]

2.3 Generative Adversarial Network (GAN)

Generative adversarial network is a kind of deep learning technique that consists of two network modules, namely generator and discriminative network. The fake data that is similar to training data has been generated using generator, while the discriminative network is responsible for differentiating between the real and fake data that has been obtained using generator network. The mostly widely used applications of GAN are image, video and voice generation. To detect the inflames in the X-ray images of the COVID-19-infected patients, a model established on GAN and fine-tuned transfer learning technique was proposed by Khalifa et al. [40]. The efficiency and robustness of the proposed model has been proved by generating 90% of the images from the dataset by training only 10% of dataset. For identifying the pneumonia in the X-ray images, deep transfer learning models such as AlexNet, GoogLeNet, Squeeznet and Resnet18 have been used because of less number of layers in their architecture that further results in reducing the complexity of the models. Moreover, results conclude that Resnet18 using GAN as augmenter achieves 99% testing accuracy with performance metrics such as recall, F1 score and precision.

2.4 Autoencoders

Autoencoder is a kind of neural network in which the input is similar to output. It utilizes unsupervised algorithm for the minimization of dimensionality in the input data and then for regenerating the output from the original data. Data denoising and dimensionality reduction for data visualization are the most widely used application areas of Autoencoders. To model the transmission progress of the COVID-19, a RIN architecture based on RNN autoencoder was proposed by Ge et al. [41]. The proposed model has been validated using data from January 22, 2020 to April 18, 2020 to estimate the number of cases around the world. The results indicate that the proposed model estimates a total of new cases and cumulative cases, and the maximum number of cumulative cases across the world as 103,872, 2,104,800 and 2,271,648, respectively, with one-week later invention. The analysis of COVID-19 using GAN and autoencoder has been depicted in Table 3.

3 Analysis of Deep Learning Techniques in Prediction and Diagnosis of COVID-19

In the analysis of COVID-19 pandemic, different approaches of deep learning have been used in the process of forecasting the future dynamics of COVID-19, categorization of COVID-19 radiography images from the radiography images of pneumonia and in the prediction of COVID-19 epidemic. These analyses done using deep

Table 3 Utilization of GANs and autoencoder in the prediction of COVID-19

Approach	Input data	Results	References
GAN and CNN	2143 chest CT images	Achieves +2.82% Pearson coefficient to enhance the quantification of COVID-19	[42]
GAN and deep transfer language	306 X-ray images	Achieved 100% testing accuracy for two classes using three deep transfer learning models and validation accuracy of 99.9% using GoogLeNet	[43]
Topological autoencoder	Center for Systems Science and Engineering (CSSE) time series data of nCOVID-19	Used in the data visualization of global trends of coronavirus transmission	[44]
Variational autoencoder with QED and SA	Moses benchmarking dataset	Generates _ 3000 novel COVID-19 drug candidates	[45]
Modified autoencoder	Time series data of COVID-19 from WHO	Estimates a total of cumulative, new and maximum number of cumulative cases could reach 75,249,909, 10,086,085 and 255,392,154, respectively, with later intervention and January 10, 2021 as case ending time	[46]
Generative deep learning approach	Protease dataset from Dr. Rao's laboratory	Developed cost and time efficient models to provide different treatment against COVID-19	[47]

learning techniques help the government authorities in implementing proper actions and the clinical experts in performing early diagnosis to inhibit the spread of the COVID-19 outbreak.

3.1 Forecasting

The loom of infectious diseases poses a serious threat to human population across the world. Advances in disease vigilance system and information technology have produced the early warning systems that are not only appropriate but also repel the spread of epidemics. Epidemic avoidance and control competence can be achieved through the development of accurate forecasting models. The process of making

Table 4 Usage of DL techniques in forecasting of coronavirus infection

Author	Approach	Input data	Outcome	Month and year	References
Chimmula et al.	LSTM	Time series data from Johns Hopkins University and Canadian Health Authority	Predicted that the probable closing point of the COVID will be approximately by June 2020 in Canada	May 2020	[48]
Yudistira	LSTM	Time series data	LSTM outperformed RNN by 281.95	May 2020	[49]
Caicedo-Torres	IseeU2 deep learning model	MIMIC-III dataset	Predicts mortality of coronavirus with ROC of 0.8629	May 2020	[50]
Azarafza et al.	LSTM	Time series data from Iran Ministry of Health and Medical Education, IRNA and ISNA	Predicted total number of cases as of May 13, 2020, was 112,725 I IRAN	January 2020	[51]
Huang et al.	CNN	Time series data from Surging News Network and WHO	RMSE of CNN for six and one-input factors are 109.439, 325.857	January 2020	[52]

predictions of the future based on the historical data is known as forecasting. The existing traditional models mainly consist of linear and nonlinear models are well suited for short-term forecasting. The application of traditional models for long-term predictions may result in gradient problem. As the LSTM of deep learning approach allows to store and access information over long periods, it reduces the gradient problem. Hence, accurate long-term predictions can be achieved using approaches of deep learning. The succeeding Table 4 represents the applicability of deep learning techniques in the estimation of COVID-19 pandemic.

3.2 Classification of COVID-19 Images

Due to the limited availability and low sensitivity of RT-PCR, radiological imaging such as X-ray and CT images is utilized in the early interpretation of nCOVID-19 disease. As deep learning enables the development of end-to-end models without

Table 5 Classification of COVID-19-infected medical images by applying DL paradigms

Author	Procedure	Input data	Outcome	Month and year	References
Angelov et al.	Deep transfer learning CNN model	852 CT images	Achieves training accuracy = 96.2264% and testing accuracy = 93.0189% respectively	May 2020	[56]
Ozkaya et al.	CNN framework utilizing deep features fusion and ranking technique	150 CT images	Accuracy = 98.27%, sensitivity = 98.93%, specificity = 97.60%, precision = 97.63% F1-score = 98.28%, MCC = 96.54%	April 2020	[57]
Abbas et al.	DeTrac CNN	196 sample X-ray images	Achieves accuracy of 95.12% in classification of X-ray images from other	March 2020	[58]
Asnaoui et al.	Deep CNN architectures	5856 X-ray images	Fine-tuned version of Resnet50, MobileNet_V2 and Inception_Resnet_V2 shows accuracy > 96%	March 2020	[59]
Amyar et al.	Multitask learning model	1044 CT images	Achieves dice coefficient > 0.78 for segmentation and ROC > 93% for the classification	January 2020	[60]

the need of human for extracting features, they have widely utilized in the screening of medical images over the machine learning approaches. Since deep learning has been profitably used in the classification of many problems such as skin cancer classification [53], breast cancer classification [54], lung segmentation [55], the present COVID-19 epidemics is also requiring the expertise of deep learning approaches in preventing the disease. The utilization of deep learning approaches in the categorization of COVID-19 images is shown in Table 5.

3.3 Diagnosis of COVID-19

As the techniques of deep learning approaches can learn from raw data during training, they can be utilized to resolve problems that are difficult to solve using traditional approaches. Compared to standard approaches, deep learning approaches have multiple hidden layers that make them well suited to learn from heterogeneous information. Several studies of deep learning revealed the capabilities of deep learning such as image recognition [61], learning from complex data [62] and so

Table 6 Diagnosis of coronavirus-infected medical images using procedures of deep learning

Author	Approach	Input data	Outcome	Month and year	References
Javaheri et al.	CovidCTNet	287 CT images	Accuracy = 90%	May 2020	[64]
Ozturk et al.	DarkCovidNet model	125 COVID-19 positive images and 500 no-findings X-ray images	Accuracy = 98.08	April 2020	[65]
Apostolopoulos et al.	VGG-19	224 positive COVID-19 and 700 pneumonia 504 no-findings X-ray images	Accuracy = 93.48	April 2020	[66]
Sethy et al.	ResNet50 and SVM	25 COVID positive and 25 COVID negative images X-ray images	Accuracy = 95.38	March 2020	[67]
He et al.	Self-trans networks	349 COVID-19 positive CT scans and 397 negative CT scans	F1 score = 0.85 ROC = 0.94	January 2020	[68]

on. Diagnosis of medical images is one the main application of deep learning [63]. Hence, deep learning is used in the diagnosis of current coronavirus pandemic. During the screening of COVID-19, appropriate deep learning approach should assist the radiologist in accurate detection of COVID-19 and to provide user-friendly tools that should assist medical community in the automatic detection of pandemic without the knowledge of computer. The applicability of procedures of DL in the identification of COVID-19 has been depicted in Table 6.

4 Critical Investigation

Based on deep learning technologies, a precise study of papers relevant to COVID-19 has been accomplished. The capability of distinguishing between bacteria and other viral pneumonia, extracting features from multimodal clinical dataset, early

prediction and visualization of epidemic patterns, etc. made the prototypes of deep learning appropriate for the analysis of the datasets related to medical field. From the studies, it can be noted that the distinct DL techniques have been profitably applied in the identification and detection of COVID-19. In this section, an analysis on the contribution of articles using various schemes of the deep learning in classification, forecasting and prediction of the novel SARS-CoV2, distribution of total number of articles in present pandemic depending on the type of input data and the analysis of the articles published week wise on COVID-19 has been represented. This investigation may assist the researches in developing more appropriate techniques for the control of the COVID-19 pandemic

4.1 Distribution of Articles Using Deep Learning Approaches Over Other Intelligent Computing Approaches

Figure 2 reveals that predominant work on the prediction and detection of COVID-19 has been supervised using the techniques of deep learning (42%). Next, 32% of research has been explored by applying the various techniques of machine learning. Only 24% of the activity has been experimented using the prototypes of the mathematical and statistical methods in the forecasting and identification of novel corona virus. From Fig. 2, it is determined that majority of the work in the prediction of present

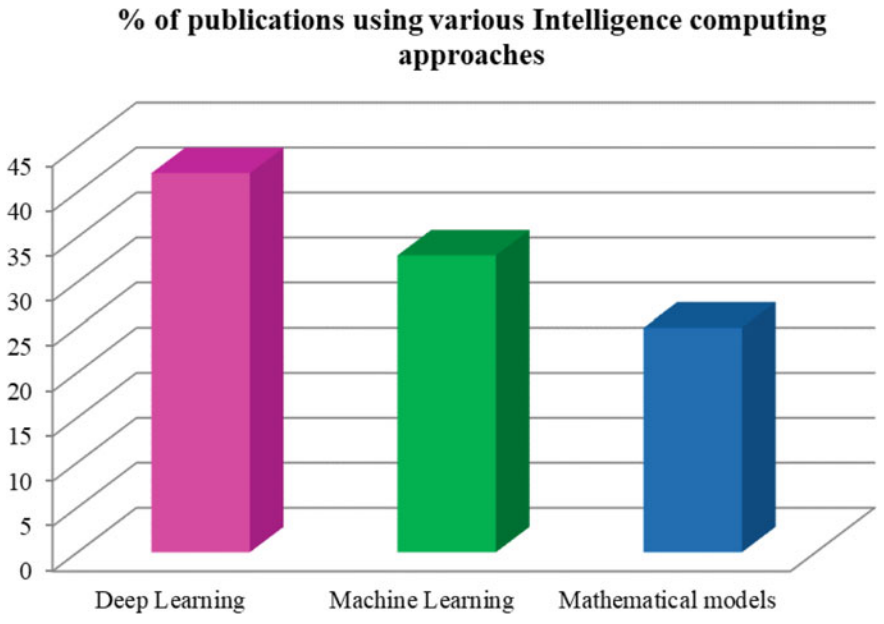

Fig. 2 Distribution of articles on COVID-19 using different approaches

pandemic has been accomplished using techniques of DL over other techniques because of the advantages such as performance excellence, handling of complex intelligent tasks, extraction of rich features without human interference.

4.2 *Distribution of Articles Using Different Deep Learning Approaches*

From Fig. 3, it is concluded that 60% of the work in the identification and prediction of SARS-CoV-2 has been implemented using convolutional neural network. Only 17% of the work has been executed using LSTM. Next, 13% of the work has been carried using GANs. Lastly, 10% of the work has been performed using autoencoders. As CNNs are capable of extracting features automatically from the images without human interference, these are more appropriate models used in the prediction of the COVID-19. Because of the disadvantages such as LSTM model results in overfitting due to the availability of limited data, GANs require lot of trial and error strategy to train the network, and autoencoders are not efficient in reconstructing the images as

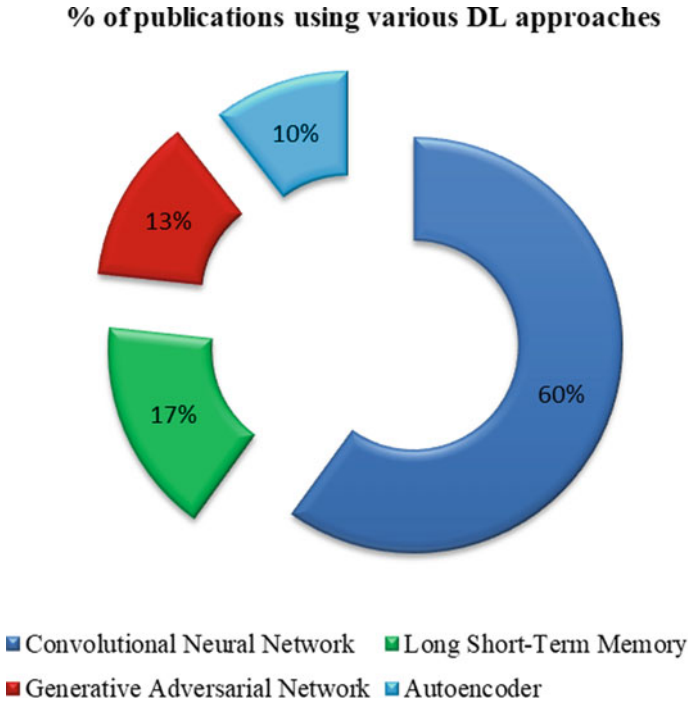

Fig. 3 Articles distribution using different approaches of deep learning

the complexity of image enhances, less work has been carried on LSTM, GANs and autoencoders in the prophecy of nCOVID-19.

4.3 Contribution of Articles on the Prognosis and Interpretation of COVID-19 Using the Techniques of Deep Learning

The analysis of articles in the classification, forecasting, diagnosis and in the development of drugs for COVID-19 using the techniques of deep learning has been depicted in Fig. 4. From Fig. 4, it can be observed that extensive work has been performed in the prophecy of current outbreak using the methods of DL (35%). After diagnosing, 32% of the work has been carried out in the classification of coronavirus-infected images from the bacterial and viral pneumonia-infected images. Next, 17% of the work has been carried out in forecasting the dynamics of COVID-19. Only 16% of work has been published in the drug discovery. As deep learning approaches are widely used in the analysis of medical images and due to the availability of less number of kits for early diagnosis, most of the work has been carried on the identification of COVID-19-infected patients and segmentation of COVID-19 medical images from other pneumonia.

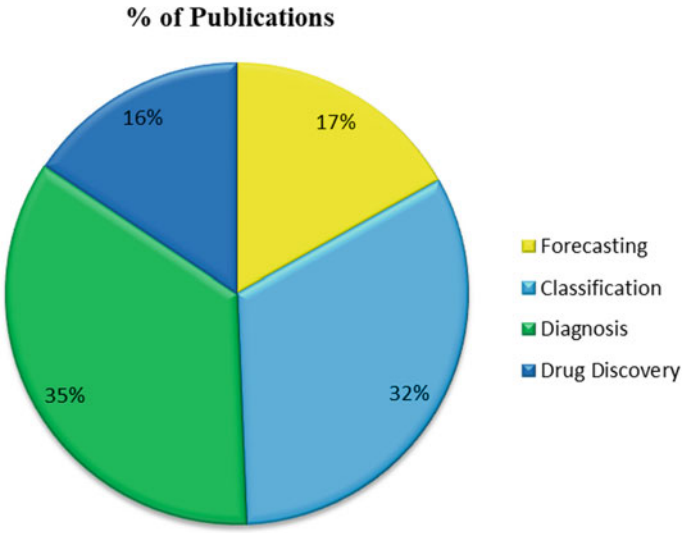

Fig. 4 Articles distribution in the prognosis and diagnosis of COVID-19

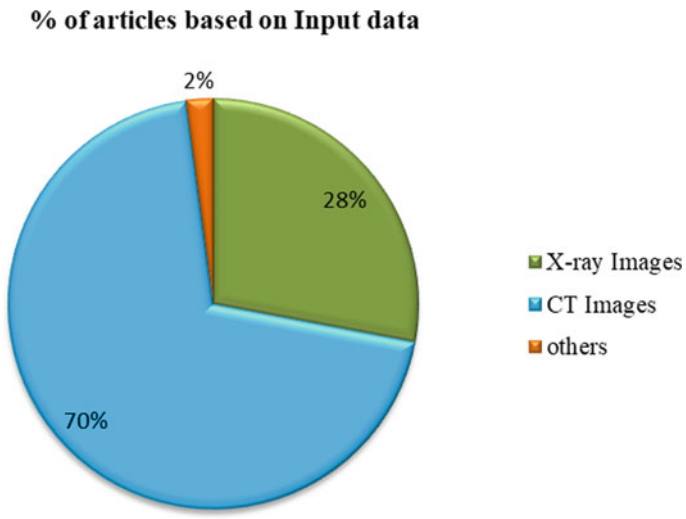

Fig. 5 Analysis of input data using deep learning

4.4 Analysis of Input Data Using Deep Learning

The methods used in DL are representation-learning algorithms that have been widely implemented in the interpretation of radiography images such as detection of abnormalities, classification of radiography images due to its multilayer processing. The analysis of input image using deep learning has been represented in Fig. 5. From Fig. 5 also, it has been concluded that most of the work is done on the analysis of medical dataset when compared to others. It is also identified that 70% of the work has been carried out using CT images and 28% of work has been accomplished using X-ray images. Only 2% of work has been contributed using other dataset as input data. Though chest X-ray images are cheaper than CT images, X-ray images result in false diagnosis. Hence, majority of the work has been carried out using chest CT images.

4.5 Growth in Publication of COVID-19 Articles

The novel coronavirus originated in December 2019 caused thrice the deaths over the combined deaths caused by SARS-CoV and MERS-CoV in the twenty-first century. As the disease is rapidly spreading across the world because of the absence of vaccine or drug and limited number of medical kits, most of the research has been performed on COVID-19 over the other pandemics. Figure 6 represents the analysis of articles published from January 13, 2020 to May 18, 2020. In the first few months of COVID-19, only 4% of articles published on COVID-19 as most of the cases were reported

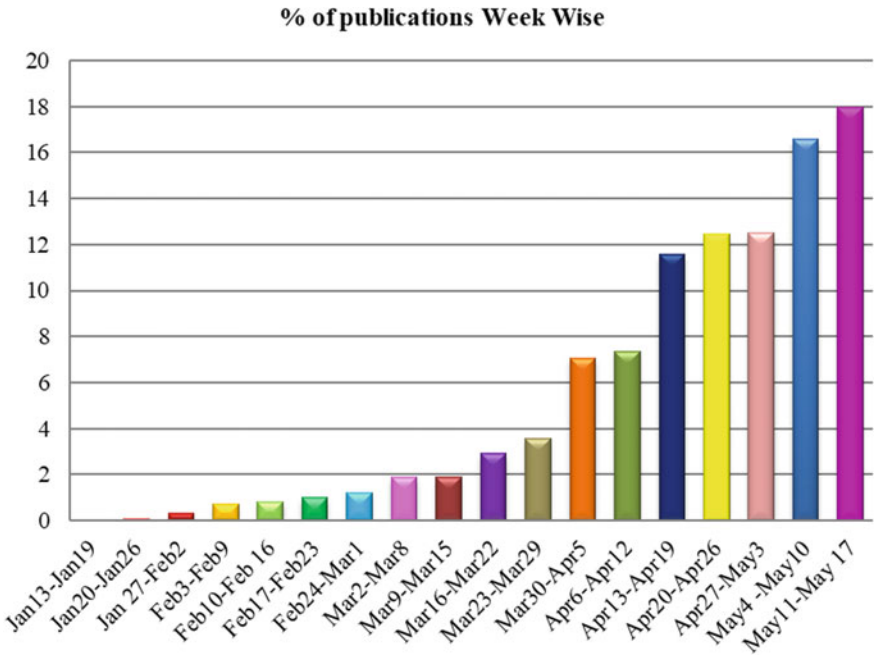

Fig. 6 Growth of publications in COVID-19

in the main land of china. In the month of March 2020, when the COVID cases in other territories are increasing outside the china, the researchers started publishing a greater number of articles on the prediction and analysis of COVID-19 to control the dissemination of disease. 17% of articles were published in March 2020 and 43% of the publications were published in the April 2020. It has been also observed from Fig. 6 that up to May 18, 2020, more number of the articles are published in April 2020.

5 Challenges

From the systematic analysis of this paper, it has been observed that techniques of deep learning have been favorably used in the development of accurate paradigms for the forecasting, classification and estimation of COVID-19 since the start of the outbreak. These prototypes have exhibited a wide scope of discrepancies in the predictions because of the existence of some challenges such as uncertainty of data that needs to be resolved for the expansion of accurate paradigms. As data is segregated in distinct zones of the world, only few datasets for the study of textual and medical images are available. Most of the approaches of deep learning require large datasets to give more accurate results. These regulation of datasets is one of

the key challenges that required to be resolved. Most of the forecasting models use online time datasets that results in poor outcomes. To overcome this problem, it is necessary to develop more real-world datasets. The other issues that need to solved are the less involvement of clinical experts while performing the classification of COVID-19 images which may result in poor outcomes.

6 Conclusion

The recent outbreak of COVID-19 in the last weeks of December 2019 has imposed a health emergency all over the world due to the rapid spread of infection across different regions of the world with an estimate of 4,951,752 confirmed cases and 322,948 deaths all over the world as on May 19, 2020. It is apparent that quarantine alone is not adequate to avoid the transmission of COVID-19. Further research is definitely required such as development of appropriate prediction and forecasting models to strengthen the government and health sectors in regulating the escalation of the epidemic. Therefore, in this paper, an overall study of distinct deep learning techniques in the forecasting and interpretation of COVID-19 has been depicted. Form the critical analysis, it has been noticed that majority of the effort has been accomplished in the categorization and prediction of novel COVID infection using CNN and LSTM network schemes. It is also observed that majority of the analysis has been done using CT or X-images rather than text data. The drawbacks such as availability of small datasets, less annotated medical images, less involvement of radiologist in lesion segmentation, not considering some features like GGO, crazy-paving patterns in diagnosis, not dealing with data irregularities require immediate attention for developing more appropriate prediction model in the prophecy and analysis of COVID-19. Also, the research analyst all over the world is facing the scarcity of real-world datasets that needs to be developed immediately for the advancement of precise models. In addition, the usage of progressive schemes such as ensemble methods, optimization methods, application of higher order and artificial neural networks and utilization of ultrasound images in the screening and prognosis of nCOVID-19 pandemic enhances the accuracy of prediction models which might be considered as further scope of research.

References

1. Henderson DA (2009) Smallpox: the death of a disease, vol 237. Prometheus Books, Amherst
2. Spreeuwenberg P, Kroneman M, Paget J (2018) Reassessing the global mortality burden of the 1918 influenza pandemic. Am J Epidemiol 187(12):2561–2567
3. Wuhan Municipal Health Commission infection data (2020) [Online]. Available: https://wjw.wuhan.gov.cn/front/web/list2nd/no/710
4. Lu H, Stratton CW, Tang Y-W (2020) Outbreak of pneumonia of unknown etiology in Wuhan, China: the mystery and the miracle. J Med Virol

5. Huang C et al (2020) Clinical features of patients infected with 2019 novel coronavirus in Wuhan, China. The Lancet 395(10223):497–506
6. Cui J, Li F, Shi Z-L (2019) Origin and evolution of pathogenic coronaviruses. Nat Rev Microbiol 17(3):181–192
7. Lai C-C et al (2020) Severe acute respiratory syndrome coronavirus 2 (SARS-CoV-2) and corona virus disease-2019 (COVID-19): the epidemic and the challenges. Int J Antimicrob Agents 105924
8. World Health Organization (2020) Laboratory testing for coronavirus disease 2019 (COVID-19) in suspected human cases: interim guidance, 2 Mar 2020. World Health Organization
9. de Moraes Batista AF et al (2020) COVID-19 diagnosis prediction in emergency care patients: a machine learning approach. medRxiv
10. Hripcsak G, Albers DJ (2013) Next-generation phenotyping of electronic health records. J Am Med Inform Assoc 20(1):117–121
11. Jensen PB, Jensen LJ, Brunak S (2012) Mining electronic health records: towards better research applications and clinical care. Nat Rev Genet 13(6):395–405
12. Luo J et al (2016) Big data application in biomedical research and health care: a literature review. Biomed Inform Insights 8:BII-S31559
13. Anthimopoulos M et al (2016) Lung pattern classification for interstitial lung diseases using a deep convolutional neural network. IEEE Trans Med Imaging 35(5):1207–1216
14. Talo M et al (2019) Application of deep transfer learning for automated brain abnormality classification using MR images. Cogn Syst Res 54:176–188
15. Ismael SA, Abdelaziz AM, Hefny H (2020) An enhanced deep learning approach for brain cancer MRI images classification using residual networks. Artif Intell Med 102:101779
16. Khalifa NEM et al (2020) Artificial intelligence technique for gene expression by tumor RNA-seq data: a novel optimized deep learning approach. IEEE Access 8:22874–22883
17. Haque IRI, Neubert J (2020) Deep learning approaches to biomedical image segmentation. Inform Med Unlocked 100297
18. Jaiswal AK et al (2019) Identifying pneumonia in chest X-rays: a deep learning approach. Measurement 145:511–518
19. Wang S et al (2020) A fully automatic deep learning system for COVID-19 diagnostic and prognostic analysis. medRxiv
20. Zheng C et al (2020) Deep learning-based detection for COVID-19 from chest CT using weak label. medRxiv
21. Razzak I et al (2020) Improving coronavirus (COVID-19) diagnosis using deep transfer learning. medRxiv
22. Hammoudi K et al (2020) Deep learning on chest X-ray images to detect and evaluate pneumonia cases at the era of COVID-19. arXiv preprint arXiv:2004.03399
23. Rajaraman S et al (2020) Iteratively pruned deep learning ensembles for COVID-19 detection in chest X-rays. arXiv preprint arXiv:2004.08379
24. Hall LO et al (2020) Finding COVID-19 from chest X-rays using deep learning on a small dataset. arXiv preprint arXiv:2004.02060
25. Xu X et al (2020) Deep learning system to screen coronavirus disease 2019 pneumonia. arXiv preprint arXiv:2002.09334
26. Apostolopoulos I, Aznaouridis S, Tzani M (2020) Extracting possibly representative COVID-19 biomarkers from X-ray images with deep learning approach and image data related to pulmonary diseases. arXiv preprint arXiv:2004.00338
27. Hemdan EE-D, Shouman MA, Karar ME (2020) Covidx-net: a framework of deep learning classifiers to diagnose covid-19 in X-ray images. arXiv preprint arXiv:2003.11055
28. Narin A, Kaya C, Pamuk Z (2020) Automatic detection of coronavirus disease (covid-19) using X-ray images and deep convolutional neural networks. arXiv preprint arXiv:2003.10849
29. Sherstinsky A (2020) Fundamentals of recurrent neural network (RNN) and long short-term memory (LSTM) network. Phys D Nonlinear Phenomena 404:132306 (5)
30. Kafieh R et al (2020) COVID-19 in Iran: a deeper look into the future. medRxiv

31. Patankar S (2020) Deep learning-based computational drug discovery to inhibit the RNA dependent RNA polymerase: application to SARS-CoV and COVID-19
32. Jelodar H et al (2020) Deep sentiment classification and topic discovery on novel coronavirus or COVID-19 online discussions: NLP using LSTM recurrent neural network approach. arXiv preprint arXiv:2004.11695
33. Tomar A, Gupta N (2020) Prediction for the spread of COVID-19 in India and effectiveness of preventive measures. Sci Total Environ 138762
34. Yang Z et al (2020) Modified SEIR and AI prediction of the epidemics trend of COVID-19 in China under public health interventions. J Thoracic Dis 12(3):165
35. Ayyoubzadeh SM et al (2020) Predicting COVID-19 incidence through analysis of Google trends data in Iran: data mining and deep learning pilot study. JMIR Public Health Surveill 6(2):e18828
36. Ibrahim MR et al (2020) Variational-LSTM autoencoder to forecast the spread of coronavirus across the globe. medRxiv
37. Jana S, Bhaumik P (2020) A multivariate spatiotemporal spread model of COVID-19 using ensemble of ConvLSTM networks. medRxiv
38. Kolozsvari LR et al (2020) Predicting the epidemic curve of the coronavirus (SARS-CoV-2) disease (COVID-19) using artificial intelligence. medRxiv
39. Bandyopadhyay SK, Dutta S (2020) Machine learning approach for confirmation of COVID-19 cases: positive, negative, death and release. medRxiv
40. Khalifa NEM et al (2020) Detection of coronavirus (COVID-19) associated pneumonia based on generative adversarial networks and a fine-tuned deep transfer learning model using chest X-ray dataset. arXiv preprint arXiv:2004.01184
41. Ge Q et al (2020) A Noel intervention recurrent autoencoder for real time forecasting and non-pharmaceutical intervention selection to curb the spread of Covid-19 in the world. medRxiv
42. Liu S et al (2020) 3D tomographic pattern synthesis for enhancing the quantification of COVID-19. arXiv preprint arXiv:2005.01903
43. Loey M, Smarandache F, Khalifa NEM (2020) Within the lack of chest COVID-19 X-ray dataset: a novel detection model based on GAN and deep transfer learning. Symmetry 12(4):651
44. Hartono P (2020) Generating similarity map for COVID-19 transmission dynamics with topological autoencoder. arXiv preprint arXiv:2004.01481
45. Chenthamarakshan V et al (2020) Target-specific and selective drug design for covid-19 using deep generative models. arXiv preprint arXiv:2004.01215
46. Hu Z et al (2020) Forecasting and evaluating intervention of Covid-19 in the world. arXiv preprint arXiv:2003.09800
47. Zhavoronkov A et al (2020) Potential COVID-2019 3C-like protease inhibitors designed using generative deep learning approaches. Insilico Medicine Hong Kong Ltd A 307:E1
48. Chimmula VKR, Zhang L (2020) Time series forecasting of COVID-19 transmission in Canada using LSTM networks. Chaos Solitons Fract 109864
49. Yudistira N (2020) COVID-19 growth prediction using multivariate long short term memory. arXiv preprint arXiv:2005.04809
50. Caicedo-Torres W, Gutierrez J (2020) ISeeU: visually interpretable ICU mortality prediction using deep learning and free-text medical notes. arXiv preprint arXiv:2005.09284
51. Azarafza M, Azarafza M, Tanha J (2020) COVID-19 infection forecasting based on deep learning in Iran. medRxiv
52. Huang C-J et al (2020) Multiple-input deep convolutional neural network model for COVID-19 forecasting in China. medRxiv
53. Codella NCF et al (2017) Deep learning ensembles for melanoma recognition in dermoscopy images. IBM J Res Dev 61(4/5):5–1
54. Celik Y et al (2020) Automated invasive ductal carcinoma detection based using deep transfer learning with whole-slide images. Pattern Recogn Lett
55. Gaál G, Maga B, Lukács A (2020) Attention U-net based adversarial architectures for chest X-ray lung segmentation. arXiv preprint arXiv:2003.10304
56. Angelov P, Soares E (2020) Classification via CT-scan

57. Ozkaya U, Ozturk S, Barstugan M (2020) Coronavirus (COVID-19) classification using deep features fusion and ranking technique. arXiv preprint arXiv:2004.03698
58. Abbas A, Abdelsamea MM, Gaber MM (2020) Classification of COVID-19 in chest X-ray images using DeTraC deep convolutional neural network. arXiv preprint arXiv:2003.13815
59. Asnaoui KE, Chawki Y, Idri A (2020) Automated methods for detection and classification pneumonia based on X-ray images using deep learning. arXiv preprint arXiv:2003.14363
60. Amyar A, Modzelewski R, Ruan S (2020) Multi-task deep learning based CT imaging analysis for COVID-19: classification and segmentation. medRxiv
61. Shin H-C et al (2016) Deep convolutional neural networks for computer-aided detection: CNN architectures, dataset characteristics and transfer learning. IEEE Trans Med Imaging 35(5):1285–1298
62. Miotto R et al (2018) Deep learning for healthcare: review, opportunities and challenges. Brief Bioinform 19(6):1236–1246
63. Lee J-G et al (2017) Deep learning in medical imaging: general overview. Korean J Radiol 18(4):570–584
64. Javaheri T et al (2020) CovidCTNet: an open-source deep learning approach to identify covid-19 using CT image. arXiv preprint arXiv:2005.03059
65. Ozturk T et al (2020) Automated detection of COVID-19 cases using deep neural networks with X-ray images. Comput Biol Med 103792
66. Apostolopoulos ID, Mpesiana TA (2020) Covid-19: automatic detection from X-ray images utilizing transfer learning with convolutional neural networks. Phys Eng Sci Med 1
67. Sethy PK, Behera SK (2020) Detection of coronavirus disease (covid-19) based on deep features. Preprints 2020030300:s2020
68. He X et al (2020) Sample-efficient deep learning for COVID-19 diagnosis based on CT scans. medRxiv

Author Index

G. T. C. Sekhar et al. (eds.), *Intelligent Computing in Control and Communication*,
Lecture Notes in Electrical Engineering 702,
https://doi.org/10.1007/978-981-15-8439-8